Complex ordering phenomena in transition metal oxides and oxyhalides

Alexander Christoph Komarek

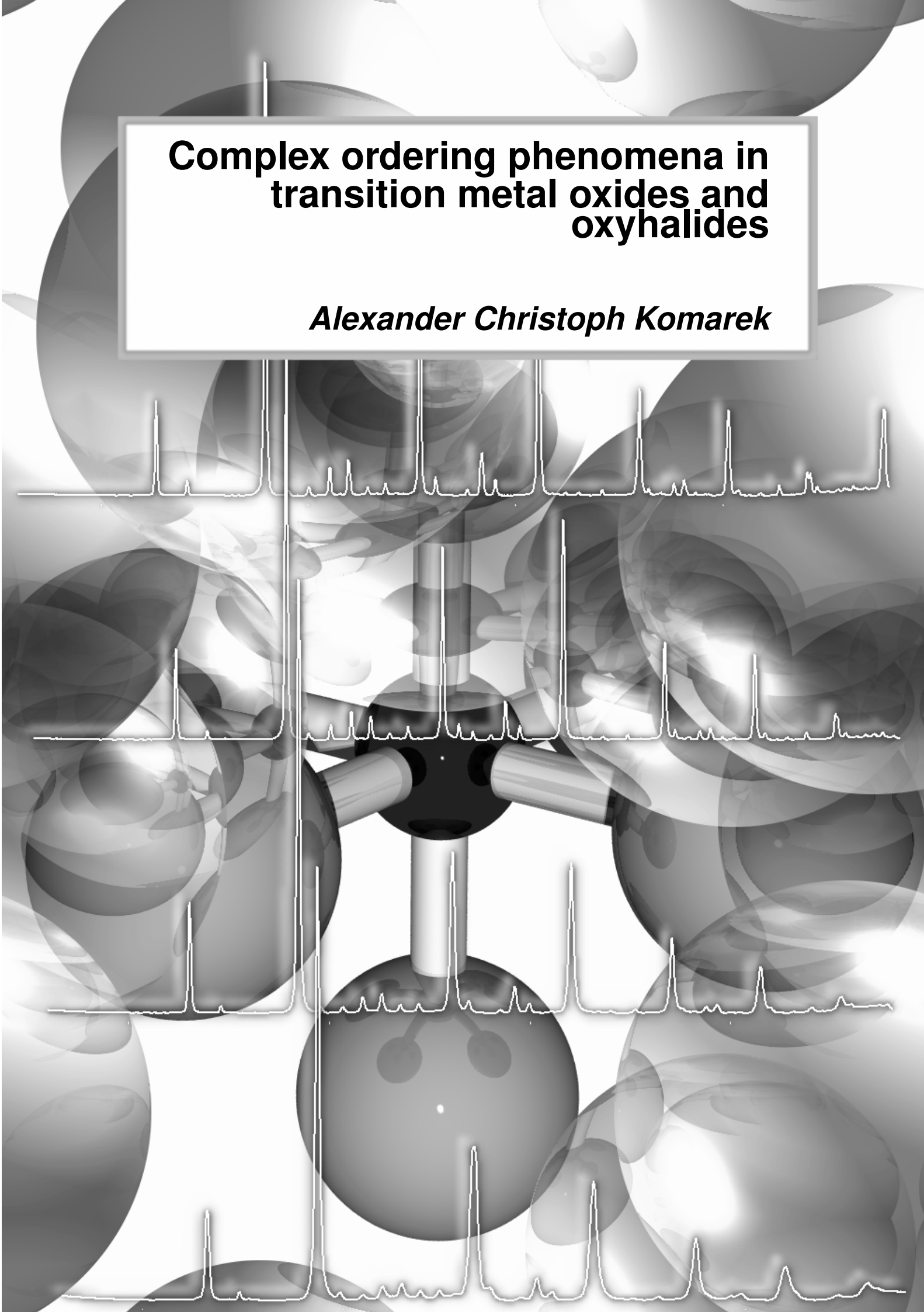

Complex ordering phenomena in transition metal oxides and oxyhalides

Inaugural Dissertation

zur

Erlangung des Doktorgrades

der Mathematisch-Naturwissenschaftlichen Fakultät

der Universität zu Köln

vorgelegt von

Alexander Christoph Komarek

aus Köln

Köln, Februar 2009

Berichterstatter:	.....	Prof. Dr. M. Braden
Berichterstatter:	.....	Prof. Dr. M. Grüninger
Vorsitzender der Prüfungskommission:	.....	Prof. Dr. L. Bohatý
Tag der mündlichen Prüfung:	.....	30.04.2009

Die Neugier steht immer an erster Stelle eines Problems, das gelöst werden will.

Galileo Galilei [1]

Contents

1 Introduction

Transition metal oxides exhibit an enormous richness and wide variety of physical properties [2] which arises from the complex interplay of spin, charge, orbital, and lattice degrees of freedom [3]. High-temperature superconductivity in the cuprates [4] and colossal magneto-resistance in the manganites [5] are some of the most prominent of these properties. In these systems complex ordering phenomena play an important role for the understanding of their outstanding physical properties.

For example charges sometimes order forming stripe or checker-board arrangements, like for example in $La_{1.48}Nd_{0.4}Sr_{0.12}CuO_4$ or in $Pr_{1-x}Ca_xMnO_3$ [6, 7]. Whereas the colossal magneto-resistance is supposed to be triggered by switching between ferromagnetic metallic and antiferromagnetic charge-ordered states [5, 8] the relationship between charge ordering and superconductivity is a more challenging question. Static charge stripe order seems to be harmful for superconductivity [9], but electron-phonon coupling might play an important role in the cuprates [10-13]. However, the direct relevance for the pairing mechanism remains an open question. This sketch of two rather prominent representatives of the class of transition metal oxides underlines the importance of charge ordering for these systems.

In this work, *charge ordering* phenomena and the concomitant appearance of electron phonon coupling have been studied within a broad spectrum of transition metal oxides using a wide variety of measurement tools, among them elastic and inelastic neutron scattering, resonant X-ray scattering, X-ray diffraction and synchrotron experiments as well as transport and thermodynamic measurements. Furthermore, a copious number of single crystals has been synthesized for these purposes.

Besides charge ordering also *orbital ordering* plays an important role for the understanding of physical properties in transition metal oxides including the colossal magneto-resistance in the manganites [14]. In this work orbital ordering has been studied by the analysis of structural distortions implied by orbital ordering or directly by means of electron density measurements at the synchrotron. The latter kinds of measurements are usually used to uncover the electron distribution within organic compounds since these materials consist of light elements only which assures a high contrast of the valence electrons compared to the core-electrons. Concerning these electron density measurements transition-metal oxides are much less studied [15-17].

Furthermore, it is also of fundamental interest to know the spin configurations as well as the spin interactions in transition metal oxides, i. e. *magnetic ordering* and dynamic spin-spin correlations. For example the spin excitation spectrum in the cuprates [18-22] has attracted enormous interest, recently, as one may assume an important role for the superconducting pairing mechanism. The overall dispersion has a so-called 'hour-glass-shape' and exhibits a much enhanced intensity around the merging point at the planar

antiferromagnetic wave vector resembling on the resonance peak in the superconducting state of $YBa_2Cu_3O_7$ [23-25]. This 'hour-glass-shape' is believed to be the unifying feature of all cuprates [20]. However, this topic is highly under debate [19]. A prerequisite of understanding spin excitations is the detailed knowledge of the magnetic structure. For the determination of static as well as for the study of dynamic spin-spin correlations, neutron scattering is an outstanding and very direct experimental probe [26]. Hence, another aim of this work was to study magnetic structures and spin wave excitations by means of elastic and inelastic magnetic neutron scattering. Magnetic ordering, charge ordering and orbital ordering are also often interwoven since charge ordering and orbital ordering may be coupled with the magnetic interactions for example by double-exchange [27] or by superexchange according to the rules of Goodenough, Kanamori and Anderson [28-30].

Regarding the materials studied, the focus of this work was on the one hand on the study of first row transition metal oxides and oxyhalides with low d-level occupation, i. e. the study of $3d^1$ and $3d^2$ systems with one or two t_{2g} electrons where the orbital degree of freedom plays an important role. Hence, three groups of 3d systems have been studied: three-dimensional perovskite *titanate* and *chromate* systems (Ti^{3+} and Cr^{4+}), different low-dimensional as well as fully three-dimensional *vanadate* systems (V^{3+} and V^{4+}) and also *titanium* and *vanadium oxychlorides* (Ti^{3+} and V^{3+}). Since the 3d-shell is only occupied by one or two electrons, these systems are also very well suited for electron density measurements as it should be more easy to separate the contributions of one or two valence electrons than the contributions of a couple of electrons in transition metal oxides with higher d-level occupation.

On the other hand the focus of this work was on the study of the first row $3d^8$ and $3d^9$ transition metal oxides, i. e. *nickelate* and *cuprate* systems with one or two holes in the 3d-shell. In contrast to the t_{2g} electron systems mentioned before, the orbital degree of freedom is almost quenched in these e_g electron systems due to a strong Jahn-Teller effect. In these systems with a layered '214' perovskite structure charge stripes play an important role and have been studied intensively in this work. Whereas the cuprates are metallic (above $\sim$5% of Sr-doping [31]) the nickelates stay insulating in the whole Sr doping regime (up to Sr-doping levels of $\sim$1 [32]). It should be noted, that like the nickelates also the layered perovskite manganites and cobaltates are insulating for moderate doping. Hence, the cuprates are different from these isostructural '214' systems. Nonetheless, the nickelate system is a prototypical charge stripe system which gives rise to the study of the properties of a charge stripe ordered phase and allows for a comparison with the isostructural cuprates.

This thesis is divided into twelve Chapters. In the first two theoretical chapters, Chapters 2 and 3, a brief survey of neutron and X-ray sources and neutron and X-ray scattering is given. In Chapter 4 a general outline of electron density measurements is given in the first, theoretical part followed by a description of the experimental requirements which have been optimized in this work. In Chapter 5 the results of crystal growth using the floating zone technique are described and the most important crystals grown in this work are presented, accompanied by measurements for sample characterization

including X-ray and neutron diffraction measurements.

In Chapter 6 to 11 the most important results of the studies of charge, orbital and magnetic order of different transition metal oxides are presented according to ascending atomic number of the transition metal element. Thus, Chapter 6 deals with Titanates with perovskite structure. In the first part the change of structural anomalies for ferro- and antiferromagnetic $R\mathrm{TiO_3}$ has been studied close to the crossover between ferroorbital and antiferroorbital ordering schemes. In the following parts charge ordering in hole-doped $R_{1-x}\mathrm{Ca}_x\mathrm{TiO}_{3+\delta}$-systems ($R$ = Y, Er, Lu) is presented. Chapter 7 deals with Vanadates - $\mathrm{K_2V_8O_{16}}$, $\mathrm{LiV_2O_5}$ and $\mathrm{ZnV_2O_4}$. In $\mathrm{K_2V_8O_{16}}$ a novel dimerized phase has been observed which resembles on the monoclinic $\mathrm{M_2}$-phase of $\mathrm{VO_2}$. For $\mathrm{LiV_2O_5}$ and $\mathrm{ZnV_2O_4}$ the electron density has been studied by means of synchrotron radiation single crystal X-ray diffraction. In Chapter 8 a study of magnetism and electronic behaviour in the $R\mathrm{CrO_3}$ (R = Ca, Sr, Pb) system is presented. The chromium ion in these compounds has a rather unusual oxidation state of $\mathrm{Cr^{4+}}$ which gives rise to interesting electronic and magnetic properties. Chapter 9 deals with electron-phonon coupling and magnetic excitations in the nickelate system $\mathrm{La}_{2-x}\mathrm{Sr}_x\mathrm{NiO_4}$ which is isostructural to the high-temperature superconducting cuprate system and which exhibits a rather robust diagonal charge stripe order. In Chapter 10 a detailed study of charge stripe ordering in the cuprates $\mathrm{La}_{2-x}\mathrm{Sr}_x\mathrm{CuO_4}$ themselves is presented with special focus to a compound in the spin-glass phase. Signatures of charge stripes have been studied directly with neutron diffraction and hard X-rays at the synchrotron as well as by the study of the coupling of phonons to such stripes. Furthermore, the impact of Ni- and Zn-doping to the phonon dispersion has been studied and compared with the Ni- and Zn-free compound $\mathrm{La_{1.88}Sr_{12}CuO_4}$ for which a 'giant electron-phonon anomaly' has been reported recently [13]. In Chapter 11 structural and magnetic studies of the oxyhalides TiOCl and VOCl are presented. For TiOCl a pressure-induced metal-insulator transition has been proposed [33], recently. Hence, pressure dependent structural studies have been performed by means of neutron diffraction revealing strong structural changes at high pressures. In synchrotron and neutron experiments on VOCl a hitherto unknown structural phase transition has been observed at low temperatures giving rise to the determination of the magnetic structure.

2 Neutron and X-ray Sources

The microscopic nature of condensed matter, i. e. the structure and the lattice or magnetic excitations, can be investigated by different diffraction and spectroscopic techniques. For these purposes X-rays and neutrons have been used in this work and, hence, the properties of X-rays and neutrons will be briefly introduced followed by a short description of the measurement techniques in the next chapters.

2.1 X-rays

X-rays have been discovered 1895 by W. C. Röntgen and the first Nobel Prize in Physics ever awarded went to him in 1901 [34]. X-rays are electromagnetic radiation with a wavelength between that of ultraviolet light and the gamma rays which is of the dimension of interatomic distances and, thus, interesting for the study of condensed matter: in 1912 M. von Laue and P. Knipping for the first time observed X-ray diffraction patterns of a crystal (1914 M. von Laue was awarded by the Nobel Prize) [34]. In home laboratories the X-rays are generated by sealed X-ray tubes or by rotating anode tubes. Here, the characteristic X-ray radiation is used: accelerated electrons hit out an orbital electron of the inner shell (K-shell) of a metal atom and when an electron from a higher shell fills up the vacancy, X-rays are generated. Characteristic X-ray radiation was discovered 1909 by C. G. Barkla and C. A. Sadler (1917 Nobel Prize to Barkla) [34].

X-ray diffraction is based on the interaction between X-rays and electrons in the shells of atoms. Constructive interference can be observed when the flight path of two scattered rays differs by the X-ray wavelength λ or an integer multiple of λ. This scattering condition is known as Bragg's law:

$$2 \cdot d \cdot \sin(\Theta) = n \cdot \lambda \tag{2.1}$$

with d the spacing between two diffracting planes in the crystal and 2Θ the scattering angle.

In the next section a more brilliant X-ray source will be presented:

2.2 Synchrotron radiation

A beam of charged particles, usually electrons or positrons [1], which has been accelerated by electric fields to relativistic speeds and which is forced on a curved trajectory by

[1] Linearly accelerated electrons hitting a tungsten target radiate gamma rays which can create electron positron pairs. The positrons can be selected by appropriate magnetic fields.

magnetic fields emits a continuous spectrum of X-rays that can be up to 10^{12}-10^{13} times as brilliant as that from sealed X-ray tubes, depending on the energy of the charged particles [35, 36]. With increasing velocity of an accelerated charge the radiation cone

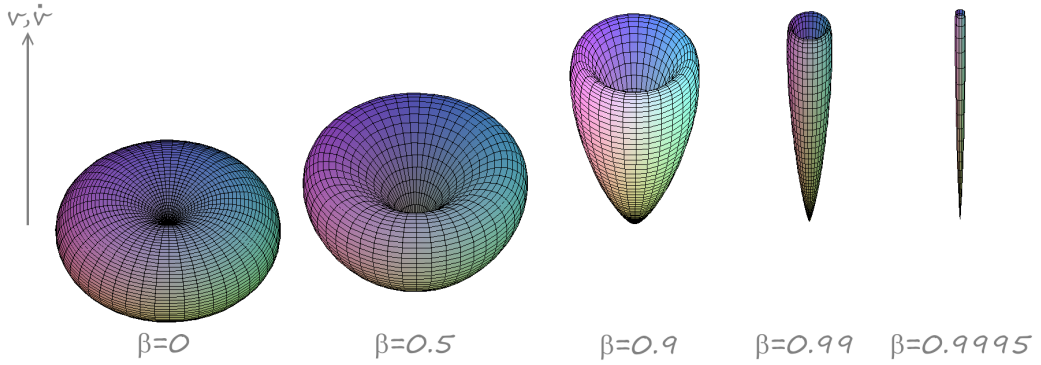

Figure 2.1: Angular distribution of $\sin^2(\Theta')/(1-\beta\cdot\cos(\Theta'))^5$ for different values of β.

shifts towards the direction of motion and the radiation power increases. For the special case $\overrightarrow{v} \| \dot{\overrightarrow{v}}$ the radiated energy per time interval dt through the angle element dΩ amounts to $dP'/d\Omega = \frac{q^2}{4\pi c^3} \cdot \dot{\overrightarrow{v}}^2 \cdot \sin^2(\Theta')/(1-\beta\cdot\cos(\Theta'))^5$ [37]; compare Fig. 2.1. Here, Θ' is the angle between $\dot{\overrightarrow{v}}$ and the direction of radiation and $\beta = v/c$ [37]. As can be seen already in this simplified special case, for highly relativistic particles most of the radiation is emitted in direction of motion, i. e. concentrated in a small cone with an opening angle which is inverse proportional to the particles energy in units of its rest energy, i. e. $1/\gamma$. In bending magnets the charged particles are forced on circular trajectories in the horizontal plane and the radiation is linearly polarized in the plane of acceleration (or elliptically polarized from other observation points) [34]. In a wiggler or undulator the charged particle beam gets deflected by an arrangement of periodic magnetic fields. A sinusoidally varying vertical field would induce also a sinusoidal beam trajectory. In a wiggler the applied magnetic fields are stronger yielding a larger deflection of the charged particles and, therefore, strongly suppressed interference effects due to the vanishing overlap of the light cones. Thus, the radiation from different periods adds incoherently. The flux is about 2· N times the flux of a bending magnet with N being the number of magnetic periods [34]. In an undulator these magnetic fields are weaker and the radiation from different periods is able to exhibit strong interference effects [34] since the deviations of the flight trajectory are smaller than in a wiggler. Roughly, the charged particles emit radiation at the wavelength of their periodic motion, which is the period length of the undulator divided by γ due to relativistic Lorentz contraction [34]. For the observer this wavelength is additionally divided by γ due to the Doppler effect. Furthermore, higher harmonics with odd values of i are observable [34]. On axis the peak intensity of the n-th harmonic is proportional to N^2. Compared to a wiggler the brilliance is higher. However, in the hard X-ray regime the wiggler has an intensity advantage since for the generation of the same photon energies as in a wiggler

the charged particles (electrons) would need an acceleration to much higher energies in the case of an undulator.

In this work experiments with synchrotron radiation have been performed at the DORIS III storage ring (*∼4.45 GeV positrons ∼140 mA*) at Hasylab/DESY in Hamburg [38], at BESSY (*∼1.7 GeV electrons ∼290 mA*) in Berlin [39] and at the ESRF (*∼6 GeV electrons ∼200 mA*) in Grenoble, France [35].

2.3 Neutrons

In 1932 J. Chadwick discovered neutrons which were emitted from beryllium metal after activation by alpha particles from a radium source: ^{4}He $+^9$ Be $\rightarrow^{12}$ C $+ n + 5.7$ MeV (1935 Nobel Prize to Chadwick) [40]. Only a few years later the diffraction of neutrons by condensed matter was studied. Neutrons are uncharged elementary particles with a finite mass $m_n = 1.675 \cdot 10^{-27}$ kg and a magnetic dipole moment μ_n = -1.913 μ_N due to their spin of 1/2 [41]. Free neutrons have a life time of roughly 886(1) s (β-decay: $n \rightarrow p + e^- + \widetilde{\nu}_e$). Due to de Broglie these particles behave also as waves with the wavelength $\lambda = \frac{h}{m \cdot v} = \frac{h}{\sqrt{2 \cdot m \cdot E}}$ [42]. The first demonstration of the diffraction of neutrons was done by Halban and Preiswerk, Mitchell and Powers using Ra-Be neutron sources [43-45]. With the advent of nuclear reactor technology the problem of the extremely low flux of Ra-Be sources was solved (first 'atomic pile' by Fermi in 1942) [40]. Nuclear fission was first discovered 1938 by O. Hahn and F. Strassmann, who bombarded a sample of uranium with a neutron beam and observed that uranium fissions into barium and krypton [46] (1944 Nobel Prize in Chemistry to O. Hahn). In nuclear reactors the neutrons are generated by the nuclear fission of ^{235}U:
$n^{(thermal)} +^{235}$ U $\rightarrow$ fragment$_1$ + fragment$_2 + 2.5 \cdot n^{(fast)} + 180$ MeV. Neutrons from the reactor core become thermalized in a moderator of heavy water D_2O ($\rightarrow$thermal neutrons). Other possible moderators are liquid H_2, CH_4 cooled to 20 K ($\rightarrow$ cold neutrons) or a block of graphite heated by the gamma rays from the core to temperatures of about 2400 K ($\rightarrow$ hot neutrons). Due to scattering processes in the moderator the peaks of the Maxwellian distribution shift to energies according to the moderator temperature. In Tab. 2.1 the properties of cold, thermal and hot neutrons are listed.

source	**E (meV)**	**T (K)**	**λ (Å)**
cold	0.1 $\rightarrow$ 10	1 $\rightarrow$ 120	30 $\rightarrow$ 3
thermal	5 $\rightarrow$ 100	60 $\rightarrow$ 1000	4 $\rightarrow$ 1
hot	100 $\rightarrow$ 500	1000 $\rightarrow$ 6000	1 $\rightarrow$ 0.4

Table 2.1: Neutron wavelength, energy and moderator temperatures for different neutron sources taken from Ref. [41].

Besides reactors the other important neutron sources are the spallation sources, where highly energetic protons hit heavy targets (metals like U, W, Ta, Pb or Hg etc.) triggering an intra-nuclear cascade. The highly excited nuclei emit neutrons and other spallation particles in order to release energy. For every proton hitting the nucleus

about 15 neutrons are emitted [47]. In contrast to the continuous flux in reactors, in spallation sources these neutrons are produced in bursts/pulses. Like in reactors, hydrogenous moderators around the target slow the high-energetic neutrons down [47]. The time structure of these neutron pulses can be used in order to compensate for the lower time-averaged flux of these polychromatic neutron beams using Time-Of-Flight methods etc., compare Chap. 3.

As can be seen in Tab. 2.1, the wavelength of thermal neutrons is of the order of the interatomic distances in solids and liquids and, hence, interference effects may occur yielding information about the microscopic properties of condensed matter. Neutron scattering is one of the most versatile techniques for probing condensed matter. 1994 the Nobel Prize in Physics was awarded to C. G. Shull and B. N. Brockhouse for their contributions to elastic neutron scattering and inelastic neutron scattering (triple-axis spectrometer invented 1961) respectively [40]. Neutron diffraction results from the nuclear interaction between neutrons and cores as well as the magnetic interaction of the neutrons magnetic moment with the moments of the atoms. The most important consequences arising from the properties of neutrons are listed in the following:

- large penetration depth since neutrons do not interact with the electron shells
- large scattering contributions from light elements as hydrogen and oxygen
- different scattering from elements with similar atomic numbers allows to distinguish between these elements
- different scattering from isotopes allows to study for example specific parts of molecules which have been deuterated etc.
- measurement of excitations accessible since the neutron energy is comparable to the energy of elementary excitations in matter
- measurement of magnetic structure and dynamical magnetic properties is possible due to the magnetic moment of the neutron.

Thus, the character of neutrons is unique and often cannot be matched by any other experimental technique. For example, the measurement of phonons with X-rays is much more difficult since the photon energies are about 7 orders of magnitude larger than the energies of neutrons for comparable wavelengths and, hence, a huge experimental effort is needed in order to resolve 1 meV energy change of a photon. Only recently, a few experimental stations at very brilliant synchrotron radiation sources were able to provide these resolutions.

In this work, neutron scattering experiments have been performed at the FRM-II in Garching (*reactor*) [48], at the reactor Orphée in Saclay, France (*reactor*) [49], at the ILL in Grenoble, France (*reactor*) [50], at ISIS in Didcot, United Kingdom (*spallation source*) [47] and at the SINQ in Villigen, Swiss (*spallation source*) [51].

3 Elastic and inelastic scattering

3.1 Powder diffraction

Four years after the pioneering work of M. v. Laue, Friedrich and Knipping on single crystals in 1912 [36, 52] Debye and Sherrer reported first experiments with polycrystals/powders [36, 53]. In the beginning, the applications of powder diffraction were limited to phase analysis mainly (Hanawalt files) [36, 54] .

Due to the extension to powder neutron diffraction by Shull and Smart [36, 55] and the development of crystal structure refinement by Rietveld [56] and the steadily growing computational power, powder diffraction became a very powerful tool for crystal and magnetic structure determination and is often used even in place of single crystal methods since the measurements are fast and the availability of powders is often much easier than for (large) single crystals.

A rather detailed description of powder diffraction methods, powder X-ray and neutron diffractometer and of the data treatment/analysis by Rietveld refinement is given in the diploma thesis of the author [57].

In this work a *Siemens D*5000 diffractometer using monochromized Cu K_α and Cr K_α radiation has been used for sample characterization. The precise measurement of the lattice parameter as a function of temperature and pressure has been performed by means of synchrotron radiation powder X-ray diffraction in several experiments at beamline B2 at Hasylab/DESY in Hamburg and beamline ID09A at the ESRF in Grenoble, France. For crystal and magnetic structure determination purposes powder neutron diffraction measurements have been performed at the SPODI diffractometer at FRM-II in Garching, at the 3T.2 diffractometer and G4.1 diffractometer at the reactor Orphée in Saclay, France, at the DMC diffractometer at pulsed neutron source SINQ at PSI in Villigen, Swiss, at the PEARL diffractometer at the pulsed neutron source ISIS in Didcot, United Kingdom, and at the D1A diffractometer, D2B diffractometer and D20 diffractometer at the ILL in Grenoble, France.

3.2 Single crystal diffraction

If single crystals are available, single crystal X-ray diffraction is the more accurate method for the determination of atomic positions and (thermal) displacement parameter. In contrast to powder methods the intensity of a very large number of reflections in reciprocal space can be measured precisely by ω-scans (or ϕ-scans).

In a scattering process the three-dimensional periodic electron density in the crystal splits the X-ray beam in several components F_{hkl}, i. e. the scattering process is

equivalent to a Fourier transformation of the electron density in the crystal and the measured intensities are proportional to the square of the amplitude of the complex structure factors $F_{hkl} \equiv F_{\overrightarrow{G}} = \sum_i f_j \exp(-i \cdot \overrightarrow{G} \circ \overrightarrow{r}_j)$ with the atomic form factor $f_j = \int dV n_j(\overrightarrow{r}) \exp(-i \cdot \overrightarrow{G} \circ \overrightarrow{r})$ being the Fourier transformation of the electron density of the j-th atom. However, the phase of F_{hkl} is not measurable and, hence, the Fourier transformation $\rho(\overrightarrow{r}) = \frac{1}{V} \cdot \sum_{\overrightarrow{G}} F_{\overrightarrow{G}} \cdot \exp(i \cdot \overrightarrow{G} \circ \overrightarrow{r})$ back to the electron density in the crystal not possible. This is the well known phase problem of X-ray crystallography. In a centrosymmetric crystal this phase problem is only limited to the determination of the sign ($\pm$). If a structure model could be derived by theoretical methods or from a known related compound, this structure model has to be optimized/refined in order to minimize the differences of the calculated and observed squares of the structure factors $|F_o^2 - F_c^2|$ (least squares refinement). In this work, the program *Jana2000* [58] was used for these purposes and the structure refinement was based on F^2. A measure for the quality of the obtained structure model are the residuals or R-values $\mathrm{R} = \sum_{\overrightarrow{G}} ||F_o| - |F_c|| / \sum_{\overrightarrow{G}} |F_o|$ and $\mathrm{R}w = [\sum_{\overrightarrow{G}} w \cdot (F_o^2 - F_c^2)^2 / \sum_{\overrightarrow{G}} w \cdot (F_o^2)^2]^{1/2}$ with weights w accounting for the accuracy of each individual reflection (in the simplest form: $w = 1/\sigma^2$ with the standard deviation $\sigma(F_o^2)$). A third measure is the goodness of fit $\mathrm{GoF} = [\sum_{\overrightarrow{G}} w \cdot (F_o^2 - F_c^2)^2 / (n-m)]^{1/2}$ with the number of reflections n and the number of refined parameters m. A more detailed description of single crystal X-ray methods and theory can be found for example in Ref. [59]. The precise measurement of the electron density by single crystal X-ray diffraction will be described in Chap. 4 and in Chap. 7.2 where the results of a synchrotron measurement are reported. In this work, a $X8Apex$ single-crystal diffractometer of *Bruker* using a CCD area detector and a $Kryo-Flex$ low-temperature device has been used for most single crystal X-ray diffraction measurements. But also several synchrotron experiments have been performed at beamline D3 at Hasylab at DESY in Hamburg and several single crystal neutron diffraction measurements have been performed at the HEIDI diffractometer and RESI diffractometer at FRM-II in Garching and at the 5C.2 diffractomter at the reactor Orphée in Saclay, France.

3.3 Triple-axis spectrometer

A triple-axis spectrometer (TAS) gives rise to the spectroscopic study of the dispersion of phonons and magnetic excitations in a wide regime of energy and momentum transfer. A drawing of the general design of a TAS is given in Fig. 3.1. The three axes being responsible for the name of this instrument are the monochromator axis, the sample axis and the analyzer axis. These axes are indicated by the *gray transparent circles* in Fig. 3.1. The polychromatic neutron beam (Maxwell distribution) from the beam tube inside the reactor gets collimated by a first collimator α_0 (usually fixed), then hits a monochromator crystal and gets diffracted according to Bragg's law - see Eq. 2.1. Thus only one wavelength with wavevector $\overrightarrow{k_i}$ and its higher harmonics pass the collimator α_1 and reach the sample. With the collimators α_2, α_3 and the analyzer crystal all

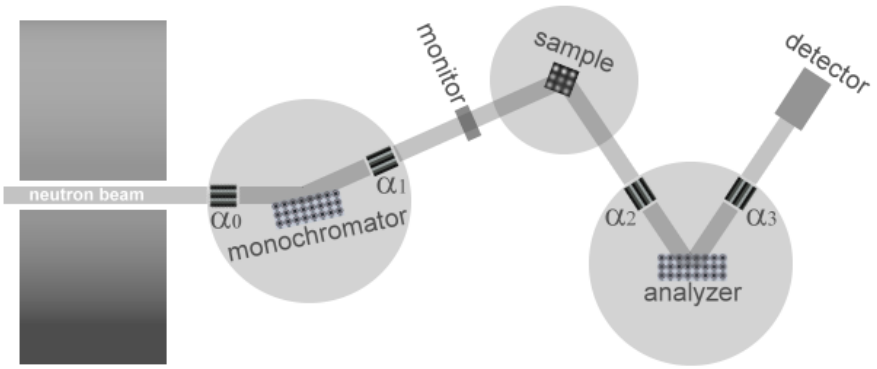

Figure 3.1: Schematic construction of a triple axis spectrometer.

scattered neutrons from the sample with a specific wavevector $\overrightarrow{k_f}$ meeting the bragg condition for the analyzer crystal can be scattered towards the detector where they will be counted. Thus, the size of energy transfer $\hbar \cdot \omega = \frac{\hbar^2}{2 \cdot m_n} \cdot (k_i^2 - k_f^2)$ and momentum transfer $\overrightarrow{Q} = \overrightarrow{k_f} - \overrightarrow{k_i}$ can be controlled by selection of $\overrightarrow{k_i}$ and $\overrightarrow{k_f}$. For an optimization of intensity and intensity-to-noise ratio the monochromator crystal should be of a material with a small unit cell volume V, a large nuclear structure factor F ($\propto$ scattering length), a low absorbtion coefficient, a small incoherent cross section and a rigid lattice (to avoid scattering by phonons) [40]. ^{58}Ni would be the ideal monochromator with no incoherent scattering and a very large value of F/V [40]. The next best materials are Be (for higher neutron energies) and pyrolytic graphite (PG) having an extremely strong preferred orientation of the (0 0 L) planes [40]. The intensities can be further optimized by choosing a focussing geometry of the monochromator (and analyzer). A vertical focussing which does not alter the good energy and momentum resolution within the scattering plane yields a factor of $\sim$4 more intensity [40]. For a further enhancement of intensity a horizontal focussing configuration can be applied in addition. (In contrast to vertical focussing, horizontal focussing influences the wavelength resolution.) In this work, double-focussing monochromator and analyzer configurations have been used in most of the inelastic neutron measurements.

Besides the mentioned key elements there are also several other elements which increase the performance of a TAS, like shielding, energy filters, diaphragms and a monitor. The shielding is necessary since the moderation is not perfect and also fast neutrons ($\gtrsim$200 meV) and gamma rays reach the monochromator. These fast neutrons need to be scattered, moderated and absorbed by different materials. Hence, a bulky shielding around the monochromator is needed. Additionally, lead may be needed to absorb the gamma rays [40]. The energy filters are needed in order to filter the higher order neutrons. Since the maximum wavelength which can be diffracted by a crystal is twice the largest d-spacing, polycrystalline materials like Be can be used as a higher order neutron filter at a cold neutron source. For a thermal TAS a PG filter is used with the c-axis parallel to the beam. The transmission conditions for this filter are rather complicated.

However, a couple of incident neutron energies with a large transmittance and a strong attenuation for $\lambda/2$ and $\lambda/3$ exists (near 14 meV, near 30.5meV etc.) [40]. Diaphragms can be used to minimize the background in a TAS experiment. A monitor measures the neutron flux behind the monochromator. Thus, measuring in a constant-k_f mode is very favourable since the angular dependence of the reflectivity of the analyzer is not changed and the monitor can be used in order to account for the changes in the monochromator reflectivity when changing k_i.

In this work several inelastic neutron scattering experiments have been performed at the IN8 spectrometer and IN20 spectrometer at the ILL in Grenoble, France, at the PUMA spectrometer and PANDA spectrometer at the FRM-II in Garching and at the 4F.1 spectrometer at the reactor Orphée in Saclay.

3.4 Time-Of-Flight techniques

Time-Of-Flight (TOF) techniques are optimal for the maximum utilization of the white neutron beam provided at pulsed spallation sources. TOF measurements base on the relation between the energy or wavelength of the neutron and its velocity which follows the law of de Broglie $\lambda = h/(m \cdot v)$. Hence, neutrons with higher energy arrive faster at sample and detector than neutrons with a smaller energy or larger wavelength. This time-structure of the detected signals allows to calculate the neutrons wavelength (measured after a time t) since the flight path l is known for each detector: $\lambda = h \cdot t/(m \cdot l)$.

For elastic scattering the d-spacing of each reflection can be calculated by Eq. 2.1 (Bragg's law): $d = h \cdot t/(m \cdot l \cdot 2 \cdot \sin(\Theta))$ [60]. Hence, the d-spacing is proportional to the time-of-flight and a large number of Bragg reflections (depending on the wavelength range) can be measured at only one fixed value of 2Θ which is in contrast to the conventional powder methods for a monochromatic instrument as described in the diploma thesis of the author [57]. Furthermore, the use of multiple detector banks increases the statistics since the data of all detectors can be merged.

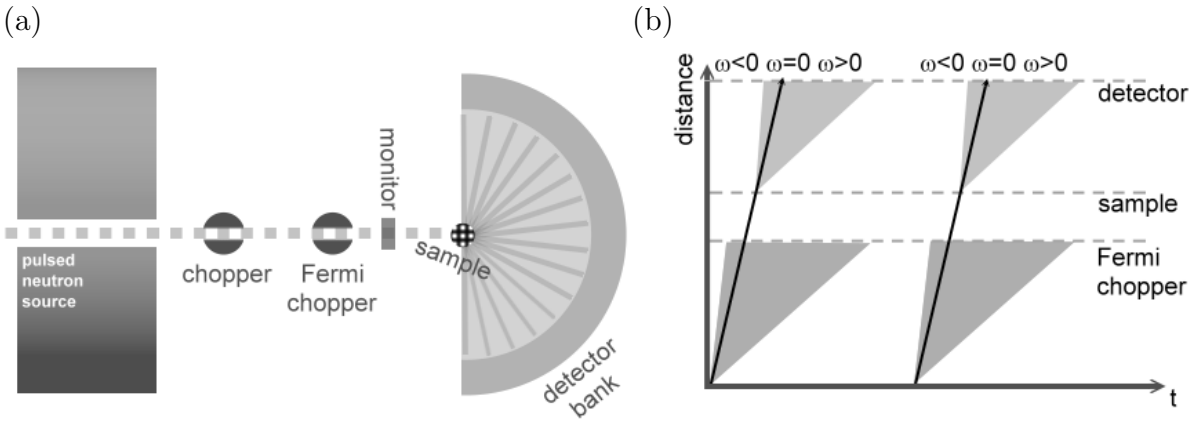

Figure 3.2: (a) Schematic construction of a TOF spectrometer. (b) Distance-time plot.

For inelastic neutron scattering the design of a chopper spectrometer is shown in Fig. 3.2 (a). The white beam coming from the moderator of the pulsed neutron source is running through a first background chopper (disk chopper) which prevents the neutrons with higher than thermal (epithermal) energies from passing further into the spectrometer where they thermalize and contribute to the background [60]. Disk choppers are rotating disks with holes which would chop a continuous neutron beam into consecutive parts. By synchronization to the proton beam hits epithermal neutrons can be cut off [60]. A second Fermi chopper monochromatizes this white neutron beam. In the Fermi chopper the hole in the middle is filled with several sheets of absorbing and transparent material with a curvature optimized for specific energy ranges [60]. The incident neutron energy can be selected by the phase of the chopper relative to the incident neutron pulse [60]. At a reactor instead of a Fermi chopper a monochromator can be used and a disk chopper divides the continuous neutron beam into pulses of neutrons. The result is always the same - pulses of monochromatic neutrons arrive at the sample. Due to scattering processes in the sample these neutrons with a fixed incident energy E_i gain or lose energy and get diffracted in one of the various detectors in the detector bank. This is drawn schematically in Fig. 3.2 (b). The black line corresponds to neutrons with energy E_i. Most of the signal can be detected in this elastic line. Neutrons which arrive earlier (later) at the detector have gained (lost) energy in an inelastic scattering process in the sample. Applying the cosine rule to the scattering triangle one obtains $\overrightarrow{Q}^2 = \overrightarrow{k_i}^2+\overrightarrow{k_f}^2-2\cdot\overrightarrow{k_i}\circ\overrightarrow{k_f}\cdot\cos(\sphericalangle(\overrightarrow{k_i},\overrightarrow{k_f}))$, thus $\hbar^2\cdot Q^2/(2\cdot m) = E_i+E_f-2\cdot\sqrt{E_i\cdot E_f}\cdot\cos(\sphericalangle\overrightarrow{k_i},\overrightarrow{k_f})$ and finally $\hbar^2\cdot Q^2/(2\cdot m) = 2\cdot E_i - \hbar\cdot\omega - 2\cdot\sqrt{E_i\cdot(E_i-\hbar\cdot\omega)}\cdot\cos(\sphericalangle(\overrightarrow{k_i},\overrightarrow{k_f}))$ [60]. Hence, each detector has a parabolic trajectory through (Q,ω)-space.

In this work, elastic TOF measurements have been performed at the PEARL diffractometer at the pulsed neutron source ISIS in Didcot, United Kingdom. Inelastic TOF neutron scattering experiments have been performed at the FOCUS spectrometer at the pulsed neutron source SINQ at PSI in Villigen, Swiss, at the IN4 spectrometer at the ILL in Grenoble, France and at the TOFTOF spectrometer at FRM-II in Garching.

3.5 Some basic neutron scattering formulas

A neutron scattering experiment measures the probability that a neutron which arrives at the sample with an incident wavevector $\overrightarrow{k_i}$ is scattered into a state with wavevector $\overrightarrow{k_f}$. Hence, the intensity is measured as a function of momentum transfer $\hbar\cdot\overrightarrow{Q} = \hbar(\overrightarrow{k_i}-\overrightarrow{k_f})$ and energy transfer $\hbar\cdot\omega = \frac{\hbar^2}{2\cdot m}\cdot(k_i^2-k_f^2)$. $\overrightarrow{Q}$ is the so called scattering vector which is (not) equal to a reciprocal lattice vector $\overrightarrow{\tau}$ for a (in-) coherent elastic scattering process with $\omega = 0$. For inelastic scattering processes the scattering vector is equal to the wavevector $\overrightarrow{q}$ of a magnetic or phononic excitation plus a reciprocal lattice vector, i. e. $\overrightarrow{Q} = \overrightarrow{q} + \overrightarrow{\tau}$. The number of neutrons scattered into an angle element dΩ with an energy transfer between $\hbar\cdot\omega$ and $\hbar\cdot(\omega+\mathrm{d}\omega)$ is called the *neutron scattering cross*

section which can be derived by Fermi's Golden Rule [26, 41]:

$$\frac{\mathrm{d}^2\sigma}{\mathrm{d}\Omega\mathrm{d}\omega} = \left(\frac{m}{2\cdot\pi\cdot\hbar^2}\right)^2 \cdot \frac{k_f}{k_i} \cdot \sum_{\lambda_i} p_{\lambda_i} \sum_{\lambda_f} |\langle \overrightarrow{k}_f, \lambda_f|\widehat{U}|\overrightarrow{k}_i, \lambda_i\rangle|^2 \cdot \delta(\hbar\cdot\omega + E_{\lambda_i} - E_{\lambda_f}) \quad (3.1)$$

with the thermal population p_{λ_i} of the initial state λ_i of the scattering system and the final state λ_f.

For nuclear scattering the interaction operator of neutron and sample can be approximated by the Fermi pseudo-potential since the nuclei have dimensions much smaller than the wavelength of a neutron: $U(\overrightarrow{r}) = \frac{2\cdot\pi\cdot\hbar^2}{m}\sum_i b_i \cdot \delta(\overrightarrow{r} - \overrightarrow{r_i})$ with the scattering length b_i of the i-th nucleus at $\overrightarrow{r_i}$ being of the order of 10^{-12} cm.

For magnetic scattering this operator $\widehat{U}$ is the product of magnetic moment operator of the neutron and the magnetic field [26, 41]: $\widehat{\mu}\overrightarrow{H}$. In the case of an electron with velocity $\overrightarrow{v_e}$ and spin $\widehat{s}$ the magnetic field $\overrightarrow{H}$ can be decomposed to contributions of spin and orbital motion [26, 41]: $\overrightarrow{H} = \mathrm{rot}\,(-2\cdot\mu_B\cdot\widehat{s}\times\overrightarrow{r}/r^3) - \frac{e\cdot\overrightarrow{v_e}\times\overrightarrow{r}}{c\cdot r^3}$. From Eq. 3.1 the following equation can be obtained for unpolarized neutrons (orbital angular momentum quenched, one magnetic ion type) [26, 41]:

$$\frac{\mathrm{d}^2\sigma}{\mathrm{d}\Omega\mathrm{d}\omega} = (\gamma\cdot r_0)^2 \cdot \frac{k_f}{k_i} \cdot F(\overrightarrow{Q})^2 \exp(-2\cdot W(\overrightarrow{Q})) \sum_{\alpha,\beta} \left(\delta_{\alpha,\beta} - Q_\alpha\cdot Q_\beta/Q^2\right)\cdot S^{\alpha\beta}(Q,\omega) \quad (3.2)$$

$$S^{\alpha\beta}(Q,\omega) = \sum_{i,j} \exp(i\cdot\overrightarrow{Q}\circ(\overrightarrow{r_i}-\overrightarrow{r_j})) \sum_{\lambda_i,\lambda_f} p_{\lambda_i} < \lambda_i|\widehat{S}_i^\alpha|\lambda_f >< \lambda_f|\widehat{S}_j^\beta|\lambda_i > \cdot\delta(\hbar\cdot\omega + E_{\lambda_i} - E_{\lambda_f}) \quad (3.3)$$

with $S^{\alpha\beta}(Q,\omega)$ the magnetic scattering function and $F(\overrightarrow{Q})$ the magnetic form factor, $\exp(-2\cdot W(\overrightarrow{Q}))$ the Debye-Waller factor, $\widehat{S}_i^\alpha$ the spin operator of the i-th ion at $\overrightarrow{r_i}$ ($\alpha = x,\ y,\ z$), γ the gyromagnetic ratio and $r_0 = 0.282\cdot 10^{-12}$cm. The pre-factor r_0 indicates that the magnetic neutron cross section is of comparable magnitude as the nuclear cross section, the factor $(\delta_{\alpha,\beta} - Q_\alpha\cdot Q_\beta/Q^2)$ indicates that neutrons couple only to magnetic moments perpendicular to the scattering vector and the factor $F(\overrightarrow{Q})$ indicates a decreasing signal with increasing value of Q since $F(\overrightarrow{Q})$ is the Fourier transform of the spatially extended spin-density.

4 Electron Density Measurements

4.1 Theoretical aspects

4.1.1 The independant atom model

The basis of structure determination by X-ray diffraction is the adoption of spherically distributed electron densities of the isolated atoms - therefore the name, independent atom model. Such a description of the atomic electron densities yields, indeed, rather good results in structure analysis and refinement and is common practice. But strictly speaking, this assumption is just an approximation, which is only very successful for the description of heavier atoms where the valence shell is just a small fraction of the total electron density. For smaller atoms this assumption becomes less reliable and finally for hydrogen, which has no core electrons at all, even wrong. In the case of hydrogen, a structure refinement based on the independent atom model even yields hydrogen positions which are shifted along the bond towards the bonding atom as its electron density is remarkably displaced along the bond [61]. Such deviations in the positional parameters appearing for hydrogen atoms can be of the order of 0.1-0.2 Å [62, 61] and can be easily revealed by comparison with neutron diffraction measurements. As can be seen from this example, the independent atom model is also not able to describe dipole electrostatic moments and charge transfer occurring between atoms of different electronegativity. Furthermore, the location of valence electrons and the occupation of orbitals within orbitally ordered materials, can not be described.

4.1.2 The κ Formalism

The spherical atom κ formalism is a first modification of the independent atom model. In this first, rather simple approach the valence electrons are separated from the inner core shells and described by two new variables - a parameter κ which describes the expansion or contraction of the valence shell and P_v which describes the valence shell population [61]. Thus, it becomes possible to describe the population and radial dependence of the valence electron shells and also enables charge transfer between atoms. The electron density in the κ formalism is defined as follows [61]:

$$\rho(r) = \rho_{core}(r) + \rho'_{valence}(\kappa \cdot r) = \rho_{core}(r) + P_v \cdot \kappa^3 \cdot \rho_{valence}(\kappa \cdot r) \tag{4.1}$$

From this equation, the structure factor can be calculated as

$$F(\mathbf{G}) = \sum_j (P_{j,c} \cdot f_{j,c}(\mathbf{G}) + P_{j,v} \cdot f_{j,v}(\mathbf{G}/\kappa)) \times exp(2 \cdot \pi \cdot i \cdot \mathbf{G} \circ \mathbf{r}_j \times T_j(\mathbf{G})) \tag{4.2}$$

with the scattering factors $f_{j,c/v}$ being the Fourier transform of the valence density component scaled to one electron, $P_{j,c/v}$ being the populations of core and valence electron shells and T_j being the temperature factor [61]. Structural analysis based on the κ formalism is able to observe net charges and dipole moments in agreement with the electronegativity of the atoms and other experimental/theoretical methods[61].

4.1.3 Multipole formalism

The next step exceeding simple spherical electron density approximations is the description of the electron density by non-spherical density functions, in the simplest case atom-centered functions. More sophisticated models either are problematical during the refinement or the interpretation of results is not easy [61]. Inspired by the s,p,d,... orbitals of the hydrogen atom the density functions are products of angular functions of θ and ϕ with certain radial functions of r. In principle the angular density functions $d_{lm\pm}(\theta,\phi)$ are linear combinations of the complex spherical harmonic functions Y_{lm}:

$$d_{lm+}(\theta,\phi) = N'_{lm} \cdot P_l^m(cos(\theta)) \cdot cos(m \cdot \phi) \tag{4.3}$$

$$d_{lm-}(\theta,\phi) = N'_{lm} \cdot P_l^m(cos(\theta)) \cdot sin(m \cdot \phi) \tag{4.4}$$

with $P_l^m(cos(\theta))$ being the associated Legendre functions and N'_{lm} some appropriate normalization factor [61]. For the radial functions an approach based on the Slater type radial functions of hydrogen orbitals omitting the radial nodes has been made:

$$R_l(r) = \kappa'^3 \cdot \frac{\zeta_l^{n_l+3}}{(n_l+2)!} \cdot (\kappa' \cdot r)^{n(l)} \cdot exp(-\kappa' \cdot \zeta_l \cdot r) \tag{4.5}$$

with κ' being an additional expansion parameter for the aspherical deformation functions being, generally, more diffuse than the spherical component of the valence density and thus needing an own expansion parameter [61]. The single-Slater ζ_l values for all subshells can be found in tables and the coefficients n_l obey the equation $n_l \geqslant l$ [61].

Thus, in the multipole formalism, the electron density is described by the following equation:

$$\rho(\mathbf{r}) = P_c \cdot \rho_c(r) + P_v \cdot \kappa^3 \cdot \rho_v(\kappa \cdot r) + \sum_{l=0}^{l_{max}} \kappa'^3 \cdot R_l(\kappa' \cdot r) \times \sum_{m=0}^{l} P_{lm\pm} \cdot d_{lm\pm}(\theta\phi) \tag{4.6}$$

A Fourier transformation of the electron densities yields the atomic form factors according to the multipole formalism and the final structure factor can then be calculated analogue as shown in the κ formalism taking into account the additional terms from the multipole formalism.

4.1.4 The residual electron density

The residual electron density $\Delta\rho(\mathbf{r})$ is the difference of the total observed electron density and the calculated electron density. To calculate $\Delta\rho(\mathbf{r})$ a Fourier transformation of the

complex coefficients ΔF has to be performed. Thereby, ΔF is the difference between the observed and calculated structure factor [61]:

$$\Delta F = F_{obs}(\mathbf{H})/scale - F_{calc}(\mathbf{H}) \tag{4.7}$$

Thus, the residual electron density is given by the following Fourier summation:

$$\Delta\rho(\mathbf{r}) = \rho_{obs}(\mathbf{r}) - \rho_{calc}(\mathbf{r}) = \frac{1}{V}\sum_{\mathbf{H}} \Delta F \cdot exp(-2 \cdot \pi \cdot \mathbf{H} \circ \mathbf{r}) \tag{4.8}$$

Usually, the structure model used for the calculation of F_{calc} is obtained from an independent atom model based on spherically averaged electron densities of the isolated atom; see Chapter 4.1.1. This model is a very good approximation, especially for heavier ions having the bulk of electrons in the core shells. But it fails in describing the electrons of valence electrons which do not have spherically distributed densities. In such a case, Eq. 4.8 is able to reveal electron densities of valence electrons, especially in orbitally ordered materials. Eq. 4.8 is a frequently used tool in structure analysis for the detection of shortcomings of the structure model in a structure refinement as it also reveals missing or wrongly set atoms etc. (see Chap. 7.1 for an example).

If a refinement with the multipole formalism has been performed, the refined electron density distribution also can be visualized by the multipole deformation map. The static multipole deformation map is the Fourier transform of the part of the calculated structure factors originating from the multipole formalism. The dynamic multipole deformation map also considers the (thermal) displacement parameters in these structure factors. But the electron density can be also visualized directly in real space by the charge density map which plots the electron density of all or only the valence electrons in real space. For an example of both, see Chap. 7.2.

4.2 Sample preparation

4.2.1 Sample shape and absorbtion correction

The sample shape is very important for electron density measurements as for a very irregular sample shape it is impossible to accurately calculate the absorbtion effects of the sample. This is especially important if smaller incident energies are used in the X-ray diffraction measurement or with rising value of $\mu \cdot R$ of the measured sample. Although numerical methods as the analytical [63] (or Gaussian quadrature...) methods probably yield the best absorption corrections, they are often not well applicable as the crystal faces are not well defined and can not be exactly measured or indexed. Also spherical/cyclindrical corrections are only accurate for perfectly shaped specimens. To cope with irregular sample shapes, semi-empirical methods have been developed. If there is a sufficiently large redundancy in the data set, multiscan absorbtion correction methods like described in Ref. [64] can be applied, analyzing the intensities of equivalent reflections using a multipolar spherical harmonic expansion. Such a multiscan absorbtion

correction is implemented in the program SADABS [65] of the Apex Suite of Bruker [66]. These corrections work remarkably well. However, a perfect description would require an extremely large redundancy only for correcting the absorbtion effects of an irregular sample shape. As the measuring time has to be very large for all images/reflections in order to measure precise intensities, especially for weaker reflections, there has to be made a compromise between measuring time and redundancy. An electron density measurement will, therefore, always suffer from the imperfect crystal shape put in the beginning. In this work, large effort has been made in order to receive close to perfectly shaped spherical crystals. Therefore, the sphere milling single crystal ball mill described in Ref. [67] was rebuilt and slightly modified with different top frames of varying exhaust radii and filter mesh widths in order to find the best milling conditions for each sample. The milling conditions of different samples distinctly vary depending on hardness and shape of the starting material. Whereas fully three-dimensional systems are more easy to handle, a quasi one-dimensional system like LiV_2O_5 - having the shape of long narrow needles which also survives after grinding - is an extremely challenging material as one can imagine (see Chapter 7.2).

The errors in the intensities for spherical samples arising from non sphericity in the sample shape have been calculated in Ref. [68]. The deviations from spherical shape ($\sigma(r)/r$) of the samples prepared for electron density measurements in this work were determined by averaging over a series of measurements under a Leica MZ16 stereomicroscope. A multiscan absorbtion correction was applied to all measurements performed at the *Apex* single crystal diffractometer. Only, for measurements performed at the synchrotron with high incident energies, where the absorbtion effects are minimal, a spherical absorbtion correction was applied for the almost perfectly spherical samples.

4.2.2 Sample stick/holder

Besides the perfect spherical sample shape there is another important point of sample preparation. The form of the (boro-silicate) glass capillary holding the sample turned out to be responsible for a sizeable contribution to the background in the (2Θ) low-angle region. The background of a standard (boro-silicate) glass capillary is shown in Fig. 4.1 (a). A rather large amount of diffuse intensity is found around the shadow of the beam-stop. From this observations it is obvious, that the glass capillary affects the measurement as it scatters (absorbs) also some intensity of the direct beam and also contributes to a larger background. Both effects might also alter in magnitude with the relative orientation of the glass capillary to the direct beam. These effects can not be corrected in any absorbtion correction procedure. In order to avoid this unknown influence of the glass capillary (plus glue), these effects of the sample holder had to be minimized. Therefore, in a first attempt, the glass capillary has been elongated under heat similar as is done by a glass-blower for macroscopic pieces of glass. Thus, only a very narrow, pointed tip is formed during this heat treatment. As can be seen in Fig. 4.1 (b), this narrowed, peaked glass capillaries contribute to a reduced background. Therefore, all common single crystal X-ray diffraction measurements within this work have been performed with spherical ground crystals mounted on the tip of such a narrow, pointed

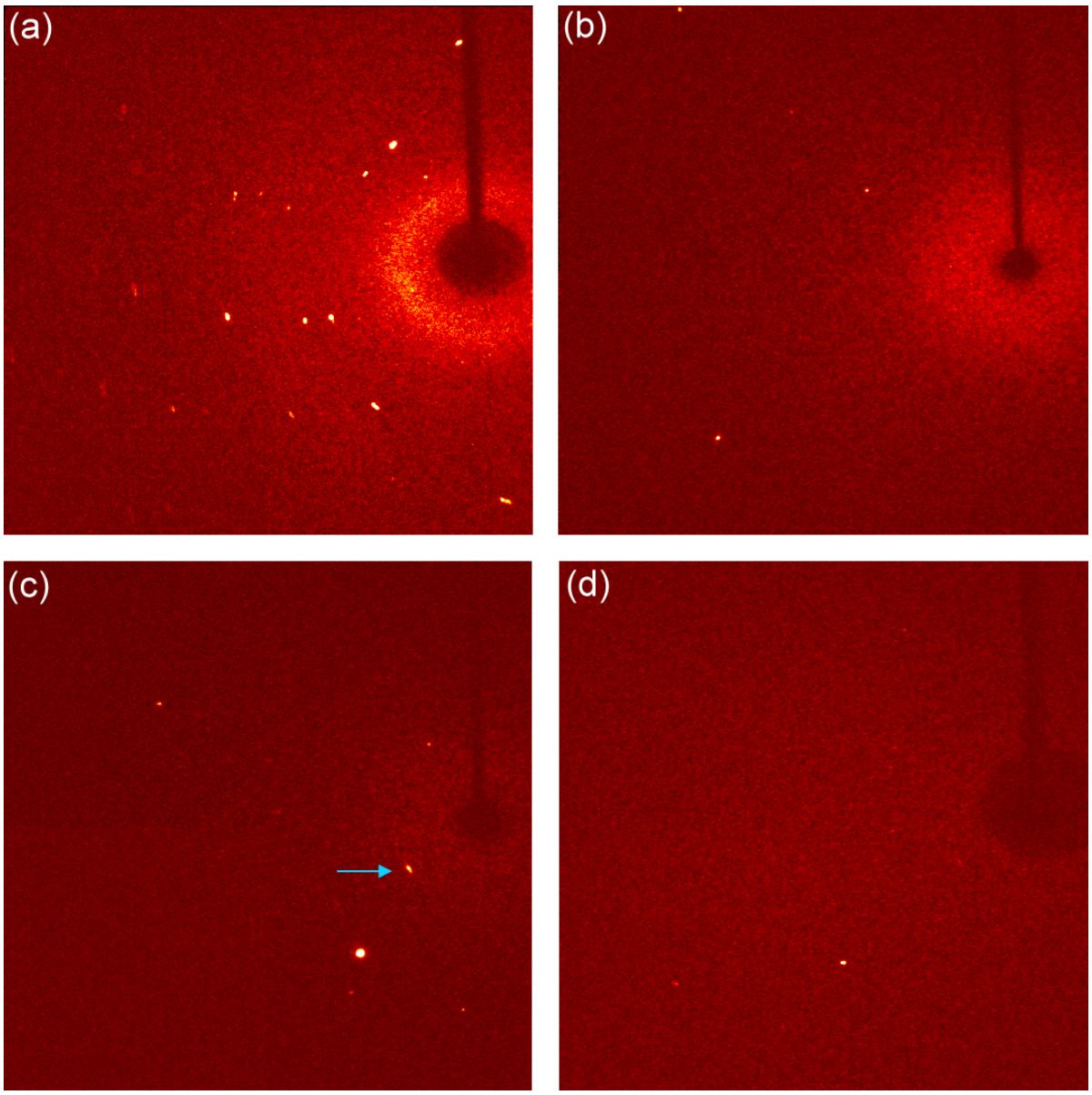

Figure 4.1: Images collected at the Apex single crystal diffractometer [66] for about similar measurement conditions (χ, ω, 2Θ) but using different sample sticks: (a) with a standard 0.1 mm glass capillary as is usually used for such kind of measurements, (b) with a narrowed glass capillary used in this work for all single crystal diffraction measurements, (c) with a carbon fibre for electron density measurements and (d) with a glass capillary specially modified for electron density measurements. The *blue arrow* indicates additional reflections from the carbon fibre. The brightness of each pixel indicates the relative measured intensity (dark-red to white). The images collected in electron density measurements (c-d) exhibit distinctly less background from the sample stick.

glass capillary treated with heat. But as there is still some background left even from this minimal mass of glass (plus glue) in the narrow glass tip, additional improvements had to be made. Instead of glass capillaries, carbon fibres contribute to a much reduced background as can be seen in Fig. 4.1 (c). Therefore, carbon fibres were used for several electron density measurements in this work. However, carbon fibres cause unwanted additional reflections. Such a reflection is indicated by a blue arrow in Fig. 4.1 (c). In order to cope with these unwanted effects, a self-written program checked for overlap with such reflections. But the further improvement of the method creating narrow peaked glass capillaries with heat finally lead to the construction of long, extremely narrow glass fibres which remain stable and which at the same time do neither vibrate nor break during rotation in ω- or ϕ-scans. Applying the spherical samples on these long and extremely narrow (but stable) tips of such glass fibres leads to a similar background reduction as the use of carbon fibres but without any additional reflections caused by the fibre - see Fig. 4.1 (d). Of cause, a minimum use of glue is as important.

5 Crystal Growth

For the study of physical properties of condensed matter it is often essential to have high quality single crystals of the compound of interest as many investigation techniques depend on having single crystals. Especially for most neutron scattering experiments even large single crystals of the order of cm^3 are needed. Furthermore, in polycrystalline samples the properties of the grain boundaries alter or sometimes even overrule the properties of the bulk material itself as can be seen for example in the resistivity of CrO_2 (see also Chap. 8.1).

In this work, the floating zone technique was used for growing single crystals.

5.1 Floating zone technique

The floating zone technique using a floating zone image furnace has established as a standard technique for preparation of transition metal oxide compounds in the past years.

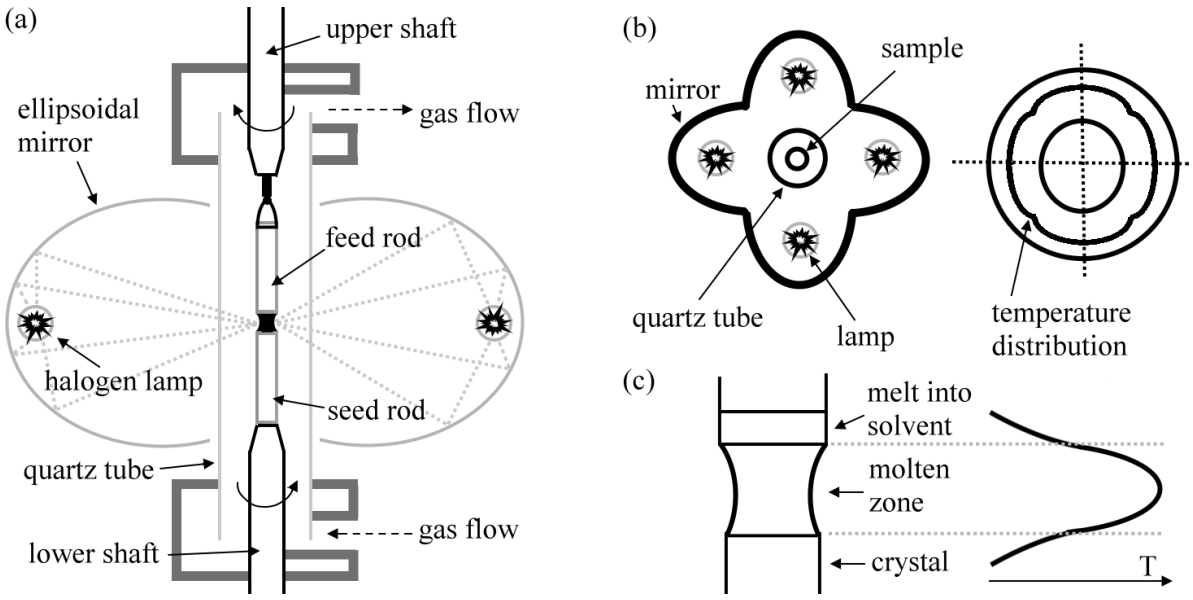

Figure 5.1: (a) Sketch of a floating zone furnace (see text). (b) Temperature distribution in the four mirror design [69] (top view). (c) Temperature distribution (side view).

The principle is as follows: four opposing ellipsoidal reflecting mirrors surround halogen lamps mounted at one side focal point of each mirror in a way that their light gets

focussed on the other side focal points. Here, the sample rod is mounted. Fig. 5.1 (a) shows a sketch of the floating zone crystallization technique. By increasing the lamp power, finally a molten zone is established which is held between the two solid sample rods by its surface tension. One of these rods is the seed rod, the other the feeding rod. The theoretical maximum stable length of the floating zone amounts to $l = \lambda \times \sqrt{\sigma/\rho \cdot g}$, where σ is the surface tension, ρ the density, g the gravitational acceleration and λ calculated to be 2.84 [70], 2.67 [71] or 2.62 [72]. The actual length of the zone depends on the lamps and the size of the filaments. Now, the molten zone can be translated along the length of the feeding rod by slowly moving the mirror system up - of cause with a well defined growth rate. Thus, the molten material recrystallizes on the seeding rod while new material is molten at the feeding rod end; see also Fig. 5.1 (c). Due to a surrounding quartz tube a controlled atmosphere can be applied during the growth process using reductive, inert or oxidizing gas flows with pressures up to 10 bar depending on the needs of the crystal system. The seeding and feeding rods have to be pressed and often also sintered before mounting them on the upper and lower shafts. Of cause, the chemical composition and stoichiometry of the feeding rod and a thorough mixture of the educts, for example achieved by thorough grinding, is also essential for a successful growth. As a seeding rod one can use either a seeding crystal or polycrystalline material or even not reacted educts, if no single crystal of the same composition is available. In the first case, it is likely that the crystal starts directly growing on the seeding crystal with the same orientation, if all other growth parameters are also correct. The upper and lower shaft can be rotated with independent velocities which has influence on the flow of the melt and is necessary for a good mixture of the molten zone as well as for stabilizing the liquid [73] during the whole growth process. Additionally, the Marangoni convection which affects the flow pattern and temperature distribution of the melt can be influenced [74]. The temperature distribution of the melt for a four lamp system can be seen in Fig. 5.1 (b) [69]. It is rather homogeneous compared to two lamp-systems with a pronounced sinusoidal temperature distribution. Fig. 5.1 (c) shows the temperature distribution from a side view. Within the hottest region, the molten zone is created, but there is also a region of high temperatures directly above and below which is affected by the filament size and where undesirable effects can occur if the liquid moves into this zone driven by the capillary force and causes objectionable pre-reactions. Two other very important growth parameters are the lamp power and the growth rate. The lamp power has to be high enough in order to melt all educts completely, especially if educts with different melting points were cold-pressed together directly without any previously applied solid state reaction or sintering. However, too high lamp power reduces the surface tension as well and it also contributes to stronger evaporation. In such systems, lamp power and growth rate are not independent and have to be adapted to each other. A too fast growth rate is also very harmful for the crystallization process and leads to twinned, polycrystalline or even not well reacted products. If all growth parameters are correct, large single crystals can be grown. The floating zone furnace used in this work is a model from CSI [75].

In Fig. 5.2 (a) an image taken during the growth-process of the $HoTiO_3$ crystal *ACK122* is shown. The bright area in the middle is a mirror image of the filaments

(a) (b)

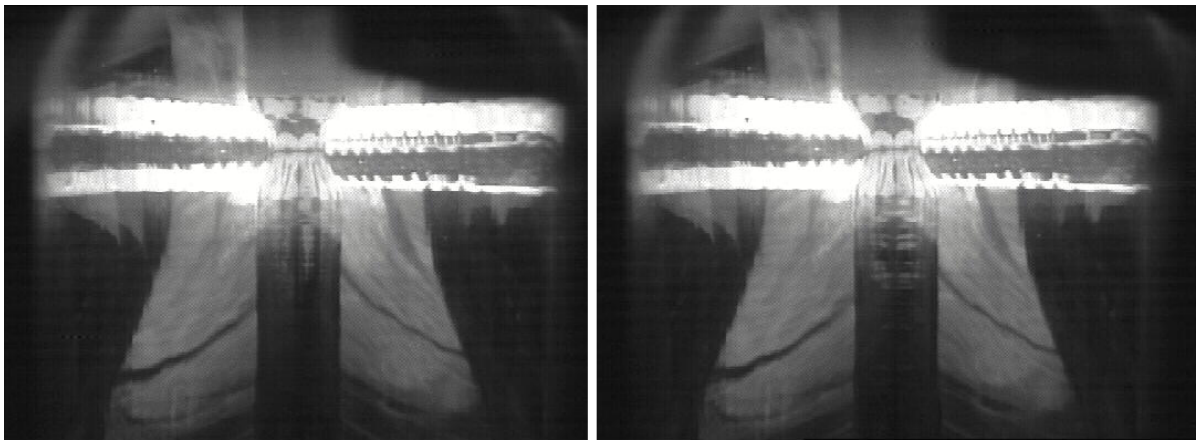

Figure 5.2: Two snapshots during the growth of $HoTiO_3$ *ACK122*.

of the 1000 W lamps generating the heat which establishes the molten zone. Above is the feeding rod and below the recrystallized material. A large facet can be seen in the middle of this crystal. This facet is very symmetric and extends over the whole length of this crystal. After a $\sim$180° rotation the image in Fig. 5.2 (b) was collected. As can be seen there is another very large facet in the middle which is exactly opposed to the first one and which extends also over the whole crystal length (from the bottom up to the molten zone). The appearance of two facets symmetrically on both sides of the crystal is indicative for a single crystal.

The advantage of the floating zone technique compared to other methods like for example the Czochralski technique is first of all the prevention of any contaminations by the crucible, which might be a severe problem for compounds with high melting points. Furthermore, due to the closed sample chamber and the use of reductive, inert or oxidizing atmospheres with well defined pressure the growth of materials with higher vapor pressure becomes also possible. Additionally, the speed of the crystal growth is rather fast, the shape of the grown crystal controllable and the crystal size rather large if compared with some other techniques like chemical transport where crystallization is carried out via the gas phase and the obtained crystals with irregular shape are often only of mm size.

5.2 $Y_{1-x}Ca_xTiO_3$

For the synthesis of the first titanate crystal within this work, $YTiO_3$, which is the parent compound of the $Y_{1-x}Ca_xTiO_3$-system a standard solid state reaction was tried.

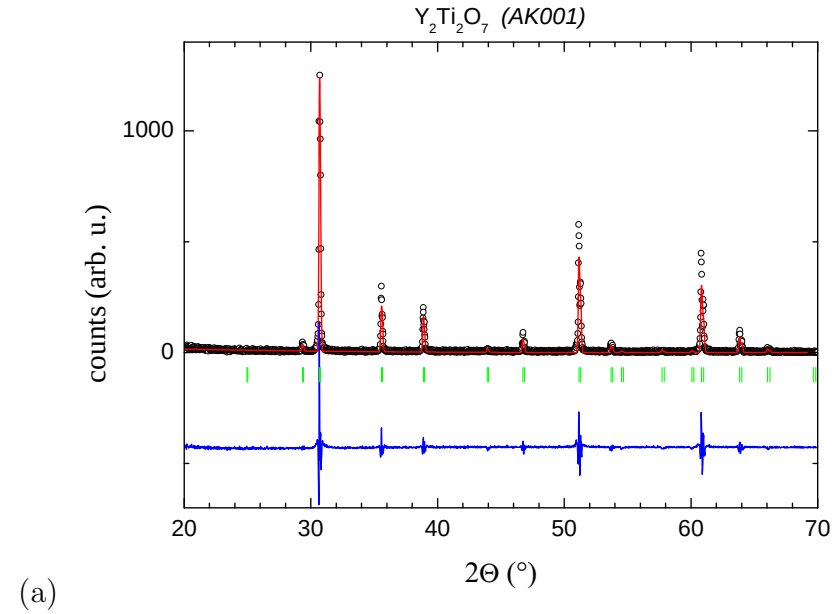

(a)

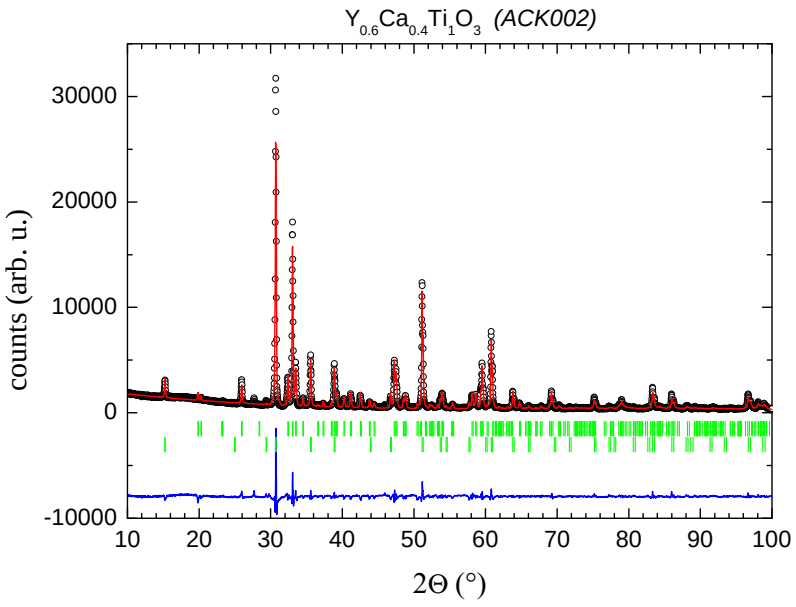

(b)

Figure 5.3: Powder X-ray diffraction patterns of (a) *AK001* and (b) *ACK002*; *black cricles:* measured data (I_{obs}), *red line:* Rietveld fit (I_{calc}), *blue line:* $I_{obs} - I_{calc}$, *green bars:* bragg peak positions.

Assuming the solid state reaction $\frac{1}{2}\times Y_2O_3 + \frac{1}{2}\times Ti_2O_3 \rightarrow YTiO_3$ would take place a stoichiometric mixture of Y_2O_3 and Ti_2O_3 was ground thoroughly in an agate mortar for about 45 minutes and pressed into pellets using a hydraulic press under application of 10-15 kbar pressure. Then, this pellet was put into an airtight chamber furnace (*'ZEUS'*) and heated with a temperature ramp of 300°C/h up to 1600°C. At this temperature the sample was left for 24 h. A constant atmosphere of 0.4 bar Ar was applied during the whole sintering process. The final product (sample *AK001*) derived by this procedure has a white color. An examination by powder X-ray diffraction reveals an absolutely pure $Y_2Ti_2O_7$ pyrochlore phase with space group $Fd\bar{3}m$ and 10.09 Å lattice parameter; see Fig. 5.3 (a). Obviously the corundum tube of the chamber furnace is not fully airtight at higher temperatures and the $YTiO_3$-mixture becomes fully oxidized.

Another 21 solid state reactions have been tried in two airtight chamber furnace (*'ZEUS'* and *'GERO'*). In these 21 additional growth processes, the total nominal oxygen content of the composition of the starting material was reduced by the exchange of Ti or TiO for Ti_2O_3. Thus, a bunch of different nominal oxygen compositions ranging from $YTiO_{2.95}$ to $YTiO_{2.75}$ and finally, also $YTiO_{2.5}$ has been tried this way. In all of these compounds (*AK002* to *AK022*) large amounts of the impurity phase ($Y_2Ti_2O_7$ etc.) could be detected in powder X-ray diffraction measurements. Also the use of carbon as a 'getter' for the oxygen and the use of a sealed Mo-container and, further, the use of welded Ta-vials did not avoid the growth of impurity phases as titanium is highly reactive and reacts with any residual oxygen or with the container material Mo or Ta. Ti even reacts with Pt which has been put into the sealed Mo-container in order to avoid the reaction with Mo. Therefore, the whole method seems not to be appropriate for the clean preparation of $YTiO_3$.

Figure 5.4: Photo of an deoxidized $Y_{1-x}Ca_xTiO_3$-crystal (*left*) and a block of TiO (*right*).

In order to get pure single crystals of $Y_{1-x}Ca_xTiO_3$ a floating zone image furnace has been used for the crystal growth (see Chap. 5.1). This furnace has the advantage of a controllable atmosphere and avoids any reactions with the crucible material. Therefore, it is a very favourable method for the growth of titanates. Nevertheless, the first tries in growing $Y_{1-x}Ca_xTiO_3$-crystals were not successful. Using forming gas (mixture of ∼95% N_2 and ∼5% H_2) as an atmosphere results in severe reduction of the whole crystal (*ACK001*). The growth of a single crystal was prevented by the formation of an unidentified yellow/golden impurity phase surrounding the whole reacted compound,

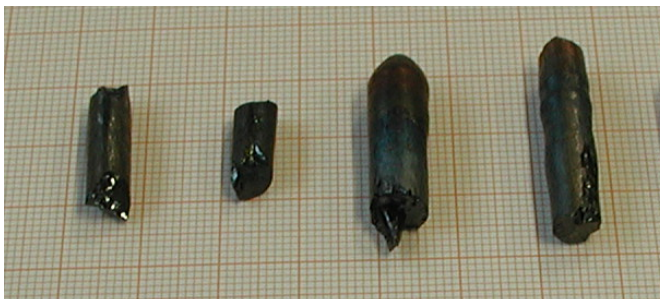

Figure 5.5: From left to right: photographs of $Y_{0.667}Ca_{0.333}TiO_3$ (*ACK015*), $Y_{0.64}Ca_{0.36}TiO_3$ (*ACK016*), $Y_{0.8125}Ca_{0.1875}TiO_3$ (*ACK045*), $Y_{0.75}Ca_{0.25}TiO_3$ (*ACK044*)obtained by the floating zone technique.

which can be seen on the crystal in the left part of Fig. 5.4. In the right part of this figure, a solid block of TiO is shown which has a very similar color as the impurity phases found in the deoxidized titanate compounds which are, hence, most likely Ti^{2+}-compounds. Thus, forming gas is a too strong deoxidising/reducing gas which can not be controlled easily and which may also give rise to possible reactions of nitrogen with the titanium since TiN is a very stable compound. Therefore, an argon atmosphere was applied throughout most of all further crystal preparation processes (see Chap. 5.7). However, the next try using an argon atmosphere resulted in the appearance of strong pyrochlore impurity phases. In Fig. 5.3 (b) a two phase fit for $Y_{1-x}Ca_xTiO_3$ and a pyrochlore phase is shown. These results indicate an excess of oxygen. Either the argon atmosphere in the sample chamber contains small impurities of oxygen or the educt Ti_2O_3 contains some excess oxygen. Indeed, the analysis of Ti_2O_3 by TGA indicates an oxygen excess of about 0.3%. This oxygen excess in the starting material has to be compensated by the removal of some oxygen from the starting materials. Furthermore, some material evaporates during the growth process and deposits on the quartz glass tube. The analysis of the evaporated material by EDX reveals Ti and Ca as the evaporating elements. Therefore, the appropriate concentration of all starting materials has to be found and in general the evaporation of Ti, Ca has to be counterbalanced. As the evaporation rate is very sensitive on the heating power and the growth rate, the three parameters of chemical doping have to be adjusted very carefully for the two chosen growth parameters with an accuracy of about 0.1-0.2%. A somewhat higher Ti-concentration leads to a higher melting point and the accumulation of Ti in the melt, which causes a rising melting point during growth process and the occurrence of the same yellow impurity phase found in the sample ACK001 which was grown with forming gas. As Ca-doping leads to an increase of the melting point, these three parameters have to be re-adjusted for every Ca-concentration again. The excess Ti was in gereral of the order of 0.5% but can be reduced to zero if the heating power is reduced. A similar growth technique was described for the manganite synthesis in Ref [76]. With this technique, no excess Ti or Ca is needed and only the excess oxygen from the Ti_2O_3 starting material has to be taken into account. However, this crystal growth process is

very difficult as shaft rotations, heating power, growth rate and the movement of the feeding rod into and out of the melting zone have to be adjusted very frequently during the whole growth process but it has the advantage that no undesirable by-products can emerge. Furthermore, the Ar-gas flow and pressure are also important parameters as all other parameters like chemical doping, heating power and growth rate have to be

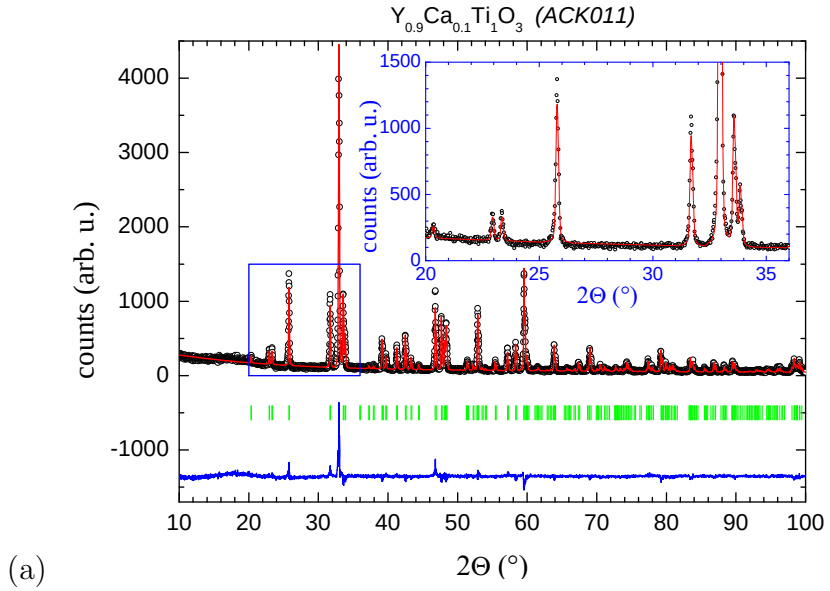

(a)

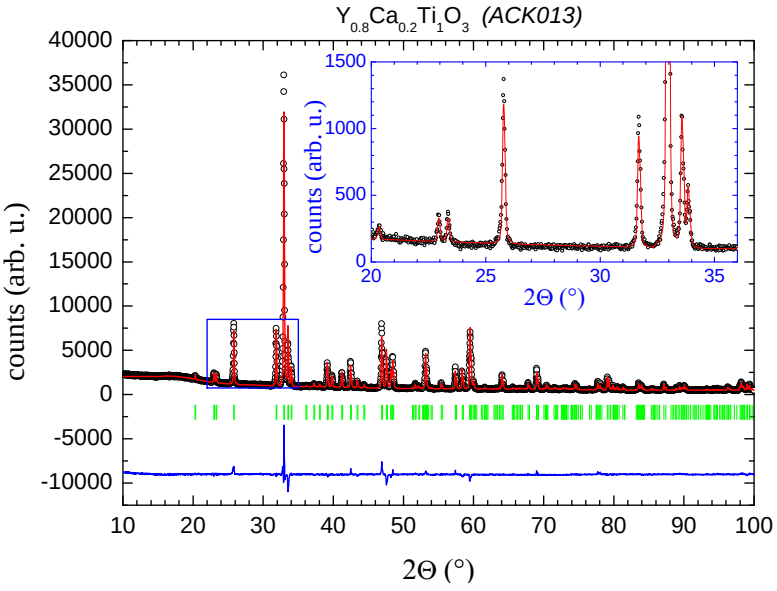

(b)

Figure 5.6: Powder X-ray diffraction patterns of (a) *ACK011* and (b) *ACK013*; *black cricles:* measured data (I_{obs}), *red line:* Rietveld fit (I_{calc}), *blue line:* $I_{obs} - I_{calc}$, *green bars:* bragg peak positions. The inset idicates an enlargement of the region marked with the *blue* box.

adjusted taking the gas flow and pressure into account. Probably, the Ar gas contains some oxygen impurities, as a higher gas pressure or gas flow have to be counterbalanced by chemical doping. Additionally, the titanate crystal growth suffers from segregation effects. Moving the melting zone a distance l leads to a concentration gradient in the recrystallized part as the concentration of a solvent in a liquid (c_l) and in the solid phase (c_s) are not equal in the thermal equilibrium [77]: on the side of the feeding rod material with a concentration of c_{ini} enters the melting zone and on the other side this material recrystallizes with a concentration $c_s = k \cdot c_l \neq c_l$. Thus, the concentration of this material in the floating zone is raised or lowered depending on whether k is smaller or larger than 1. If no concentration gradient was applied over the whole feeding rod in the $Y_{1-x}Ca_xTiO_3$-synthesis, impurity phases could appear in the further growth process or a pulldown of the floating zone could be unavoidable or, in the simplest case, the beginning and the end of the grown crystal have different properties, for example in the electrical

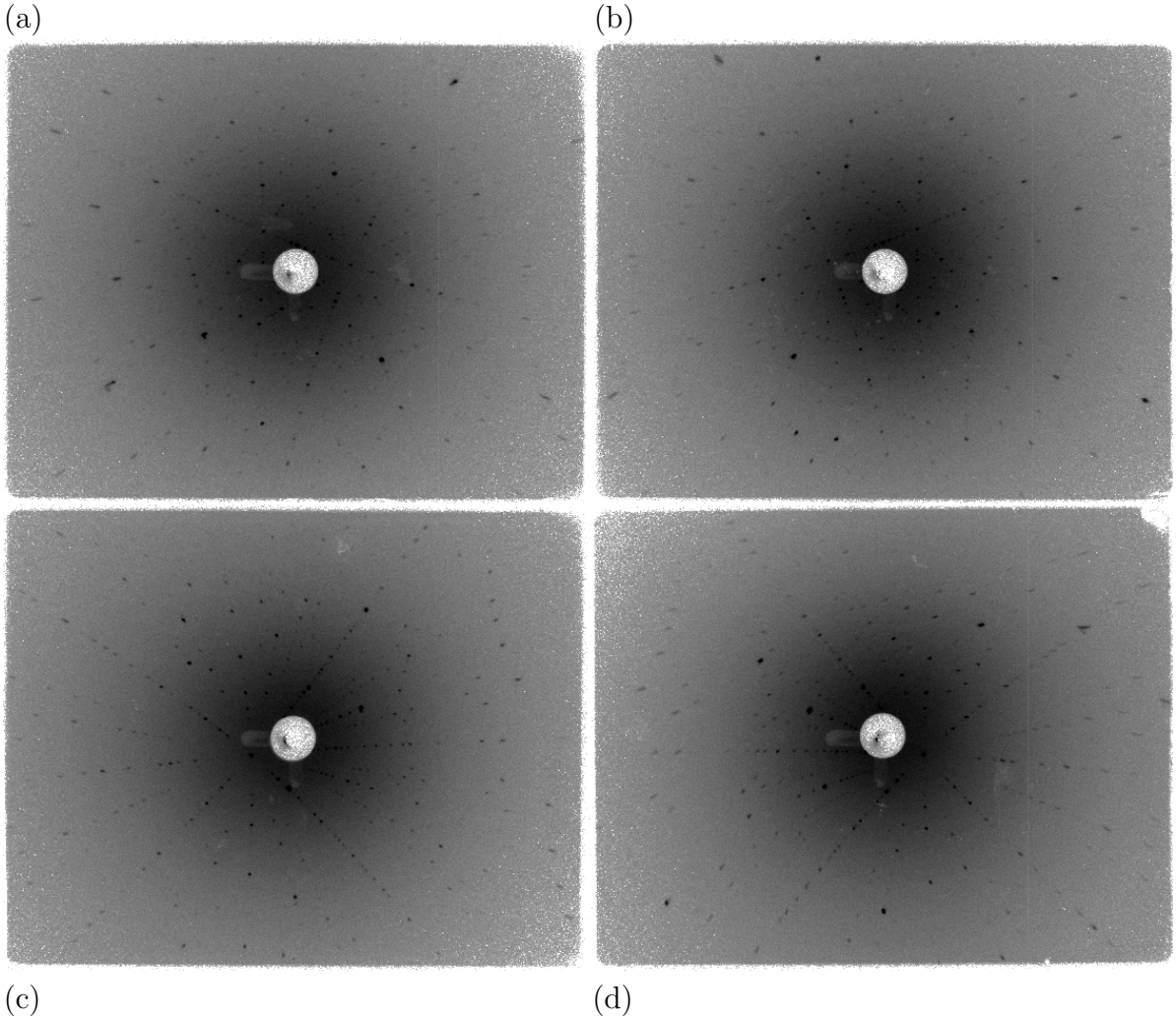

Figure 5.7: Laue photos of crystal ACK011 (a,b) and ACK044 (c,d).

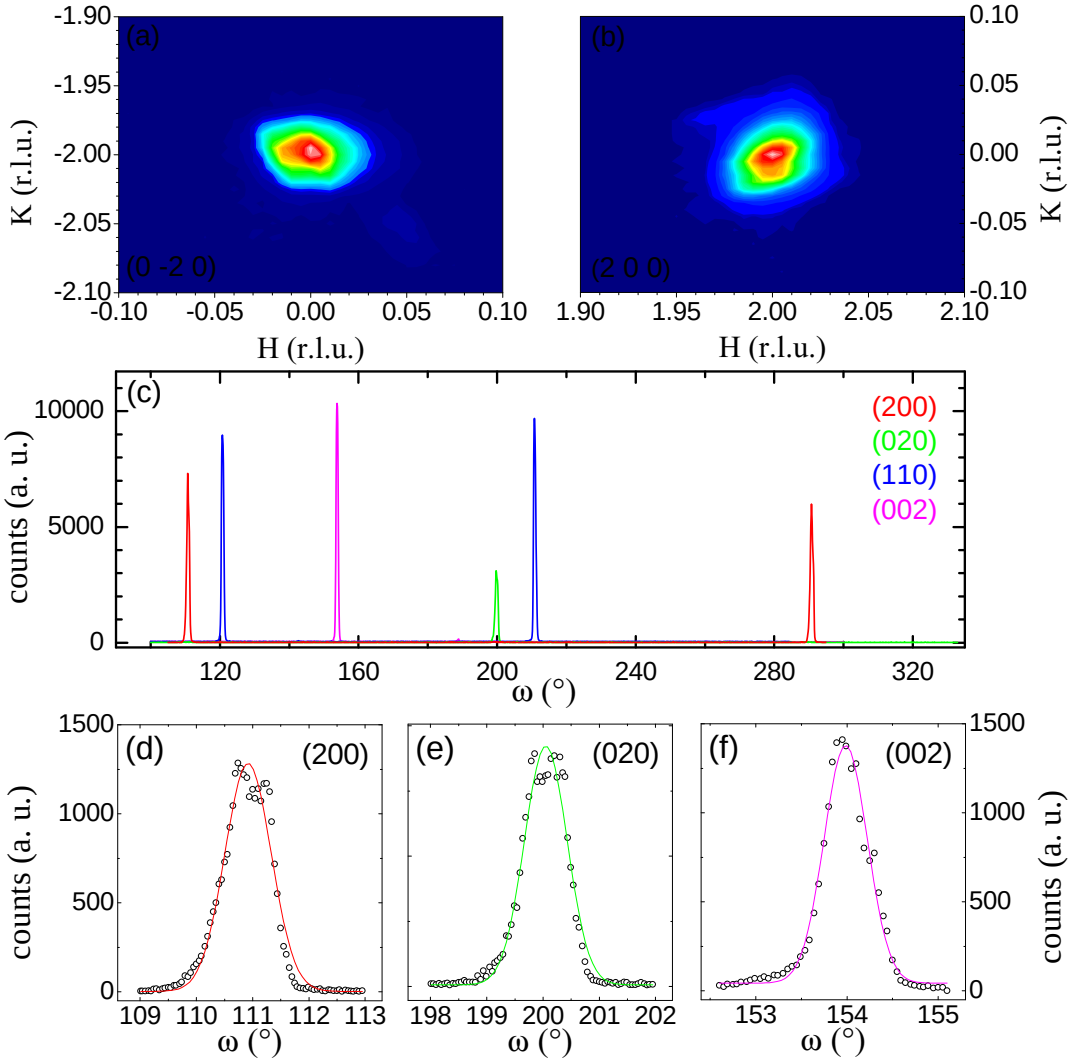

Figure 5.8: (a-b) Elastic neutron scattering intensity of $Y_{0.64}Ca_{0.36}TiO_3$ *ACK017* measured within the HK-plane with a 15'-S-40' collimation. (c) Large rocking scans (ω-scans) for different reflections with 15'-S-40' collimation. (d-e) Rocking scans of single reflections with 15'-S-10' collimation.

resistivity etc. Therefore, a gradient of Ti, O (Ca) has been applied over the whole feeding rod, which had to be adjusted for each $Y_{1-x}Ca_xTiO_3$-compound depending on the Ca concentration, the chosen growth conditions like growth rate, heating power or argon flow and on the amount of the Ti-/Ca-/O-doping. In order to get a more continuous distribution of this gradient, the whole feeding rod was made of more than six different

parts by filling a rubber tube successively with starting materials of slightly changing concentration yielding a more continuous distribution over the whole rod followed by pressing the tube in a hydraulic press. If the feeding rod was divided into two or three different parts only, an abrupt change of the growth conditions could be observed when the neighbouring part enters the floating zone. Such an abrubt change can even induce the pulldown of the floating zone, if the gradient is large enough. However, these effects can be fine tuned also by the Ar gas flow. Oxygen rich and oxygen poor melting zones have slightly different properties of the liquid. If a change of the melt is recognized early enough during the growth, the Ar- gas flow or pressure can be lowered or enlarged in order to balance the melt again. Of cause the heating power has to be adjusted again, if the pressure is changed.

Fig. 5.5 shows some of the $Y_{1-x}Ca_xTiO_3$ single crystals grown in this work by the floating zone technique and in Fig. 5.6 the X-ray powder diffraction patterns of (a) $Y_{0.90}Ca_{0.10}TiO_3$ and (b) $Y_{0.80}Ca_{0.20}TiO_3$ are shown. As can be seen in the inset of these figures, there is no oxidized pyrochlore impurity phase. In Fig. 5.7 (a-b) two Laue photos of $Y_{0.90}Ca_{0.10}TiO_3$ from the front side and the 180° rotated backside of a ∼cm large crystal are shown. These Laue photos obtained from both sides of the crystal indicate the single crystallinity.

The $Y_{0.64}Ca_{0.36}TiO_3$ crystal was also examined at the 3T.1 diffractometer at the reactor Orphée in Saclay, France. A collimation of 15'-S-40' has been used for these measurements. Large rocking scans of various reflections are shown in Fig. 5.8 (c). Only the expected number of reflections is visible in an ω-range of more than 180°. This indicates that there are no crystallites in this single crystal. In Fig. 5.8 (a-b) the neutron scattering intensity maps of Q-scans within the reciprocal HK-plane are shown. Red (rosy) regions are regions of high intensity and dark blue areas are regions of low intensity. These scans indicate that this single crystal of $\lesssim$cm^3 dimension is untwinned. Also a single crystal neutron diffraction measurement performed with this crystal at the 5C.2 diffractometer at the reactor Orphee in Saclay, France exhibits no indications for twinning. Scans with 15'-S-10' collimation are shown in Fig. 5.8 (d-f) indicating a quite fair mosaic spread of the crystal which amounts to 0.59(7)° for the (002) reflection and 0.83(11)° and 0.90(9)° for the (020) and (200) reflections.

The stoichiometry of the $Y_{1-x}Ca_xTiO_3$-samples was tested by EDX measurements over the whole crystal length. These measurements prove the overall stoichiometry of the $Y_{1-x}Ca_xTiO_3$-single crystals grown in this work. However, the accuracy of EDX measurements is not perfect as these measurements suffer from some uncertainties. For example the chosen standard materials for calibration may not be appropriate reference materials for the $Y_{1-x}Ca_xTiO_3$-system and the shape of the crystal surface may alter the intensities of lighter versus heavier elements etc. Therefore, also complementary single crystal X-ray diffraction measurements have been performed in order to get additional information about the Ca-content. Especially, some synchrotron radiation single crystal X-ray diffraction measurements which have been performed for $Lu_{1-x}Ca_xTiO_3$ etc. give very accurate Ca compositions (which differ from the according EDX measurements). In Tab. 5.1 the Ca-concentrations determined by single crystal X-ray diffraction measurements are shown together with the values of EDX measurements. Also the goodness

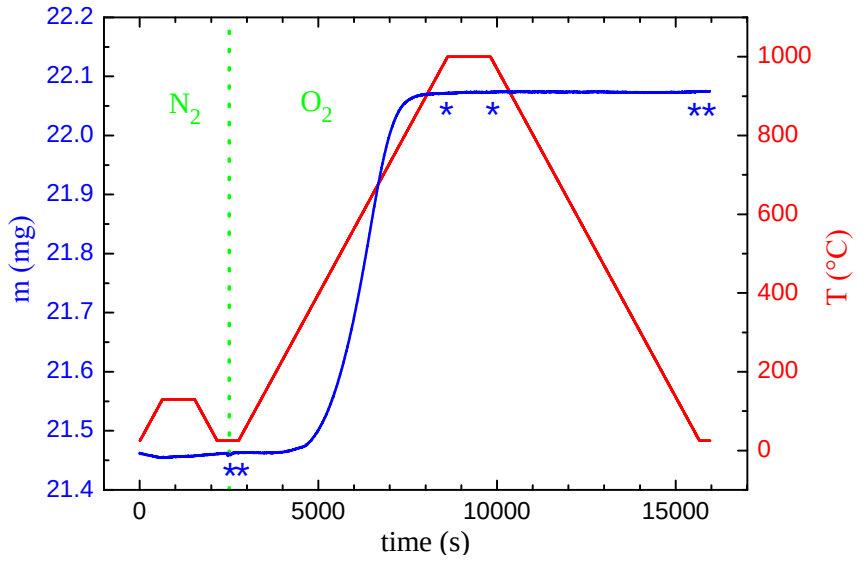

Figure 5.9: TGA measurement of $Y_{0.64}Ca_{0.36}TiO_3$ (*ACK016*), *red:* temperature curve, *blue:* sample mass.

of fit, R and weighted R-values of the X-ray measurements are listed.

crystal	x **(nom.)**	x **(EDX)**	x **(X-ray)**	**GoF/R/Rw**	δ **(TGA)**
ACK011	0.10		10.3(2)%	1.74/2.16%/3.17%	0.001(1)
ACK012	0.10	11.7%			0.010(1)
ACK013	0.20		21.1(2)%	1.68/1.88%3.46%	
ACK015	0.333	33.8%	33.9(2)%	1.78/1.81%/2.62%	0.005(1)
ACK016	0.36	36.1%	34.2(2)%	2.49/1.95%/3.37%	-0.013(1)
ACK017	0.36				
ACK027	0.45	44.2%			
ACK044	0.25	22.7%	22.9(2)%	2.52/1.77%/2.91%	-0.007(2)
ACK045	0.1875	19.4%	19.8(4)%	1.99/1.97%/3.70%	-0.005(1)
ACK047	0.5		49.8(3)%	1.78/1.57%/2.91%	
ACK083	0.37				0.018(1)
ACK088	0.5				-0.009(1)
ACK090	0	-	-	-	-0.010(1)
HR08+71	0				0.025(1)
HR99+100	0.38				0.012(1)
HR120	0.35				0.007(1)
HR139	0.5				0.020(3)
HR155	0.55				0.016(1)
Agung	0.40				0.046(1)

Table 5.1: Calcium and oxygen content of $Y_{1-x}Ca_xTiO_{3+\delta}$ determined by EDX, single crystal X-ray diffraction and TGA respectively.

Furthermore, the oxygen content has been determined by TGA after some improvements of the measuring sequence. The main improvement of the new measuring sequence

is a sintering process of the sample at 130°C for 15 minutes in an inert gas flow (N_2) before the oxidation process in order to get rid of any water etc. After this sintering at 130°C, the sample was cooled down to 25°C again and, then, the gas flow was changed to O_2 and an oxidation process at 1000°C has been started. The whole measurement is shown in Fig. 5.9. The (starting) oxygen composition in the $Y_{1-x}Ca_xTiO_{3+\delta}$-compound can be calculated from the change of mass in this chemical reaction of titanium with oxygen: $Y_{1-x}Ca_xTiO_{3+\delta} + \frac{1-x-2\cdot\delta}{4}\cdot O_2 \longrightarrow \frac{1-x}{2}\cdot Y_2Ti_2O_7 + x\cdot CaTiO_3$. The excess oxygen δ is listed for the $Y_{1-x}Ca_xTiO_{3+\delta}$-compounds grown in this work in Tab. 5.1.

In general, the oxygen stoichiometry as well as the Ca-composition could be adjusted quite well within the accuracy of each measurement technique by the synthesis route described in this chapter. For a comparison, the oxygen content was also measured for $Y_{1-x}Ca_xTiO_3$-samples synthesized in Ref. [78] and listed in Tab. 5.1. Obviously, these samples tend to have a slightly larger oxygen excess than the samples grown in this work. Also the $Y_{1-x}Ca_xTiO_3$-crystals grown by A. Nugroho exhibit severe oxygen problems.

In Fig. 5.10 the lattice parameter of several $Y_{1-x}Ca_xTiO_3$-samples grown in this work ($0 \leq x \leq 0.5$) determined by powder X-ray diffraction are shown. For the exact determination of the lattice parameter, Si was used as a standard. As can be seen in Fig. 5.10 (d) the unit cell volume decreases with hole doping. Thus, a differing oxygen or calcium concentration would induce changes in the lattice parameter and unit cell volume. The lattice parameter of the crystals grown in this work (*circles*) exhibit very similar values as the lattice parameter reported in Ref. [79] (*triangles*) which underlines the stoichiometry of the samples grown in this work.

In summary, untwinned single crystals of $Y_{1-x}Ca_xTiO_3$ having close to stoichiometric Ca and O compositions have been grown by the synthesis route developed in this work.

5.3 $R\mathrm{TiO}_3$

The crystal synthesis of rare earth titanates was focussed on the growth of ferromagnetic $R\mathrm{TiO}_3$-single crystals. Among this group crystals with R = Gd, Tb, Dy, Y, Ho and Yb have been grown in this work using the floating zone image furnace. Therefore, a very similar crystal synthesis procedure as for the $Y_{1-x}Ca_xTiO_3$-system described in Chap. 5.2 has been applied. In this chapter the growth optimization and control process will be reported in detail on the example of $GdTiO_3$. Although the $R\mathrm{TiO}_3$ crystal growth is more simple due to the absence of Ca, all growth parameters have to be adjusted for each system again. Especially, the growth of $R\mathrm{TiO}_3$ with smaller R-ionic radii turned out to be rather difficult. The reason might be that the well-known Goldschmidt tolerance factor t [80], defined

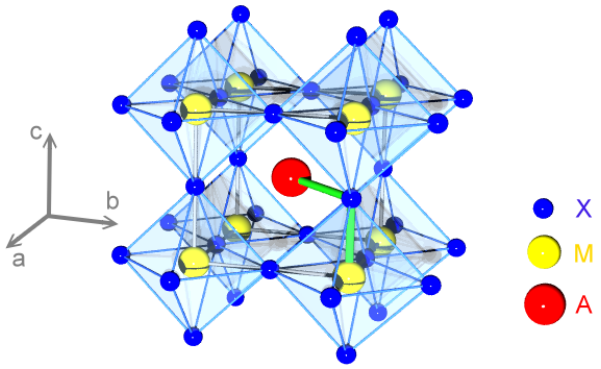

Figure 5.11: Unit cell of the undistorted perovskite AMX_3 with corner-sharing MX_6-octahedra.

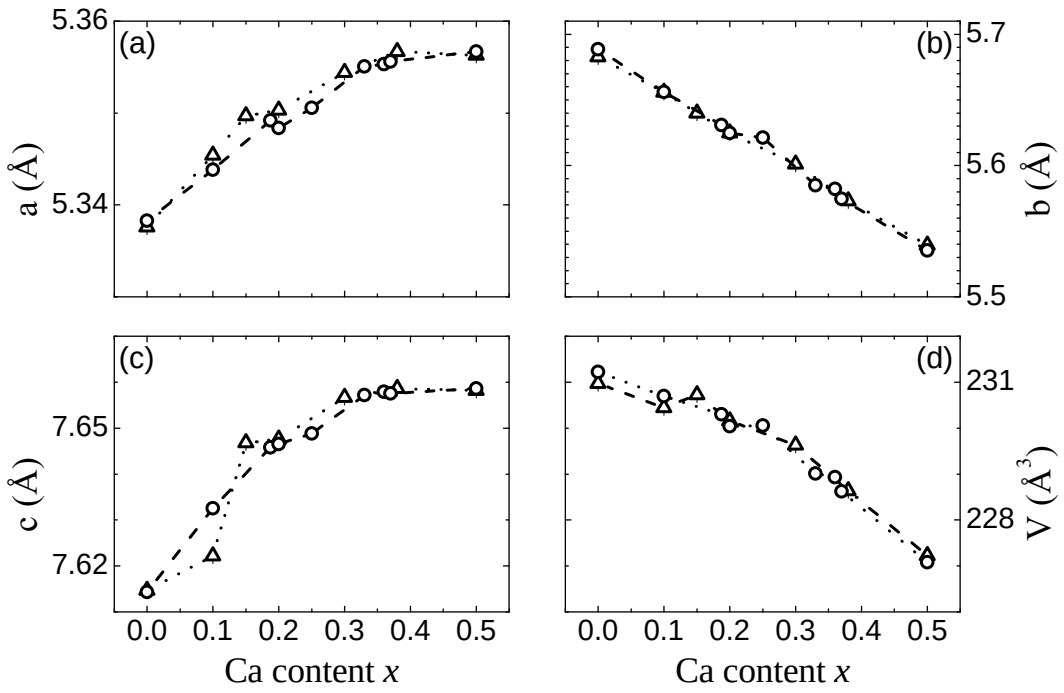

Figure 5.10: (a-d) Room-temperature lattice parameter and unit cell volume of *ACK090*, *ACK011*, *ACK045*, *ACK013*, *ACK044*, *ACK015*, *ACK016*, *ACK083* and *ACK088* (*circles*) and from Ref. [79] (*triangles*).

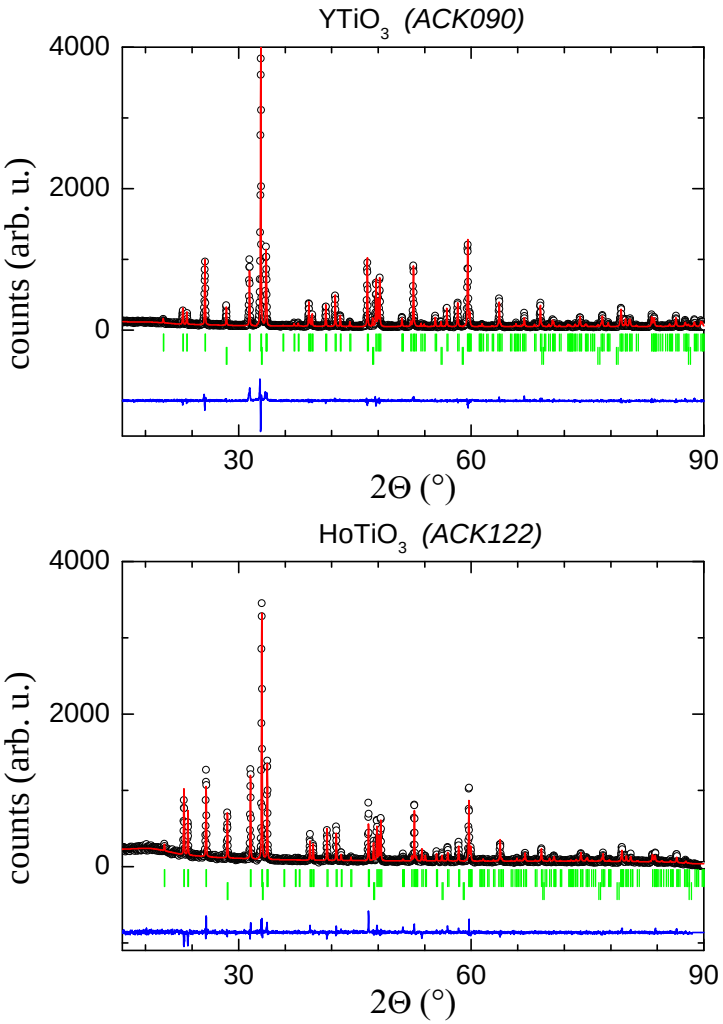

Figure 5.13: Powder X-ray diffraction patterns and Rietveld fits for $YTiO_3$ *ACK090* and $HoTiO_3$ *ACK122*; *black cricles:* measured data (I_{obs}), *red line:* Rietveld fit (I_{calc}), *blue line:* $I_{obs} - I_{calc}$, *green bars:* bragg peak positions.

by Eq. 5.1

$$t = \frac{r_A + r_X}{\sqrt{2} \cdot (r_M + r_X)} \tag{5.1}$$

is already too far away from the ideal value of 1 for these type of perovskite compounds. For the ideal closed packing the A-X bondlength has to be $\sqrt{2}$ times larger than the M-X bond lengths (*green lines* in Fig. 5.11). Hence, the tolerance factor is 1 for the ideal, undistorted perovskite structure. In the titanate series, only $EuTiO_3$ and $SrTiO_3$ have the ideal perovskite structure with a $3d^0$ configuration of the Ti^{4+}-ion. But as the ionic radius of the Yb^{3+}-ion is about 0.27 Å smaller than the radius of the Sr^{2+}-ion (for a coordination of 8) [82], the tolerance factor is far from the ideal value of 1. This effect

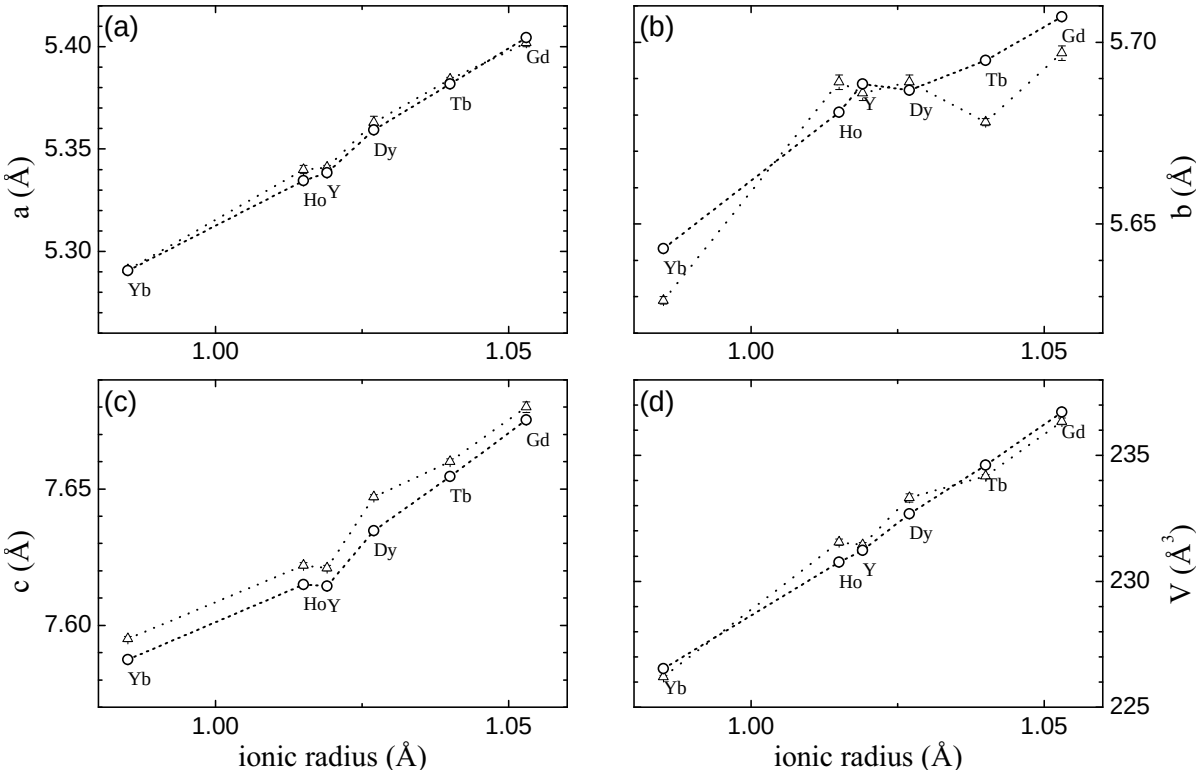

Figure 5.14: Lattice parameter and unit cell volume of $R\mathrm{TiO_3}$ (R = Gd, Tb, Dy, Y, Ho and Yb). *Circles* denote the values for *ACK043*, *ACK121*, *ACK115*, *ACK090*, *ACK122* and *ACK123* grown in this work and *triangles* the lattice parameter from Ref. [81]

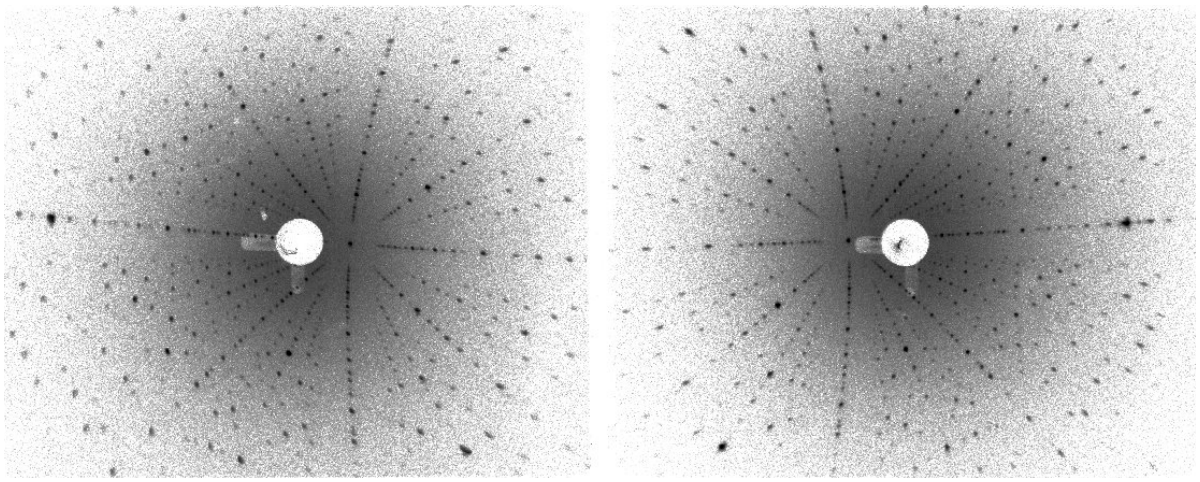

Figure 5.15: Laue photos from two sides of $\mathrm{DyTiO_3}$ (*ACK115*).

is even enhanced as the Ti^{3+}-ion in $YbTiO_3$ has an about 10% larger ionic radius than the Ti^{4+}-ion in (Sr/Eu)TiO_3. Unfortunately no ionic radius for a coordination of 12 is given for the Yb^{3+}-ion in Ref. [82]. But a linear extrapolation of the given values for coordinations of 6, 7, 8 and 9 to a value of 12 indicates an extrapolated radius of 1.215 Å (compared to 1.44 Å for $SrTiO_3$). Assuming this extrapolated ionic radius for the Yb^{3+}-ion, the tolerance factor decreases from 1.009 for $SrTiO_3$ to 0.928 for $YbTiO_3$. Probably, this rising deviation from the ideal close-packing makes the growth of RTiO$_3$ with smaller R-ionic radius more difficult. One try to grow $LuTiO_3$ with an even smaller R-ionic radius than for $YbTiO_3$ was not successful.

Finally, RTiO$_3$ with smaller R-ionic radius have been grown successfully in this work using the floating zone technique (see Fig. 5.12) among which $YbTiO_3$ is the compound with the smallest R-ionic radius. In Fig. 5.13 the powder X-ray diffraction patterns for two RTiO$_3$crystals are shown. All RTiO$_3$ samples are single phase. For the exact determination of the lattice parameter at room-temperature, Si was used as a standard (second phase in Fig. 5.13). The resulting lattice parameter are plotted in Fig. 5.14 as a function of the R-ionic radius [82] for a coordination of 8 as this is a coordination which is available for all R-ions. Furthermore, one may argue, that the orthorhombic distortions in the $GdFeO_3$ structure lift the equal size of the twelve R-O distances reducing the effective coordination of the R ion a little bit such that a smaller coordination than 12 may be justified. The unit cell volume exhibits the expected monotonic increase from $YbTiO_3$ to $GdTiO_3$. A comparison with the lattice parameter of Ref. [81] indicates very similar values.

Figure 5.12: Photos of RTiO$_3$ crystals (top down: $YTiO_3$, $SmTiO_3$, $DyTiO_3$, $GdTiO_3$, $TbTiO_3$, $HoTiO_3$ and $YbTiO_3$).

Furthermore, Laue photographs from the front and the back side of a RTiO$_3$- single crystal prove the single crystallinity of these crystals grown in this work. As an example in Fig. 5.15 the two Laue photos of both sides of the $DyTiO_3$ crystal *ACK115* grown in this work is shown.

EDX measurements indicate a close to stoichiometric composition of the RTiO$_3$-crystals grown in this work. For example, the Gd concentration in the $GdTiO_3$-crystal *ACK043* amounts to 98.6(1.5)% averaged over 13 EDX measurements for two different pieces. Since the EDX measurements seem not to be perfectly reliable for the $Y_{1-x}Ca_xTiO_3$- and $R_{1-x}Ca_xTiO_3$- system, complementary information was drawn from the refinement of single crystal X-ray diffraction data. The refinement of the R content/occupation indicates a value which is not far from the stoichiometric composition. The Gd concentration in the $GdTiO_3$-crystal *ACK043* amounts to 99.1(1)% [1]. Further-

[1] GoF: 2.32, R/Rw: 1.72%/3.11%; 29024 reflections collected up to $2\Theta_{max} = 120.3°$ with a redundancy of 16.3 and an internal R-value of 3.09%.

more, the oxygen excess is close to zero within the accuracy of the TGA measurements. For example for $GdTiO_3$, the excess oxygen of the crystal *ACK043* amounts to 0.007(1), which is not far from the stoichiometric value with regard to the general accuracy of these measurements. Additionally, the sample quality can be checked by the magnetic ordering temperature, which is higher for samples with higher sample quality. This might be the best method to test the sample quality since defects and a non stoichiometric composition usually lower the magnetic ordering temperature, whereas EDX measurements suffer from measurement and even systematic errors and TGA measurements are also difficult if an extremely high accuracy is demanded. In Fig. 5.16 the magnetic

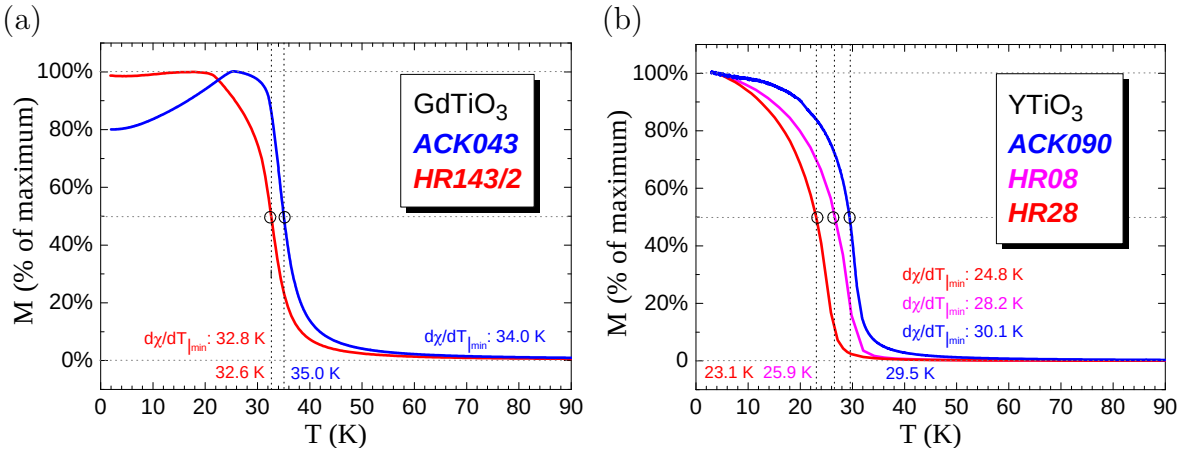

Figure 5.16: Magnetic susceptibility or magnetisation measurements for the determination of the magnetic ordering temperature of (a) $GdTiO_3$, (b) $YTiO_3$.

susceptibility is shown for two $R\mathrm{TiO}_3$-samples grown in this work comparing it with other crystals grown in Ref. [78, 83] which are also published in Ref. [84, 85]. As can be seen, the magnetic ordering temperatures are higher for the new $YTiO_3$ and $GdTiO_3$ crystals grown in this work underlining their high crystal quality. In this work, the value of T_C of each crystal was determined by the derivative of the magnetization as a function of temperature. The temperature exhibiting an extremal value of $\partial M/\partial \mathrm{T}$ can be considered to be the magnetic ordering temperature [86]. In Ref. [78] changes of the inverse susceptibility were used for the determination of T_C yielding slightly overestimated values of T_C: for example a value of 34 K was given for T_C of $GdTiO_3$ (*HR143/2*) in Ref. [78]. But the value determined by the method applied in this work yields a value of 32.8 K for the same sample *HR143/2* and a value of 34.0 K for the $GdTiO_3$ crystal *ACK043* grown in this work.

In Fig. 5.17, the inverse magnetic susceptibility for the $GdTiO_3$ crystals *ACK032*, *ACK022*, *ACK033*, *ACK021* and finally *ACK043* (from left to right) are shown which have been measured by M. Reuther using a vibrating sample magnetometer (VSM). For the example of $GdTiO_3$ the result of the growth optimization process is visualized in this figure. This process includes the optimization of the growth rate, the lamp power, the Ti doping x within the feeding rod etc. For the feeding rod the following starting

materials have been mixed together and ground for at least 45 minutes: $\frac{1}{2}\times Gd_2O_3 + \frac{1}{2}\times Ti_2O_3 + x\times Ti \rightsquigarrow Gd_{1.00}Ti_{1.00+x}O_{3.00}$. The Ti-doping in the seeding rod of each crystal is summarized in Tab. 5.2. In general, a smooth gradient $\Delta(l)$ of Ti-doping x has been applied over the whole length l_{tot} of the feeding rod with $x \equiv x(l)$ tending towards zero at the end of the feeding rod. This drift of Ti-doping $x(l) = x_0 - \Delta(l)$ is important, as the crystals become deoxidized otherwise and the properties of the crystal change between the upper and lower part of the crystal. The oxygen content has been weighted stoichiometrically. Hence, only two chemical parameters had to be adjusted, the Ti-doping and the gradient $(x_0 - \Delta(l))$ within the feeding rod. One of the most important parameters, the lamp power which determines the evaporation rates on the one hand and guarantees a complete melting and mixture of all educts on the other hand has to be adjusted for each growth process again as it is always different since it depends on the translucency of the glass tube and the thickness of the feeding rod etc. (Hence, the lamp power is not listed in the Tab. 5.2.) The lamp power has to be adjusted

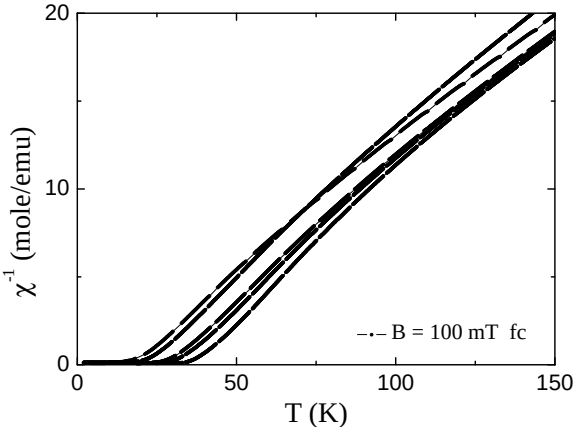

Figure 5.17: Inverse magnetic susceptibility of $GdTiO_3$ (compare Tab. 5.2).

crystal	**Ti-doping**	**lamps**	**atmosphere, flow, p**	**growth**	T_C
ACK021	+0.40%	1000 W	Ar, 0.5 l/min, 2.0 bar	8 mm/h	29.9 K
ACK022	+0.80%	1000 W	Ar, 1 l/min, 2.4 bar	7 mm/h	18.7 K
ACK032	+1.20%	1000 W	Ar 0.7 l/min, 2.0 bar	5 mm/h	17.7 K
ACK033	+0.04%	1000 W	Ar, 1 l/min, 1.7 bar	4 mm/h	22.6 K
ACK043	+0.86%	1000 W	Ar, 1 l/min, 3.0 bar	5 mm/h	34.0 K

Table 5.2: Growth parameters for $GdTiO_3$ together with T_C (VSM-measurement).

carefully until the properties of the melting zone are optimal - no unreacted material should be found in the crystal afterwards and the evaporation rates should be adopted to the Ti-doping x. Also the growth rate was modified during the whole growth process in order to optimize the melting zone and the duration of evaporation etc. Typically, this parameter varies somewhere between 2 mm/h and 6 mm/h, for $GdTiO_3$ which was the first $RTiO_3$-crystal grown in this work, the growth rate is listed in Tab. 5.2.

Returning to the magnetic measurements shown in Fig. 5.17 and 5.18 (a), the $GdTiO_3$ crystal *ACK043* has a magnetic ordering temperature of 35.0 K where the Ti-sublattice (Ti-array) orders ferromagnetically. Then, at ∼25 K the Gd-sublattice orders ferromagnetically but antiferromagnetically to the Ti-sublattice. The magnetization curve shows no hysteresis as can be seen in Fig. 5.18 (a). A comparison of T_C with literature data is listed in Tab. 5.3 and the value of T_C for the $GdTiO_3$ crystal *ACK043* is larger than for other crystals reported in literature.

In Tab. 5.3 also the magnetic ordering temperatures of all other $R\mathrm{TiO_3}$-crystals grown in this work are compared with literature data. Furthermore, the magnetic susceptibility and magnetization curves of all ferromagnetic $R\mathrm{TiO_3}$-crystals grown in this work are shown in Fig. 5.18. The magnetization measurements of the other $R\mathrm{TiO_3}$ crystals not discussed yet have been performed by S. Heiligen using a SQUID.

Titanate	T_C(*R*-array)	**ACK series** T_C(Ti-array)	**Ref. [81]** T_C(Ti-array)	**Ref. [87]** T_C(Ti-array)
$GdTiO_3$	25 K	**34.0 K**	32 K	**34 K**
$TbTiO_3$	12 K	**57.3 K**	49 K	49 K
$DyTiO_3$	14 K	**64.6 K**	60 K	64 K
$YTiO_3$	–	**30.1 K**	**30 K**	29 K
$HoTiO_3$	8 K	**57.3 K**	56 K	56 K
$YbTiO_3$		**44.1 K**	36 K	41 K

Table 5.3: Magnetic ordering temperatures for ferromagnetic $R\mathrm{TiO_3}$ grown in this work compared with ordering temperatures from Ref. [81, 87]. The ordering temperatures for the crystals grown in this work have been determined by the position of the extremal value of the derivative of χ. The largest value for the magnetic ordering temperature is indicated with bold letters/numerics.

For the $TbTiO_3$ crystal *ACK121* the magnetic susceptibility was measured for all three crystallographic axes. The temperature dependency of χ is very similar for the *a*- and *c*-direction. However, the absolute values are two orders of magnitude (factor ∼80) larger for the *c*-direction. This result does not support the F_x type ferromagnetic order reported for both the Ti- and *R*- sublattice [87]. The behaviour of χ in *b*-direction, however, aggrees with the C_y type AFM order of the *R*-sublattice (*R*-array) [87], but, the magnetic ordering temperature of the *R*-ions is usually distinctly lower than for the Ti-sublattice. This result either indicates strong *R*-O-Ti interactions starting at the magnetic ordering temperature of the Ti-sublattice or it points to some participation of the Ti-sublattice on the C_y-type AFM order. An additional measurement with 50 mT field-cooled and $c\|H$-orientation has been perfomed after measuring the hysteresis loop $M(H)$ (*dashed line*), i. e. with a large remanence. These measurements turned out to indicate the ordering temperature of the *R*-sublattice very accurately. As is indicated by the *black arrow* the magnetic susceptibility attains very large values below the *R*-sublattice ordering temperature. The derivative of this second measurement of χ has a sharp maximum at ∼12 K. Hence, the ordering temperature of the *R*-sublattice is roughly 12 K which is distinctly lower than the magnetic ordering temperature of the Ti-sublattice of about 57.3 K. Of cause, the additional contribution of the Ti-sublattice

may biase the values determined for the R-ordering temperature slightly since it might shift the extremum of the derivative of χ.

The $DyTiO_3$-crystal *ACK115* has a magnetic ordering temperature of 64.6 K (ordering of the Ti-sublattice). The first (#1) field-cooled (fc) susceptibility measurement (*black dotted line*) was measured after a *M-H* hysteresis curve has been measured and the magnetic field was reduced from +7 T to 50 mT. The second (#2) susceptibility measurement (*gray dashed line*) has been measured on the same sample directly (50 mT, fc) without any previous $M - H$ measurement. These two measurements indicate the ordering temperature of the Dy-sublattice which amounts to ∼14 K. Additionally, three oriented magnetic susceptibility measurements have been performed. In these zero-field cooled measurements (zfc) the value of the magnetic susceptibility is negative for the orientations along the b- and c-axis. The diamagnetic signal must have something to do with some remaining fields in the SQUID magnetometer but is not finally understood. The susceptibility in b direction is one order of magntitude larger than in c-direction (factor 17) and even two to three orders of magnitude larger than in a-direction (factor 700). This is fully in accordance with the F_y type ferromagnetic order of the Ti- and R-arrays [87]. The *M-H* hysteresis loops (inset of Fig. 5.18 (c)) exhibits large remanences and coercivities and unusually abrupt changes at the coercitivities which are much more pronounced than for the samples reported in Ref. [81]. Similar as in Ref. [81], $DyTiO_3$ exhibits the largest values for remanences and coercivities among the $R TiO_3$-series.

The $YTiO_3$ crystal *ACK090* has a magnetic ordering temperature of 30.1 K and exhibits no visible or very small coercivities and remanences similar to the observations in Ref. [81].

As can be seen in Fig. 5.18 (e) the $HoTiO_3$ crystal *ACK122* exhibits a magnetic ordering temperature of 57.3 K. In a second fc measurement after application of high magnetic fields at 2 K, the magnetic ordering temperature of the R-sublattice could be determined as ∼8 K.

The magnetical susceptibility of $YbTiO_3$ crystal *ACK123* which has the smallest rare earth ion in this series has been measured by M. Reuther using a VSM magnetometer. This (not oriented) $YbTiO_3$ crystal has a magnetic ordering temperature of 44.1 K. Additionally, the M-H hysteresis loop (not oriented) has been measured by S. Heiligen. As can be seen, the magnetization exhibits a very linear developing for high fields and no saturation can be observed even at highest fields which is very similar to the observations for $YbTiO_3$ in Ref. [81].

In summary, the magnetic susceptibility measurements document the high crystal quality of the $R TiO_3$-samples grown in this work. The magnetic ordering temperatures are listed in Tab. 5.3 and these values are also plotted in Fig. 6.1 (d) of Chap. 6.1 together with values for T_C of other crystals for a comparison. The transition temperatures of the crystals grown in this work (which have been determined by the derivative of the magnetic susceptibility) belong to the highest transition temperatures reported in literature.

Furthermore, for $TbTiO_3$, $DyTiO_3$, $HoTiO_3$ and $YbTiO_3$ powder neutron diffraction measurements have been performed at the 3T.2 diffractometer at the reactor Orphée in Saclay, France. $YTiO_3$ has been measured already in the Diploma thesis of the author

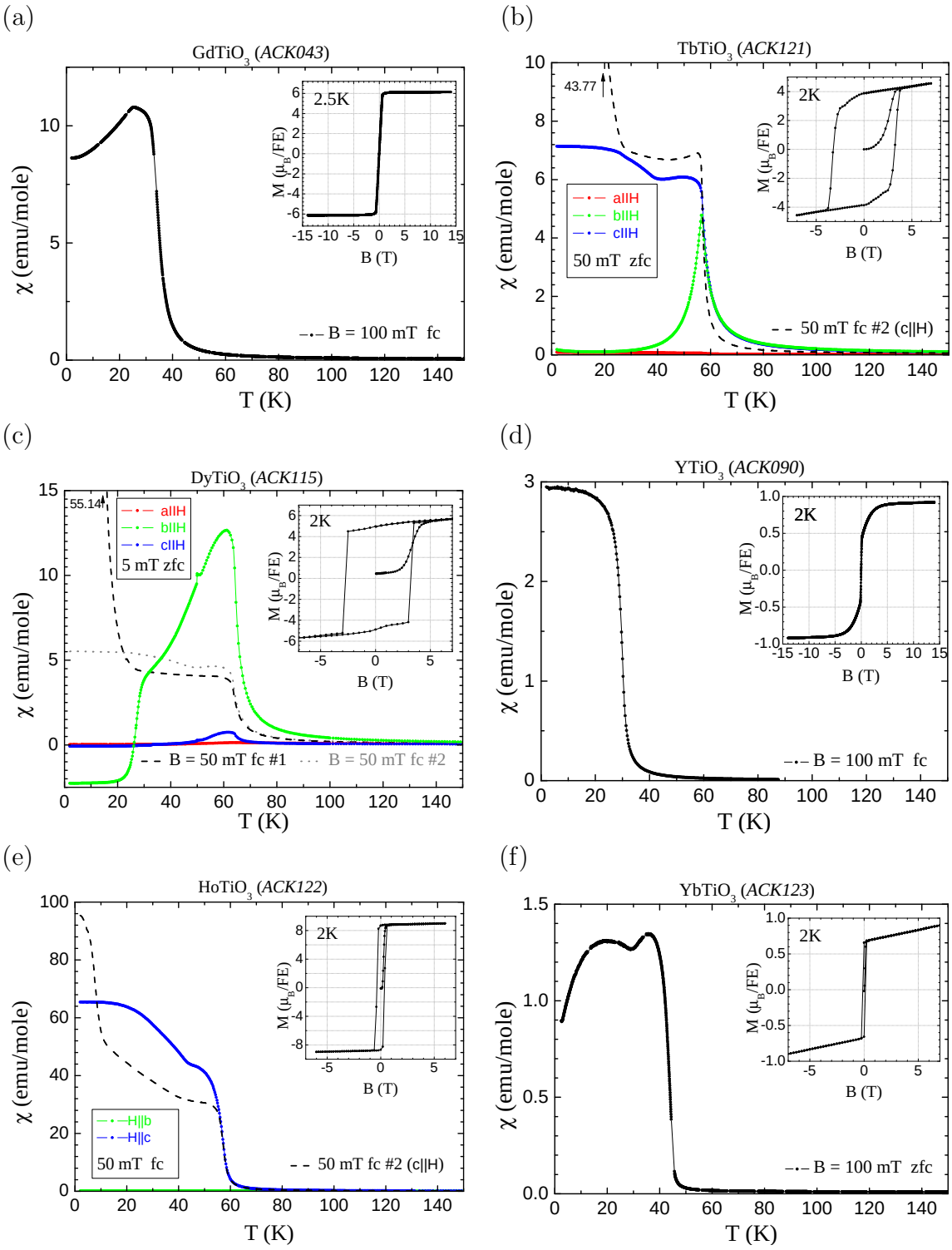

Figure 5.18: Magnetisation measurements of (a) $GdTiO_3$, (b) $TbTiO_3$, (c) $DyTiO_3$, (d) $YTiO_3$, (e) $HoTiO_3$ and (f) $YbTiO_3$.

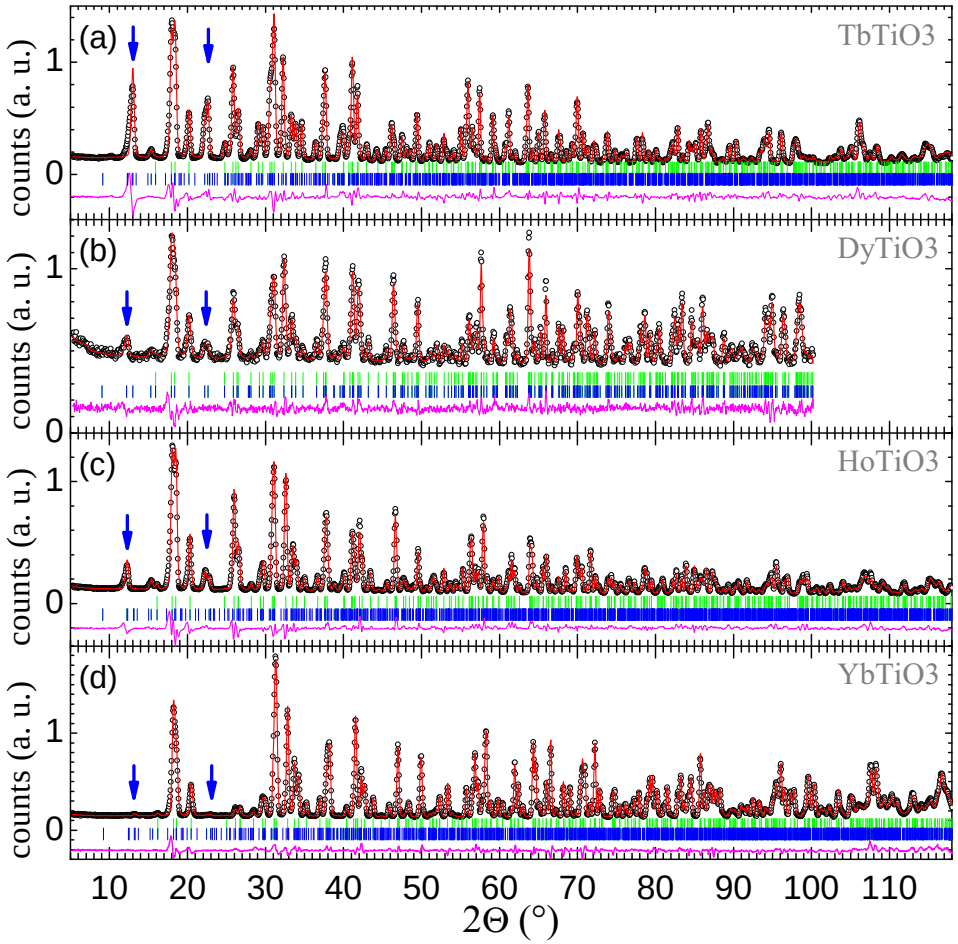

Figure 5.19: Powder neutron diffraction measurements of (a) $TbTiO_3$, (b) $DyTiO_3$, (c) $HoTiO_3$ and (d) $YbTiO_3$ measured at 2 K; *black circles*: measured data I_{obs}, *green/blue bars*: peak positions of the nuclear/magnetic peaks; *red line*: Rietveld fit (I_{calc}); *blue dotted line*: calculated contribution of the magnetic structure to I_{calc}; *blue arrows*: marked magnetic peaks.

[57]. Due to the large absorbtion of Gd, the $GdTiO_3$ sample could not be measured. Also in $DyTiO_3$ the already significant absorbtion of the Dy ions has diminished the data quality and only the data for $2\Theta \leq 100°$ could be evaluated properly. The powder neutron diffraction patterns have been analyzed and fitted using the programs *BasIreps* for the calculation of all possible irreducible representations and *FullProf* for Rietveld refinement [88]. The irreducible representations for spacegroup *Pbnm* have been also calculated and reported in Ref. [89]. Whenever possible, only one irreducible representation has been used in order to describe the magnetic symmetry at the Ti- and *R*-sites. The results of Rietveld refinement are shown in Fig. 5.19 (a-d). The strongest antiferromagnetic intensities are marked with *blue arrows*. In overall, the magnetic structures for these $RTiO_3$-compounds are in accordance with the magnetic structures reported in

Ref. [90, 91, 87] (with one exception).

For $TbTiO_3$ the irreducible representation with a ferromagnetic moment in x-direction and a C-type antiferromagnetic (AFM) moment in y-direction (F_xC_y) yields the best description of the measured data. But, exactly as described in Ref. [91] the antiferromagnetic (100) peak appears somehow skewed and highly asymetrically broadened: there is a lot of intensity which is distributed exactly between the (100) and (010) peaks as can be seen at the position of the first *blue arrow* in Fig. 5.19 (a). In Ref. [91] this problem was solved by attributing some of the integrated intensity with a ratio of 1 : 5.9 to the (010) peak. Since this ratio would be 1 : 1.2 for an antiferromagnetic moment along the z-direction, it was thought that the C-type AFM moment also has a small component in z-direction [91]. In this work, Rietveld refinement was used and the refinement of another C_z-type component did not yield an appropriate description of the data since the measured intensity is very low at the (010) peak and the largest amount of the additional intensity is distributed exactly between the (010) and (100) peaks. However, all other magnetic peaks are sharp and symmetric. Thus, the idea to fit another C_z-type component to the data does not solve the problem and there must be another reason for the additional intensity between the (010) and (100) peaks. Further neutron measurements with a higher resolution would be necessary in order to analyze the origin of these additional magnetic intensities which were observed in Ref. [91] and also in this work, now. Since another C_z component fails in describing the data, only the F_xC_y magnetic structure was fitted to the data in this work. Additionally, a ferromagnetic moment in x-direction was fitted at the Ti-site. The resulting Ti- and Tb-moments are listed in Tab. 5.4. The ordered moment at the Ti-sies amounts to $\sim 0.6\mu_B$ which is $\sim 0.15\mu_B$ lower than the ordered moment observed in the diploma thesis of the author for $YTiO_3$ - in this system without any magnetic R-ion the ordered moment amounts to $\sim 0.75(8)\mu_B$ at 2 K [57]. The concomitant appearance of ferromagnetically ordered moments at Ti- and R-sites may induce a slight biasing of the small Ti-moments. The ordered Tb-moment of $\sim 8.3\ \mu_B$ is in agreement with the total Tb-moment of 8.1(4) μ_B observed in Ref. [91].

The measurement of $DyTiO_3$ suffers from the sizeable neutron absorbtion of the Dy-ions. Therefore, the data with larger 2Θ had to be dismissed. The refinement of the magnetic moment is in accordance with the results in Ref. [91]. During the refinement the Ti-moment had to be fixed to the value of -0.6 μ_B which is between the measured values for $TbTiO_3$ and $HoTiO_3$ ($r(\mathrm{Tb}) < r(\mathrm{Dy}) < r(\mathrm{Ho})$) since the value determined by Rietveld refinement was too small and, hence, unphysical. (As there were difficulties with the neutron absorbtion of this compound, no further efforts have been made in order to investigate the origin of this small Ti-moment.) The total Dy-moment amounts to 9.0(1) μ_B which is about 7% smaller than the value of 9.7(7) μ_B reported for the Dy-moment in Ref. [91] but which agrees with this value within the error bars.

For $HoTiO_3$ the magnetic structure is in agreement with the results reported in Ref. [90]. The ordered Ti-moment is similar as in $TbTiO_3$ and the total Ho-moment amounts to 8.7(1) μ_B which is within the error bars very close to the value of 8.1(5) μ_B reported for the Ho-moment in Ref. [90].

The magnetic structure of $YbTiO_3$ exhibits some hitherto unknown features. As can

	$TbTiO_3$	$DyTiO_3$	$HoTiO_3$	$YbTiO_3$	$YbTiO_3$ *(test)*
crystal:	*ACK121*	*ACK115*	*ACK122*	*ACK123*	~
mag. order (Ti):	$\mathbf{F}_x$	$\mathbf{F}_y$	$\mathbf{F}_y$	$\mathbf{F}_z$	$\mathbf{C}_y\mathbf{F}_z$
1st component size:	-0.58(4) μ_B	-0.6 μ_B	-0.61(4) μ_B	-0.44(8) μ_B	0.77(7) μ_B
2nd component size:	-	-	-	-	-0.44(8) μ_B
total moment:	0.58(4) μ_B	0.6 μ_B	0.61(4) μ_B	0.44(8) μ_B	0.89(8) μ_B
mag. order (R):	$\mathbf{F}_x\mathbf{C}_y$	$\mathbf{C}_x\mathbf{F}_y$	$\mathbf{C}_x\mathbf{F}_y$	$\mathbf{C}_y\mathbf{F}_z$	$\mathbf{F}_z$
1st component size:	6.82(6) μ_B	4.05(7) μ_B	3.22(3) μ_B	-0.71(6) μ_B	1.72(6) μ_B
2nd component size:	4.67(4) μ_B	8.07(11) μ_B	8.11(6) μ_B	1.72(6) μ_B	-
total moment:	8.26(7) μ_B	9.03(12) μ_B	8.73(6) μ_B	1.86(6) μ_B	1.72(6) μ_B
magnetic R-factor:	6.41%	6.27%	7.17%	8.50%	8.18%

Table 5.4: Ordered magnetic moments of $R\mathrm{TiO_3}$ grown in this work compared determined at 2 K.

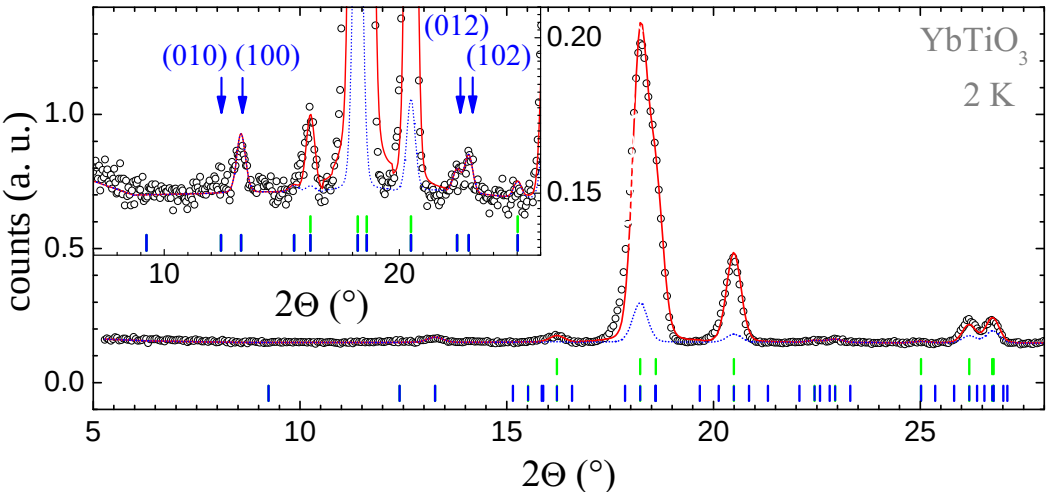

Figure 5.20: Powder neutron diffraction pattern of $\mathrm{YbTiO_3}$ crystal *ACK123* measured at 2 K at the 3T.2 diffractometer; *black circles*: measured data I_{obs}; *green/blue bars*: peak positions of the nuclear/magnetic peaks; *red line*: Rietveld fit (I_{calc}); *blue dotted line*: calculated contribution of the magnetic structure to I_{calc}.

be seen in the inset of Fig. 5.20 there are small but significant intensities at the (100), (012) and (102) peak positions which are indicative for a C-type antiferromagnetic order but there is no intensity of the (010) reflection. Thus, a C_y antiferromagnetic moment is either located at the Ti-site or at the Yb-site. Since all other compounds studied exhibit only ferromagnetic order at the Ti-site, most likely, the AFM C_y component can be attributed to the Yb-moments. However, for a final decision a temperature dependent study would be necessary, since the Yb- ordering temperature is distinctly lower than the Ti-ordering temperature. Nevertheless also the results of a fit for the C_y-component at

the Ti-sites is listed in Tab. 5.4 and denoted by the word 'test'. It should be noted that due to representation analysis of spacegroup *Pbnm* a C_y type antiferromagnetic order belongs to the irreducible representation Γ_2 with $F_xC_yG_z$ components at the Ti-site [89]. However, a fit with a F_x-type ferromagnetic order at the Ti-site yields unphysical values for the total moments of 1.2(1) μ_B and enhanced magnetic R-values of 9.7%. Also for the *R*-site the irreducible representation Γ_2 allows for F_xC_y magnetic components only. A fit with such an ordering scheme at the *R*-site yields strongly enhanced magnetic *R*-values of 12.2% and unphysical total moments of 1.7(1)μ_B (F_z) at the Ti-sites. Hence, these possibilities can be excluded and the moments at the Yb-site belong to two different irreducible representations. Other magnetic structures where the spins on one site belong to two different irreducible representations have been reported for example for $ErCrO_3$ (the Cr-moment has G_x and G_y components belonging to the irreducible representations Γ_4 and Γ_1 respectively) and also for the $RTiO_3$-system [92, 90, 91]. Concluding, the C_y-type AFM order observed in this work for $YbTiO_3$ has not been reported in literature so far. Hitherto, only ferromagnetic F_z-components were reported for the magnetic ions in $YbTiO_3$. Finally, it should be noted that the magnetic structure can be described with the same irreducible representation in $LaTiO_3$ to $YTiO_3$, i. e. Γ_4 [89] with $G_xA_yF_z$ components. Only the size of G_x versus F_z components changes between AFM $LaTiO_3$ and FM $YTiO_3$, see Chap. 6.1. But this ordering scheme is obviously changed by the introduction of heavier rare earth ions (*RE*) which affect the ordering at the Ti-sites via *RE*-Ti interactions, see Tab. 5.4.

In Tab. 5.5, the structural parameters derived from Rietveld refinement are listed. A discussion of these values is given in Chap. 6.1.

	$TbTiO_3$	$DyTiO_3$	$HoTiO_3$	$YbTiO_3$
crystal:	*ACK121*	*ACK115*	*ACK122*	*ACK123*
a (Å) :	5.3804(2)	5.3526(5)	5.3131(2)	5.2798(1)
b (Å) :	5.6809(2)	5.6856(5)	5.6864(2)	5.6422(1)
c (Å) :	7.6284(3)	7.6174(7)	7.5825(3)	7.5555(1)
x (R) :	0.9826(6)	0.9789(4)	0.9777(5)	0.9763(2)
y (R) :	0.0708(5)	0.0738(3)	0.0750(4)	0.0761(2)
z (R) :	1/4	1/4	1/4	1/4
x (Ti) :	0	0	0	0
y (Ti) :	1/2	1/2	1/2	1/2
z (Ti) :	0	0	0	0
x (O1) :	0.1131(8)	0.1175(10)	0.1202(7)	0.1269(3)
y (O1) :	0.4609(7)	0.4598(12)	0.4570(7)	0.4509(4)
z (O1) :	1/4	1/4	1/4	1/4
x (O2) :	0.6919(5)	0.6911(7)	0.6899(5)	0.6875(3)
y (O2) :	0.3081(5)	0.3097(8)	0.3097(5)	0.3120(3)
z (O2) :	0.0553(4)	0.0580(5)	0.0575(3)	0.0609(2)
$B_{iso}^{(R)}$ *(Å²)* :	0.293(4)	0.140(0)	0.140(3)	0.051(1)
$B_{iso}^{(Ti)}$ *(Å²)* :	0.299(84)	0.311	0.311(83)	0.071(42)
$B_{iso}^{(O1)}$ *(Å²)* :	0.467(3)	0.424	0.424(3)	0.171(1)
$B_{iso}^{(O2)}$ *(Å²)* :	0.467(3)	0.424	0.424(3)	0.171(1)
Rp/Rwp :	6.42%/8.91%	2.80%/3.58%	5.66%/7.62%	3.90%/5.33%

Table 5.5: Structural parameters of $R\mathrm{TiO_3}$ measured at 2 K at the 3T.2 diffractometer. As the $\mathrm{DyTiO_3}$ sample suffers from neutron absorbtion, the (thermal) displacement parameters have been fixed to the values derived from the refinement of $\mathrm{HoTiO_3}$. The displacement parameter of O2 has always been restricted to the value of O1 in order to avoid too many free fitting parameter.

5.4 $R_{1-x}\mathbf{Ca}_x\mathbf{TiO}_3$

The insulator-to-metal transition in the $R\mathrm{TiO_3}$-system shifts with decreasing R-ionic radius to higher levels of hole-doping. Whereas, the $\mathrm{LaTiO_3}$-system becomes metallic around $x \approx 0.05$ [93-95], the $\mathrm{Y_{1-x}Ca_xTiO_3}$-system stays insulating up to hole doping levels of roughly 35-40% [96-98]; see also Chap. 6.2. In order to extend the insulator-to-metal transition to higher hole doping levels, the Y-ion in $\mathrm{Y_{1-x}Ca_xTiO_3}$ has been substituted with smaller Er- and Lu- ions. Hence, a series of samples of the $\mathrm{Er_{1-x}Ca_xTiO_3}$-, $\mathrm{Er_{(1-x)/2}Lu_{(1-x)/2}Ca_xTiO_3}$- and the $\mathrm{Lu_{1-x}Ca_xTiO_3}$-system have been grown in this work using the floating zone furnace.

For the $\mathrm{Lu_{1-x}Ca_xTiO_3}$-system the difficulties of the growth of $R\mathrm{TiO_3}$-systems with small R-ionic radius and the difficulties of the growth of Ca-doped titanate systems

come together. However, large single crystals of $Lu_{1-x}Ca_xTiO_3$ have been grown after an optimization of the growth conditions; see Fig. 5.24.

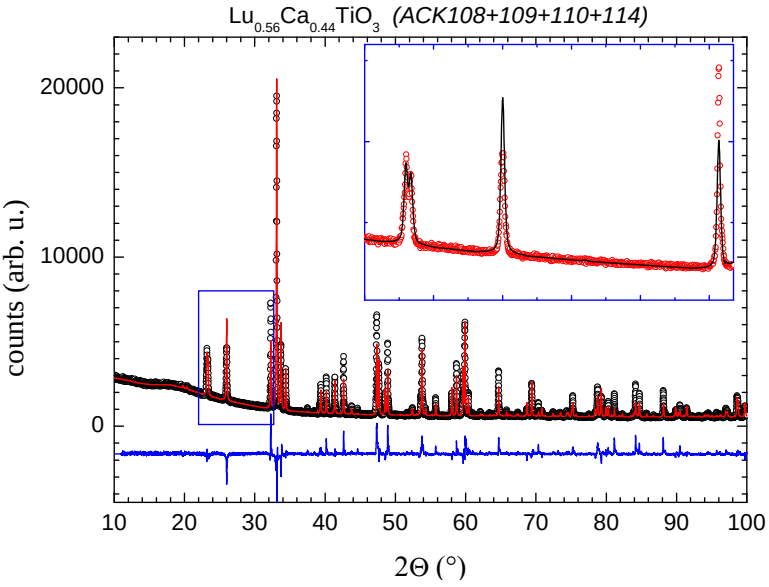

Figure 5.22: Powder X-ray diffraction patterns of *ACK108 + ACK109 + ACK110 + ACK114*; *black cricles:* measured data (I_{obs}), *red line:* Rietveld fit (I_{calc}), *blue line:* $I_{obs} - I_{calc}$, *green bars:* bragg peak positions.

Powder X-ray diffraction measurements of $Lu_{0.56}Ca_{0.44}TiO_3$ (mixture of *ACK108 + ACK109 + ACK110 + ACK114*) are shown in Fig. 5.22. As can be seen in the inset, there is no impurity phase visible. Hence, these samples are single phase. The lattice parameter amount to 5.31813(7) Å, 5.55200(8) Å and 7.63365(10) Å.

Figure 5.21: Photos of $Lu_{0.56}Ca_{0.44}TiO_3$ (*ACK110* and *ACK114*).

Neutron Laue diffraction measurements have been performed in collaboration with B. Ouladdiaf and M. T. Fernandez-Diaz at the Neutron Laue diffractometer Orientexpress at the ILL in Grenoble, France. Laue images were collected at different parts over the whole crystal length. Reflections resulting from the neutron Laue diffraction measurements of three different parts of the $Lu_{0.56}Ca_{0.44}TiO_3$ crystal *ACK110* are shown in Fig. 5.23. Red points indicate the positions of the indexed reflections using the Laue indexation program OrientExpress [99]. These measurements of the bulk crystal shown in Fig. 5.24 (top) prove the single crystallinity of this crystal as the neutron beam penetrates the whole crystal. This fact together with the broader neutron beam also explains the broader reflection profiles of these Neutron Laue measurements compared to the X-ray case. These laue diffraction photos indicate an untwined sample since Laue photos of

twinned crystals exhibit additional reflections in vicinity of the reflections of the first domain.

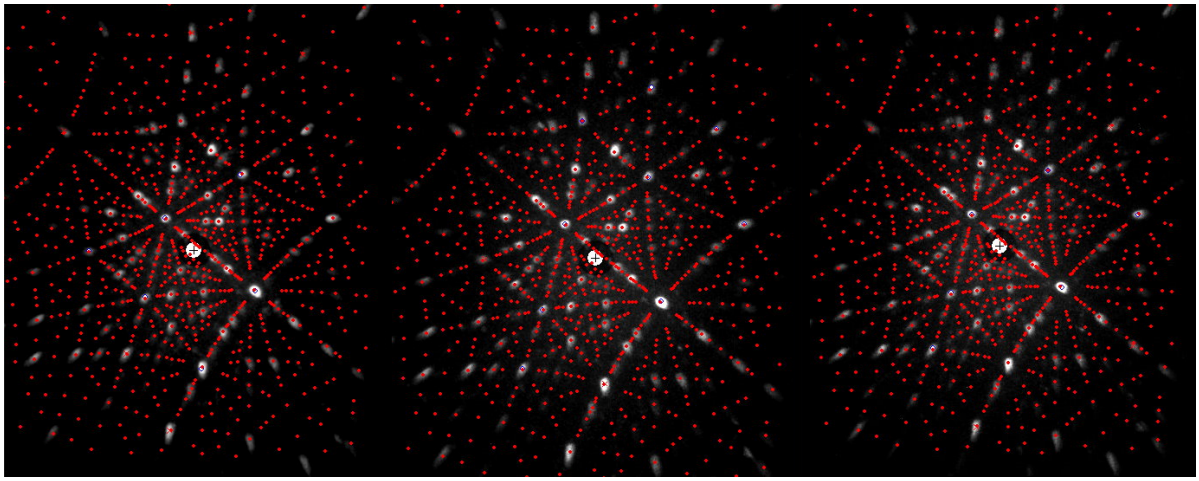

Figure 5.23: Neutron Laue diffraction photos from three different parts of the $Lu_{0.56}Ca_{0.44}TiO_3$ crystal *ACK110*. Red points indicate fits to the data.

crystal	x **(nom.)**	R**-ion**	x **(EDX)**	x **(X-ray)**	**GoF/R/Rw**	δ **(TGA)**
ACK024	0.40	Er	39(1)%	39.9(1)%	1.46/2.03%/2.81%	-0.004(1)
ACK026	0.43	Er	42(1)%	43.7(1)%	1.46/1.79%/2.83%	
ACK028	0.45	Er	44(2)%	43.3(1)%	1.89/1.83%/3.84%	
ACK030	0.47	Er	45(2)%	47.2(1)%	3.49/1.75%/4.16%	
ACK031	0.50	Er	50(2)%	50.3(1)%	2.10/2.91%/3.75%	
ACK039	0.40	$Er_{\frac{1}{2}}Lu_{\frac{1}{2}}$		40.3(2)%	1.44/1.90%/2.91%	
ACK041	0.43	$Er_{\frac{1}{2}}Lu_{\frac{1}{2}}$	40.0(3)%	45.4(2)%	1.79/1.94%/3.93%	0.013(1)
ACK038	0.36	Lu		35.9(2)%	2.55/2.14%/4.39%	
ACK042	0.50	Lu	45.4(4)%	50.1(4)%	1.99/1.98%/4.11%	0.018(1)
”	∼	∼	∼	49.6(1)%	1.54/2.04%/2.86%	∼
”	∼	∼	∼	49.8(4)%	1.61/3.01%/4.40%	∼
”	∼	∼	∼	48.6(2)%	1.61/3.01%/4.40%	∼
ACK048	0.45	Lu		48.6(1)%	1.64/1.75%/3.30%	0.017(1)
ACK055	0.43	Lu		46.9(1)%	1.42/1.87%/2.83%	-0.002(0)
ACK082	0.44	Lu		44.2(1)%	2.46/2.57%/4.87%	0.022(1)
ACK114	0.44	Lu		44.2(1)%	2.46/2.57%/4.87%	-0.012(1)

Table 5.6: Calcium and oxygen content of $R_{1-x}Ca_xTiO_{3+\delta}$ determined by single crystal X-ray diffraction and TGA respectively.

The Ca-content determined by EDX and that refined in single crystal X-ray diffraction measurements are shown together with the oxygen stoichiometry determined by TGA in Tab. 5.6. However, the EDX measurements did not seem reliable, especially for the determination of the compositions in the titanates containing Lu. In order to study the large discrepancies of EDX measurements and the nominal Ca concentration, an

intensive study of the Ca content has been performed on the half-doped $Lu_{0.5}Ca_{0.5}TiO_3$ crystal *ACK042*. In total, 20 EDX measurements on several sample pieces have been made indicating a rather constant Ca concentration of 45.4(4)% in average which is far away from the nominal composition of 50%. In order to get further information, four different samples taken from the $Lu_{0.5}Ca_{0.5}TiO_3$ crystal have been ground carefully to spheres of 38μm to 110μm radius and measured with very precise single crystal X-ray diffraction measurements. One of these measurements is a synchrotron radiation single crystal X-ray diffraction measurement performed at the beamline D3 at Hasylab/DESY in Hamburg which is used for electron density measurements usually. All these measurements on four samples from different parts of the crystal including the synchrotron measurement indicate a Ca concentration of 49.5(3)% in average which is close to the nominal composition; see Tab. 5.6. Hence, the EDX measurements do not seem to be reliable, probably the Lu standard is not appropriate. Also for the $Er_{1-x}Ca_xTiO_3$-system the EDX measurements often indicate a lower Ca-stoichiometry but with a larger statistical spread which may result from surface effects as the relative orientation of the sample surface to the emitted X-ray beam plays an important role on the the intensities of heavier versus lighter elements. Therefore, the analysis of the Ca-content by single crystal X-ray diffraction may be more accurate and more reliable for the (Lu,Er,Ca)TiO_3-system than EDX measurements and no further EDX measurements have been applied for the $Lu_{1-x}Ca_xTiO_3$-crystals grown later.

5.5 $La_{2-x}Sr_xNiO_4$

Using the floating zone image furnace a $La_{2-x}Sr_xNiO_4$ (LSNO) single crystal with $x = 0.12$ (*ACK117*) has been grown. A growth strategy more similar to the $Y_{1-x}Ca_xTiO_3$-synthesis route described in Chap. 5.2 than to the strategies described in Ref. [100, 101] has been applied for the growth of the $La_{2-x}Sr_xNiO_4$-system. Some reasons for this choice are that the La_2NiO_4- and $La_{2-x}Sr_xNiO_4$- systems tend to intercalate excess oxygen - see Chap. 9.1 - which is a somehow similar problem as in the titanate system where the Ti^{4+}-ion has the most stable oxidation state and any oxidation of the Ti^{3+}-ion has to be prevented during the synthesis. Furthermore, also the evaporation of Ni has to be counterbalanced. In order to cope with this Ni-evaporation, some extra Ni has been added to the starting materials, very similar to the growth strategy in the titanate case. For the feeding rod the following starting materials have been mixed together and ground for about one hour: $(1-\frac{x}{2})\times La_2O_3 + (\frac{x}{2}+y)\times SrCO_3 + (\frac{x}{2}-y)\times SrO_2 + (1+y)\times NiO \rightsquigarrow La_{2-x}Sr_xNi_{1.00+y}O_4 + (\frac{x}{2}+y)\times CO_2\uparrow$. For the crystal *ACK117* an Ni-excess y of 0.5% has been applied. In this work, hygroscopic R_2O_3 starting materials like La_2O_3 always have been heated for 12 hours at 900°C before weighing. In the growth process the main attention has been turned to the establishment of growth conditions which support a minimum of Ni-evaporation very similar as described for the $Y_{1-x}Ca_xTiO_3$-system in Chap. 5.2.

Figure 5.24: Photo of LSNO $x = 0.12$ (*ACK117*).

Powder X-ray diffraction measurements from a piece of the bottom of this crystal prove that the crystal *ACK117* is single phase right from the beginning of the growth. In Fig. 5.25 a Rietveld fit with space group *Cmca* is shown. The second phase is the Si standard. In the inset of this figure the splitting of the (2K0) and (0K2) peaks with K = 0, 4 are shown. Hence, the LSNO-sample is orthorhombic at room-temperature with an orthorhombic splitting $\epsilon = 2\cdot\frac{a-b}{a+b}$ of 0.465×10^{-2}. This value is close to the value of ϵ of a $La_{2-x}Sr_xNiO_4$-sample with $x = 0.10$ which amounts to 0.426×10^{-2} [102]. This value fits also nicely in the LSNO phase diagram reported in Ref. [103] where a sample with $x + 2\cdot\delta \approx 0.09$ has a value $\epsilon \approx 0.57\times10^{-2}$. These results indicate that no significant amount of excess oxygen is incorporated in the LSNO-crystal *ACK117*. The lattice parameters of this crystal amount to 5.48056(19)Å, 12.60571(40)Å and 5.45511(20)Å (space group *Cmca*).

Laue photographs from two sides of the crystal indicate the single crystallinity of this crystal; see Fig. 5.26.

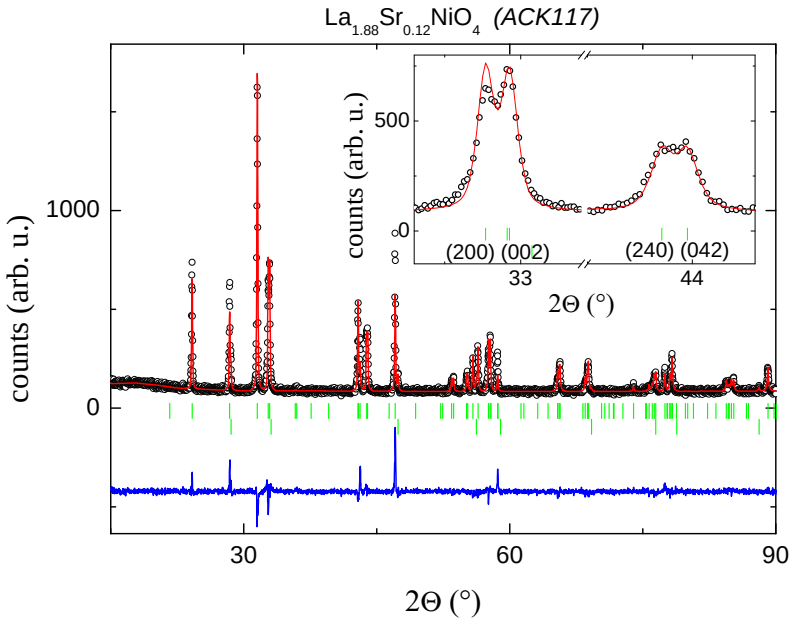

Figure 5.25: Powder X-ray diffraction patterns and Rietveld fits of $La_{1.88}Sr_{0.12}NiO_4$ *ACK117*; *black cricles:* measured data (I_{obs}), *red line:* Rietveld fit (I_{calc}), *blue line:* $I_{obs} - I_{calc}$, *green bars:* bragg peak positions.

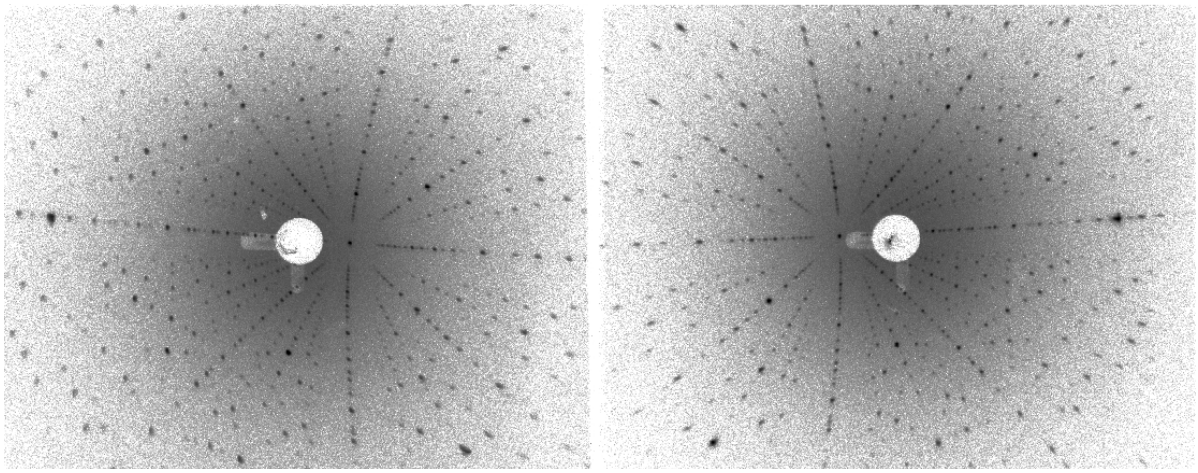

Figure 5.26: Laue photos from two sides of $La_{1.88}Sr_{0.12}NiO_4$ (*ACK117*).

5.6 $R\mathbf{MnO_3}$

For neutron scattering experiments [104] RMnO$_3$-crystals have been grown in this work. Therefore, a similar synthesis route as for the RTiO$_3$-system has been applied and adopted to the manganite system which has the great advantage, that there are not such

severe oxidation problems as in the titanate synthesis and, hence, only the evaporation of Mn has to be counterbalanced, which is a similar problem as the Ti-evaporation in the titanate growth. In order to cope with the evaporation of Mn, few extra Mn x has been added to the stoichiometrically composed starting materials in the feeding rod and the growth conditions have been optimized for a minimization of Mn-evaporation very similar as in the titanate synthesis; see Chap. 5.2. Therefore, the following starting materials have been ground together for at least 45 minutes: $\frac{1}{2} \times R_2O_3 + \frac{1}{2} \times Mn_2O_3 + x$ Mn $\rightsquigarrow R\mathrm{Mn}_{1.00+x}\mathrm{O}_3$. The basic growth parameters are listed in Tab. 5.7. A photo of some $R\mathrm{MnO}_3$-crystals grown in this work is shown in Fig. 5.27. (from top to the bottom: TbMnO_3 *ACK103*, GdMnO_3 *ACK105* and DyMnO_3 (*ACK116*)). The (Tb/Dy)MnO_3-cyrstals have the tendency to crack easily. One possible explanation might be that these compounds are close to the hexagonal perovskite phase [105] which appears for smaller R-ionic radius in the manganite system and which may be connected somehow to this problem. A GdMnO_3-crystal grown also in this work does not exhibit such problems which may support this interpretation.

As indicated by powder X-ray diffraction, the $R\mathrm{MnO}_3$-crystals grown in this work are single phase and contain no impurity phases; see Fig. 5.28. The analysis with Laue diffraction indicates the single crystallinity of the analysed $R\mathrm{MnO}_3$-samples as shown in Fig. 5.28 for the example of DyMnO_3. The magnetic suseptibility of TbMnO_3 measured by M. Reuther using a vibrating sample magnetometer (VSM) with the crystallographic c-axis parallel to the magnetic field indicates two magnetic transition temperatures - one at 42.0 K and another at 27.5 K for the TbMnO_3-crystal *ACK106*; see Fig. 5.30 (a). The first TbMnO_3-crystal exhibits slightly lower transition temperatures 41.8 K and 27.1 K. Also, the whole magnetic susceptibility is higher and the transitions are slightly smeared out. One interpretation might be that the excess Mn doping x of 1.0% is already too large and that magnetic impurities of manganese oxides might be responsible for the slightly higher magnetic susceptibility. Hence, the doping with extra Mn should be avoided, if possible (there is only very few extra Mn in *ACK106*).

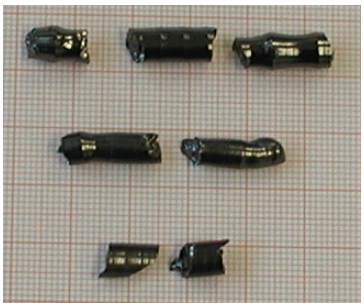

Figure 5.27: Photo of $R\mathrm{MnO}_3$.

In neutron scattering experiments performed by T. Finger and M. Braden the ex-

crystal	$R\mathbf{MnO}_3$	**Mn-doping**	**lamps**	**atmosphere**	**growth**
ACK101	TbMnO_3	+1%	1000 W	Ar	3 mm/h
ACK102	TbMnO_3	+0.5%	1000 W	Ar	6 mm/h
ACK103	TbMnO_3	+0.1%	300 W	Ar	2 mm/h
ACK105	GdMnO_3	±0%	300 W	Ar	2 mm/h
ACK106_1	TbMnO_3	+0.04%	1000 W	Ar	2 mm/h
ACK106_2	TbMnO_3	+0.04%	300 W	Ar	2 mm/h
ACK116	DyMnO_3	+0.80%	1000 W	∼80%Ar ∼20%O_2	2 mm/h

Table 5.7: Growth parameters of the $R\mathrm{MnO}_3$-synthesis in this work.

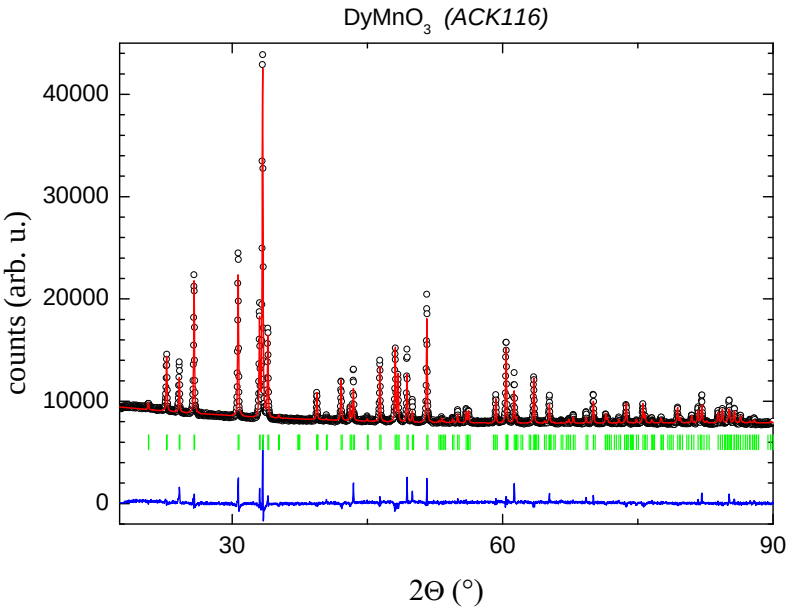

Figure 5.28: Powder X-ray diffraction patterns and Rietveld fits of $DyMnO_3$ *ACK116*; *black cricles:* measured data (I_{obs}), *red line:* Rietveld fit (I_{calc}), *blue line:* $I_{obs} - I_{calc}$, *green bars:* bragg peak positions.

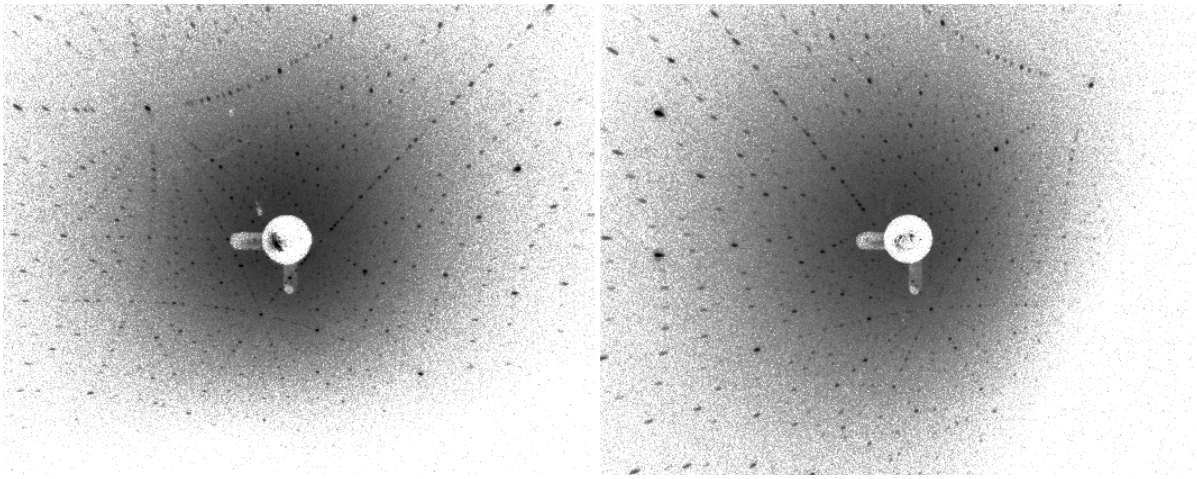

Figure 5.29: Laue photos from two sides of $DyMnO_3$ (*ACK116*).

pected magnetic intensities of the incommensurate magnetic reflections were observed. In Fig. 5.30 (b) a K-scan is shown. These intensities exhibit a distinct rise at temperatures which can be connected to the observed transition temperatures in the VSM measurements and affirm the consistency with the $TbMnO_3$-phase diagram [104]. Hence, the crystal quality of the $TbMnO_3$-single crystals is affirmed by neutron diffraction.

For the growth of $DyMnO_3$ an oxygen-rich atmosphere has been used in order to stabilize the orthorhombic perovskite phase versus the hexagonal one. Similar strategies have been reported in literature [106].

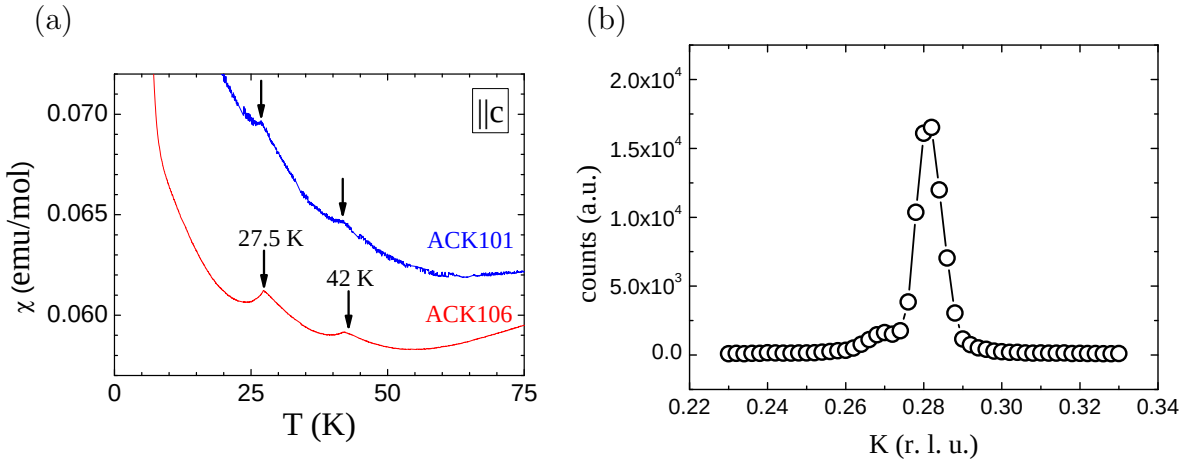

Figure 5.30: (a) Magnetic susceptibility of $TbMnO_3$ (*ACK101* and *ACK106*) with $H \| c$. (b) K-scan of an incommensurate magnetic reflection in $TbMnO_3$ measured at 17 K.

5.7 Table of Crystals

A list of all crystals grown at the floating zone image furnace follows. It also contains the most important growth parameter which were constant during growth. Some other growth parameters like growth rate, (maximum) lamp power and shaft rotations and even the gas pressure usually were often changed during the whole growth process and therefore not listed in this table. The table is built in the following manner: the first column contains the sample name followed by the composition of the sample. Special signs indicate whether the crystal has successfully grown as a single crystal (♢), polycrystal (♭), with impurities (§) or not at all(♯,‡,†). In the following columns (maximum) lamp power and atmosphere are listed followed by the total length during the growth process.

crystal	***composition***	***lamps***	***gas***	***length***
ACK001	$Y_{0.6}Ca_{0.4}TiO_3$ §	1000 W	Ar	30 mm
ACK002	$Y_{0.75}Ca_{0.25}TiO_3$ §	1000 W	Ar	63.3 mm
ACK003	$Yb_{0.5}Ca_{0.5}TiO_3$ §	1000 W	Ar	46.5 mm
ACK004	$Y_{0.64}Ca_{0.36}TiO_3$ ♭	1000 W	Ar	80 mm
ACK005	$Y_{0.64}Ca_{0.36}TiO_3$ ♭	1000 W	Ar	74.1 mm
ACK006	Sr_2TiO_4 ♭	1000 W	Ar	55 mm
ACK007	La_2TiO_4 ♯	1000 W	FG	11.6 mm
ACK008	La_2TiO_4 ♯	1000 W	Ar	5.4 mm
ACK009	$LaSrTiO_4$ ♯	1000 W	Ar	-
ACK010	$YCaTiO_4$ §	1000 W	Ar	60 mm
ACK011	$Y_{0.90}Ca_{0.10}TiO_3$ ♢	1000 W	Ar	43.2 mm
ACK012	$Y_{0.90}Ca_{0.10}TiO_3$ ♢	1000 W	Ar	64.3 mm
ACK013	$Y_{0.80}Ca_{0.20}TiO_3$ ♢	1000 W	Ar	70.6 mm
ACK014	$LaSrTiO_4$ §	1000 W	Ar	46.7 mm
ACK015	$Y_{0.667}Ca_{0.333}TiO_3$ ♢	1000 W	Ar	70.6 mm
ACK016	$Y_{0.64}Ca_{0.36}TiO_3$ ♢	1000 W	Ar	65.3 mm
ACK017	$Y_{0.64}Ca_{0.36}TiO_3$ ♢	1000 W	Ar	50.1 mm
ACK018	$Y_{0.5}Ca_{0.5}TiO_3$ ♢	1000 W	Ar	57.8 mm
ACK019	$Y_{0.5}Ca_{0.5}TiO_3$ ♭	1000 W	Ar	23.5 mm
ACK020	$Y_{0.5}Ca_{0.5}TiO_3$ ♭	1000 W	Ar	66.8 mm
ACK021	$GdTiO_3$ ♢	1000 W	Ar	73.4 mm
ACK022	$GdTiO_3$ ♢	1000 W	Ar	36.4 mm
ACK023	$Gd_2CaTi_2O_7$ ♭	1000 W	Ar	66.8 mm
ACK024	$Er_{0.6}Ca_{0.4}TiO_3$ ♢	1000 W	Ar	60.9 mm
ACK025	$YTi_{0.5}Ni_{0.5}O_3$ §	1000 W	Ar	63.4 mm
ACK026	$Er_{0.57}Ca_{0.43}TiO_3$ ♢	1000 W	Ar	64.9 mm
ACK027	$Y_{0.55}Ca_{0.45}TiO_3$ ⋄	1000 W	Ar	48.7 mm
ACK028	$Er_{0.55}Ca_{0.45}TiO_3$ ♢	1000 W	Ar	51.0 mm
ACK029	$Er_{0.53}Ca_{0.47}TiO_3$ ⋄	1000 W	Ar	18.3 mm
ACK030	$Er_{0.53}Ca_{0.47}TiO_3$ ♢	1000 W	Ar	58.0 mm
ACK031	$Er_{0.5}Ca_{0.5}TiO_3$ ♢	1000 W	Ar	45.1 mm
ACK032	$GdTiO_3$ ♢	1000 W	Ar	34.5 mm
ACK033	$GdTiO_3$ ♢	1000 W	Ar	34.5 mm
ACK034	$Er_{0.3}Ca_{0.7}TiO_3$ ‡	1000 W	Ar	45.1 mm
ACK035	$Er_{0.59}Ca_{0.41}TiO_3$ ♢	1000 W	Ar	53.2 mm
ACK036	$La_{1.15}Sr_{0.85}CrO_4$ ‡	1500 W	Ar	45.1 mm
ACK037	$Y_{0.6}Mg_{0.07}Ca_{0.33}TiO_3$ §	1000 W	Ar	28.5 mm
ACK038	$Lu_{0.64}Ca_{0.36}TiO_3$ ♭	1000 W	Ar	46.5 mm
ACK039	$Er_{0.3}Lu_{0.3}Ca_{0.4}TiO_3$ ♢	1000 W	Ar	57.4 mm
ACK040	$Er_{0.285}Lu_{0.285}Ca_{0.43}TiO_3$ ♢	1000 W	Ar	34 mm

Table 5.8: Table I of grown crystals at the CSI[75] floating zone furnace. (FG: $5\%H_2+95\%N_2$; ♯: No stable melt could be established; ‡: no melt could be established; † feeding rod broken accidentally; §: contaminated with impurities; ♭: polycrystalline; ♢: single crystal.)

crystal	*composition*	*lamps*	*gas*	*length*	*TGA*
ACK041	$Er_{0.285}Lu_{0.285}Ca_{0.43}TiO_3$ ♢	1000 W	Ar	44.3 mm	
ACK042	$Lu_{0.5}Ca_{0.5}TiO_3$ ♢	1000 W	Ar	36.7 mm	
ACK043	$GdTiO_3$ ♢	1000 W	Ar	45.0 mm	$\delta O = 0.0009(1)$
ACK044	$Y_{0.75}Ca_{0.25}TiO_3$ ♢	1000 W	Ar	63.5 mm	
ACK045	$Y_{0.8125}Ca_{0.1875}TiO_3$ ♢	1000 W	Ar	53.0 mm	
ACK046	$LaTiO_3$ †	1000 W	Ar	0.0 mm	δTi=0.00
ACK047	$Y_{0.5}Ca_{0.5}TiO_3$ ♢	1000 W	Ar	64.7 mm	
ACK048	$Lu_{0.55}Ca_{0.45}TiO_3$ ♢	1000 W	Ar	59.2 mm	
ACK049	$YCaTiO_4$ §	1000 W	Ar	54.2 mm	
ACK050	$LuFe_2O_4$ ♭	300 W	FG	36.7 mm	
ACK051	$LuFe_2O_4$ ♢	300 W	Ar	42.3 mm	
ACK052	$ErFe_2O_4$ ♢	300 W	Ar	52.2 mm	
ACK053	$ErFe_2O_4$ ♭	1000 W	Ar	9.7 mm	
ACK054	$Sr_{1.94}La_{0.06}TiO_4$ ♭	1000 W	Ar	50.0 mm	
ACK055	$Lu_{0.57}Ca_{0.43}TiO_3$ ♢	1000 W	Ar	45.0 mm	
ACK056	$Sr_{1.85}La_{0.15}TiO_4$ ♭	1000 W	Ar	30.0 mm	
ACK057	$Sr_{1.82}La_{0.18}TiO_4$ ♭	1000 W	Ar	24.5 mm	
ACK058	Eu_2TiO_5 ♢	1000 W	Ar	54.2 mm	
ACK059	$Eu_{1.5}La_{0.5}TiO_4$ §	1000 W	Ar	26.1 mm	
ACK060	$Sr_{1.85}La_{0.15}TiO_4$ ♭	1000 W	Ar	2.6 mm	
ACK061	$LaBaTiO_4$ §	300 W	Ar	49.0 mm	
ACK062	$Eu_{1.5}Gd_{0.5}TiO_4$ §	1000 W	Ar	18.3 mm	
ACK063	$Eu_2Nb_{0.2}Ti_{0.8}O_5$ §	1000 W	Ar	12.9 mm	
ACK064	$Lu_{0.34}Ca_{0.66}TiO_3$ §	1000 W	Ar	23.1 mm	
ACK065	Eu_2TiO_4 §	1000 W	Ar	1.9 mm	
ACK066	$Eu_2V_{0.15}Ti_{0.85}O_5$ ♢	1000 W	Ar	45.0 mm	
ACK067	Gd_2VO_5 §	1000 W	Ar	37.3 mm	
ACK068	$Sr_{1.9}La_{0.1}TiO_4$ ♭	1000 W	FG	2.0 mm	
ACK069	$LaSrCrO_4$ ♯	1000 W	FG	0 mm	
ACK070	$Gd_{0.64}Ca_{0.36}Ti_{0.97}Co_{0.03}O_3$ ♭	1000 W	Ar	44.8 mm	
ACK071	Sr_2TiO_4 ♭	1000 W	Ar	57.3 mm	
ACK072	$Sr_{1.75}La_{0.25}TiO_4$ §	1000 W	Ar	24.2 mm	
ACK073	Sr_2FeO_4 ♭,§	1000 W	O_2	51.2 mm	
ACK074	$La_{0.5}Ba_{0.5}Ti_{0.97}Co_{0.03}O_3$ §	1000 W	Ar	1.3 mm	
ACK075	$Y_{0.59}Ca_{0.41}Ti_{0.98}Co_{0.02}O_3$ ♭	1000 W	Ar	1.3 mm	
ACK076	$Y_{0.61}Ca_{0.39}TiO_3$ ♢	1000 W	Ar	45.4 mm	
ACK077	$MgCuO_2$ ‡	300 W	Ar	0 mm	
ACK078	$CuTiO_2$ ♯	300 W	Ar	0 mm	
ACK079	$SrLaTiO_4$ §	1000 W	Ar	60.5 mm	
ACK080	$YBa_2Ti_3O_7$ §	1000 W	Ar	33.9 mm	

Table 5.9: Table II of grown crystals at the CSI[75] floating zone furnace. (FG: 5%H_2+95%N_2; ♯: No stable melt could be established; ‡: no melt could be established; † feeding rod broken accidentally; §: contaminated with impurities; ♭: polycrystalline; ⋄: small single crystals; ⋄: small single crystals; ♢: single crystal.)

crystal	***composition***	***lamps***	***gas***	***length***	***TGA***
ACK081	$SrLaTiO_4$ ♯	1000 W	Ar	3.4 mm	
ACK082	$Lu_{0.56}Ca_{0.44}TiO_3$ ♢	1000 W	Ar	49.6 mm	
ACK083	$Y_{0.63}Ca_{0.37}TiO_3$ ♢	1000 W	Ar	87.0 mm	
ACK084	$Lu_{0.4}Sc_{0.1}Ca_{0.5}TiO_3$ ♭	1000 W	Ar	31.5 mm	
ACK085	$Lu_{0.4}Sc_{0.1}Ca_{0.5}TiO_3$ ♭	1000 W	Ar	31.0 mm	
ACK086	$Lu_{0.4}Sc_{0.1}Ca_{0.5}TiO_3$ ⋄	1000 W	Ar	50.0 mm	
ACK087	$Y_{0.5}Ca_{0.5}TiO_3$ ⋄	1000 W	Ar	46.1 mm	
ACK088	$Y_{0.5}Ca_{0.5}TiO_3$ ♢	1000 W	Ar	72.4 mm	
ACK089	$YRu_{0.2}Ti_{0.8}O_3$ ♢	1500 W	Ar	22.3 mm	
ACK090	$YTiO_3$ ♢	1000 W	Ar	60 mm	
ACK091	Yb_2VO_5 §	1000 W	Ar	55.0 mm	
ACK092	Er_2TiO_5 ⋄	1000 W	Ar	6.4 mm	
ACK093	$SmTiO_3$ ♭	1000 W	Ar	30 mm	
ACK094	$Sm_{0.1}Gd_{0.9}TiO_3$ ♢	1000 W	Ar	8.6 mm	
ACK095	$SmTiO_3$ ♢	1000 W	Ar	53.3 mm	
ACK096	$Sm_{0.2}Gd_{0.8}TiO_3$ ♢	1000 W	Ar	8.6 mm	
ACK097	$Sm_{0.3}Gd_{0.7}TiO_3$ ♢	1000 W	Ar	22.0 mm	
ACK098_1	$Sm_{0.4}Gd_{0.6}TiO_3$ ♢	1000 W	Ar	19.0 mm	
ACK098_2	$Sm_{0.4}Gd_{0.6}TiO_3$ ♢	1000 W	Ar	9.1 mm	
ACK099_1	$Sm_{0.5}Gd_{0.5}TiO_3$ ♢	1000 W	Ar	22.5 mm	
ACK099_2	$Sm_{0.5}Gd_{0.5}TiO_3$ ♢	1000 W	Ar	8.5 mm	
ACK100	$Sm_{0.6}Gd_{0.4}TiO_3$ ♢	1000 W	Ar	15.4 mm	
ACK101	$TbMnO_3$ ♢	1000 W	Ar	60 mm	
ACK102	$TbMnO_3$ ♢	1000 W	Ar	94.7 mm	
ACK103	$TbMnO_3$ ♢	300 W	Ar	88 mm	
ACK104	$Ba_{1.2}Mn_8O_{16}$ §	300 W	Ar	5.8 mm	
ACK105	$GdMnO_3$ ♢	300 W	Ar	30 mm	
ACK106_1	$TbMnO_3$ ♢	1000 W	Ar	46.6 mm	
ACK106_2	$TbMnO_3$ ♢	300 W	Ar	46.0 mm	
ACK107	YTi_2O_5 §	1000 W	Ar	72.3 mm	
ACK108	$Lu_{0.56}Ca_{0.44}TiO_3$ ⋄	1000 W	Ar	63.7 mm	
ACK109	$Lu_{0.56}Ca_{0.44}TiO_3$ ⋄	1000 W	Ar	71.4 mm	
ACK110	$Lu_{0.56}Ca_{0.44}TiO_3$ ♢	1000 W	Ar	75.8 mm	
ACK111	$Eu_{0.991}Eu_{0.009}TiO_3$ ♢	1000 W	Ar	75.8 mm	
ACK112	$EuSrTiO_4$ §	1000 W	Ar	34.7 mm	
ACK113	$Lu_{0.38}Sc_{0.12}Ca_{0.5}TiO_3$ ♭	1000 W	Ar	26.2 mm	
ACK114	$Lu_{0.56}Ca_{0.44}TiO_3$ ♢	1000 W	Ar	74.8 mm	
ACK115	$DyTiO_3$ ♢	1000 W	Ar	96.8 mm	
ACK116	$DyMnO_3$ ♢	1000 W	Ar	∼20 mm	
ACK117	$La_{1.88}Sr_{0.12}NiO_4$ ♢	1000 W	Ar	78.3 mm	
ACK118	$YTi_{0.5}Mn_{0.5}O_3$ ⋄	1000 W	Ar	55.2 mm	
ACK119	$La_{1.5}Sr_{0.5}TiO_4$ ♯	1000 W	Ar	-	
ACK120	$La_{1.85}Ce_{0.15}NiO_4$ §	1000 W	Ar	36.8 mm	

Table 5.10: Table III of grown crystals at the CSI[75] floating zone furnace. (FG: 5%H_2+95%N_2; ♯: No stable melt could be established; ‡: no melt could be established; † feeding rod broken accidentally; §: contaminated with impurities; ♭: polycrystalline; ⋄: small single crystals; ♢: single crystal.)

crystal	***composition***	***lamps***	***gas***	***length***	***TGA***
ACK121	$TbTiO_3$ ♢	1000 W	Ar	64.5 mm	
ACK122_1	$HoTiO_3$ ♢	1000 W	Ar	44.0 mm	
ACK122_2	$HoTiO_3$ ♢	1000 W	Ar	60.0 mm	
ACK123	$YbTiO_3$ ♢	1000 W	Ar	97.4 mm	
ACK124	$Eu_2TiO_{4.9}$ ⋄	1000 W	Ar	35.5 mm	
ACK125	$LuTiO_3$ ♭,§	1000 W	Ar	≈70 mm	
ACK126	$NaTiSi_2O_6$ §	150 W	Ar	≈40 mm	

Table 5.11: Table IV of grown crystals at the CSI[75] floating zone furnace. (FG: 5%H_2+95%N_2; ♯: No stable melt could be established; ‡: no melt could be established; † feeding rod broken accidentally; §: contaminated with impurities; ♭: polycrystalline; ⋄: small single crystals; ♢: single crystal.)

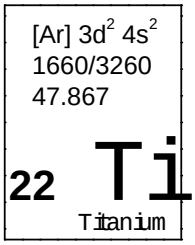

6 Titanates

Titanium is widely spread throughout the earth´s crust - 0.6% by mass with the main ores Rutile and Ilmenite [107]. It is a less corrodible metal with high strength and melting point and a rather low density making it a desired material for technical applications like for example jet engines [107]. One of the most prevalent titanium oxides, TiO_2, is a common substance which is used as a white pigment for example in wall paint or in paper [107, 108] (maybe also in the paper this work is written on).

The first experimental Chapter of this work dealing with the properties of transition metal oxides will tie in with the results observed in the Diploma Thesis of the author [57]. In the first section a short survey of the perovskite rare earth titanates (RTiO$_3$) is given which will be followed by the new results measured in this work. Afterwards, in the second and third section, a special focus will be given on the metal-insulator transition in the hole-doped R_{1-x}Ca$_x$TiO$_3$-system and the observations of charge ordering within this system. Finally, in the fourth section, first results of a layered perovskite titanate system will be presented.

6.1 Interplay of magnetic and orbital order in RTiO$_3$

6.1.1 Introduction

The pseudocubic perovskite compound RTiO$_3$ (with R = trivalent rare earth ion or Y) is a prototypical example of a Mott-Hubbard insulator [2]. With decreasing R ionic radius in the series La to Lu [82] the magnetic ordering scheme of the Ti-array changes from antiferromagnetism to ferromagnetism [81, 109-119]. (EuTiO$_3$ exhibits an exceptional behaviour as the Eu-ion has a valency of 2+ within this perfectly cubic perovskite compound resulting in a 3d^0 configuration of the Ti-ion [120] according to the preferred Ti(IV+) oxidation state of the titanium ion. Only the 7 μ_B of the Eu^{2+}-ion order antiferromagnetically below about 5 K [120]. See also Appendix C.) By decreasing the R-ionic radius, the Ti-O-Ti bond angles and concomitantly the one-electron bandwidth of the RTiO$_3$-system decrease [121, 122]. The changes in the bond-angles can be understood by the structure. The RTiO$_3$-compounds, with exception of EuTiO$_3$, have an orthorhombic distorted perovskite structure of GdFeO$_3$-type. The tolerance factor t=d$_{R-O}$/$\sqrt{2}$·d$_{Ti-O}$ [123] is smaller than the value 1 for the ideal structure resulting in a compressive stress in the Ti-O bondlengths. In order to relieve this stress, the TiO$_6$-octahedra are coop-

eratively tilted around the cubic (110)-axis and rotated around the c-axis which leads to a decreasing Ti-O-Ti bond angle and an enlargement of the pseudocubic unit cell to the orthorhombic $\sqrt{2} \times \sqrt{2} \times 2$ unit cell with space group $Pbnm$. This is shown in Fig. 6.1 (a-b). The Ti-O-Ti interactions are responsible for the electronic properties of the $R\mathrm{TiO_3}$ system and the orbital (and magnetic) ordering changes with decreasing Ti-O-Ti bond angle from ferroorbital ordering in $\mathrm{LaTiO_3}$ to $\mathrm{SmTiO_3}$ to antiferroorbital ordering in $\mathrm{GdTiO_3}$ to $\mathrm{LuTiO_3}$ and $\mathrm{YTiO_3}$ [124, 117]. In accordance with the rules of Goodenough, Kanamori and Anderson [28-30], these two types of orbital ordering induce antiferromagnetism in $\mathrm{LaTiO_3}$ to $\mathrm{SmTiO_3}$ and ferromagnetism in $\mathrm{GdTiO_3}$ to $\mathrm{LuTiO_3}$ and $\mathrm{YTiO_3}$. Concomitant with these types of orbital ordering also two corresponding $\mathrm{TiO_6}$-octahedral distortions appear. These are shown schematically for the shape of the $\mathrm{TiO_6}$-octahedral basal plane (O2) in Fig. 6.1 (c). In the case of ferroorbital ordering the $\mathrm{TiO_6}$-octahedral basal plane exhibits a rectangular distortion and the difference of the two O2-O2 bond-lengths differs most ($\Delta(O2 - O2) \neq 0$). For antiferroorbital ordering a rhombic octahedral basal plane is observed [121, 118, 84] and the two Ti-O2 bond-lengths show the strongest changes ($\Delta(Ti - O2) \neq 0$) [1]. The magnetic phase diagram of this system is shown in Fig. 6.1 (d). $\mathrm{LaTiO_3}$ having a relative large Ti-O-Ti bond angle of about 153.5° [84] is a G_x-type [2] antiferromagnetic Mott-insulator with a Néel-temperature of about 145 K whereas $\mathrm{YTiO_3}$ (or $\mathrm{LuTiO_3}$) having a roughly 10° smaller Ti-O-Ti bond angle [84] is a ferromagnetic (F_z) insulator with a Curie-temperature of about 30 K. However, also weak G_x-type and A_y-type antiferromagnetic components have been found in $\mathrm{YTiO_3}$ [125]. Thus, these two different types of magnetic ordering correspond to the same irreducible representation, determined in Ref. [89] for the $\mathrm{GdFeO_3}$ structure, and the change from antiferromagnetism to ferromagnetism corresponds to a redistribution of the ordered moment among the the three different G_x, A_y and F_z components of the irreducible representation labeled Γ_4 [89]. However, the magnetic order at the R-sites may alter this rule since the anisotropic rare earth ions (RE) affect the ordering at the Ti-sites via RE-Ti interactions, see Chap. 5.3.

The occurrence of ferromagnetism and insulating electrical properties together is always interesting as the coexistence of these two properties deviates from the usual observation of ferromagnetism in metals. Like in the case of $\mathrm{YTiO_3}$ [117], orbital ordering often explains the coexistence of these two properties [126].

In the past years, $\mathrm{LaTiO_3}$ has attracted large interest due to an orbital liquid model which has been proposed for this system assuming that the splitting between the t_{2g} states is sufficiently low to allow orbital fluctuations to determine the physical properties of this system [129, 130]. However, the t_{2g}-level splitting of the order of 200 meV is contraindicative for this scenario as it should effectively suppress orbital fluctuations [118, 124, 131-133]. This is in accordance with recent calculations which are able to describe the magnetic properties of this system quite well within a conventional scenario [134, 135].

[1] $\Delta(Ti-O2) = dist(Ti-O2) : dist(Ti-O2') - 1$ shown schematically in Fig. 6.1 (c) left. $\Delta(O2-O2) = dist(O2 - O2') : dist(O2 - O2'') - 1$; see Fig. 6.1 (c) right.

[2] moment of all six nearest neighbour Ti-sites are coupled antiferromagnetically; all moments are parallel to the x/a-axis.

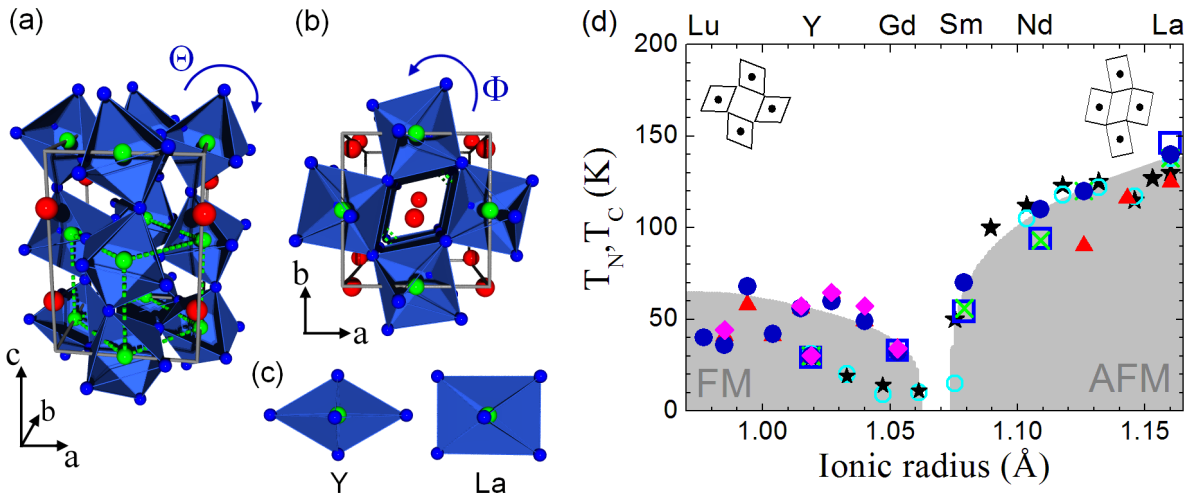

Figure 6.1: (a-b) $GdFeO_3$-structure (*Pbnm*); *green dotted lines*: (pseudo-)cubic unit cell. (c) Schematic figures of basal TiO_6-distortions in $YTiO_3$ and $LaTiO_3$. (d) Phasediagram of $RTiO_3$ from Ref. [84]. The magnetic ordering temperatures are plotted versus the R-ionic radius. This extended version also contains the value for $LuTiO_3$ from Ref. [81] (*dark blue dot*). *Open squares/triangles/crosses/open circles/stars/dots*: values from Ref. [84]/[87]/[127]/[122]/[128]/[81] and *diamonds*: values of T_C for crystals synthesized in this work (ACK). The insets show the prominent octahedral distortions of $YTiO_3$/$LaTiO_3$.

Additionally to the magnetic ordering within the Ti-array the R-array (with exception of R = Y, La, Lu) orders also magnetically:

1. for R = Ce to Sm: AFM below $T_{N2} < T_{N1}$ [3] which is of C_z/F_y- type for Nd, Sm [111, 112].

2. for R = Gd to Yb (without Tb, Dy, Ho): FM ordering antiparallel to the FM moment of the Ti-array.

3. for Tb, Dy, Ho: FM and AFM components; see Ref. [81, 87, 136-138].

The ordering temperatures of these moments are distinctly smaller than for the Ti-sublattice which allows a separation of the effects of magnetic ordering of the R-sublattice.

In the Diploma Thesis of the author [57] a coupling between orbital degrees of freedom and the crystal structure has been found within the titanate system extending the observations in $LaTiO_3$ [118, 139] to other AFM $RTiO_3$ with R = Nd, Sm. These measurements show an anomalous rise of the a- and decrease of the b-lattice parameter below T_N. These effects sum up in the orthorhombic splitting $\varepsilon = (a-b)/(a+b)$. In Fig. 6.2 (e) the orthorhombic splitting is shown for different $RTiO_3$. The arrows indicate the magnetic ordering temperature. Usually, ε should be negative for undistorted octahedra

[3] AFM: antiferromagnetic; T_{N1} is the Néel-temperature for the G-type AFM ordering of the Ti-array.

as these octahedra tilt around b. But octahedral basal planes which are elongated in a-direction - see Fig. 6.1 (c) - can even lead to positive values of ε as in $LaTiO_3$. In Ref. [57] (Diploma Thesis) the anomalous rise of ε in the series La, Nd, Sm strengthens from La to Sm. This anomaly was interpreted as a change of the orbital ground state at the magnetic ordering temperature with a strengthening of the ferroorbital arrangement. For one of these compounds, it was shown by neutron scattering [57, 84] that tilt and rotational angles do not change with temperature, but that the internal octahedral distortions $\Delta(O2-O2)$ shown in Fig. 6.1 (c) exhibit a strong temperature dependence. Hence, the octahedral distortions are decoupled from the tilts and the anomalous structural effects can be interpreted to be mainly caused by orbital effects. Thus, on the one hand the crystal field splitting is induced by the tilting angles (and the shifts of the R-ions) [124, 131], but on the other hand, below T_N, the ferroorbital arrangement gets strengthened following the crystal-field splitting already induced by the tilts [57, 84]. It turned out that the orthorhombic splitting which is directly accessible by the lattice parameter is a direct indicator for these octahedral distortions ($\Delta(O2-O2)$) as only the tilt and the octahedral distortion $\Delta(O2-O2)$ determine the value of ε and the tilt is constant over the whole temperature range. Furthermore, it was also shown that the ε - $\Delta(O2-O2)$ curve is linear over the whole temperature range [57, 84].

Also for a ferromagnetic compound, $YTiO_3$, which is on the other end of the phase diagram the tilting and rotational angles are temperature invariant [57]. Some first weak structural anomalies around T_C were also visible in the lattice parameter and the thermal expansion of $YTiO_3$ [57, 84, 140].

In this work, these observations for the antiferromagnetic (AFM) titanates (and $YTiO_3$) have been further extended to measurements of a ferromagnetic (FM) compound which is close to the FM/AFM-crossover: $GdTiO_3$.

6.1.2 Experimental

The older RTiO$_3$ samples (R = La, Nd, Sm, Gd and Y) were grown by H. Roth [78]. New $GdTiO_3$ (*ACK043*) and $YTiO_3$ (*ACK090*) samples with higher T_C and, additionally, the ferrimagnetic RTiO$_3$ samples $TbTiO_3$ (*121*), $DyTiO_3$ (*115*), $HoTiO_3$ (*ACK122*) and $YbTiO_3$ (*123*) were grown within this work using a floating zone image furnace. The magnetic transition temperatures have been measured by M. Reuther by a vibrating sample magnetometer (VSM) or were taken from Ref. [84, 78, 85]. Powder X-ray diffraction measurements have been performed using a Siemens D5000 X-ray diffractometer with Cu-/Cr- K_α radiation. The program *FullProf* [88] has been used for rietveld-refinement. Single crystal X-ray diffraction has been performed on a Bruker X8 Apex CCD diffractometer using Mo-K_α radiation. For the structural refinement on F^2 the program *Jana2000* [58] has been used. Thermal-expansion coefficients of $GdTiO_3$, $TbTiO_3$ and $DyTiO_3$ have been measured by J. Rohrkamp and T. Lorenz on a high-resolution capacitance dilatometer using the RTiO$_3$ samples grown in this work.

High pressure studies of the $GdTiO_3$-sample grown in this work have been performed by means of angle dispersive powder X-ray diffraction using synchrotron radiation at beamline ID09A at ESRF in Grenoble, France using a wavelength of 0.413071 Å. There-

fore, a $GdTiO_3$ single crystal (*ACK043*) has been crushed and a piece smaller than 1 mm^3 has been ground thoroughly for at least two hours to an extremely fine powder. Diamond anvil cells of the cylinder-piston type with a He gas driven membrane for pressure generation have been used with He as the pressure medium. For the determination of the pressure the ruby fluorescence method has been used. Two-dimensional diffraction images have been measured with an image plate detector. The data reduction has been performed with the FIT2D software [141]. (See also Chapter 8.4.)

Additionally, resonant X-ray diffraction measurements at the Ti K-edge have been performed by and in collaboration with C. Schüßler-Langeheine, H.-H. Wu and C. Trabant at beamline MagS at BESSY in Berlin.

6.1.3 Results

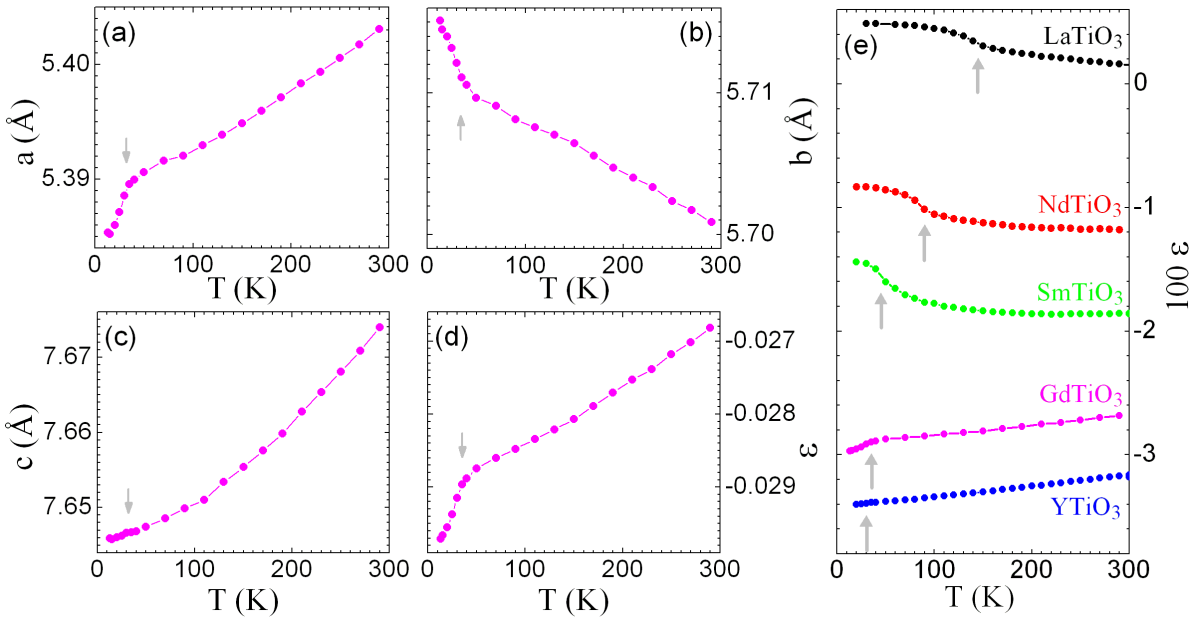

Figure 6.2: (a-d) Lattice parameter and $\varepsilon = (a-b)/(a+b)$ of $GdTiO_3$. (e) Orthorhombic splitting ε of $RTiO_3$ with R = La (*black*), Nd (*red*), Sm (*green*), Gd (*magenta*) and Y (*blue*) measured in the Diploma thesis of the author [57] and in this work. The two groups of antiferromagnetic (AFM) and ferromagnetic (FM) titanates exhibit anomalies of opposite sign at the magnetic ordering temperature and the compounds close to the AFM/FM crossover, i. e. $SmTiO_3$ and $GdTiO_3$, exhibit the strongest anomalies within their group.

X-ray diffraction measurements

The lattice parameter of $GdTiO_3$ [4] have been measured as a function of temperature by means of powder X-ray diffraction; see Fig. 6.2. At the magnetic ordering temperature

[4] old sample grown by H. Roth

which is indicated by an arrow in the figure, anomalies of the lattice parameter are observable. But the *a*- and *b*- lattice parameter show a completely different behaviour than for the antiferromagnetic titanates - instead of increasing a and decreasing b the a-lattice parameter of $GdTiO_3$ decreases and the b-lattice parameter increases below T_C. Thus, the orthorhombic splitting ε exhibits anomalies of opposite sign; see Fig. 6.2 (d-e). Much weaker anomalies but of similar sign have been also reported for another FM titanate - $YTiO_3$ [140]. These structural anomalies of the FM titanates with magnetic moment parallel to c do not seem to arise from simple spin-orbit coupling as one could expect an elongation along c [142], which, however, could also be observed in these compounds additionally to the effects mentioned above as described in the Diploma thesis [57] and in Ref. [140]. But additionally to a possible influence of the spin orbit coupling, also orbital effects may drive the anomalous rise of c, as the energetically lowest orbital in $YTiO_3$ is also extended in c-direction [124, 143, 144].

The thermal-expansion has been measured for the three orthorhombic directions (α_a, α_b, α_c) on the $GdTiO_3$ sample *ACK043* grown in this work. The results are plotted in Fig. 6.3 (a). These measurements are of higher accuracy than powder X-ray diffraction measurements. At $T_C \approx 34$ K the anomalies give rise to extrema in the thermal expansion coefficient. As known from the lattice parameter, these anomalies are opposite in sign compared to the thermal expansion anomalies in the AFM titanates. As can be seen in these accurate measurements there are also anomalies at a lower temperature $T_{C2} \approx 25$ K. This is most likely the ordering temperature of the Gd moments which order ferromagnetically but antiparallel to the Ti moments. Concerning α_a and α_b the anomalous peaks are very narrow compared to the anomalous peaks around T_C. As the peak width is very small, the integrated area under these additional peaks is negligible which is also confirmed in a calculation omitting these Gd-contributions. In Fig. 6.3 (b) the measured a lattice parameter is plotted as a function of temperature (*triangles*). Additionally, the calculated a-lattice parameter derived from the thermal expansion measurement (*blue*) is shown. Together with these values a calculated line omitting the Gd-contributions (*red*) is shown. The corresponding modified thermal expansion is shown in the inset (*red line*). As can be seen, the effect of Gd-ordering is small and would not have been seen in a X-ray diffraction measurement. Therefore, the main contribution on the structural distortions is caused by the Ti-sublattice and the effect of Gd-ordering on the lattice can be neglected.

In Fig. 6.4 (a-c) the thermal expansion of $GdTiO_3$ is compared with the thermal expansion of $RTiO_3$ wit smaller rare-earth ionic radius. As found in the X-ray diffraction measurements the structural anomalies are strongest for $GdTiO_3$ which is close to the AFM/FM crossover in the phase diagram. $TbTiO_3$ with a slightly smaller rare-earth ionic radius exhibits already distinctly smaller anomalies than $GdTiO_3$. And $DyTiO_3$ exhibits the same absolute values for the thermal expansion α_b at T_C as $YTiO_3$ [84] (with a very similar rare-earth ionic radius) for α_a. This indicates that the size of the structural anomalies at T_C depends on the size of the R-ion rather than on its magnetic moment as the Y^{3+}-ion is non-magnetic which is in contrast to the Dy^{3+}-ion. The magnetic R-ions either seem to have only small impact on α at the magnetic ordering temperature as could be observed for $GdTiO_3$ or its effect is smeared out over a large temperature

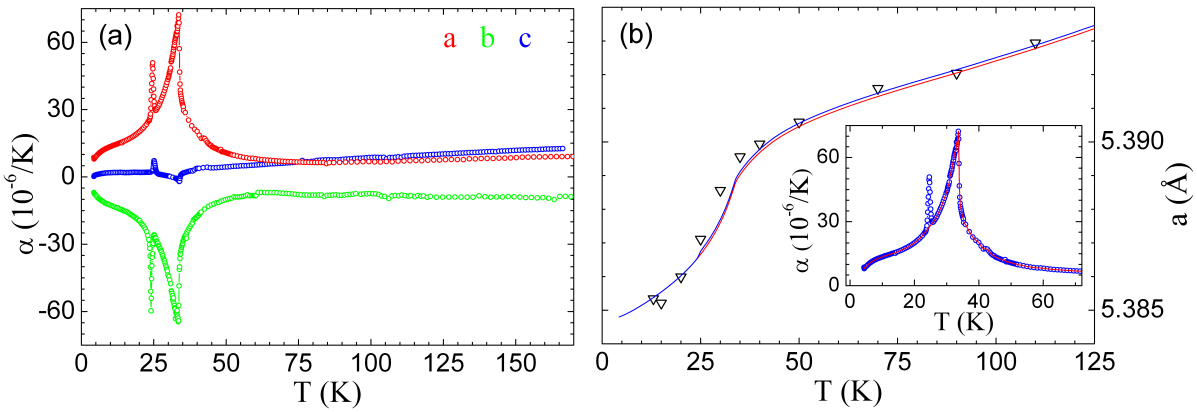

Figure 6.3: (a) Thermal expansion α_j of $GdTiO_3$. (b) a-lattice parameter; *triangles*: measured values for a from Fig. 6.2; *lines*: calculated values from the measured thermal expansion of $GdTiO_3$ (*blue*) and for a hypothetic thermal expansion of $GdTiO_3$ with subtraction of the Gd contribution (*red*) as shown in the inset.

interval as could be observed for $TbTiO_3$, see Fig. 6.4 (b). A similar smeared out bump of α between 20 and 150 K could also be observed for $TbMnO_3$ [145] and, hence, may be attributed to the Tb-array.

These new observations give now a complete picture of the phase diagram of the titanates. Both, the AFM and the FM titanates exhibit structural anomalies below the magnetic ordering temperature which can be observed directly in the orthorhombic splitting ε or in the thermal expansion α. For the FM titanates these anomalies of ε and the thermal expansion along a and b exhibit a sign change compared to the AFM

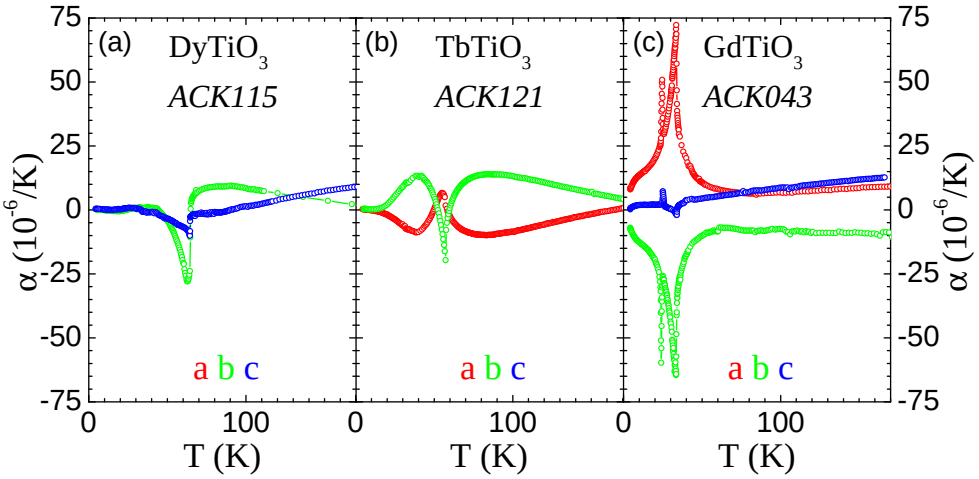

Figure 6.4: (a-c) Comparison of the thermal expansion α of $DyTiO_3$, $TbTiO_3$ and $GdTiO_3$.

side as these anomalies of ε and α are connected to the ferroorbital and antiferroorbital ab-plane arrangement. As the structural anomalies are induced by orbital ordering and as ferroorbital and antiferroorbital ordering is coupled to antiferromagnetic and ferromagnetic ordering respectively, also magnetism and structural anomalies couple. This is verified by the fact that the structural anomalies are strongest at the magnetic ordering temperature; see thermal expansion measurements in [57, 84]. Thus, magnetism induces a change in the orbital arrangement which strengthens the prevalent orbital ordering already induced by the tilts and R-shifts (which exists already at room-temperature). Furthermore, for both sides the anomalies get the stronger the closer the compound is to the AFM/FM crossover of the phase diagram as can be clearly seen in Fig. 6.2 (e) where the anomalies of ferromagnetic $GdTiO_3$ and antiferromagnetic $SmTiO_3$ are strongest.

Single crystal X-ray diffraction measurements of the old $GdTiO_3$-sample and of the new RTiO$_3$-samples (R = Tb, Dy, Ho, Yb) grown in this work have been performed (at room-temperature) in order to measure the full structure and observe the octahedral tilts and distortions in this compound close to the AFM/FM crossover. In Fig. 6.5 the values of these structural distortions are plotted and compared with the other RTiO$_3$-compounds measured in the Diploma Thesis of the author [57]. As can be seen, the Ti-O-Ti angles which are a direct measure of the octahedral tilting and rotational angles increase continuously with increasing R-ionic radius. The close examination of the structure shows that also the two prominent octahedral distortions vary continuously

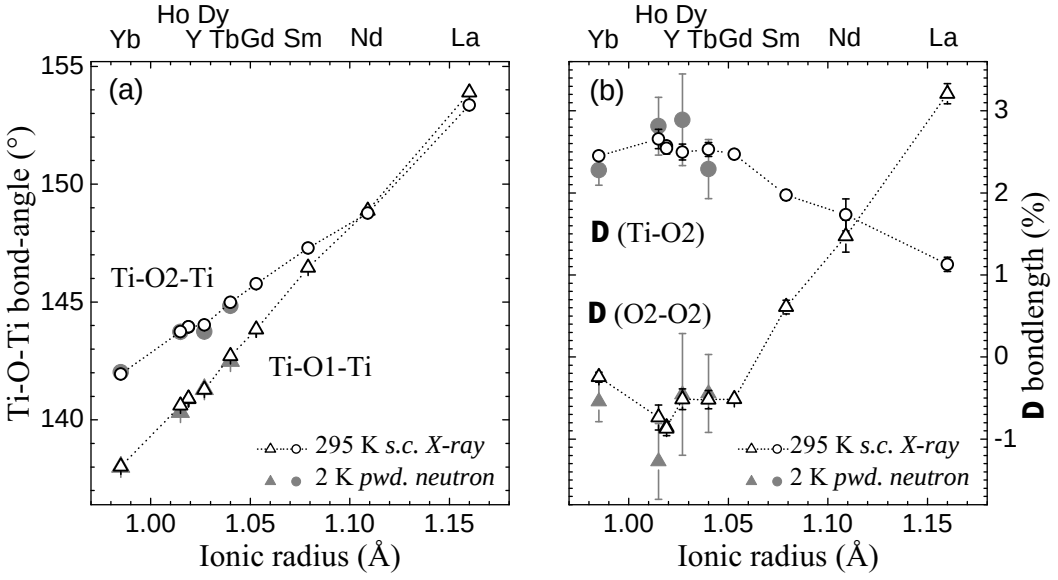

Figure 6.5: (a) Ti-O-Ti bondlengths of RTiO$_3$ which are a measure of the octahedral tilting and rotational angles and (b) the two prominent basal/ab-plane distortions of the TiO_6-octahedra; *black open symbols*: single crystal X-ray diffraction data (room-temperature); *gray symbols*: powder neutron diffraction data (2 K). (Lines are guide to the eyes.)

from $HoTiO_3$ to $LaTiO_3$. In Ref. [118] and also in the Diploma Thesis [57] somehow the values for the bondlength ratios $r_{O2-O2} = \Delta(O2-O2)+1$ and $r_{Ti-O2} = \Delta(Ti-O2)+1$ are always bigger than 1. But if one uses constantly the same oxygen ions O2, O2' and O2" for the calculation of the octahedral distortions the 'real' dependency of the ratios r_{O2-O2} and r_{Ti-O2} on the R ionic radius gets visible which is shown in Fig. 6.5 (b). Due to the correct procedure the artificial minimum in r_{O2-O2} and r_{Ti-O2} has vanished. Now, it can be seen, that also the TiO_6-octahedral distortions change continuously and smoothly with increasing R-ionic radius from $HoTiO_3$ to $LaTiO_3$. Thus, the R-ionic radius can be considered as an external control parameter which continuously drives the magnetic and orbital transition from ferromagnetic and antiferroorbital to antiferromagnetic and ferroorbital ordering. Such transitions controlled by an external ordering parameter are well known for other systems. Especially, for a quantum phase transition the expected change of the sign of the thermal expansion anomalies on crossing the transition [146] and also the observed sign change of the thermal expansion across the metamagnetic transition in $Ca_{2-x}Sr_xRuO_4$ [147] resembles on the observations of the sign change of the thermal expansion anomalies across the FM/AFM crossover in the RTiO$_3$-system.

Additionally, the values of powder neutron diffraction measurements at 2 K are shown, compare Tab. 5.5 in Chap. 5.3. As can be seen, the octahedral tilts and rotations can be determined accurately by powder neutron diffraction (the error bars are small) and there is nearly no change between room-temperature and 2 K. Unfortunately, the two prominent octahedral distortions $\Delta(O2-O2)$ and $\Delta(Ti-O2)$ exhibit larger error bars and, hence, the single crystal X-ray diffraction measurements are more accurate. However, within the accuracy of these powder neutron measurements, there is no indication for a significant change of $\Delta(O2-O2)$ and $\Delta(Ti-O2)$ between room-temperature and 2 K.

high pressure studies

Synchrotron radiation studies of the lattice parameter of $GdTiO_3$ have been performed at 298 K and at 42 K. Fig. 6.6 (a-c) shows the lattice parameter as a function of pressure. No phase transition could be observed up to pressures of roughly 40 GPa. As reported for $YTiO_3$ the b-axis is less compressible than the other two axes [148]. But whereas the b axis is about half (50%) as compressible than a or c in $YTiO_3$, this anisotropy has decreased for $GdTiO_3$, which is closer to the ferroorbital versus antiferroorbital border within the RTiO$_3$ phase diagram, and the difference amounts to 15% only. In Fig. 6.6 (d) the unit cell volume is shown together with the fits of the Birch equation of state (EOS); see Eq. 8.1 in Chapter 8.4. These fits of the V-P curve to the Birch EOS give a bulk modulus B_0 of 185.8(0.8)/187.5(2.2) GPa at 298/42 K. Therefore, $GdTiO_3$ is less compressible than the d^0 titanate compound $CaTiO_3$ having a bulk modulus of 170.9(1.4) GPa [149]. Astonishingly, $GdTiO_3$ is also much less compressible than $YTiO_3$ which has a bulk modulus of 163(6) GPa [148].

As the used sample volume is very small in these synchrotron measurements, preferred orientation effects appeared despite the extremely thorough grinding procedure. Unfortunately, these preferred orientation effects render a reliable determination of the atomic positions impossible. Neutron scattering would be an alternative to avoid pre-

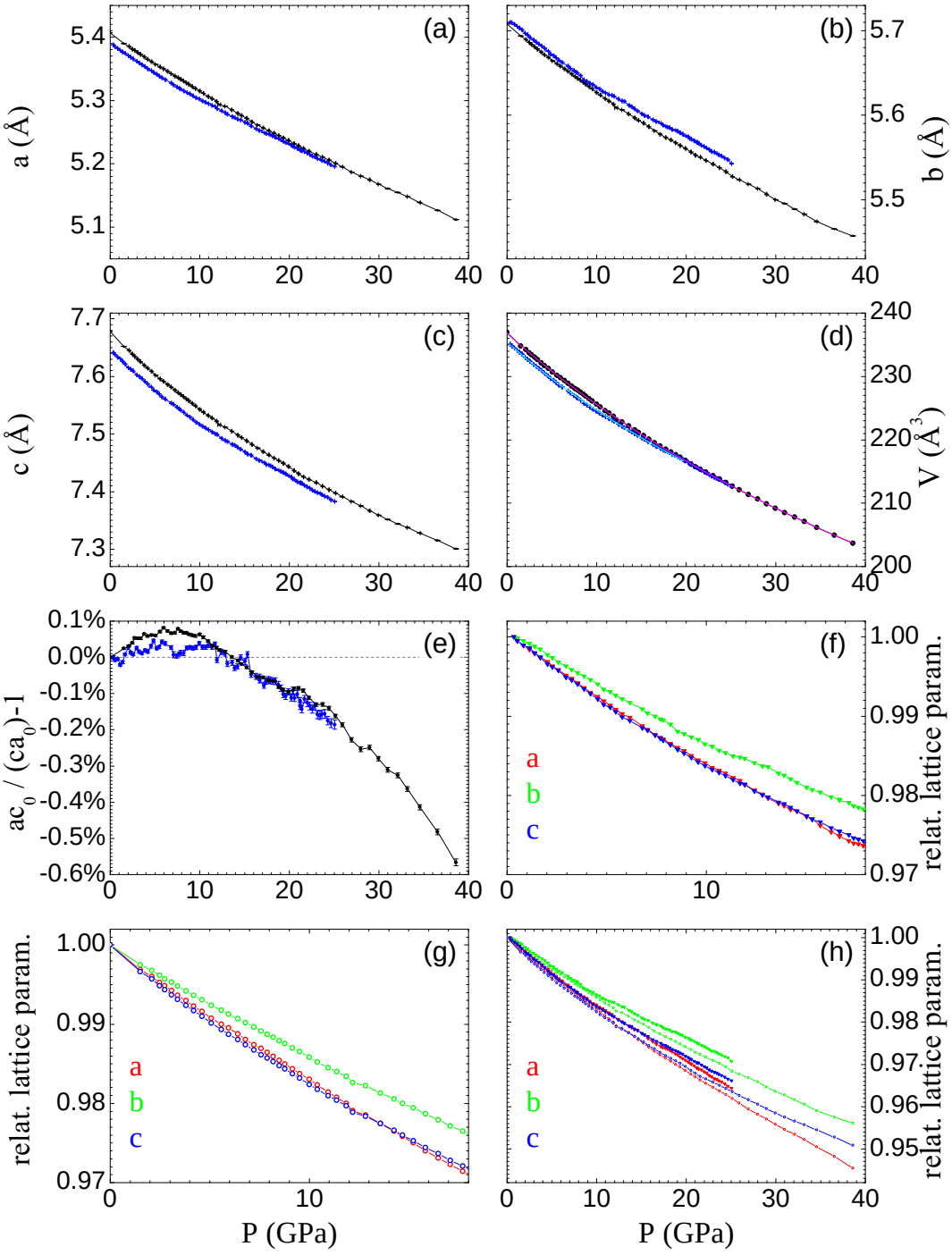

Figure 6.6: (a-d) Lattice parameter and V of $GdTiO_3$; *black/blue*: 298/42 K data; *magenta/cyan lines*: fit of 298/42 K data to Birch EOS. (e) Change of a/c-ratio relative to the value at P = 0; *black/blue*: 298/42 K. (f-h) Pressure dependence of the relative lattice parameter a/a_0; *circles/triangles*: 298/42 K data.

ferred orientation effects as the used sample volume is usually much larger in these kind of experiments. However, the large absorbtion of the Gd-ion [5] makes this alternative impossible or very expensive as special Gd-isotopes would be needed. Therefore, reliable information has to be deduced from the lattice parameter.

Related high-pressure studies on $YTiO_3$ exhibit a flattening of the TiO_6-octahedra along c-direction at high pressures which could indicate the occupation of a d_{xy}-orbital and thus a pressure-induced change in orbital ordering [148]. Although there are some concerns in theoretical calculations, the reported high pressure phase resembles on $SmTiO_3$, [148, 151], which is already on the AFM side of the phase diagram. About concomitant with this change a crossing of the relative lattice parameter a/a_0 and c/c_0 could be observed in Ref. [148] (a exhibits a lower compressibility). Such a crossing could be also observed in the high resolution synchrotron measurements of this work at 298 K as well as at 42 K; see Fig. 6.6 (f-h). At 42 K this crossing is more subtle but still detectable. Fig. 6.6 (e) shows the change of the value of a/c relative to the value at ambient pressure (in %), i. e. $100 \cdot (a \cdot c_0/(a_0 \cdot c) - 1)$ %. The 298 K measurement exhibits a crossing around 13.6 GPa. The 42 K data has a larger statistical spread, but a similar crossing is located somewhere between 12 GPa and 15 GPa. In the data of Ref. [148] the same crossing is observable between 16 GPa and 20 GPa. Thus, this crossing of the normalized a/c lattice parameter occurs around 4(2) GPa lower in the $GdTiO_3$-system. This observation would favour a model where the antiferroorbitally ordered (and ferromagnetic) titanates are shifted by pressure towards the ferroorbitally ordered (and antiferromagnetic) side of the phase diagram as $GdTiO_3$ is already closer to this side than $YTiO_3$. For this reasons, $GdTiO_3$ may be also the better candidate to examine this possible pressure induced crossing of the orbital ordering schemes.

The best proof of such a change in orbital ordering would be to identify the associated types of magnetic ordering as a function of pressure at very low temperatures. Neutron scattering could be a possible method. But in this case, the difficulties would be of more practical nature, as the larger pressure cells need to be cooled down to very low temperatures, i. e. the needed pressure and temperature range might be a problem.

In conclusion, the high pressure studies of $GdTiO_3$ indicate a crossing of the relative a/a_0 and c/c_0 lattice parameters which is very similar to the observations in $YTiO_3$ and, thus, also might be connected to a pressure-induced change of the orbital ordering schemes from antiferroorbital to ferroorbital ordering. In favour of this interpretation is, that this pressure induced cross-over in $GdTiO_3$ (which is already closer to the AFM side of the phase diagram) appears at lower pressures than in $YTiO_3$. Furthermore, this crossing seems to be rather temperature independent and driven by pressure only, since the 42 K and 298 K measurements yield similar results.

resonant X-ray diffraction measurements

The temperature dependency of orbital ordering in $DyTiO_3$ was analyzed in resonant X-ray diffraction measurements at the 7 T multipole wiggler beamline MagS at the synchrotron source BESSY in Berlin. For a brief description of the measurement technique,

[5] 49700(125) barn [150]

see Chap. 6.2 or Ref. [152].

Very recently, thermal conductivity (κ) measurements for the whole RTiO$_3$-series have been reported in Ref. [153]. For all samples κ(T) exhibits a strong increase below the magnetic ordering temperature [153]. This result was interpreted as an evidence for a transition from an orbital liquid to an orbitally ordered phase at the magnetic transition temperature, which is common for both the AFM and the FM compounds [153]. In this scenario, the low, glassy κ(T) for T > T$_{C/N}$ is induced by strong scattering from orbital fluctuations and the phonon-like κ(T) for T < T$_{C/N}$ is interpreted by orbital ordering [153]. This result was supposed to give an answer to the issue of orbital order versus an orbital-liquid phase in the RTiO$_3$-system which was discussed controversially in the recent years (see introduction). However already the structural studies of the series of rare earth titanates RTiO$_3$ [6] indicate that the distortions indicative for orbital ordering appear above T_C or T_N (see discussion below).

The resonant X-ray measurements of DyTiO$_3$ (*ACK115*), which will be presented in the following, reveal a completely different scenario and, hence, disprove this attempt to reconcile the orbital liquid picture and the orbital order picture in the RTiO$_3$-system. But, already the structural results indicating a small temperature dependency of the octahedral distortions (which are mainly doping dependent) can exclude this interpretation as can be seen in Fig. 6.5 for example.

In Fig. 6.7 (a) the energy dependence of the resonant X-ray scattering intensity of the forbidden (0 1 1) reflection is plotted for different temperatures. The intensity in the non-rotated σ-σ channel has a structural origin whereas the intensity in the rotated σ-σ channel originates from orbital ordering [154]. Both contributions appear for this reflection. In order to avoid contaminations by multiple scattering the energy scans have been performed at several different azimuthal angles. The fluorescence of DyTiO$_3$ is shown additionally in the background (*gray area*). The two resonant peaks which can be seen in these plots emerge at the maximum of the absorbtion and about 10 eV higher, i. e. at ∼4973 eV and at ∼4983 eV. The temperature dependence of the first of these two peaks is plotted as a function of temperature for both channels and for two different azimuthal angles in the inset of Fig. 6.7 (a). As can be seen there is almost no temperature dependence.

In Fig. 6.7 (b) energy scans of the forbidden (0 0 1) reflection are shown for different temperatures. The intensity of the unrotated channel (*dotted lines*) is much smaller for this reflection and most of the intensity can be found in the rotated channel (*solid lines*). Also for this (0 0 1) reflection two resonant peaks emerge at ∼4971 eV and at ∼4983 eV. Additionally, a weak peak can be observed at the pre-edge, see the inset of Fig. 6.7 (b). The resonant X-ray scattering intensity at the pre-edge is expected to reflect the 3d orbital state directly [140]. They become accessible via a dipole transition from the 1s state because of the hybridization of the Ti 4p with the orbitally ordered Ti 3d orbitals [140]. The usually forbidden (0 0 1) reflection becomes detectable due to the non-scalar interaction due to orbital ordering and the intensity is a measure for this orbital ordering [155]. (Nevertheless, orbital ordering is in accordance with space group

[6] of this work and of the Diploma thesis of the author [57] and for LaTiO$_3$ of Ref. [118]

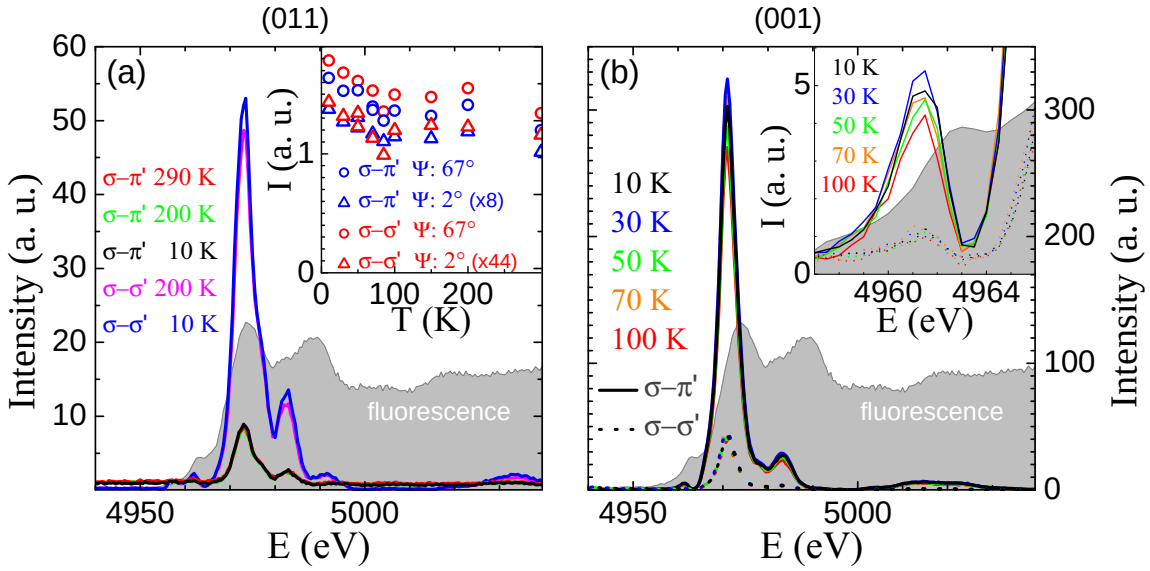

Figure 6.7: (a) Fluorescence (*gray*) together with energy scans of the (0 1 1) reflection in the (un-)rotated $\sigma - \sigma$ ($\sigma - \pi$) channel at different temperatures. In the inset the temperature dependency of the intensity of the (0 1 1) reflection measured at resonance energy for the (un-) rotated channels and for two different values of the azimuth is shown. (b) Energy scans of the (001) reflection at different temperatures for the rotated (*solid lines*) and the unrotated (*dotted lines*) channel. The inset shows the region around the pre-edge.

Pbnm.)

All these observations are very similar to the observations in $YTiO_3$ [140] where the orbital order was studied at the same reflections. Hence, these measurements indicate an orbital order in $DyTiO_3$ similar to that in $YTiO_3$.

The temperature dependence of the main and pre-edge peaks in $DyTiO_3$ is again rather weak. There is no strong rise of any intensity at the magnetic ordering temperature ($T_C = 64.6$ K). Similar observations were made for $YTiO_3$ [140] where the RXS intensities of the (001) reflection at the main edge exhibit no anomalies at T_C (which was also reported for the pre-edge RXS intensities).

As these resonant peaks are a fingerprint of orbital ordering these measurements of $DyTiO_3$ show, that there is no transition between an orbital liquid state and an orbitally ordered state and that the interpretation in Ref. [153] which is in particular based on the analysis of $DyTiO_3$ and $LaTiO_3$ seems rather questionable [7].

[7] ***X-ray absorption magnetic circular dichroism measurements***
Complementary X-ray absorption magnetic circular dichroism (XMCD) measurements at the Ti $L_{2,3}$ edge which have been performed by Z. Hu and N. Hollmann using the $DyTiO_3$ crystal *ACK115* grown in this work reveal that the orbital moment of the Ti^{3+} ions is strongly quenched by using the XMCD sum rule reported in Ref. [156]. These experimental results further rule out the orbital

As mentioned above, this could already be seen in the structural studies between room-temperature and 2 K which indicate neither changes of the octahedral tilt (which is important for the orbital ordering scheme [124]) nor in the rhombic or rectangular TiO_6 octahedral basal plane distortions which are indicative for distortions arising from orbital ordering, see Fig. 6.5. In conclusion, the interpretation that magnetic order in $DyTiO_3$ is accompanied by a transition from an orbital liquid to an orbital ordered state can be fully ruled out.

6.1.4 Conclusion

From the single crystal X-ray diffraction measurements of $RTiO_3$ a continuous variation of the octahedral tilts and rotations as well as the TiO_6-octahedral distortions with decreasing R-ionic radius has been observed. Thus, the R-ionic radius can be considered as an external control parameter which continuously drives the magnetic ordering from AFM to FM ordering. Powder X-ray as well as thermal expansion measurements for R = La, Nd, Sm, Gd and Y exhibit anomalies of the orthorhombic splitting ε and the thermal expansion α at the magnetic ordering temperature which are of opposite sign for AFM and FM titanates. These anomalies get stronger for the compounds closer to the FM/AFM crossover and are indicative for a magnetically driven change in the orbital arrangement which strengthens the prevalent orbital ordering already induced by the tilts and R-shifts. The thermal expansion measurements on $GdTiO_3$ exhibit also structural anomalies at the magnetic ordering temperature of the Gd-ions. But these effects can be neglected compared to the contribution of the Ti-sublattice. Hence, these structural effects and the increase of the thermal expansion anomalies towards the AFM/FM crossover are not induced by the R-ions and their magnetic moments (magneto-elastic coupling) but are intrinsic effects within the Ti-sublattice. Thus, this change of the sign of the thermal expansion anomalies and the increase for compounds close to the AFM/FM-crossover resembles on a quantum phase transition [146] or on the metamagnetic transition in $Ca_{2-x}Sr_xRuO_4$ [147].

The results of the synchrotron high pressure studies of $GdTiO_3$ in this work exhibit a crossing of the relative a/a_0 and c/c_0 lattice parameters which occurs at distinctly lower pressures than in $YTiO_3$ where a concomitant change in the oxygen environment of the Ti-ion indicating a change in orbital ordering has been observed [148]. Since $GdTiO_3$ is already closer to the antiferromagnetic side of the magnetic phase diagram, the observations within this work support such a model where the ferromagnetic and antiferroorbital ordered titanates are shifted by pressure towards the antiferromagnetic and ferroorbital ordered side of the phase diagram. Furthermore, this crossing of the relative lattice parameters could be observed at room-temperature as well as in the 42 K measurement at about the same pressures. Thus, these (presumable) crossings of the orbital ordering schemes in $GdTiO_3$ seem to be rather temperature independent and almost fully driven by pressure.

In resonant X-ray scattering measurements of $DyTiO_3$ similar signatures of orbital

liquid scenario in $DyTiO_3$ [157].

ordering as in $YTiO_3$ [140] could be observed. In $DyTiO_3$ the resonant peaks associated with this orbital ordering exhibit almost no temperature dependence and, especially, no anomalies at T_C. Thus, the resonant X-ray scattering measurements indicate an orbitally ordered state already at room-temperature. Hence, the interpretation of the thermal conductivity measurements of $DyTiO_3$ reported in Ref. [153] where a transition from an orbital liquid to an orbitally ordered state at T_C has been assumed in an attempt to reconcile the orbital liquid and the orbital ordering picture can be ruled out. This could be observed also directly in the structural measurements, since no significant structural changes which might be connected to a change in orbital ordering etc. could be observed between room-temperature and 2 K. Hence, the interpretation of a transition from an orbital liquid to an orbitally ordered state [153] could already be excluded from the structural measurements of $RTiO_3$.

6.2 Charge order in $Y_{1-x}Ca_xTiO_3$

6.2.1 Introduction

Metal Insulator transitions controlled by carrier-doping into a Mott insulator are a central theme in contemporary solid-state physics partly due to their relevance for the phase diagram of the high-T_C-superconducting cuprates [158, 2]. The titanates $LaTiO_3$ and $YTiO_3$ are particularly interesting since they posses a single electron in the 3d-shell compared to the cuprates with a single hole. But in contrast to the cuprates, the orbital degree of freedom plays an important role in the titanates whereas it is quenched in the cuprates. Furthermore, these titanates exhibit a three-dimensional crystal structure. In contrast to the cuprates, but, especially in contrast to the $La_{1-x}Sr_xTiO_3$ system the $Y_{1-x}Ca_xTiO_3$-system stays insulating up to rather high hole-doping levels which was the motivation to study the properties of this system in more detail.

Doping Sr and Ca into $LaTiO_3$ and $YTiO_3$, respectively, allows one to render these titanate systems metallic as the substitution of the trivalent R-ion by the divalent earth alkaline ion introduces holes into this system. Besides turning these titanates metallic also the magnetic order gets suppressed by hole-doping. However, whereas a small amount of Sr (approximately 5%) is sufficient to render $LaTiO_3$ metallic, $Y_{1-x}Ca_xTiO_3$ samples stay insulating up to Ca-doping levels of about 39% (at room-temperature) [159]. This surprising difference could only be explained by reduced bandwidths induced by increasing octahedral tilts so far [122]. But there are several other phase diagrams known, where doping into a Mott-insulator does not yield metallic behavior even at high amounts of doping. In such systems charges sometimes order, forming checker-board or stripe arrangements, like for example in $Pr_{1-x}Ca_xMnO_3$ or in $La_{2-x}Sr_xNiO_4$ [7, 160]. In the titanates, however, so far no evidence for charge ordering has been reported.

The $Y_{1-x}Ca_xTiO_3$-system shows some rather anomalous properties for the compounds in the metal-insulator transition region with Ca-doping levels of 30%-40%. First of all, the samples have insulating properties at high temperatures. However, the samples show a temperature-driven insulator-to-metal transition and become metallic at low temperatures [159, 161] which is rather anomalous. Usually, other systems like V_2O_3 exhibit an opposite behaviour with insulating properties at low temperatures and metallic properties at high temperatures [162]. Also other charge ordered systems exhibit metallic properties at high temperatures and insulating properties at low temperatures [163].

Furthermore, the magnetic susceptibility of $Y_{1-x}Ca_xTiO_3$ shows an anomalous rise on heating and an anomalous hysteresis as a function of temperature [159, 164, 165]. K. Kato *et al.* found phase separation occurring in this system at low temperatures [161] and could qualitatively assign the metallic properties to one of these phases - a low-temperature orthorhombic phase (LTO) with a small unit cell volume which appears besides the original insulating phase with a larger unit cell volume. It turned out that the large volume phase is orthorhombic at high temperatures (HTO) but becomes monoclinic at low temperatures (LTM) [161].

In the Diploma Thesis of the author [57] $Y_{1-x}Ca_xTiO_3$-samples with $x = 0.35$, 0.38 and

0.41 have been studied [8] and phase separation could be observed also in the sample with $x = 0.38$ which is right in the MI transition regime [57]. However, the resolution of the home diffractometer using Cu-K_α radiation was on the border of the detection limit and the LTM phase emerged as a shoulder in the diffraction patterns. Nevertheless, a quantitative description of macroscopic properties like electrical resistivity ρ and magnetic susceptibility χ could be achieved by weighting the metallic and insulating contributions of ρ and χ with the volume fractions determined in these X-ray measurements and summing up both contributions: $\chi_{total} = n_{LTO} \cdot \chi_{0,const} + (1 - n_{LTO}) \cdot C_{LTM}/(T + \Theta_{LTM})$ with n_{LTO} being the volume fraction of the metallic LTO phase as determined by X-ray diffraction and C_{LTM} (Curie constant) and Θ_{LTM} obtained by fitting this Curie Weiss term to the high temperature tail where $n_{LTO} = 0$. Thus, only $\chi_{0,const}$ remains a free parameter which has to be determined or fitted to the data. With this quantitative description the overall anomalous features of the magnetic susceptibility can be understood - the anomalous rise can be explained as a rise of the volume fraction of the insulating LTM phase which has a larger value of χ and the hysteresis is explained by the hysteresis of the volume fractions [57]. Furthermore, in a first powder neutron diffraction measurement of the sample with $x = 0.38$ a first (weak) indication for charge ordering was found within the insulating LTM phase [57].

In this work, first, high resolution synchrotron measurements extended the structural studies on phase separation and on the lattice parameter. Furthermore, various powder and single crystal neutron measurements have been performed in order to search for and finally establish charge ordering. Finally, the results of the neutron measurements have been affirmed by complementary resonant X-ray diffraction measurements using synchrotron radiation. For all these purposes several new $Y_{1-x}Ca_xTiO_3$ single crystals with more precise oxygen stoichiometry have been grown (see Chap.5.7) and characterized by electrical resistivity and magnetic susceptibility measurements as well as specific heat and thermal expansion measurements.

6.2.2 Experimental

A Siemens D5000 X-ray diffractometer was used for powder X-ray diffraction. $\Theta/2\Theta$-scans with step widths of 0.01° and 0.02° were made using Cu- and Cr-K_α-radion. Powder X-ray diffraction measurements using synchrotron radiation have been performed on beamline B2 at Hasylab/DESY in Hamburg. A wavelength of $\lambda = 0.74950$ Å (E = 16541.7 eV) was chosen in order to avoid fluorescence of the Y-ions (electron binding energy for K 1s electrons: 17038 eV). Powder neutron diffraction measurements have been performed at the reactor FRM-II in Garching using the SPODI diffractometer ($\lambda = 1.548$Å) and at the reactor Orphée in Saclay using the 3T2 diffractometer ($\lambda = 1.2251 - 1.2252$Å). Single crystal neutron diffraction measurements have been performed at the reactor Orphée in Saclay using the 5C2 diffractometer ($\lambda = 0.83$ Å, 0.831 Å) and at the PANDA spectrometer at the FRM-II in Garching. Single crystal X-ray diffraction has been performed on a Bruker Apex X8 CCD diffractometer

[8] The sample with x=0.40 probably suffers from larger inhomogeneities.

using Mo-K_α radiation (structural refinement with *Jana2000* [58]). Resonant X-ray diffraction using synchrotron radiation have been performed at the MagS beamline of BESSY in Berlin in collaboration with C. Schüßler-Langeheine, H.-H. Wu and C. Trabant. Resistivity measurements have been performed using an AC four-point method. The magnetic susceptibility was measured by M. Reuther with a vibrating sample magnetometer (VSM). The specific heat has been measured by O. Heyer in a physical property measurement system (PPMS, Quantum Design) using the relaxation time method. Measurements of the thermal expansion have been performed by J. Rohrkamp using a high-resolution capacitance dilatometer.

For the first diffraction measurements of this work old samples grown by H. Roth were used. These samples *HR120*, *HR99+HR100*, *HR134*, *HR139* and *HR155* with $x = 0.35$, 0.38, 0.41, 0.50 and 0.55 respectively tend to have some excess oxygen as indicated by TGA measurements (see Chap. 5.2) or by the comparison of the volume fractions of the metallic LTO phase measured for *HR99+HR100* with the values observed in Ref. [166] for a $Y_{1-x}Ca_xTiO_3$-sample with $x = 0.39$ which are very similar for both measurements; see Fig. 6.10 (f). Two other samples with $x = 0.40$, 0.52 were grown by A. Nugroho. Since the new $Y_{1-x}Ca_xTiO_3$-samples (*ACK*-series) were not available then, only these old $Y_{1-x}Ca_xTiO_3$-samples could be measured in the very first synchrotron and some of the very first neutron measurements. Many of the $R_{1-x}Ca_xTiO_3$-samples grown later in this work have a better oxygen stoichiometry (see Chap. 5.7) and have been used for all further neutron, resistivity, magnetic susceptibility, thermal expansion and specific heat measurements as well as resonant X-ray diffraction measurements.

6.2.3 Results and Discussion

Resistivity and magnetic susceptibility measurements

For a detailed characterization of the $Y_{1-x}Ca_xTiO_3$-phase diagram the electrical resistivity as well as the magnetic susceptibility have been measured mainly using the new samples grown in this work (*ACK*-series) for different doping levels ranging from $x = 10\%$ to 50%. These measurements are shown in Fig. 6.8 (a-b). Up to roughly 30% of Ca-doping, the $Y_{1-x}Ca_xTiO_3$-system stays insulating. Between about 30% and 40% of doping there is a broad MI-transition regime. In this regime a temperature driven MI-transition can be observed (T_{MI}). This MI-transition is rather unusual as the metallic phase emerges at low temperatures. Such anomalous behaviour could be observed for the layered 327-manganites (see for example Ref. [167]), but usually, like in V_2O_3, the metallic phase emerges at high temperatures and the insulating phase at low temperatures [162]. The $Y_{1-x}Ca_xTiO_3$-compounds in this MI-transition regime also exhibit anomalies in the magnetic susceptibility which shows a hysteresis and an anomalous rise with temperature. This anomalous susceptibility could be well described within the phase separation scenario by attributing a constant Pauli paramagnetic term to the metallic phase and fitting a Curie-Weiss term to the high-temperature tail where 100% of the insulating HTO phase persists (see Introduction) [57].

powder X-ray diffraction measurements

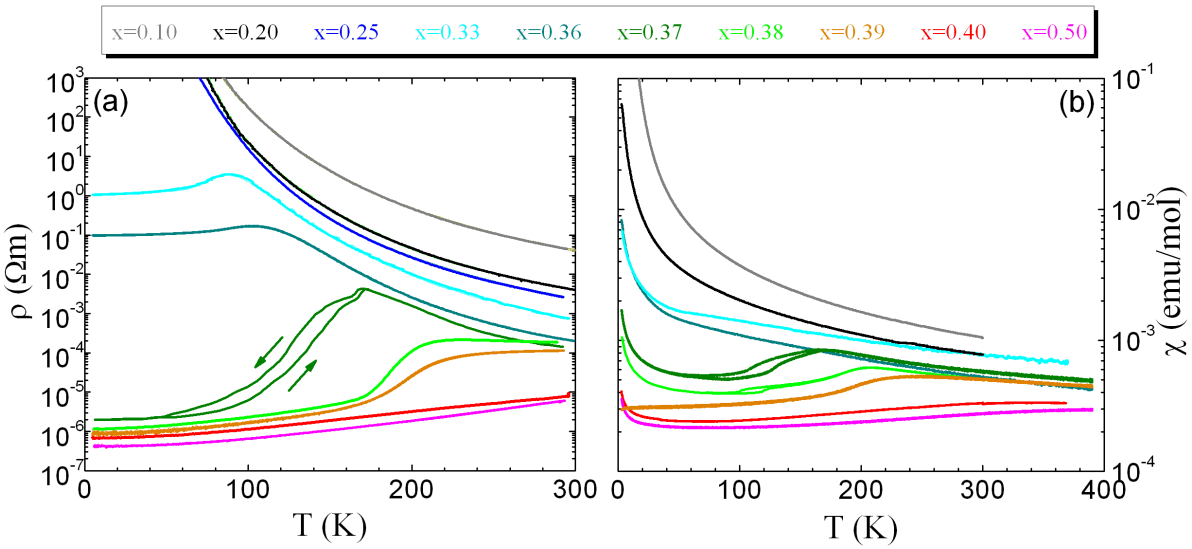

Figure 6.8: (a) Electrical resistivity and (b) magnetic susceptibility measurements of $Y_{0.9}Ca_{0.1}TiO_3$ (*ACK012*), $Y_{0.8}Ca_{0.2}TiO_3$ (*ACK013*), $Y_{0.75}Ca_{0.25}TiO_3$ (*ACK044*), $Y_{0.67}Ca_{0.33}TiO_3$ (*ACK015*), $Y_{0.64}Ca_{0.36}TiO_3$ (*ACK016*), $Y_{0.63}Ca_{0.37}TiO_3$ (*ACK083*), $Y_{0.62}Ca_{0.38}TiO_3$ (*HR100*), $Y_{0.61}Ca_{0.39}TiO_3$ (*ACK076*), $Y_{0.6}Ca_{0.4}TiO_{3+\delta}$ (*Agung*), $Y_{0.5}Ca_{0.5}TiO_3$ (*ACK047*).

Synchrotron radiation powder X-ray diffraction measurements have been performed in order to study the lattice parameter, the monoclinic angle and the occurrence of phase separation in the $Y_{1-x}Ca_xTiO_3$-system (old samples grown by H. Roth). As the LTO phase has a smaller unit cell volume caused by a smaller *b*-lattice parameter [57] the (020) peak is a good reflection to distinguish between the HTO/LTM and the LTO phase [9]. This peak is compared in Fig. 6.9 (a-c) for three different types of measurements. A first improvement to the powder X-ray diffraction measurements of the Diploma Thesis [57] could be achieved by using Cr-K_α-radiation instead of Cu-K_α-radiation as Cr-K_α radiation has a distinctly larger wavelength. The use of a larger wavelength succeeds in giving a better resolution as can be seen impressively in Fig. 6.9 (a-b), but the use of such a large wavelength renders these measurements more surface sensitive since the absorbtion increases. Therefore, the results of these measurements can be biased by surface effects. Additionally, fewer reflections can be measured making the Rietveld fits less reliable. Therefore, the structural studies have been extended to synchrotron measurements in this work. These synchrotron measurements benefit from the small divergence of the X-ray beam at the synchrotron which gives a much better resolution even at higher incident energy (smaller wavelength). Clips out of the diffraction patterns of measurements of the same $Y_{1-x}Ca_xTiO_3$-sample are plotted in Fig. 6.9 (c). In the left part of the figure the splitting of the (020) peak can be observed with better resolution

[9] The (020) reflection has the largest intensity of all reflections exhibiting a peak-splitting due to phase separation.

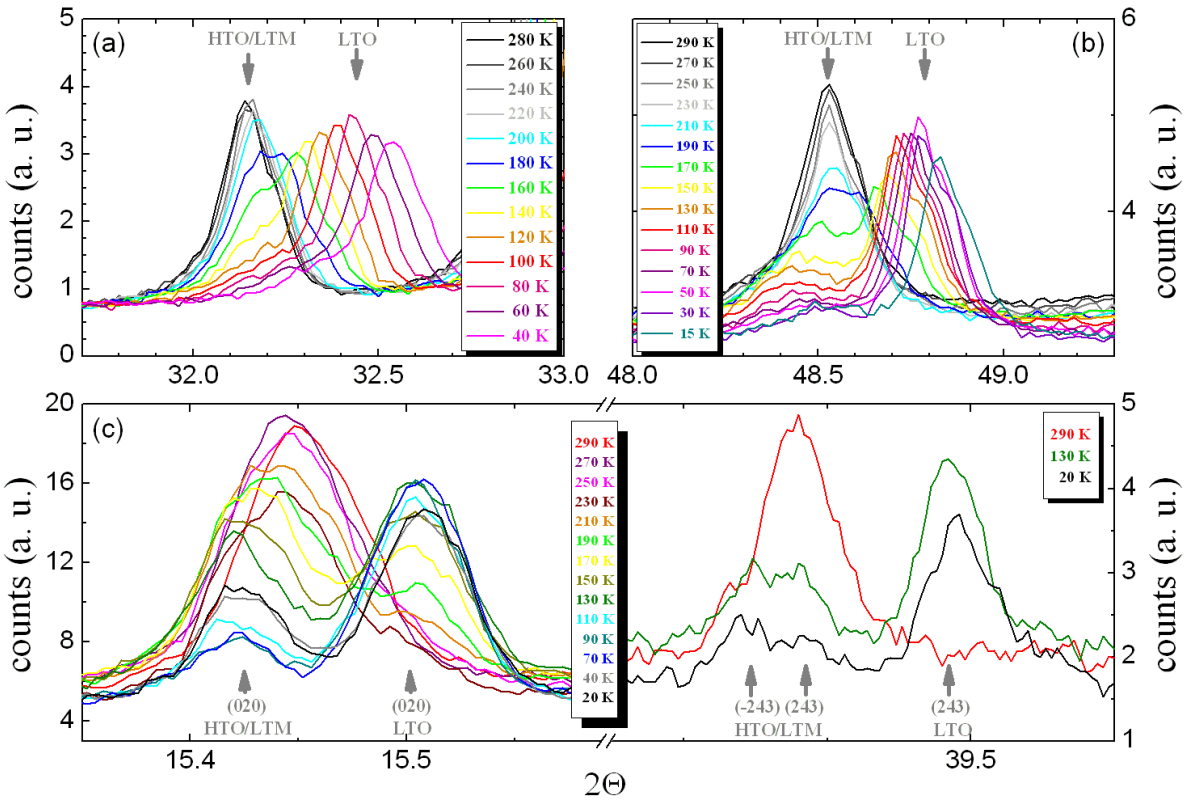

Figure 6.9: Clips out of powder X-ray diffraction patterns of $Y_{0.62}Ca_{0.38}TiO_{3.01}$ using (a) Cu-K_α radiation [57], (b) Cr-K_α radiation and (c) synchrotron radiation (λ = 0.7495 Å).

than in the measurement using Cr-K_α-radiation although the wavelength is more than three times smaller. In the right part of this figure the (243) reflection is shown which is also split into the LTO and the LTM contribution. Additionally, the (243) peak of the LTM phase exhibits a significant peak broadening at low temperatures and indicates the splitting into a (-243) and a (243) peak. The Rietveld refinement reveals a monoclinic angle which starts to deviate from 90° below about 200 K and amounts to 90.1° at low temperatures; see Fig. 6.10 (e). Thus, the insulating HTO phase becomes monoclinic on cooling. The corresponding volume fraction of the metallic LTO phase is shown in Fig. 6.10 (f) and the lattice parameter and unit cell volume are plotted in Fig. 6.10 (a-d). Besides the sample with $x = 0.38$ also the other samples with $x = 0.35$, 0.41, 0.50 and 0.55 and the sample with $x = 0.40$ (grown by A. Nugroho) have been measured. The results of these measurements were plotted in Fig. 6.10 (a-f).

One of the main important results which can be drawn from these measurements is that phase separation occurs in the systems around the MI-transition and that the volume ratio of the metallic phase increases with increasing hole doping level; see Fig. 6.10 (f). For completeness also the volume ratio of the sample with $x = 0.37$ from Ref. [166] is added to the plot. The samples which are already in the metallic regime

($x = 0.40$, 0.41) also exhibit phase separation and minor parts of the HTO phase survive into this metallic regime and even exhibit a small increase on heating. This explains the rise of the magnetic susceptibility with temperature which could be observed for the metallic samples with $x \geq 0.40$; see Fig. 6.8 (and the Diploma Thesis [57]). With increasing temperature, the volume fraction of the HTO phase rises and causes a small rise of the total susceptibility as $\chi_{HTO/LTM} \gg \chi_{LTO}$. For the samples with $x = 0.40$ and 0.41 this could be observed directly, for the samples with higher hole-doping level this could not be observed directly as the lattice constants may have become more similar, but the anomalous rise of the susceptibility for these samples would suggest a similar scenario as for the samples with $x = 0.40$ and 0.41 where phase separation could be confirmed.

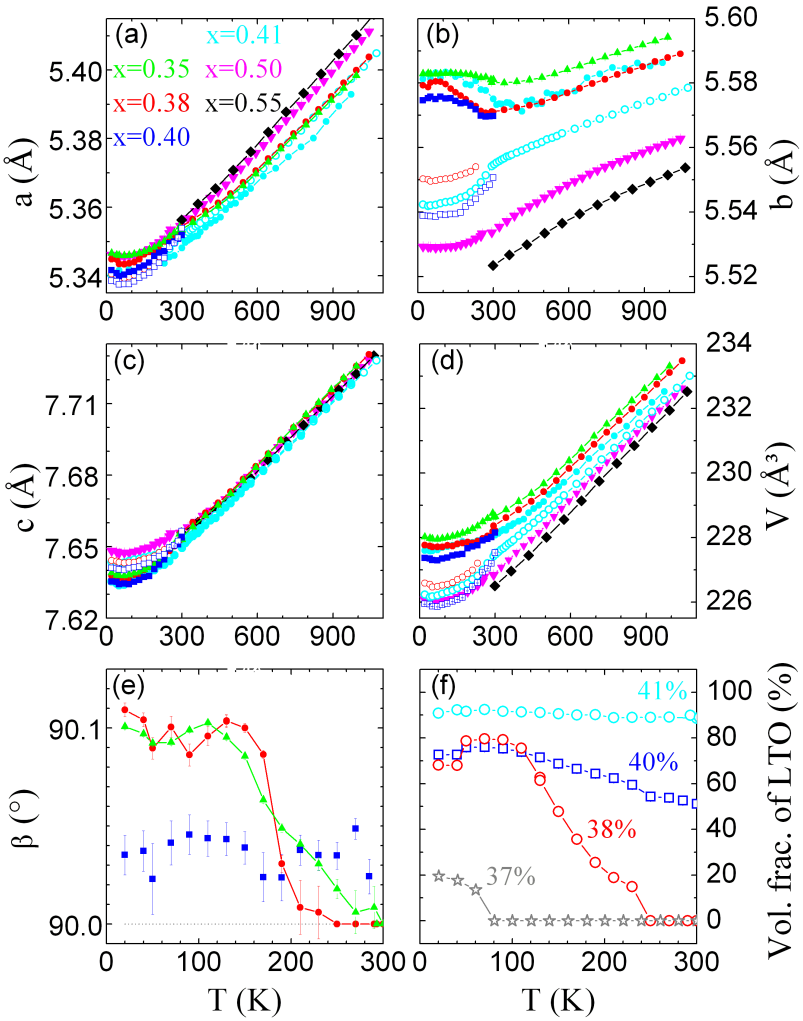

Figure 6.10: (a-e) Lattice parameter a, b, c, β and V of $Y_{1-x}Ca_xTiO_3$ for different doping levels x. (f) Volume fraction of the metallic LTO phase. Values for $x = 0.37$ (*gray*) were taken from Ref. [166].

Furthermore, the phase separated samples in the MI-transition regime ($0.30 < x < 0.40$) have a monoclinic phase with a monoclinic angle β which starts to deviate from 90° below about 200-250 K and attains its maximum value of about 90.1° at lowest temperatures. This was also observed in Ref. [161]. However, for the samples in the metallic regime ($x \geq 0.40$) the monoclinic angle gets small and can not be unambiguously distinguished from 90°. Also in Ref. [161] it was reported that the sample with $x = 0.41$ shows phase separation with two orthorhombic phases ($Pbnm$) at room-temperature [10].

Another interesting result is the temperature dependence of the b lattice parameter of the LTM phase. For all samples measured in this work ($x = 0.35$, 0.38, 0.40 and 0.41) an anomalous rise of the b-lattice parameter on cooling could be observed. Such an anomalous rise could be indicative for orbital ordering (see for example Chapter 6.1) or other interesting effects occurring in the insulating LTM phase. The b lattice constant is also the lattice constant which shows the strongest difference for the LTO and the LTM phase. These interesting findings give reason to further investigations.

neutron diffraction measurements

Single crystal neutron diffraction measurements have been performed for $Y_{0.64}Ca_{0.36}TiO_{3.00}$ (ACK016) and $Y_{0.67}Ca_{0.33}TiO_{3.00}$ (ACK015) at the PANDA spectrometer at FRM-II in Garching. In these measurements superstructure reflections could be observed on cooling; see Fig. 6.11 (a-b). The space group $Pbnm$ has a b glide mirror plane ($\perp$a) which induces the zonal reflection condition $0kl$, $k = 2n$. Thus, the (011) and (013) reflections are superstructure reflections which indicate the breaking of the glide mirror symmetry. In synchrotron radiation powder X-ray diffraction measurements for similar $Y_{1-x}Ca_xTiO_3$ samples a phase transition from the orthorhombic space group $Pbnm$ to the monoclinic space group $P2_1/n$ has been observed (see previous section and Ref. [161]). In the monoclinic space group $P2_1/n$ the zonal reflection condition mentioned above is absent and the (0kl) reflections with odd values of k are allowed. Thus, the rise of the (011) and (013) superstructure reflections indicates the orthorhombic → monoclinic phase transition which is in accordance with the synchrotron measurements (see previous section). The (011) and (013) reflections are the $(1/2\ 1/2\ 1/2)_{cub}$ and $(1/2\ 1/2\ 3/2)_{cub}$ reflections of the pseudocubic unit cell of the Ti-array (blue cell in the inset of 6.11 (a)) and, thus, are indicative for distortions/modulations which alternate for all Ti-ions. Due to the loss of symmetry elements in the monoclinic phase the oxygen environment of a Ti ion can be different compared to its six neighbouring Ti-ions. The remaining n glide mirror plane induces equivalent oxygen environments among these six neighbourring Ti-ions. Thus, there are two different Ti-sites (Ti1, Ti2) in the monoclinic phase which alternate in all three directions (a_{cub}, b_{cub}, c_{cub}). As the average charge at all Ti sites is close to 3.5+, this observation could suggest charge ordering in the RTiO$_3$-system which should be embodied by an alternating Ti^{4+}-/Ti^{3+} checkerboard pattern such that each $Ti^{4+}O_6$-octahedron is connected with six neighbouring $Ti^{3+}O_6$-octahedra. If the

[10] At low temperatures (20 K), again, a monoclinic phase has been reported for this sample but the monoclinic angle was not shown. Only the temperature dependency of β for the samples with $x = 0.37$ and 0.39 has been plotted.

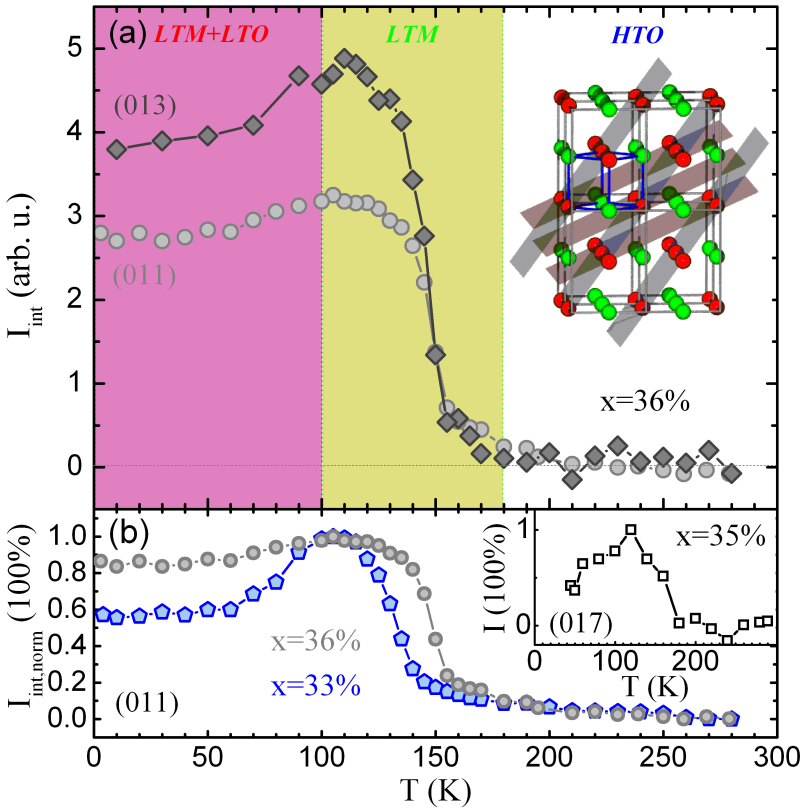

Figure 6.11: (a) Intensity of the (011) and (013) reflections (in *Pbnm*) for $Y_{0.64}Ca_{0.36}TiO_{3.00}$ (ACK016); background and multiple scattering subtracted. In the inset a model with 8 unit cells (*Pbnm*) filled with alternating Ti^{3+}/Ti^{4+}-ions and the (011) and (013) planes is shown. (b) Comparison of the temperature dependency of the (011) reflections for $Y_{0.64}Ca_{0.36}TiO_{3.00}$ (ACK016) and $Y_{0.67}Ca_{0.33}TiO_{3.00}$ (ACK015). The inset shows the temperature dependency of a (017) superstructure reflection for the sample with $x = 0.35$ after multiple scattering subtraction.

Ca doping x is less than 50% some additional Ti^{3+}- ions have to be placed randomly at Ti^{4+}-sites. A very similar type of ordering can be observed in the $A_2BB'O_6$-type perovskites with A = Nd, B = Ti and B' = Mg, where the B/B'-sites are almost fully ordered and each TiO_6-octahedron is surrounded by 6 MgO_6 octahedra and vice versa [168]. This type of Mg/Ti-ordering is very similar to a Ti^{4+}-/Ti^{3+}-ordering and also results in a reduction of the symmetry from *Pbnm* to $P2_1/n$ with a monoclinic angle β very close to 90°. Besides the similar symmetry reduction, the charge ordering in the $Y_{1-x}Ca_xTiO_3$-system is supported by the following findings. The transition temperature for the $Y_{1-x}Ca_xTiO_3$-sample with $x = 0.33$ is 15 K lower as the transition temperature for the sample with x=0.36; see Fig. 6.11 (b). These superstructure reflections can not be caused by orbital ordering and concomitant oxygen displacements as the larger Ti*3d*-orbital occupation in the sample with $x = 0.33$ should stabilize any orbital ordering and the ordering temperature should be higher for the sample with $x = 0.33$ instead.

Furthermore, these superstructure reflections are not magnetic in origin as the magnetic susceptibility shows no anomalies at 150 K (see Fig. 6.8) and as the magnitude increases with Q which is in contrast to the expected Q-dependency due to the magnetic form factor. Last, any ionic Y/Ca order can be excluded because the fully reversible rise of the superstructure reflections at 150 K is too steep and sudden for such types of ordering phenomena. And additionally, any oxygen-order can be excluded by the almost perfect oxygen stoichiometry.

A similar temperature dependency of the (017) superstructure reflection of a sample with $x = 0.35$ (HR120) could be observed in a different single crystal neutron diffraction measurement at the 5C.2 diffractometer at the reactor Orphée in Saclay, France. This measurement suffers from larger multiple scattering contributions. In order to remove this multiple scattering, a linear intensity contribution has been subtracted from this data. Hence, the $x = 0.35$ intensity-temperature curve has some uncertainties, but at least the overall progression of the intensity with temperature can be estimated from the inset of Fig. 6.11 (b).

The loss of intensity of the (01L) superstructure reflections at about T_{MI} can be well understood by the phase separation scenario. As can be seen in Fig. 6.8 the electrical resistivity of $Y_{0.67}Ca_{0.33}TiO_{3.00}$ (ACK015) and $Y_{0.64}Ca_{0.36}TiO_{3.00}$ (ACK016) starts to decrease below about 100 K. This is about the same temperature where these superstructure reflections start to decrease slightly; see Fig. 6.11 (b). Therefore, it is likely that phase separation occurs at these temperatures and that the metallic LTO phase emerges besides the insulating and charge ordered monoclinic $P2_1/n$ (LTM) phase. As this metallic phase which is not charge ordered exhibits no superstructure reflections, the intensity of the superstructure reflections decreases together with the volume fraction of the LTM phase.

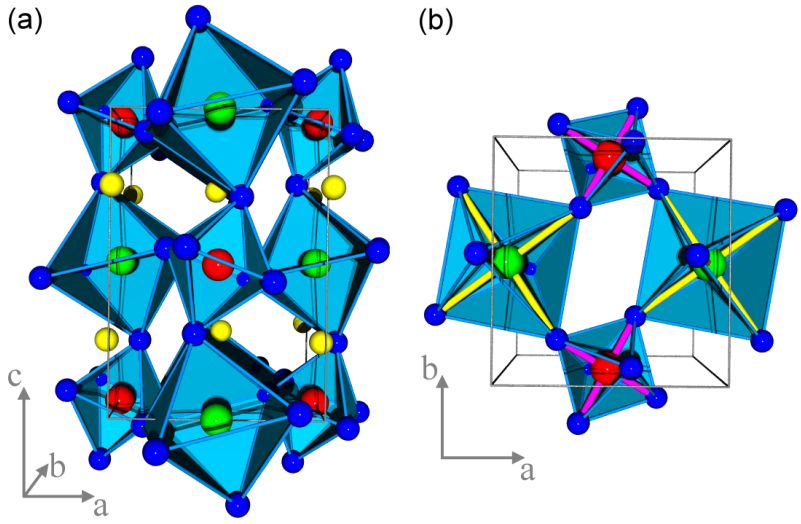

Figure 6.12: (a-b) Schematic model for the distortions in the LTM phase.

For a more detailed analysis of the charge ordering occuring in this system, single

crystal neutron diffraction measurements have been performed at the 5C.2 diffractometer at the reactor Orphée in Saclay, France. In these measurements the samples with $x = 0.35$ (HR120) and $x = 0.36$ (ACK017) have been measured at 120 K, 298 K and at 110 K, 298 K respectively, i. e. one measurement in the HTO and one measurement in the pure LTM phase for each sample. Due to the loss of symmetry elements after the phase transition from the HTO phase ($Pbnm$) to the LTM phase ($P2_1/n$) there are two different Ti sites with inequivalent oxygen environments in the unit cell of the LTM phase as shown schematically in Fig. 6.12 (a-b). The results of the structure refinement of these measurements indicate elongated basal Ti-O distances for one Ti-ion and compressed basal Ti-O distances for its six neighbouring Ti ions. This is indicative for charge ordering which is affirmed by the bond valence sum analysis (calculated for both Ti-ions from the measured crystal structure) which provides clear evidence for charge ordering. Thus, the insulating large-volume HTO phase becomes monoclinic at low temperatures due to charge ordering. In this charge ordering pattern the Ti^{4+}- and Ti^{3+}-ions are placed alternatingly at the Ti1 and Ti2 sites. But as the doping level of 35%-36% is not sufficient for a fully developed three-dimensional Ti^{3+}/Ti^{4+} checkerboard charge ordering pattern the additional electrons have to be placed randomly at the Ti^{4+} sites.

The analysis of the internal R-values for the monoclinic settings "a", "b", and "c" ("2/m") yields the following R_{int} values: 4.32%, 3.37% and 4.42% (redundancy: 1.9, 1.8 and 1.9 respectively) for the sample with $x = 35\%$ and 1.83%, 1.13% and 1.86% (redundancy: 1.8, 1.9, and 1.8 respectively) for the sample with $x = 36\%$. Thus, the results of the synchrotron measurements finding the monoclinic angle β are supported by these neutron measurements.

The results of the structural refinements of these single crystal neutron diffraction measurements are listed in Tab. 6.1. Due to these measurements, the four Ti-O2 distances are larger for the Ti2-site than for the Ti1-site; see Tab. 6.1. (The two Ti-O1 distances exhibit an opposite behaviour of minor extent.) This leads to different bond valence sums for these two Ti-ions. The bond valence sum (BVS) is an empirical value which indicates the nominal valency of an ion M_i calculated from the M_i - oxygen distances by equation 6.1 [169].

$$V_i = \sum_j s_{ij} = \sum_j \exp((r_0 - r_{ij})/B) \tag{6.1}$$

The constants B and r_0 have been determined for each ion M_i from a crystal structure database and can be found in tables [169]. If the M_i-O_j distance r_{ij} is small, the bond valence s_{ij} increases and indicates a stronger oxidation of the M_i-ion. As the constants B and r_0 have not been calculated for such compact structures as the perovskite structure, the BVS V_i for these type of compounds always indicates slightly larger values than expected. But as was shown in Ref. [170, 57] the BVS is an excellent measure for *differences* in the oxidation state of two ions within the same class of compounds or within the same crystal. The calculation of the BVS for the Ti-ions in the samples with $x = 0.35$ (HR120) and $x = 0.36$ (ACK017) reveals a difference in the nominal oxidation state which amounts to about 0.23 - 0.30 electrons; see Tab. 6.1. In the refinement with space group $P2_1/n$ the anisotropic thermal displacement parameters U_{ij} for Ti2

and O3 sites have been restricted to the corresponding values at the Ti1 and O2 sites respectively, assuming that these ions have very similar thermal displacement parameters as in the *Pbnm* parent structure. This restriction to the same thermal displacement parameters according to space group *Pbnm* avoids any additional distortions which may occur in the structure refinement if the (thermal) displacement parameters of Ti1 and Ti2 get different. (For example if U_{ij} of Ti1 would be very large and U_{ij} of Ti2 would be very small one could easily introduce distortions similar to charge ordering artificially.) Although the observation of the (01L) superstructure reflections in both measured samples clearly indicates the monoclinic symmetry $P2_1/n$, for a comparison the low-temperature single crystal neutron data has also been refined with a structure model which is restricted to an undistorted *Pbnm* structure which does not allow charge ordering (‡). The refinement within this structure model yields enhanced R-values. This supports the charge ordering model. On the other hand a refinement of the 298 K room-temperature data for the sample with $x = 0.35$ with the monoclinic structure $P2_1/n$ and the atomic positions from the charge ordered 120 K structure as starting parameters yields structural parameters which do not show any indication for charge ordering. At 298 K the nominal valency of both Ti sites amounts to 3.534(6) for Ti1 and 3.530(6) for Ti2. This result is in accordance with a drop of the (017) superstructure reflection around roughly 150 K measured for the sample with $x = 0.35$ at the 5C.2 diffractometer which indicates the onset temperature for charge ordering (T_{CO}) which is similar to the sample with $x = 0.36$; see Fig. 6.11 (b). The difference of the nominal valencies of both Ti sites derived from the BVS analysis is plotted for different temperatures in Fig. 6.13 (a). Additionally, the temperature dependency of the (011) superstructure reflection of $Y_{0.64}Ca_{0.36}TiO_3$ is shown in the background (*gray*). Hence, these single crystal neutron diffraction measurements give evidence for a checkerboard type charge ordering in the $Y_{1-x}Ca_xTiO_3$-system which is shown schematically in Fig. 6.13 (b).

Unfortunately, the two single crystals which are untwined at room-temperature become twinned below the orthorhombic to monoclinic phase transitions with two (monoclinic) twin domains of about 50.0% volume fraction. This twinning is inherent to the phase transition and can not be avoided. The existence other twin domains can possibly biase the results of the structural refinement. In order to avoid any effects by twinning, both samples with $x = 0.35$ (HR120) and $x = 0.36$ (ACK017) have also been studied with complementary powder neutron diffraction measurements at 130 K, 298 K and 110 K, 298 K respectively. The sample with $x = 0.35$ has been measured at the SPODI diffractomter at FRM-II in Garching and the sample with $x = 0.36$ has been measured at the 3T.2 diffractometer at the reactor Orphée in Saclay. In the less accurate powder neutron diffraction data, the weak superstructure reflections could not be observed anymore. Nevertheless, these measurements have to be in accordance with the structure model determined in the single crystal neutron measurements. Therefore, the structure model was refined *simultaneously* for powder neutron diffraction data and single crystal neutron data using the program Jana2006 [171]. The R-values obtained for the refinement of the charge ordered structure model ($P2_1/n$) and the R-values obtained for the undistorted structure model (*Pbnm*) are very similar for the powder neutron data: R_p/R_{wp}=5.88%/7.92% ($P2_1/n$), R_p/R_{wp}= 5.90%/7.97% (*Pbnm*) for the sample

x:	**0.35**	**0.35**	**0.35**	**0.36**	**0.36**	**0.36**
SG:	$P2_1/n$	*Pbnm* ‡	*Pbnm*	$P2_1/n$	*Pbnm* ‡	*Pbnm*
s.c. neutron:						
T:	120 K	‡	298 K	110 K	‡	298 K
all refl.:	1538	‡	1553	1790	‡	366
$\mathbf{2\Theta_{max}}$**:**	78.9°	‡	85.1°	85.3°	‡	85.5°
redun.:	1.79	‡	2.83	1.88	‡	1.07
$\mathbf{R}_{int}$**:**	2.26%	‡	4.16%	1.13%	‡	0.79%
GoF:	3.96	4.65	11.43	2.96	3.22	8.00
R:	4.03%	5.35%	3.46%	3.31%	5.59%	5.36%
$\mathbf{R}_w$**:**	8.35%	9.87%	5.76%	3.06%	3.38%	5.85%
x(Y1/Ca1):	0.9834(1)	0.9834(1)	0.9841(1)	0.9847(1)	0.9847(1)	0.9849(2)
y(Y1/Ca1):	0.0641(1)	0.0642(1)	0.0631(1)	0.0623(1)	0.0623(1)	0.0612(4)
z(Y1/Ca1):	0.2476(2)	0.25	0.25	0.2488(3)	0.25	0.25
U(Y1/Ca1):	0.0095(2)	0.0095(2)	0.0136(2)	0.0047(1)	0.0046(1)	0.0063(7)
x(Ti1/Ti2):	0 / 0.5	0 / -	0 / -	0 / 0.5	0 / -	0 / -
x(Ti1/Ti2):	0.5 / 0	0.5 / -	0.5 / -	0.5 / 0	0.5 / -	0.5 / -
z(Ti1/Ti2):	0 / 0	0 / -	0 / -	0 / 0	0 / -	0 / -
U(Ti1/Ti2):	0.0085(3)	0.0082(3)	0.0111(3)	0.0029(1)	0.0029(1)	0.0038(11)
x(O1):	0.1039(1)	0.1040(1)	0.1030(2)	0.0999(1)	0.0998(1)	0.1002(2)
y(O1):	0.4656(1)	0.4657(2)	0.4658(1)	0.4678(1)	0.4679(1)	0.4668(5)
z(O1):	0.2507(3)	0.25	0.25	0.2526(4)	0.25	0.25
U(O1):	0.0125(2)	0.0122(2)	0.0154(2)	0.0068(1)	0.0068(1)	0.0088(8)
x(O2):	0.6993(3)	0.6958(1)	0.6956(1)	0.7004(3)	0.6964(1)	0.6964(2)
y(O2):	0.3057(2)	0.3017(1)	0.3013(1)	0.3035(3)	0.3000(1)	0.3003(3)
z(O2):	0.0554(2)	0.0534(1)	0.0529(1)	0.0493(3)	0.0516(1)	0.0517(1)
U(O2):	0.0125(2)	0.0127(2)	0.0159(1)	0.0066(1)	0.0070(1)	0.0085(6)
x(O3):	0.8079(3)	-	-	0.8077(3)	-	-
y(O3):	0.7977(3)	-	-	0.7965(3)	-	-
z(O3):	0.0514(2)	-	-	0.0540(3)	-	-
U(O3):	0.0122(1)	-	-	0.0066(1)	-	-
Ti1-O1:	2.011(2) Å	2.006(1) Å	1.993(1) Å	2.018(3) Å	1.999(1) Å	1.995(1) Å
Ti1-O2:	1.991(1) Å	2.016(1) Å	2.019(1) Å	1.984(2) Å	2.015(1) Å	2.004(1) Å
Ti1-O2':	1.997(1) Å	2.029(1) Å	2.045(1) Å	1.996(2) Å	2.020(1) Å	2.005(1) Å
Ti2-O1:	2.001(2) Å	-	-	1.980(3) Å	-	-
Ti2-O2:	2.060(1) Å	-	-	2.044(2) Å	-	-
Ti2-O2':	2.041(2) Å	-	-	2.047(2) Å	-	-
Δ***BVS:***	0.32(1) e	-	-	0.23(1) e	-	-

Table 6.1: Results of single crystal neutron diffraction measurements of $Y_{1-x}Ca_xTiO_3$; $U \equiv U_{iso}$ (Å^2); ‡: same low-temperature measurement as in column before but fitted with restrictions equivalent to space group *Pbnm*.

with $x = 0.35$ and R_p/R_{wp}=2.92%/3.68% ($P2_1/n$), R_p/R_{wp}=2.89%/3.64% (*Pbnm*) for the sample with $x = 0.36$. Thus, the powder diffraction data is presumably not sensible enough to distinguish clearly between the undistorted and the charge ordered structure model. This could have already been assumed for these measurements, as the charge ordering superstructure reflections are completely hidden in the background. Whereas

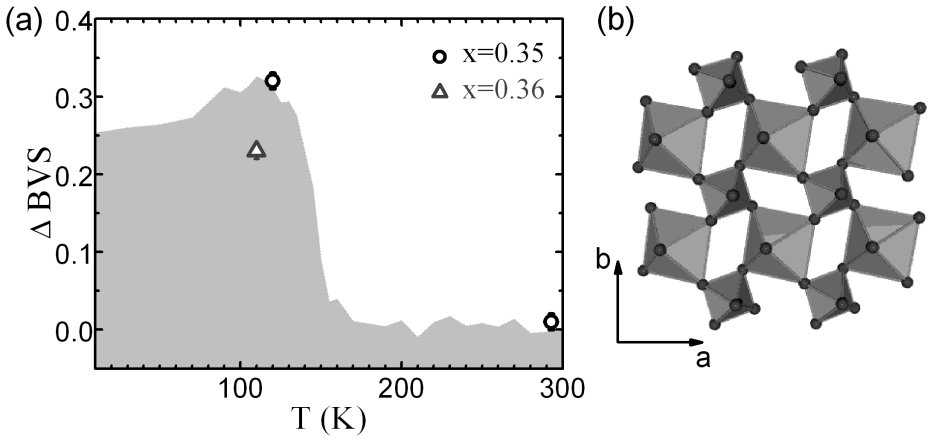

Figure 6.13: (a) Difference of the BVS for both Ti sites for different temperatures. Additionally, the temperature dependency of the (011) superstructure reflection for the sample with $x = 0.36$ is shown (*lt. gray*). (b) Schematic model of the LTM phase.

the powder diffraction data set is not very sensible to a change between these two structure models (*Pbnm* and $P2_1/n$) in this simultaneous refinement, the single crystal data set still exhibits enhanced R-values for the *Pbnm* structure and the results are fully in accordance with the first refinement of the single crystal data solely. Thus, this *simultaneous* refinement with powder and single crystal neutron data supports the results of single crystal neutron diffraction as it shows, that there are no major discrepancies due to twinning.

Unfortunately, the $Y_{1-x}Ca_xTiO_3$-system becomes metallic for doping levels exceeding 40%. Therefore, the optimum doped sample with $x = 50\%$ can not exhibit charge ordering at low temperatures. Instead, the charge ordering regime extends to lower Ca-doping levels x where the $Y_{1-x}Ca_xTiO_3$-system is still insulating.

X-ray diffraction measurements

Additional single crystal X-ray diffraction measurements of the sample with x=0.35 have been performed with the accuracy of an electron density measurement. Images have been collected with 30 s/ 45 s/ 50 s for the low/medium/high 2Θ-angle region. For a detailed description of the measurement method see Chapter 4. The spherical sample with 75(3) μm radius has been measured at 298 K and at 115 K and the resulting Ti-O distances and bond valence sums are listed in Tab. 6.2. In these measurements the difference in the BVS is significantly enlarged compared to the results in the single crystal neutron measurements although the atomic positions of the neutron measurements have been used as starting parameters and the oxygen positions were refined last. This discrepancy in the BVS mainly results from an increased apical Ti-O distance for the Ti^{3+} ion which is absent in the neutron results. Thus the TiO_6-octahedra are elongated in all three directions for the Ti^{3+} ion as is shown in Fig. 6.12. This discrepancy between

x:	**0.35**	**0.35**	**0.35**	**0.35**
SG:	$P2_1/n$	*Pbnm* †	$P2_1/n$	*Pbnm* †
s.c. X-ray:				
T:	115 K	‡	298 K	‡
all refl.:	27382	‡	24851	‡
$\mathbf{2\Theta_{max}}$**:**	126.8°	‡	125.0°	‡
redun.:	7.85	‡	6.92	‡
$\mathbf{R}_{int}$**:**	3.05%	‡	2.37%	‡
GoF:	1.96	2.12	2.10	2.09
R:	1.86%	2.00%	1.61%	1.71%
$\mathbf{R}_w$**:**	3.68%	4.02%	3.15%	3.33%
Ti1-O1:	1.986(2) Å	1.998(1) Å	1.996(2) Å	2.000(1) Å
Ti1-O2:	1.9564(15) Å	2.009(1) Å	2.011(2) Å	2.012(1) Å
Ti1-O2':	1.9844(15) Å	2.023(1) Å	2.025(1) Å	2.021(1) Å
Ti2-O1:	2.010(2) Å	-	2.005(2) Å	-
Ti2-O2:	2.0636(15) Å	-	2.017(1) Å	-
Ti2-O2':	2.0615(15) Å	-	2.014(2) Å	-
BVS(Ti1):	4.04(1)	3.68(1)	3.66(1)	3.66(1)
BVS(Ti2):	3.36(1)	-	3.65(1)	-
Δ***BVS:***	0.68(1) e	-	0.01(1)	-

Table 6.2: Results of the refinement of single crystal X-ray diffraction measurements of $Y_{1-x}Ca_xTiO_3$. ‡: same measurement as in the column before but fitted with *Pbnm*.

single crystal neutron and single crystal X-ray data has not been fully understood. Either the sample quality of a small single crystalline sphere is higher than that of a large single crystal of roughly 0.5 cm^3 volume which causes an enhanced difference of the BVS in the X-ray case or one of these measurements has less accuracy than the other. The relatively weak scattering by the oxygen ions in the X-ray case is disfavourable for these types of measurements, but extinction effects may be disfavourable for the neutron measurements. A synchrotron radiation single crystal X-ray diffraction measurement could give additional information as extinction and absorbtion effects are small at high X-ray energies and as the large statistics due to the high intensities at the synchrotron may overcompensate the relative small scattering by oxygen.

Single crystal X-ray diffraction measurements have been performed for the whole series of $Y_{1-x}Ca_xTiO_3$ at room-temperature (HTO phase with space group *Pbnm*) in order to determine the TiO_6-octahedral tilts and rotations which are important for the electronic bandwidth W of this system. As has been discussed in the previous Chapter, the TiO_6-octahedral tilts and rotations in $RTiO_3$ decrease with increasing R ionic radius. Thus, the enlargement of Ti-O-Ti bond angle versus 180° supports the effective d-electron hopping interaction and increases the electronic bandwidth W since the d-electron transfer is governed by superexchange interaction via the oxygen 2p orbitals rather than by d-d hopping. In Fig. 6.14 (b) the Ti-O-Ti bond angles are shown as a function of Ca doping (x). These bond angles are a measure for the TiO_6-octahedral tilts and rotations. For a comparison also the corresponding values of the

pure RTiO$_3$-system are shown in Fig. 6.14 (a). As the Ca^{2+}-ion has a larger ionic radius (1.12 Å) for the same coordination (of 8) than the Y-ion (1.019 Å) [82], the doping with Ca can be expected to decrease also the octahedral tilts and rotations in addition to the introduction of holes into the system. Indeed, a continuous rise of the Ti-O-Ti angle with increasing Ca doping level x could be observed in these measurements of $Y_{1-x}Ca_xTiO_3$ with $0.00 \leq x \lessapprox 0.50$; see Fig. 6.14 (b). A doping with 50% of Ca even induces TiO$_6$-octahedral tilts and rotations which are smaller than for NdTiO$_3$ which is already far in the antiferromagnetic regime of the magnetic phase diagram of RTiO$_3$. It is interesting to note, that the MI-transition regime of the $Y_{1-x}Ca_xTiO_3$-system starts at Ca doping levels $x \approx 0.30$ where the octahedral tilts are exactly between the corresponding values of ferromagnetic GdTiO$_3$ and antiferromagnetic SmTiO$_3$, i. e. around the values for a compound which is at the crossover of the magnetic phase diagram of RTiO$_3$ concomitantly with a crossover between ferro- and antiferroorbital ordering schemes. And the metallic $Y_{1-x}Ca_xTiO_3$-sample with $x = 0.40$ has already even smaller octahedral tilts than SmTiO$_3$ which has a larger electronic bandwidth than YTiO$_3$ [127]. These effects are caused by the large ionic radius of the Ca^{2+} ion which is already distinctly larger than that of the Nd^{3+} ion (1.109 Å) [82]. The Ti-O-Ti angles and octahedral distortions have been calculated for CaTiO$_3$ ($x = 1.0$) from the crystal

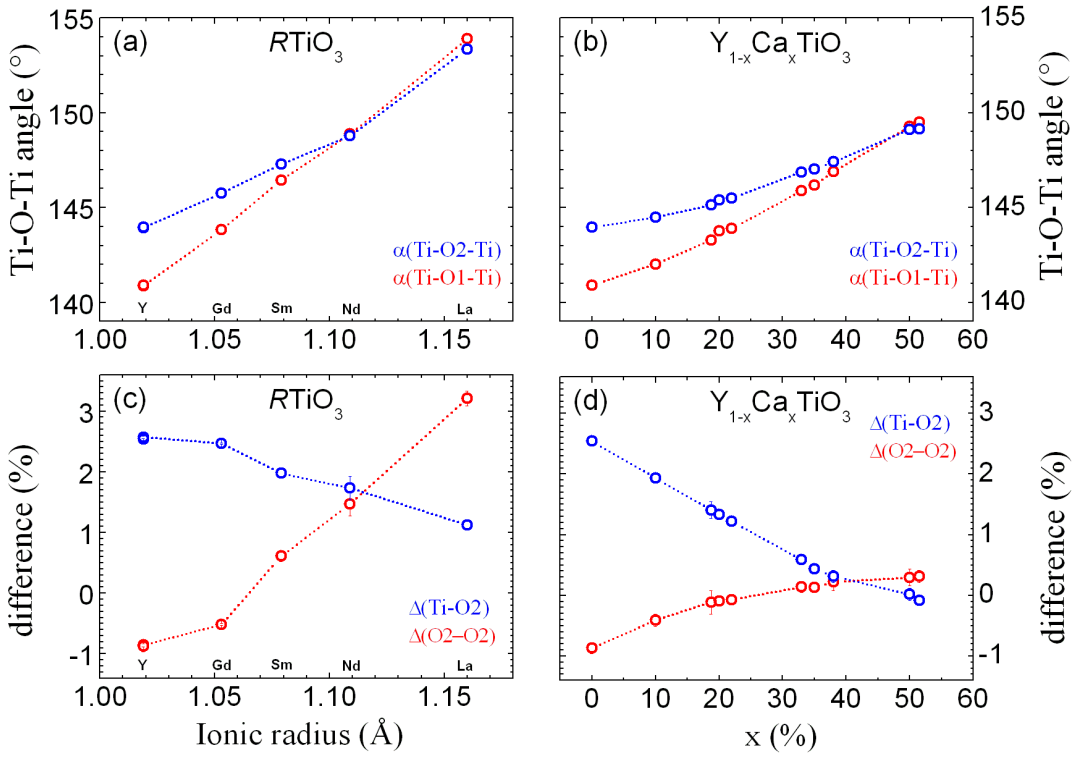

Figure 6.14: Ti-O-Ti angles for (a) the RTiO$_3$-system (see also Ref. [84]) and (b) for the $Y_{1-x}Ca_xTiO_3$-system and the two prominent distortions of the TiO$_6$-octahedral basal plane for (c) RTiO$_3$ and (d) $Y_{1-x}Ca_xTiO_3$.

structure at 296 K [172] and exhibit Ti-O1-Ti/Ti-O2-Ti angles of about 156.0°/155.6° which are even larger than the Ti-O-Ti angles for $LaTiO_3$. These strong structural changes have a direct impact on the electronic properties. Hence, Ca doping enhances the metallic properties of the $Y_{1-x}Ca_xTiO_3$-system on two ways - by hole doping and also by increasing of the electronic bandwidth W. So far, only the first mechanism has been accounted for.

Besides the Ti-O-Ti angles also the distortions of the TiO_6-octahedral basal plane change with increasing Ca-doping as can be seen in Fig. 6.14 (d). If refined with a single orthorhombic phase, the octahedral distortions indicative for antiferroorbital ordering in $YTiO_3$ continuously decrease from $x = 0$ to about $x = 0.4$ and vanish above this critical Ca concentration. Hence, in the metallic regime the octahedral distortions vanish and the TiO_6-octahedra become regular. In Ref. [79] a similar result has been reported for the octahedral distortions based on less reliable powder X-ray diffraction measurements.

resonant X-ray diffraction measurements

Using synchrotron radiation resonant X-ray diffraction measurements have been performed at the 7 T multipole wiggler beam line MagS at the synchrotron source BESSY in Berlin. In Fig. 6.16 (a) the temperature dependency of the (011) superstructure reflection of $Y_{0.64}Ca_{0.36}TiO_3$ (ACK016) measured at two different energies, one at the resonance energy (E_{res} = 4967.7 eV) and one below (E' = 4900 eV) is shown. Whereas the intensity of this superstructure reflection is close to zero at room-temperature, a strong rise can be observed at low temperatures. This temperature dependency is very similar to the one observed in the single crystal neutron diffraction measurements reported in the previous section. However, in the synchrotron measurements there is a much stronger decrease of intensity at low temperatures than in the neutron case. A very similar discrepancy between the intensities in neutron and synchrotron measurements was also observed for charge ordering superstructure reflections in the stripe ordered nickelates [173]. Thus, this stronger decrease at low temperatures compared to the neutron measurements may be inherent to the measurement technique. The untwined single crystal used in this synchrotron measurement was derived from the same large single crystal used for the neutron measurements reported in the previous section. However, small gradients within the large single crystal can not be fully excluded and may also explain the different observation in the synchrotron measurements at low temperatures.

In order to verify the charge ordering scenario spectroscopically the energy dependence of the superstructure reflection was studied around the Ti 1s⟶4p (K) resonance. In Fig. 6.16 (b) energy scans of the (011) superstructure reflection and a (022) fundamental reflection are shown together with the fluorescence signal (*gray*). The fundamental reflection exhibits a distinct decay at the absorbtion threshold. Contrarily to this normal behaviour, the (011) superstructure reflection shows a well pronounced resonant enhancement at this energy which is indicative for charge ordering. In order to exclude orbital ordering to be the driving mechanism of this resonant enhancement polarization analysis was performed. Therefore, the linear polarized X-ray beam with $\overrightarrow{E}$-vector in the horizontal plane of the synchrotron ring and parallel to the sample surface (σ-polarized) was scattered by the sample and analyzed with an additional analyzer crystal; see Fig. 6.15. Analyzer crystal and detector were mounted in a way that the diffraction angle 2Θ for the analyzer crystal is $180°\text{-}\Theta_{Brewster}$. Thus, the scattered X-ray beam meets the Bragg condition and at the same time makes an angle with the normal of the analyzer crystal surface which is equal to the brewster angle $\Theta_{Brewster} = arctan(n_2/n_1)$. Thus, only light with an $\overrightarrow{E}$-vector parallel to the ana-

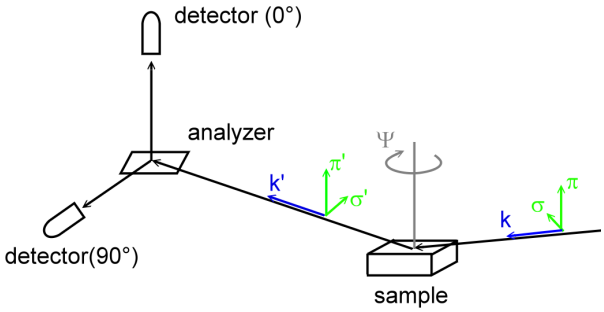

Figure 6.15: Arrangement of the experimental configuration in the resonant X-ray scattering measurement.

lyzer crystal surface will be diffracted into the detector. In the first setting the detector is mounted vertically above the analyzer such that the incident X-ray beam on the sample, the diffracted beam of the sample and the diffracted beam of the analyzer crystal are within the same vertical plane. In this setting, only X-rays with horizontal linear polarization (σ) parallel to the sample surface will be scattered by the analyzer into the detector. This setting is called the σ-σ channel, as both, incident and scattered X-ray beam (of the sample) are σ polarized. The other configuration is the σ-π' setting where the analyzer crystal and detector are rotated by 90° such that only the component with a polarization rotated by 90° and perpendicular to the sample surface will be detected. As the incident X-ray beam has σ polarization and only the π'-component perpendicular to the sample surface is measured, this setting is called the σ-π' channel (see also Ref. [152]).

In Fig. 6.16 (c) ω-scans of the (011) reflection for the σ-σ and the σ-π' channel are shown. They have been measured at resonance energy at two different temperatures: 300 K and 110 K. As can be seen, the polarization of the scattered photons is unrotated. The small residual intensity in the σ-π' channel can be attributed to an imperfect polarization analysis or may be caused by some very weak orbital ordering component which occurs in addition to charge order. Therefore, not orbital ordering but charge ordering is mainly responsible for the rise of these superstructure reflections. This is a clear affirmation of charge ordering in the $Y_{1-x}Ca_xTiO_3$-system.

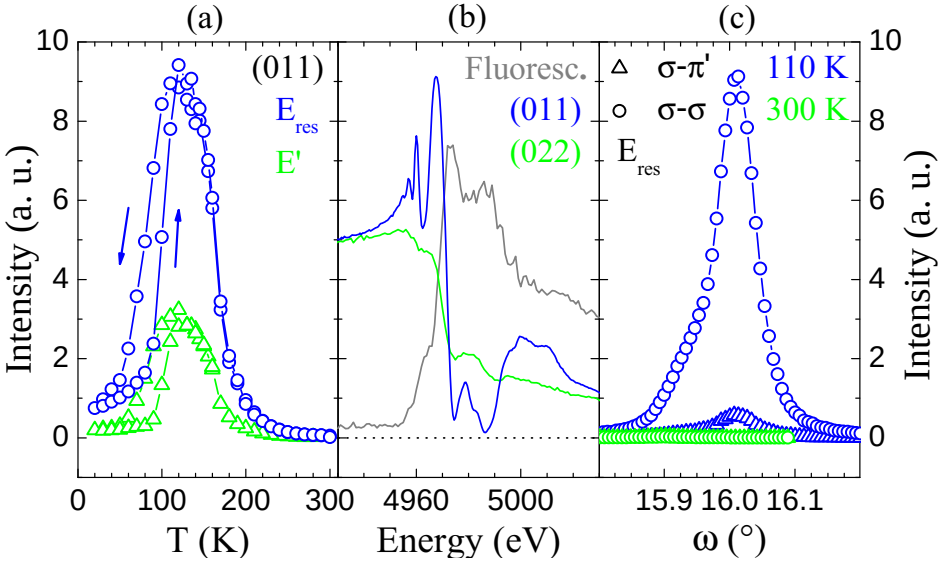

Figure 6.16: (a) Temperature dependency of the (011) reflection for two different energies. (b) Energy scans for the (011) and (022) reflections together with the fluorescence. (c) ω-scans of the (011) reflection at resonance energy for different polarization channels.

In Fig. 6.17 (a) the intensity of the (011) charge ordering superstructure reflection is plotted versus temperature for different doping levels $x = 0.33$ (ACK015), $x = 0.36$

(ACK016) and $x = 0.37$ (ACK083). The values are normalized to 100% in order to get a better comparison of the onset of charge ordering. With increasing hole concentration n, the onset of charge ordering shifts to higher temperatures as can be clearly seen in this plot. This is in accordance with the results observed by single crystal neutron diffraction for the samples with $x = 0.33$ and $x = 0.36$ where the onset of charge ordering was 15 K lower for the sample with $x = 0.33$. Thus, the charge ordering transition temperature T_{CO} shifts to higher values with increasing hole-doping level n. As discussed in the previous section, such a $T_{CO}n$ dependency could be expected for charge ordering as the values of n closer to the optimum doped value of 50% should stabilize charge ordering. In Fig. 6.17 (c) energy scans of the (011) superstructure reflection for the sample with $x = 0.33$, 0.36, 0.37 and 0.5 are shown. The resonant enhancement at the absorbtion threshold affirms the relation of this superstructure reflection to charge ordering.

Finally, for the sample with $x = 0.50$ far in the metallic regime, still a weak (011) charge ordering superstructure reflection could be observed. The temperature dependency of this (011) reflection is plotted as a function of temperature and normalized to 100% in Fig. 6.17 (b). As the sample is metallic, no (011) reflection would have been expected. Fig. 6.17 (c) shows an energy scan of the (011) superstructure reflection at 550 K [11] and compares it to the fundamental (022) reflection (measured at 295 K). Thus, the (011) superstructure reflection is also related to charge ordering in the sample with $x = 0.50$ in the metallic regime and small volume fractions of the insulating charge ordered LTM phase may survive into this metallic regime. Already in the magnetic susceptibility measurements of this sample a rise of χ could be observed with increasing temperature; see Fig. 6.8 (b). This rise of χ is very similar to the rise in the sample with $x = 0.38$ which has been analyzed with powder X-ray diffraction measurements in the Diploma Thesis of the author [57]. These measurements could explain the rise of χ with an increasing volume ratio of the insulating LTM/HTO phase in the phase separated regime and could describe the measured susceptibility even quantitatively; see the Introduction of this chapter. Thus, the same mechanism can be expected to drive the rise of χ also for the sample with $x = 0.50$. But as no phase separation could be observed directly in the synchrotron radiation powder X-ray diffraction measurements of this work for a similar sample with with $x = 0.50$, the volume fraction of the insulating phase has to be very small and thus below the detection limit. As the lattice parameters of the LTO and LTM phase could also be more equal in these compounds of the metallic regime, possibly any volume ratio smaller than 10% could not have been detected in these kind of measurements. Indeed, as shown in Fig. 6.10 (f) such small values have been measured in this work for the metallic sample with $x = 0.41$. Due to the Ca-doping dependency x shown in Fig. 6.10 (f) even smaller values can be expected for the sample with $x = 0.50$. The existence of few percents of the LTM phase could explain the rise of χ with temperature (see Fig. 6.8 (b)) and also the anomalies of the electrical resisitivity ρ at higher temperatures which have been measured for the sample with $x = 0.50$ in this work. Furthermore it could also explain the occurrence of the weak (011) charge ordering superstructure reflection in this resonant X-ray diffraction measurement. Hence, small

[11] Another energy scan at 295 K shows very similar values.

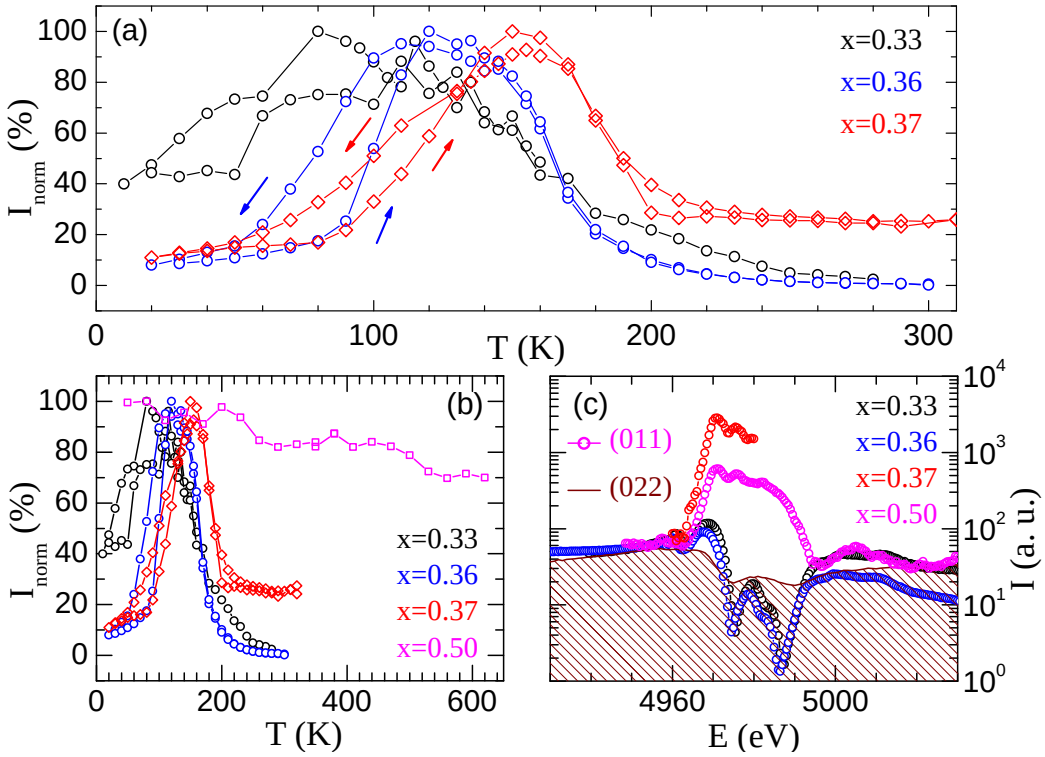

Figure 6.17: (a-b) Temperature dependency of the (011) reflection for different values of x. (c) Energy scan of the (011) and (022) reflection at 550 K and 295 K respectively.

volume fractions of the insulating and charge ordered LTM phase can be even found even far in the metallic regime around Ca doping levels of $x = 50\%$.

Finally, a discussion follows whether orbital order instead of charge order is the possible origin of the (0 1 1) resonance peak. In Ref. [140] orbital order in $YTiO_3$ was studied by the measurement of the forbidden (1 0 0), (0 0 1) and (0 1 1) peaks in resonant X-ray scattering experiments at the Ti K-edge and, hence, under similar conditions as in the measurements of this work. Like for the Ca-doped system the (0 1 1) peak in $YTiO_3$ exhibits a resonant enhancement at the absorption threshold and also a larger intensity in the σ-σ channel compared to the rotated σ-π channel [140]. What is different though is the energy dependence. In order to compare $YTiO_3$ directly with a 33% Ca doped $Y_{1-x}Ca_xTiO_3$-sample these two crystals have been measured in the same RXS synchrotron experiment. The resulting energy scans for different azimuthal angles of both compounds are shown in Fig. 6.18 (a-b). (Some scans are contaminated with multiple scattering which should not be taken into account.) The big difference between these two measurements is the position of the resonance peaks. For $YTiO_3$ the maxima of the resonance peaks appear at the maximum of the fluorescence whereas the maxima of the resonance peaks in $Y_{0.67}Ca_{0.33}TiO_3$ appear at distinctly lower energies right at the maximum of the slope the fluorescence signal, i. e. the (0 1 1) resonance resembles the

derivative of the fluorescence signal. This derivative-like resonance shape is the general signature of charge ordering [174-178]. reflecting a fundamental difference to the spectra of $YTiO_3$. Thus, the origin of these reflections is different in both compounds and in contrast to $YTiO_3$ the peak positions in $Y_{0.67}Ca_{0.33}TiO_3$ are compatible with charge ordering. Hence, the (0 1 1) peak which is the $(\frac{1}{2}\ \frac{1}{2}\ \frac{1}{2})$ peak in the pseudocubic cell (which describes the Ti-array) is able to reflect antiferroorbital ordering as in $YTiO_3$ and charge ordering as in $Y_{1-x}Ca_xTiO_3$ for $x \sim 0.33$. There are also some RXS studies of $Y_{1-x}Ca_xTiO_3$ in literature [79, 179, 180]. However, in these studies the interpretation focuses on the signatures of orbital ordering. Especially the RXS intensity at the pre-edge which reflects orbital ordering is analyzed [79]. As suggested for $YTiO_3$ [140], these pre-edge intensities arise from the dipole transition 1s → 3d which is allowed due to the hybridization of Ti 4p and neighbouring Ti 3d electrons. The intensities of these reflections (at the pre-edge) rapidly decrease with increasing Ca doping level x. Above Ca concentrations of $x = 0.15$ these peak intensities are strongly suppressed. This critical Ca concentration corresponds roughly to the Ca concentration where the ferromagnetic order is destroyed. Above Ca concentrations of $x = 0.4$ this signal completely vanishes which corresponds to Ca concentrations where the $Y_{1-x}Ca_xTiO_3$-system becomes metallic.

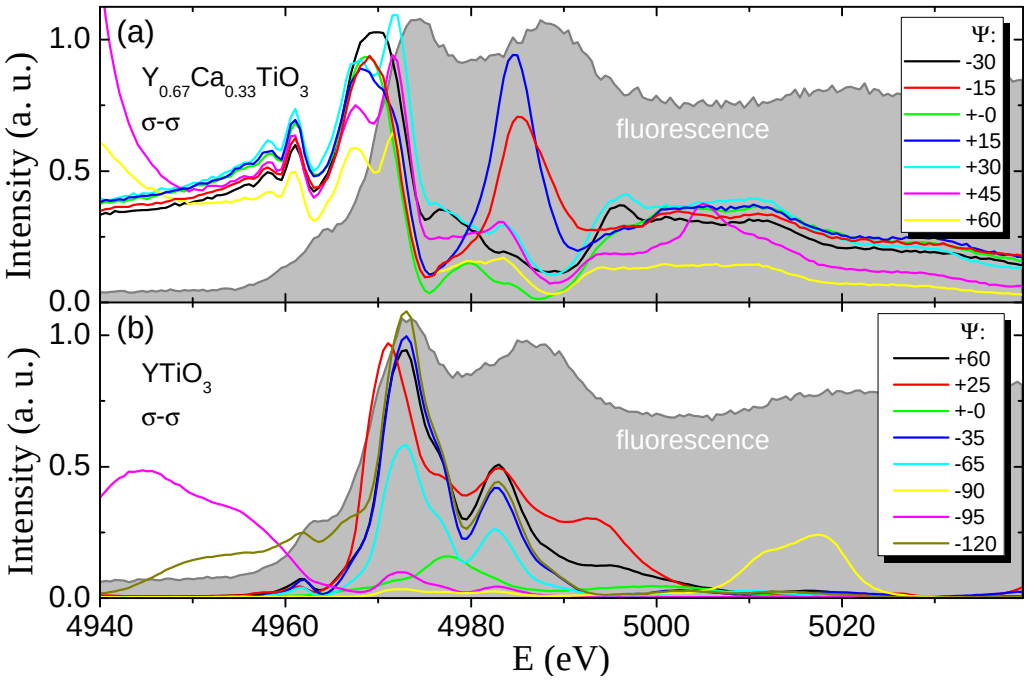

Figure 6.18: For several azimuthal angels the energy dependence of RXS intensity of the (0 1 1) reflection measured in the unrotated σ-σ channel for (a) $Y_{0.67}Ca_{0.33}TiO_3$ at 110 K and (b) $YTiO_3$ at 295 K is shown. The *gray line* indicates the fluorescence of each compound.

Interestingly, fairly strong pre-edge peaks could be observed in the RXS measurements

of this work, see Fig. 6.18 (a) or Fig. 6.16 (b). This may indicate the presence of orbital order also for doping levels distinctly higher than 0.15, but the pre-edge intensity could also be a consequence of charge ordering, see Ref. [152].

In contrast to the pre-edge intensities, the intensities at the main-edge may arise also from the local crystal structure [179]. The qualitatively different energy dependencies of the main-edge intensities of the (0 1 1) reflections of $YTiO_3$ and $Y_{1-x}Ca_xTiO_3$ which have been measured in this work (see Fig. 6.18 (a-b)) indicate a different origin of these superstructure reflections in the $Y_{1-x}Ca_xTiO_3$-system, i. e. a structural origin rather than orbital ordering. This structural origin can not be related to the alternating octahedral tilting pattern since the temperature dependency of these superstructure reflections is very disfavourable for such an interpretation (see Fig. 6.17 (a)): At room temperature this intensity is about zero for the samples with $x = 0.33$ and 0.36 and it starts to rise at low temperatures T_C. Furthermore, this transition temperature T_C increases with growing value of x which can be neither explained with octahedral tilts nor with orbital ordering. Hence, the charge ordering scenario is in accordance with the temperature and with the energy dependence of these superstructure reflections.

specific heat and thermal expansion measurements

The thermal expansion α has been measured for the sample with $x = 0.33$ along the crystallographic b-direction ($Pbnm$) and for the sample with $x = 0.37$ in the pseudocubic $[111]_{cub}$ direction which is the [011] direction in the orthorhombic cell ($Pbnm$); see Fig. 6.19 (a,c). Additionally, the temperature dependency of the (011) superstructure reflection measured at beamline MagS at BESSY (*lt. gray*) and measured with neutrons (*dk. gray*) is shown together with the electrical resisitivity (*dk. gray*). The measurement of α clearly indicates strong structural anomalies around the MI-transition temperature. At about these temperatures the superstructure reflection intensity is decreasing again. In the previous sections this decrease at low temperatures was explained with phase separation and the formation of the metallic LTO phase which is not charge ordered and thus leads to a reduction of the total intensity of the charge ordering superstructure reflections. The strong anomalies of the thermal expansion α of the sample with $x = 0.37$ support this interpretation, as the LTO phase has a smaller b lattice parameter than the LTM phase. Thus, the formation of the metallic LTO phase would induce a decay of the crystal length in [011] direction [12] and, thus, qualitatively the same anomalies of α as observed in the measurement of the sample with $x = 0.37$. Of cause, also the resistivity ρ which already exhibits a drop at T_{MI} supports this interpretation; see also Fig. 6.8 (a). As the electrical resistivity is much more sensitive to the occurrence of small volume fractions of the metallic LTO phase, the decrease of ρ may even start at little higher temperatures than the decrease of the superstructure reflection intensity which have only a linear dependence on the volume fractions. Clear anomalies in the thermal expansion of the sample with $x = 0.33$ can not be resolved. This may be attributed to the fact that this sample is already close to the insulating regime and that there are

[12] The a and c lattice parameter of the LTO and LTM phase are very similar and do not change much; see Fig. 6.10.

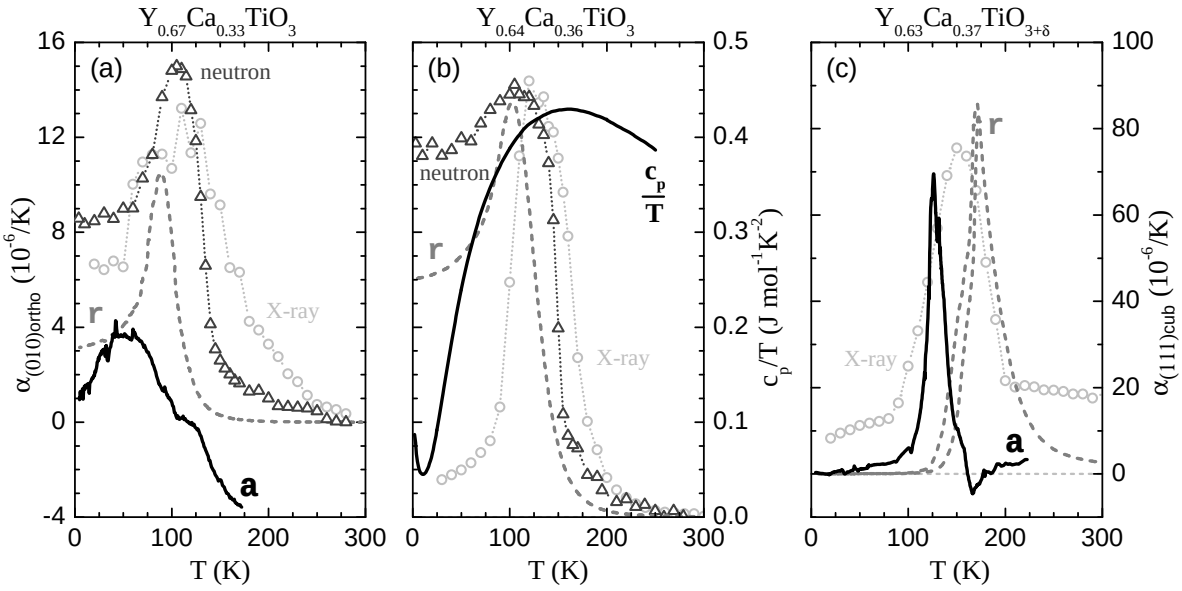

Figure 6.19: (a) Thermal expansion α for $Y_{0.67}Ca_{0.33}TiO_3$ (*ACK015*) with the intensity of the (011) superstructure reflection (*lt. gray*) measured with X-rays at the synchrotron and neutron scattering (*dk. gray*) and the electrical resistivity ρ (*gray*) in the background. (b) Specific heat for $Y_{0.64}Ca_{0.36}TiO_3$ (*ACK016*) with the (011) superstructure reflection intensity measured by neutron scattering (*dk. gray*) and X-rays at the synchrotron (*lt. gray*). (c) Thermal expansion α for $Y_{0.63}Ca_{0.37}TiO_{3+\delta}$ (*ACK083*) with the intensity of the (011) superstructure reflection (*lt. gray*) measured with X-rays at the synchrotron and the electrical resistivity ρ (*gray*) in the background.

only small volume fractions of the metallic phase which contribute to the reduction of b. However, these small volume fractions of the metallic phase are able to change the electrical resistivity significantly as was discussed in the Diploma thesis of the author [57].

In Fig. 6.19 (b) the specific heat divided by temperature (c_p/T) of $Y_{0.64}Ca_{0.36}TiO_3$ is plotted as a function of temperature. Additionally, the resistivity ρ and the intensities of the (011) superstructure reflections measured by neutron and synchrotron measurements are shown for a comparison of the transition temperatures. Anomalies of the specific heat are neither visible around the onset temperature of charge ordering nor at T_{MI}. Thus, the are only minor differences in entropy of the HTO and the LTM phase.

6.2.4 Conclusion

In this work, a three-dimensional checkerboard Ti^{3+}/Ti^{4+} charge ordering has been observed in the insulating LTM phase of $Y_{1-x}Ca_xTiO_3$ by various neutron and synchrotron diffraction techniques. With the onset of charge ordering a rise of the (01L) superstruc-

ture reflections was detected both by neutron and synchrotron measurements. These superstructure reflections arise from charge ordering as could be verified with resonant synchrotron radiation X-ray diffraction together with polarization analysis. Single crystal neutron diffraction measurements indicate a difference of about 0.3 electrons for the valency of the two Ti-sites derived from the analysis of the bond-valence sums. However, highly precise single crystal X-ray diffraction measurements indicate a distinctly higher value of about 0.6 electrons. This discrepancy could not be finally explained, but, it arises either from the higher sample quality of a small 100 μm sphere compared to the large single crystal of about 1/2 cm^3 size or from the different accuracy of neutron and X-ray diffraction measurements.

To the best knowledge of the author, no observation of charge ordering in a titanate system has been reported in literature so far. This occurrence of charge ordering may also explain the expansion of the insulating properties of the $Y_{1-x}Ca_xTiO_3$-system to such high hole-doping values of 40%. So far, this fact has been attributed to the bandwidth reduction induced by the stronger tilts in this system only. But as shown by the single crystal X-ray diffraction measurements, the tilting angles for the compounds with $x = 0.40/0.50$ have already become even smaller than in antiferromagnetic (Sm/Nd)TiO_3 which have distinctly larger electronic bandwidths W than $YTiO_3$ [127] [13]. Thus, charge ordering can be an additional explanation for enforcing the insulating properties of the $Y_{1-x}Ca_xTiO_3$-system to these rather high levels of hole doping.

With increasing Ca-doping the metallic properties of the $Y_{1-x}Ca_xTiO_3$-system get amplified by two mechanisms - first by hole doping and second by an increase of the electronic bandwidth W. This combined effect finally turns the whole system metallic at $x \approx 0.40$. Thus, unfortunately, the optimum doped compound for a three-dimensional checkerboard charge ordering ($x = 0.50$) is in the metallic regime and the ideal Ti^{3+}/Ti^{4+} charge ordering pattern could not be observed directly by structure determination. However, resonant X-ray diffraction measurements reveal a small volume fraction of the charge ordered LTM phase also for the metallic sample with $x = 0.50$ which can explain the anomalies in the magnetic susceptibility and resistivity at high temperatures. But the existence of a pure LTM phase, at least at one temperature point, is necessary in order to measure the nuclear structure of the charge ordered LTM phase with neutron or X-ray diffraction and to analyze the oxygen environment of the Ti-ions. In order to extend the insulating properties of this system closer to the ideal value of 50% hole-doping, a further reduction of the electronic bandwidth W has been aimed at by the substitution of the already small Y^{3+} ion with even smaller R^{3+} ions - see the next Chapter.

[13] This effect is caused by the large ionic radius of the Ca^{2+} ion which has a distinctly larger size than the Sm^{3+} and Nd^{3+} ion [82].

6.3 Charge order in $(Lu,Er)_{1-x}Ca_xTiO_3$

6.3.1 Introduction

As has been stated in the previous Chapter, the observation of charge ordering in the $Y_{1-x}Ca_xTiO_3$ system suffers from the imperfect Ti^{3+}/Ti^{4+} charge ordering pattern for the compounds in the insulating regime with $x < 0.40$. The ionic radius of the Y^{3+} ion is already rather small (1.019 Å [82]) resulting in stronger TiO_6-octahedral tilt and rotational distortions. In order to increase the insulating properties of the $R_{1-x}Ca_xTiO_3$-system, the effect of substitution with the smaller Er^{3+} (1.004 Å [82]) and Lu^{3+} ions (0.977 Å [82]) has been studied in this work. Due to the smaller R ionic radius an increase of the octahedral tilts and distortions could be expected to diminish the electronic bandwidth W and, thus, to enhance the insulating properties of this system.

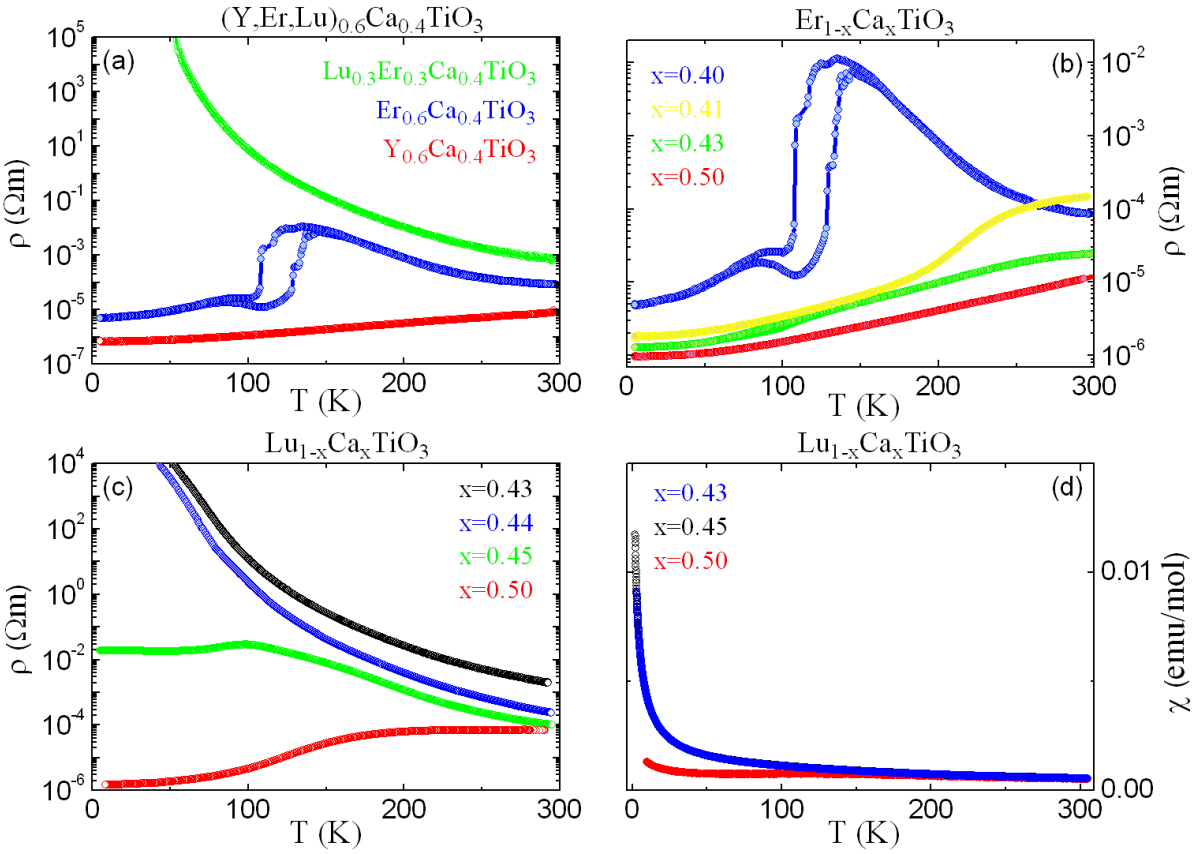

Figure 6.20: Electrical resistivity of (a) $R_{0.6}Ca_{0.4}TiO_3$ (b) $Er_{1-x}Ca_xTiO_3$ and (c) $Lu_{1-x}Ca_xTiO_3$. (d) Magnetic susceptibility measurements of $Lu_{1-x}Ca_xTiO_3$.

6.3.2 Experimental

Single crystal X-ray diffraction has been performed on a Bruker Apex X8 diffractometer using Mo-K_α radiation. Synchrotron radiation single crystal X-ray diffraction measurements have been performed at beamline D3 at HASYLAB/DESY in Hamburg using a MarCCD area detector ($\lambda = 0.47686$ Å). For the structural refinement the program *Jana2000* [58] has been used. Resistivity measurements have been performed using an AC four-point method. Resonant X-ray diffraction using synchrotron radiation have been performed at BESSY in Berlin in collaboration with C. Schüßler-Langeheine and H.-H. Wu. The magnetic susceptibility was measured by M. Reuther with a vibrating sample magnetometer (VSM).

6.3.3 Results

resistivity and magnetic susceptibility measurements
In Fig. 6.20 (a) the electrical resistivity of three different $R_{0.6}Ca_{0.4}TiO_3$ samples is plotted versus temperature. With decreasing R-ionic radius the metallic susceptibility of $Y_{0.6}Ca_{0.4}TiO_3$ changes to insulating properties in $(Lu_{1/2}Er_{1/2})_{0.6}Ca_{0.4}TiO_3$. Thus, the decreasing R-ionic radius has the expected effect on the electronic properties of this system. In Fig. 6.20 (b) the resistivity of the $Er_{1-x}Ca_xTiO_3$ series is shown. Obviously, these samples become metallic above 41% of hole-doping. The resistivity of the sample with $x = 0.41$ is very similar to the resistivity of the $Y_{1-x}Ca_xTiO_3$-sample with $x = 0.39$. In order to get a more pronounced effect regarding the insulating properties, the $Lu_{1-x}Ca_xTiO_3$-system was synthesized and studied. The electrical resistivity and magnetic susceptibility of this system are shown in Fig. 6.20 (c-d). The sample with $x = 0.50$ has a similar resistivity as the $Y_{1-x}Ca_xTiO_3$-sample with $x = 0.39$. Also, the $Lu_{1-x}Ca_xTiO_3$-sample with $x = 0.45$ has a very similar resistivity as the $Y_{1-x}Ca_xTiO_3$-sample with $x = 0.36$. Thus, in the $Lu_{1-x}Ca_xTiO_3$-system the insulating properties are extended distinctly closer to the half-doped sample and the MI-transition boundary is shifted by roughly 0.10 to higher values of Ca doping x.

X-ray diffraction measurements
Single crystal X-ray diffraction measurements for various $R_{1-x}Ca_xTiO_3$-samples have been performed at room-temperature (HTO phase, *Pbnm*) in order to study the octahedral tilts and rotations for the systems with R = Er, $(Er_{1/2}Lu_{1/2})$, Lu. The resulting Ti-O-Ti angles are shown in Fig. 6.21. Whereas the $Er_{1-x}Ca_xTiO_3$-system exhibits only about 0.4° larger tilts than the $Y_{1-x}Ca_xTiO_3$-system, the octahedral tilts in the $Lu_{1-x}Ca_xTiO_3$-system are about 3.5° larger than in the $Y_{1-x}Ca_xTiO_3$-system. A comparison of the compounds at the MI-transition boundary of the systems with R = Y, Er, Lu shows that these compounds have quite similar TiO_6-octahedral tilts or Ti-O1-Ti angles. For all these compounds with x =0.39, 0.41 and 0.50 respectively, the Ti-O1-Ti angle attains values around 147°-146°. Thus, from R = Y to Lu the octahedral tilts change about 3.5° for the samples with the same values of x (x =0.50, 0.50, 0.50) but change less than about 1° for the samples at the MI-transition

boundary (x =0.39, 0.41, 0.50). Thus, the bandwidth W which is dependent on the octahedral tilts and rotations has a strong impact on the MI-transition which may be even more important than the band filling which is dependent on the hole concentration $n = x + 2 \cdot \delta_O$.

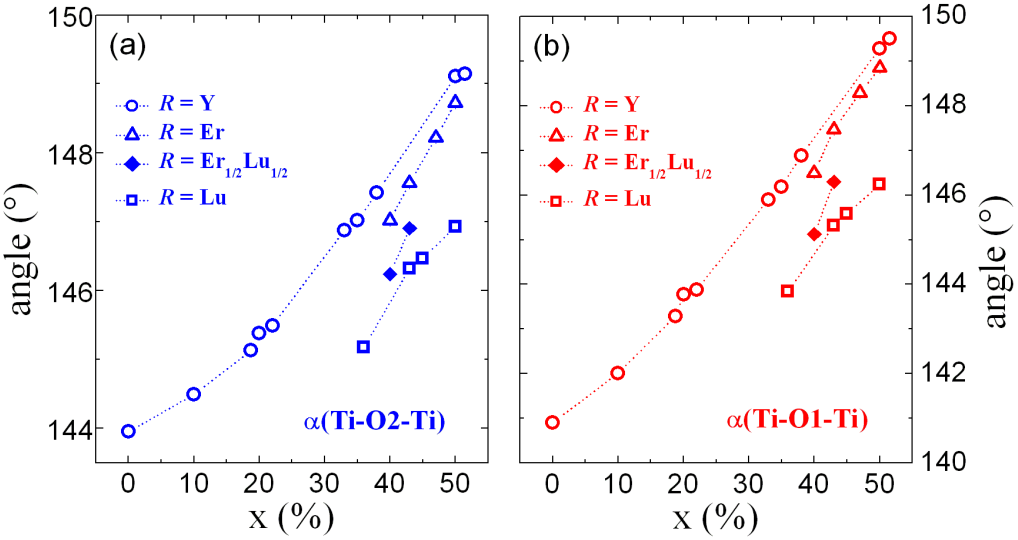

Figure 6.21: Ti-O-Ti bond angles for $R_{1-x}Ca_xTiO_3$ measured with single crystal X-ray diffraction at room-temperature.

Synchrotron radiation single crystal X-ray diffraction measurements using an CCD area detector have been performed at beamline D3 at DESY in Hamburg. In these synchrotron measurements the crystal structure of $Lu_{0.3}Er_{0.3}Ca_{0.4}TiO_3$ and $Lu_{0.5}Ca_{0.5}TiO_3$ has been studied at about 10 K. Two small single crystalline spheres of roughly 60 μm in diameter have been chosen in order to minimize absorption effects which are already minimized by the high incident X-ray energy. As can be seen in Fig. 6.20 (a,c) the first compound belongs still to the insulating regime whereas the second compound is just at the MI-transition boundary but exhibits already a completely metallic temperature dependency of the electrical resistivity. The resulting Ti-O distances of the structural refinement of both compounds are listed in Tab. 6.3. A refinement of the Lu, Er and Ca concentrations verifies the stoichiometry of both compounds within about 1% accuracy. For $Lu_{0.3}Er_{0.3}Ca_{0.4}TiO_3$ a better description could be achieved with the charge ordering model ($P2_1/n$) compared to a model which is restricted to the undistorted $Pbnm$ structure. The structure refinement within the monoclinic space group $P2_1/n$ indicates elongated Ti2-O2 distances whereas the Ti2-O1 distances are not elongated (compared to the corresponding Ti1Oν distances). This result is in accordance with the neutron measurements of $Y_{1-x}Ca_xTiO_3$ in Chap. 6.2. However, the bond valence sums (BVS) calculated from the Ti-O distances indicate a difference of about 0.72(3) electrons in the nominal valency at both Ti-sites. This value is distinctly higher than for the $Y_{1-x}Ca_xTiO_3$-compounds with x = 0.35 and 0.36 measured in Chapter 6.2 but still in accordance with the nominal hole-doping level in this compound.

x:	**0.40**	**0.40**	**0.50**	**0.50**	**0.44**	**0.44**
SG:	$P2_1/n$	*Pbnm* ‡	$P2_1/n$	*Pbnm* ‡	$P2_1/n$	*Pbnm* ‡
s.c. X-ray:						
T:	8 K	‡	≈10 K	‡	125 K	‡
all refl.:	17368	‡	9410	‡	7853	‡
$\mathbf{2\Theta_{max}}$**:**	64.2°	‡	63.8°	‡	87.0°	‡
redun.:	6.76	‡	4.01	‡	5.42	‡
$\mathbf{R}_{int}$**:**	7.42%	‡	2.87%	‡	2.91%	‡
GoF:	1.43	1.47	1.48	1.57	2.20	2.46
R:	2.83%	3.05%	2.14%	2.16%	2.25%	2.57%
$\mathbf{R}_w$**:**	5.49%	5.67%	4.39%	4.41%	4.33%	4.87%
Ti1-O1:	2.002(4) Å	2.003(1) Å	2.003(3) Å	1.996(1) Å	1.976(4)	1.998(1)
Ti1-O2:	1.952(4) Å	2.011(1) Å	2.011(2) Å	2.011(1) Å	1.950(4)	2.004(1)
Ti1-O2':	1.966(4) Å	2.018(1) Å	2.014(3) Å	2.011(1) Å	1.967(3)	2.013(1)
Ti2-O1:	2.003(4) Å	-	1.991(3) Å	-	2.020(4)	-
Ti2-O2:	2.071(4) Å	-	2.009(3) Å	-	2.059(3)	-
Ti2-O2':	2.070(4) Å	-	2.009(2) Å	-	2.062(4)	-
BVS(Ti1):	4.00(2)	3.63(1)	3.64(1)	3.67(1)	4.15(2)	3.72(1)
BVS(Ti2):	3.28(2)	-	3.70(1)	-	3.33(1)	-
ΔBVS:	0.72(3) e	-	0.06(2) e	-	0.82(2) e	-

Table 6.3: Results of the refinement of synchrotron radiation single crystal X-ray diffraction measurements of $Lu_{0.3}Er_{0.3}Ca_{0.4}TiO_3$ ($x = 0.40$) and $Lu_{0.5}Ca_{0.5}TiO_3$ ($x = 0.50$) and of a single crystal X-ray diffraction measurement of $Lu_{0.56}Ca_{0.44}TiO_3$ ($x = 0.44$) is ‡: same low-temperature measurement as in column before but fitted with restrictions equivalent to space group *Pbnm*.

The structure refinement of $Lu_{0.5}Ca_{0.5}TiO_3$ using starting parameters from the distorted $P2_1/n$ structure of $Lu_{0.3}Er_{0.3}Ca_{0.4}TiO_3$ exhibits only minor TiO_6-octahedral distortions and the difference in the nominal valency of both Ti-sites amounts to 0.06 only. A refinement with restrictions to the undistorted *Pbnm* structure yields very similar R-values. Hence, $Lu_{0.5}Ca_{0.5}TiO_3$ does not exhibit any indications for charge ordering which is in accordance with its almost metallic properties.

An additional single crystal X-ray diffraction measurement has been performed for a $Lu_{0.5}Ca_{0.5}TiO_3$ sample (ACK082) at the Apex X8 single crystal X-ray diffractometer using Mo-K_α radiation. A larger single crystalline sphere with 110 μm radius has been chosen in order to yield more intensity of the weaker (superstructure) reflections. Resonant X-ray diffraction measurements on the same sample revealed the strongest charge ordering superstructure reflection intensity at temperatures around 125 K; see the next section. Thus, the same temperature was chosen for this single crystal X-ray diffraction measurement. The results of the structural refinement with space group $P2_1/n$ and for a structure model restricted to the undistorted *Pbnm* structure are listed in Tab. 6.3. The refinement of the structure model without charge ordering exhibits moderately enhanced R-values. Analyzing the Ti-O distances with the BVS formalism reveals a difference of the nominal oxidation states of both Ti-ions which amounts to 0.82(2) electrons. This value is even larger than the value of about 0.72 electrons for $Er_{0.6}Ca_{0.4}TiO_3$ which sup-

ports the overall picture of a stabilization of charge ordering for the compounds with Ca concentrations closer to the optimum-/half-doped value of 50%.

resonant X-ray diffraction measurements

Resonant X-ray diffraction measurements at the Ti K edge using synchrotron radiation have been performed at beamline MagS at BESSY in Berlin. In Fig. 6.22 (a) the (011) superstructure reflection intensity is plotted for four different $R_{1-x}Ca_xTiO_3$-compounds as a function of temperature. For $Er_{0.6}Ca_{0.4}TiO_3$ the onset temperature of charge ordering (T_{CO}) is distinctly higher than for $Y_{0.63}Ca_{0.37}TiO_{3+\delta}$ and $Y_{0.64}Ca_{0.36}TiO_3$. For these three compounds T_{CO} increases continuously with hole-doping n. Such a behaviour supports the charge ordering model, as the compounds closer to the optimum half-doped sample exhibit higher values for T_{CO}. However, further hole doping ($x = 0.44$-0.45) does not increase T_{CO} any further; see Fig. 6.22 (c). Instead, the whole temperature dependency becomes smoother with no sharp transition. For these higher doped compounds small volume fractions of the sample exhibit charge ordering even at room-temperature, but the bulk of the sample orders always below about 250 K.

In Fig. 6.22 (b) the half width at half maximum (HWHM) for the (011) charge ordering superstructure reflections is shown. For all samples the HWHM increases below T_{MI} where the metallic LTO phase appears. This effect is most strongly for $Er_{0.6}Ca_{0.4}TiO_3$ which exhibits the strongest changes in the electrical resistivity around T_{MI}. As there is no charge ordering in the metallic LTO phase, the broadening of the (011) charge ordering superstructure reflection can be attributed to the insulating LTM phase only. Hence, the appearance of the metallic phase seems to induce a peak broadening of peaks belonging to the charge ordered phase. An explanation might be that the metallic and the charge ordered phase get more mixed on a microscopic scale rather than forming large, well separated metallic and charge ordered domains (see Ref. [181]). Such an effect could be responsible for the reduction of the coherence length and, thus, for the peak broadening. The correlation length calculated from the peak width is of the order of 450 Å (in a-direction of $Er_{0.6}Ca_{0.4}TiO_3$ far away from the MI-transition). However, it shrinks to about 140 Å in the MI-transition region [14]. The hysteresis of the peak-width as well as of the intensity itself corresponds to the hysteresis in the electrical resistivity as can be seen by comparing Fig. 6.20 (b) with Fig. 6.22 (a-b) for $Er_{0.6}Ca_{0.4}TiO_3$.

In Fig. 6.22 (d) energy scans for the same reflections as in Fig. 6.22 (c) at the temperature of maximum intensity are shown. The fluorescence of $Y_{0.64}Ca_{0.36}TiO_3$ is plotted (*gray*) in the background indicating the Ti K-edge. Additionally, the behaviour of the fundamental (022) reflection of $Lu_{0.56}Ca_{0.44}TiO_3$ is shown (*brown*). These energy scans of the (011) reflections exhibit a strong resonant enhancement at the Ti K edge very unlike to the behaviour of the fundamental (022) reflection indicating the charge ordering nature of these superstructure reflections for all compounds.

In Fig. 6.22 (e) energy scans of the (011) and (013) superstructure reflections and the fundamental (022) reflection of $Lu_{0.56}Ca_{0.44}TiO_3$ (ACK110) are plotted together with

[14] Further synchrotron measurements are planned to analyze the distribution of the charge ordered and metallic domains more in detail.

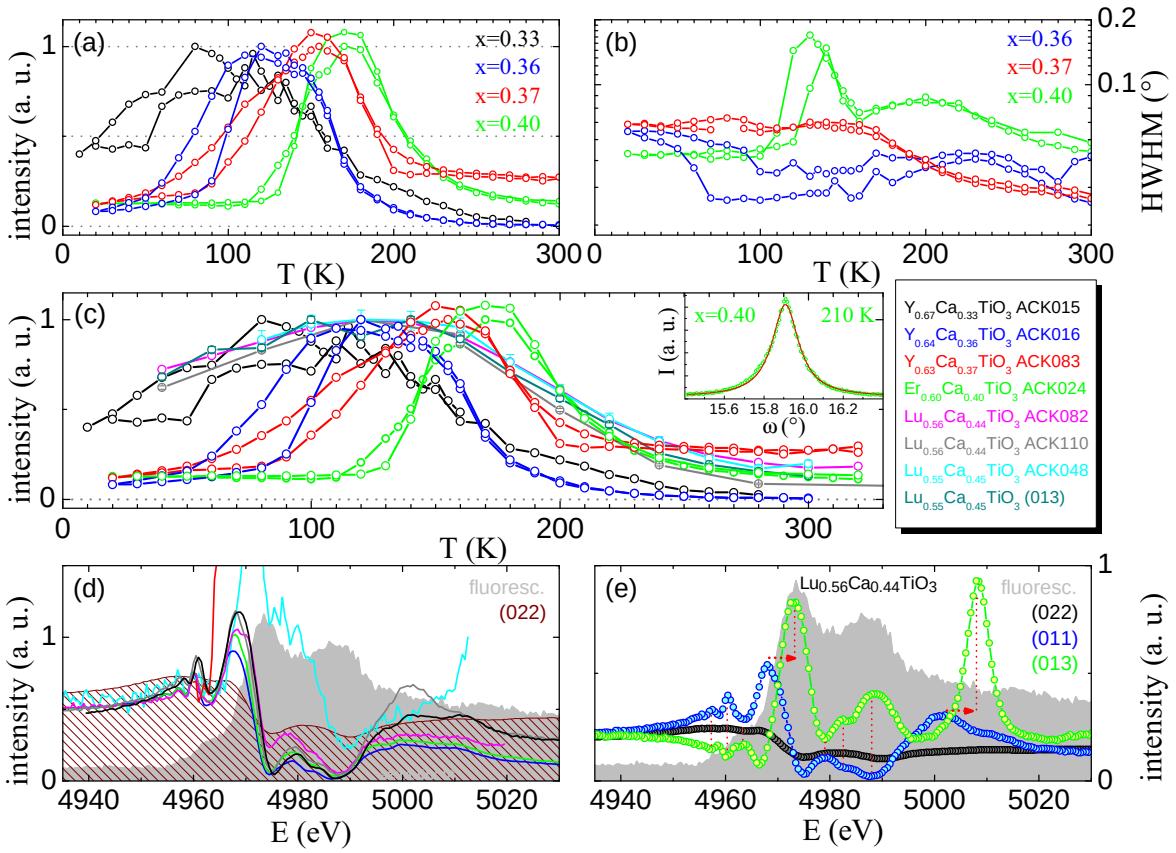

Figure 6.22: (a-b) Intensity and HWHM of the (011) reflection for $Y_{0.67}Ca_{0.33}TiO_3$, $Y_{0.64}Ca_{0.36}TiO_3$, $Y_{0.63}Ca_{0.37}TiO_3$ and $Er_{0.6}Ca_{0.4}TiO_3$. (c) Intensity of the (011) reflection for different $R_{1-x}Ca_xTiO_3$-systems. For $Lu_{0.55}Ca_{0.45}TiO_3$ the (011) and (013) reflections are shown (*cyan* and *dk. cyan*). (d) Energy scans for these reflections shown in figure (c). Additionally the fluorescense of $Y_{0.64}Ca_{0.36}TiO_3$ (*gray*) and the fundamental (022) reflection of $Lu_{0.56}Ca_{0.44}TiO_3$ (*brown*) are shown. (e) Energy scans for different reflections of $Lu_{0.56}Ca_{0.44}TiO_3$ (ACK110) on top of the fluorescense of $Y_{0.64}Ca_{0.36}TiO_3$ (*gray*).

the fluorescence of $Y_{0.64}Ca_{0.36}TiO_3$. A very interesting effect is visible in these energy scans - the (013) and (011) reflection exhibit resonance with an anti-phase modulation. This is indicated by the six dotted vertical lines. Additionally, the peak at the Ti K edge is shifted to little higher energies. Another peak around 5010 eV also shows a similar displacement, but whether this second peak is true or an artifact of multiple scattering is not clear. During these measurements a strong azimuthal dependency was revealed which may also be the reason for this anti-phase behaviour. As shown in Fig. 6.22 (c) the intensity of the (011) and (013) superstructure reflections of $Lu_{0.55}Ca_{0.45}TiO_3$ show an identical temperature dependency. Thus, both reflections are connected to charge ordering, but the anti-phase energy dependency of the (011) and (013) reflections have

to be analyzed further.

6.3.4 Conclusion

In conclusion, the substitution of the Y ion with smaller R ions (R = Er, Lu) is successful in the enhancement of the insulating properties of the $R_{1-x}Ca_xTiO_3$-system. Compared to $Y_{1-x}Ca_xTiO_3$, this improvement is achieved by the reduction of the electronic bandwidth W induced by larger TiO_6-octahedral tilts and rotations as could be shown by single crystal X-ray diffraction measurements. With these increased insulating properties these samples stay insulating closer to the optimum/half-doped regime. As shown by resonant X-ray diffraction, these compounds exhibit charge ordering at low temperatures with an increasing charge ordering temperature T_{CO} for the samples with higher Ca doping level x. At high Ca doping levels around $x = 0.45$ the charge ordering transition is smeared out and T_{CO} attains its maximum value in the broad temperature range 200 K to 250 K. However, small volume fractions of the sample may be even charge ordered at room-temperature as there is still some superstructure reflection intensity left around 300 K. The (011) and (013) charge ordering superstructure reflections exhibit a not yet understood anti-phase resonance with an additional strong resonant peak at the absorbtion threshold which is shifted to higher energies compared to the (011) reflection. In summary, these measurements demonstrate the shift of charge ordering to higher temperatures with increasing hole-doping value n. Single crystal X-ray diffraction measurements for samples with larger Ca doping level $x = 0.40$, 0.44 also indicate enhanced values for the difference of the nominal valency of both Ti-sites. This observation is in accordance with the expected stabilization of charge ordering for doping levels closer to the optimum doped value of 50%.

6.4 Comparison and Summary of $R_{1-x}Ca_xTiO_3$

The $R_{1-x}Ca_xTiO_3$-system (R = Y, Er, Lu) exhibits a temperature-driven insulator-to-metal transition with the metallic phase appearing at low temperatures. This is in contrast to the usually observed MI-transition in other compounds like V_2O_3, VO_2 or other charge ordered systems like for example $K_{0.5}CoO_2$ where the metallic phase appears at high temperatures and where the insulating phase instead at low temperatures [162, 163]. However, there exist also other systems with such an 'inverse MI-transition' as for example the 327-manganites $(La,Sr,Ca)_3Mn_2O_{7\pm\delta}$ [167]. In Fig. 6.23 (a) the phase diagram of the $Y_{1-x}Ca_xTiO_3$-system is shown. At high temperatures there is an insulating phase (HTO phase) which first becomes charge ordered at lower temperatures (LTM phase) and finally metallic (LTO phase) at even lower temperatures. Additionally, in Fig. 6.23 (b) the MI-transition temperatures derived from electrical resistivity measurements are plotted as a function of Ca-doping level x (*gray dashed lines*). In this unified $R_{1-x}Ca_xTiO_3$-phase diagram the curves of all three systems with R = Y, Er and Lu are shown together (*gray dashed lines*) separating the insulating regime from the metallic regime [15].

Besides these unusual features the doping driven MI-transition appears at rather high hole doping levels x ∼0.39, ∼0.41 and ∼0.5 for R = Y, Er, Lu [16]. This is in contrast to the $La_{1-x}Sr_xTiO_3$-system where the MI-transition appears at rather low hole-doping levels of x ∼0.05 [2, 94, 182]. So far, this difference has been attributed to the bandwidth reduction induced by the stronger tilts of the $Y_{1-x}Ca_xTiO_3$-system solely. But as could be derived from single crystal X-ray diffraction measurements, these octahedral tilts strongly decrease with Ca doping since the Ca^{2+} ion has a larger ionic radius than the R^{3+}-ions and since the Ti^{4+}-ion has a smaller ionic radius than the Ti^{3+}-ion: 1.120 Å for Ca with a coordination of VIII and 1.019 Å, 1.004 Å and 0.977 Å for Y, Er and Lu respectively [82]; 0.605 Å for Ti^{4+} and 0.67 Å for Ti^{3+} with a coordination of VI [82]. For pure metallic $Y_{1-x}Ca_xTiO_3$ with hole-doping levels x ∼0.40, the octahedral tilts have already become smaller than in $SmTiO_3$ which has distinctly larger electronic bandwidths W than $YTiO_3$ and exhibits an 'inverse MI-transition' between x = 0.20 and 0.24 [127]. This could be an indication that additional effects - like charge ordering - might explain the enforced insulating properties of the $R_{1-x}Ca_xTiO_3$-systems with R = Y, Er, Lu. In other perovskites (like for example $Pr_{1-x}Ca_xMnO_3$ or $La_{2-x}Sr_xNiO_4$) which stay insulating up to high amounts of hole-doping sometimes charge ordering is observed [7, 160]. However, no evidence for charge ordering has been reported for a titanate system so far.

In this work, the monoclinic low-temperature phase (LTM) in $Y_{1-x}Ca_xTiO_3$ which has been reported in Ref. [161] could be confirmed by synchrotron radiation powder X-ray diffraction measurements. In this monoclinic structure with space group $P2_1/n$ there are two different Ti-sites which alternate three-dimensionally in all directions. Furthermore, the structural data derived from several neutron, synchrotron and single crystal X-ray

[15] The metallic regime is below this curve and the insulating regime above.

[16] The electrical resistivity of these samples exhibits a very similar temperature dependency with an almost metallic character.

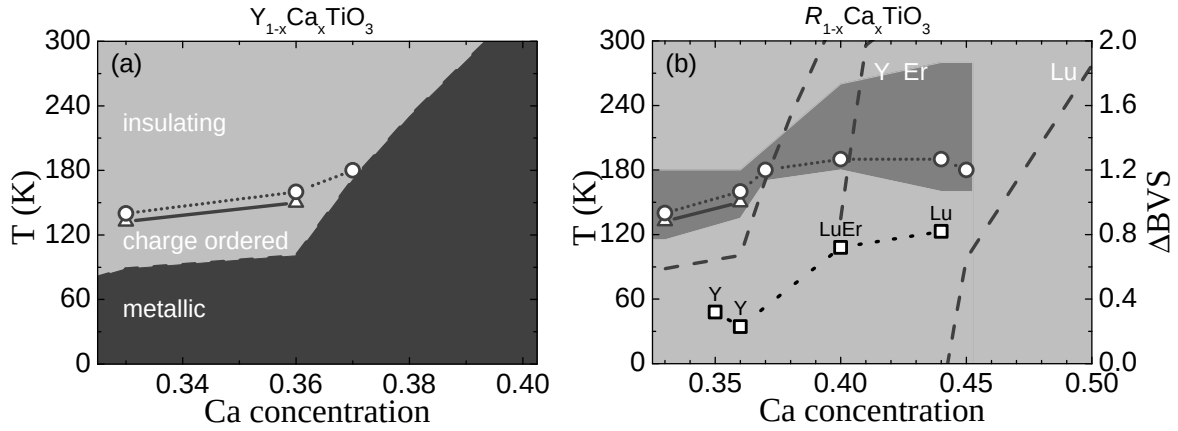

Figure 6.23: (a) Phase diagram of the $Y_{1-x}Ca_xTiO_3$-system; *gray circles/triangles*: CO-transition temperature determined by the derivative of the superstructure reflection intensities in the resonant X-ray/neutron measurements (beamline MagS/PANDA diffractometer); the *dark gray shaded area* indicates the metallic regime as derived from electrical resistivity measurements. (b) Phase diagram of the $R_{1-x}Ca_xTiO_3$-system; *dark gray dashed lines*: MI-transition temperature of $Y_{1-x}Ca_xTiO_3$, $Er_{1-x}Ca_xTiO_3$ and $Lu_{1-x}Ca_xTiO_3$ systems derived from the resistivity; *gray circles/triangles*: CO-transition temperature determined by the derivative of the superstructure reflection intensities in the resonant X-ray/neutron measurements (beamline MagS/PANDA diffractometer); *gray shaded area*: temperature region where the superstructure reflection intensities rise on cooling (beamline MagS); *black squares*: difference of the nominal valency of the distinct Ti sites in the charge ordered LTM phase.

diffraction measurements indicates a different oxygen environment of the two distinct Ti-sites in the LTM phase which is indicative for charge ordering. The nominal valency of both Ti-sites which could be calculated by the bond-valence-sum formalism [169] reveals a difference of about 0.3 electrons for the $Y_{1-x}Ca_xTiO_3$-compounds with $x \sim 0.35$. In Fig. 6.23 (b) the difference of the nominal valencies of both Ti-sites (ΔBVS) is plotted as a function of hole-doping (*black squares*). With increasing hole-doping level x this difference of the nominal valencies further increases in the RTiO$_3$-system [17] and attains its maximum value of about 0.8 electrons for a compound with $x \sim 0.44$. This doping dependency supports the charge ordering picture since the half-doped compound should exhibit the most stable charge ordering pattern.

Additionally, charge ordering superstructure reflections (0 1 L) could be observed by neutron diffraction. These reflections are the $(\frac{1}{2}\ \frac{1}{2}\ \frac{1}{2})$ reflections of the pseudocubic unit cell (Ti-sublattice) and are indicative for three-dimensionally alternating oxygen

[17] This could be observed only in systems having a pure LTM phase and, hence, systems which are fully insulating at the measured temperatures. Thus, the RTiO$_3$-systems have been measured at 120 K for $Y_{0.65}Ca_{0.35}TiO_3$, 110 K for $Y_{0.64}Ca_{0.36}TiO_3$, 8 K for $Er_{0.3}Lu_{0.3}Ca_{0.4}TiO_3$ and 125 K for $Lu_{0.56}Ca_{0.44}TiO_3$.

environments of the Ti-ions. The Q-dependence of these reflections indicates, that the origin of these reflections is not magnetic. And the charge ordering temperature associated with the onset of these superstructure reflection intensities rises for compounds with increasing hole-doping level x. This is also in accordance with a stabilization of charge ordering for doping levels closer to the half-doped compound since a half-doped compound should exhibit the ideal Ti^{3+}/Ti^{4+}-charge ordering pattern. The charge ordering temperatures T_{CO} derived from these reflections are plotted in the $R_{1-x}Ca_xTiO_3$-phase diagram (*gray triangles*), see Fig. 6.23 (a-b).

Complementary resonant X-ray diffraction measurements have been performed at the synchrotron exhibiting the same superstructure reflections. The charge ordering onset temperatures T_{CO} derived from these superstructure reflection intensities are plotted in Fig. 6.23 (a-b). The circles denote the temperatures with the largest slope and the gray shaded region indicates the whole temperature regime where the intensities of these reflections increase on cooling. As can be seen, the overall charge ordering temperature T_{CO} increases with increasing Ca content x which has also been observed in the neutron measurements [18]. But for higher doped samples this transition somehow smears out. Furthermore, the charge ordering character of these superstructure reflections could be verified by energy scans and with polarization analysis. Thus, orbital order could be excluded as an origin for these reflections.

Summarizing, comprehensive neutron, synchrotron, single crystal X-ray and resonant X-ray diffraction measurements reveal charge ordering in the $R_{1-x}Ca_xTiO_3$-system (R = Y, Er, Lu) which extends from hole-doping levels around $x \sim 0.35$ towards the half-doped regime and which is stabilized with increasing Ca content x as can be seen in the increase of T_{CO} and in the increasing difference of the Ti-valencies. However, the metallic properties finally prevail at high doping levels since the introduction of Ca-ions strengthens the metallic properties by hole doping as well as by an increase of the electronic bandwidth W due to decreasing octahedral tilts. The substitution of Y by even smaller R-ions succeeded in counteracting this decrease of the octahedral tilts and it was possible to extend the insulating properties towards higher hole-concentrations. However, the optimum doped sample with $x \sim 1/2$ is still metallic in the compound with the smallest R-ion, $Lu_{0.5}Ca_{0.5}TiO_3$.

[18] The sample with $x = 0.45$ might have a lower sample quality.

6.5 The quasi two-dimensional titanate system $Sr_{2-x}La_xTiO_4$

6.5.1 Introduction

Among layered perovskites with K_2NiF_4-structure (214-structure, see Chap. 9.1) the compound Sr_2RuO_4 is so far the only compound exhibiting superconductivity [183] besides the superconducting cuprates [158]. Doped $SrTiO_3$ was one of the first transition metal oxides where superconductivity was found [184]. But compared to the two-dimensional CuO_2-layers in the high-T_C cuprates, $SrTiO_3$ has a fully three-dimensional (3D) crystal structure. Therefore, the effect on the electronic properties for 2D strontium titanate compounds could be of interest. There exists only one study dealing with this topic. In Ref. [185] epitaxial films of $Sr_{2-x}La_xTiO_4$ were grown in the concentration range $2\% \leq x \leq 7\%$. For 2% of La-doping, a beginning conversion to metallic behaviour could be observed, whereas the samples with 5%-7% are already metallic.

In this work, polycrystalline $Sr_{2-x}La_xTiO_4$-samples with La-concentrations ranging from 0% to 18% have been grown at the floating zone image furnace. Despite slow growth rates (∼1 mm/h) it was not possible to obtain single crystals. It should be noted, that even simple 113-perovskite (La,Sr)TiO_3 compounds like $La_{0.96}Sr_{0.04}TiO_3$ are reported to grow only as polycrystalline samples using the floating zone technique [78, 83]. Furthermore, there seems to be also a similar problem during growth of Sr_2VO_4 [186], where the synthesis of tetragonal (*I4/mmm*) Sr_2VO_4 was rendered difficult due to its metastability: at high temperatures above 1373 K the tetragonal phase transforms to an orthorhombic phase [186] which disturbs or prevents the growth of single crystalline samples using the floating zone technique. It is also possible, that a similar problem is inherent in the synthesis of 214-titanates. Hence, several problems might even merge in the growth process of $Sr_{2-x}La_xTiO_4$. In this work, all $Sr_{2-x}La_xTiO_4$-crystals have been grown as polycrystalline products, even if the growth rate was reduced to 1 mm/h and varying Sr-, Ti- and oxygen-concentrations have been tried. The compounds with lower La-doping level x are single phase but for higher La-concentrations around 18% some small volume fractions of impurity phases appear. Finally, above 18% of La-doping, no stable zone could be established at all.

6.5.2 Experimental

High resolution synchrotron radiation powder X-ray diffraction measurements have been performed at beamline B2 at the synchrotron facility HASYLAB/DESY in Hamburg, Germany. A wavelength of 0.7763 Å (E = 15970.6 eV) was chosen from the direct white synchrotron beam using a Si (111) double flat-crystal monochromator in order to suppress the Sr-fluorescence (K 1s: 16105 eV). The diffraction patterns have been collected using an on-site readable position-sensitive image-plate detector.

Powder neutron diffraction measurements have been performed at the high resolution D2B diffractometer at ILL in Grenoble, France ($\lambda = 1.59439$ Å). The electrical resistivity

has been determined by an AC four-point method and the capacitance of a cylindrical sample was measured by S. Jodlauk using an ultra-high precision capacitance bridge.

6.5.3 Results

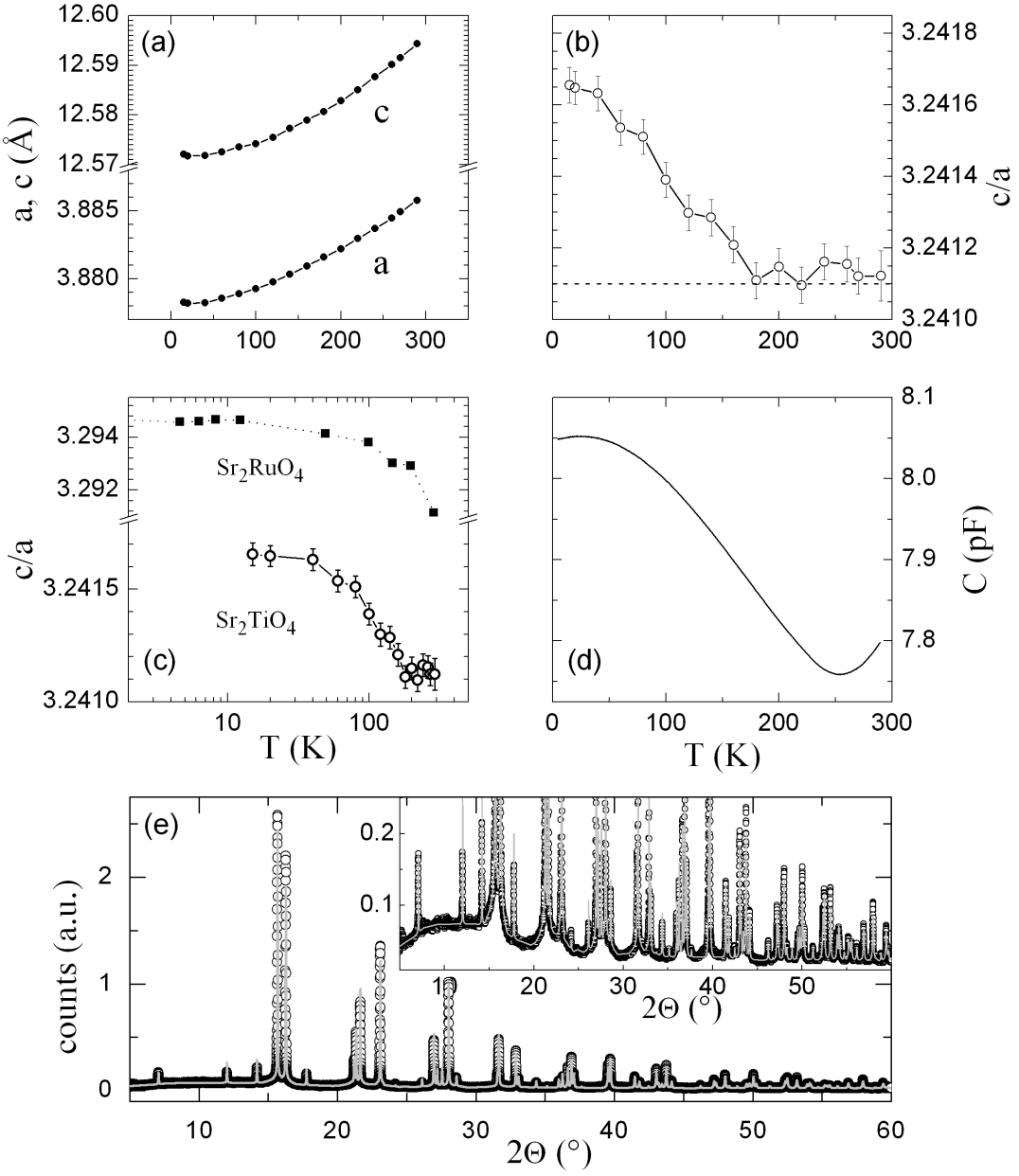

Figure 6.24: (a-b) Lattice parameter of Sr_2TiO_4. (c) c/a-ratio for Sr_2TiO_4. For comparison the values for Sr_2RuO_4 from Ref. [187] are plotted. (d) Capacity of a cylindrical Sr_2TiO_4-sample. (e) Synchrotron radiation powder X-ray diffraction patterns of Sr_2TiO_4(beamline B2).

powder X-ray diffraction measurements

Synchrotron radiation experiments have been performed in order to study the lattice parameter of Sr_2TiO_4 between room-temperature and about 10 K. A diffraction pattern of the measured sample grown in this work is plotted in Fig. 6.24 (e). These synchrotron measurements prove that the Sr_2TiO_4-sample grown in this work contains no impurities. The temperature dependency of the a- and c-lattice parameter is shown in Fig. 6.24 (a). A closer look to the data reveals, that the ratio c/a shows an anomalous rise at around 170 K. This rise of the ratio is unusually linear down to lowest temperatures as can be seen in Fig. 6.24 (b). A similar situation, but without a kink, was observed for Sr_2RuO_4 [187]. In Sr_2RuO_4 the ratio c/a also exhibits an anomalous rise on cooling which resembles to the one found in this work; see Fig. 6.24 (c). In Ref. [187] this anomalous rise was connected with localized moments and associated with a transition from a localized to an itinerant state. With regard to the new results found in this work these similar changes in Sr_2RuO_4 may also be driven by purely structural effects only, as Sr_2TiO_4 is a d^0-system. Finally, it should be noted that these effects are rather small and could be resolved only due to the high resolution at the synchrotron.

In order to study whether the rise of c/a may be indicative for some kind of ferroelectric transition, the dielectric constant ϵ ($\propto C$) was measured by S. Jodlauk on the same sample. Therefore, a cylindrical sample was sputtered with gold at the top and bottom faces and the capacity C was measured as a function of temperature. As can be seen in Fig. 6.24 (d), there is no strong rise visible comparable to that in $SrTiO_3$ [188]. However there is a small rise parallel to the rise of c/a. The anomalous behaviour around room-temperature is an extrinsic effect of the measuring method and should be ignored.

neutron measurements

The influence of La-doping on the lattice parameter of the $Sr_{2-x}La_xTiO_4$-system measured by means of powder neutron diffraction is shown in Fig. 6.25 (a-b). Whereas a decrease of the c-lattice parameter can be observed with increasing La-doping level, the a-axis shows the opposite behaviour. In total, the system exhibits a rise of the unit cell volume with increasing La-doping; see Fig. 6.25 (c). The inset within this figure shows the bond-valence sum (BVS, see Eq. 6.1) for all compounds measured. As expected, the BVS decreases with increasing La-concentration as the trivalent La-ion introduces electrons in this system. The fact that the initial value for Sr_2TiO_4 starts at a higher value of about 4.1 is common for perovskite systems as the BVS parameters have not been determined for systems with such a compact structure. Nevertheless, a comparison within a series yields reliable relative values (see Chapter 6.2). Comparing the values determined for $Sr_{2-x}La_xTiO_4$ in this work, the continuous electron doping with further La-substitution is clearly demonstrated. However, not the full difference expected for $x = 0$ and $x = 0.15$ is attained.

The value for c/a shown in Fig. 6.25 (d) exhibits a decreasing La-doping dependency. However the Ti-O2 distances [19] distinctly increase with further electron doping instead

[19] The apical Ti-O2 bond is parallel to the c-axis.

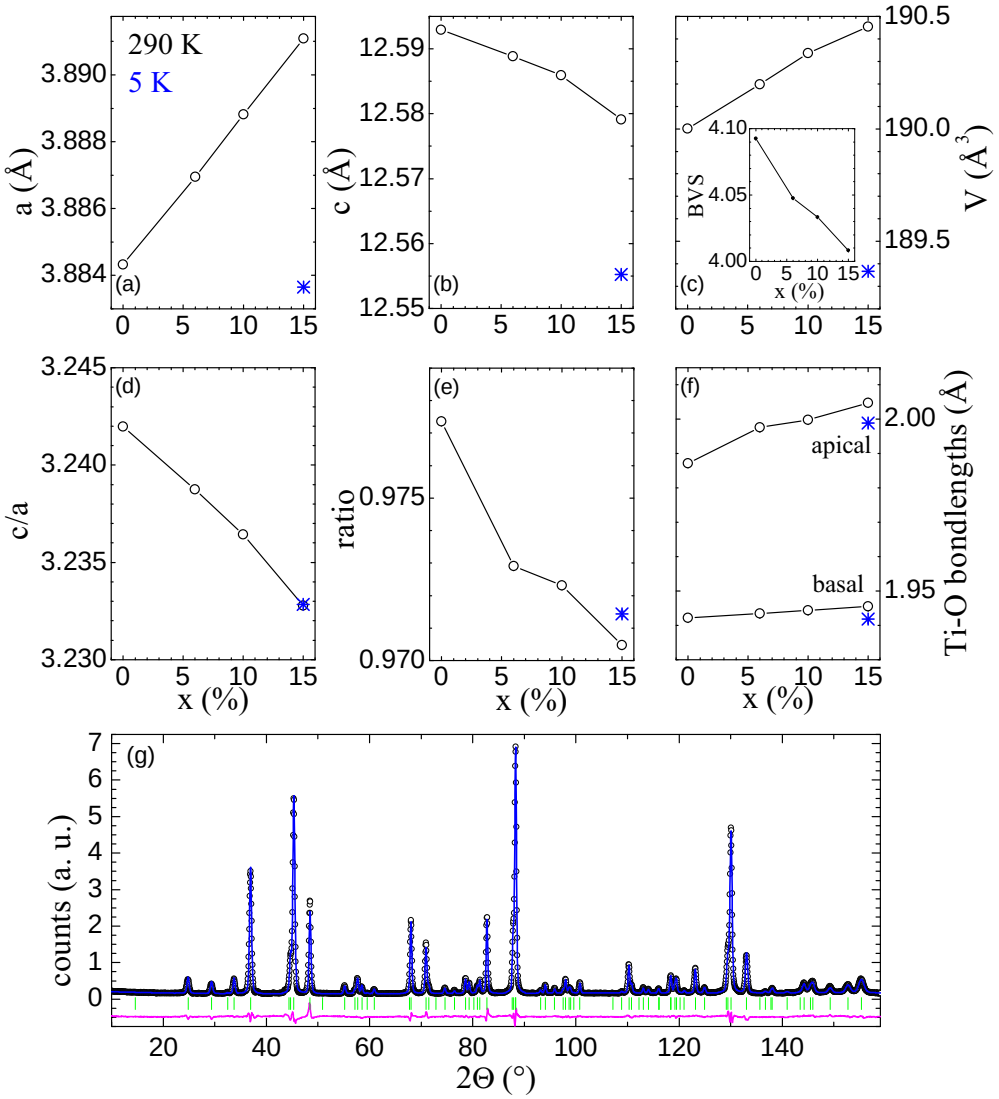

Figure 6.25: (a-c) Lattice parameter and unit cell volume of $Sr_{2-x}La_xTiO_4$ with the BVS in the inset. (d) c/a-ratio. (e) Ratio of Ti-O bondlength (basal versus apical). (f) Apical and basal Ti-O bondlength. (g) Powder neutron diffraction pattern for $Sr_{1.94}La_{0.06}TiO_4$ (D2B diffractometer).

of decreasing as the behaviour of c/a would suggest. The doping dependency of the two Ti-O distances is plotted in Fig. 6.25 (f). This rise of the apical Ti-O2 distance is even stronger than the rise of the basal Ti-O1-distance although the a-lattice parameter exhibits a rise and the c-lattice parameter a decay with increasing La-doping. This surprising result may indicate that the d_{xz} and d_{yz} orbitals get successively occupied with the introduction of electrons into the $Sr_{2-x}La_xTiO_4$-system (if there are no other effects).

The resistivity of this system has already been measured for epitaxial films up to La-

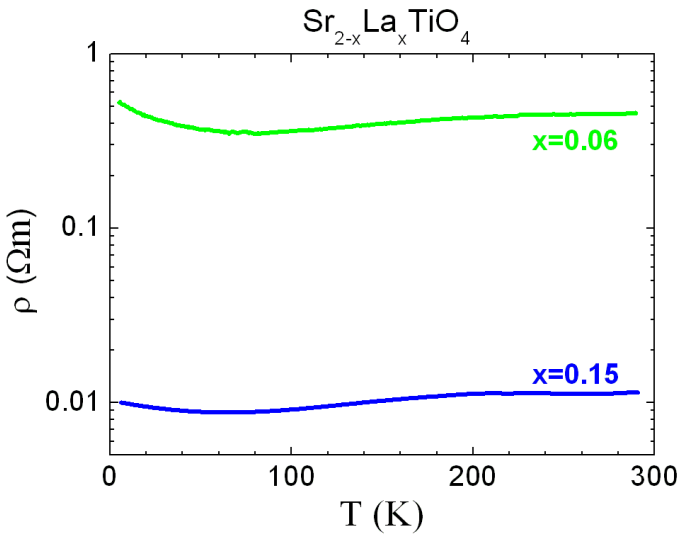

Figure 6.26: Resistivity of $Sr_{2-x}La_xTiO_4$.

doping levels of 7% only [185]. Therefore, the resistivity of higher doped 214-titanates is of greatest interest. In Fig. 6.26 the resistivity of the 15% La-doped compound is shown and compared to the (known) resistivity of the 6% doped sample which has a similar temperature dependency. The difference in the absolute value of the resistivity of $Sr_{1.94}La_{0.06}TiO_4$ compared to Ref. [185] can be explained by grain boundary effects as the samples grown in this work are polycrystalline. Compared to the 6% doped sample, $Sr_{1.85}La_{0.15}TiO_4$ has more metallic temperature dependency with a smaller resistivity. However, both samples show no superconductivity down to 6 K.

6.5.4 Conclusion

In summary, polycrystalline $Sr_{2-x}La_xTiO_4$-samples have been grown in this work. High-resolution synchrotron measurements on the undoped parent compound Sr_2TiO_4 exhibit an anomalous rise of the c/a ratio which resembles on the rise of c/a in the isostructural Sr_2RuO_4-system [187]. But as the titanate has no d-electrons indicating a purely structurally driven effect, probably also the origin of this anomaly in the ruthenate-system has to be re-analyzed.

New $Sr_{2-x}La_xTiO_4$-compounds with higher La-doping levels have been synthesized within this work. Neutron scattering studies indicate increasing apical Ti-O distances (parallel to c) although the ratio of the lattice parameter c/a decreases. These results may point to the occupation of d_{xz} and d_{yz} orbitals in this system on electronic doping. The 6% and 15% doped samples are metallic down to 6 K. The larger absolute values may be induced by the polycrystallinity of these materials. Single crystalline samples might have distinctly lower absolute values. Further resistivity measurements down to

300 mK are planned in order to search for superconductivity within these samples. Also the growth of even higher doped samples and maybe even single crystalline samples is a future aim.

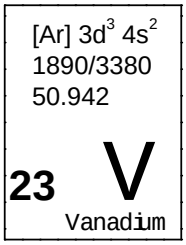

7 Vanadates

Vanadium is a common element in the earth's crust with a distribution of 0.02% by mass [107]. Its applications range from the use in iron or titanium alloys such as steel to the use in reactors due to its structural strength and small neutron cross section. The vanadium oxide V_2O_5 (see Chap. 7.2) is used as a catalyst for the industrial production of chemicals like sulfuric acid [107].

7.1 A novel dimerized phase in Hollandite

7.1.1 Introduction

Although discovered about 30 years ago [189] not much is known about the hollandite $K_2V_8O_{16}$ which may be related to the elaborate high-pressure preparation procedure which renders the availability of this vanadium oxide rather difficult. Due to the large number of possible oxidation states of the vanadium ion ranging from +2 to +5 a large variety of different vanadium oxide compounds exists. Some of these compounds exhibit very interesting properties as for example the vanadium bronzes β-$Na_{0.33}V_2O_5$, β-$Ag_{0.33}V_2O_5$ and β'-$Cu_{0.65}V_2O_5$ which exhibit superconductivity under pressure [190-192]. Vanadium oxides show a large variety of structural and electromagnetic properties of which the metal-insulator (MI) transition in the binary vanadium oxides V_2O_3 and VO_2 is one of the most famous ones. This MI transition is accompanied by a strong and sharp rise of the electrical resistivity by several orders of magnitude[193, 194, 162]. The comprehension of the MI transition in these compounds is still a puzzling task as the role of electron correlations and the role of electron-lattice interactions, concomitant with structural distortions, is highly under debate. On the one hand, the MI transition in VO_2 was found to be a predominantly Peierls transition [195], on the other hand it was thought to be a Mott-Hubbard transition [196].

Mixed-valent vanadium oxides such as V_4O_7, additionally, exhibit charge ordering at the MI transition accompanied by dimerization of spin singlets which becomes noticeable in a drop in the magnetic susceptibility [197-199]. The hollandite compound $K_2V_8O_{16}$ is such a mixed-valent vanadium oxide with an average valency of 3.75+. Originally, the first *Hollandite* was a manganese oxide mineral[200], but all compounds with the general formula $A_xM_8O_{16}$ ($x \leq 2$) are counted to this class of compounds. Byström and Byström were the first who reported the hollandite type structure for manganese minerals [200]. A series of other hollandite compounds quickly followed [201-209]. At room-temperature,

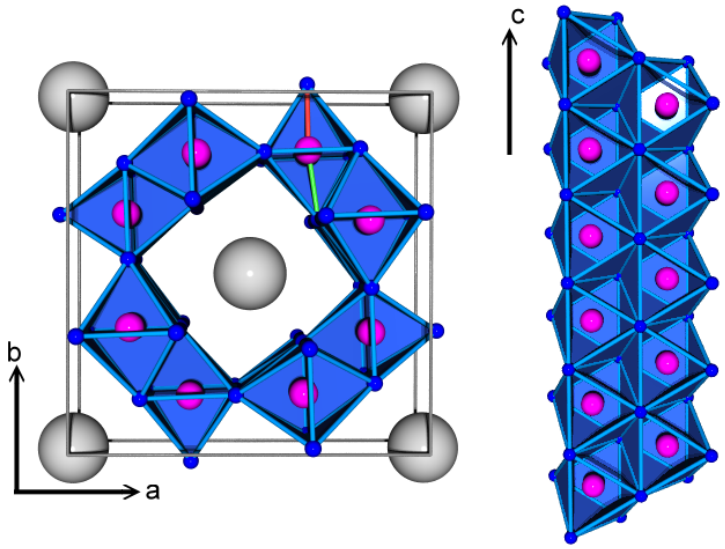

Figure 7.1: The tetragonal high temperature structure of $K_2V_8O_{16}$; *blue:* oxygen ions, *gray:* potassium ions, *magenta:* vanadium ions. The *green/red* bonds indicates long/short apical V-O bonds. The right figure shows a VO_6-octahedral double chain running in c_{tet}-direction.

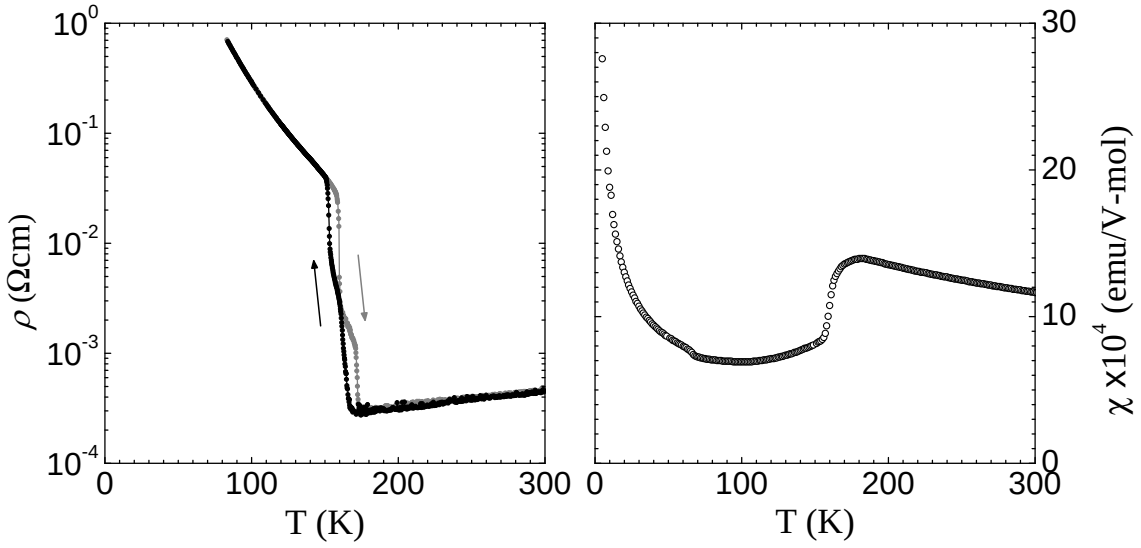

Figure 7.2: (a) Electrical resistivity of $K_2V_8O_{16}$ measured by M. Isobe [210]. (b) Magnetic susceptibility of $K_2V_8O_{16}$ measured by M. Isobe [210].

the vanadium oxide hollandite compound $K_2V_8O_{16}$ has a tetragonal structure with lattice parameters of about 10 Å × 10 Å × 2.9 Å (see Fig. 7.1). The structure is built of VO_6-

octahedral double chains running along the tetragonal c-direction. Due to the four-fold symmetry four octahedral double chains form tubes extending in c_{tet}-direction. The potassium ions align along the free space within these tubes surrounded by vanadium oxide double-chains and, thus, form themselves chains in c-direction as can be seen in Fig. 7.1.

$K_2V_8O_{16}$ exhibits a (split) metal-insulator (MI) transition at $T_{MI} \sim 160$ K with the insulating behaviour appearing below this temperature [210], see Fig. 7.2 (a). Concomitantly with the MI-transition there is a structural phase transition from the tetragonal to a monoclinic structure with an enlarged $\sqrt{2} \times \sqrt{2} \times 2$ cell. As the average valence of the vanadium ions amounts to 3.75+ it is obvious to search for a charge disproportionation corresponding to a V^{3+}:V^{4+}-ratio of 1:3 below T_{MI}. Such charge order could explain the insulating properties below T_{MI}. However, concomitantly with the metal-insulator transition the magnetic susceptibility exhibits a well pronounced drop below 160 K (see Fig. 7.2 (b) and Fig. 7.8 (b)) and this effect can not be explained by a charge ordering scenario alone.

7.1.2 Experimental

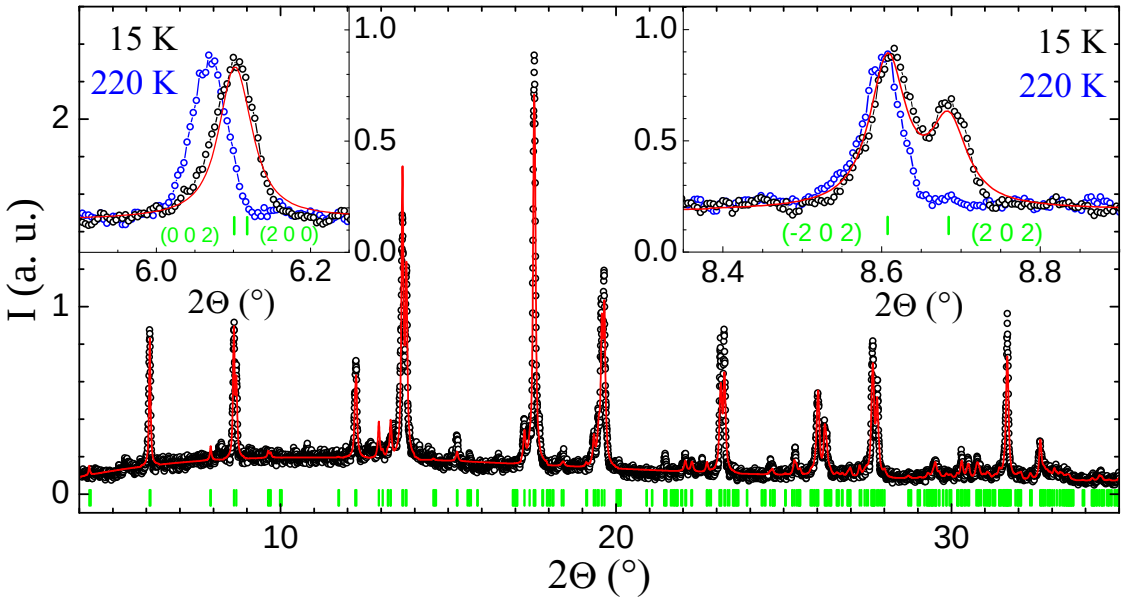

Figure 7.3: Synchrotron radiation powder X-ray diffraction pattern of $K_2V_8O_{16}$ measured at beamline B2; *black circles*: measured intensity at 15 K, *red line*: Le Bail fit, *green bars*: Bragg peak positions, *blue circles*: measured intensity at 220 K $\gg T_C$.

Polycrystalline samples of $K_2V_8O_{16}$ were grown by M. Isobe using a high-pressure technique with pressures of about 3-4 GPA. Within the polycrystalline samples it was

possible to find some single crystalline grains as well. In this work four different samples (A, B, C, D) have been studied. Regarding impurity phases, sample A and C are high quality samples, whereas sample B has a somewhat minor quality and sample D is a sample with an acceptable quality in between. Sample C' will be defined as sample C plus an additional large amount of sample volume with the same high sample quality. The samples A_ν, B_ν, C_ν and D_ν ($\nu = 1, 2, ...$) are single crystalline spheres derived from the polycrystalline bulk of sample A, B, C and D respectively. Elastic and inelastic powder neutron diffraction measurements have been performed at the D2B diffractometer (sample B and C') and the IN4 spectrometer (sample C') at the ILL in Grenoble, France and at the DMC diffractometer (sample B) and the FOCUS spectrometer (sample B) at the PSI in Villigen, Swiss. Synchrotron radiation powder X-ray diffraction measurements have been performed on sample D at beamline B2 at Hasylab/DESY. A *Bruker X8 Apex* single crystal X-ray diffractometer was used for single crystal X-ray-diffraction measurements on sample C_1 using Mo-K_α radiation. The magnetic susceptibility of sample C was measured by M. Isobe using a SQUID-magnetometer. The specific heat was measured by D. Meier on sample A using a home-built calorimeter. The ESR studies were carried out together with J. Hemberger with a Bruker ELEXSYS E500 CW spectrometer at X-band frequency ($\nu = 9.36$ GHz) in a nitrogen gas flow cryostat Bruker ER4131VT for 100 K $\leq$ T $\leq$ 300 K.

7.1.3 Results and Discussion

neutron and X-ray measurements

Fig. 7.3 shows the synchrotron radiation powder X-ray diffraction patterns of $K_2V_8O_{16}$ measured at 15 K (*black circles*) together with the corresponding Le Bail fit (*red line*). Additionally, the measured data at 220 K in the high-temperature tetragonal phase with space group $I4/m$ is shown (*blue circles*). As can be seen, at low temperatures a peak splitting is observable. Additionally, other peaks slightly broaden. The best description could be obtained with a monoclinic symmetry with space group *I2/m* and a $\sqrt{2}\times 2\times\sqrt{2}$ enlarged unit cell with monoclinic angle β [1]. The Bragg peaks in Fig. 7.3 are labeled in notation of this enlarged monoclinic unit cell. As can be seen in the right inset of Fig. 7.3 the tetragonal $(2\ 0\ 0)_{tet}$ and $(0\ 2\ 0)_{tet}$ peaks are clearly split. This peak splitting can be described by the $\sqrt{2} \times 2 \times \sqrt{2}$ monoclinic unit cell. In notation of this monoclinic cell these peaks are the $(\pm 2\ 0\ 2)_{mono}$ peaks and the splitting of these peaks can be described

[1] The superstructure reflections according to this enlarged unit cell with $a_{mono} \sim \sqrt{2} \times a_{tet}$ $b_{mono} \sim 2 \times c_{tet}$ and $c_{mono} \sim \sqrt{2} \times b_{tet}$ were barely visible in these powder diffraction patterns but have been observed by single crystal X-ray diffraction as will be presented later.

a (Å)	13.98027(81)
a (Å)	5.85981(24)
a (Å)	14.01861(79)
β (°)	90.50777(31)

Table 7.1: Lattice parameters of $K_2V_8O_{16}$ at 15 K (space group *I2/m*).

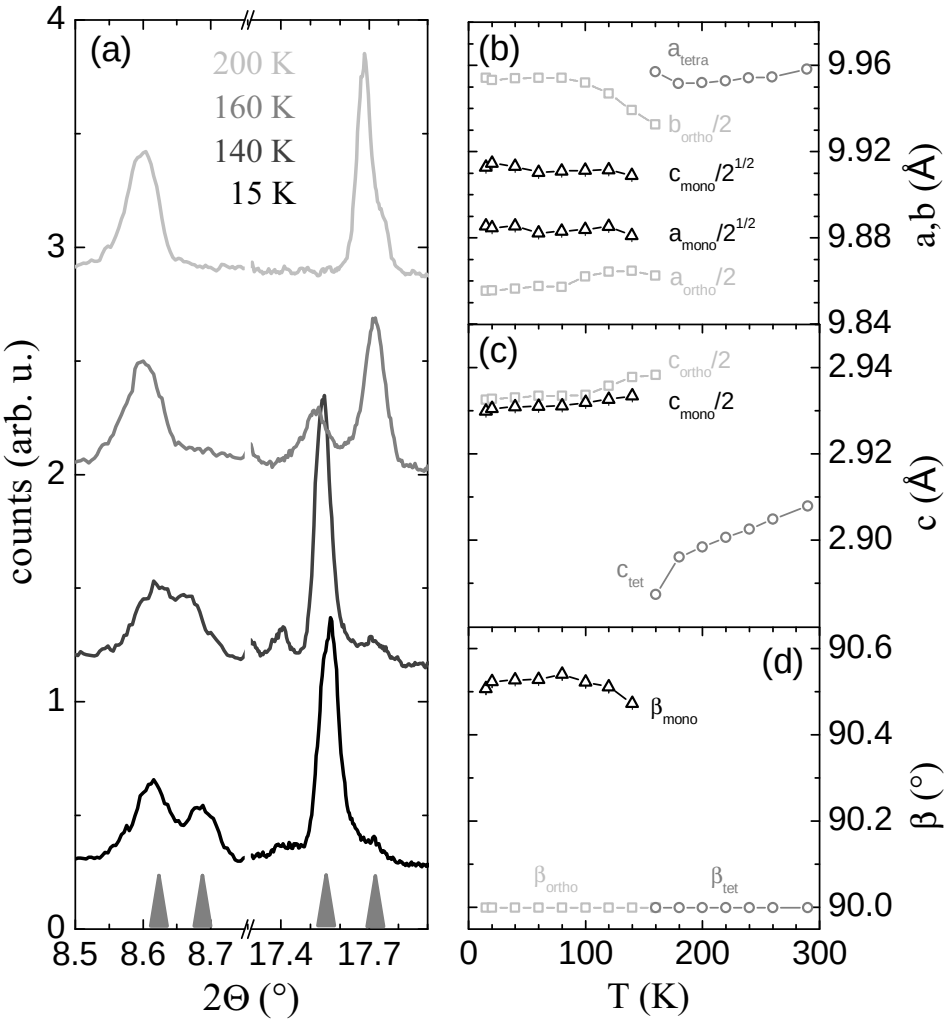

Figure 7.4: (a) Powder diffraction patterns of $K_2V_8O_{16}$ at different temperatures indicating phase separation at 160 K. (b-d) The lattice parameter of $K_2V_8O_{16}$ measured by means of synchrotron radiation powder X-ray diffraction. Additionally to the values of the low-temperature monoclinic cell (*I2/m*) for a comparison, also the values derived from a fit of an F-centered orthorhombic unit cell are shown. This enlarged orthorhombic cell is also able to describe the distinct peak splitting observed for one class of reflections but fails in describing a small peak broadening (splitting) of a second class of reflections.

with a monoclinic angle of about 90.5°. However, this splitting can be also described by a F-centered orthorhombic unit cell which exhibits a further doubling of the unit cell and which is rotated by about 45°compared to the monoclinic unit cell. Hence, this F-centered orthorhombic cell would be $2 \times 2 \times 2$ the size of the tetragonal cell and the split peaks mentioned above would be the $(4\ 0\ 0)_{ortho}$ and $(0\ 4\ 0)_{ortho}$ peaks.

However, also the $(1\ \pm1\ 0)_{tet}$ peaks, i. e. the $(2\ 0\ 0)_{mono}$ and $(0\ 0\ 2)_{mono}$ peaks

in monoclinic notation, are broadened below T_C, see the left inset of Fig. 7.3. This could be verified by gaussian fits yielding a peak width (FWHM) of 0.03862(79)° at 220 K and 0.03249(49)° at 15 K. This is a clear indication for a further peak splitting of the monoclinic $(2\ 0\ 0)_{mono}$ and $(0\ 0\ 2)_{mono}$ peaks which could not be resolved in these synchrotron measurements. Such a peak splitting can not be described with the orthorhombic $2 \times 2 \times 2$ unit cell since these peaks correspond to the $(2\ \pm 2\ 0)_{ortho}$ peaks in this F-centered orthorhombic cell which exhibit no splitting in powder diffraction patterns. Hence, a monoclinic symmetry is needed in order to describe also these slightly broadened peaks. The lattice parameters at 15 K obtained by a Le Bail fits using the monoclinic symmetry are listed in Tab. 7.1. As can be seen, the difference between the monoclinic a_{mono} and c_{mono} lattice parameters is significant. Hence, an orthorhombic symmetry is less probable.

Concluding, the distinct peak splitting of the $(2\ 0\ 0)_{tet}$ and $(0\ 2\ 0)_{tet}$ peaks observed in $K_2V_8O_{16}$ below T_C can be attributed either to a monoclinic distortion with a monoclinic angle of about 90.5° or to an orthorhombic distortion with a difference of about 1% between the orthorhombic a and b-lattice parameters. Furthermore, a tiny peak broadening below T_C could be observed for the $(1\ \pm 1\ 0)_{tet}$ peaks which is indicative for a small peak splitting. This peak splitting can be only described by the monoclinic symmetry yielding a difference of about 0.27% in the monoclinic a and b lattice parameters. The values of the I-centered monoclinic (*black triangles*) and, for a comparison, also the values of a fit with a F-centered orthorhombic unit cell (*light gray squares*) are plotted together with the values of the high-temperature tetragonal unit cell (*gray circles*) in Fig. 7.4 (b-c). Besides the failure in describing the small peak broadening of the $(1\ \pm 1\ 0)_{tet}$ peaks the transition from the tetragonal cell (*I4/m*) to a F-centered orthorhombic cell is not a continuous phase transition [211]. In contrast, the transition *I4/m* → *I2/m* (or *I4/m* → *C2/c* or *I4/m* → *I2*) is a continuous phase transition [211]. Hence, it is very unlikely that the low-temperature phase in $K_2V_8O_{16}$ has an orthorhombic symmetry and only the monoclinic space groups *I2/m*, *C2/c* and *I2* are possible symmetries which describe continuous phase transitions and which are able to describe the small peak broadening of the second class of reflections in the high-resolution synchrotron measurements. Due to these synchrotron data and also due to single crystal X-ray and powder neutron diffraction data, there is no indication for an even lower symmetry.

Furthermore, from Fig. 7.4 (a) it can be seen, that phase separation occurs around 160 K: the tetragonal high temperature and the monoclinic low temperature structure coexist in this temperature region. But at 140 K the phase separated region has already vanished and only one monoclinic phase persists down to lowest temperatures.

It should be noted that the c-axis exhibits a distinct rise below T_C (see Fig. 7.4 (c)) which is very similar to the rise of the rutile c-axis in VO_2 by about 1% [212, 213]. Hence, even at this early stage of data analysis the temperature dependency of the lattice parameters of $K_2V_8O_{16}$ reveals similarities with VO_2.

In order to elucidate the low temperature structure of $K_2V_8O_{16}$, single crystal X-ray diffraction measurements using Mo-K_α radiation have been performed. A single crystalline sphere of about 100 μm in diameter (sample C_1) has been measured between

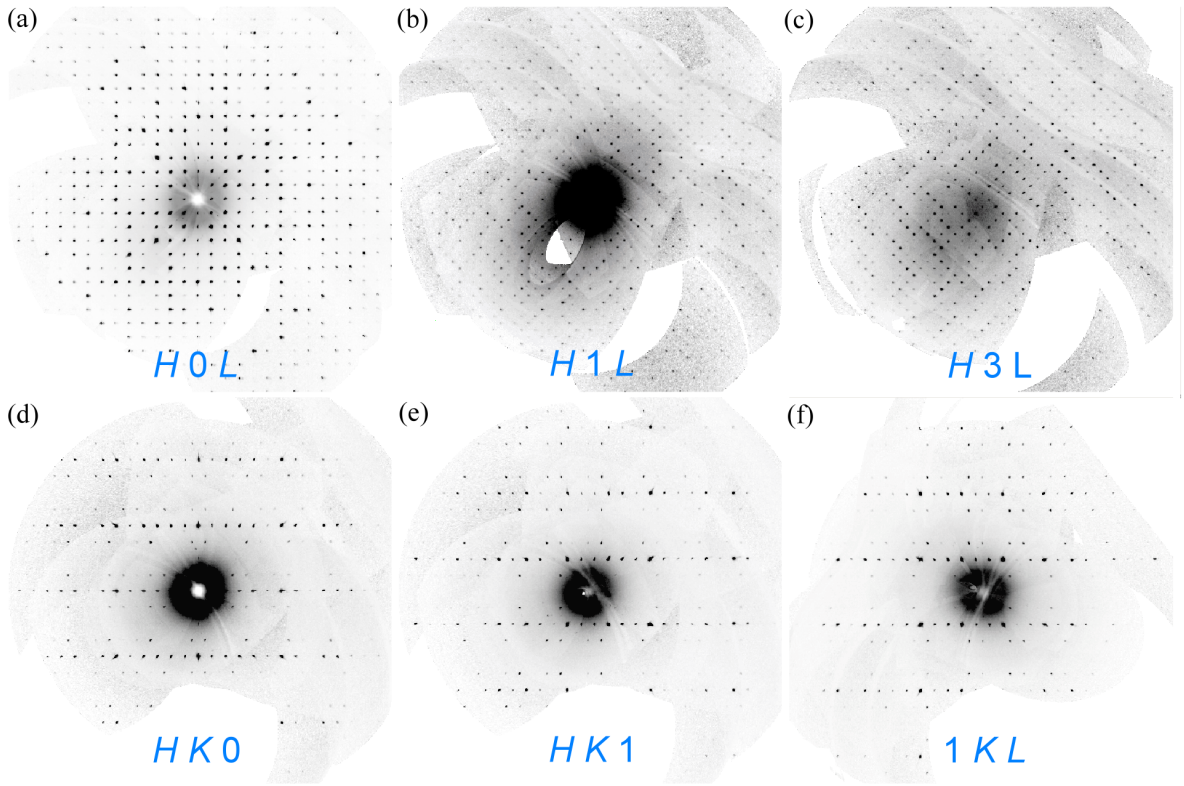

Figure 7.5: Clips out of precession maps measured at 100 K in *monoclinic notation* (first axis in horizontal direction, second in vertical direction). (a) $(H\ 0\ L)_{mono}$ plane, first reflections in H-/L- direction are $(2\ 0\ 0)_{mono}$ and $(0\ 0\ 2)_{mono}$. (b) $(H\ 1\ L)_{mono}$ and (c) $(H\ 3\ L)_{mono}$ plane showing the superstructure reflections, first reflections in H-/L-direction are $(1\ 3\ 0)_{mono}$ and $(0\ 3\ 1)_{mono}$. (d) $(H\ K\ 0)_{mono}$ plane. (e) $(H\ K\ 1)_{mono}$ plane. (f) $(1\ K\ L)$ plane.

290 K and 100 K. A close analysis of the 290 K structure reveals, that the V-ions in the high-temperature structure are not located in the center of its surrounding VO_6 octahedron but shifted towards an apical oxygen as indicated by the red and green V-O bonds in Fig. 7.1. In fact, this could be derived from the structural parameters already measured in Ref. [189], but nevertheless an octahedral oxygen environment has been reported in this publication. The sample measured in this work exhibits two different apical V-O distances of 1.8604(5) Å and 1.9713(5) Å. Thus, the V-O coordination has already become a square pyramid rather than an octahedron. This observation is in accordance with the expected V-O coordination for a vanadium valency of about 4+ [214]. And as the neighbouring vanadium chain within each V-double chain exhibits the same split apical V-O distances, but, in opposite direction, the vanadium ions within these double chains become more separated and isolated from each other.

Fig. 7.5 (a-f) shows (central) parts of the precession maps of $K_2V_8O_{16}$ at 100 K. In Fig. 7.5 (b-c,e-f) all reflections shown are superstructure reflections. In this work, only

superstructure reflections with $K = 2 \cdot n + 1$ and $H + L = 2 \cdot n + 1$ in monoclinic notation ($\sqrt{2} \times \sqrt{2} \times 2$ cell) could be observed, i.e. for $(H\ K\ L)_{tet}$-reflections with half-integer values. Fig. 7.5 (b) shows the large number of reflections in the $(H\ 3\ L)_{mono}$ plane which are all superstructure reflections - with most of them having rather strong intensities of the order of $\sim\frac{3}{4}\%$ of the strongest fundamental reflection [2]. In contrast, in the $(H\ 0\ L)_{mono}$ plane only fundamental reflections could be detected, see Fig. 7.5 (a). The main purpose of showing the precision maps in Fig. 7.5 (a-f) is to show the vast number of strong superstructure reflections which could be observed in this X-ray diffraction measurement. Note, that all the reflections which can be seen in Fig. 7.5 (b-c,e-f) are superstructure reflections solely.

Due to Ref. [211] there are three possible monoclinic space groups which have an unit cell volume $V_{mono} = 4 \times V_{tet}$ and which describe a continuous tetragonal to monoclinic phase transition: *I2/m*, *C2/c* and *I2*. These three symmetries have to be considered since the orthorhombic F-centered symmetries could be excluded according to the synchrotron measurements. For the last of these space groups there would be a large number of about 30 atoms in the asymmetric unit. For the other two possibilities, the number is still large but only of the order of 20 atoms. Hence, first of all only the two symmetries *I2/m* and *C2/c* will be compared. The unit cell in the first case (*I2/m*) roughly is a 14 Å × 5.8 Å × 14 Å cell with a monoclinic angle $\beta \sim 90.5°$, compare Tab. 7.1. The unit cell in the second case roughly is a 19.9 Å × 5.8 Å × 14 Å cell with a monoclinic angle $\beta \sim 135°$. The symmetry reduction from the tetragonal symmetry $I4/m$ with a unit cell size of about 9.9 Å × 2.9 Å × 9.9 Å to the monoclinic symmetries *I2/m* and *C2/c* and the calculation of the possible twin laws arising concomitantly with the loss of symmetry elements has been performed using the 'cell transformation', 'origin shift transform' and 'go to subgroup structure' tools provided by the program *Jana2000* [58]. Finally, it was possible to solve the structure with space group $I2/m$ yielding acceptable R-values which were of the order of 5% to 8.5% for several different single crystalline spheres measured. A refinement with space group $C2/c$ did not yield satisfactory results and the R-values were of the order of 17%. After solving the low-temperature structure of $K_2V_8O_{16}$ and regarding the differences between space groups $I2/m$ and $C2/c$ this result can be understood also from the physical point of view. But first the solved low-temperature structure of $K_2V_8O_{16}$ has to be presented and afterwards, the problems of describing such a structure with space group $C2/c$ will be discussed. It is also possible to describe the low-temperature structure of $K_2V_8O_{16}$ with space group $I2$. The R-values even decrease by up to 1% and all distortions which can be observed in the structure with space group $I2/m$ can be still observed in the structure with space group $I2$. However, the refinement is not satisfactory since too many displacement parameters are negative or not positive definite. Thus a refinement with such a huge number of atoms in the asymmetric unit seems not very stable [3]. Also this refinement with space group

[2] Most fundamental reflections are distinctly weaker. For example these superstructure reflection intensities are of the order of 1.5% of the intensity of the second strongest fundamental reflection which has been measured. In average, these superstructure reflections can be estimated to be of the order of roughly 1-5% of most strong fundamental reflections.

[3] For these reasons it was also not possible to refine structure models with lower monoclinic symmetry

$I2$ does not yield any completely new distortions compared to space group I2/m which could have justified the use of such a low symmetry. Thus, the highest symmetry which is able to describe the low temperature structure of $K_2V_8O_{16}$ satisfactory is $I2/m$ (a satisfactory description with space group $C2/c$ was not possible).

Several single crystalline samples A_1, A_2, A_3, A_4, B_1, B_2, B_3, B_4, C_1 and D_1, have been measured at the *Apex* single crystal diffractometer. For all of these samples which have been measured at low temperatures, the observed distortions appearing below the tetragonal to monoclinic phase transition were qualitatively and also quantitatively almost the same. Also the volume fractions of the twin domains calculated by the program *Jana*2000 [58] were distributed about equally among two twin domains, with the exception of one sample (C_1) which exhibits only one large twin domain and, hence, only few twinning below the phase transition. Usually, all symmetry elements which get lost due to a symmetry reduction should appear in the twin laws of the twinned structure which appears below the phase transition. After a tetragonal to monoclinic phase transition twin domains ν with the following twin laws can be expected:

$$\mathbf{T_1} = \begin{pmatrix} 1 & 0 & 0 \\ 0 & 1 & 0 \\ 0 & 0 & 1 \end{pmatrix} \quad \mathbf{T_2} = \begin{pmatrix} -1 & 0 & 0 \\ 0 & 1 & 0 \\ 0 & 0 & 1 \end{pmatrix} \quad \mathbf{T_3} = \begin{pmatrix} 0 & 0 & -1 \\ 0 & 1 & 0 \\ 1 & 0 & 0 \end{pmatrix} \quad \mathbf{T_4} = \begin{pmatrix} 0 & 0 & 1 \\ 0 & 1 & 0 \\ 1 & 0 & 0 \end{pmatrix}$$

As mentioned above, there was one sample (sample C_1) which shows only minor twinning as was indicated by the refinement of the volume ratios of all twin domains. Since the obtained fit was rather good and since the structural results were almost identical to the results of the other fully twinned samples, this less twinned sample has been considered as the ideal sample for structural studies of $K_2V_8O_{16}$ and measured in great detail at different temperatures. Presumably some kind of strain due to imperfections or impurities might enforce the growth of one twin domain only. Besides the less twinned sample C_1 also the 'fully twinned' samples A_3 and A_4 have been studied in great detail at several temperatures [4]. In the following the low temperature structure of $K_2V_8O_{16}$ derived from the measurements of sample C_1 will be discussed. The results of the refinement of the 'untwined' sample C_1 at 100 K are listed in Tab. 7.2.

The low-temperature structure of $K_2V_8O_{16}$ exhibits three different structural distortions which are displayed in Fig. 7.6. First of all, one half of all vanadium ions exhibits a quite remarkable dimerization along chains in c_{tet}-direction. A measure for this dimerization are the V-V-bondlengths of the dimerized V-ions within the same dimer and between two dimers, see Fig. 7.7. The difference of these V-V-bond lengths amounts to ∼0.3 Å at 100 K and is plotted as a function of temperature in Fig. 7.8 (d). The second distortion is found in the other half of vanadium chains which are the neighbouring V-chains of the dimerized V-chains within the VO_6-double chains. In these neighbouring V-chains the vanadium ions move away from the dimers on the one hand

like $P2/m$ or $P2$ having even 42 atoms and 56 atoms in the asymmetric unit respectively.

[4] The volume ratios $\mathbf{r}_\nu \equiv \mathbf{r}(\mathbf{T}_\nu)$ of the twin domains of these three very well studied samples amount to $\mathbf{r_1^{(A_3)}}$= 61.4(8)%, $\mathbf{r_2^{(A_3)}}$= 0.1(2)%, $\mathbf{r_3^{(A_3)}}$= 38.3(8)%, $\mathbf{r_4^{(A_3)}}$= 0.1(2)%, $\mathbf{r_1^{(A_4)}}$= 47.6(2)%, $\mathbf{r_2^{(A_4)}}$= 0.1(1)%, $\mathbf{r_3^{(A_4)}}$= 52.2(2)%, $\mathbf{r_4^{(A_4)}}$= 0.1(1)%, $\mathbf{r_1^{(C_1)}}$= 86.5(7)%, $\mathbf{r_2^{(C_1)}}$= 0.3(1)%, $\mathbf{r_3^{(C_1)}}$= 13.2(7)%, $\mathbf{r_4^{(C_1)}}$= 0.0(0)%. Hence, sample C_1 is almost untwined.

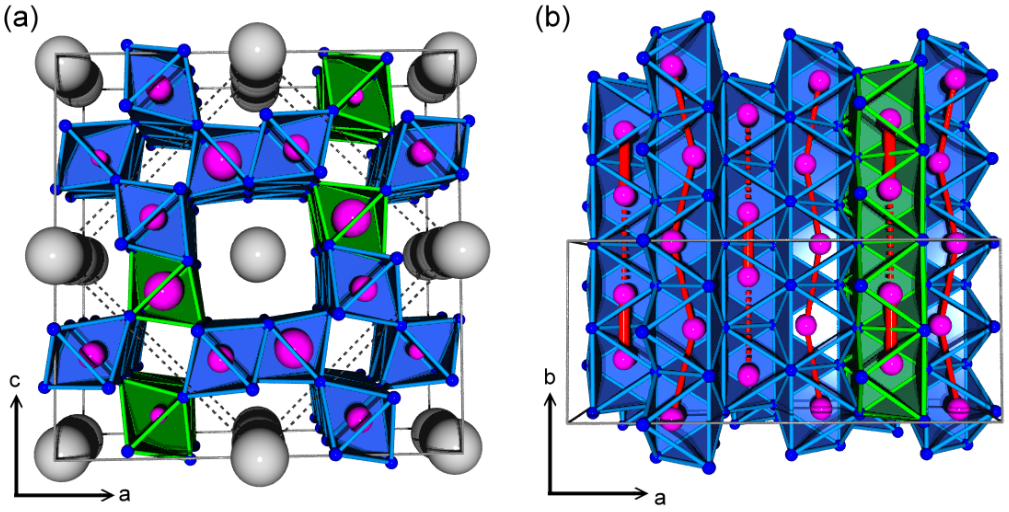

Figure 7.6: Low temperature structure of $K_2V_8O_{16}$. (a) The measured structure at 100 K; *blue:* oxygen ions, *gray:* Potassium ions, *magenta:* vanadium ions, small/large/medium sized spheres denote V-ions which are dimerized with a V-ion: in the same unit cell (moving down)/the next upper unit cell (moving up)/ within zig-zag-chains. *Green octahedra* indicate $V^{3+}O_6$-octahedra and *blue octahedra* indicate $V^{4+}O_6$-octahedra thus visualizing the charge ordering. The black dotted lines identify the small 10 Å × 10 Å × 2.9 Å unit cell of the high-temperature structure whereas the gray cell is the $\sqrt{2} \times \sqrt{2} \times 2$ cell of the low temperature structure. (b) Two unit cells rotated by 90° with respect to Fig. (a). Here, all K^+-ions are omitted and the distortions are exaggerated in order to demonstrate the dimerization and zig-zag-chain formation more clearly.

and move towards the free space between two dimers in a manner which leads to a zig-zag-chain formation as can be seen in Fig. 7.6 (b). As a quantitative measure the V-V-V bond-angle within one selected zig-zag chain is plotted versus temperature in Fig. 7.8 (e). A distinct deviation from the non-distorted value of 180° can be observed below T_{MI}. The value at 100 K amounts approximately 174.7°. This dimerization and zig-zag-chain formation strongly resembles on the monoclinic M2-phase in VO_2[212] or $V_{0.976}Cr_{0.024}O_2$ which also exhibits astonishingly similar anomalies in the lattice parameter at the phase transition from the high temperature tetragonal rutile structure to the monoclinic M2-structure around 345 K[215] (rise of c etc.). It should be noted that these rather strong structural distortions were observable below T_{C} for all samples measured at low temperatures, also the 'fully twinned' samples A_3 and A_4. The values of the V-V distances and V-V-V bond angles is listed in Tab. 7.3.

Furthermore, on top of that, there occurs charge ordering in the low-temperature structure of $K_2V_8O_{16}$ in a way that one half of all dimerized vanadium chains contains V^{4+} ions and the other half V^{3+} ions. This charge ordering was found by analysis of the bond valence sums of the vanadium ions. It turned out that all vanadium ions located in zig-zag-chains have all the same oxidation state of about 4+. Therefore, the

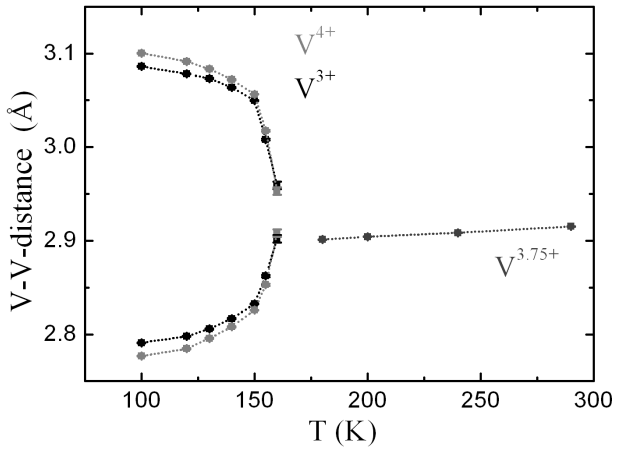

Figure 7.7: V-V-distances within dimerized chains along c in $K_2V_8O_{16}$ determined by single crystal X-ray diffraction.

charge ordering must take place within the dimerized chains. Within the monoclinic space group $I2/m$ there are only two V-sites within these dimerized chains - V1 and V4 - opposed to the four V-sites attributed to the zig-zag-chains - V2, V3, V5 and V6. The difference in the oxidation state of the V1 and V4 ions compared to the average valency of the remaining four vanadium sites reveals that the V4-site contains V^{4+} ions whereas the V1 sites are occupied by V^{3+} ions. This difference in the oxidation state is plotted as a function of temperature in Fig. 7.8 (f) and amounts to about 0.5 electrons at low temperatures. The deviation from the ideal value of one electron was also observed in other charge ordered systems like the manganites which show even much smaller values of about 0.2. It should be noted that this distribution of electrons which naturally comes out by bond valence sum analysis of the diffraction measurements is fully in accordance with the nominally expected ratio of V^{4+}:V^{3+} ions for $K_2V_8O_{16}$ where the V-ions should have the nominal valency of 3.75+, i. e. a ratio of 3:1. The structural parameter of $K_2V_8O_{16}$ measured at 100 K are given in Tab. 7.2. Whereas the dimerization and zig-zag chain formation are stable in the structural refinements of all three samples and could be observed without any doubts, the charge ordering in $K_2V_8O_{16}$ is not unambiguously clear since the twinned samples A_3 and A_4 exhibit almost no indications for charge ordering.

In the following, the low-temperature structure of $K_2V_8O_{16}$ will be discussed in order to explain all distortions and features of this rather complex structure. Afterwards, also a possible solution with space group $C2/c$ will be discussed. Fig. 7.6 (a) shows a view of the monoclinic 14 Å × 5.8 Å × 14 Å cell from c-direction and the distribution of the dimerized chains within the cell. Here, large V-ions *(magenta)* indicate dimerized V-ions where the topmost V-ion moves upwards and thus dimerizes with a vanadium ion

	a (Å)	*b* (Å)	*c* (Å)	*β* (°)
	13.9773(9)	5.8773(4)	13.9773(9)	89.481°†
atom	*x*	*y*	*z*	U_{iso} (Å^2)
K1	0	0.25014(6)	0	0.00435(14)
K2	0.5	0.5	0	0.0344(5)
K3	0.5	0	0	0.0347(5)
V1	0.24290(10)	0.26262(6)	0.09062(10)	0.00592(13)
V2	0.73881(9)	0.5	0.09262(9)	0.00560(15)
V3	0.74587(10)	0	0.08644(9)	0.00544(14)
V4	0.09103(10)	0.26386(6)	-0.24409(11)	0.00618(13)
V5	0.09519(9)	0.5	-0.73930(10)	0.00465(14)
V6	0.08842(10)	0	-0.74616(11)	0.00685(15)
O1	0.1774(6)	0	0.0196(7)	0.0067(10)
O2	0.6755(6)	0.25173(14)	0.0214(7)	0.0049(9)
O3	0.1751(6)	0.5	0.0156(7)	0.0060(9)
O4	0.3144(5)	0	0.1499(5)	0.0089(12)
O5	0.8142(4)	0.24852(14)	0.1507(4)	0.0034(9)
O6	0.3176(5)	0.5	0.1514(5)	0.0085(12)
O7	0.0247(5)	0	-0.1791(4)	0.0023(7)
O8	0.0179(5)	0.25143(15)	-0.6757(5)	0.0072(8)
O9	0.0225(5)	0.5	-0.1771(5)	0.0033(7)
O10	0.1501(6)	0	-0.3162(6)	0.0082(9)
O11	0.1461(5)	0.24978(13)	-0.8148(4)	0.0032(7)
O12	0.1507(5)	0.5	-0.3199(5)	0.0073(9)
# refl.	# av. refl.	R_{int}	*redund.*	$2\Theta_{max}$
31852	4861	2.54%	6.55	92.5°
R	R_w	GoF		
3.06%	5.14%	2.58		

Table 7.2: Results of single crystal X-ray diffraction measurements of $K_2V_8O_{16}$ at 100 K: lattice parameter, atomic positions, displacement parameter (isotropical), number of reflections/averaged reflections, internal R-value, redundancy, maximum value of 2Θ, R- and weighted R-value and GoF; †: the monoclinic angle β was taken from the synchrotron measurements.

in the next unit cell above (and not shown here). Very small V-ions indicate dimerized V-ions which move downward and dimerize with another V-ion in the same unit cell shown here. For a better understanding, see also Fig. 7.6 (b) which shows a view of the same unit cell rotated by 90° around the a_{mono}-axis. The medium sized V-ions in Fig. 7.6 (a) indicate V-ions within the zig-zag-chains. The blue VO_6 octahedra indicate the VO_6-octahedra containing V^{4+}-ions and the green ones the octahedra containing V^{3+}-ions. As mentioned above, Fig. 7.6 (b) shows a view of the same cell with the b_{mono}axis rotated by 90° towards c_{mono}. But here, the potassium ions have been omitted and dimerization- and zig-zag-chain distortions have been exaggerated a little in order to present a more clear picture.

Now the structure with monoclinic symmetry $C2/c$ will be discussed briefly. Besides

	sample A_3	*sample* A_4	*sample* C_1
temperature	100 K	90 K	100 K
V1-V1 distance	3.126(2) Å	3.094(1) Å	3.087(1) Å
V1-V1 distance	2.745(2) Å	2.769(1) Å	2.790(1) Å
V4-V4 distance	3.092(2) Å	3.107(1) Å	3.102(1) Å
V4-V4 distance	2.779(2) Å	2.756(1) Å	2.776(1) Å
V-V-V angle	173.8(1)°	173.8(1)°	174.9(1)°
V-V-V angle	174.2(1)°	173.8(1)°	174.7(1)°
#reflections	9072	35591	31852
av. reflections	2337	6885	4861
redundancy	3.9	5.2	6.6
R_{int}	2.53%	3.41%	2.54%
$2\Theta_{max}$	92.5°	110.8°	92.5°
R-value	4.06%	4.21%	3.06%
R_w-value	8.48%	6.75%	5.14%
GoF	2.15	1.88	2.58

Table 7.3: V-V distances and V-V-V bond angles indicating the dimerization and zig-zag-chain formation of three different samples measured at low temperatures. It should be noted that the R-values of the refinements of samples A_3 and A_4 can be further minimized if anisotropic displacement parameters for the potassium ions would have been introduced in order to describe shifts of the K-ions within their tubes which has been also observed for other hollandite materials [202], compare the discussion in the following sections.

the distinctly worse R-values, there is also a physical reason which renders this solution very unfavourable. In Fig. 7.9 two unit cells of this structure are shown. As can be seen, the V1 (*green*) and V2 ions (*yellow*) always appear within the same vanadium oxide double chain. The same is true for the V3 (*red*) and V4 ions (*magenta*). Hence, if there is dimerization in one chain, there is also dimerization in the neighbouring vanadium chain within the same VO_6-double chain. But as Pouget *et al.* and Paquet and Leroux-Hayon [216, 217, 196] already pointed out for the monoclinic M2 phase of VO_2, the zig-zag displacement is directly coupled to the pairing on the neighbouring chain. Therefore, it would be energetically unfavourable to replace any zig-zag chain by a second dimerized chain creating double chains with two dimerized chains and double chains with two non-dimerized chains. The only possibility might be that all four vanadium sites dimerize, but as can be seen in Fig. 7.2 (b) and Fig. 7.8 (b) the susceptibility χ decreases only to about one half of its value above T_C. Hence, only one half of all V-ions may dimerize. (That this drop of χ is really connected to a dimerization and not to antiferromagnetic order will be corroborated by neutron and ESR-measurements as presented in the following sections.)

This kind of charge ordering which was indicated by the measurement of sample C_1

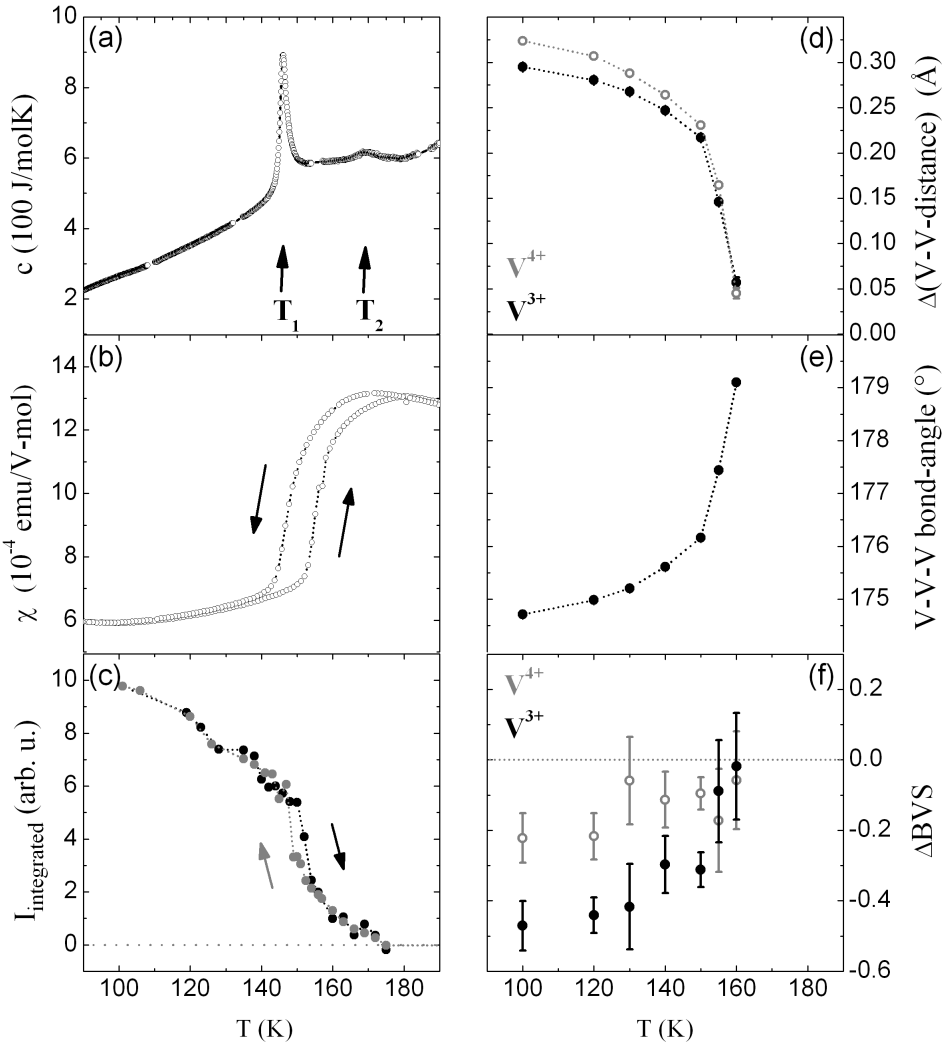

Figure 7.8: (a) Specific heat of sample A. (b) Magnetic susceptibility of sample C. (c-f) Results of single crystal X-ray diffraction measurements of sample C_1. (c) Intensity of the $(0.5\ 1.5\ 1.5)_{tet} = (2\ 1\ 3)_{mono}$ superstructure reflection normalized to the fundamental $(0\ 2\ 2)_{tet} = (2\ 2\ 4)_{mono}$ reflection. (d) Difference of the V-V bond-length indicating the dimerization; *black:* V1-V1 , *grey:* V4-V4. (e) V5-V6-V5 bond-angle, i.e. the angle of the zig-zag-chains. (f) Difference in the oxidation state of the dimerized V1 and V4 ions compared to the average valency of the V-ions within the zig-zag chains which are all very close to a V^{4+} valency. Due to the BVS formalism only the V1-ion exhibits a distinct deviation from a V^{4+} valency which indicates charge ordering: in the low-temperature structure V1 has the oxidation state 3+ whereas V2 to V6 have the oxidation state 4+.

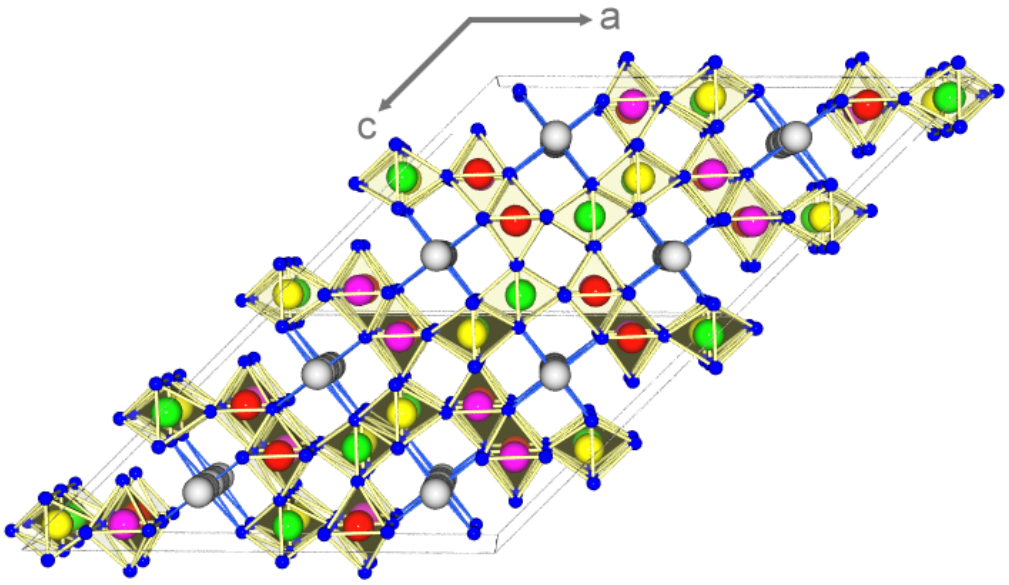

Figure 7.9: Two unit cells of the $C2/c$ structure; *blue*: O-ions, *white*: K-ions, *green/yellow/red/magenta*: V1-/V2-/V3-/V4-ions.

may explain the symmetry reduction from tetragonal to monoclinic below T_{MI} as the fourfold symmetry is broken. In Fig. 7.10 (a-b) the charge ordering pattern observed for sample C_1 is compared with another charge ordering pattern where the charges are more equally distributed. Indeed, a simple estimation of the electrostatic lattice energy $U = 1/2 \times \sum_{i \in Cell} Q_i \times \sum_{j \neq i} Q_j / \mid \overrightarrow{r_j} - \overrightarrow{r_i} \mid$ [218] for electrons located at the V^{3+}-sites (*green octahedra*) yields a slightly lower energy for the other ordering pattern which is shown in Fig. 7.10 (b) [5]. Thus, other charge ordering patterns with lower electrostatic energy are possible, compare Tab. 7.4. However, all these other charge ordering models would lead to a symmetry reduction from $I2/m$ to $\mathrm{P}2/m$ etc. For example the charge ordering model shown in Fig. 7.10 (b) would violate the I-centering. But no additional superstructure reflections indicating such a further symmetry reduction could be observed as can be seen for example in Fig. 7.5. Nevertheless, other charge ordering patterns with lower energy are possible and can not be excluded, if the symmetry is lower than $I2/m$ or if one introduces an additional doubling of the monoclinic b_{mono} axis (which has also not been observed experimentally). At least the charge ordering pattern found in this work is energetically lower than the uniform distribution of 0.25 electrons at all vanadium sites and as the charge ordering model proposed by M. Isobe *et al.* [210] which is even higher than that for the uniform electron distribution as was already pointed out in Ref. [221].

Returning to the single crystal X-ray diffraction measurements, also one superstruc-

[5] For a better convergence the charges at the border of summation have been count only half/quarter/$\frac{1}{8}$, if they are located at faces/edges/corners [219]. An improvement of this simple summation would be to calculate the Madelung energy using the Ewald summation as described for example in Ref. [220].)

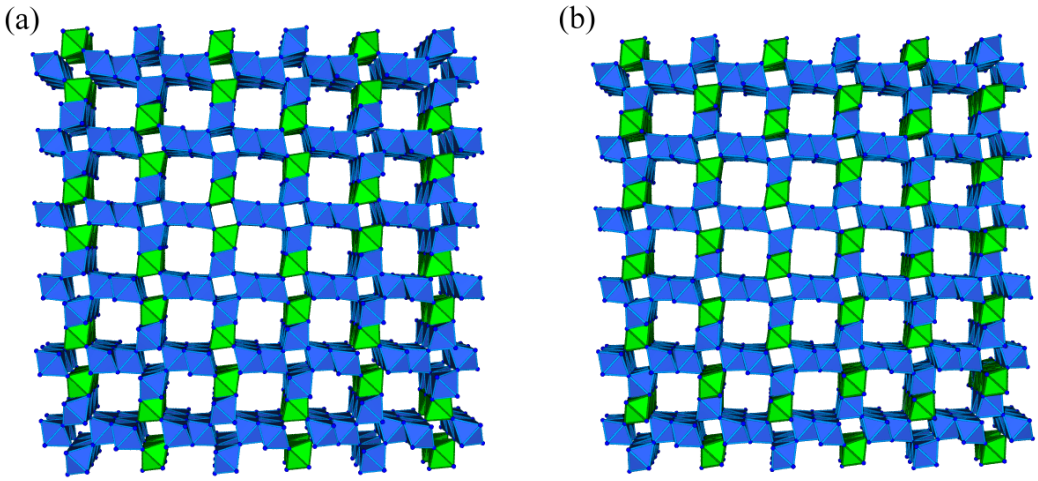

Figure 7.10: Charge ordering patterns for (a) the low temperature monoclinic structure and (b) another charge ordering model with V^{3+}-ions at dimerized chains and zig-zag-chains. *Blue/green* octahedra indicate V^{4+}-/V^{3+}-ions.

energy U (eV)	***# monoclinic unit cells***	***CO model***
252633.210542	51×51×51	average 0.25 elec.
252630.326116	51×51×51	this work
252621.569976	51×51×51	Fig. 7.10 (b)
252609.273865	51×51×51	Horiuchi [221]
252639.898987	51×51×51	Isobe [210]

Table 7.4: Simple calculation of the electrostatic lattice energy U [218] for different charge ordering models considering only electrons located at the V^{3+}-sites.

ture reflection has been traced with temperature, see Fig. 7.8 (c). If compared with the magnetic susceptibility data (χ) of the bulk sample C from which sample C_1 was derived, a hysteresis of the intensity of the superstructure reflection is observable in about the same temperature region where the hysteresis of χ of the bulk sample occurs. This indicates that the structural distortions leading to these superstructure reflections are directly related to the drop of the magnetic susceptibility and thus underlines the dimerization scenario. The larger hysteresis loop in the bulk sample may be caused by small oxygen or most likely potassium gradients (or other inhomogenities) within the bulk sample.

The specific heat measurement of another bulk sample of high crystal quality indicates two different transition temperatures T_1 and T_2. Our synchrotron diffraction measurements exhibit phase separation around 160 K which is between these two transition temperatures. Therefore, this feature may be connected with phase separation (or even sample inhomogenities) rather than two different phase transitions. Thus, also the single crystal X-ray diffraction results between T_1 and T_2 are questionable. It remains unclear wether the small values for dimerization-shifts are the real values of this dimerization or

only appear to be small due to phase separation effects. On the other hand these two transition temperatures measured within the specific heat correspond very well with the two-step phase transition measured in the electrical resisitivity which was reported by Isobe *et al.* [210], see Fig. 7.2 (a). Therefore, there may be also another explanation: Analyzing the structural data more in detail, one finds that the dimerized V^{4+} chains exhibit stronger dimerized V^{4+}-V^{4+} pairs than the V^{3+}-V^{3+} chains, see Fig. 7.8 (d). Thus, the V^{4+}-V^{4+} dimerization seems energetically more favoured and may set in at little higher temperatures than the V^{3+}-V^{3+} dimerization. This could be another explanation of the two-step phase transition, which was experimentally observed in the electrical resistivity [210], and phase separation is just an additional effect then.

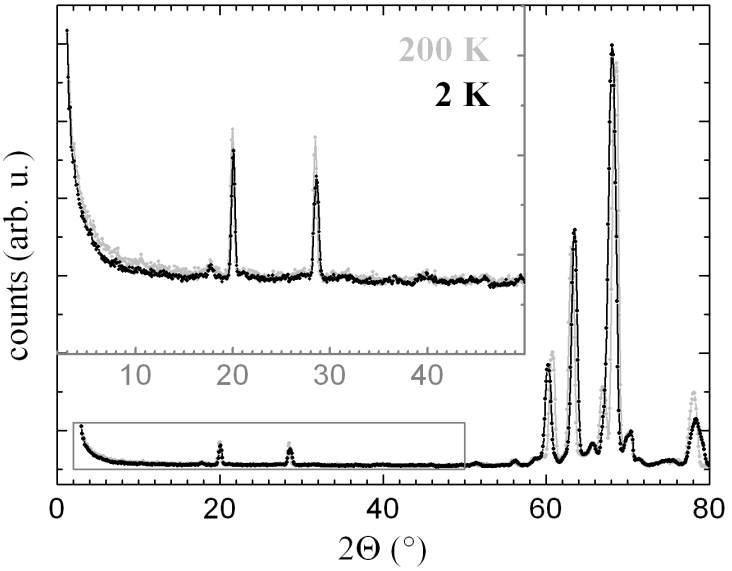

Figure 7.11: Powder neutron diffraction patterns measured at the DMC diffractometer (measured at 2 K and 200 K > T_{MI}).

In order to verify whether the drop in χ is related with magnetic order, magnetic reflections have been also searched for by powder neutron diffraction at the DMC diffractometer at PSI in Viligen, Swiss using a wavelength of 2.4503 Å in a temperature range from 2 K to 250 K (in 50 K steps). In the $K_2V_8O_{16}$-sample there is no sign of antiferromagnetic ordering below T_{MI}. Fig. 7.11 shows the diffractograms at 2 K and at 200 K with an cut-out of the interesting low-theta-angle region in the inset. This finding is fully contrary to the observations in the manganese hollandite compound $Ba_{1.2}Mn_8O_{16}$, where quite sizeable magnetic reflections have been observed by powder neutron diffraction recently [222]. (Nevertheless, a direct comparison of these measurements with $K_2V_8O_{16}$ seems difficult since no absolute values for neighbouring structural peak intensities etc. could be found in Ref. [222].) The absence of any magnetic reflections in the neutron diffraction measurements of $K_2V_8O_{16}$ underlines the observation of dimerization (which can explain the drop of χ) as there are no indications for antiferromagnetic ordering down to 2 K.

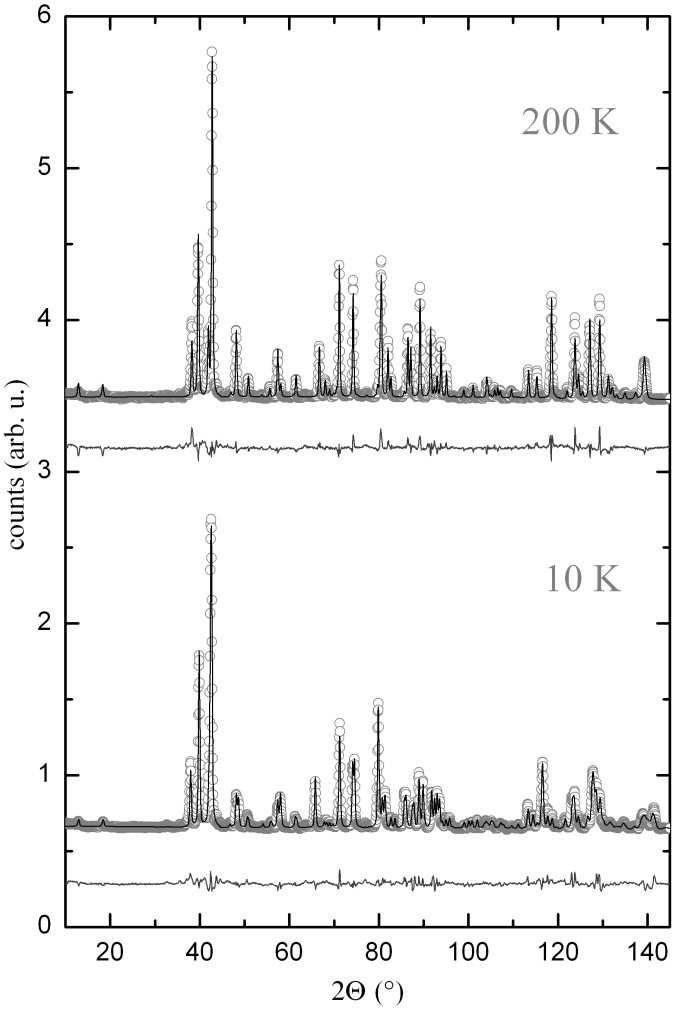

Figure 7.12: Powder neutron diffraction patterns measured at the D2B diffractometer measured at 10 K and 200 K. The 200 K data was fit with space group I4/m and the 10 K data was fit by using the atomic positions (fixed) of the single crystal X-ray diffraction measurements at 100 K (SG I2/m). *Gray:* data points, *black:* calculated values, *dark gray:* difference of observed and calculated values.

Powder neutron diffraction measurements have been also performed at the D2B diffractometer on the high quality sample C' using a neutron wavelength of 1.59439 Å. The low-temperature data at 10 K can be fitted with the low-temperature structure found by single crystal X-ray diffraction (measured at 100 K). As shown in Fig. 7.12 the single crystal X-ray data is able to describe the low-temperature structure of $K_2V_8O_{16}$ as well as a regular fit of the tetragonal high-temperature structure is able to describe the

200 K data. The R- and R_w-values of the measurement at 10 K amount to 4.71% and 6.22% which is of similar size as the R- and R_w-values of the measurement at 200 K, i. e. 5.02% and 6.92% respectively. (Also another $K_2V_8O_{16}$-sample B of slightly lower sample quality has been measured at 5 K, 100 K and 200 K at the D2B diffractometer which can be fitted with about the same quality in the same way.) Although one of the best high resolution powder diffractomters was used, this powder diffraction data turned out not to be sufficient to refine the large number of atomic parameters of all 21 atoms in the asymmetric unit of the low-temperature structure of $K_2V_8O_{16}$ reliably. Nevertheless, these measurements are important as the measured intensities can be perfectly described by the structure derived from the single crystal X-ray diffraction. Thus, larger errors by possible hidden twinning within the X-ray data can be excluded. Furthermore, these measurements on the high quality sample C' as well as on sample B neither show any additional magnetic peaks nor any magnetic intensities on top of the structural peaks down to 10 K and 5 K respectively. Thus, these measurements underline the results of the DMC measurement exhibiting also no indications for magnetic ordering at low temperatures.

Now, a brief discussion of the arrangement of the zig-zag chains and the dimerized chains within the crystal follows. First it should be noted, that the direction of the displacements of the V-ions within the zig-zag chains fully 'harmonizes' with the directions of the dimerization displacements within the neighbouring chains. If one regards one zig-zag chain, it has three neighbouring dimer chains. First of all, V^{4+} ions within a zig-zag chain are strongest influenced by the dimers within the same VO_6 octahedral double chain and move off the chain axis towards an apical oxygen away from the V-V-dimer within the same double chain. Second, the dimerized V-ions within the next V-chain which is directly connected over this apical oxygen exhibit dimerization displacements in a way that dimerized V-V-pairs are as far away from these former zig-zag V-ions as possible. This ordering scheme is identical to the one in the M2 phase of VO_2 [215]. Finally, the dimerized ions in the third and last neighbouring V-chain which is neither within the same double chain nor coupled via an apical oxygen of the zig-zag chain, shows the smallest dependency on the displacement directions of the zig-zag chain as the displacements also point more or less in a perpendicular direction. This third group is first of all influenced by the other two neighbouring zig-zag-chains of its own in the same way as mentioned above.

Further on, there is another parallel to the M2 phase of VO_2. If one regards the positions of the dimers (running along the b axis) in VO_2, they are all at same height y comparing dimers in c-direction. But different dimers appear at alternating heights y if one compares dimers in a direction. A similar situation can be observed in $K_2V_8O_{16}$. But instead of one direction one has to follow a circular path within a whole tube (of size of the 10 Å × 10 Å × 2.9 Å-cell). In every second of all such tubes surrounding the potassium ions one can observe dimers beeing at the same height y and in the other half of tubes the dimers are located at alternating heights y; see Fig. 7.6. This is the same situation as in VO_2 but instead of linear directions one has to follow circular rings. Regarding this, $K_2V_8O_{16}$ shows similar physics with regard to dimerization and zig-zag chain formation as VO_2 but with two linear dimensions transformed into circular rings

which may be an interesting situation for theoretical calculations.

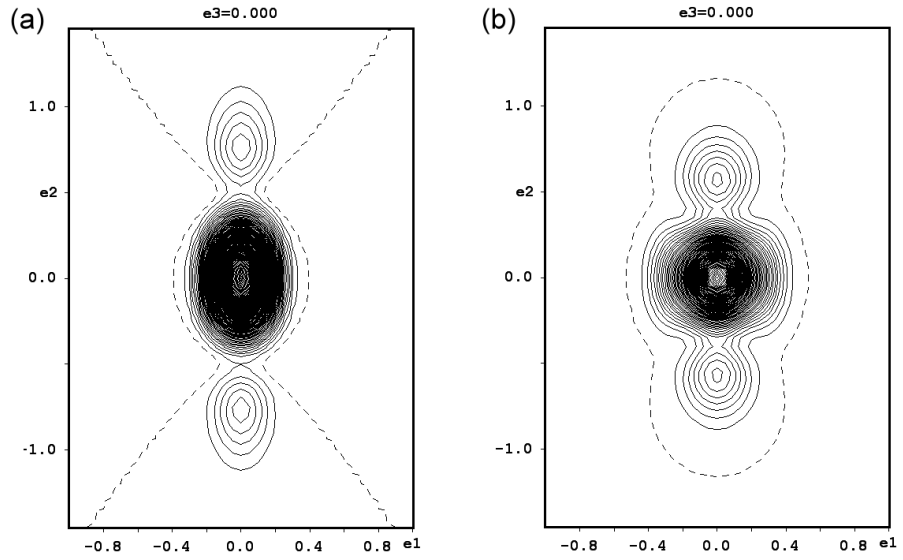

Figure 7.13: Joint probability density function (pdf) for the K1-ion with 0.25 atom/Å^3 contour intervals for the measurements of (a) sample C_1 at 100 K and (b) sample A_1 at 298 K. e1/e2: $(100)_{tet}$-/$(001)_{tet}$-directions and units in Å.

Next, another aspect of the intriguing structure of $K_2V_8O_{16}$ will be discussed. Similar as observed for the Ba-ions in $Ba_{1.2}Mn_8O_{16}$ [222], the K-ions in $K_2V_8O_{16}$ exhibit a kind of diffusion within the large tunnels built of four VO_6 double chains in which they are located as they have only other K-ions below and above them and thus the potential holding them in c_{tet}-direction is only created by the oxygen ions very far away from them. This results in large U_{33} displacement parameters and additionally remaining electron density directly of 1.4 e/Å^3 above and below the nominal K-sites. In order to describe these effects two different methods turned out to be applicable: either the adding of further K-ions above and below the K-ions shifted in c_{tet}-direction or a refinement of anisotropic thermal displacement parameters for the K-ions. In the first method the z_{tet}-, occupation and isotropic atomic displacement parameters (U_{iso}) of the additional K-ions were refined. It turned out, that a fraction of about 2% of all K-ions is located at these sites. Applying the second method, extremely large values for the anharmonic displacement parameters D3333 and F333333 were obtained in the refinement whereas all other anharmonic displacement parameters stayed reasonably small. The joint probability density function (jpdf) [223] for the K1 ion of such a refinement is shown in Fig. 7.13 for two different temperatures below and above the phase transition. (For the 100/298 K measurement anharmonic displacement parameters up to the order of 4/6 have been refined.) The jpdf are very similar to the jpdf reported for the potassium ions in $K_xMg_{(8+x)/3}Sb_{(16-x)/3}O_{16}$ [202]. This may suggest that this effect in $K_2V_8O_{16}$ originates in a small off-stoichiometric potassium occupation of the samples which leads to a small displacement of K-ions sitting next to a vacant K-site (of the order of 1%).

The fact that the jpdf for the K1-ions in $K_2V_8O_{16}$ look very similar at 100 K and 298 K corroborates that no potassium ordering is the origin of the superstructure reflections. Also, a potassium ordering could not describe the drop of the magnetic susceptibility at T_C.

Old samples [6] of bad sample quality which have lost their superstructure reflections even exhibit values of only 81% K-ions sitting at the regular sites and 10% K-ions directly above and below and the remaining percent even being located at positions further away in c_{tet}-direction.

inelastic neutron scattering measurements

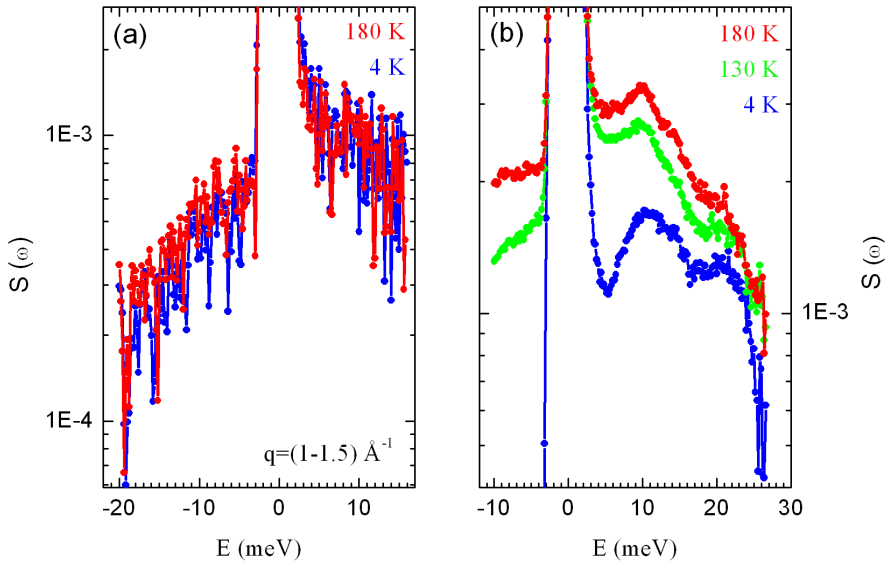

Figure 7.14: Neutron scattering intensity measured at the TOFTOF spectrometer: (a) S(ω) for momentum Q within a range of 1 Å^{-1} <Q< 1.5 Å^{-1}. (b) Total of S(ω).

Next, spin excitations have been searched for by means of inelastic powder neutron diffraction measurements at three time-of-flight spectrometer: FOCUS (PSI, Villigen, Switzerland), IN4 (ILL, Grenoble, France) and TOF-TOF (FRM-II, Garching, Germany). Due to the dimerization within the V^{3+}- and V^{4+}-chains one would expect a singlet-triplett excitation with an energy of the order of roughly $k_B \times T_{MI}$. In different measurements at the FOCUS spectrometer using various incident energies down to neutron wavelengths of $\lambda = 1.7$ Å, no signal could be detected below about 17 meV (sample B, measured at 2 K). Another measurement at the TOF-TOF spectrometer

[6] After leaving these samples one year at room-temperature in air.

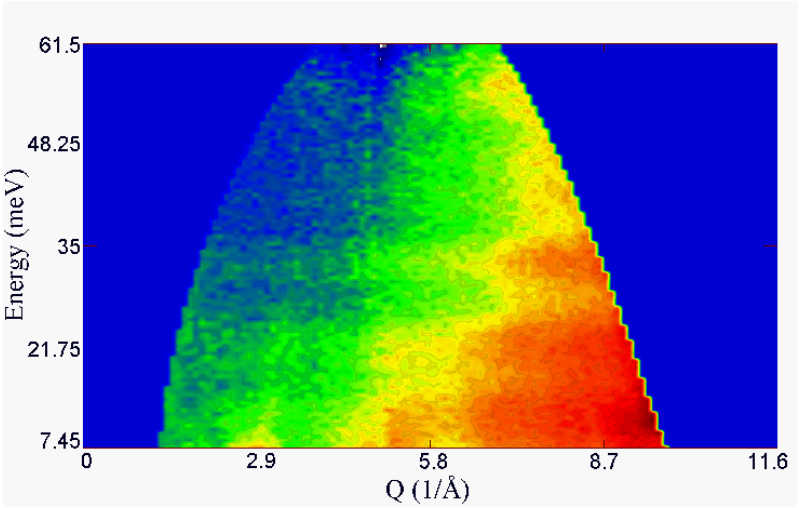

Figure 7.15: Neutron scattering intensity as a function of energy and wavevector transfer measured at 2 K at the IN4 spectrometer using a neutron wavelength of 1.08 Å.

with higher flux was performed (sample C'). The used neutron wavelength was 1.6 Å. The results of these measurements were shown in Fig. 7.14 (vanadium normalization and background subtraction already applied). Also these measurements do not exhibit any indications for a magnetic excitation. The rise of intensity with temperature seen in the overall scattering function S(ω) in Fig. 7.14 (b) is due to phonon contributions. These can be minimized for smaller values of momentum transfer Q which was done by binning the detector intensities for small values of Q as shown in Fig. 7.14 (a). There is no indication for any magnetic excitations up to 15 meV. Therefore, magnetic excitations have been searched for in the higher energy range at the IN4 spectrometer (using the high quality sample C'). Unfortunately, the low-angle detector bank was missing in the configuration of the IN4 spectrometer rendering the search for weaker magnetic excitations quite difficult (compare Eq. 3.2). Therefore, the high flux of this instrument did not compensate the problems occurring due to the strong incoherent scattering of vanadium and the rather large phonon contributions. In principle one could expect one very broad signal as the dimerized V^{3+}-chains and the dimerized V^{4+}-chains should have different excitation energies which probably leads to a merging of the magnetic signal in a broad peak. This makes the detection of the searched signal even more difficult. Fig. 7.15 shows the resulting signal of the IN4 measurement using a wavelength of 1.08 Å and with already applied vanadium normalization and background correction (with measured background data counted for the same time). At least, there are two energy regions in which there are first weak indications of a very broad magnetic signal which also has the right Q-dependency for a magnetic signal - these are around 28 and 57 meV. For a distinct decision further investigations are needed. It may be possible that the spin excitations are even higher in energy.

electron density measurements

Furthermore, precise electron density measurements at 298 K have been performed with an *Apex* single crystal diffractometer of *Bruker* [66] using Mo Kα radiation and a CCD area detector. In order to attain the high accuracy needed for this kind of measurements, large effort has been made to obtain a nearly perfectly shaped sphere of about 100(2) μm in diameter. In order to avoid background, the sample preparation procedures described in Chapter 4 have been applied. For an almost perfect background reduction a carbon fibre was used instead of a glas capillary. The collected reflections were checked for overlap with possible reflections from the carbon fibre by a self-written program. For a very good statistics of measured reflections, also of weaker reflections, the measuring time for all frames was enlarged to 60-90 seconds per image (0.5° rotation in ω-/ϕ-scans; κ-geometry) with 60 seconds for the low-angle and 75 and 90 seconds for the medium and high angle region. To cancel out small absorbtion effects due to tiny imperfections of the spherical shape of the sample a reasonably large redundancy of 14.92 has been attained. 18788 reflections have been collected in total with a completeness of 100% up to a value of 1.173 Å^{-1} for sinθ/λ and 98.9% for sinθ_{max}/λ = 1.242 Å^{-1} or, equivalently, $2\theta_{max} = 123.93°$. The internal R-value of this set of reflections amounts to 2.38.

The structure refinement has been performed with *Jana*2000 [58]. Isotropic extinction correction has been applied. In order to describe potassium vacancies which are common for other hollandite compounds the occupancy of K1 has also been refined. The final resulting goodness of fit, R-value and weighted R-value amount to 2.55, 1.34% and 2.73%. The structural parameters are listed in Tab. 7.5.

The residual electron density maps (compare Chap. 4) ±1Å around the V1-ion are shown in Fig. 7.16 (a-c). In the xz plane there are obviously additional densities with a kind of fourfold symmetry as could be expected for the occupation of the $d_{x^2-z^2}$ orbital in the tetragonal unit cell or a d_{xy} orbital in an coordinate system of the V1-ion and its six surrounding oxygen ions. For convenience, from now on, the local coordinate system of the V1 ion will be referred to. In this coordinate system the z-axis points in direction of the apical oxygens and the x- and y- axis are pointing in direction of the basal oxygens. Furthermore, in the residual electron density maps additional electron density can be observed which is located in direction of the apical oxygen O^+_{apic}, which is most far away from the V1-ion (green distance in Fig. 7.1). Such an electron density could indeed be expected for the V1 ion, as it is shifted towards the apical oxygen O^-_{apic}. Therefore, the V1-O^-_{apic} distance is the shortest V-O distance in this system (red distance in Fig. 7.1). This leads to a rise of the energy levels of all e_g and t_{2g} orbitals having an orientation in z-direction, i. e. the d_{xz}, d_{yz} and $d_{3r^2-z^2}$ orbitals. Thus, one would naturally expect the occupation of a d_{xy} orbital in this system. And as the V1-ion is shifted out of the basal oxygen plane towards the apical oxygen O^-_{apic} one could also expect some admixture of an orbital in direction of the apical oxygen O^+_{apic} which resembles on a 'sp-orbital'. This is exactly what the residual electron density maps reveal. The ionic radius of the V^{4+} ion amounts to 0.58 Å [82]. This is about the distance where the maximal electron density in the residual electron density maps could be observed. Therefore, the electron density

	a (Å)	*b* (Å)	*c* (Å)	
	9.9518(2)	9.9518(2)	2.9085(1)	
atom	*x*	*y*	*z*	U_{iso} (Å^2)
K1	0	0	0.5	0.02222(15)
V1	0.33083(1)	0.14859(1)	0.5	0.00750(2)
O1	0.19777(3)	0.15502(3)	0	0.00724(6)
O2	0.46145(3)	0.16506(3)	0	0.00796(6)
atom	U_{11} (Å^2)	U_{22} (Å^2)	U_{33} (Å^2)	
K1	0.02406(12)	0.02406(12)	0.0185(4)	
V1	0.00708(3)	0.00751(3)	0.00791(2)	
O1	0.00756(10)	0.00725(10)	0.00692(10)	
O2	0.00593(9)	0.01058(11)	0.00738(9)	
atom	U_{12} (Å^2)	U_{13} (Å^2)	U_{23} (Å^2)	
K1	0	0	0	
V1	0.00045(2)	0	0	
O1	0.00040(8)	0	0	
O2	-0.00040(8)	0	0	
# refl.	# av. refl.	R_{int}	*redund.*	$2\Theta_{max}$
18788	1259	2.38%	14.92	123.93°
R	R_w	GoF		
1.34%	2.73%	2.55		

Table 7.5: Results of a (precise) single crystal X-ray diffraction measurement of $K_2V_8O_{16}$ at room-temperature.

measurement points to the occupation of a d_{xy} orbital with some additional density in direction of the most far apical oxygen (O^+_{apic}). For a three-dimensional visualization of the residual electron density, the 0.2 e/Å^3-isosurface is shown in Fig. 7.16 (d) together with a 'wire model' of the orbital lobes on top.

The occupation of an orbital which has large d_{xy} character (in the local V1-coordinate system) may also have some relevance for the dimerization at low temperatures observed in this work by single crystal X-ray diffraction. If such orbitals are occupied, there are always lobes pointing in $\pm z_{tet}$direction at the vanadium sites. Thus, there may be even direct overlap of orbitals in chain-direction. Such a one-dimensional metallic chain may be instable versus static lattice deformations with wavevector $2 \times k_F$ [224], i. e. exhibit a Peierls instability.

However, the resulting residual electron densities of these measurements can be only regarded as a first indication for such an orbital occupation. For a more reliable analysis of the electron density of $K_2V_8O_{16}$ synchrotron measurements would give more accurate information since the noise in the background and absorbtion (extinction) effects are much lower and the intensity and, thus, the statistics is much higher in these measurements yielding a much higher precision and reliability of the results (see Chap. 7.2).

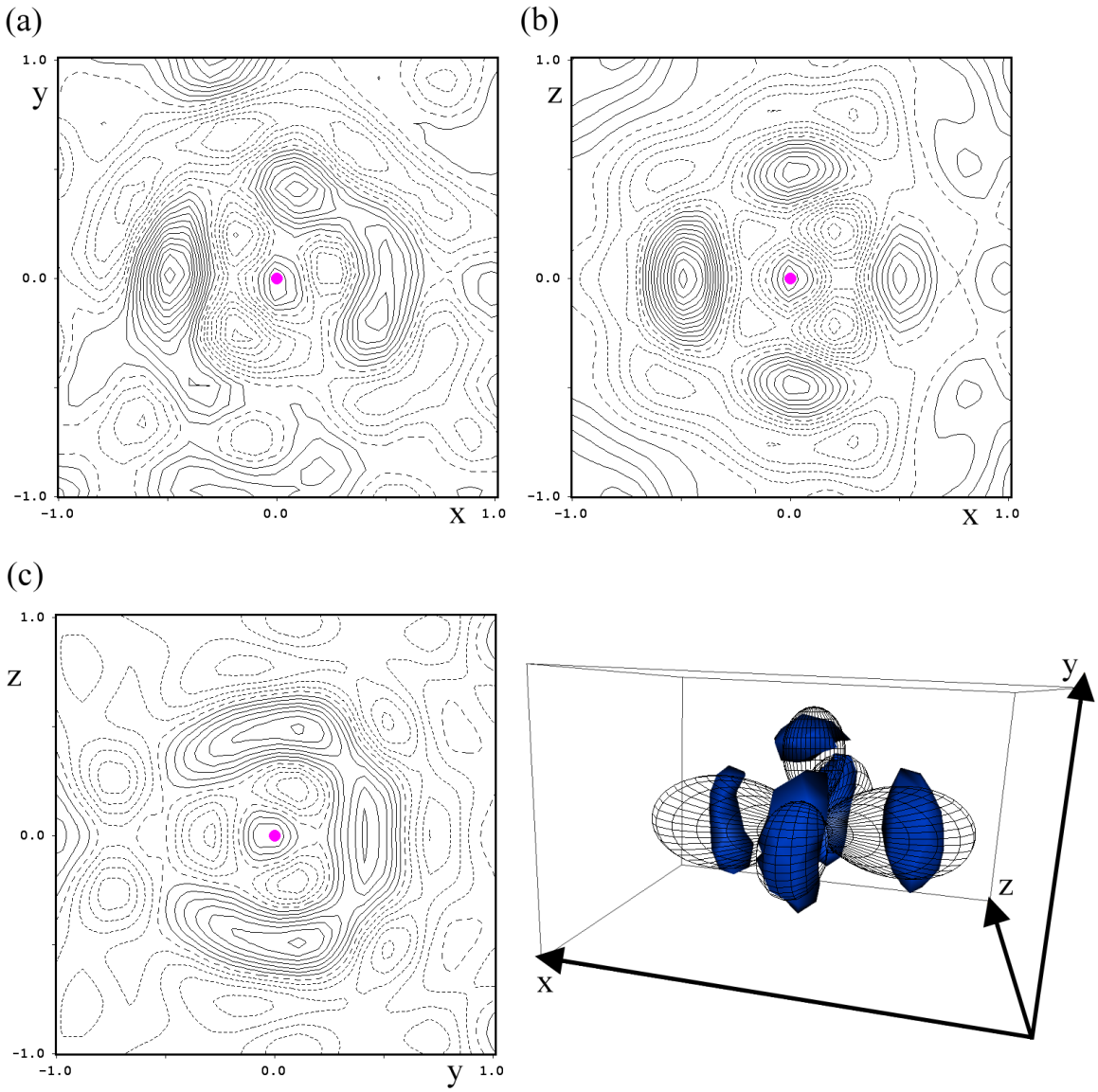

Figure 7.16: Residual electron density maps of $K_2V_8O_{16}$ at room temperature in the (a) xy-plane, (b) xz-plane and (c) yz-plane (tetragonal unit cell); units are in Å; *magenta:* position of the V1-ion. The contours are at 0.05 e/Å^3; negative lines are dashed; the extremal values are +0.655/-0.466 e/Å^3. (d) *blue:* the 0.2 e/Å^3 iso-surface around the V1-ion (tetragonal unit cell). Additionally, a model of a $d_{x^2-z^2}$ orbital with an additional lobe is shown.

ESR measurements

In Fig. 7.17 (b) the measured ESR signal as a function of magnetic field and temperature

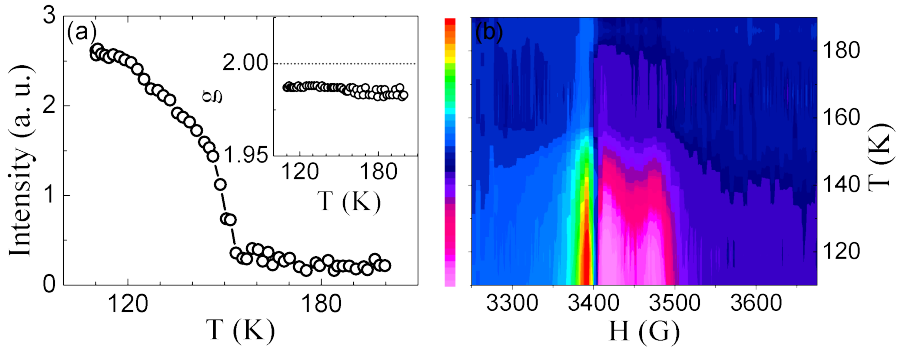

Figure 7.17: (a) Intensity of ESR peak as a function of temperature. The corresponding value of g is shown in the inset. (b) T-H plot of the measured ESR-signal.

is shown. The corresponding values of the intensity and the g factor fitted by J. Hemberger are shown in Fig. 7.17 (a). A T-H plot of the raw data of this measurement is shown in Fig. 7.17 (b). These measurements reveal a strong localization of t_{2g}-electrons of the V-ions below T_{MI} which would be accordance with a localization of one half of all V-ions in the zig-zag chains [7]. Furthermore, these ESR measurements support no antiferromagnetic phase transition since the g-factor should exhibit a strong kink at the magnetic ordering temperature with g extrapolating to extremely high values then [226]. Such a behaviour could not be seen in the g-T diagram of Fig. 7.17 (a). Thus, these ESR measurements indicate no antiferromagnetism in the $K_2V_8O_{16}$-system. Regarding the strong decay of the magnetic susceptibility at T_{MI}, this ESR measurement is an indirect evidence for dimerization in $K_2V_8O_{16}$ below T_{MI} and, hence, nicely supports the neutron measurements detecting no antiferromagnetic ordering at low temperatures.

7.1.4 Conclusion

In this work the low-temperature crystal structure of $K_2V_8O_{16}$ was measured by single crystal X-ray diffraction and solved for the first time. A dimerization of one half of all vanadium chains running in c-direction could be observed together with zig-zag-chain formation of the neighbouring vanadium chains. This resembles on the monoclinic M2-phase of VO_2. Furthermore, there is some evidence that charge ordering occurs in this

[7] This effect resembles on the rise of the ESR signal at the phase transition of the triclinic T-phase to the monoclinic M2-phase in $V_{0.99}Cr_{0.01}O_2$ [225]. In the T-phase all V-ions are paired resulting in the vanishing ESR signal. When coming into the M2-phase only half of all chains are dimerized and, thus, the localized and unpaired V^{4+}-ions in the zig-zag chains induce the rise of the ESR signal. This is very similar as in the case of $K_2V_8O_{16}$ with the difference that the vanishing ESR signal at high temperatures is caused due to the metallic conductivity of the tetragonal phase. Below T_{MI} the localized V^{4+}-ions in the zig-zag chains of the monoclinic low-temperature phase contribute to the growing ESR signal similar as in the M2-phase of VO_2.

system in a manner that one half of all dimerized chains contains V^{3+} ions and the other half V^{4+} ions. This additional charge ordering is indicated by the analysis of the V-O distances and explains the monoclinic symmetry of this system being in accordance with the highest possible symmetry ($I2/m$). Other charge ordering patterns could be imagined if an even lower symmetry or a doubling of the b_{mono}-lattice parameter was assumed, but there is no evidence for such lower symmetries.

Finding the dimerization by solving the low-temperature structure of $K_2V_8O_{16}$ now explains the drop of the magnetic susceptibility below T_{MI} and the metal-insulator transition. An additional charge ordering is not needed but fits into this overall picture [8]. Also the decrease of χ by about 50% below T_C nicely fits to the dimerization of one half of all vanadium chains. The observation of dimerization of the vanadium ions in this work is corroborated by powder neutron diffraction measurements exhibiting no signs of antiferromagnetic ordering down to 2 K. This is, furthermore, supported by ESR measurements.

Precise electron density measurements have been performed giving some evidence for an orbital occupation with large d_{xy} character. These orbitals would exhibit direct overlap in c_{tet}-direction indicating $K_2V_8O_{16}$ to be a quasi one-dimensional system. This is also supported by the close analysis of the high-temperature structure indicating a square pyramidal rather than an octahedral oxygen environment which isolates the vanadium ions in each double chain, thus, enhancing the 1D-character of each V-chain. This quasi one-dimensional metal may exhibit a Peierls instability below T_{MI} which explains the dimerization found in this work. Thus, in this work a new structure with a complex ordering scheme could be solved which may be interesting for further theoretical calculations as it is in some sense an analogue of VO_2 but with two linear dimensions transformed into 'circular rings'.

[8] It might be interesting to note, that the vanadium oxide β-SrV_6O_{15} with a similar structure of Sr-ions in tunnels of vanadium chains also exhibits a very similar charge ordering temperature of 170 K [227].

7.2 Electron density measurement of LiV_2O_5

7.2.1 Introduction

The vanadate family of oxides AV_2O_5 shows a variety of low-dimensional phenomena originating from their peculiar crystal structures [228]. The parent compound of AV_2O_5 is V_2O_5 which crystallizes in the orthorhombic *Pmmn* structure. In this structure the V^{5+}-ions are surrounded by oxygen square pyramids which can be described as an oxygen basal plane together with one apical oxygen of strongly distorted VO_6 octahedra in which the vanadium ion has moved out of the basal plane towards the apical oxygen; see Fig. 7.18 (a). The other apical oxygen has moved away and the free space in between enables the intercalation of (earth) alkaline A-cations like sodium or lithium. These VO_5 square pyramids form edge-sharing zig-zag chains which are connected via corner-shared oxygen ions. This arrangement of VO_5 square pyramids in the *ab*-plane describes ladders in *b*-direction with rungs in *a*-direction. Such a lattice is also known as the Trellis lattice [229-231]. The intercalated A-cations act as electron donators and α'-NaV_2O_5 and γ-LiV_2O_5 are the end compounds in the bronze system $A_xV_2O_5$. The structure of α'-NaV_2O_5 is shown in Fig. 7.18 (b). α'-NaV_2O_5 is one of the most studied vanadates as this system was believed to be the second inorganic spin-Peierls system with a much enhanced transition temperature of 34 K compared to the first discovered inorganic spin-Peierls system $CuGeO_3$ with a transition temperature of 14 K [232-235, 231]. The discovery of the spin-Peierls transition in $CuGeO_3$ has attracted large experimental and theoretical interest [232]. $CuGeO_3$ [236] is an almost ideal prototype of the S 1/2 frustrated chain, the antiferromagnetic Heisenberg $J_1 - J_2$ chain (J_1: nearest neighbour coupling, J_2: next nearest neighbour coupling). The spin-Peierls transition is an instability below a critical temperature T_{SP} arising from magnetoelastic effects and is characterized by the opening of a spin gap together with a lattice dimerization. It was first predicted for the non-frustrated S 1/2 chain [237]. But also the properties of the $J_1 - J_2$ chain suggest that it is also a natural instability for this chain, as the ground state of that model is spontaneously dimerized for $J_2/J_1 \geq 0.24$ [238]. Recently, TiOCl was assumed to be another spin-Peierls system which may even have a higher transition temperature of 67 K [239-242]; see Chap. 11.1.

In older structural studies NaV_2O_5 has been described with the non-centrosymmetric space group $P2_1mn$ in which V^{4+}/V^{5+}-charge ordering was postulated [243]. But more recent studies find an average valency of 4.5+ for the vanadium ions in NaV_2O_5 which crystallizes in a centrosymmetric orthorhombic structure with space group *Pmmn* [244, 245]. This structure describes two-leg spin ladders which are quarter filled (1 electron per rung). Band structure calculations indicate that the electrons are not localized at the vanadium sites but form V-O-V molecular orbitals between them [244]. Due to these new findings and due to other studies [246-248] NaV_2O_5 is not supposed to be a spin-Peierls system and the transition at 34 K is associated with charge ordering inducing a $2 \times 2 \times 4$ supercell [249] which was also confirmed in ^{51}V-NMR measurements [250]. Simultaneously with charge ordering and the respective lattice distortions a spin gap opens, indicating substantial spin-charge coupling in α'-NaV_2O_5 [250, 234, 251, 252].

X-ray diffraction measurements indicate a monoclinic symmetry of this charge ordered phase [253, 254] with space group $A112$ having the lattice parameter $a' = a$ - b, $b' = 2 \cdot b$, $c' = 4 \cdot b$ and $\gamma \approx 107.6°$. In this V^{4+}/V^{5+}-charge ordered structure the V^{5+}-ions form zig-zag chains along each ladder (one V^{4+}- and one V^{5+}-ion per rung). There are four possible arrangements of these zig-zag-chains within one layer (A, A', B, B') and two possibilities for a stacking of these layers which are in accordance with the quadrupled c-lattice parameter and with the space group A112 (ABA'B', AAA'A').

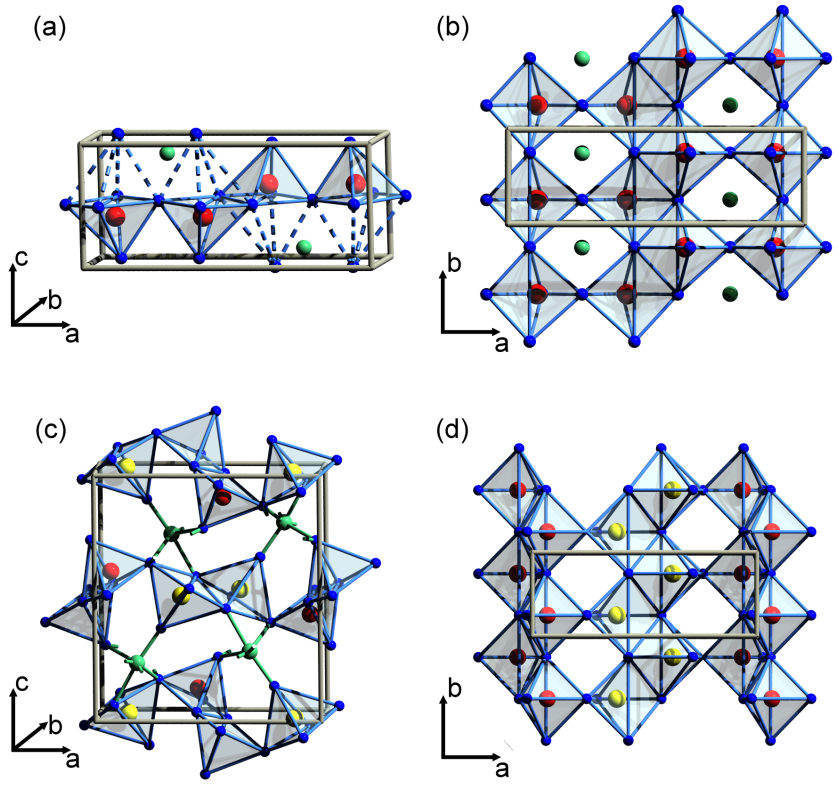

Figure 7.18: Structure of (a) AV_2O_5, (b) NaV_2O_5, (c) γ-LiV_2O_5 and (d) charge ordered V^{4+}- and V^{5+}- zig-zag chains in LiV_2O_5; *green*: A^+-cations, *blue*: O^{2-}-ions, *red*: V^{4+}-ions, *yellow*: V^{5+}-ions.

Whereas charge ordering was observed in α'-NaV_2O_5 only below 34 K, γ-LiV_2O_5 which has a much more corrugated crystal structure exhibits charge ordering already at room-temperature; see Fig. 7.18 (c). In the charge ordered unit cell with a c-lattice parameter being about twice as large as in NaV_2O_5, magnetic V^{4+}- zig-zag chains running in b-direction are separated by non-magnetic V^{5+}- zig-zag chains; see Fig. 7.18 (d). This charge ordering was confirmed by ^{51}V-NMR measurements [255]. Contrarily to α'-NaV_2O_5, γ-LiV_2O_5 has no singlet ground state and exhibits no magnetic ordering down to 0.5 K [233, 256]. The magnetical susceptibility of γ-LiV_2O_5 exhibits a broad maximum around 200 K [233, 257] which can be fitted with a one-dimensional (1D) linear antiferromagnetic Heisenberg chain model [258, 259]. Depending on the size of

the magnetic exchange interactions along the zig-zag chains (J_1) or along the legs of the ladders (J_2) this 1D spin system can be regarded either as a double-linear chain with independent linear chains ($J_1 \ll J_2$) or as a zig-zag chain ($J_1 \gg J_2$) or even something in between ($J_1 \approx J_2$). Inelastic neutron scattering measurements of Ref. [260] indicate that the magnetic chains in γ-LiV_2O_5 are independent S 1/2 AF double-linear chains with $J_1 \ll J_2$. This result is supported by infra-red and Raman measurements [261, 262].

Quasi-1D quantum antiferromagnets show interesting properties at low temperatures. Due to recent theoretical calculations, γ-LiV_2O_5 has been proposed to be a good candidate for a novel tetramerized phase [238] which should induce a further doubling of the zig-zag chain periodicity. With increasing ratio J_2/J_1, the weakly coupled J_2-chains may undergo a spin-Peierls transition of their own and for large enough frustration the tetramerized phase has been proposed [238]. The doubling of the zig-zag chain periodicity in this scenario should induce new superstructure peaks which could be detected by neutron or X-ray diffraction, and also two non-equivalent V^{4+}- sites, a feature that could be observed in NMR experiments [238].

Of cause, the observation of superconductivity in the vanadium bronzes β-$Na_{0.33}V_2O_5$, β-$Ag_{0.33}V_2O_5$ and β'-$Cu_{0.65}V_2O_5$ [190-192] is another highlight of the interesting low temperature physics of this class of compounds.

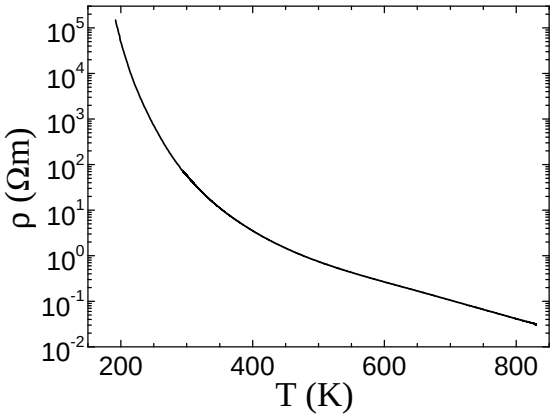

Figure 7.19: Electrical resistivity of LiV_2O_5.

7.2.2 Experimental

Single crystals of γ-LiV_2O_5 have been grown by M. Isobe. The electrical resistivity of γ-LiV_2O_5 was measured with an AC four point method. For the high temperature measurement a furnace was used and a vacuum of approximately 10^{-5} mbar was applied. Single crystal neutron diffraction measurements have been performed at the HEIDI

diffractometer at FRM-II in Garching and at the 4F.2 diffractometer at the reactor Orphée in Saclay, France. High precision synchrotron radiation single crystal X-ray diffraction measurements have been performed at beamline D3 at Hasylab/DESY in Hamburg ($\lambda = 0.45$ Å).

7.2.3 Results

electrical resistivity measurements
In Fig. 7.19 the electrical resistivity of γ-LiV_2O_5 is plotted as a function of temperature. The γ-LiV_2O_5-sample was measured in about 10^{-5} mbar vacuum in a temperature range of 192 K < T < 830 K. Below about 192 K the electrical resistivity gets too large for a reliable measurement due to a saturation of the voltmeter. No kink in the electrical resistivity could be observed up to 830 K. This indicates that the charge ordering appearing at room-temperature possibly also persists up to 800 K and above.

X-ray diffraction measurements
A single crystal X-ray diffraction measurement has been performed at room-temperature at the Bruker X8-Apex single crystal diffractometer using Mo-K_α radiation. This measurement has been performed with the accuracy of an electron density measurement (see next sections and Chap. 4). The CCD images have been collected starting with 25 s per image for the low-2Θ-angle region and 45 s per image for the high-2Θ-angle region. 77439 reflections have been collected up to $sin(\Theta)/\lambda = 1.221$ ($2\Theta_{max} = 120.8°$) with a redundancy of 25.54. The internal R-value amounts to 3.73. The structural refinement using the programm Jana2000 [58] yields a Goodness of Fit, R and R_w- value of 3.49, 2.08% and 4.29% respectively. The analysis of the refined structural parameters reveals

measurement:	**X-ray at 295 K**	**neutron at 2 K**	**synchrotron at 10 K**
V1-O1 (Å):	1.9467(6)	1.97(2)	1.9560(9)
V1-O3 (Å):	1.6104(8)	1.62(3)	1.6141(10)
V1-O4 (Å):	1.9744(7)	1.97(2)	1.9726(8)
V1-O4 (Å):	1.9435(2)	1.949(9)	1.9390(4)
V1-O4 (Å):	1.9435(2)	1.949(9)	1.9390(4)
V2-O1 (Å):	1.7411(6)	1.72(2)	1.7290(8)
V2-O2 (Å):	1.6172(8)	1.64(3)	1.6133(10)
V2-O5 (Å):	1.9738(7)	1.98(3)	1.9740(10)
V2-O5 (Å):	1.8917(2)	1.895(9)	1.8870(3)
V2-O5 (Å):	1.8917(2)	1.895(9)	1.8870(3)
BVS(V1):	4.14(1)	4.05(14)	4.13(1)
BVS(V2):	5.04(1)	4.98(15)	5.12(1)

Table 7.6: V-O distances and BVS of V1 and V2.

differences in the V-O distances which point to charge ordering; see Tab. 7.6. Due to the analysis of the bond-valence sums the nominal oxidation states of the V1 and V2 ions amount to 4.14(1) and 5.04(1) respectively. Thus the difference in the oxidation state of both V-ions amounts to 0.90(1) electrons confirming the charge ordering of γ-LiV_2O_5 at

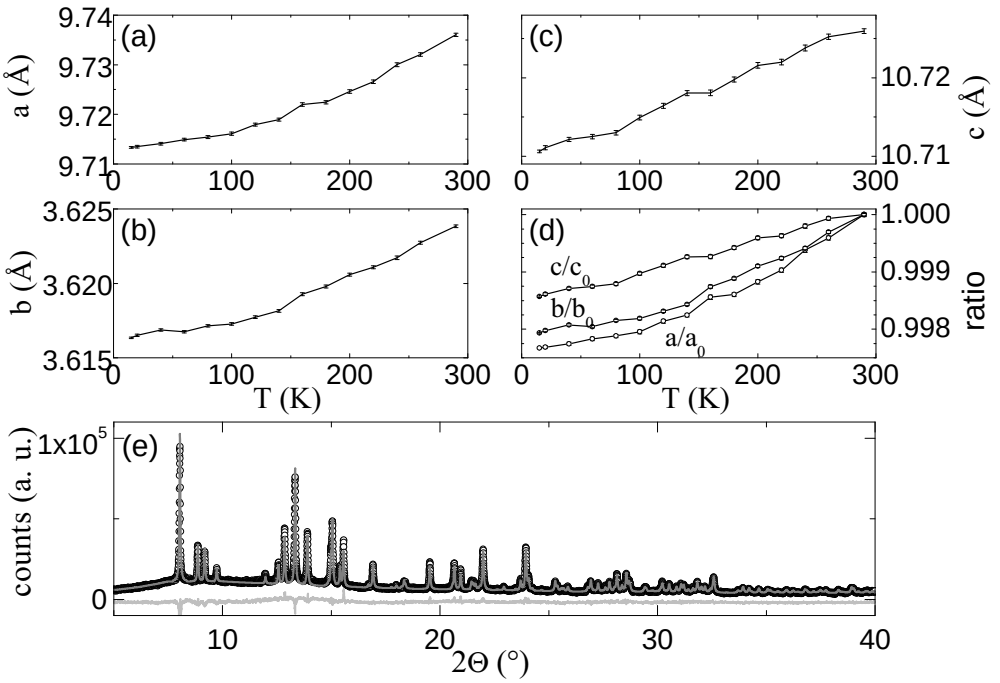

Figure 7.20: (a-c) Lattice parameter of γ-LiV_2O_5. (d) Ratio of lattice parameter versus value at 290 K. (e) Diffraction pattern at 15 K; *black*: measured data, *gray*: rietveld fit, *lt. gray*: difference $I_{obs} - I_{cal}$.

room-temperature described in the introduction. A similar result (with less accuracy) has been obtained in Ref. [263] for γ-LiV_2O_5 at room-temperature. In Ref. [264] the non-centrosymmetric space group $Pna2_1$ has been used with all atomic parameters fixed to $y = 0$ in order to simulate a centrosymmetric structure. However, this data has been refined with space group $Pnma$ later [263].

Synchrotron radiation powder X-ray diffraction measurements have been performed at beamline B2 at Hasylab/DESY using a X-ray wavelength of 0.75 Å. A diffraction pattern measured at 15 K is shown in Fig. 7.20 (e). The resulting lattice parameter are plotted in Fig. 7.20 (a-d) and exhibit a weak temperature dependency. There is no indication for any structural phase transition down to 15 K (no symmetry changes or superstructure reflections etc.).

single crystal neutron diffraction measurements

Single crystal neutron diffraction measurements have been performed at 2 K at the HEIDI diffractometer using a neutron wavelength of 0.875 Å. 1740 reflections have been collected up to $sin(\Theta)/\lambda = 0.776$ and a redundancy of 2.5. The R_{int}-value amounts to 8.8. The structure refinement using the program Jana2000 [58] yields a GoF, R and R_w value of 2.34, 4.05% and 6.47% respectively. As the V-scattering length is very small in the neutron case, the thermal displacement parameters of all vanadium ions have

been refined isotropically. The resulting V-O distances of the refinement are listed in Tab. 7.6. Both vanadium sites exhibit a different oxygen environment which indicates a difference of the valency of both V-ions due to the bond-valence sum formalism, see Eq. 6.1. The nominal valencies of both vanadium ions amount to 4.05(14) and 4.98(15). Thus, the persistance of charge ordering in γ-LiV_2O_5 down to very low temperatures has been ascertained.

An elastic neutron scattering experiment has been performed at the 4F.2 spectrometer in order to search for superstructure reflections down to very low temperatures which would indicate a tetramerized phase as described in the introduction. Therefore, a dozen LiV_2O_5-single crystals have been coaligned using a Laue camera. However, in these measurements there were no clear indications for superstructure reflections indicating a tetramerized phase nor any additional peaks of magnetic origin etc. As described in the next section, additional synchrotron measurements have been performed for the further search of such superstructure reflections.

electron density measurements

Careful synchrotron radiation single crystal X-ray diffraction measurements have been performed at 10 K at beamline D3 at Hasylab/DESY in order to search for superstructure reflections in γ-LiV_2O_5 and to measure the electron density of this compound. Therefore, a single crystalline sphere of 45(2) μm radius has been prepared with great effort from the needle-like single crystals and the accurate preparation procedure described in Chap. 4 has been applied (this is the same sample as used for the *Apex* single crystal X-ray diffraction measurement described in the previous sections). For the minimization of extinction and absorbtion effects an incident X-ray wavelength of 0.45 Å with the highest possible energy at a reasonable flux has been chosen. For the measurement of the reflections (ω-scans) an NaJ point detector has been used. Contrarily to neutron

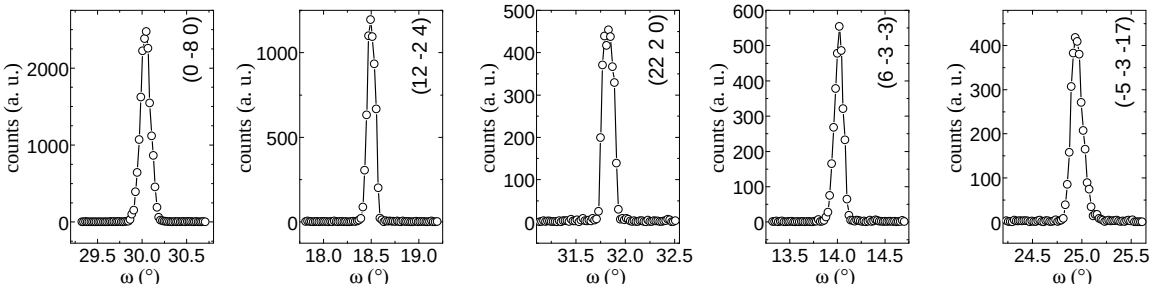

Figure 7.21: Typical ω-scans for HKL reflections of γ-LiV_2O_5.

measurements, synchrotron measurements have the advantage of a large contribution of the scattering of the vanadium ions and rather high intensities of the incident X-ray beam which is both important for the detection of weak superstructure reflections due to tiny shifts of the vanadium ions as expected for a tetramerized phase. Nevertheless, in these measurements there were no clear signs of superstructure reflections indicating a tetramerized phase as proposed in Ref. [238].

For the precise measurement of the electron density 4460 reflections with a redundancy of 1.794 have been collected with the NaJ point detector. The internal R-value amounts to 1.78%. Typical reflections measured performing ω-scans are shown in Fig. 7.21. These scans of randomly chosen reflections with medium-sized intensities demonstrate the high accuracy of this electron density measurement compared to the neutron measurement or the measurement at the *Apex* single crystal diffractometer using a CCD area detector. The background of all peaks is almost zero in this synchrotron measurement. A fit of the randomly chosen (0 -8 0) reflection yields an average background of 2.2(2) counts and a peak-amplitude of 2460(23) counts. This level of accuracy is fully in contrast to the neutron measurement suffering from large incoherent scattering contributions to the background and also to the measurement at the CCD *Apex* single crystal diffractometer suffering from the dark current noise of the CCD area detector and the absence of any diaphragms etc. In the *Apex* CCD measurement the equivalent (0 8 0) reflection has a fitted background of 47.0(1.4) counts at a fitted peak amplitude of 2699(42) counts. Thus, the peak to background ratio is nearly a factor 20 worse than in the synchrotron measurement although the elaborate sample preparation procedure for electron density measurements described in Chap. 4 has been applied as the sample in the CCD measurement is exactly the same sample as in the synchrotron measurement. In the neutron measurement, the situation is even worse as vanadium has a large incoherent scattering contribution. Just to get an impression, the (400) reflection has a fitted background of 238(4) counts at a fitted peak-amplitude of 924(19) counts. Due to the high energy of the synchrotron radiation X-ray beam (27.55 keV) and as the sample contains only the light elements Li, O, and V, the spherical absorption correction had only minor effects on the intensities of the collected reflections reaching from 0% to 0.1% for highest angles. The maximum value of $\sin\Theta/\lambda$ obtained in this measurement amounts to 1.274. For the structure refinement the program *Jana*2000 [58] has been used. The goodness of fit (GoF), the R and R_w-values amount to 1.84, 1.51% and 2.94%. These rather small values underline the accuracy of this measurement compared to the values obtained in the neutron or the *Apex* CCD measurement (see previous sections). The structural parameters are listed in Tab. 7.7 and the V-O distances in Tab. 7.6. The bond valence sum (BVS) for the vanadium ions calculated from the V-O distances amounts to 4.13(1) for the V^{4+}-ion and 5.12(1) for the V^{5+}-ion. Thus, the difference of the oxidation state of both vanadium ions amounts to 0.99(1) electrons which confirms the persistence of charge ordering down to 10 K. Note, that the BVS tends to overestimate the nominal valency but it yields reliable values for differences of valencies of two ions.

Fig. 7.22 (b) shows the difference Fourier map which is the Fourier transformation of the difference of the observed and the calculated structure factors and which indicates additional electron densities which have not been described by the spherical electron densities of the applied structure model. Usually, this feature is used for the detection of missing ions like hydrogen ions during a structural refinement. But in a precise electron density measurement it may also indicate orbitally ordered electrons which can not be described by the standard spherical model. This additional electron density shown is also the largest electron density within the whole unit cell and amounts to +0.48 e/Å^3 in the peak. These rather low values within the whole map underline the high precision

(a) (b)

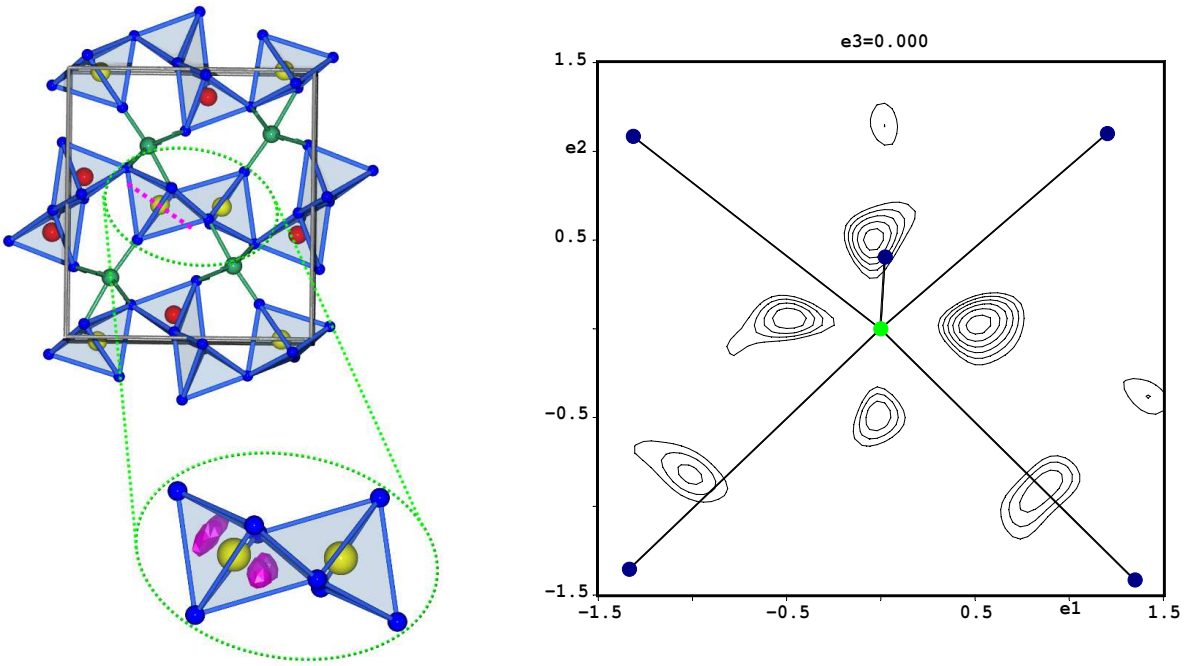

Figure 7.22: (a) A model of LiV_2O_5 where the plane of the difference Fourier map of figure (b) is shown (*magenta*). Additionally, the +0.25 e/Å^3 isosurface (*magenta*) of the 3D difference Fourier map within the model of a VO_5-square pyramid is painted below. (b) Difference Fourier map around the V^{4+}-ion in γ-LiV_2O_5; maximum (minimum) electron density in the region shown: +0.48 (-0.39) e/Å^3; maximum (minimum) electron density in the whole unit cell: +0.49 (-0.57) e/Å^3; only electron density $\geq$ 0.25 e/Å^3 is shown; *solid/dotted lines:* positive/negative 0.05 e/Å^3 countour lines *Green:* V-ion, *blue:* O-ions.

of this measurement as there is no significant deviation from the structure model over the whole cell. In Fig. 7.22 (a) the three-dimensional +0.25 e/Å^3 isosurface (*magenta*) of this electron density is also shown together with a model of the VO_6-square pyramid. The electron density in Fig. 7.22 (a) is located around the V^{4+}-ion and points between the surrounding four oxygen ions. This electron density indicates the occupation of a d_{xy} orbital within the basal plane of the VO_6-square pyramid; see Fig. 7.22 (a-b). In order to avoid the noisy background, electron densities smaller than 0.25 e/Å^3 have been omitted.

A multipole refinement as described in Chap. 4 has been tried describing all ions with the full multipole formalism as reported in Chap. 4. This multipole refinement starts with the structural parameter derived in the first refinement (see Tab. 7.7) and uses anharmonic displacement parameters up to the third order. But, due to the huge amount of parameters from the multipole formalism no stable and reliable solution could be obtained. Therefore, in a another refinement all ions have been described with the

SG:	**a (Å)**	**b (Å)**	**c (Å)**	α (°)	β (°)	γ (°)
Pnma	9.6558(23)	3.5949(6)	10.6445(24)	90	90	90
	x	**y**	**z**	**U_{iso} (Å^2)**		
Li1	0.1640(3)	0.25	0.2223(3)	0.0118(4)		
V1	0.37602(2)	0.25	0.49878(2)	0.002250(15)		
V2	0.065971(19)	0.25	0.59999(2)	0.002186(14)		
O1	0.24069(8)	0.25	0.63552(9)	0.00425(7)		
O2	0.48085(9)	0.25	0.76959(9)	0.00608(8)		
O3	0.27737(9)	0.25	0.37637(9)	0.00603(8)		
O4	0.57331(8)	0.25	0.45067(10)	0.00397(7)		
O5	0.44037(9)	0.25	0.04633(10)	0.00482(7)		
	U_{11} (Å^2)	**U_{22} (Å^2)**	**U_{33} (Å^2)**	**U_{12} (Å^2)**	**U_{13} (Å^2)**	**U_{23} (Å^2)**
Li1	0.0122(6)	0.0152(7)	0.0081(6)	0	-0.0028(5)	0
V1	0.00212(2)	0.00200(2)	0.00263(3)	0	-0.00004(2)	0
V2	0.00206(2)	0.00197(2)	0.00252(3)	0	-0.00012(2)	0
O1	0.00332(10)	0.00481(12)	0.00463(14)	0	-0.00011(10)	0
O2	0.00532(11)	0.00773(14)	0.00520(15)	0	-0.00155(11)	0
O3	0.00600(12)	0.00681(14)	0.00528(15)	0	-0.00156(11)	0
O4	0.00374(10)	0.00302(11)	0.00516(14)	0	0.00049(10)	0
O5	0.00556(11)	0.00291(11)	0.00600(15)	0	0.00187(11)	0
	C_{111}	**C_{113}**	**C_{122}**	**C_{133}**	**C_{223}**	**C_{333}**
Li1	-0.0001(3)	-0.00021(18)	-0.0014(17)	-0.00007(17)	-0.0018(14)	-0.0001(2)
V1	0.000023(9)	0.000039(6)	-0.00002(4)	0.000042(7)	-0.00001(5)	0.000062(12)
V2	-0.000025(9)	-0.000031(6)	-0.00005(4)	0.000020(7)	0.00001(5)	-0.000062(13)
O1	-0.00009(4)	-0.00002(3)	-0.0002(2)	-0.00005(3)	0.0000(2)	0.00003(5)
O2	-0.00001(5)	0.00002(3)	0.0006(2)	0.00000(4)	0.0002(3)	0.00018(6)
O3	0.00006(5)	0.00003(3)	0.0000(2)	0.00000(4)	0.0003(3)	0.00017(6)
O4	-0.00004(4)	0.00004(3)	-0.00035(19)	-0.00002(3)	0.0000(2)	0.00009(6)
O5	-0.00001(5)	0.00003(3)	0.0000(2)	0.00007(4)	0.0001(2)	0.00003(6)
R_{int}	**GoF**	**R**	**R_w**			
1.78%	1.50	1.50%	3.31%			

Table 7.7: Structural parameters of the synchrotron measurement (beamline D3) at 10 K.

standard spherical model using V^{5+}-form factors for the vanadium ions and setting an additional electron at the V^{4+}-site. This single electron at the V^{4+}-site has been described with the multipole formalism, using the ζ-values etc. for a vanadium 3d electron. As the electron density distribution of a 3d orbital can be described by the population of multipole terms with even values of l up to $l = 4$ in Eq. 4.6, only the $P_{2m\pm}$- and $P_{4m\pm}$- terms have been refined within this multipole refinement. In a first multipole refinement of this kind the charge density distribution of the additional electron at the V^{4+}-site was very similar to the one in Fig. 7.22 (b), hence, supporting the picture with an occupied d_{xy} orbital at the V^{4+}-site. This electron density remains qualitatively similar, if anharmonic displacement parameters up to the fifth order were refined for all ions additionally in a second multipole refinement of this kind. The fact, that the use of anharmonic displacement parameters up to the fifth order does not alter the electron density distribution of the additional electron at the V^{4+}-site substantially underlines the reliability of this multipole refinement and indicates that the additional electron

density is not caused by some anharmonic vibrational effect of the vanadium ions. With this knowledge and as the multipole parameters were not perfectly uncorrelated with the higher order anharmonic displacement parameters, the highest order of the anharmonic displacement parameters at the V^{4+}-site has been reduced to three again in order to avoid any correlations between the multipole and anharmonic displacement parameters within a third and last multipole refinement of this kind. This final multipole refinement yields a goodness of fit (GoF), R and R_w values of 1.80, 1.38% and 2.67% respectively. The static multipole deformation maps are plotted in Fig. 7.23 (a-c) for different xz-planes within the unit cell at three different values of y: 0.17, 0.25 and 0.33 respectively. The V^{4+}-ion (*green*) is located at $y = 0.25$ and the maps at $y = 0.17$ and 0.33 indicate the accumulation of electron density in the lobes of the d_{xy} orbital. In Fig. 7.23 (d) the summation of the whole electron density from $y = 0.00$ to 0.50 is plotted. As this large region covers the whole space around the V^{4+}-ion, the total electron density distribution of the additional d-electron at the V^{4+}-site is projected in this map. In Fig. 7.23 (e) the static multipole deformation map of a plane through the V^{4+}-ion and the d_{xy}-like electron distribution is plotted. This plane is similar to the magenta plane in Fig. 7.22 (a). This figure shows how the electron density points between the four oxygen ions (*blue*) as could be expected for a d_{xy} orbital. The fifth oxygen ion in the middle is located below this plane and below the V^{4+}-ion; see also Fig. 7.22 (a). Finally, in Fig. 7.23 (f) the charge density map of the valence density of the 3d-electron at the V^{4+}-site is shown within the same plane as in Fig. 7.23 (e). This map directly shows the electron density generated by the multipole formalism in real space, see Chap. 4, and is not effected by termination effects as the Fourier maps before. All these maps in Fig. 7.23 (a-f) show how the electron distribution of the additional electron at the V^{4+}-site has been modelled during the multipole refinement. Finally, an electron distribution qualitatively similar to that of a d_{xy} orbital has been obtained. This result has already been derived in the difference Fourier map of the standard refinement; see Fig. 7.22 (b). Thus, the difference Fourier map can already be regarded as a good indicator of non-spherical electron density distributions. However, the difference Fourier map suffers from more noise.

The occupation of the d_{xy} orbital is physically sound, as the apical V-O distance is distinctly shorter than the other four basal V-O distances: 1.611(1) Å versus 1.957(1) Å, 1.973(1) Å, 1.939(0) Å, 1.939(0) Å. Hence, the d_{xy} orbital is most likely energetically lower than d_{xz} or d_{yz} orbitals corroborating the results of the multipole refinement. This is also supported by electronic structure calculations of the ground state of LiV_2O_5 by H. Wu [265] using the structural parameters measured in the synchrotron measurement of this work.

7.2.4 Conclusion

Summarizing, in this work, single crystal X-ray and neutron diffraction measurements of γ-LiV_2O_5 reveal the persistence of charge ordering down to lowest temperatures (2 K). No structural phase transitions could be observed in synchrotron measurements studying the lattice parameter. Furthermore, neither neutron nor single crystal X-ray diffraction

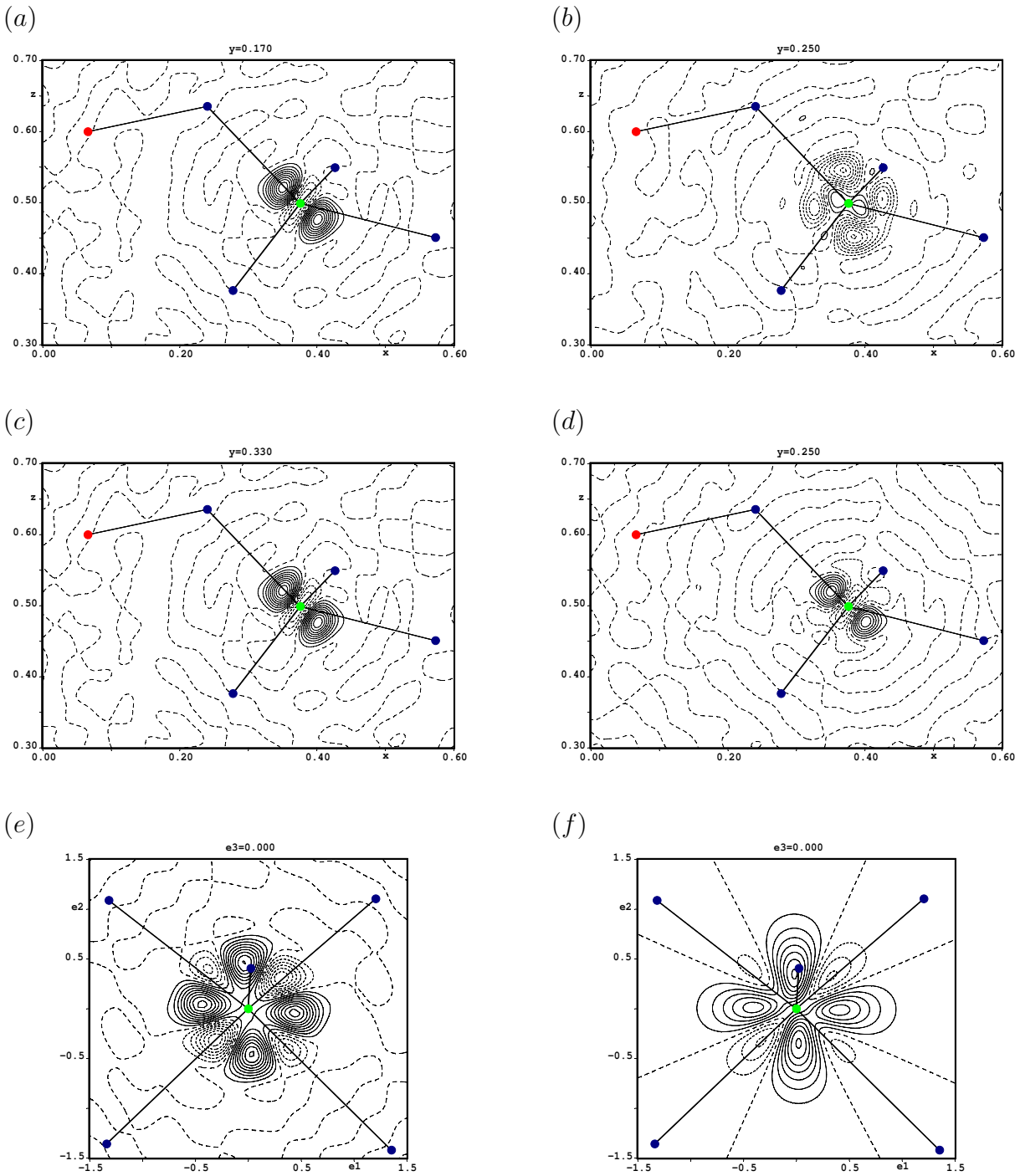

Figure 7.23: (a-e) Static multipole deformation maps, (f) charge density map (valence density). *Solid/dotted lines:* positive/negative 0.1 e/Å^3 contour lines. *Green:* V^{4+}-ion, *blue:* O^{2-}-ion, *red:* V^{5+}-ion.

measurements at the synchrotron give any evidence for a tetramerized phase at low temperatures as was proposed in Ref. [238]. Furthermore, electrical resistivity measurements up to 830 K indicate that the charge ordering is quite robust and persists up to such high temperatures.

Beyond the search for phase transitions, a careful electron density measurement has been performed at the synchrotron. The data has been refined with a standard structure refinement and, additionally, with a multipole refinement of the single d-electron at the V^{4+}-site. The difference Fourier map of the first as well as the static multipole deformation map of the multipole refinement both point to the occupation of the d_{xy} orbital of the V^{4+}-ion in the charge ordered structure at 10 K. Such a ground state could be expected for the V^{4+}-ion as the four V-O distances are much larger within the xy plane (of the local coordinate system) than the 'apical' V-O distance.

7.3 Structural and electron density studies on ZnV_2O_4

7.3.1 Introduction

Geometrical frustration is one of the central themes in contemporary condensed matter physics since it gives rise to interesting and exotic ground states [266]. The cubic spinells AM_2X_4 with magnetic M ions may form frustrated systems [267]. The ideal spinel structure can be described as a cubic close-packed array of anions X in which one eighth of the tetrahedral and one half of the octahedral interstices are occupied by cations A and M respectively [268, 269]. Some of the most prominent representatives of this class of compounds are magnetite $Fe^{3+}[Fe^{3+}Fe^{2+}]O_4$ with the inverse spinell structure (i. e. all tetrahedrally coordinated sites are occupied by Fe^{3+}-ions) exhibiting ferrimagnetism (A-array vs. M-array) below ∼850 K [270] and the well known Verwey transition at 120 K [271]. A further example is $LiTi_2O_4$ which exhibits superconductivity at ∼12 K [272, 273] or LiV_2O_4 which is a metallic transition-metal oxide exhibiting a heavy Fermi liquid behaviour at low temperatures ($C_P \sim \gamma \cdot T$, $\rho \sim \rho_0 + A \cdot T^2$, $\chi \sim$ const) with the d-electrons having the largest Sommerfeld constant among d-electron systems: $\gamma \sim 0.42$ J·mol^{-1}·K^{-2} and an effective mass about equal to that in UPt_3 [9] [274, 275]. With successive substitution of the monovalent Li^+-ion in LiV_2O_4 by the divalent Zn^{2+}-ion and after crossing a metal-insulator transition for Zn-doping levels of 65(5)% [276] one finally obtains the Mott-Hubbard insulator ZnV_2O_4 which was studied in this work. ZnV_2O_4 also crystallizes in the cubic spinel structure with space group $Fd\bar{3}m$, see Fig. 7.24 (a-c). The

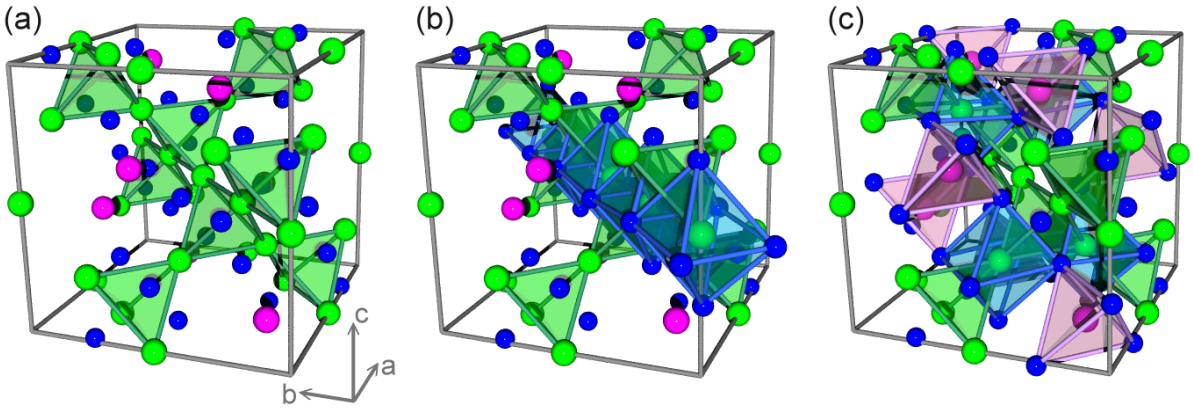

Figure 7.24: (a-c) Crystal structure of ZnV_2O_4; *green*: V-ions, *blue*: O-ions, *magenta*: Zn-ions. In figure (a) only the V-tetrahedra (*green*) are shown, whereas in figure (b) a chain of edge-sharing VO_6 octahedra (*blue*) is added. In figure (c) ZnO_4 tetrahedra (*magenta*) and some other VO_6 octahedra (*blue*) are shown additionally with the V-tetrahedra (*green*).

[9] $C_P = \gamma \cdot T + A \cdot T^3 \approx \gamma \cdot T = \frac{\pi^2}{2} \cdot N \cdot k_B \cdot T \cdot \frac{k_B}{\epsilon_F}$ with $\epsilon_F = \frac{\hbar^2 \cdot k_F^2}{2 \cdot m}$; thus the Sommerfeld parameter γ is inversely proportional to the Fermi energy ϵ_F and, hence, $\gamma \propto m$ [224] which gives rise to the values of m for LiV_2O_4 and UPt_3 in experiment.

vanadium ions form tetrahedra which run in chains along the [1 ±1 0]-, [±1 0 1]- and [0 1 ±1]-directions, compare Fig. 7.24 (a). This tetrahedral coordination of the vanadium ions gives rise to the frustration in this system. Furthermore, all vanadium ions are coordinated octahedrally by six oxygen ions forming edge-sharing VO_6 octahedral chains, compare Fig. 7.24 (b). In contrast, the Zn-ions are located in a tetrahedral oxygen environment and isolated from the other Zn-ions, compare Fig. 7.24 (c).

Whereas metallic LiV_2O_4 is not magnetically ordered at low temperatures and whereas a spin-glass state appears in the $Li_{1-x}Zn_xV_2O_4$-system for Zn-doping levels $0.1 \lesssim x \lesssim 0.9$, pure ZnV_2O_4 orders antiferromagnetically below $T_N \sim 40$ K [277]. Furthermore, the susceptibility of this insulating $3d^2$ system exhibits an additional distinct drop at $T_C \sim 50$ K which can be explained by a structural phase transition from a high temperature cubic phase ($a_{cub} = 8.39941(5)$ Å) to a low temperature tetragonal phase ($c_{tet}/\sqrt{2} < a_{tet} = b_{tet}$; $c_{tet} = 8.37532(1)$ Å, $a_{tet} = 5.94807(5)$ Å) [278, 277, 279]. Powder neutron diffraction measurements have been described with space group $I4_1/amd$. Neutron measurements studying the magnetic structure in the low temperature tetragonal phase at 4.2 K reveal an antiferromagnetic ordering with one-dimensional antiferromagnetic spin chains in [1 1 0] and [1 -1 0] direction which are staggered in c-direction [279, 280]. The ordered moment amounts to 0.61 μ_B/V [278-280].

The orbital order in ZnV_2O_4 and other vanadium spinels like CdV_2O_4 and MgV_2O_4 is highly debated as the competition between spin, orbital, and lattice degrees of freedom is rather complex in these systems [281-283]. Since the tetragonal c-axis is compressed one may assume that the first electron of the $3d^2$-system ZnV_2O_4 occupies the d_{xy} orbital whereas the other t_{2g} orbitals are degenerate giving rise to different possible orbital ordering patterns. If spin frustration is cancelled out by a magnetoelastic interaction a spontaneous symmetry breaking in the crystal lattice is calculated in Ref. [284]. In the $Tsunetsugu - Motome$ ('antiferroorbital' ordering) model [285], where the orbital degree of freedom due to the degeneracy of the t_{2g} orbitals which are not completely occupied is considered, the structural phase transition is supposed to induce orbital order with a spatially modulated interaction between the spins and, thus, reduced frustration in this system. In the ground state of this model the first electron occupies the d_{xy} orbital and d_{yz} and d_{xz} orbitals are alternatingly occupied along the c-direction. The competing $Tchernyshyov$ ('ferroorbital' ordering) model which is presented in Ref. [286] considers also the orbital moment of the V^{3+}-ion and regards the relativistic spin-orbit coupling as the driving force for orbital ordering. Treating the Jahn-Teller effect as an perturbation, finally a uniform ferroorbital order is obtained with a $d_{xz} \pm i \cdot d_{yz}$ occupied orbital state. Yet another model which might be applicable to the orbital ordering scheme in ZnV_2O_4 is reported in Ref. [287] and will be referred to as the $Khomskii - Mizokawa$ ('orbital- Peierls') model in which the d_{yz} and d_{zx} orbital are aligned as $yz - yz - xz - xz$ chains along the [1 0 1]- and [0 1 1]- direction (cubic notation) [288]. In this model the first electron occupies the d_{xy} orbital and the d_{yz} and d_{xz} orbitals are alternatingly occupied as is illustrated in Fig. 7.25 (c). Due to tiny structural changes induced by the particular orbital ordering pattern, these three basic models which are shown in Fig. 7.25 (a-c) are connected to three different crystal structures with space group $I4_1/a$ ($Tsunetsugu - Motome$), $I4_1/amd$ ($Tchernyshyov$)

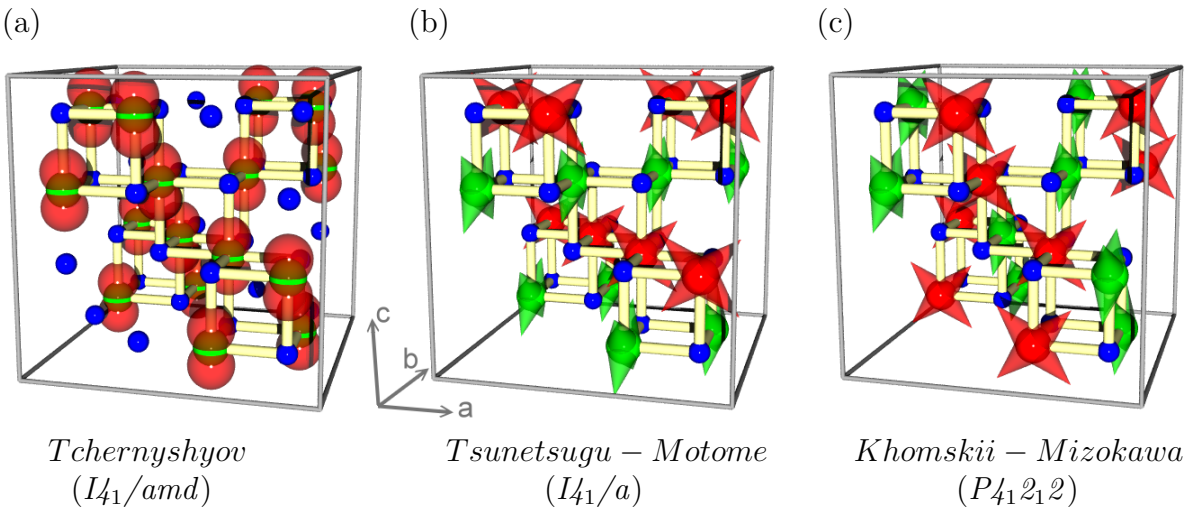

Figure 7.25: (a-c) The three major orbital ordering patterns proposed for the tetragonal phase of ZnV_2O_4 [289, 288]; *green/red spheres*: V-ions, *blue spheres*: O-ions. The occupied orbitals are indicated schematically by *transparent cones* or *spheres*. The d_{xy} orbitals occupied by the first d-electron of the V^{3+}-ions have been omitted.

and $P4_12_12$ ($Khomskii - Mizokawa$) respectively. Although in powder diffractions measurements [10] the low-temperature tetragonal structure is described using space group $I4_1/amd$ [279, 290], the low temperature structure can not be regarded as finally solved and, hence, the orbital ordering model applicable for ZnV_2O_4 remains an open issue.

Recent neutron scattering measurements observe a one-dimensional spin chain structure in the tetragonal phase and a three-dimensionally tangled spin chain structure in the cubic high temperature phase [278]. The data was interpreted in terms of an orbital ordering model equivalent to the $Tsunetsugu - Motome$ model [285]. A change from symmetric to asymmetric spin excitations appeared at the cubic $\rightarrow$ tetragonal phase transition indicating a change from three-dimensional to low-dimensional magnetic correlations [278]. An agreement between a one-dimensional chain model and the data below the structural phase transition supports the picture of ZnV_2O_4 being an one-dimensional antiferromagnetic spin chain system [278]. More recent calculations with an *ab initio* density functional theory approach find a uniform orbital ordering with magnetic moment close to the experimentally observed one [283] resembling on the complex orbitals of the $Tchernyshyov$ model [291]. Finally, very recent electronic structure calculations indicate that partial electronic delocalization induces a formation of V-V dimers along the [0 1 1] and [1 0 1] directions [292]. This model will be referred to as the $Pardo$ model.

[10] Powder diffraction measurements usually fail in detecting rather weak superstructure peaks.

7.3.2 Experimental

Single crystals of ZnV_2O_4 have been grown by M. Isobe. Precise synchrotron radiation single crystal X-ray diffraction measurements have been performed at beamline D3 at Hasylab/DESY in Hamburg using an incident wavelength of 0.5 Å.

7.3.3 Results

Very precise synchrotron radiation single crystal X-ray diffraction measurements have been performed at 70 K and 10 K at beamline D3 at Hasylab/DESY in order to measure the electron density of ZnV_2O_4 and in order to distinguish between the orbital ordering models (10 K measurement). A tiny single crystal of octahedral shape and about 30 μm in diameter (apex distance: 22 μm, (111)-face distance: 15 μm) has been chosen in order to minimize absorbtion effects which is also achieved due to the rather high incident X-ray energy of the synchrotron radiation. This tiny sample was mounted cautiously with a minimum of glue on a small carbon fibre in order to minimize background and absorbtion from the sample holder/stick. The reflections have been measured using a NaJ point detector. In order to exclude wrong intensities due to the Renninger effect, all reflections have been collected at two different values of Ψ differing by 0.5°. Due to the extremely high resolution at the synchrotron this value is fully sufficient in order to detect reflections contaminated by the Renninger effect.

Unfortunately the cubic to tetragonal phase transition is accompanied by twinning with three possible twin domains. And this twinning renders the results rather unreliable since the twinning causes an uncontrollable overlap with reflections from other twin domains. In order to minimize these effects, also a larger wavelength of 0.7 Å has been tried in an additional measurement at 10 K for a higher resolution. Furthermore, the detector diaphragms of the χ-circle have been closed further in order to avoid overlap with any peaks from other twin domains. However, also these efforts were not successful and twin contributions could be observed in the peak shapes of several reflections. Thus, a reliable structure model could not be obtained from both measurements at 10 K. Recently a study of MnV_2O_4 succeeded in determining the low temperature structure of this compound by using magnetic fields in order to suppress the formation of the other two unwanted twin domains, thus establishing a single-domain structure in the tetragonal phase under a magnetic field [288]. However this method will only work for ferrimagnetic MnV_2O_4.

In contrast, the ZnV_2O_4 synchrotron measurement at 70 K did not suffer from such twinning effects since the temperature is comfortably above the structural phase transition but, nonetheless, low enough to minimize thermal vibrations (displacement parameter) in order to optimize the conditions for detecting the electron density. In this measurement 1919 reflections have been collected with a redundancy of 9.05 and an internal R-value of 2.68% up to the maximum value of $\sin(\Theta_{max})/\lambda = 1.145$. Some randomly chosen typical reflections (with non-zero intensity) are shown in Fig. 7.26. As can be seen, the background is almost zero for these reflections. For example the (6 6 6) reflection has an average background of 1.47(23) counts (averaged over 42 ω-steps) and

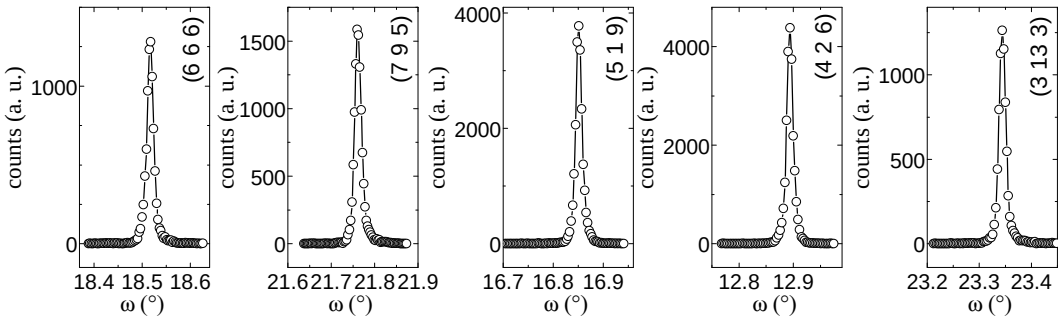

Figure 7.26: Typical ω-scans of reflections of ZnV_2O_4 measured at 70 K.

a maximum peak intensity of 1281 counts, i. e. a ratio of peak to background of about 873; in contrast, a peak with a similar intensity in the measurement of γ-LiV_2O_5 at the *ApexX*8 single crystal diffractometer with all optimizations for electron density measurements (see Chap. 4) has an average background of 37.76(70) counts and a maximum (-1 -8 9) peak intensity of 1354 counts and, hence, a ratio of peak to background of about 36 only. Thus, the peak to background ratio is nearly a factor 24 worse than in the synchrotron measurement. This example gives a rough impression of the high accuracy of these synchrotron measurements compared to a laboratory 'state-of-the-art' study. The high incident X-ray energies at the synchrotron minimize absorbtion and extinction effects and, thus, further increase the accuracy of these measurements.

For the structure refinement of the 70 K data with space group $Fd\bar{3}m$ the program *Jana*2000 [58] has been used. For all ions anharmonic displacement parameters have been refined up to the order of 5. The goodness of fit (GoF), the R and R_w-values amount to 1.73, 1.48% and 3.95%. and the resulting structural parameters are listed in Tab. 7.8. The positional parameters of the oxygen ion $x(O) > 0.25$ indicate a trigonal distortion of the VO_6 octahedra which are elongated parallel to the roto-inversion axis. This drawn schematically in Fig. 7.27 (a-b). This trigonal distortion of the VO_6 octahedra indicates that something with the three theoretical models (*Tchernyshyov*, $Tsunetsugu - Motome$ and $Khomskii - Mizokawa$ model) might be wrong and that a description with trigonal orbitals like a_{2g} orbitals might be more appropriate for this system. Within this refinement the anharmonicity of the atomic displacements was modeled using the Gram-Charlier expansion of the probability density function for atomic displacements up to tensors of the fifth rank. The probability density function (PDF) of the V1-ion within a plane spanned by the vectors $\overrightarrow{e}_1$ = (1 1 1) and $\overrightarrow{e}_2$ = (1 -1 0) is shown in Fig. 7.28. These figures visualize the effect of the largest significant anharmonic components $D_{\mu\mu\nu\nu} = 0.000076(14)$ and D_{1123}, D_{1223} and $D_{1233} = 0.000014(4)$ which describe an anharmonicity along the roto-inversion axis. Without the use of anharmonic parameters in the refinement the R-, R_w-values and GoF increase to 2.03%, 5.33% and

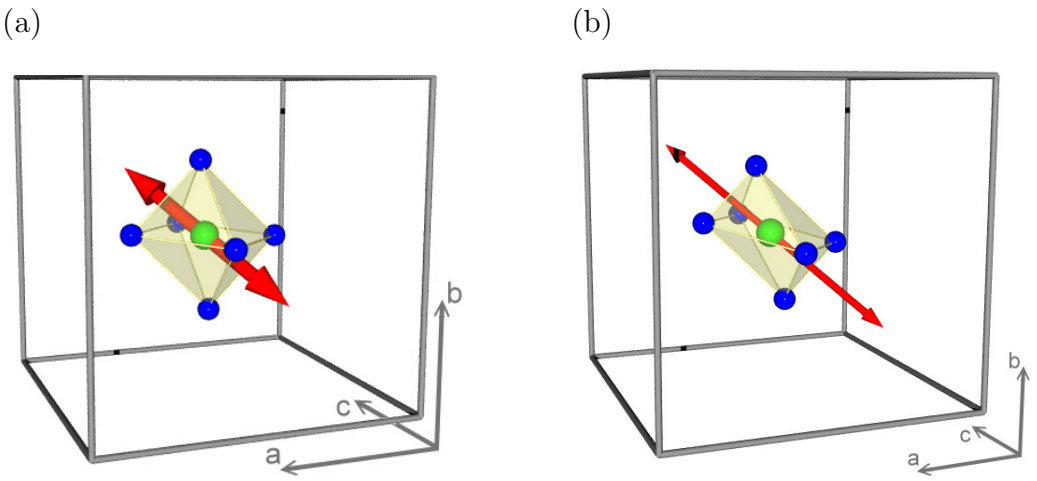

Figure 7.27: Schematic model of the trigonally distorted VO_6 octahedron; *green sphere*: V^{3+}-ion, *blue spheres*: O^{2-}-ions; *red arrows*: $\pm(1\ 1\ 1)$-direction (3-fold roto-inversion axis). Figure (a) is based on measured values and figure (b) is an exaggerated schematic model.

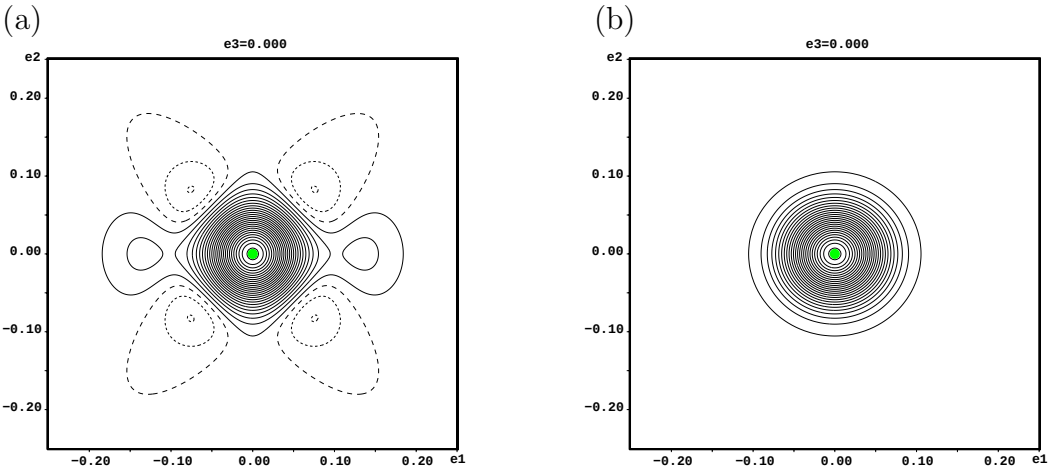

Figure 7.28: PDF of the vanadium ion. The distance of the contour lines amounts to $50/Å^3$; *green dot*: position of the V1-ion; *solid/dashed lines*: positive/negative values. (a) plane spanned by vectors e_1 = (1 1 1) and e_2 = (1 -1 0) and (b) a plane spanned by e_1 = (1 -1 0) and e_2 = (1 1 -2); (units of e_ν: Å).

2.21. Furthermore, the effects in the difference Fourier map which will be described in the following stay qualitatively the same but are even much more pronounced (extremal values: -1.50 e/Å^3 and +1.41 e/Å^3 in a refinement without anharmonic parameters compared to 0.54 e/Å^3 and -0.75 e/Å^3 in a refinement with anharmonic parameters to the fifth order).

Fig. 7.29 (a) shows the difference Fourier map for the refinement with anharmonic

SG:	**a (Å)**	**b (Å)**	**c (Å)**	α (°)	β (°)	γ (°)
$Fd\bar{3}m$	8.3652(288)	8.3652(288)	8.3652(288)	90	90	90
	x	**y**	**z**	$\mathbf{U}_{iso}$ **(Å^2)**		
Zn1	1/8	1/8	1/8	0.0025(2)		
V1	1/2	1/2	1/2	0.0032(2)		
O1	0.2607(2)	0.2607(2)	0.2607(2)	0.0046(2)		
	$\mathbf{U}_{11}$ **(Å^2)**	$\mathbf{U}_{22}$ **(Å^2)**	$\mathbf{U}_{33}$ **(Å^2)**	$\mathbf{U}_{12}$ **(Å^2)**	$\mathbf{U}_{13}$ **(Å^2)**	$\mathbf{U}_{23}$ **(Å^2)**
Zn1	0.0025(3)	0.0025(3)	0.0025(3)	0	0	0
V1	0.0032(3)	0.0032(3)	0.0032(3)	0.00000(9)	0.00000(9)	0.00000(9)
O1	0.0046(4)	0.0046(4)	0.0046(4)	-0.0004(3)	-0.0004(3)	-0.0004(3)
	$\mathbf{C}_{111}$	$\mathbf{C}_{112}$	$\mathbf{C}_{113}$	$\mathbf{C}_{122}$	$\mathbf{C}_{123}$	
Zn1	0	0	0	0	-0.00005(7)	
V1	0	0	0	0	0	
O1	0.0008(4)	0.00010(16)	0.00010(16)	0.00010(16)	-0.0002(2)	
	$\mathbf{C}_{133}$	$\mathbf{C}_{222}$	$\mathbf{C}_{223}$	$\mathbf{C}_{233}$	$\mathbf{C}_{333}$	
Zn1	0	0	0	0	0	
V1	0	0	0	0	0	
O1	0.00010(16)	0.0008(4)	0.00010(16)	0.00010(16)	0.0008(4)	
	$\mathbf{D}_{1111}$	$\mathbf{D}_{1112}$	$\mathbf{D}_{1113}$	$\mathbf{D}_{1122}$	$\mathbf{D}_{1123}$	
Zn1	-0.00006(3)	0	0	0.000025(12)	0	
V1	-0.00001(4)	-0.000001(7)	-0.000001(7)	0.000076(14)	0.000014(4)	
O1	0.00003(6)	-0.00001(3)	-0.00001(3)	0.00008(3)	-0.000008(17)	
	$\mathbf{D}_{1133}$	$\mathbf{D}_{1222}$	$\mathbf{D}_{1223}$	$\mathbf{D}_{1233}$	$\mathbf{D}_{1333}$	
Zn1	0.000025(12)	0	0	0	0	
V1	0.000076(14)	-0.000001(7)	0.000014(4)	0.000014(4)	-0.000001(7)	
O1	0.00008(3)	-0.00001(3)	-0.000008(17)	-0.000008(17)	-0.00001(3)	
	$\mathbf{D}_{2222}$	$\mathbf{D}_{2223}$	$\mathbf{D}_{2233}$	$\mathbf{D}_{2333}$	$\mathbf{D}_{3333}$	
Zn1	-0.00006(3)	0	0.000025(12)	0	-0.00006(3)	
V1	-0.00001(4)	-0.000001(7)	0.000076(14)	-0.000001(7)	-0.00001(4)	
O1	0.00003(6)	-0.00001(3)	0.00008(3)	-0.00001(3)	0.00003(6)	
	$\mathbf{E}_{11111}$	$\mathbf{E}_{11112}$	$\mathbf{E}_{11113}$	$\mathbf{E}_{11122}$	$\mathbf{E}_{11123}$	$\mathbf{E}_{11133}$
Zn1	0	0	0	0	-0.000004(4)	0
V1	0	0	0	0	0	0
O1	0.00011(6)	-0.000005(15)	-0.000005(15)	0.000014(11)	-0.000006(12)	0.000014(11)
	$\mathbf{E}_{11222}$	$\mathbf{E}_{11223}$	$\mathbf{E}_{11233}$	$\mathbf{E}_{11333}$	$\mathbf{E}_{12222}$	$\mathbf{E}_{12223}$
Zn1	0	0	0	0	0	-0.000004(4)
V1	0	0	0	0	0	0
O1	0.000014(11)	0.000006(8)	0.000006(8)	0.000014(11)	-0.000005(15)	-0.000006(12)
	$\mathbf{E}_{12233}$	$\mathbf{E}_{12333}$	$\mathbf{E}_{13333}$	$\mathbf{E}_{22222}$	$\mathbf{E}_{22223}$	$\mathbf{E}_{22233}$
Zn1	0	-0.000004(4)	0	0	0	0
V1	0	0	0	0	0	0
O1	0.000006(8)	-0.000006(12)	-0.000005(15)	0.00011(6)	-0.000005(15)	0.000014(11)
	$\mathbf{E}_{22333}$	$\mathbf{E}_{23333}$	$\mathbf{E}_{33333}$			
Zn1	0	0	0			
V1	0	0	0			
O1	0.000014(11)	-0.000005(15)	0.00011(6)			
$\mathbf{R}_{int}$	**GoF**	**R**	$\mathbf{R}_{w}$			
2.68%	1.73	1.48%	3.95%			

Table 7.8: Structural parameters of the synchrotron measurement of ZnV_2O_4 at 70 K.

parameters within a plane through the central vanadium ion at ($\frac{1}{2}$ $\frac{1}{2}$ $\frac{1}{2}$) spanned by the vectors (1,1,1) and (1,-1,0). The ±[1 1 1]-directions (3-fold roto-inversion axis) are indicated by the red arrows in Fig. 7.27 (a). The electron densities range between 0.54 e/Å^3 (maximum value) and -0.75 e/Å^3 (minimum value). These are also the extremal values observed in the whole cell $0 \leq x, y, z \leq 1$. Additionally, in Fig. 7.29 (b) a plane perpendicular to the roto-inversion axis spanned by vectors (1,-1,0) and (1,1,-2) is shown. Here, only minor intensities can be found which are distributed in a kind of ring around the vanadium ion. However, these intensities are rather small and might be artifacts due to termination effects [11]. The difference Fourier maps indicate additional electron density parallel to the roto-inversion axes through the vanadium ions and, hence, the occupation of the trigonal a_{2g} orbital which is rather remarkable since the VO_6 octahedra are elongated in this direction (*red arrows* in Fig. 7.27 (a-b)) and the oxygen ions are closer to the roto-inversion axis ($\bar{3}$) for such elongated octahedra. This elongation in direction of the *red arrows* in Fig. 7.27 (a) is connected to the positional parameters of the oxygen ion O1 which has a value of $x \sim 0.26$ ($y = z = x$). A similar observation for the oxygen positions was reported in Ref. [279], i. e. $x \sim 0.26$. However, it should be noted that there are also studies reporting compressed VO_6 octahedra with a value of $x \sim 0.24$ [293, 294], i. e. with a different sign of the deviation from the ideal oxygen position $x = 0.25$.

Furthermore, in Fig. 7.30 (c) the three-dimensional ±0.35 e/Å^3 isosurfaces of the difference Fourier maps are shown. Positive/negative isosurfaces are colored *brown/cyan*. In Fig. 7.30 (a) the shown volume is indicated by the *blue dashed/dotted lines*. As can be seen, the negative (*brown*) lobes point towards the six oxygen ions and might indicate an electron transfer to the electronegative oxygen ions which seems rather reasonable. And the positive (*cyan*) lobes extend along the three-fold roto-inversion axis indicating an a_{2g} orbital occupation.

In order to describe these additional electron densities better also a multipole refinement as described in Chap. 4 has been applied for the additional vanadium 3d electrons whereas all other ions have been described with the standard spherical model but using V^{5+}-form factors for the vanadium ion. The d-electrons at the V^{3+}-site have been described with the multipole formalism, using the ζ-values etc. for vanadium 3d electrons. Since the electron density distribution of a 3d orbital can be described by the population of multipole terms with even values of l up to $l = 4$ in Eq. 4.6, only these even terms have been refined within this multipole refinement. Anharmonic displacement parameters have been refined up to the order of 6 for all ions. The goodness of fit (GoF), the R and R_w-values amount to 2.25, 1.74% and 3.63%. The results of the multipole refinement are shown in Fig. 7.29 (c-d) where the static multipole deformation and charge density maps are shown. The charge density map directly shows the electron density generated by the multipole formalism in real space, (Chap. 4) and is not effected by termination effects like the Fourier maps, thus, giving a better impression of the electron distribution. In Fig. 7.30 (d-i) also the three-dimensional iso surfaces of the static multipole deformation maps are shown giving information about the (additional)

[11] The multipole refinement does not describe these minor electron densities.

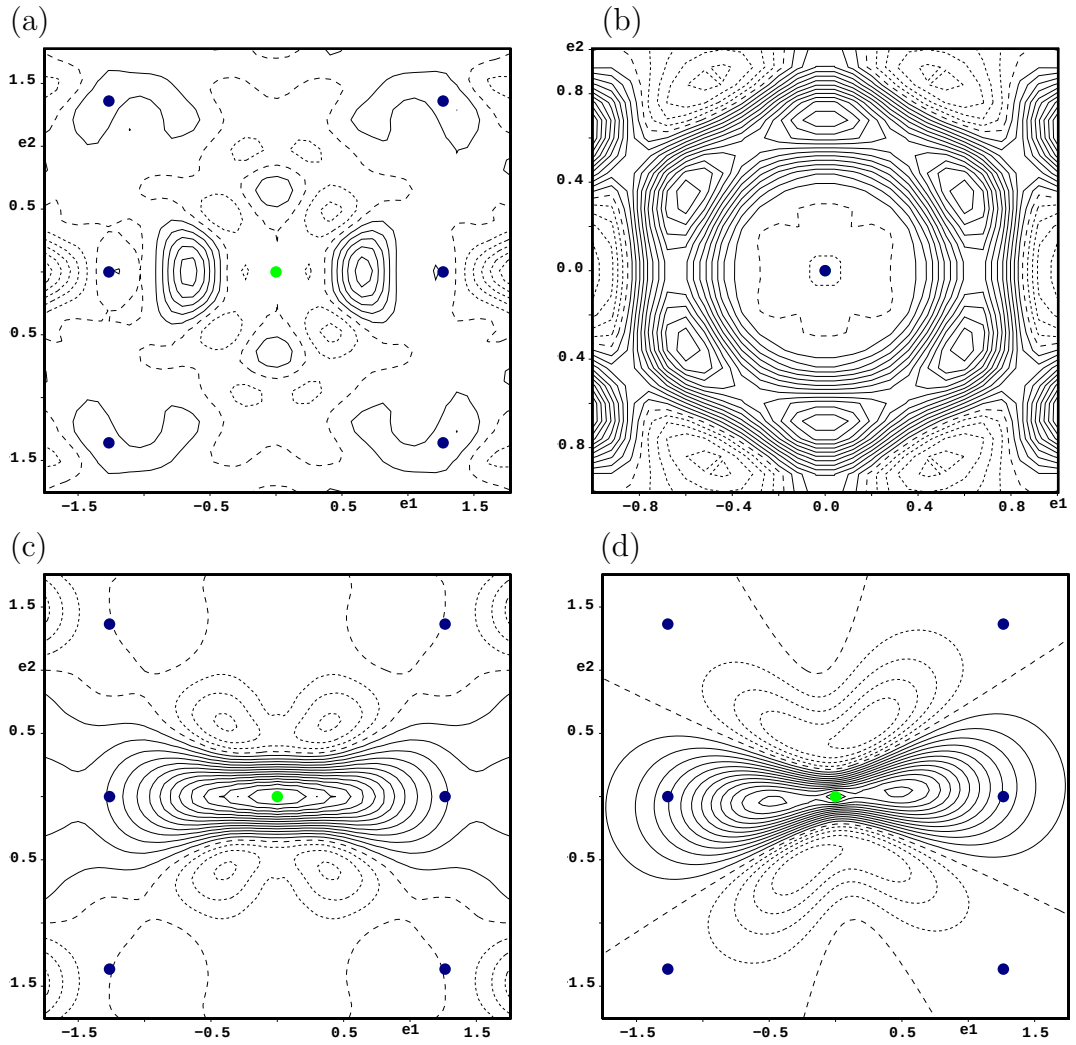

Figure 7.29: (a) Difference Fourier map in plane spanned by vectors $e_1 \propto (1,1,1)$ and $e_2 \propto (1,-1,0)$; *solid/dotted lines:* positive/negative 0.1 e/Å^3 contour lines with maximum (minimum) electron density: 0.54 e/Å^3 (-0.75 e/Å^3). (a) Difference Fourier map in plane spanned by vectors $e_1 \propto (1,-1,0)$ and $e_2 \propto (1,1,-2)$; *solid/dotted lines:* positive/negative 0.02 e/Å^3 contour lines with maximum (minimum) electron density: 0.26 e/Å^3 (-0.09 e/Å^3). (c) Static multipole deformation map n plane spanned by vectors $e_1 \propto (1,1,1)$ and $e_2 \propto (1,-1,0)$ with $\Delta = \pm 0.1$ e/Å^3 contour lines and 1.44 e/Å^3 maximum and -0.84 e/Å^3 minimum electron density. (d) charge density map (valence density) with $\Delta = \pm 0.15$ e/Å^3 contour lines and 2.50 e/Å^3 maximum and -1.87 e/Å^3 minimum electron density. (a-c) *blue dots*: projection of oxygen ions into the 3.5 Å × 3.5 Å plane spanned by vectors $e_1 \propto (1,1,1)$ and $e_2 \propto (1,-1,0)$ centered at the V^{3+}-ion at $(\frac{1}{2}\ \frac{1}{2}\ \frac{1}{2})$ (*green dot*). (d) Structure model; *green sphere*: V^{3+}-ion at $(\frac{1}{2}\ \frac{1}{2}\ \frac{1}{2})$, *blue spheres*: O^{2-}-ions; *red arrows*: $\pm(1\ 1\ 1) \equiv \pm e_1$ direction (3-fold roto-inversion axis).

electron density distribution within the crystal. In Fig. 7.30 (a-b) the volume shown in Fig. 7.30 (d-i) is indicated by the *blue dashed/dotted lines*. These results support the picture of the occupation of an a_{2g} orbital.

However, there might be also another interpretation. Since the difference Fourier maps indicate missing electron density in the structure model, these missing electron densities could also be explained if the vanadium ions would exhibit a shift along the roto-inversion axes (or [1 1 1]- and equivalent directions). A shift of the vanadium ions in this direction is also supported by the PDF of the vanadium ion in Fig. 7.28. Such shifts have also been observed for other spinells - see Ref. [268]. In order to describe such shifts of the vanadium ions in ZnV_2O_4 within the cubic phase, ZnV_2O_4 has to be described with the non-centrosymmetric space group $F\bar{4}3m$. These shifts of the vanadium ions along the [1 1 1]-directions would induce a 'dimerization' of the vanadium ions. Such a dimerization was already proposed in Ref. [294] as there are indications for this type of dimerization in EXAFS (Extended X-ray Absorbtion Fine structure) measurements. Furthermore, this idea might have become more significance due to the publication of the *Pardo* model which calculates a V-V dimerization [292]. In Tab. 7.9 the reflection conditions of space

space group	**reflections**	**reflection conditions**	**abbreviation**
$F\bar{4}3m$	hkl	$h+k,\ h+l,\ k+l = 2n$	$F\bar{4}3m$ #1
	$0kl$	$k,\ l = 2n$	$F\bar{4}3m$ #2
	hhl	$h+l = 2n$	$F\bar{4}3m$ #3
	$h00$	$h = 2n$	$F\bar{4}3m$ #4
$Fd\bar{3}m$	hkl	$h+k,\ h+l,\ k+l = 2n$	$Fd\bar{3}m$ #1
	$0kl$	$k+l = 4n$ and $k,\ l = 2n$	$Fd\bar{3}m$ #2
	hhl	$h+l = 2n$	$Fd\bar{3}m$ #3
	$h00$	$h = 4n$	$Fd\bar{3}m$ #4

reflection:	**I**	**σ(I)**	**I/σ(I)**	**cond. violated**	**cond. fulfilled**
4 2 0	2.1	0.1	21.0	$Fd\bar{3}m$ #2	$F\bar{4}3m$ #2
6 0 4	2.2	0.2	11.0	$Fd\bar{3}m$ #2	$F\bar{4}3m$ #2
8 0 10	3.9	0.5	7.8	$Fd\bar{3}m$ #2	$F\bar{4}3m$ #2
4 1 2	0.7	0.1	7.0	$Fd\bar{3}m$ #1	-
0 14 0	3.3	0.5	6.6	$Fd\bar{3}m$ #4	$F\bar{4}3m$ #4
10 12 0	2.1	0.4	5.2	$Fd\bar{3}m$ #2	$F\bar{4}3m$ #2
8 0 10	1.6	0.4	4.0	$Fd\bar{3}m$ #2	$F\bar{4}3m$ #2

Table 7.9: Reflection conditions for space groups $F\bar{4}3m$ and $Fd\bar{3}m$ from Ref. [295] followed by a list of measured reflections at 70 K. For these reflections I, σ(I) and I/σ(I) are listed as well as the violated reflection condition of space group $Fd\bar{3}m$. Additionally, if this reflection is allowed in space group $F\bar{4}3m$ the corresponding reflection condition in listed.

groups $F\bar{4}3m$ and $Fd\bar{3}m$ are listed. Furthermore, also the reflections with largest values of I/σ(I) violating the reflection conditions of space group $Fd\bar{3}m$ ('*cond. violated*')

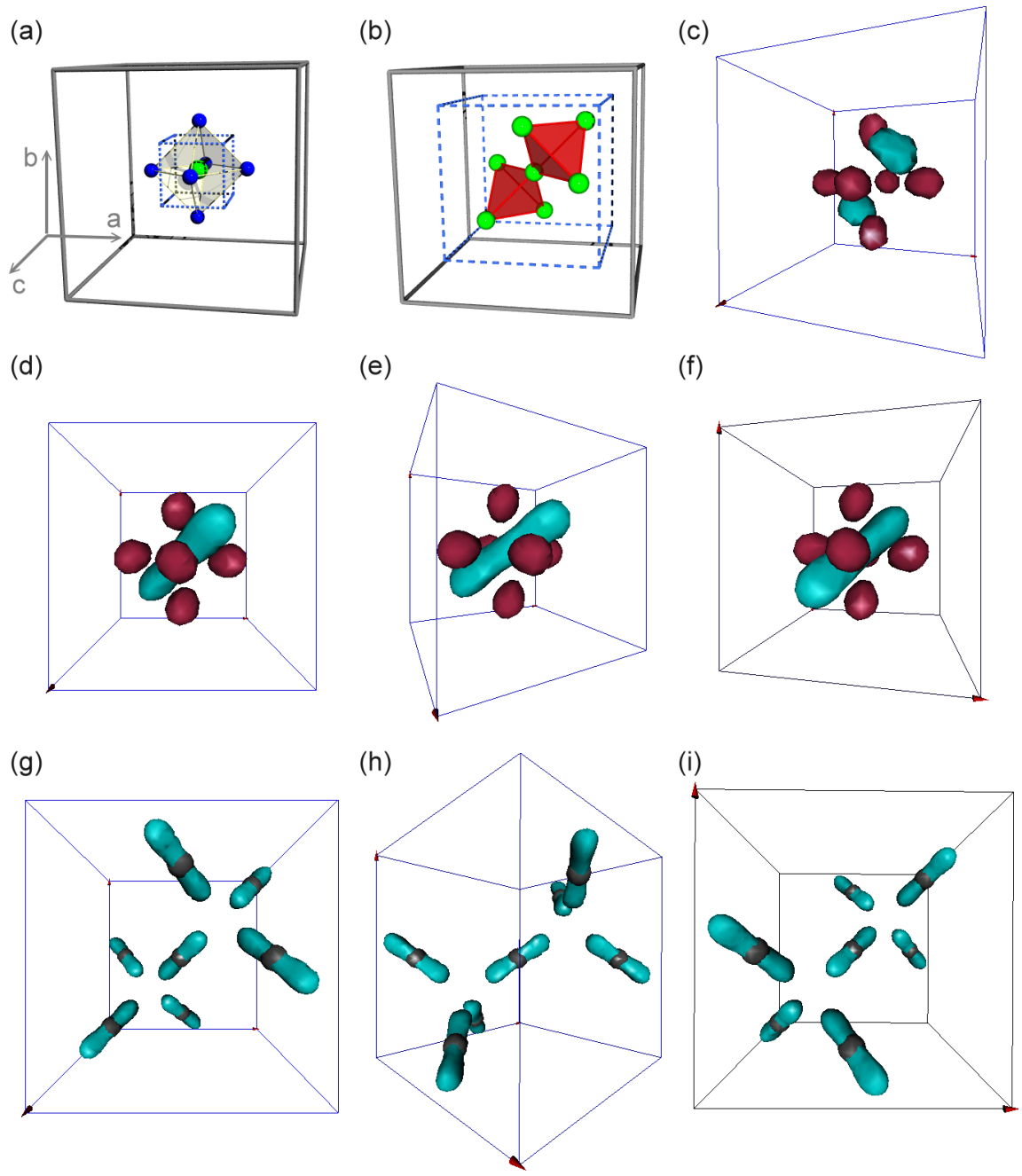

Figure 7.30: (a-b) Selected volume A and B (*blue dotted cubes*) within the unit cell (*grey*); *green*: V-ions, *blue*: O-ions. (c) ± 0.35 e/Å^3 isosurface of the difference Fourier map within A. (d-f) ± 0.45 e/Å^3 isosurface of the static multipole deformation maps within A. (g-i) ± 0.45 e/Å^3 isosurface of the charge density map within B; *grey spheres*: V-ions. (c-i) Positive/negative isosurfaces are colored *brown*/*cyan*.

are shown. Nearly all of these reflections are allowed in space group $F\bar{4}3m$ ('*cond.*

fulfilled'). Multiple scattering can be excluded since all reflections have been measured at two different values of Ψ in order to detect multiple scattering contributions. Thus, the detection of these forbidden peaks might be a first indication for such a 'dimerization model'. A refinement with space group $F\bar{4}3m$ finally yields some improvements for the R- and R_w-values which amount to 1.23% and 3.51%. These values are better than the values of 1.48% and 3.95% for a fully equivalent refinement with space group $Fd\bar{3}m$, compare Tab. 7.8 and Tab. 7.12 or see tab. 7.11. However, the goodness of fit amounts

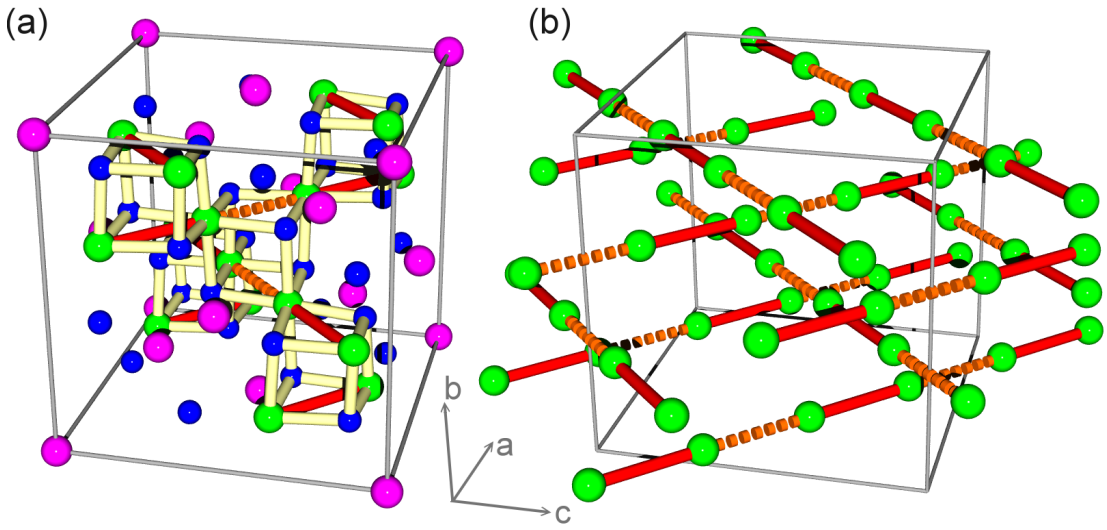

Figure 7.31: (a-b) The structure of ZnV_2O_4 measured at 70 K and refined with space group $F\bar{4}3m$; *green*: V-ions, *blue*: O-ions, *magenta*: Zn-ions, *red lines*: short V-V bonds, *orange dashed lines*: long V-V bonds.

to 1.69 which is almost identical to 1.73 obtained in the refinement with space group $Fd\bar{3}m$. Since $Fd\bar{3}m$ is a non-centrosymmetric space group, an additional twin domain has to be considered in the refinement (with $T_2 = -E_3$). As can be seen from Tab. 7.11, the refinement with space group $F\bar{4}3m$ has even advantages compared to the multipole refinement [12] further supporting the 'dimerization' model. The V-V distances and V-O distances obtained by this refinement are listed in Tab. 7.10 and exhibit small but significant deviations from the average value of the undistorted $Fd\bar{3}m$-structure. For example the distances between the vanadium ions differ by 0.013(3) Å which supports the 'dimerization model'. This is also shown in Fig. 7.31 (a-b) where the structure of ZnV_2O_4 obtained by this refinement (with space group $F\bar{4}3m$) is shown. The *green spheres* indicate the vanadium positions which are connected by *red* and *orange dotted lines* for small and large V-V bonds respectively. Additionally, the vanadium oxygen cubes typical for the spinel structure are indicated with *white/light yellow lines*. As can be seen, each cube contains either only small or only large V-V bonds. Whereas there is

[12] The comparably larger goodness of fit in the multipole refinement may arise from the additional fitting parameters and the comparably small number of averaged reflections in this cubic symmetry. Then the weighted R-values might be a better comparison.

only one V1-site in this structure there are two different oxygen sites O1 and O2. The (pseudo-) cubes with small V-V bonds contain only O2 ions, whereas the cubes with large V-V bonds are build of O1 ions only. These two types of corner-sharing (pseudo-) cubes alternate three dimensionally in all directions. Due to the deviations in the V-V bond lengths these cubes exhibit a trigonal distortion which is different for both types of cubes, see Tab. 7.10. For the trigonal distorted cubes (rhombohedra) containing V1-ions with large V1-V1 distances only, the V1-O1-V1 bond angle amounts to 94.1(2)° and for the other pseudo-cubes (rhombohedra) with small V1-V1 distances the V1-O2-V1 bond angle amounts to 96.0(2)° and in the 'undistorted' structure with space group $Fd\bar{3}m$ these angles have an intermediate value of 95.0(1)° due to the trigonal distortion of the VO_6 octahedra.

type	***lengths/angles***	
	70 K	**290 K**
V1-V1	2.964(2) Å (3×)	2.9806(18) Å(3×)
V1-V1	2.951(2) Å(3×)	2.9676(18) Å(3×)
V1-O1	2.025(5) Å (3×)	2.044(5) Å (3×)
V1-O2	1.985(5) Å (3×)	1.992(4) Å (3×)
V1-O1-V1	94.1(2)° (3×)	93.63(19)° (3×)
V1-O2-V1	96.0(2)° (3×)	96.28(19)° (3×)

Table 7.10: Bond length for all ions around the V1-ion within a sphere of 3 Å radius obtained from a refinement of the 70 K synchrotron measurement and the 290 K single crystal X-ray diffraction measurement with space group $F\bar{4}3m$.

However, a distinct decision between both space groups seems difficult although there are some points in favour of space group $F\bar{4}3m$: The occurrence of superstructure reflections with $I/\sigma(I) > 10$ (Renninger effect can be excluded), the better R- and weighted R-values in a refinement with space group $F\bar{4}3m$, the PDF of the vanadium ion which exhibits local maxima along the three-fold roto-inversion axis and the electron density in the difference Fourier map of the refinement with space group $Fd\bar{3}m$ which might indicate a vanadium shift rather than an occupied orbital. However, this might be only some evidence in favour of such a model and further, complementary measurements are needed for a final decision. Such complementary measurements are for example the EXAFS studies reported in Ref. [294] which indicate that one half of all V-V distances are enlarged and the other half diminished by the same value which indicates a dimerization. Furthermore, the V-O distances shrink for one half (i. e. three) of all V-O distances within the VO_6 octahedron and are larger for the others. But this is exactly what could be observed in the structural refinement by space group $F\bar{4}3m$: the vanadium ions move in [1 1 1]-direction and, thus, equally towards three oxygen ions (or their center of mass etc.) whereas the other three oxygen ions are more far away and, thus, there are two different V-O distances for one half of all V-O bonds as well as two different V-V distances for one half of all V-V distances - compare Tab. 7.10. Hence, the EXAFS

measurements would strongly support the 'dimerization model'. Also an alternative explanation of the EXAFS measurement was given in Ref. [294]: an asymmetrical electron density distribution of the oxygen ions which points towards Zn- and V-ions could also explain the measured signal. However, the electron density measurements of this work (space group $Fd\bar{3}m$) do not indicate such an electron density distribution and hence, this interpretation of the EXAFS data seems not likely. Since these EXAFS measurements are nearly temperature independent, this kind of dimerization might already exist in the cubic phase which would support a dimerization also occuring at 70 K.

Complementary single crystal X-ray diffraction measurements at room-temperature at the *ApexX*8 single crystal X-ray diffractometer with the accuracy of an electron density measurement - see Chap. 4 - have also been performed. Therefore, a second single crystalline sample with octahedral shape and about 55 μm in diameter has been measured using Mo-K_{alpha} radiation. 2283 reflections have been collected with a redundancy of 5.09 (449 averaged reflections) and an internal R-value of 1.48% up to $\sin(\Theta_{max})/\lambda = 1.2621$ ($\Theta_{max} = 127.1°$). In Tab. 7.11 the obtained R-values are compared for structure refinements with space group $F\bar{4}3m$ versus space group $Fd\bar{3}m$ (290 K measurement). Here, the differences between both structure models are even more apparent: as can be clearly seen the R-values and also the goodness of fit are better with space group $F\bar{4}3m$. The different V-V and V-O bond lengths are listed in Tab. 7.10 together with the results for the 70 K synchrotron measurement. Also, in this measurement reflections could be observed which violate the reflection condition $0kl$, $k + l = 4n$ and which have significant values of $I/\sigma(I)$. Furthermore, the difference Fourier maps of the refinement

	70 K			***290 K***	
	$Fd\bar{3}m$	$Fd\bar{3}m$ †	$F\bar{4}3m$	$Fd\bar{3}m$	$F\bar{4}3m$
R-value:	1.48%	1.74%	1.23%	1.67%	1.31%
R_w-value:	**3.95%**	**3.63%**	**3.51%**	**4.45%**	**3.16%**
GoF:	1.73	2.25	1.69	1.80	1.17
Δd(V-V):	0	0	0.013(3) Å	0	0.0130(25) Å

Table 7.11: Comparison of the R-values and goodness of fit for a structural refinement with space group $Fd\bar{3}m$ and $F\bar{4}3m$ for the synchrotron measurement at 70 K as well as for the measurement at the single crystal X-ray diffractometer *ApexX*8 at 290 K. Additionally, the difference of the long and short V-V bonds Δd(V-V) is listed. †: fit with multipole refinement.

with space group $Fd\bar{3}m$ exhibit the same excess electron densities distributed along the roto-inversion axis as observed in the synchrotron measurement at 70 K. This indicates that either the occupation of the trigonal a_{2g} orbital or this kind of 'dimerization' phase appears already at room-temperature. Regarding now also the clear differences of R_w-values and GoF for the room-temperature measurement the 'dimerization' model with space group $F\bar{4}3m$ may be favourized. Since the V-V distances of all four V1 ions within a cube or rhombohedron are of the same size (either large or small), compare Fig. 7.31, this phase might be a kind of 'tetramerization' phase [238] rather than a 'dimerization'

phase.

(a) (b)

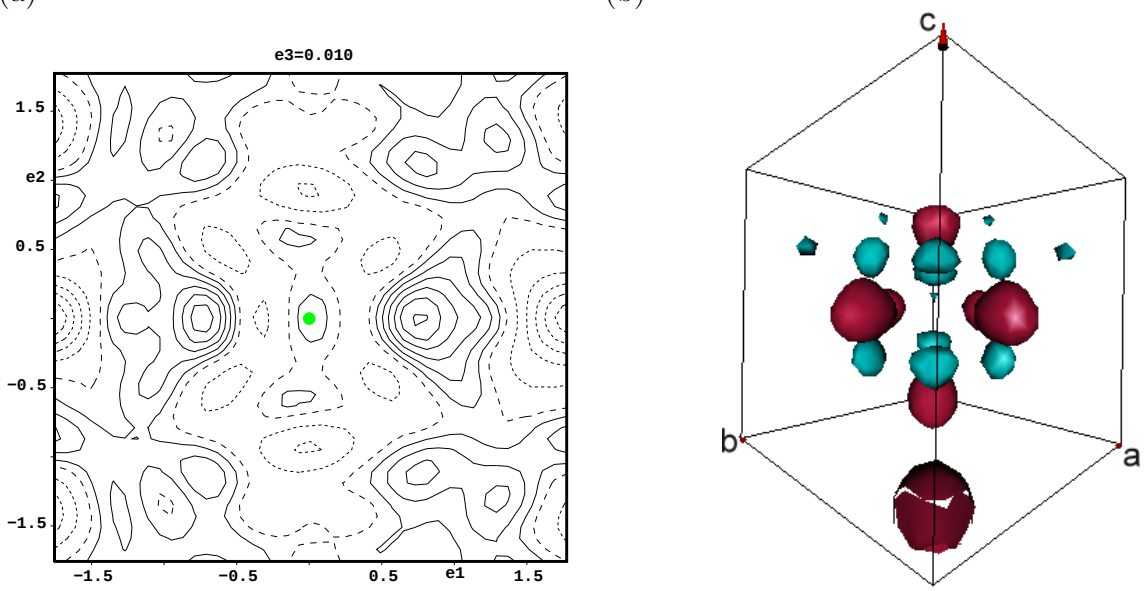

Figure 7.32: (a) Difference Fourier map with +0.05 e/Å^3- (-0.1 e/Å^3-) contour lines; maximum (minimum) elecctron density: 0.321 e/Å^3 -0.561 e/Å^3; the plane is spanned by vectors e_1 = (1 1 1), e_2 = (1 -1 0); all distances in Å. (b) +0.2 e/Å^3-iso-surface (*cyan*) and -0.25 e/Å^3-iso-surface (*brown*) of the difference Fourier map around the V1-ion in the center.

It might be also possible, that both effects, i. e. the occupation of the a_{2g} orbital and a 'dimerization' of the vanadium ions ($F\bar{4}3m$) occur simultaneously. However, since a second twin domain has to be introduced if the non-centrosymmetric structure model ($F\bar{4}3m$) is applied, the detection of such electron densities might be not reliable. Usually, the residual electron densities etc. are severely biased by the refinement of the volume ratios of other twin domains. For completeness, also the difference Fourier maps within a plane spanned by the vectors (1 1 1) and (1 -1 0) are shown in Fig. 7.32 (a). (At least these maps may indicate the quality of the structure model or shortcomings of the structure refinement.) Also a +0.2 e/Å^3- (-0.25 e/Å^3-) iso-surface of the Difference Fourier map in a cubic volume around the vanadium ion is shown in Fig. 7.32 (b). As mentioned above, the significance of these maps is rather questionable due to twinning effects. However, the negative electron densities (brown iso-surfaces) exactly point towards the oxygens, i. e. are located in the vanadium $d_{x^2-y^2}$ and $d_{3r^2-z^2}$ orbitals. This feature could be also observed in the difference Fourier maps of the 'undistorted' structure ($Fd\bar{3}m$) as can be seen in Fig. 7.30 (c-f). Hence, this 'electron drain' from the vanadium ion towards its six neighbouring oxygen ions is still observable in the refinement with space group $F\bar{4}3m$. The positive electron densities in Fig. 7.32 (a) still point to an occupation of the a_{2g} orbital, but there are now some additional electron densities and the overall picture resembles on the occupation of the (trigonal) xz+yz and xz-yz

orbitals now. But as stated above, these orbital occupations might be artifacts of the refinement with a second twin domain - a problem which is absent in the refinement with the centrosymmetric space group $Fd\bar{3}m$.

70 K						
SG:	**a (Å)**	**b (Å)**	**c (Å)**	α (°)	β (°)	γ (°)
Fd$\bar{3}$m	8.3652(288)	8.3652(288)	8.3652(288)	90	90	90
	x	**y**	**z**	**U_{iso} (Å^2)**		
Zn1	0.25	0.25	0.25	0.0027(2)		
Zn2	0	0	0	0.0027(2)		
V1	0.62527(18)	0.62527(18)	0.62527(18)	0.0036(2)		
O1	0.3835(6)	0.3835(6)	0.3835(6)	0.0049(3)		
O2	-0.1381(5)	-0.1381(5)	-0.1381(5)	0.0049(3)		
	U_{11} (Å^2)	**U_{22} (Å^2)**	**U_{33} (Å^2)**	**U_{12} (Å^2)**	**U_{13} (Å^2)**	**U_{23} (Å^2)**
Zn1	0.0027(4)	0.0027(4)	0.0027(4)	0	0	0
Zn2	0.0027(4)	0.0027(4)	0.0027(4)	0	0	0
V1	0.0036(4)	0.0036(4)	0.0036(4)	0.00019(11)	0.00019(11)	0.00019(11)
O1	0.0049(6)	0.0049(6)	0.0049(6)	0.0014(8)	0.0014(8)	0.0014(8)
O2	0.0049(6)	0.0049(6)	0.0049(6)	-0.0014(8)	-0.0014(8)	-0.0014(8)
R_{int}	**GoF**	**R**	**R_w**			
2.68%	1.69	1.23%	3.51%			

290 K						
SG:	**a (Å)**	**b (Å)**	**c (Å)**	α (°)	β (°)	γ (°)
Fd$\bar{3}$m	8.4120(13)	8.4120(13)	8.4120(13)	90	90	90
	x	**y**	**z**	**U_{iso} (Å^2)**		
Zn1	0.25	0.25	0.25	0.0153(4)		
Zn2	0	0	0	0.0153(4)		
V1	0.62527(15)	0.62527(15)	0.62527(15)	0.0159(5)		
O1	0.3825(5)	0.3825(5)	0.3825(5)	0.0184(6)		
O2	-0.1387(5)	-0.1387(5)	-0.1387(5)	0.0184(6)		
	U_{11} (Å^2)	**U_{22} (Å^2)**	**U_{33} (Å^2)**	**U_{12} (Å^2)**	**U_{13} (Å^2)**	**U_{23} (Å^2)**
Zn1	0.0153(8)	0.0153(8)	0.0153(8)	0	0	0
Zn2	0.0153(8)	0.0153(8)	0.0153(8)	0	0	0
V1	0.0159(8)	0.0159(8)	0.0159(8)	-0.00050(13)	-0.00050(13)	-0.00050(13)
O1	0.0184(11)	0.0184(11)	0.0184(11)	0.0032(6)	0.0032(6)	0.0032(6)
O2	0.0184(11)	0.0184(11)	0.0184(11)	-0.0032(6)	-0.0032(6)	-0.0032(6)
R_{int}	**GoF**	**R**	**R_w**			
1.48%	1.17	1.31%	3.16%			

Table 7.12: Structural parameters of ZnV_2O_4 measured at 70 K (synchrotron) and 290 K (Mo-K_α) for the refinements with space group $F\bar{4}3m$ (anharmonic displacement parameters omitted).

7.3.4 Conclusion

In conclusion, precise single crystal X-ray diffraction measurements have been performed at the synchrotron (70 K measurement) and at the *ApexX*8 single crystal diffractometer (290 K measurement) on two different ZnV_2O_4 samples. Both measurements indicate an excess electron density around the V-ion which extends along the three-fold roto-inversion axis in the cubic phase. This might be an indication of the trigonal a_{2g} orbital which would give rise to completely new orbital ordering schemes also in the low temperature tetragonal phase.

However, there might be also another explanation: the excess electron density might indicate a shift of the vanadium ions along the [1 1 1]-direction and equivalent directions (former roto-inversion axes) instead of a real electron density. Such a phase can be described with space group $F\bar{4}3m$. Indeed, the fits indicate better R/R_w-values for this structure model and also superstructure reflections violating the $0kl$, $k + l = 4n$ reflection condition of space group $Fd\bar{3}m$ could be observed in both measurements. These reflections are allowed in space group $F\bar{4}3m$. Thus, ZnV_2O_4 might exhibit a tetramerized phase already at high temperatures, i. e. in the cubic phase. Hence, the cubic to tetragonal phase transition might be a transition from a tetramerized phase to a dimerized phase which has been reported recently in the *Pardo* model [292].

Either the occupation of an a_{2g} orbital or the formation of V-V dimers/tetramers in the cubic phase gives rise to new basis for theoretical calculations of the ground state of ZnV_2O_4. Unfortunately, the tetragonal low temperature structure could not be measured at the synchrotron due to severe twinning problems.

[Ar] $3d^5$ $4s^1$
1857/2482
51.996

24 Cr
Chromium

8 Chromates

Chromium is a comparatively rare transition metal with the main ore Chromite ($FeCr_2O_4$) [107]. As vanadium, it is mainly used in the production of steel.

8.1 Magnetic order and electrical properties in $CaCrO_3$

8.1.1 Introduction

$CaCrO_3$ is a transition metal oxide with an orthorhombic $GdFeO_3$-type perovskite structure (see Fig. 8.1). Two electrons occupy the d-shell of the chromium ion (S=1). In such materials with low d-level occupation one may expect the orbital degree of freedom to cause exciting effects [296-299, 119, 300, 301]. As $CaCrO_3$ has two d-electrons it resembles either on the metallic $4d^4$ system (Ca,Sr)RuO_3 (S=1, low spin with two holes in the t_{2g} shell) or on the insulating $3d^2$-system RVO_3 with a similar structure and which show such interesting effects as for example temperature-induced magnetization reversals in YVO_3 with a concomitant change in the magnetic structure from C-type to G-type antiferromagnetism induced by orbital ordering where the first electron occupies an d_{xy}-orbital and the second one occupies alternatingly the d_{xz}- and d_{yz}-orbitals in a way that C-type orbital ordering leads to G-type antiferromagnetism and G-type orbital ordering leads to C-type antiferromagnetism [296-299]. Regarding the magnetism in such correlated electron systems, the relation to electrical conductivity is in principle the following: ferromagnetism comes along with metallic conductivity and antiferromagnetism with insulating properties [302]. Systems with a behaviour differing from this rule often attract strong attention. An example for an insulating ferromagnet is $YTiO_3$ which plays an important role in Chapter 6.1. In this fully three-dimensional system antiferroorbital ordering [117] induces ferromagnetism as is in accordance with the rules of Goodenough [28], Kanamori [29] and Anderson [30]. Thus, orbital ordering can often explain the occurrence of ferromagnetism in insulating transition-metal oxide systems [126]. The other possibility of antiferromagnetism occurring in a fully three-dimensional metallic transition metal oxide may be even more interesting, as the few systems with these two properties are quasi low dimensional with regard to their structure and antiferromagnetism is realized by stacking of ferromagnetic layers. Such systems are for example $Ca_3Ru_2O_7$ [303] and $(La,Sr)_3Mn_2O_7$ [304]. In this work, the fully three-dimensional pseudocubic perovskite chromate compound $CaCrO_3$ was found to exhibit antiferromagnetic ordering. Optical reflectivity measurements carried out and

analyzed by T. Möller reveal metallic properties of this system which is consistent with previous reports of metallic properties of single crystalline samples of $CaCrO_3$ [305]. Therefore, it is likely, that $CaCrO_3$ is the rare example of a fully three-dimensional antiferromagnetic transition metal oxide.

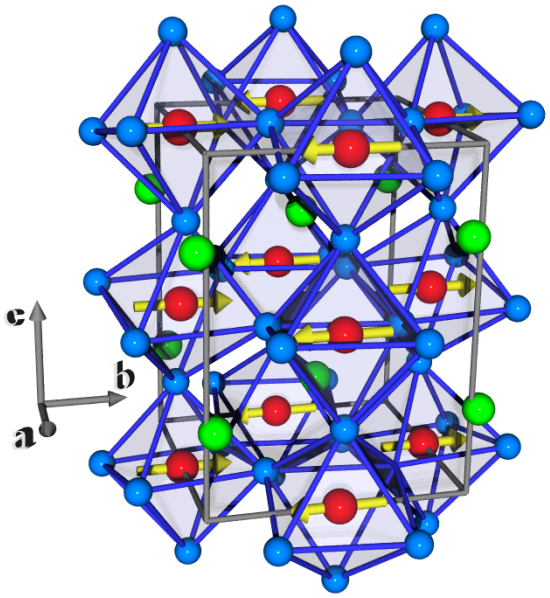

Figure 8.1: The structure of $CaCrO_3$ at 3.5 K with space group *Pbnm* derived from powder neutron diffraction; *red:* Cr^{4+}, *blue:* O^{2-}, *green:* Ca^{2+}. The *yellow arrows* indicate the spin directions.

The oxidation state 4+ of the chromium ion is rather unusual and the samples have to be grown by an elaborate high pressure synthesis. Among perovskite Cr^{4+} compounds, $SrCrO_3$, $CaCrO_3$ and $PbCrO_3$ have been studied. However, for most of them, there is no detailed knowledge of the crystal and magnetic structure and sometimes even the same group reports two conflictive observations within shortest time as in the case of $SrCrO_3$:

> ... No magnetic diffraction peaks are evident in the 10 K neutron diffraction profile of $SrCrO_3$ ..The 50 K magnetic transition in $SrCrO_3$ therefore appears to be to a weakly ferromagnetic itinerant state ... [306]

followed about one year later by:

> ...observation of two very weak magnetic peaks ... These peaks index on an antiferromagnetic (1/2 1/2 0) superstructure of the tetragonal $SrCrO_3$ phase ... [307]

Returning to $CaCrO_3$, also the electronic properties are not reported unanimously with reports ranging from metallic [305, 308] to insulating properties [309, 310]. For $CaCrO_3$ Goodenough *et al.* reported a structural O-orthorhombic → O'-orthorhombic

transition at about 90 K [309]. This transition manifests itself through a crossover of the pseudo-cubic a_{cub}- and c_{cub}- lattice parameters.

Besides its exciting physical properties the system $La_{1-x}A_xCr_{1-y}M_yO_3$ (A=Ca,Sr; M=Mg,Ti), of which $CaCrO_3$ is an end compound, has attracted interest in the past decades due to its importance for technical applications in solid oxide fuel cells [311-313] and as electrodes in magnetohydrodynamic generators [314].

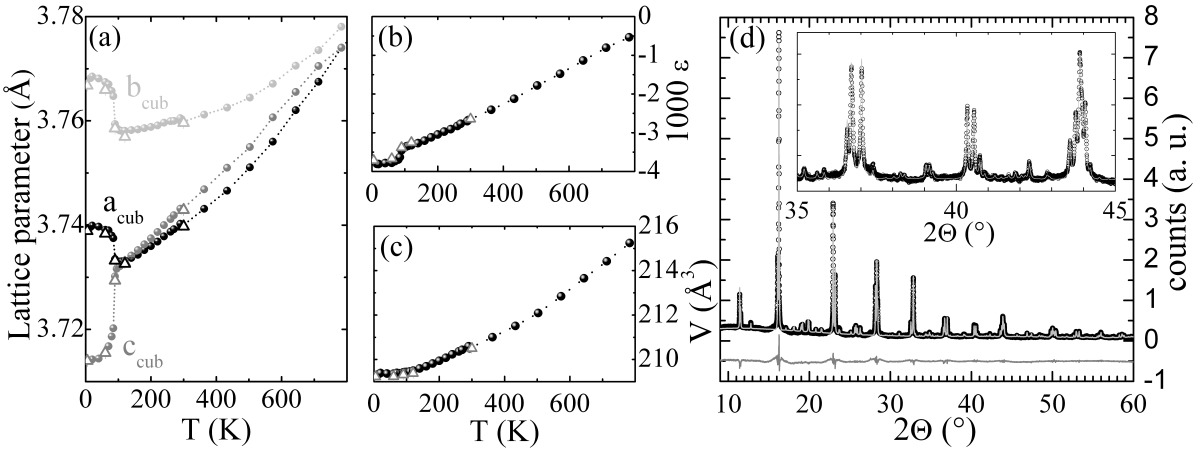

Figure 8.2: (a) The lattice parameter $a_{cub} = a/\sqrt{2}$, $b_{cub} = b/\sqrt{2}$, $c_{cub} = c/2$ (in pseudo-cubic notation), (b) the orthorhombic splitting $\varepsilon = (a-b)/(a+b)$ scaled with factor $\times 1000$. (c) and the unit cell volume V of $CaCrO_3$ measured with powder x-ray and neutron diffraction. The O-orthorhombic $\rightarrow$ O'-orthorhombic phase transition manifests itself in a crossover of the a_{cub}- and c_{cub}- lattice parameters. *circles:* synchrotron X-ray data , *open triangles:* neutron data. (d) A diffraction pattern measured at 20 K; *black:* measured intensities I_{obs}, *light gray:* rietveld fit I_{calc}, *gray:* $I_{obs} - I_{calc} - I_{offset}$.

8.1.2 Experimental

Polycrystalline samples of $CaCrO_3$ were grown by M. Isobe using high pressure techniques. The magnetic ordering temperature was determined by M. Isobe using a SQUID-magnetometer and amounts to $\sim$90 K. Powder neutron measurements have been performed at the SPODI diffractometer at the FRM-II reactor in Garching ($\lambda = 1.548$Å) and at the D20 high flux diffractometer at ILL, Grenoble ($\lambda = 2.4233$ Å). The lattice parameters have been studied with synchrotron radiation X-ray powder diffraction at beamline B2 at Hasylab/DESY in Hamburg ($\lambda = 0.7466$ Å) and structural studies down to 90 K have been performed with an $BrukerApexX8$ single crystal diffractometer [66]. The electrical resistivity was measured by an AC four-point method. And the reflectivity spectra were measured using a Bruker IFS 66v/S Fourier transform spectrometer with an Au mirror used as a reference.

8.1.3 Results

$CaCrO_3$ has an orthorhombic perovskite structure with space group *Pbnm*. The Cr-ions are surrounded by six oxygen ions forming corner-sharing CrO_6-octahedra with O1 being the apical and O2 the basal oxygen.

powder X-ray diffraction measurements
The precise lattice parameters of $CaCrO_3$ have been measured by means of synchrotron radiation X-ray powder diffraction at the beamline B2 at DESY, Hamburg using an incident wavelength of 0.75 Å and an image plate detector for the temperature range between 15 K and 1063 K. Fig. 8.2 (d) gives an impression of the accuracy of these measurements; note, that the pseudocubic lattice parameters are very similar.

With the onset of magnetic ordering at 90 K a distinct rise of the *a*- and *b*- lattice parameters is observable (on cooling). Concomitantly the *c*-lattice parameter shows a strong decrease. The last plot in Fig. 8.2 shows the a_{cub}- and c_{cub}- lattice parameters with an apparent crossover at 90 K. Therefore, the system undergoes an O-orthorhombic $\rightarrow$ O'-orthorhombic phase transition together with a pronounced suppression of ε which indicates some orbital reoccupation or ordering processes [84].

The high temperature data shows an approximation of the lattice parameters towards cubic symmetry. At 713 K a second phase emerges which may be due to a temperature induced decay of the sample (or phase separation). Therefore, only the data below 800 K is shown in Fig. 8.2.

It should be stressed, that in these high resolution synchrotron measurements of $CaCrO_3$ there is no phase mixture apparent as was reported recently for $SrCrO_3$ in Ref. [307].

single crystal x-ray diffraction measurements
Although the sample mass of $CaCrO_3$ is polycrystalline it was finally possible to find a single domain single crystalline grain within the whole sample. This grain was ground to a sphere with roughly 100(5) μm in diameter (*sample 1*). This sample was used for a temperature dependant single crystal X-ray diffraction measurement down to 90 K. Unfortunately these measurements revealed a twinned structure with 6 different twin domains which can be described by a threefold rotation around the pseudocubic (1 1 1) axis combined with or without mirroring at the (1 1 0) plane. The six twin matrices $\mathbf{T_j}$ in notation of the conventional *Pbnm* cell are:

$$\mathbf{T_1} = \begin{pmatrix} 1 & 0 & 0 \\ 0 & 1 & 0 \\ 0 & 0 & 1 \end{pmatrix} \quad \mathbf{T_2} = \begin{pmatrix} -\frac{1}{2} & \frac{1}{2} & \frac{1}{2} \\ \frac{1}{2} & -\frac{1}{2} & \frac{1}{2} \\ 1 & 1 & 0 \end{pmatrix} \quad \mathbf{T_3} = \begin{pmatrix} 0 & 1 & 0 \\ 1 & 0 & 0 \\ 0 & 0 & -1 \end{pmatrix}$$

$$\mathbf{T_4} = \begin{pmatrix} -\frac{1}{2} & \frac{1}{2} & -\frac{1}{2} \\ -\frac{1}{2} & \frac{1}{2} & -\frac{1}{2} \\ 1 & 1 & 0 \end{pmatrix} \quad \mathbf{T_5} = \begin{pmatrix} \frac{1}{2} & \frac{1}{2} & \frac{1}{2} \\ -\frac{1}{2} & -\frac{1}{2} & \frac{1}{2} \\ 1 & -1 & 0 \end{pmatrix} \quad \mathbf{T_6} = \begin{pmatrix} \frac{1}{2} & \frac{1}{2} & -\frac{1}{2} \\ \frac{1}{2} & \frac{1}{2} & \frac{1}{2} \\ 1 & -1 & 0 \end{pmatrix}$$

The volume ratios of these 6 different twin domains $\mathbf{r_j} \equiv \mathbf{r}(\mathbf{T_j})$ are:
$\mathbf{r_1}$= 39.7(1.4)%, $\mathbf{r_2}$= 2.9(6)%, $\mathbf{r_3}$= 39.5(7)%, $\mathbf{r_4}$= 2.6(6)%, $\mathbf{r_5}$= 11.2(6)% and $\mathbf{r_6}$=

4.2(6)% at room-temperature and do not change for the refinements at all lower temperatures. The results of these measurements are listed in Tab. 8.1. Afterwards a second single crystalline grain was searched for. In order to avoid twinning like in *sample 1*, a very small grain was selected. This grain was ground to an accurate sphere with 20(2) μm in diameter (*sample Elec*) and prepared with large effort for an electron density measurement at room-temperature; for further details see Chap. 4. Images/frames have been collected with 60 s per image up to $2\Theta_{max}$=124.5° using Mo-K_α-radiation. But unfortunately, also this measurement revealed a twinned structure with 6 different twin domains. The volume ratios of these 6 different twin domains are:
$\mathbf{r_1}$= 4.1(3)%, $\mathbf{r_2}$= 2.7(1)%, $\mathbf{r_3}$= 11.5(1)%, $\mathbf{r_4}$= 4.2(1)%, $\mathbf{r_5}$= 39.2(1)% and $\mathbf{r_6}$= 38.2(1)%. As the divergence of the X-ray beam is rather large compared to synchrotron measurements for example, the reflections of different twin domains merge into a single broad intensity-spot, which can be integrated and includes the intensity of all possible reflections from other twin domains which may contribute to this (broad) spot. Therefore, it is possible to analyze and refine the data with a program which can calculate the intensity contributions of all twin domains to the total intensity $I^{(tot)}(hkl) \propto \sum_{\nu=1}^{6} \mathbf{r}_\nu^2 \cdot I(\mathbf{T}_\nu(hkl))$. But an electron density analysis becomes impossible as all tiny features of any possible valence electron density distribution will be hidden by the refinement of the volume ratios of the six different twin domains. Therefore, this single crystal X-ray diffraction measurement which has been prepared with the precision of an electron density measurement has been used for precise structure determination purposes only. In a third try to

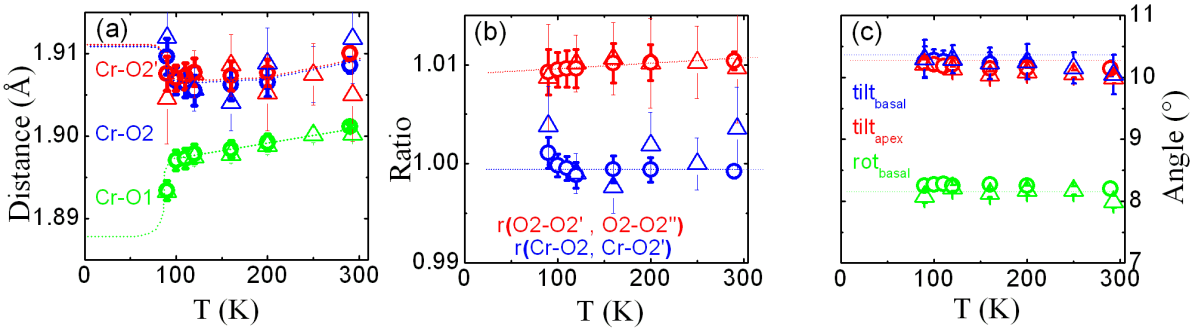

Figure 8.3: Results of single crystal X-ray diffraction measurements; *open circles: sample Elec* and *sample 2*, *open triangles: sample 1*. (a) Cr-O distances; (b) ratio of the O2-O2 bondlengths (*red*) and ratio of the basal Cr-O2 distances (*blue*); (c) tilt and rotational angles of the CrO_6 octahedron.

find an untwined sample another single crystalline specimen has been found within the polycrystalline sample mass. This sample was ground to a sphere of roughly 20(4) μm in diameter (*sample 2*). Afterwards a second, temperature dependant structural study has been applied from 200 K to 90 K. This second temperature measurement has been performed in order to check, whether the results from the first measurement can be reproduced despite their heavily twinned composition, in order to measure some more temperature points in the low temperature region close to the phase transition and also

in order to improve the data quality and to diminish the statistical spread of the data points. Unfortunately, also this sample was twinned despite its tiny dimensions. The volume ratios of these 6 different twin domains are:
$\mathbf{r_1}$= 1.5(6)%, $\mathbf{r_2}$= 1.3(3)%, $\mathbf{r_3}$= 1.1(3)%, $\mathbf{r_4}$= 3.4(4)%, $\mathbf{r_5}$= 30.3(2)% and $\mathbf{r_6}$= 62.4(4)%. These ratios stayed about constant for all temperatures. The results of this second measurements are listed in Tab. 8.2. A comparison between the results of both measurements can be seen in Fig. 8.3. The three different Cr-O distances - with O2 and O2' being in the CrO_6-octahedral basal plane and O1 the apical oxygen - are shown in Fig. 8.3 (a). The ratios of the two different O2-O2 bondlengths, i. e. the ratio of the two basal Cr-O2 distances and the ratio of the edges of the CrO_6 octahedral basal plane are plotted in Fig. 8.3 (b). Finally, in Fig. 8.3 (c) the tilt and rotation angles of the CrO_6 octahedron are plotted. These values are calculated from the tilt of the apical oxygen and also for the tilt and rotation of the basal plane. As can be seen, the results of all measurements are quite consistent as the values do not differ within the error bars. Therefore, the results are reproducible (within the error bars). But the measurement with *sample Elec* and *sample 2* yield much better results with respect to error bars and statistical spread. Especially, the O2-ions seems to suffer from this statistical spread in the data of *sample 1*. Therefore, only the data of *sample Elec* and *sample 2* will be taken for further data analysis and interpretation as will follow in the next section.

Furthermore, a synchrotron radiation single crystal X-ray diffraction measurement at beamline D3 at DESY, Hamburg has been performed using the MAR CCD area detector and a wavelength of 0.47686 Å. In this experiment *sample 2* which only has two major twin domains has been measured at 10 K [1]. But at the synchrotron the resolution is much higher than at the *Apex* single crystal diffractometer. Therefore, the reflections of both different twin domains were resolved and detected separately, although the pseudocubic lattice parameter of $CaCrO_3$ are very similar. Unfortunately, this is an obstacle for the integration software which can not deal with twinned structures. Thus, this measurement could not be further evaluated.

neutron measurements

Powder neutron diffraction measurements have been performed at the high resolution diffractometer SPODI at FRM-II, Garching and at the high-flux diffractometer D20 at ILL, Grenoble. In the SPODI measurement the atomic positions could be determined down to 3.5 K. The results are listed in Tab. 8.3. Together with the single crystal diffraction data the whole temperature region between room-temperature and 3.5 K has been measured and the results are shown in Fig. 8.4. The rotation Φ and tilt Θ of the CrO_6-octahedra characteristic for the $GdFeO_3$ perovskite structure (see also Chapter 6.1 and Ref. [84]) do not change much with temperature as can be seen in Fig. 8.4. There are two prominent distortions determining the shape of the basal oxygen plane of this CrO_6-octahedra. The first is the ratio of the basal oxygen (O2) bondlengths between each other ($r_{O2-O2',O2-O2''}$). The other is the ratio of the bondlength of the Cr-ion to these basal oxygens ($r_{Cr-O2,Cr-O2'}$). If the first ratio is large, the basal oxygen plane is

[1] *Sample 1* and *sample Elec* have both three twin domains with significantly large volume ratios.

	90 K	***120 K***	***160 K***	***200 K***	***250 K***	***293 K***
Lattice:						
a (Å):	5.2806(15)	5.2772(14)	5.2789(13)	5.2806(13)	5.2835(11)	5.2888(2)
b (Å):	5.3178(17)	5.3104(16)	5.3096(15)	5.3106(14)	5.3131(13)	5.3169(2)
c (Å):	7.4532(25)	7.4714(23)	7.4750(21)	7.4781(21)	7.4837(18)	7.4858(3)
Atoms:						
Ca1:						
x:	0.9944(2)	0.99437(9)	0.9946(1)	0.9949(2)	0.9949(1)	0.9952(2)
y:	0.0332(2)	0.0329(1)	0.0324(2)	0.0322(2)	0.0315(2)	0.0305(2)
z:	0.25	0.25	0.25	0.25	0.25	0.25
U_{iso} ***(Å²):***	0.0042(2)	0.00494(9)	0.0056(1)	0.0063(2)	0.0072(1)	0.0086(2)
Cr1:						
x:	0	0	0	0	0	0
y:	0.5	0.5	0.5	0.5	0.5	0.5
z:	0	0	0	0	0	0
U_{iso} ***(Å²):***	0.0026(2)	0.0033(1)	0.0034(1)	0.0040(2)	0.0043(1)	0.0047(2)
O1:						
x:	0.0627(4)	0.0624(2)	0.0618(3)	0.0621(4)	0.0619(3)	0.0616(5)
y:	0.04897(4)	0.4896(2)	0.4898(3)	0.4898(4)	0.4895(3)	0.4907(4)
z:	0.25	0.25	0.25	0.25	0.25	0.25
U_{iso} ***(Å²):***	0.0040(6)	0.0050(3)	0.0052(4)	0.0052(8)	0.0065(4)	0.0070(6)
O2:						
x:	0.7133(6)	0.7137(3)	0.7141(4)	0.7134(5)	0.7139(4)	0.7138(7)
y:	0.2852(6)	0.2861(3)	0.2861(4)	0.2857(5)	0.2857(4)	0.2849(7)
z:	0.0325(2)	0.0324(1)	0.0322(2)	0.0323(2)	0.0319(1)	0.0316(2)
U_{iso} ***(Å²):***	0.0043(5)	0.0048(3)	0.0049(4)	0.0055(5)	0.0066(4)	0.0077(6)
Data:						
all refl.:	2625	31380	11263	4508	11244	4119
av.refl.:	1104	1785	1644	1600	1645	1527
$\mathbf{2\Theta_{max}}$**:**	74.2°	84.6°	84.1°	83.2°	84.12°	82.4°
redun.:	2.38	17.58	6.85	2.82	6.84	2.70
$\mathbf{R}_{int}$**:**	2.26%	3.85%	3.29%	2.81%	3.34%	2.61%
Fit:						
GoF:	1.73	2.05	1.92	1.43	1.76	1.63
R:	2.76%	1.86%	2.55%	2.82%	2.34%	3.13%
$\mathbf{R}_w$**:**	5.03%	3.25%	4.01%	4.72%	3.69%	4.89%

Table 8.1: Results of single crystal X-ray diffraction measurements of $CaCrO_3$ *sample 1.*

rectangular, if it is close to 1 it is square (or rhombic). On the other hand, if the second ratio is large the basal plane has an rhombic shape and if it is close to 1 it is square (or rectangular). These ratios are shown in Fig. 8.4 (a). As the second ratio, $r_{Cr-O2,Cr-O2'}$, is very close to 1 over the whole temperature range, the oxygen basal plane has no rhombic shape at all. Only the first ratio differs from 1 and amounts approximately 1.01. The oxygen basal plane therefore has a square shape with a small rectangular distortion of the order of 1% which also shows no significant change with temperature. Therefore,

	90 K	***100 K***	***110 K***	***120 K***	***160 K***	***200 K***	***290 K***
Lattice:							
a (Å):	5.2806(15)	5.2765(15)	5.2768(15)	5.2772(14)	5.2789(13)	5.2806(13)	5.2888(2)
b (Å):	5.3178(17)	5.3112(17)	5.3112(17)	5.3104(16)	5.3096(15)	5.3106(14)	5.3169(2)
c (Å):	7.4532(25)	7.468(2)	7.4697(25)	7.4714(23)	7.4750(21)	7.4781(21)	7.4858(3)
Atoms:							
Ca1:							
x:	0.9944(1)	0.9944(1)	0.9943(1)	0.9944(1)	0.9945(1)	0.9947(1)	0.99486(5)
y:	0.0326(1)	0.0326(1)	0.0324(1)	0.0323(1)	0.0320(1)	0.0317(1)	0.03116(5)
z:	0.25	0.25	0.25	0.25	0.25	0.25	0.25
U_{iso} ***(Å^2):***	0.0054(1)	0.0056(1)	0.0056(1)	0.0057(1)	0.0063(1)	0.0067(1)	0.00806(4)
Cr1:							
x:	0	0	0	0	0	0	0
y:	0.5	0.5	0.5	0.5	0.5	0.5	0.5
z:	0	0	0	0	0	0	0
U_{iso} ***(Å^2):***	0.0032(1)	0.0033(1)	0.0034(1)	0.0033(1)	0.0036(1)	0.0038(1)	0.00441(4)
O1:							
x:	0.0628(2)	0.0629(2)	0.0627(2)	0.0629(2)	0.0625(2)	0.0625(2)	0.0625(1)
y:	0.04895(2)	0.4895(2)	0.4896(2)	0.4898(2)	0.4897(2)	0.4894(2)	0.4899(1)
z:	0.25	0.25	0.25	0.25	0.25	0.25	0.25
U_{iso} ***(Å^2):***	0.0061(2)	0.0059(2)	0.0061(3)	0.0062(3)	0.0069(3)	0.0069(3)	0.0077(1)
O2:							
x:	0.7135(2)	0.7134(2)	0.7133(2)	0.7132(2)	0.7133(2)	0.7134(2)	0.7136(1)
y:	0.2863(2)	0.2861(1)	0.2862(2)	0.2860(2)	0.2861(2)	0.2861(2)	0.2858(1)
z:	0.0324(1)	0.0324(1)	0.0323(1)	0.0322(1)	0.0322(1)	0.0321(1)	0.0319(1)
U_{iso} ***(Å^2):***	0.0056(2)	0.0058(2)	0.0059(2)	0.0061(2)	0.0061(2)	0.0068(2)	0.0073(1)
Data:							
all refl.:	9946	10193	10340	8951	8967	8614	27617
av.refl.:	1699	1689	1686	1665	1667	1700	3799
$\mathbf{2\Theta_{max}}$**:**	82.6°	84.3°	84.4°	84.4°	84.3°	84.12°	124.5°
redun.:	2.38	6.04	6.133	5.38	5.38	5.07	7.27
$\mathbf{R}_{int}$**:**	2.26%	2.40%	2.66%	2.67%	2.77%	2.57%	2.90%
Fit:							
GoF:	1.78	1.84	1.73	1.67	1.70	1.77	1.58
R:	2.21%	2.10%	2.30%	2.37%	2.42%	2.40	1.95%
$\mathbf{R}_w$**:**	3.80%	3.78%	3.83%	3.32%	4.23%	4.28	3.20%

Table 8.2: Results of single crystal X-ray diffraction measurements of $CaCrO_3$ *sample Elec.*

the nearly square shape of the oxygen basal plane remains unchanged over the full temperature range. But a comparison of the basal Cr-O2 distances with the apical Cr-O1 distances reveals a strong change with the onset of magnetic ordering, see Fig. 8.4 (c): The Cr-O1 distance starts to decline at 90 K whereas the Cr-O2 distances increase. Hence, the CrO_6-octahedra are compressed in z-direction and stretched/elongated in the xy-plane - without changing the shape of the basal oxygen plane. This octahedral

compression in z-direction is an indication for an orbital redistribution of the t_{2g}-orbitals and points to a stronger d_{xy} occupation due to this anisotropic oxygen environment. For Ca_2RuO_4 with similar electronic properties such effects are also known and have been interpreted in terms of an orbital rearrangement [315-317]. In Ca_2RuO_4 these effects are even one order of magnitude larger than in $CaCrO_3$.

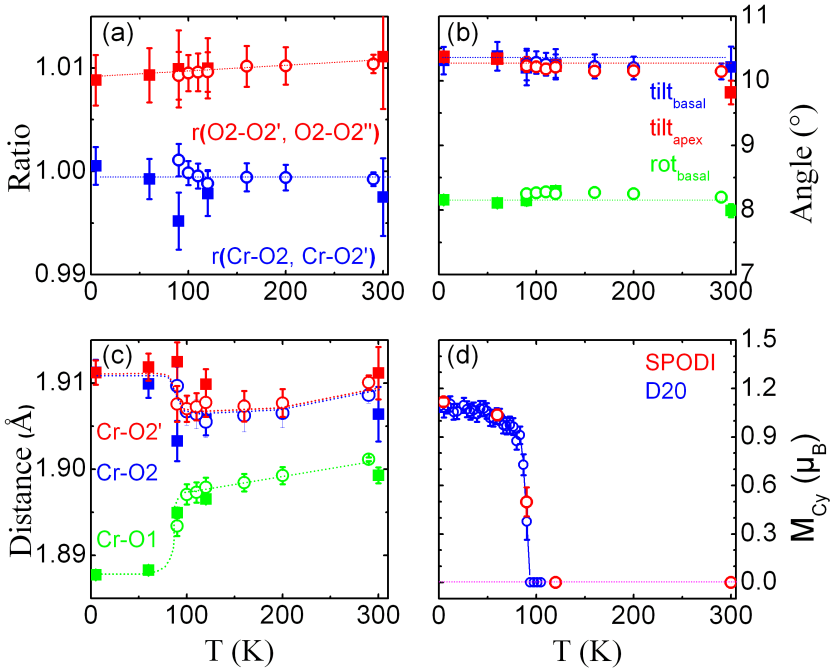

Figure 8.4: Results of powder neutron and single crystal X-ray diffraction measurements; *open circles:* X-ray results of *sample Elec* and *sample 2*, *squares:* neutron results. (a) Ratio of the O2-O2 bondlengths (*red*) and ratio of the basal Cr-O2 distances (*blue*); (b) tilt and rotational angles of the CrO_6 octahedron; (c) Cr-O distances; (d) antiferromagnetic moment of Cr^{4+}.

From the octahedral distortions, in principle, it can be understood why the orthorhombic splitting ε is an indicator for orbital (re-)occupation (which causes these distortions). As the CrO_6-octahedra get elongated in their basal plane without changing their shape, the elongation in b-direction has a stronger effect on the b-lattice parameter than the elongation in a-direction on the a-lattice parameter because of the octahedral tilt Θ which points along a-direction and reduces any effect of an octahedral elongation on the a-lattice parameter by the factor of $\cos(\Theta)$ whereas the effect on the b-lattice parameter is not reduced. Therefore, the occupation of the d_{xy}-orbital which leads to the elongation of the octahedral basal plane causes a stronger rise of the b-lattice parameter than of the a-lattice parameter which leads to a decay of $\varepsilon = (a-b)/(a+b)$.

Fig. 8.5 (a) shows powder neutron diffraction patterns measured on heating on the high-flux D20 diffractometer. Below 90 K two strong magnetic peaks emerge which can only be described by a C-type antiferromagnetic order. From the intensities an

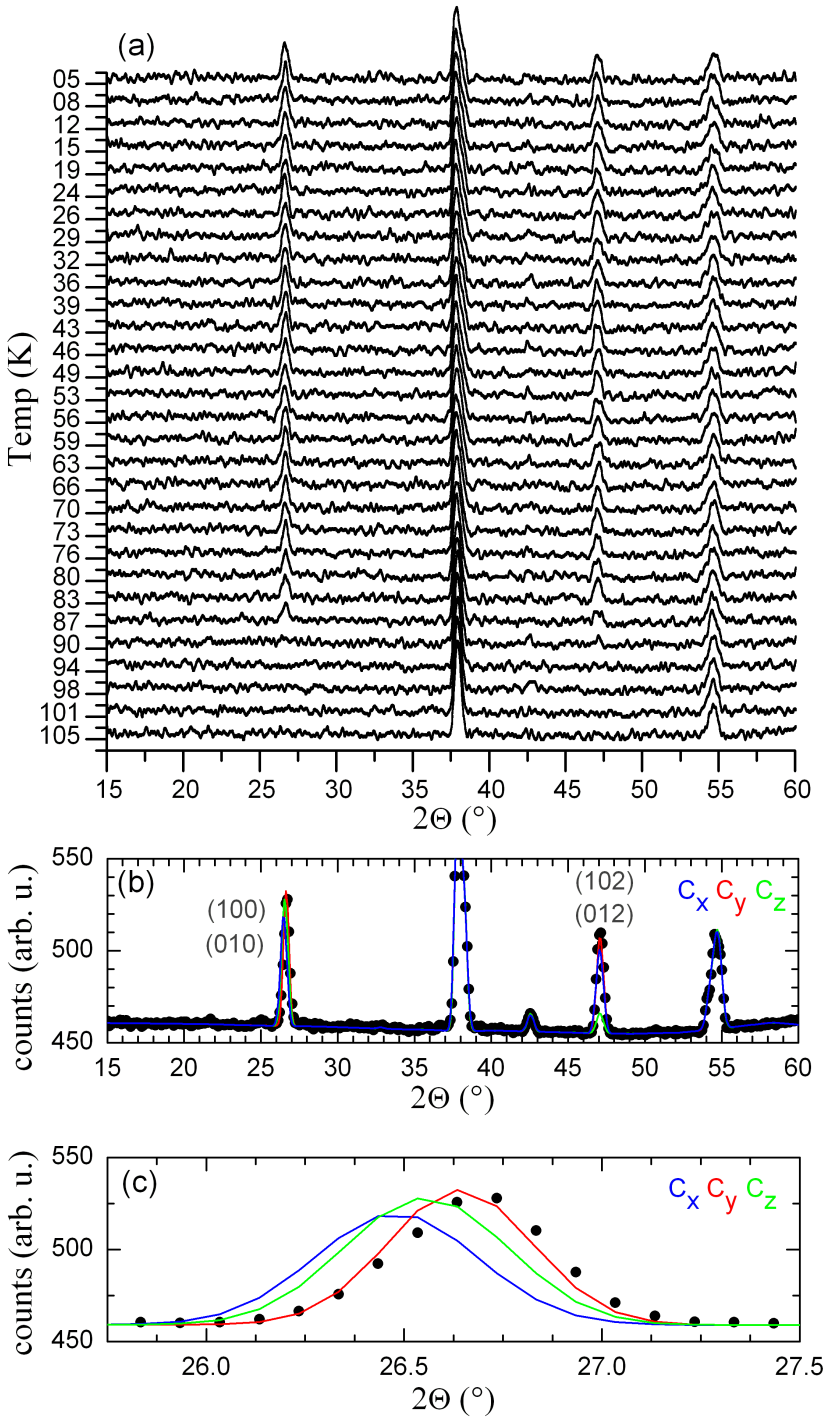

Figure 8.5: (a) Powder neutron diffraction patterns measured at the D20 diffractometer. (b-c) Rietveld-fits to the 2 K data for C_x, C_y and C_z type AFM order.

C_z-type-AF moment can be excluded as the scattering vector is perpendicular to the ordered moment for the magnetic (100)- and (010)-reflections which causes their cal-

culated intensities to be too large compared to the ones for the magnetic (102)- and (012)-reflections and vice versa; see Fig. 8.5 (b). The position of the magnetic (010)-reflection is shifted to lower 2Θ-values due to a larger *b*-lattice parameter ($b/a > 1$). Thus, the ordered magnetic moment can not be perpendicular to this direction and an C_x-type-AF is excluded; see Fig. 8.5 (c). Indeed the fit for the remaining C_y-type-AF ordering fits well to the data. In this ordering scheme the magnetic moment points in $\pm y$-direction. In Fig. 8.1 *yellow arrows* indicate the direction of the magnetic moments at the Cr-sites.

Generally, there exist four different types of magnetic ordering which are allowed within the space group *Pbnm* for the magnetic Cr^{4+}-ions sitting at the 4*b*-sites. As the ordered state has to be symmetric according to the glide plane $x = \frac{1}{4}, \frac{3}{4}$ and the mirror plane $z = \frac{1}{4}, \frac{3}{4}$, only the $G_xA_yF_z$-, $A_xG_yC_z$-, $C_xF_yA_z$- and $F_xC_yG_z$- types of magnetic ordering are allowed belonging to the four different irreducible representations Γ_{1g} to Γ_{4g} from representation theory [89]. As the predominating magnetic mode in $CaCrO_3$ is of C_y-type, the magnetic structure of $CaCrO_3$ is of $F_xC_yG_z$-type according to the irreducible representation Γ_{2g}. However, even in a long measurement at the high-flux diffractometer D20 it was not possible to detect any (weak) intensities unambiguously indicating any other components besides the predominant C_y-type moment. However, an F_x component would be in accordance with the observation of weak ferromagnetism in the susceptibility. Therefore, there may be an additional, weak F_x component which is difficult to separate from the structural peaks. The results of the Rietveld-refinement are shown in Fig. 8.5 (b-c). The total magnetic moment at 2 K amounts to 1.094(37) μ_B using the form factor of the Cr^{4+}-ion [2].

The magnetic structure of the series $La_{1-x}Ca_xCrO_3$ has the irreducible representation Γ_{1g} ($A_xG_yC_z$) for x=0.00 to x=0.30 as was found in Ref. [319]. The predominating component is a magnetic G_y-mode with an magnetic moment of 2.49(2) μ_B for the compound with x=0.00. Thus, the magnetic moment points in the same direction ($\pm y$) as in $CaCrO_3$, which is the end compound of this series. The only difference is, that the magnetic moments are also aligned antiferromagnetically in *c*-direction, whereas the moments are aligned ferromagnetically in this direction in $CaCrO_3$. This might be connected to the metallic versus insulating properties of $CaCrO_3$ and $LaCrO_3$ respectively. Therefore, an examination of the whole series with respect to their electronic and magnetic properties would be of interest.

Furthermore, it should be remarked that the neutron measurements which are very sensitive to the oxygen content (see Chap. 2), show nearly no deviations from the stoichiometric formula $CaCrO_3$ if the calcium and oxygen occupations are refined (versus the Cr-occupation of 0.5): occ(O2)=1.007(4), occ(Ca)=0.502(3) and occ(O1)=$\frac{1}{2}$·occ(O2). Therefore, the $CaCrO_3$-sample measured in this work can be assumed to be close to stoichiometric, which is also corroborated by the high value for T_N.

Finally, orbital-order superstructure reflections have been searched for in a long powder neutron diffraction measurement at the high-flux diffractometer D20 at 2 K. In this

[2] A different chromium form factor has been used in the refinement reported in Ref. [318] yielding a slightly higher ordered moment.

	3.5 K	*60 K*	*90 K*	*120 K*	*300 K*
Lattice:					
a (Å)	5.2876(1)	5.2869(1)	5.2796(2)	5.2786(1)	5.2888(2)
b (Å)	5.3270(1)	5.3258(1)	5.3154(2)	5.3131(1)	5.3169(2)
c (Å)	7.4279(1)	7.4309(2)	7.4587(2)	7.4655(2)	7.4858(3)
Atoms:					
x(Ca1)	0.9930(5)	9919(6)	0.9919(13)	0.9942(10)	0.9950(18)
y(Ca1)	0.0330(5)	0.0328(5)	0.0315(7)	0.0322(5)	0.0296(10)
z(Ca1)	0.25	0.25	0.25	0.25	0.25
x(Cr1)	0	0	0	0	0
y(Cr1)	0.5	0.5	0.5	0.5	0.5
z(Cr1)	0	0	0	0	0
x(O1)	0.0634(4)	0.0632(4)	0.0629(6)	0.0630(5)	0.0603(10)
y(O1)	0.4900(4)	0.4901(4)	0.4888(6)	0.4898(5)	0.4896(9)
z(O1)	0.25	0.25	0.25	0.25	0.25
x(O2)	0.7138(3)	0.7141(3)	0.7140(5)	0.7133(4)	0.7147(6)
y(O2)	0.2857(3)	0.2856(3)	0.2868(4)	0.2868(3)	0.2856(5)
z(O2)	0.0328(1)	0.0329(2)	0.0322(3)	0.0323(2)	0.0321(4)
B (Å^2):					
B(Ca1)	0.50(4)	0.52(4)	0.58(6)	0.64(4)	0.99(8)
B(Cr1)	0.57(4)	0.41(4)	0.32(6)	0.33(5)	0.55(7)
B(O1)	0.63(3)	0.62(4)	0.53(5)	0.47(4)	0.86(8)
B(O2)	0.64(3)	0.59(3)	0.53(4)	0.63(3)	0.75(5)
Fit:					
R	2.68%	2.96%	4.08%	3.29%	5.35%
R$_w$	3.43%	3.79%	5.17%	4.19%	6.76%

Table 8.3: Results of the rietveld refinement of the SPODI powder neutron diffrection measurements of $CaCrO_3$ at different temperatures.

measurement, superstructure reflections could not be observed and can be excluded with an accuracy of 10^{-3} of strong fundamental reflections. Also a refinement of the SPODI high-resolution data with an orbital order model similar to YVO_3 did not yield any evidence for such kind of orbital ordering.

resistivity measurements

The electrical resistivity ρ was measured on a pellet of $CaCrO_3$-powder cold-pressed at 12.5 kbar. The resistivity has a characteristic semiconductive developing but with rather small values at room-temperature; see Fig. 8.6. Moreover the resistivity tends to a finite value for T→0, which is a real effect and not due saturation of the voltmeter as the measured voltage (< 0.04 V) remains two orders of magnitude below the saturation limit of 3 V. This finite resistance at low temperatures is indicative for itinerant electron behaviour. The overall semiconductive temperature dependency may be dominated by grain boundary effects. On the first cooling there is a jump at about 90 K which may be caused by cracks within the pellet induced by strains occurring at the first order phase transition. On heating again, as well as on further cooling and heating cycles, this jump vanishes nearly completely (see Fig. 8.6). It should be noticed, that a similar jump was observed in the resistivity of the *metallic* $CaCrO_3$-sample of Ref. [305]. As the jump is exactly at the same temperature as in the pellet measured in this work both samples most likely exhibit the same Néel-temperature. This shows, that the single crystalline

sample of Ref. [305] has a similar stoichiometry as minor deviations from perfect stoichiometry usually alter the Néel-temperature in transition metal oxides distinctly - see for example the $La_{2-x}Sr_xCuO_4$ or the $La_{1-x}Sr_xTiO_3$ phase diagram [31, 2].

In the inset of Fig. 8.6 the Arrhenius plot of ρ is shown. It can be seen that ρ proceeds to a finite value for T $\rightarrow$ 0 K and that the activation energy Δ vanishes for T $\rightarrow$ 0 K. The second inset (within the first) shows this activation energy calculated from a simple $\rho = \rho_0 \cdot exp(\Delta/(2 \cdot k_B \cdot T))$ model for the second measurement (without a jump of ρ). Below the phase transition, Δ seems to accelerate its decrease towards 0 eV. Of course, this is a too simple model for any quantitative result but at least it shows, that $CaCrO_3$ is not a simple insulator or semiconductor.

Concluding, the question whether single crystalline and bulk $CaCrO_3$ is metallic or insulating could not be unambiguously solved by resistivity measurements of polycrystalline pellets. On the one hand, the temperature dependency $\partial\rho/\partial$T < 0 is an indication for insulating or semiconductive behaviour, but it may be caused by grain boundary-effects and by barrier oxide layers on the surface of the powder particles. On the other hand, the lack of a divergence of ρ for T $\rightarrow$ 0 K and the somewhat lower room-temperature values of ρ are indications for an itinerant electron behaviour of $CaCrO_3$.

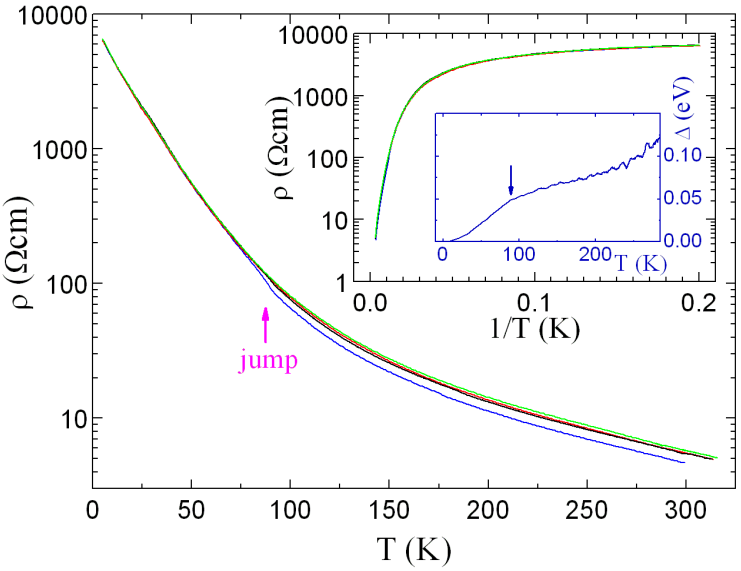

Figure 8.6: Electrical resistivity ρ of $CaCrO_3$ measured with a current of 1 μA. The first inset shows the arrhenius plot; the second inset (within the first) shows the activation energy Δ calculated from a simple model. Four heating/cooling measurements have been performed: 1st cooling (blue), 2nd heating (red), 3rd cooling (black), 4th heating (green).

Finally, it is interesting to note, that in single crystals, metallic properties have been observed [305], whereas in polycrystalline powders insulating properties have been observed [309]. Also in the polycrystalline powder samples of this work, the temperature dependency of the resistivity ρ exhibits a semiconductive character. The comparism with another Cr^{4+} compound - CrO_2 - reveals astonishing similarities. CrO_2 is a half metall with a metallic conductivity. But wheras bulk single crystalline films exhibit metallic properties [320], cold-pressed polycrystalline powders exhibit insulating properties. In cold-pressed CrO_2-powders the different particles have a natural barrier oxide layer of Cr_2O_3 covering them. This insulating Cr_2O_3-layers have a thickness of 2-3 nm which is sufficient for turning the properties of the whole pellet insulating [320, 321]. Such an insulating temperature dependency of the electrical resistivity of $CaCrO_3$ could have been observed for similar reasons in Ref. [309] and in this work. Possibly, the unusual oxidation state of the Cr^{4+}-ion leads in both compounds to a different oxygen stoichiometry at the surface. Therefore, the resistivity of polycrystalline $CaCrO_3$ may be governed by grain boundary effects.

optical measurements

In order to get more insight in the electronic properties of $CaCrO_3$ optical reflectivity measurements of a cold-pressed pellet of $CaCrO_3$-powder have been performed and analyzed by T. Möller in the spectral range between 7 meV and 0.9 eV at quasi-normal incidence; see also Ref. [318]. As is shown in Fig. 8.8 (a) the reflectivity $R(\omega)$ tends to 1 for $\omega \rightarrow 0$ which is typical for a metal. The additional peaks between 20 and 80 meV are phonons which are obviously strongly screened as could be expected for a metal.

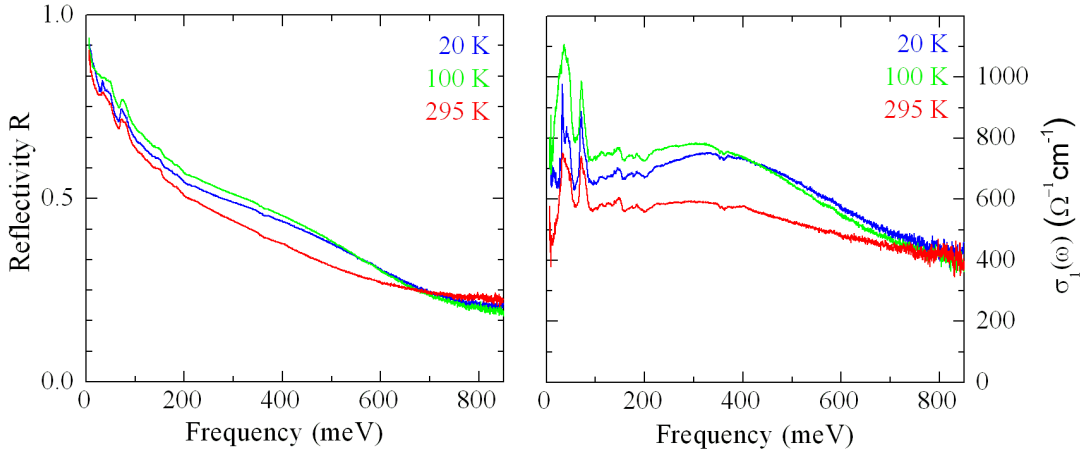

Figure 8.7: (a) Optical reflectivity R and (b) optical of conductivity σ_1 of $CaCrO_3$ measured by T. Möller [318].

Thus $R(\omega)$ clearly indicates the itinerant electron behaviour in $CaCrO_3$.

Furthermore, the real part $\sigma_1(\omega)$ of the optical conductivity has been calculated by T. Möller using Kramers-Kronig relations; see Fig. 8.8 (b). The fact, that a polycrystalline sample with finite grain size of 10-20 μm in average has been used for this measurement can explain the small decrease of $\sigma_1(\omega)$ for small values of $\omega \to 0$ since the wavelength of $\lambda = 20$ μm corresponds to a photon energy of about 60 meV. Also the broad peak around 350 meV could be attributed to excitations from the lower to the upper Hubbard band. For further, more detailed information, see Ref. [322].

Hence, the optical measurements reveal the metallic properties of $CaCrO_3$ with a moderate conductivity of the order of several hundred $\Omega^{-1}\mathrm{cm}^{-1}$.

magnetic susceptibility

The magnetic susceptibility has been measured by M. Isobe; see also Ref. [318]. The temperature dependency of χ above T_N is small and almost temperature independent which is indicative for itinerant magnetism. Therefore, these measurements corroborate the itinerant properties of $CaCrO_3$. Indeed, the magnetic susceptibility of $CaCrO_3$ has some similarities with the susceptibility in the metallic (Sr,Ca)RuO_3-system [323].

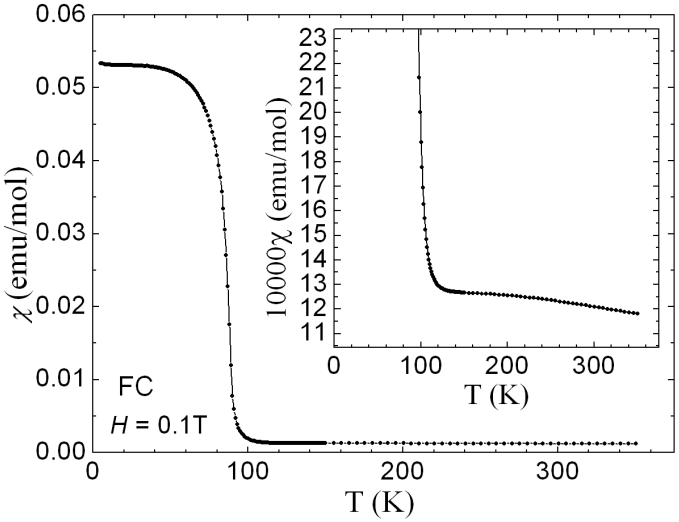

Figure 8.8: The magnetic susceptibility of $CaCrO_3$ measured by M. Isobe [318].

This itinerant scenario would also be in accordance with the observations in Ref. [310] where a magnetic moment μ_{eff} of 3.7 μ_B was obtained by fitting $\chi(T)$ to the Curie-Weiß-law. This value is distinctly higher than the measured value of 1.1 μ_B determined by neutron scattering in this work. Such a failure of the Curie-Weiß-law is usually indicative for a non-localized system.

band structure calculations
In order to understand the electrical and magnetic properties of $CaCrO_3$ better, S. V. Streltsov has performed band structure calculations using the structural data measured in this work; see Ref. [318]. The results of the LSDA calculation for $CaCrO_3$ retrieve metallic solutions for all possible types of (collinear, commensurate) magnetic ordering. Due to these calculations, the C-type antiferromagnetic structure has the lowest energy. This is in accordance with the magnetic structure measured in this work. The calculated magnetic moment of about 1.5 μ_B is only little higher than the measured moment of about 1.1 μ_B. A value lower than 2 μ_B can be explained by strong pd-hybridisation. In these LSDA calculations, the C-type antiferromagnetic ordering could be explained by the interplay of three different exchange constants J, J' and J" - see Fig. 8.9. Here, J is the exchange constant between the nearest neighbours (nn) within the *ab*-plane. J' is a similar coupling constant between nearest neighbours in *c*-direction and J" is the next nearest neighbour (nnn) exchange constant in a diagonal direction; see Fig. 8.9. S. V. Streltsov found strong antiferromagnetic nn coupling constants J = 80 K and J' = 60 K. This can not explain the observed magnetic structure, as it would cause a G-type antiferromagnetic structure as measured for example for insulating $LaCrO_3$ [319]. But the nnn coupling constants were found to be remarkably high: J" = 33 K. Since there are four times more nnn than nn, the nnn coupling overrules the nn coupling (J is also AFM). This explains the C-type antiferromagnetic order in $CaCrO_3$. Furthermore, the flattening of the octahedra observed in this work fits to this scenario since it yields an increased d_{xy} occupation thereby lowering J'.

S. V. Streltsov also made LSDA+U calculations (Ref. [318]). In these calculations $CaCrO_3$ is insulating and the resulting C-type magnetic structure is related to orbital ordering very similar as in the G-type orbital ordered phase of YVO_3 which leads to C-type antiferromagnetism [296-299].

On the one hand these two solutions were the two possibilities right from the beginning, on the other hand these calculations show, that the C-type antiferromagnetism can be well explained in a metallic scenario.

8.1.4 Discussion

In the literature, the descriptions of the electronic properties of $CaCrO_3$ range from metallic [305, 308] to insulating properties [309, 310]. Whereas metallic properties have been observed in single crystals, all polycrystalline powders exhibit insulating properties. A similar difference in the behaviour of ρ in single- and polycrystalline samples has also been observed for the *metallic* Cr^{4+} compound CrO_2 [320, 321]. This may be caused by the unusual oxidation state of the Cr^{4+} ion leading to an oxidation at the surface. Thus, the resistivity of polycristalline samples may be governed by grain boundary effects also in $CaCrO_3$ and, indeed, there is strong evidence that bulk $CaCrO_3$ is metallic.

The first indication for an itinerant electron behaviour in $CaCrO_3$ is the finite value of ρ for $T \rightarrow 0$ K.

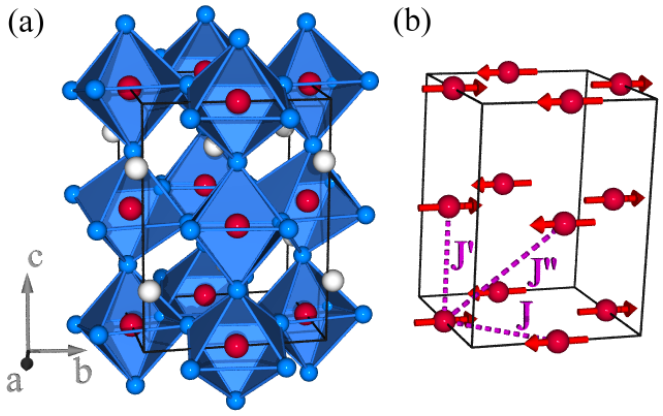

Figure 8.9: (a) The measured crystal structure of $CaCrO_3$ and (b) a model of the measured magnetic structure together with the exchange interactions J, J' and J" used in the band structure calculations of S. V. Streltsov [318].

The metallic scenario of $CaCrO_3$ is, furthermore, supported by the fact that the *metallic* samples of Ref. [305] show an anomalous jump in the resistivity at the same temperature, 90 K, as was also observed in the resistivity in this work. It is very unlikely that the transition temperature of the *metallic* samples in Ref. [305] is exactly as high as in stoichiometric samples, if these were not stoichiometric. Therefore, these *metallic* samples in Ref. [305] can be regarded as stoichiometric $CaCrO_3$.

The small and almost temperature independent magnetic susceptibility is also indicative for itinerant electron behaviour. And the failure of Curie-Weiss fits - 3.7 μ_B reported in Ref. [310] versus 1.1 μ_B measured in this work - corroborate the non-localized electron behaviour scenario.

Moreover, the optical reflectivity measurements of the cold-pressed $CaCrO_3$-sample of this work, which were performed and analyzed by T. Möller, revealed the metallic nature of $CaCrO_3$ as the reflectivity tends towards 1 for $\omega \rightarrow 0$.

Even, if band structure calculations do not give a clear picture (LSDA: metal, LSDA+U: insulator), at least the LSDA calculations are able to explain the C-type antiferromagnetic properties of $CaCrO_3$ also in a metallic scenario.

8.1.5 Conclusion

Concluding, a comprehensive structural, magnetic and electronic study of $CaCrO_3$ including synchrotron and neutron measurements as well as macroscopic resistivity, susceptibility and optical reflectivity measurements has been performed and revealed the unique nature of $CaCrO_3$. The neutron measurements reveal a C_y-type antiferromagnetic ordering with a total antiferromagnetic moment of about 1.1 μ_B at 2 K. From the structural data a compression of the CrO_6-octahedra in c-direction with an concomitant elongation in a- and b-direction was found below T_N indicating a higher occupation of the d_{xy}-orbital. Finally, the optical reflectivity measurements [318] reveal the itiner-

ant properties of $CaCrO_3$. However, $CaCrO_3$ is not a typical metal and close to the itinerant/localized crossover, but on the metallic side. Hence, $CaCrO_3$ possibly is the unique example of an antiferromagnetic and metallic transition metal oxide with a fully three-dimensional crystal structure.

8.2 Magnetic order in $PbCrO_3$

8.2.1 Introduction

$PbCrO_3$ is an undistorted perovskite with a simple cubic crystal structure. In Ref. [324] insulating properties were reported for this compound with a room-temperature value of ρ which is three orders of magnitude higher than that for $CaCrO_3$ and an activation energy of 0.27 eV. Also in this compound ρ tends to a finite value for $T \rightarrow 0$ K after reaching a maximum value around 100 K. At this temperature, where the anomalies in the electrical resistivity appear, also the magnetic susceptibility shows its sharpest increase. However, a Néel-temperature of 160 K is reported in the same study [324]. In Ref. [325] the Néel-temperature was observed at 240 K. But in this neutron scattering study a small intensity tail was attributed to the onset of magnetic ordering and the error bars are already rather large at 200 K with about 160 K being the next data point below. As the powder samples in the neutron scattering study [325] contain impurity phases but no impurity phases have been detected by X-rays within the single crystalline samples in the thermodynamics and transport study [324], the Néel-temperature of 160 K [324] is probably more reliable.

8.2.2 Experimental

Polycrystalline samples of $PbCrO_3$ were grown by a high pressure technique by M. Azuma. Unfortunately these samples contain impurity phases as was determined by X-rays. Powder neutron diffraction measurements have been performed at the G4.1 diffractometer at the reactor Orphée in Saclay ($\lambda = 2.4226$ Å). The lattice parameter have been studied with synchrotron radiation X-ray powder diffraction at beamline B2 at Hasylab/DESY in Hamburg ($\lambda = 0.49342$ Å).

8.2.3 Results

powder X-ray diffraction measurements
Using synchrotron radiation, temperature dependant powder X-ray diffraction measurements have been performed. A rather high incident energy has been chosen in order to penetrate these plumbiferous samples during the measurement in Debye-Scherrer geometry. As the sample contains some impurity phases it was not possible to decide whether $PbCrO_3$ has a lower than cubic symmetry or not; see Fig. 8.10 (b). In the rietveld refinement the thermal displacement parameters attained non-physical large values. It could not be determined whether this is due to bad sample quality or other effects (absorbtion). The temperature dependency of the a-lattice parameter is shown in Fig. 8.10 and shows a very linear developing.

neutron measurements
Powder neutron diffraction measurements have been performed at 1.5 K and at 200 K;

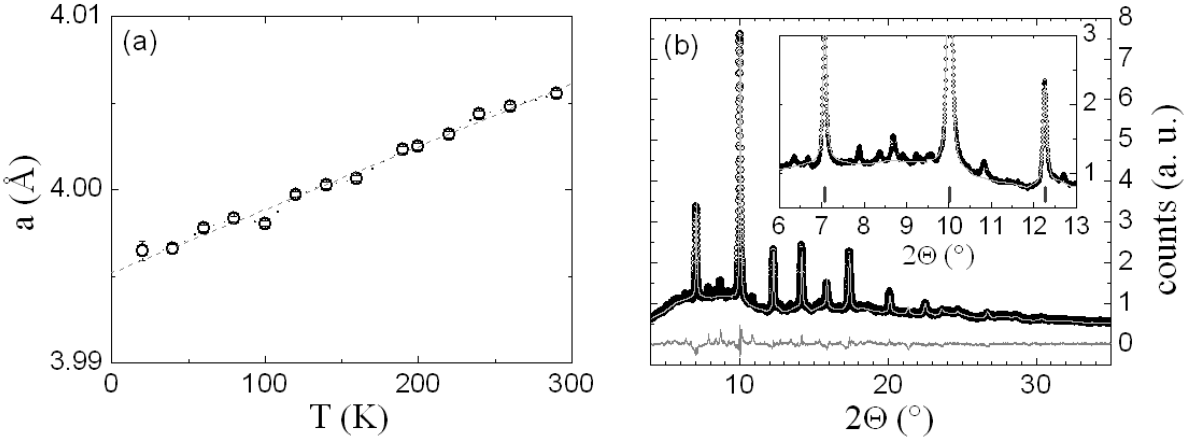

Figure 8.10: (a) a-lattice parameter of $PbCrO_3$. (b) Synchrotron radiation powder X-ray diffraction pattern measured at 13 K (beamline B2); *black:* measured intensities I_{obs}, *light gray:* rietveld fit I_{calc}, *gray:* $I_{obs} - I_{calc} + I_{offset}$; *dark gray:* positions of bragg peaks (only in the inset).

see Fig. 8.11. Contrarily to the neutron scattering study in Ref. [325] the magnetic peaks have already vanished at 200 K. This can be seen in Fig. 8.11 (b). On the one hand, this would be in accordance with the observations in single phase single crystals of Ref. [324]. On the other hand it is possible that T_N is somewhat lower in the sample measured in this work due to a different sample quality. The magnetic moment measured at 1.5 K amounts to 2.09(33) μ_B per Cr^{4+}-ion. This value is close to the value of 1.9 μ_B reported in Ref. [325]. Therefore, the sample quality of the sample studied in Ref. [325] and in this work may be comparable. In Ref. [325] it was noted that the sample quality was bad (impurity phases) which resulted in relatively poor-quality intensity data [325]. Therefore, it can be assumed that the transition temperature could not be determined as accurately as in Ref. [324] and that the value of 160 K for T_N determined in Ref. [324] is more reliable. Both values of the antiferromagnetic moment are close to the spin value expected for a $3d^2$ system.

8.2.4 Conclusion

Concluding, synchrotron radiation studies and powder neutron diffraction measurements have been performed on a sample of $PbCrO_3$, which contains some impurities. A G-type antiferromagnetic moment of 2.09(33) μ_B has been measured at 1.5 K confirming the observations in Ref. [325]. However, opposed to the observations in Ref. [325], at 200 K there is already no sign of magnetic ordering. The rather high magnetic moment suggests that $PbCrO_3$ is more insulating than $CaCrO_3$ which was also observed in resistivity measurements in Ref. [324]. The reason for this more insulating behaviour in spite of the less distorted cubic structure most likely is the much larger unit cell of $PbCrO_3$ compared to the pseudocubic unit cell of $CaCrO_3$ which supports localization effects.

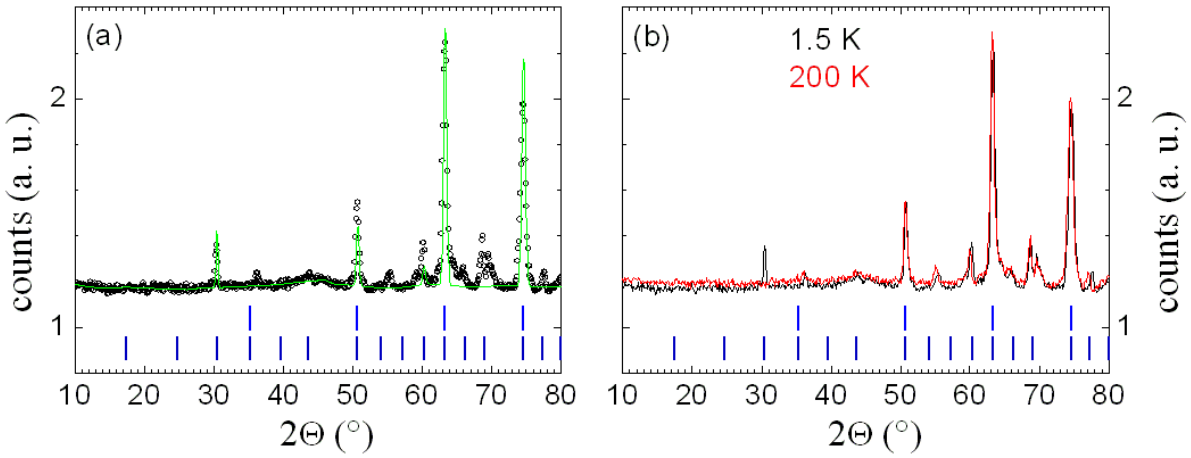

Figure 8.11: (a) Powder neutron diffraction pattern measured at 1.5 K (G4.1 diffractometer); *black:* measured intensities I_{obs}, *green:* rietveld fit I_{calc}, *blue/dark blue:* positions of structural/magnetic bragg peaks. (b) Comparison between 1.5K and 200 K data.

The pseudocubic lattice parameters of $CaCrO_3$ are around 3.75 Å at room-temperature whereas the cubic lattice parameters are close to 4.00 Å.

8.3 Magnetic order in $SrCrO_3$

8.3.1 Introduction

$SrCrO_3$ which only has slightly larger lattice parameter ($a \approx 3.82$ Å) compared to the pseudocubic unit cell of $CaCrO_3$, but which already has an undistorted cubic crystal structure like $PbCrO_3$, might also be of interest with regard to the coexistence of antiferromagnetism and metallic properties.

More than 40 years ago, in the first studies, metallic properties have been observed for $SrCrO_3$ between room-temperature and liquid helium temperature [326]. In the same study the magnetic properties of $SrCrO_3$ have been described in terms of paramagnetism. There are not so many studies of $SrCrO_3$ due to the elaborate high pressure synthesis technique which renders the availability of all these chromates rather difficult. However, in the last few years $SrCrO_3$ has re-attracted considerable interest [310, 306, 307, 327]. Regarding the magnetism of the d^2-system $SrCrO_3$, there are already two conflictive observations within the same group as was already stated in Chapter 8.1 [306, 307]. In Ref. [310] a fit of the magnetic susceptibility to the Curie-Weiss law yields a too large value of 8.3 μ_B indicating a failure of the Curie-Weiss law similar to the case of $CaCrO_3$. This supports a non-localized electronic picture for $SrCrO_3$ [310]. In the same study it was also reported that the anomalous electronic and magnetic properties of $SrCrO_3$ are driven by Cr-O bond-length fluctuations due to Cr-O bond lengths differing from ionic bonds as well as from covalent or metallic bonds [310].

In Ref. [307] phase separation has been reported for $SrCrO_3$ at low temperatures. A further tetragonal phase ($P4/mmm$) appears beneath the cubic high-temperature phase. Whereas no magnetic peaks have been observed in powder neutron diffraction measurements of Ref. [306], weak magnetic peaks within a very noisy background were observed in powder neutron diffraction measurements of Ref. [307]. These magnetic peaks were interpreted by orbital ordering in the tetragonal phase in which the occupation of a d_{xy} orbital was assumed. Due to this orbital occupation a spin ordering equivalent to C-type antiferromagnetic ordering was fitted to the data. Therefore, the magnetic order was supposed to occur only within the tetragonal phase and it was claimed, that no magnetic ordering was observed for the cubic phase.

8.3.2 Experimental

Polycrystalline samples of $SrCrO_3$ were grown by M. Isobe using a high pressure and high temperature technique. One of these samples, *sample A*, is contaminated by impurity phases but the other *sample B* has only minor impurity contributions (which may be neglected). Powder neutron diffraction measurements have been performed at the SPODI diffractometer at the FRM-II in Garching ($\lambda = 1.548$ Å, *sample A*) and at the D1A diffractometer at ILL in Grenoble, France ($\lambda = 1.3897$ Å, *sample B*).

8.3.3 Results

neutron measurements

Both samples have been measured by means of powder neutron diffraction between 100 K and about 3 K; see Fig. 8.12. In both samples phase separation was observed at lowest temperature similar to the observations in Ref [307]. However, at higher temperatures (35 K) the tetragonal phase has already vanished. The diffraction patterns could be described by a cubic ($Pm\bar{3}m$) and a tetragonal phase ($P4/mmm$) with $a, b > c$. Since the atoms are all sitting at high symmetry positions in both phases, no refinement of the atomic positions was necessary. The volume ratio of both phases was fitted and the magnetic moment was attributed only to the tetragonal phase. In Tab. 8.4 the results of the Rietveld refinement are shown.

The Rietveld refinement yields a value of about 30.4% for the volume fraction of the tetragonal phase in *sample A* at 3 K. Fig. 8.12 (c) shows the related Rietveld fit. In the 3 K data there is a small magnetic peak visible which is temperature dependent as it vanishes at 100 K; see Fig. 8.12 (f). This peak could be indexed as a $(\frac{1}{2}\ \frac{1}{2}\ 0)$ peak and a a C-type antiferromagnetic (AFM) structure model could be fitted to the data. From the comparison of fits with magnetic moments parallel to the c_{tet}-direction (*green line*) or within the a_{tet}/b_{tet}-plane (*blue line*) a C_z antiferromagnetic structure could be unambiguously identified: For C_x-type AFM ordering the calculated intensity of the $(\frac{1}{2}\ \frac{1}{2}\ 0)_{tet}$-peak is too low and for the $(\frac{1}{2}\ \frac{1}{2}\ 1)_{tet}$-peak the calculated intensity is too large. In case of C_z-type AFM ordering the magnetic moment is more parallel to the $(\frac{1}{2}\ \frac{1}{2}\ 1)$-scattering vector which has a large L-component. Thus, the scattered intensity of this reflection is much reduced (compare Chap. 3) which is in accordance with the experiment; see Fig. 8.12 (d). This result is contrarily to the observations in Ref. [307] where a moment within the *ab*-plane was found.

In *sample B* the refinement yields a value of only 17.5% for the tetragonal phase. Such a sample dependent fraction of the tetragonal phase was also observed in Ref. [307]. In *sample B*, this small volume fraction of the tetragonal phase makes the detection of the small magnetic moment even harder as the magnetic moment is smaller than 1 μ_B. Therefore, a distinct magnetic peak could *not* be detected. The data and fit are shown in Fig. 8.12 (e). Nevertheless, it was possible to fit a magnetic moment of similar value as for the tetragonal phase in *sample A* to these data. This shows, that the magnetic moment is really related to the tetragonal phase (and its volume fraction) and not to the cubic phase: when the tetragonal phase has nearly vanished, also the magnetic peaks have vanished. This was already assumed in Ref. [307] but without having the data for comparison [3].

8.3.4 Conclusion

In conclusion, powder neutron diffraction measurements have been performed for two different $SrCrO_3$-samples. At lowest temperatures ($\approx$ 3 K) both samples exhibit phase

[3] Probably, in Ref. [307] it was implicitly assumed that the cubic phase would exhibit G-type antiferromagnetism and not C-type.

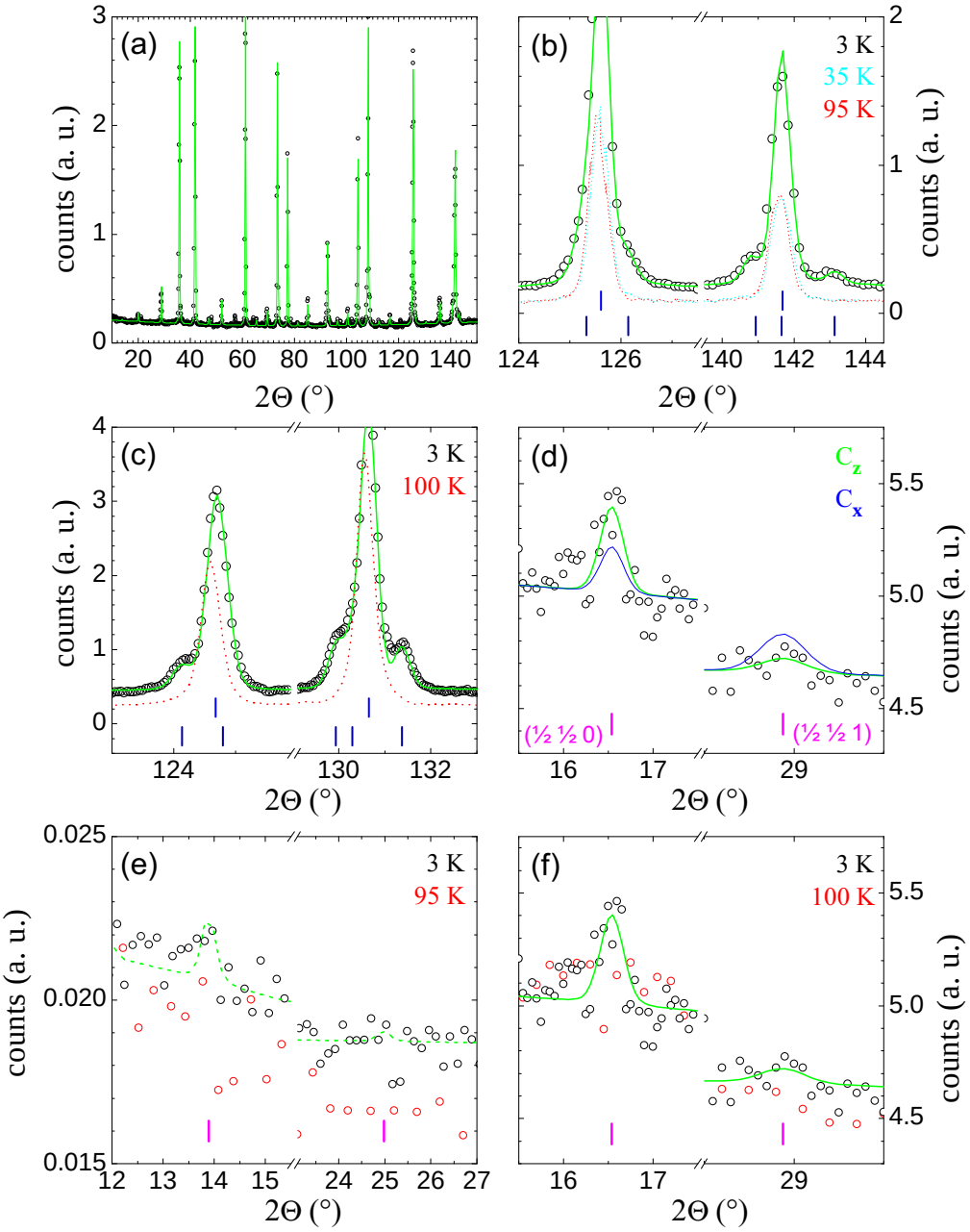

Figure 8.12: (a,b,e) Powder neutron diffraction pattern measured at 3.5 K (*black*), 35 K (*cyan*) and 95 K (*red*) at the D1A diffractometer ($\lambda = 1.3897$Å) and (c,d,f) measured at 3 K (*black*) and at 100 K (*red*) at the SPODI diffractometer ($\lambda = 1.548$ Å). The *green* lines are fits; *blue*/*dark blue*/*magenta bars*: Bragg positions of the cubic/tetragonal/magnetic phase. *Green* and *blue lines* in (d): fits for C_z- and $C_{x/y}$-type AFM.

separation similar to the observations in Ref. [307]. But whereas the low-temperature-

sample	***A***	***A***	***B***	***B***	***B***
T:	***3 K***	***100 K***	***3.5 K***	***35 K***	***95 K***
Cubic phase					
a (Å):	3.81028(7)	3.81151(7)	3.81230(6)	3.81246(8)	3.81306(8)
Tetragonal phase					
a (Å):	3.82117(19)	-	3.82257(2)	-	-
c (Å):	3.79392(23)	-	3.79447(4)	-	-
vol% :	30.4(8)%	0	17.5(8)%	0	0
M (μ_B/***Cr***$^{4+}$***):***	0.83(28)	0	≈0.87(45) ‡	0	0

Table 8.4: Lattice parameter, volume fraction and magnetic moment of the two phases in $SrCrO_3$. ‡: Due to the small volume fraction of the tetragonal phase in the D1A measurement, a magnetic peak could hardly be detected. Nevertheless, the (not reliable) value of the fit is shown here.

tetragonal (LTT) phase amounts to 30.4% in the first sample, the second sample exhibits only 17.5% of the LTT phase. At these low temperatures a small magnetic peak can be observed for the first sample but not for the second. This gives evidence for the connection between the magnetic and the tetragonal phase - if the volume fraction of the LTT phase is sufficient, a weak magnetic peak can be observed, and if the fraction of the LTT phase gets further diminished, also this weak magnetic peak vanishes or gets hidden in the background. Furthermore, the type of magnetic ordering could be unambiguously determined as a C_z-type AFM ordering with moments parallel to the c_{tet}-axis. This result is different to the observations in Ref. [307]. Also the magnetic moment, which was not determined in the noisy measurement of Ref. [307] could be determined roughly in this work. The C_z-type AFM moment amounts to 0.83(28) μ_B. This moment is of the order of the AFM moment of 1.1 μ_B of the chromium ion in $CaCrO_3$ and even a little lower. With respect to these new results, especially the low ordered moment, the situation in the LTT phase of $SrCrO_3$ may be similar as in $CaCrO_3$ and antiferromagnetism and metallic properties may coexist in this phase. Therefore, further examination of the LTT phase of $SrCrO_3$ would be of interest. But for these purposes, samples with a volume fraction of 100% of the tetragonal phase would be desirable in order to avoid any biasing by the cubic phase. All samples used in this work do not meet these requirements, but the existence of such a sample has been reported in Ref. [307].

8.4 Pressure studies on chromates

8.4.1 Introduction

High pressure studies provide a powerful tool to probe the behaviour of condensed matter as a function of decreasing inter-atomic distance omitting any complications introduced by the change of chemistry. An example may be the doping of chromium into VO_2 which has a similar effect on the structure (dimerized M2-phase) as the application of pressure, but which introduces a different element into this vanadate for example causing changes in ESR measurements [328]. In this work, high pressure synchrotron radiation experiments have been performed in order to determine the lattice parameter of $CaCrO_3$ and $SrCrO_3$ as a function of pressure.

For determination of the bulk modulus B_0, its pressure derivative B_0' and the volume at ambient pressure V_0, a third-order Birch-Murnaghan equation of state has been fitted to the data.

$$P = \frac{3}{2} \cdot B_0 \times \left[\left(\frac{V_0}{V} \right)^{7/3} - \left(\frac{V_0}{V} \right)^{5/3} \right] \times \left(1 + \frac{3}{4} \cdot (B_0' - 4) \cdot \left[\left(\frac{V_0}{V} \right)^{2/3} - 1 \right] \right) \quad (8.1)$$

Here, V_0 is the volume at 0 GPa, B_0 is the bulk modulus at 0 GPa and B_0' is its pressure derivative (see for example Ref. [329-331]).

8.4.2 Experimental

High pressure studies have been performed on the chromates $CaCrO_3$ and $SrCrO_3$ [4] discussed in Chapters 8.1 and 8.3. The pressure dependent lattice parameter have been measured by means of angle dispersive synchrotron radiation powder diffraction at beamline ID09A at ESRF in Grenoble, France ($\lambda = 0.413115$ Å). Diamond anvil cells of the cylinder-piston type with a He gas driven membrane for pressure generation have been used with He as the pressure medium. The pressure was determined by the ruby fluorescence method. And the scattered intensities have been detected with an image plate detector. Such a measured intensity map is shown in Fig. 8.13. Data reduction has been performed with the FIT2D software [141].

8.4.3 Results

$CaCrO_3$

The unit cell volume of $CaCrO_3$ as a function of pressure if plotted for two different temperatures in Fig. 8.14 (a). For rising pressures, the unit cell volume at 49 K $< T_C$ tends towards the value at room-temperature. Two diffraction patterns measured at low and high pressures are shown in Fig. 8.14 (g). By comparing the FWHM of the Bragg peaks at 2 GPa and at 33 GPa the pressure broadening effect is illustrated quite

[4] *sample B*

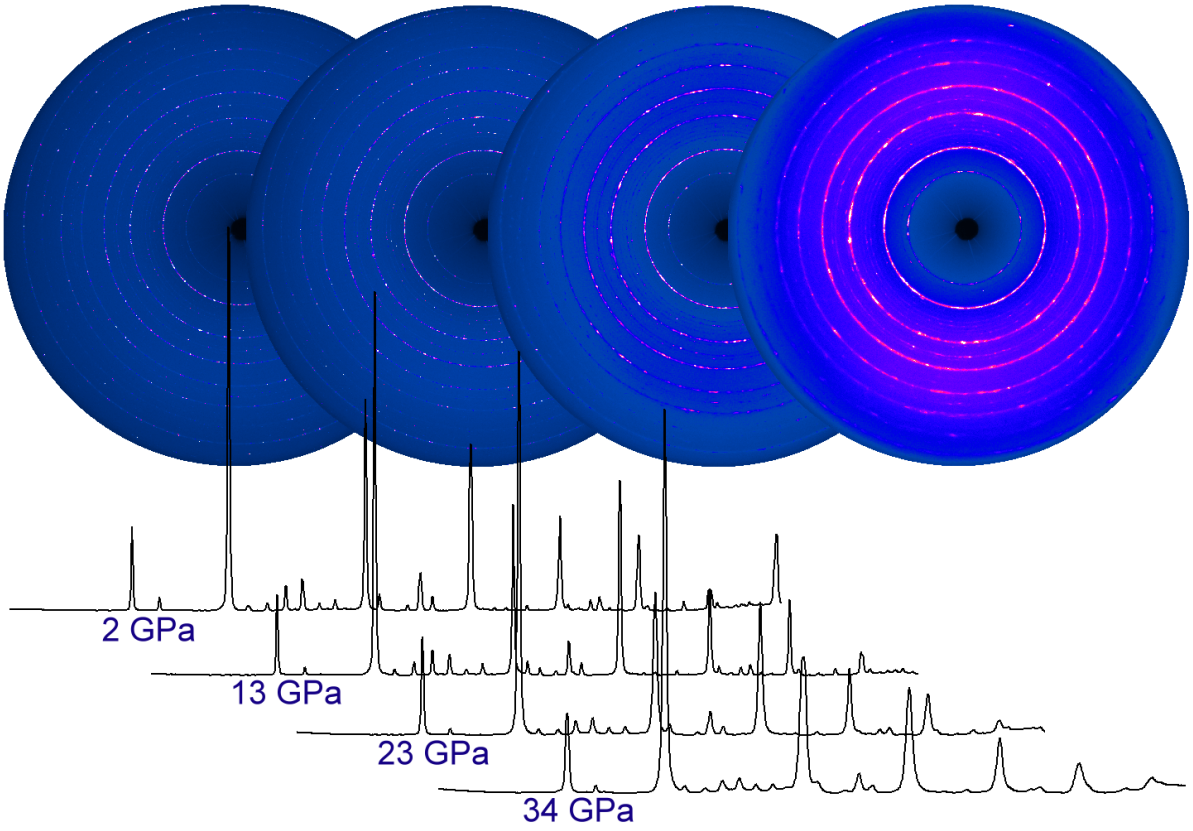

Figure 8.13: Diffraction patterns of $CaCrO_3$ for different pressures measured at room-temperature indicating the pressure-induced peak broadening.

impressively. This pressure broadening effect is caused, if the hydrostatic conditions get worse at higher pressures and was also initially shown in Fig. 8.13.

In Fig. 8.14 (b) the ratio of the lattice parameter at a given pressure to the value at ambient pressure is shown. This value is a measure for the compressibility of the related lattice parameter or axis. As can be seen, the c-lattice parameter is less compressible than a and b. This is somehow astonishing since the c-lattice parameter exhibits a strong anomalous drop on cooling; see Chapter 8.1. Below the phase transition, at 49 K the a-lattice parameter becomes also less compressible and only b stays the most compressible axis. Around 15 GPa a crossover of the pseudocubic c_c and b_c lattice parameter can be observed. This resembles on the O-orthorhombic $\rightarrow$ O'-orthorhombic phase transition on cooling where a crossing of the pseudocubic c_c and a_c lattice parameter can be observed; see Chap. 8.1. But here, c_c behaves opposite and crosses the other pseudocubic b_c lattice parameter.

Unfortunately, preferred orientation effects can not be avoided in such kind of synchrotron measurements as the used sample volume within these pressure cells is very small. Therefore, the atomic parameters could not be fitted to the data. Thus, the lattice parameter are the only reliable information which can be drawn out of these

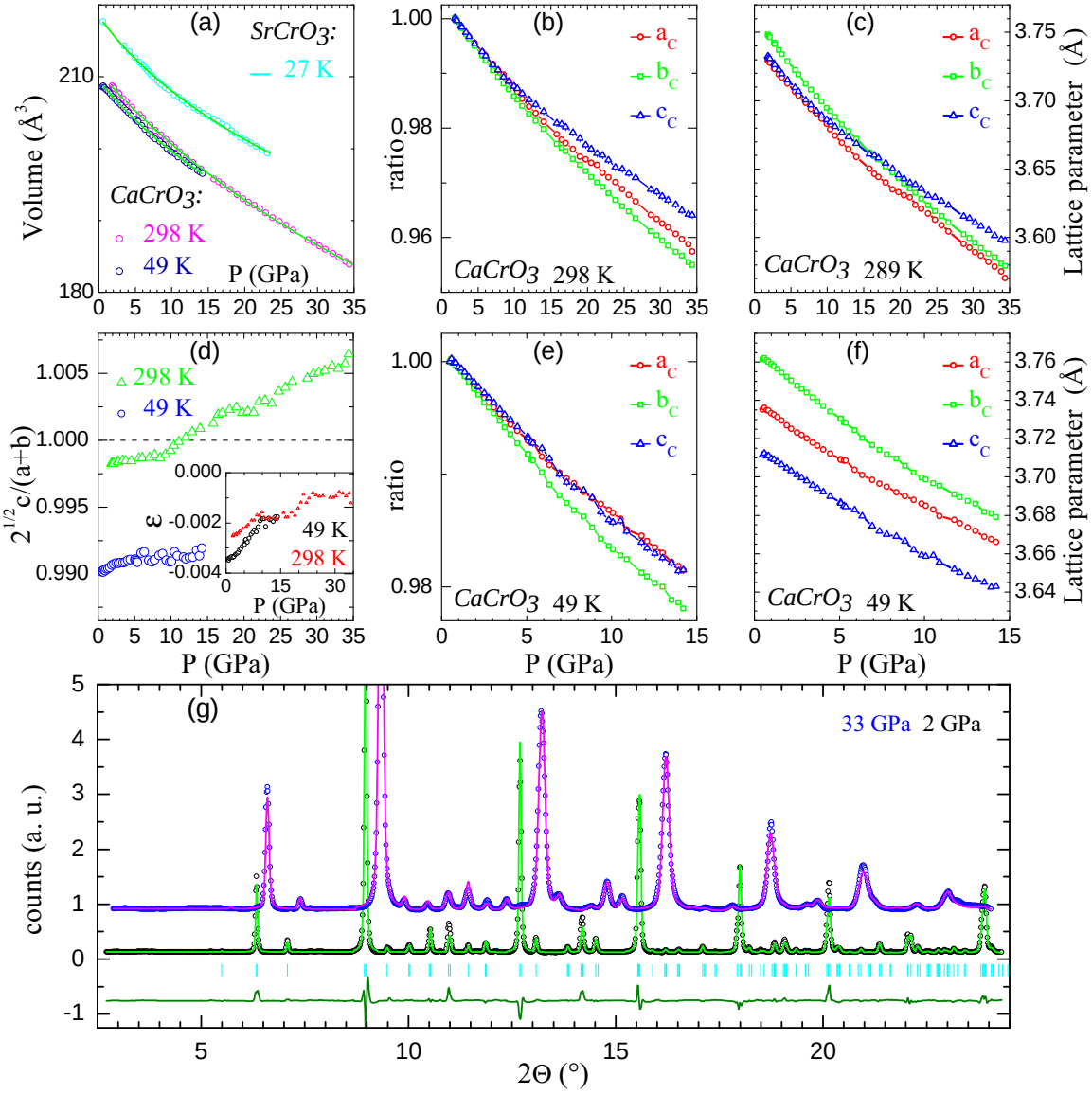

Figure 8.14: (a) Unit cell volume of $CaCrO_3$ at 298 K and 49 K and of $SrCrO_3$ (cubic) at 27 K; *green lines*: fits to the Birch EOS. (b) Ratios of the lattice parameter $a/a_{(0GPa)}$ etc. of $CaCrO_3$ measured at 298 K. (c) Pseudocubic lattice parameter of $CaCrO_3$ at 298 K. (d) Ratio $\sqrt{2} \cdot c/(a+b)$; inset: $\varepsilon = (a-b)/(a+b)$. (e) Ratios of the lattice parameter $a/a_{(0GPa)}$ etc. of $CaCrO_3$ measured at 49 K. (f) Pseudocubic lattice parameter of $CaCrO_3$ at 49 K. (g) Powder diffraction patterns of $CaCrO_3$ at 298 K; *black/blue circles*: 2 and 33 GPa data respectively; *green/magenta lines*: corresponding Rietveld fits of 2 and 33 GPa data respectively; *cyan bars*: Bragg positions at 2 GPa; *dark green line*: I_{obs}-I_{calc} for the '2 GPa refinement'.

measurements and interpretation has to be done without knowledge of the atomic positions. Either pure structural effects like CrO_6-octahedral tilts or orbital occupations inducing octahedral distortions can have impact on the lattice parameter. Generally, with higher pressure orbital ordering should be diminished and a metallic state should be supported. As $CaCrO_3$ is close to the itinerant/localized crossover, pressure may have a remarkable effect on the electronic structure.

The reason for the *b*-axis being the most compressible axis at all temperatures probably can have something to do with the octahedral tilts. The CrO_6-octahedra are tilted around the *b*-axis. If the octahedral tilts decrease with increasing pressure, this should stabilize the *c*- and also the *a*-axis. As was observed in the neutron and X-ray diffraction measurements of this work, the CrO_6-octahedral tilts have a constant value of about 10° for all measured temperatures (see Chap. 8.1). Thus, there is the same initial situation at 298 K and 49 K leading to the same compressibility of *b*. However, the octahedral rotations should be more stable (relative to the tilts) then, since decreasing rotations would also stabilize the *a*- and *b*-lattice parameter. If this simple interpretation is right, *a* and *b* should become more equal. Indeed, this is the case for both temperatures as can be seen in Fig. 8.14 (c) and (f). Furthermore, this theory is supported by the pressure dependence of the ratio $c \cdot \sqrt{2}/(a+b) \equiv c_{\mathrm{cub}}/\frac{a_{\mathrm{cub}}+b_{\mathrm{cub}}}{2}$ with the pseudocubic lattice parameters $a_{\mathrm{cub}} = a/\sqrt{2}$, $b_{\mathrm{cub}} = a/\sqrt{2}$ and $c_{\mathrm{cub}} = c/2$, see Fig. 8.14 (d). For both temperatures, this ratio exhibits an increase with increasing pressure (and even a crossover for the room-temperature measurement). Furthermore the 'orthorhombicity', i. e. the absolute value of the orthorhombic splitting $\varepsilon = (a-b)/(a+b)$, decreases with increasing pressure as can be seen in the inset of Fig. 8.14 (d). However, up to the highest pressures measured, the symmetry stays *Pbnm* and in the diffraction patterns there is no indication for a transition to a higher symmetry like for example $P4/mmm$ as in $SrCrO_3$ or $I4/mcm$ as in $Sr_{1-x}Ca_xCrO_3$ with x = 0.4-0.5 [327] or like *Ibmm* as in $La_{1-x}Sr_xTiO_3$ for high Sr-doping [116].

Fits of the unit cell volume of $CaCrO_3$ to the Birch EOS, Eq. 8.1, yield values of 181(2) GPa at 298 K and 168(4)GPa at 49 K for the bulk modulus B_0. The value at room-temperature is of the same order as the value observed in Ref. [310] - 189(2) GPa.

$SrCrO_3$

The unit cell volume of the cubic phase of $SrCrO_3$ at 27 K as a function of pressure is plotted in Fig. 8.14 (a). As can be seen in Fig. 8.15 (c-d) at 27 K there is no phase separation observable at ambient pressure. But after loading some pressure, at 3.5 GPa phase separation sets in and the LTT phase emerges. The lattice parameter of both phases are plotted in Fig. 8.15 (a) and the volume fraction of the LTT phase is shown in Fig. 8.15 (b). After reaching its maximum value right in the beginning, the volume ratio of the tetragonal phase decreases again. At higher pressures the peaks were broadened as could be also seen for $CaCrO_3$. Increasing peak widths and decreasing volume ratios of the LTT phase render the determination of the lattice parameter of the LTT phase difficult. Therefore, only a simple cubic phase has been fitted to the data for higher pressures (and also the data shown for pressures above 13 GPa might already

suffer from these effects). Additionally to the lattice parameters the unit cell volume of the tetragonal phase is shown indirectly by plotting $V_{tet}^{1/3}$ together with the a_{cub}-lattice parameter of the cubic phase. As can be seen the unit cell volume of both phases is about equal in the reliable pressure regime. For example at 3.5 GPa (where the volume fractions of the tetragonal phase are large) the unit cell volumes of the tetragonal and cubic phase amount to 53.552(17)Å^3 and 53.575(5)Å^3 respectively. This is about equal within the error bars and, hence, within the resolution of this measurement.

The pressure dependency of the volume fraction indicates a full conversion of the LTT phase to the cubic phase at high pressures (which could be expected). The fact that the sample did not exhibit any phase separation at 0.5 GPa pressure [5] but directly after measuring the next pressure point indicates that the formation of the LTT phase is affected by strain within the crystal. This was also concluded in Ref. [307] where a slowly varying strain field was supposed to support the growth of the LTT phase whereas large local variations of strain would be harmful for the LTT phase. Therefore, the application of 3.5 GPa pressure could have smeared out local peaky variations of microstrain thus creating more ideal [6] conditions for the LTT phase. And the effect is really large: as *sample B* shows no phase separation at 27 K and only a LTT-volume fraction of 17.5(8)% at the much lower temperature of 3.5 K in the neutron measurement, it is really remarkable that at 27 K the same sample exhibits even three times higher volume fractions of the LTT phase if 3.5 GPa pressure is applied.

After increasing the pressure by 13.5 GPa the c_{tet}-lattice parameter has decreased by 2.33% whereas the a_{tet}-lattice parameter has lost only 1.5% of its value. The relative incompressibility of the a_{tet} axis may indicate a higher occupation of the d_{xy} orbital. This was also assumed in Ref. [307].

A fit of the V-P data of the cubic phase of $SrCrO_3$ to the Birch-Murnagham EOS, Eq. 8.1, yields a bulk modulus $B_0 = 153(9)$ GPa. This is much lower than the value of 178(5) GPa observed in the room-temperature measurements of Ref. [310] for the low pressure regime ($P < P_{crit} = 4$ GPa), but it is closer to the value of 144(2) GPa which was reported in the same study for the high pressure regime ($P > P_{crit}$). This would suggest a similar high compressibility than in the $P > P_{crit}$ regime of the room-temperature studies of Ref. [310]. On the other hand the phase diagram shown in Ref. [310] predicts the shift of P_{crit} towards much higher pressures on cooling [7]. Therefore, the bulk modulus of $SrCrO_3$ should be much higher at 27 K, i. e. of the order of 178(5) GPa [310]. Thus, the results of this work are inconsistent with the model of Ref. [310] and vice versa. No phase separation has been reported in Ref. [310]. It may be possible that also at room-temperature a pressure of 4 GPa may be sufficient to induce some kind of phase separation which may have been confound with peak broadening effects. If these data would have been fitted with a single cubic phase then, a small kink in the P-V diagram as observed in Ref. [310] could be explainable. Unfortunately, no diffraction

[5] A temperature of 27 K was already reached before starting the 0.5 GPa measurement.
[6] with respect to the criteria of Ref. [307]
[7] for example: $P_{crit}(240\ K) \approx 23$ GPa [310] indicating that all pressures observed in this work are below P_{crit}.

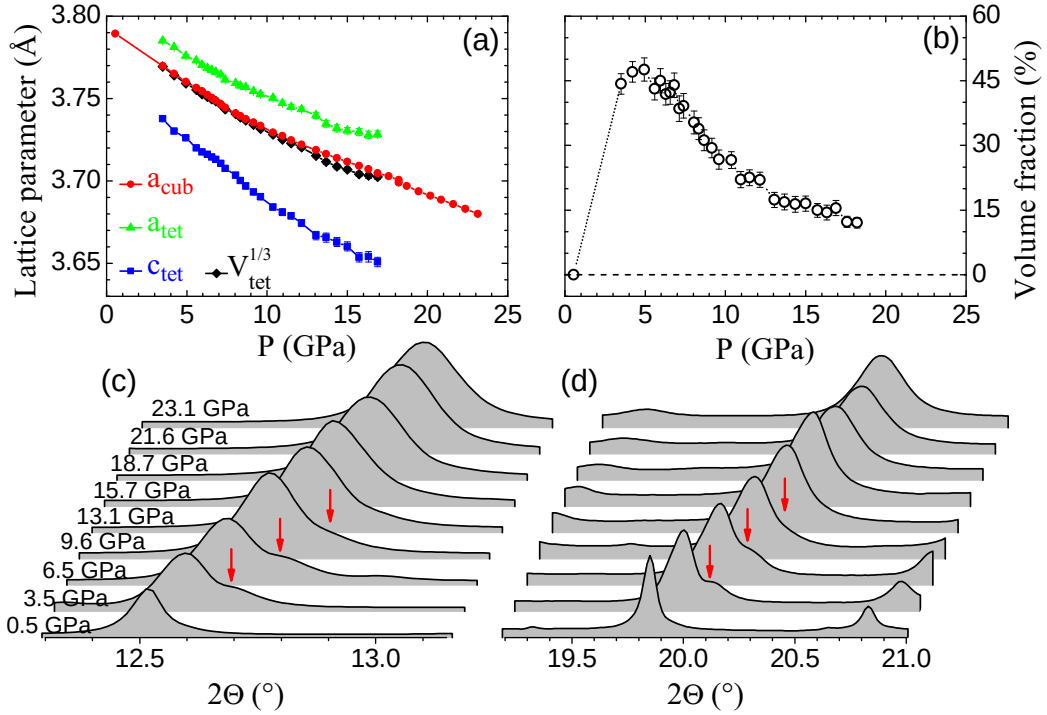

Figure 8.15: (a) Lattice parameter of the cubic (a_{cub}) and tetragonal phase (a_{tet}, c_{tet}). Also the tetragonal unit cell volume is indicated by the value of $V_{tet}^{1/3}$. (b) Volume ratio of the LTT phase. (c-d) Diffraction patterns; *red arrows* indicate peaks of the LTT phase.

patterns were shown in Ref. [310]. A careful reinvestigation of the room-temperature phase with special attention to phase separation could give further insights.

8.4.4 Conclusion

Concluding, for $CaCrO_3$ the lattice parameter have been measured at two different temperatures, 298 K and 49 K $< T_C$. There is no change in symmetry up to 35 GPa for both temperatures although the absolute value of the orthorhombic splitting steadily decreases. Similar to the O-orthorhombic → O'-orthorhombic phase transition on cooling, the c_c-lattice parameter also crosses another pseudocubic lattice parameter with increasing pressure in the 298 K measurement. But instead of decreasing and crossing a_c, the c_c lattice parameter is the most incompressible lattice parameter at 298 K and crosses the initially higher b_c lattice parameter. The reason may be the higher compressibility of b_c which could be driven by a decreasing CrO_6-octahedral tilt. This is also supported by the pressure driven increase of the ratio $c_{\mathrm{cub}}/\frac{a_{\mathrm{cub}}+b_{\mathrm{cub}}}{2}$. However, also orbital effects could be responsible. In order to get further information, either theoretical calculations using the measured lattice parameter or powder neutron diffraction measurements are

necessary. The last possibility may be the best. Pressure cells for neutron scattering are much larger as in the synchrotron case. Therefore, much larger amounts of sample can be loaded into the pressure cell which diminishes preferred orientation effects and, thus, also gives access to the atomic positions.

In the $SrCrO_3$-system a pressure-induced phase separation has been observed at 27 K. Showing no phase separation at 0.5 GPa pressure, the application of 3.5 GPa pressure results in a phase separated sample with roughly 50% LTT phase. This is even three times more than the value observed at 3.5 K in the neutron measurements (without pressure). Therefore, the theory that strong but slowly varying strains support the growth of the LTT phase [307] may be reasonable. The observation of a less compressible a_{tet}-axis may also indicate an orbital (re-)occupation of the d_{xy} orbital within the LTT phase. Finally, at higher pressures, the LTT phase begins to vanish again and can not be detected within the resolution around 18 GPa. This is in accordance with the expectation, that very high pressures should turn the whole system cubic. Finally, the observation of a distinctly higher compressibility of the cubic phase of $SrCrO_3$ at 27 K than in Ref. [310] at room-temperature may indicate either discrepancies with the model reported in Ref. [310] as a much higher bulk modulus would haven been expected due to the phase diagram shown there, or it indicates a general lowering of the bulk modulus with decreasing temperature in $SrCrO_3$. Probably, a reinvestigation of the pressure dependant lattice parameter in $SrCrO_3$ at room-temperature with focus on indications for phase separation might be of interest.

8.5 Comparison and Summary of Chromates

In this work the structural, magnetic and electronic properties of the $R\mathrm{CrO_3}$-system with divalent R-ions Ca, Sr and Pb have been studied. The R-ionic radius increases in this series from Ca to Pb : $r(\mathrm{Ca^{2+}}) < r(\mathrm{Sr^{2+}}) < r(\mathrm{Pb^{2+}}) \Leftrightarrow 1.34$ Å < 1.44 Å < 1.49 Å (for *coordination: XII*). Concomitantly with this ionic radius [82], also the pseudocubic (perovskite) unit cell volume increases in this series as can be seen from the values of the corresponding lattice parameter: $a_c^{(Ca)} \sim 3.75$ Å, $a_c^{(Sr)} \sim 3.82$ Å, $a_c^{(Pb)} \sim 4.00$ Å. Whereas the compound with the largest R-ion, $\mathrm{PbCrO_3}$, has the ideal cubic perovskite structure with space group $Pm\bar{3}m$, the compound with the smallest R-ion in this series, $\mathrm{CaCrO_3}$, has the orthorhombic $\mathrm{GdFeO_3}$ structure with space group *Pbnm*. At room-temperature, the compound with the interjacent R-ion size, $\mathrm{SrCrO_3}$, also crystallizes in an undistorted cubic perovskite structure with space group $Pm\bar{3}m$, but at low temperatures ($<$ 35-70 K) this system exhibits a structural phase transition from the cubic phase to a tetragonal phase with space group *P4/mmm* accompanied by phase separation as has been reported in Ref. [307] and as could be also observed in various neutron and synchrotron measurements in this work.

The $\mathrm{Cr^{4+}}$ oxidation state in these compounds is rather unusual and all these compounds have to be grown by an elaborate high-pressure synthesis route. Besides detailed information about the structure, for most of these compounds there is also no detailed knowledge about the electronic and magnetic properties. These materials have been studied in this work by means of neutron diffraction and electrical resistivity measurements. Furthermore, in this context the optical reflectivity of $\mathrm{CaCrO_3}$ has been studied by T. Möller [322]. And accompanying band structure calculations have been performed by S. V. Streltsov [318] which were based on the detailed crystal structure measured by neutron diffraction in this work.

$\mathrm{PbCrO_3}$ which has the largest cubic unit cell volume clearly is an insulator [324]. For both compounds with a smaller (pseudo-cubic) unit cell volume, $\mathrm{SrCrO_3}$ and $\mathrm{CaCrO_3}$, the electronic properties reported in literature range from insulating to metallic properties [310, 308, 305, 309]. Despite these controversial observations it seems beyond doubt that these compounds are close to the crossover from localized to itinerant electronic behavior [310, 318].

In this work, the electrical properties of $\mathrm{CaCrO_3}$ have been studied by electrical resistivity measurements revealing room-temperature values of ρ which are three orders of magnitude smaller than those reported for insulating $\mathrm{PbCrO_3}$ [324]. Despite its semiconductive temperature dependency the electrical resistivity of $\mathrm{CaCrO_3}$ might exhibit already first indications for its itinerant character since the value of ρ for $\mathrm{T} \rightarrow 0$ K is finite. Also the small and nearly temperature independent magnetic susceptibility of $\mathrm{CaCrO_3}$ and the failure of Curie-Weiss fits is indicative for itinerant electron behaviour. Furthermore, the optical reflectivity of $\mathrm{CaCrO_3}$ has been measured and analyzed by T. Möller [322]. As is typical for a metal, the reflectivity extrapolates to 1 for $\omega \rightarrow 0$. These measurements clearly indicate the metallic character of $\mathrm{CaCrO_3}$ with a moderate conductivity of several hundred to thousand $\Omega^{-1}\mathrm{cm}^{-1}$. Hence, grain boundary effects may biase the electrical resistivity measurements of polycrystalline $\mathrm{CaCrO_3}$-samples sim-

ilar to the observations for half-metallic CrO_2 [320, 321].

In this work, the magnetic structures of all three chromates have been studied by means of powder neutron diffraction and the magnetic structure of $CaCrO_3$ has been solved for the first time. The magnetic properties of $SrCrO_3$ which are reported controversially in literature [306, 307] have been reanalyzed. Furthermore, the reported magnetic structure of $PbCrO_3$ could be affirmed.

Below T_N∼90 K, $CaCrO_3$ exhibits a C-type antiferromagnetic order with an ordered moment of 1.09(4) μ_B pointing in the crystallographic *b*-direction. These results together with the optical data of T. Möller [322] indicate that $CaCrO_3$ is the rare case of a metallic and antiferromagnetic transition-metal oxide with a fully three-dimensional crystal structure.

For $SrCrO_3$ a weakly ferromagnetic itinerant state and a C-type antiferromagnetic structure with moments within the *ab*-plane has been reported in literature [306, 307]. In this work, a C-type antiferromagnetic structure has been found. In contrast to the studies reported in Ref. [307] the size of the ordered moment could be unambiguously determined in this work, yielding an ordered moment of 0.83(28) μ_B pointing in *c*-direction. This direction is different from the direction (*ab*-plane) reported in Ref. [307] where an extremely noisy measurement was presented. Furthermore, by the comparison of neutron measurements of $SrCrO_3$-samples with different volume fractions of the tetragonal and cubic phases, the magnetic properties of $SrCrO_3$ could be directly attributed to the tetragonal low temperature phase. This model has been also proposed in Ref. [307]. $SrCrO_3$ has the lowest magnetic ordering temperature of these three chromates, i. e. $T_N \approx 40$ K [307].

Insulating $PbCrO_3$ exhibits a G-type antiferromagnetic structure with an ordered moment of 2.1(3) μ_B. Among the studied chromates, $PbCrO_3$ is the compound with the highest Néel-temperature of about 160 K [324] which might be related to the fact that this material already is an insulator.

chromate:	**$CaCrO_3$**	**$SrCrO_3$**	**$PbCrO_3$**
T_N	∼90 K	∼ 40 K [307]	∼160 K [324]
magnetic order	C-type AFM	C-type AFM	G-type AFM
moment direction	b_{ortho}	c_{tet}	a_{cub} †
moment size	1.09(4) μ_B	0.83(28) μ_B	2.1(3) μ_B

Table 8.5: Summary of magnetic properties of $RCrO_3$; †: since this system is cubic also any other direction is possible.

Comparing these types of magnetic ordering and the size of the magnetic moments the similarities between $CaCrO_3$ and $SrCrO_3$ show up (the magnetic properties of these three chromates are listed in Tab. 8.5). Whereas insulating $PbCrO_3$ exhibits a G-type antiferromagnetic order with the full moment of roughly ∼2 μ_B which can be expected for this d^2-system, the other two systems exhibit a different C-type antiferromagnetic order with an ordered moment of half this size, i. e. roughly ∼1.1 μ_B and ∼0.8(3) μ_B respectively, and lower magnetic ordering temperatures. These different magnetic properties underline the difference between insulating $PbCrO_3$ and the other two chromates

$CaCrO_3$ and $SrCrO_3$. As mentioned above, $CaCrO_3$ has metallic properties. The less distorted crystal structure of $SrCrO_3$ and the slightly lower ordered moment suggest that this compound is even more metallic than $CaCrO_3$.

Complementary band structure calculations of S. V. Streltsov [318] based on the detailed structural data of $CaCrO_3$ measured in this work give an ambivalent answer to the question of the electronic properties of $CaCrO_3$: LSDA+U calculations indicate that $CaCrO_3$ is an insulator whereas LSDA calculations indicate that $CaCrO_3$ is a metal. At least, these calculations can explain the C-type antiferromagnetic properties of $CaCrO_3$ also in the metallic scenario, which are caused by comparably large diagonal exchange interactions induced by a strong pd-hybridization. Hence, these band structure calculations verify the self-consistency of the metallic picture.

Regarding the vicinity to the crossover between itinerant and metallic properties, pressure studies of the $CaCrO_3$- and $SrCrO_3$-systems seem rather interesting. Therefore, the lattice parameter of $CaCrO_3$ and $SrCrO_3$ have been also measured at the synchrotron as a function of pressure and temperature [8]. For $CaCrO_3$ no change in symmetry was observable in the whole pressure and temperature range. The study of the lattice parameters reveals that b_{ortho} is the most compressible axis. Together with a pressure driven increase of the ratio $c_{\mathrm{cub}}/\frac{a_{\mathrm{cub}}+b_{\mathrm{cub}}}{2}$ this could be indicative for a decrease of the octahedral tilts with pressure. However, also orbital effects could be responsible.

In pressure-dependent synchrotron measurements of $SrCrO_3$ the tetragonal phase of the used $SrCrO_3$-sample only appeared after applying pressure (3.5 GPa at 27 K). The volume fraction of this tetragonal phase amounts to 50% which is distinctly higher than that observed in the neutron measurements at ambient pressure. This supports the theory that strong but slowly varying strains support the growth of the tetragonal phase in $SrCrO_3$ [307]. With further increasing pressure the volume fractions of the tetragonal phase in $SrCrO_3$ decrease and, finally, at high pressures these volume fractions vanish. Interestingly, the larger tetragonal a_{tet}-axis ($a_{tet} > c_{tet}$) exhibits a lower compressibility than the already smaller tetragonal c_{tet}-axis. This lower compressibility of the a_{tet}-axis may be connected to the occupation of the d_{xy} orbital in the tetragonal phase of $SrCrO_3$ which is in accordance with the (in c_{tet}-direction) compressed CrO_6 octahedra and which was, therefore, also assumed in Ref. [307].

Concluding, the study of structural, magnetic and electronic properties of $CaCrO_3$ (and related systems) reveals the unique case of an antiferromagnetic and metallic transition metal oxide with a three-dimensional electronic structure - $CaCrO_3$. The few antiferromagnetic and metallic transition metal oxides are low dimensional with regard to their electronic structure and antiferromagnetism is realized by stacking of ferromagnetic layers like in $Ca_3Ru_2O_7$ [303] and $(La,Sr)_3Mn_2O_7$ [304]. Like $CaCrO_3$, also $SrCrO_3$ might be such a metallic and antiferromagnetic transition metal oxide since its metallic properties should be even more pronounced than in $CaCrO_3$ as it has a less distorted crystal structure and since the indications for antiferromagnetism which have

[8] $CaCrO_3$: T = 298 K and 49 K, P $\leq$ 34.4 GPa and P $\leq$ 14.2 GPa respectively;
$SrCrO_3$: T = 27 K, P $\leq$ 23.1 GPa.
The pressure dependence of the unit cell volume of $CaCrO_3$ and $SrCrO_3$ up to pressures of about 8 GPa has also been reported in literature [310].

been reported in Ref. [307] could be verified by neutron measurements which have been performed in this work.

[Ar] $3d^8$ $4s^2$
1453/2732
58.693

28 Ni
Nickel

9 Nickelates

Nickel is the 24th most abundant element in the earth crust and can be found in ores bonded with arsenic, antimony or sulfur [107]. This hardly corrodible metal with quite good electrical conductivity is commonly used in the production of alloys such as steel.

9.1 Electron-phonon coupling and magnon dispersion in $La_{2-x}Sr_xNiO_4$

9.1.1 Introduction

Within contemporary research of strongly correlated electron systems spin, charge and orbital ordering phenomena play an important role in the understanding of the physical properties of a broad range of materials. The discovery of the charge stripe ordering in the high-T_C superconducting cuprate materials $La_{2-x-y}Nd_ySr_xCuO_4$ [6] has attracted a lot of interest, recently. The role of the stripe instability in the pairing mechanism, however, remains unclear. Whereas static stripes definitely are harmful to superconductivity, dynamic stripes might have some relevance for the understanding of high-T_C superconductivity. Stripe ordering has been predicted theoretically as a combined charge and spin-density wave already long before (see for example Ref. [332]) and was first observed in neutron diffraction measurements of the isostructural $La_2NiO_{4+\delta}$-system ($\delta = 0.125$) [160, 333] after incommensurate magnetic correlations have been observed with neutrons in the NiO_2 planes of the $La_{2-x}Sr_xNiO_4$-system [334] and superlattice peaks indicative for charge ordering were found in the $La_{2-x}Sr_xNiO_{4+\delta}$-system by electron diffraction [335].

The $La_{2-x}Sr_xNiO_{4+\delta}$-system is isostructural to the high-T_C cuprates with a K_2NiF_4-type single-layered perovskite structure and like La_2CuO_4, La_2NiO_4 is an antiferromagnetic insulator with $T_N \approx 330$ K [336], rendering this system ideal for a comparison to the $La_{2-x}Sr_xCuO_4$-system, especially with regard to the charge ordering observed in different nickelate systems $(La/Nd)_{2-x}Sr_xNiO_{4+\delta}$ [160, 337-343]. But in contrast to the $La_{2-x}Sr_xCuO_4$-system where the antiferromagnetic, insulating phase is rapidly destroyed by hole-doping and becomes metallic around hole-concentrations of $n = x \approx 0.05$ [344, 2] (see Chap. 10.1), the $La_{2-x}Sr_xNiO_{4+\delta}$-system remains insulating to up to rather high concentrations of hole-doping $n = x+2\cdot\delta \approx 1$ [32]. In the parent compound La_2NiO_4 the Ni^{2+}-ion has a $3d^8$ high-spin configuration with S=1 and is a charge transfer insulator

with a charge transfer gap of 4 eV [345-348]. Compared to this, the Cu^{2+}-ion in the charge transfer insulator La_2CuO_4 has a $3d^9$ S=1/2 electron configuration but a much smaller charge transfer energy of 2 eV [349].

There are mainly four relevant basic structural variations of the $La_{2-x}Sr_xNiO_4$- and $La_{2-x}Sr_xCuO_4$-systems which are commonly referred to as '214 compounds'. The basic structure which is also known as the high-temperature tetragonal (HTT) phase consists of NiO_2 (CuO_2) planes separated by $(La,Sr)_2O_2$ layers. In principle, within the NiO_2 (CuO_2) planes the Ni- (Cu-) ions form a square lattice connected by oxygen ions within the plane. These planes are staggered in *c*-direction and each unit cell contains two of these plains shifted by [1/2 1/2 1/2]. Additionally, each Ni- (Cu-) ion has also an (apical) out-of-plane neighbouring oxygen ion in *c*-direction forming a tetragonally-distorted NiO_6- (CuO_6-) octahedral oxygen environment. The (La,Sr)-ions are placed below and above the centers of the Ni- (Cu-) square lattice within the plane of the apical oxygens above and below the NiO_2 (CuO_2) planes. Changes of this well known K_2NiF_4-type structure can be best described in terms of NiO_6- (CuO_6-) octahedral tilts θ_1 around the [1-10] and θ_2 around the [110] axis; see Fig. 9.1 (a). Depending on the size of these two tilts one can distinguish between three (distorted) structural variants in '214' compounds which all have a $\sqrt{2} \times \sqrt{2} \times 1$ enlarged unit cell as shown for one of these structures in Fig. 9.1 (b). These structures are the low-temperature orthorhombic structure (LTO), the low-temperature tetragonal structure (LTT) and the low-temperature less orthorhombic structure (LTLO). In Tab. 9.1 the according values for the octahedral tilts and the space group are shown.

name:	θ_1	θ_2	**unit cell**	**space group**
HTT	0°	0°	$1 \times 1 \times 1$	$I4/mmm$
LTO	0°	α	$\sqrt{2} \times \sqrt{2} \times 1$	$Bmab$
LTT	α	α	$\sqrt{2} \times \sqrt{2} \times 1$	$P4_2/ncm$
LTLO	α	β	$\sqrt{2} \times \sqrt{2} \times 1$	$Pccn$

Table 9.1: Parameters of some common (distorted) K_2NiF_4-structures with tilting angles Θ_1, Θ_2 around [1 1 0] and [1 -1 0]; α, $\beta \neq 0°$, $\alpha \neq \beta$.

The structural phase diagram of the $La_{2-x}Sr_xNiO_4$-system exhibits a tetragonal to orthorhombic phase transition from the HTT to the LTO phase at 781 K for the undoped La_2NiO_4-compound and an almost linear decrease of the transition temperature which can be extrapolated down to 0 K for $x \rightarrow 0.23$ [102, 336]. The $La_{2-x}Sr_xCuO_4$-system has a very similar phase diagram. But compared to the decrease of 320 K for $\Delta x = 0.1$ in the $La_{2-x}Sr_xNiO_4$-system, the transition temperature of the $La_{2-x}Sr_xCuO_4$-system decreases with 230 K in the same doping interval only [102, 350]. On the other hand the transition temperature of the undoped parent compound La_2CuO_4 amounts to 530 K [102, 351]. Furthermore, a second structural phase transition can be observed in the $La_{2-x}Sr_xNiO_4$-system. A transition of the LTO phase to a phase which can be described with space group *Pccn* (LTLO) occurs around 83 K [102]. For this second transition also a linear decrease of the transition temperature has been reported. But as the orthorhombic splitting of the LTO phase decreases with further Sr doping, this second

phase transition could only be traced up to doping levels $x \approx 0.15$ where the transition temperature was reduced to approximately 55 K [102].

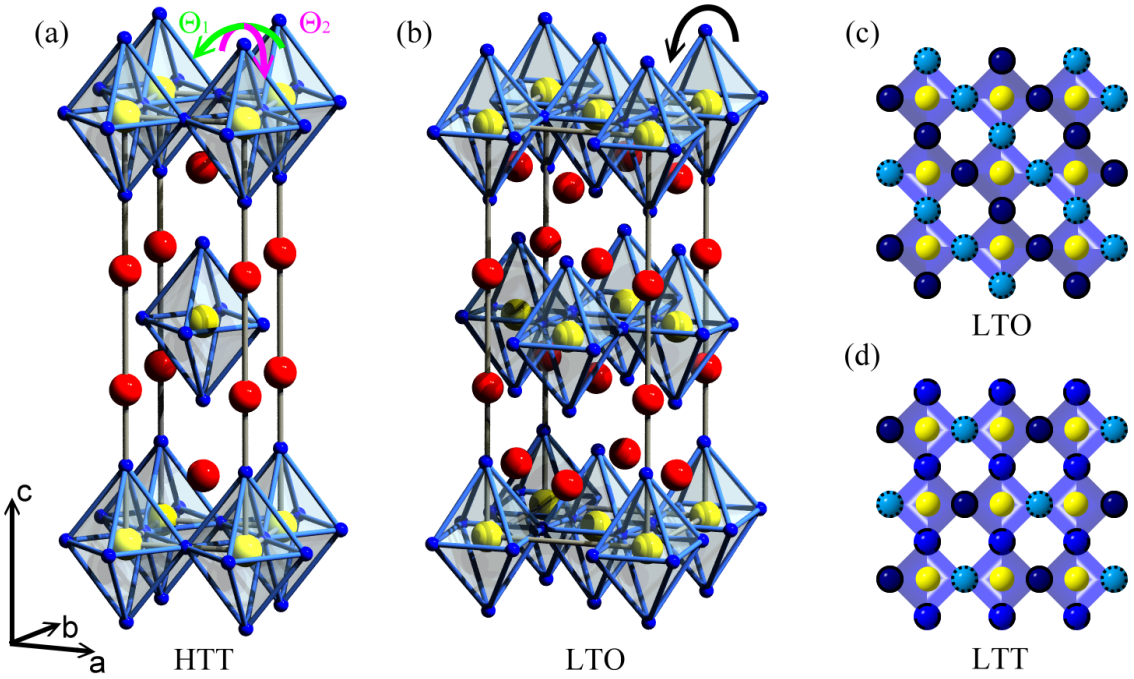

Figure 9.1: (a) HTT and (b) LTO structure; *blue:* O-ions, *red:* La-ions, *yellow:* M-ions (M = Ni/Cu), *green/magenta arrows* indicate the two tilts Θ_1 and Θ_2 of the MO_6 octahedra. (c-d) octahedral tilt patterns for LTO and LTT structure within a MO_2 plane; *yellow:* M-ions, *dark blue (solid):* O-ion displaced downwards out of plane, *blue (dashed):* in-plane O-ion, *light blue (dotted):* O-ion displaced upwards out of plane.

Whereas the higher doped $La_{2-x}Sr_xNiO_4$-samples ($x \gg 0.5$) have the tendency to exhibit stoichiometric oxygen contents [32], the lower doped $La_{2-x}Sr_xNiO_4$-samples have the affinity to accommodate excess oxygen. Especially, the parent compound La_2NiO_4 is able to incorporate a large amount of extra oxygen and has a very rich phase diagram as a function of oxygen doping [352-354]. The intercalation of extra oxygen is accompanied by NiO_6-octahedral tilts about the tetragonal [110] axis similar to the tilts occurring in the LTO structure with space group *Bmab*. The interstitial extra oxygen ions tend to localize between the adjacent LaO layers at the (1/4 1/4 1/4) sites of the LTO structure repelling its four neighbouring oxygen ions and, thus, disrupting the local octahedral tilt pattern. At higher oxygen doping ($0.06 \leq x < 0.11$), this intercalation of oxygen ions preferably occurs within separate layers which are staggered periodically in *c*-direction and induce superstructure reflections of the type (0 K L$\pm\Delta$) with K even and L odd [352, 355]. Thus, the modulation wave vectors are (0 1 $\pm\Delta$) and the characteristic LTO peaks with the modulation wave vector (0 1 0) are absent. Although charge stripe ordering coexists with the interstitial oxygen ordering [333], such a disruption of the

octahedral tilting pattern may not seem favourable for a study of the effects of charge stripe ordering solely, like the electron-phonon coupling of Ni-O bond-stretching phonon modes for example.

In the charge stripe ordered phase the holes form charge stripes which act as antiphase domain walls for the antiferromagnetically ordered Ni-spins. The modulated charge density induces nuclear displacements with modulation wave vectors ($\pm\varepsilon$ ε 1) in tetragonal notation. The in-plane component indicates that the charge stripes are running in diagonal [$\pm$110] direction with a spacing of $a/(\sqrt{2}\cdot\varepsilon)$ between them and the out-of-plane component indicates that the charge stripes in neighbouring NiO_2-layers are staggered in a body-centered manner. This staggering is a consequence of the Coulomb repulsion between the stripes running parallel to each other. Acting as antiphase domain walls for the antiferromagnetic host structure with the wavevector ($\frac{1}{2}$ $\frac{1}{2}$ 0), the charge stripe ordering induces magnetic superstructure reflections which can be characterized by the modulation wave vectors ($\pm\frac{1}{2} \mp \frac{\varepsilon}{2}$ $\frac{1}{2} - \frac{\varepsilon}{2}$ 0). The two different modulation wave vectors ($\pm$) correspond to the two different twin domains either in the magnetic or in the structural case. Note, that the charge and magnetic superstructure reflections of the nickelate system are often measured in the orthorhombic (LTO) setup, where the stripes run parallel to the b_{ortho}-direction. In this notation, the charge and magnetic satellites can be found in reciprocal space at positions with q= (2ε 0 1) and (1-ε 0 0) respectively.

The observation of higher harmonics [356] indicates that the stripe ordering is not a sinusoidal modulation of charge and spin densities but that these stripes are rather narrow. Due to the dependency of the neutron intensity on the angle between the scattering vector and the magnetic moment or spin direction the Ni spins were found to be oriented perpendicular to the modulation direction and, thus, parallel to the stripes in the $La_2NiO_{4+\delta}$-system [333]. However, in the $La_{2-x}Sr_xNiO_4$-system the spin-direction seems to be rotated away from the charge and spin stripe direction within the NiO_2 plane [357]. A model of these stripes within the NiO_2 planes is shown in Fig. 9.2 (a-b) for the two possible domains. The corresponding superstructure reflections are shown in Fig. 9.2 (c). In the nickelates the 1/3 doped compound exhibits a very stable type of commensurate stripe order which induces distinct anomalies in the electrical resistivity [345]. This compounds exhibits a constant value of $\varepsilon = 1/3$ over the whole temperature range where charge ordering exists. The value of the incommensurability ε for other hole-doping concentrations in a wide range around this 1/3 doped sample is temperature dependent and converges towards the commensurate value of 1/3 on heating [337]. Also the charge (and spin) ordering temperatures are highest for the 1/3 doped sample and continuously decrease from about 250 K for x = 1/3 to approximately 60 K for x $\approx$ 0.13 [340]. The low-temperature value of the incommensurability ε is proportional to the hole-doping concentration $n = x + 2\cdot\delta$ indicating for all hole concentrations n the same hole-density of 1 hole per site within the stripes. The possibility that the incommensurate charge ordering superstructure reflections found for various $La_{2-x}Sr_xNiO_4$-samples [334, 342, 343, 358, 340] are induced by a spin density wave as for example in Cr [359] can be excluded as the charge ordering temperature is always distinctly higher than the magnetic ordering temperature.

Resonant X-ray diffraction measurements at the Ni $L_{2,3}$ absorbtion edge indicate that

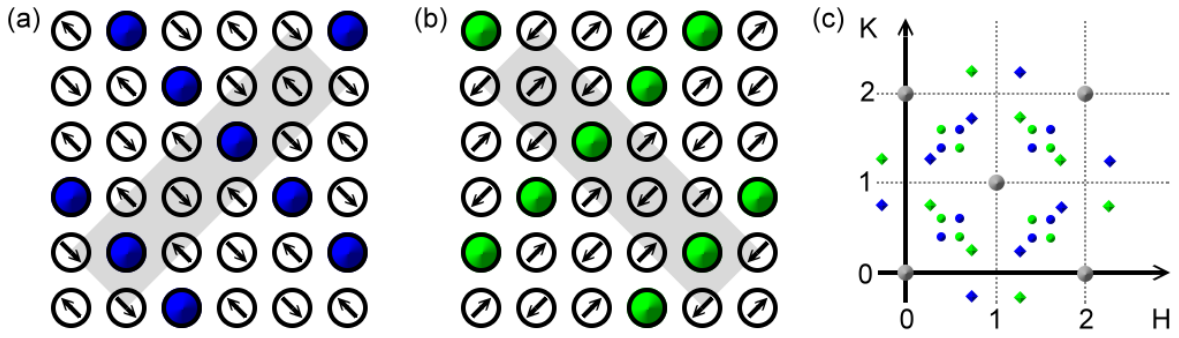

Figure 9.2: (a-b) Schematic model of diagonal stripes within the NiO_2 plane. Only the Ni-ions are shown (*circles*). Holes are indicated by filled circles and the spin directions by the arrows. A magnetic unit cell of this arrangement is indicated by the gray shaded region. (c) (HK0)-zone in reciprocal space; *gray circles:* bragg reflections, *blue/green circles (diamonds):* the magnetic (structural) superstructure reflections of the stripe domains in figure (a)/(b).

the holes within the stripes are not located at the Ni-site but are mainly located on NiO_2 in-plane oxygen ions surrounding the Ni^{2+}-ion with antiferromagnetically coupled spins [360, 361] resembling on a Zhang-Rice singlet in the cuprates [362].

On increasing the hole doping level n an additional commensurate checkerboard charge ordering emerges abruptly at $n \geq 0.5$ which persists up to rather high temperatures. However, the stripe order coexists with this commensurate checkerboard ordering at lower temperatures up to doping levels of $n \approx 0.7$ [363]. Thus the electronic phase diagram of the $La_{2-x}Sr_xNiO_4$-system exhibits a stripe ordering which has a maximum T_C for the 1/3 doped sample around 240 K and an (incommensurate) magnetic ordering temperature of about 180 K, which both decrease monotonically while n moves away from 1/3. In the regime $n \leq 0.45$ the incommensurability ε is proportional to n and no checkerboard charge ordering occurs. Then, for $n \geq 0.5$ a commensurate checkerboard charge ordering emerges abruptly and coexists with the stripe odering whose incommensurability $\varepsilon \approx 0.44$ is nearly doping-independent up to $n \approx 0.7$ while the commensurate checkerboard charge ordering exhibits a much higher T_C which decreases from 480 K to 400 K within the same doping range ($n = 0.5$ to 0.7) [363, 364].

Contrarily to the diagonal charge stripe order in the nickelates which is well established, in the isostructural cuprate system static charge stripes have been found only in the Nd co-doped $La_{2-x}Sr_xCuO_4$-system with $x \approx 0.125$ [6] and in the $La_{2-x}Ba_xCuO_4$-system at $x \approx 0.125$ [365]. The stripes in the latter systems are rotated by 45° compared to the charge stripes observed in the isostructural nickelates. In these systems, the distinctly different size of the larger Ba- or the smaller Nd-ions distorts the lattice and the system exhibits a low-temperature phase transition to the LTT phase where the lattice potential seems to pin or stabilize the vertical stripes. For the pure $La_{2-x}Sr_xCuO_4$-compounds only the magnetic satellites were observed (see Chap. 10.1) which rotate by 45° on entering the spin-glass regime of this class of compounds. Thus, a diago-

nal charge stripe ordering could be assumed also in the spin glass (SG) phase of the $La_{2-x}Sr_xCuO_4$-system as the magnetic satellites observed in this regime are rotated by 45° in a diagonal direction. However, no charge ordering superstructure reflections of such a diagonal stripe phase have been observed for this system so far and a chiral model is also able to explain the diagonal magnetic satellites without any stripe ordering [366]. With regard to these two possible scenarios the nickelate-system with a diagonal charge stripe ordering is an important reference system. Besides the direct (structural) comparison of the diagonal charge stripes in the nickelates and the vertical stripes in the cuprates a comparison of the nature of the physical properties of these stripe ordered systems is of high interest.

On the one hand, the magnetic excitations in the cuprates [18-22, 367] are discussed controversially. Recent neutron scattering experiments in the stripe ordered state of the $La_{1.875}Ba_{0.125}CuO_4$-system exhibit spin wave excitations which start at the incommensurate positions $(\frac{1}{2} \pm \delta\ \frac{1}{2}\ 0)$ and $(\frac{1}{2}\ \frac{1}{2} \pm \delta\ 0)$ and merge at the antiferromagnetic zone center $(\frac{1}{2}\ \frac{1}{2}\ 0)$ around 55 meV [20]. But above this merging point the spin excitations continue further (up to at least 200 meV) with the main intensities at positions rotated by 45° compared to the excitations below the merging point [20]. Thus, the overall dispersion has a so-called 'hour-glass-shape' and exhibits a much enhanced intensity around the merging point around 55 meV resembling on the resonance peak in the superconducting state of $YBa_2Cu_3O_7$ [23-25]. This feature has has been expected already before due to theoretical work [368]. The spin wave dispersion is in quite good agreement with linear spin-wave calculations [369, 370]. The 'hour-glass-shape' is believed to be the unifying feature of all cuprates [20]. However, this topic is under debate and there are also different views [19]. As the $La_{2-x}Sr_xNiO_4$-system is a prototypical stripe ordered system it may be a very interesting system to test models on the spin-fluctuations of the stripe phases etc. and to compare its properties with the cuprate-system. Low energy spin dynamics of the $La_2NiO_{4+\delta}$-system ($\delta = 0.133$) has been reported in Ref. [371]. Besides this oxygen doped compound suffering from the additional influence of oxygen ordering as described above, only the commensurate 1/3 doped system $La_{5/3}Sr_{1/3}NiO_4$ [372-374] and the half-doped system $La_{3/2}Sr_{1/2}NiO_4$ have been studied [375]. Chosing the compound $La_{5/3}Sr_{1/3}NiO_4$ with a small commensurate magnetic unit cell with only two Ni^{2+}-ions has the advantage of a very stable charge ordering (as described above). Close to the elastic peaks, these inelastic neutron measurements find a spin-wave velocity of about 300 meVÅ [372, 373] which is comparable to 340 meVÅ in the parent compound La_2NiO_4 [376]. The description of the spin-wave dispersion needs only two magnetic interaction parameters, one for the nearest neighbour interaction and a second one with similar magnitude for the interaction across the stripes. The spin wave dispersion merges at the antiferromagnetic zone center $(\frac{1}{2}\ \frac{1}{2}\ 0)$. However, this could be expected in the commensurate case and presumably can not be connected directly to the cuprate resonance. Furthermore, only a single magnon branch can be expected in the commensurate case and, thus, no dispersion was found above the merging point. Hence, there is few similarity with a 'hour-glass-shape'. Also the spin wave dispersion of $La_{1.725}Sr_{0.275}NiO_4$ strongly resembles on the dispersion in the 1/3 doped compound [374] although, in principle, additional magnon branches could be expected above the

merging point for incommensurate stripe phases [370]. Obviously, this composition is still too close to the commensurate compound and the commensurability seems to lock the magnetic structure.

On the other hand electron-phonon coupling has been studied within the cuprate system [13] and giant phonon anomalies at the phase transition into the stripe order have been reported. Regarding the polarization patterns a coupling of bond stretching phonon modes to charges at the metal site is possible. These modes induce a modulation of the bond-distances which favours the occupation of positive charges at sites with short M-O bonds and, thus, can be considered as a kind of dynamic precursors of charge ordering. In Fig. 9.3 (a-b) two examples of such a coupling of phonons and charge stripes are shown. The *black arrows* indicate the oxygen displacements within these polarization

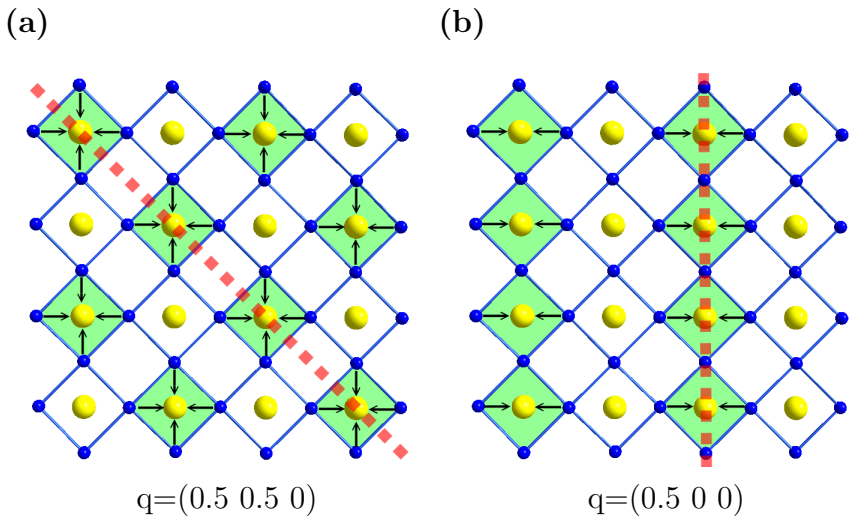

Figure 9.3: Polarization patterns of (a) the planar full breathing mode with q=(0.5 0.5 0) and (b) the half- breathing mode with q=(0.5 0 0); *yellow circles:* M-ions, *blue circles:* O-ions, *black arrows:* O-displacements, *red dotted lines:* diagonal (a) or collinear (b) charge stripes.

patterns. In Fig. 9.3 (a) the polarization pattern for the high energy Σ_1-mode is shown for a propagation vector of $(\frac{1}{2}\ \frac{1}{2}\ 0)$. As is indicated by the red dotted line, this planar full breathing mode can couple to a diagonal charge stripe instability. In Fig. 9.3 (b) the situation for the topmost Δ_1 mode is shown. This half breathing mode obviously is able to couple to vertical charge stripes. The dispersion of the Δ_1 mode is qualitatively similar for nickelates and cuprates and, astonishingly, also for many other perovskites [377-379]. The dispersion starts flat from the zone center, then steeply decreases around $(\frac{1}{4}\ 0\ 0)$ and gets flat again in the Brillouin zone boundary with respect to the small perovskite mesh. Qualitative differences are found in the dispersion of the Σ_1 mode. Whereas distinct changes can be observed in the dispersion of the nickelates [380], the metallic cuprates exhibit only an almost flat dispersion [381]. This difference may be connected to the different charge stripe instabilities in both systems: In the nickelates the dispersion exhibits anomalies in [110]-direction which is the propagation direction of

the diagonal stripes and in the cuprates where charge ordering has only been observed in stripes running in [100]-direction the dispersion in [100] direction exhibits a over-screening [381]. And comparing several cuprates among which also static stripe order appears, a giant phonon anomaly has been reported at the transition into the stripe order [13]. These large phonon frequency renormalization effects are an interesting topic to compare with the nickelate system, especially for lower hole-concentrations, far away from the commensurate value of 1/3 which have not been measured (to the knowledge of the author) until now.

9.1.2 Experimental

Single crystals of $La_{1.8}Sr_{0.2}NiO_{4+\delta}$ and $La_{1.83}Sr_{0.17}NiO_{4+\delta}$ were grown by A. A. Nugruho using a floating-zone image furnace.

In order to study the electron phonon coupling, inelastic neutron scattering experiments have been performed at the IN8 triple axis spectrometer at the ILL in Grenoble, France. A Cu (200) monochromator and a pyrolytic graphite (002) analyzer was used, each of which was vertically and horizontally focused. The analyzer was used in a constant-k_f mode with a final energy of 14.7 meV. Two pyrolytic graphite filters were placed after the sample in order to diminish undesirable neutrons at higher harmonic wavelengths. In a first experiment only one PG filter has been used and in a second experiment two PG filters have been placed after the sample. The sample was mounted with the [100]/[010] axes in the scattering plane (tetragonal notation).

For a study of the spin dynamics in this compound inelastic neutron scattering experiments have been performed at the triple axis spectrometer PUMA at FRM-II in Garching and at the IN20 spectrometer at the ILL in Grenoble, France.

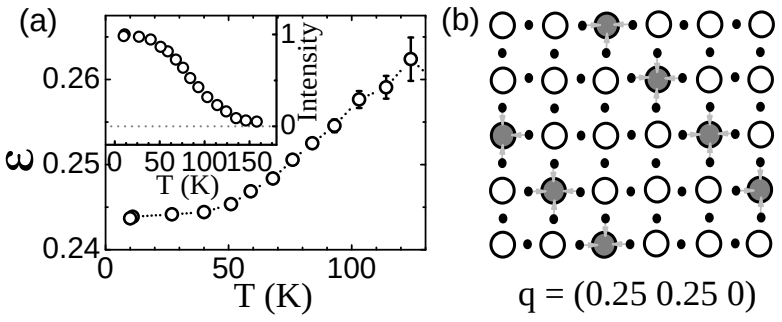

Figure 9.4: (a) Incommensurability of charge stripes ε plotted versus temperature. In the inset the intensity of the according superstructure reflections is shown. (b) Model of diagonal charge stripes with $\varepsilon = 0.25$ and coupling of a full breathing mode.

9.1.3 Results and Discussion

lattice dynamics

For a characterization of the charge stripe modulation and the corresponding incommensurability ε in $La_{2-x}Sr_xNiO_{4+\delta}$ the positions of a charge ordering superstructure reflection in reciprocal space has been traced with temperature. The associated values of ε are plotted as a function of temperature in Fig. 9.4 (a). These values exceed the expected value of $\varepsilon \approx x$ by about 0.045. Hence, this sample contains a small excess of oxygen which is of the order of $\delta = 0.02$. With increasing temperature the value of the incommensurability ε tends towards the commensurate value of 1/3. A similar behaviour was observed also for other nickelates [343]. In the inset of Fig. 9.4 (a) the temperature dependency of the intensity of this superstructure reflection is shown. From this plot one obtains an onset temperature for static stripe ordering (T_{CO}) which amounts to roughly 150 K. In Fig. 9.4 (b) a model for the charge stripe ordering with $\varepsilon = 0.25$ is shown. The *black dots* denote the oxygen ions whereas the larger *filled/open circles* indicate the Ni-sites with/without a hole. Additionally, the most significant parts of the polarization pattern of a breathing mode with $q = (0.25\ 0.25\ 0)$ is shown. If there are diagonal charge stripes, a coupling of such a phonon mode to the local charges could be expected.

The octahedral tilts in $La_{2-x}Sr_xNiO_4$ induce distortions doubling the primitive unit cell and the number of phonon branches. Additionally, twinning may further increase the possible modes at a given value of Q. For the phonon modes in [1 1 0]-direction a broadening can be expected. But these (small) effects are difficult to resolve in a typical neutron measurement and will be ignored in this work. Thus, the results presented in this work refer to the tetragonal notation. In Fig. 9.5 (b) the dispersion of the topmost Σ_1 phonon modes at 2 K (*black*) are plotted. The energies were derived from gaussian fits to the according constant-Q scans. The dispersion of the Σ_1 mode rises from $\zeta = 0.0$ to 0.5 by about 2 meV and exhibits a distinct dip at a value of ζ which nicely fits to the measured incommensurability of the charge stripes; see Fig. 9.5 (b). This new observation is a direct evidence for electron phonon coupling in the nickelates and gives rise for a comparison with the $La_{2-x}Sr_xCuO_4$-compounds in the spin glass phase, where similar anomalies should be observable, if the diagonal stripe picture is applicable. A direct comparison with a LSCO sample in the spin-glass phase is shown in Chap. 10.1.

For the $La_{1.8}Sr_{0.2}NiO_{4+\delta}$-sample the constant-$Q$ scans exhibit a well pronounced broadening around $\zeta = \varepsilon$. In Fig. 9.5 (c) the full-width at half maximum (FWHM) of the corresponding energy scans is plotted below the dispersion (*lt. gray* data). Hence, this broadening may indicate a splitting of the Σ_1 branch into two modes similar to the interpretation proposed for $La_{2-x}Sr_xCuO_4$ in Ref. [13], i. e. one for phonons propagating parallel and one for phonons propagating perpendicular to the stripes. The corresponding constant-Q scans are shown in Fig. 9.5 (a).

The highest-energy longitudinal optical mode (Δ_1) exhibits a softening of about 20% between the Brillouin zone center and the zone boundary; see Fig. 9.6 (a). This observation is similar to the findings for the Δ_1 mode in Ref. [380]. However, in contrast to the Σ_1-mode there is no broadening of the phonon peaks visible for any value of q; see Fig. 9.6 (b).

In Fig. 9.5 (d-f) the constant-Q scans for $\zeta = 0.00$, 0.25 and 0.50 are shown for different temperatures. The resulting energies from gaussian fits are plotted together with the dispersion at 2 K in Fig. 9.5 (b). First of all, the overall dispersion decreases by a constant energy which can be interpreted in terms of thermal expansion effects. It seems that the dispersion exhibits a larger decrease around $\zeta = 0.25$, i. e. at the q-vector of the anomaly in the Σ_1 branch. This can be seen in Fig. 9.5 (e) where the phonon peak exhibits an anomalous large shift to lower energies between above T_{CO}. This can be also seen in the dispersion Fig. 9.5 (b): at the zone center $\omega(q)$ decreases by about 2 meV and $q = \varepsilon$ the dispersion $\omega(q)$ decreases by more than 3 meV on heating from 2 K to 300 K. Second, the dispersion shows a rather interesting effect at 300 K for $\zeta = 0.5$ where the intensity of the dispersion is smeared out which may be interpreted as a strong damping in this region of the Brillouin zone.

In Fig. 9.7 the neutron scattering intensity is plotted as a function of energy and wavevector transfer. The open circles denote the phonon dispersions and the black

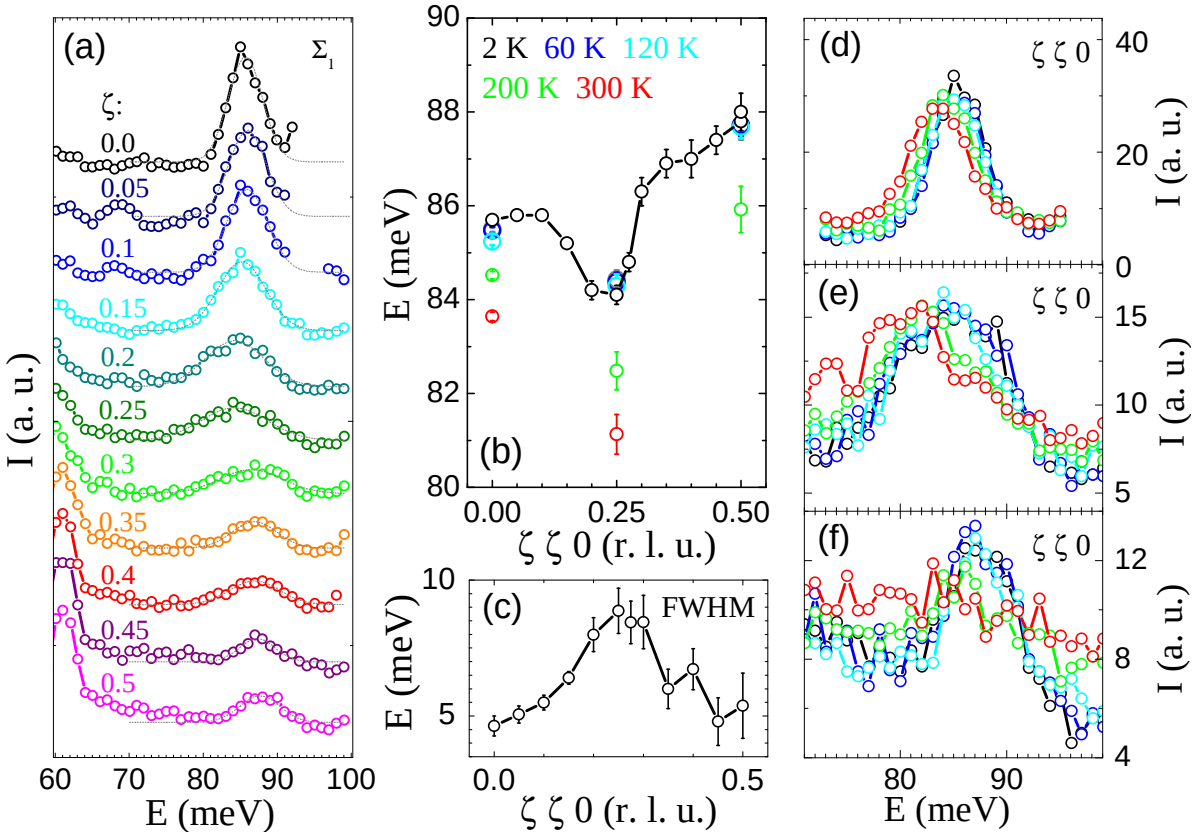

Figure 9.5: (a) Constant-Q scans at 2 K ($q = \zeta\zeta 0$) measured at (3-ζ 3-ζ 0); *gray dotted lines* indicate gaussian fits with constant background. (b) Phonon dispersion of the topmost Σ_1 phonon mode for different temperatures. (c) peak widths (FWHM) at 2 K. (d-f) Constant-Q scans ($q = \zeta\zeta 0$) measured at different temperatures are plotted for (d) $\zeta = 0.00$, (e) $\zeta = 0.25$ and (f) $\zeta = 0.50$. (IN8 measurement)

dotted line indicates some additional intensity which may be contributed to a further splitting into an additional branch. Clear indications for a split branch have been reported in Ref. [380] for a $La_{1.69}Sr_{0.31}NiO_4$-sample. This additional branch was attributed to the coupling of the phonons to localized charges which may also occur in the $La_{1.8}Sr_{0.2}NiO_{4+\delta}$-sample measured in this work. However, this signal is distinctly weaker than the observations for $La_{1.69}Sr_{0.31}NiO_4$ [380] and may even be absent for this $La_{1.8}Sr_{0.2}NiO_{4+\delta}$-sample. In this case, the anomalous dip in the phonon dispersion around $\zeta = 0.25$ is purely an effect induced by electron-phonon coupling and is not related to a merging of the Σ_1-branch with this additional branch (*dashed line*). However, such a merging can not be fully excluded although there are some severe arguments against such a scenario. This is especially the fact, that the structure factor or intensity of this additional branch for the $La_{1.69}Sr_{0.31}NiO_4$-sample strongly decreases with decreasing value of ζ from $\zeta = 0.5$ to $\zeta = 0.25$. In the measurement of this work, the intensity of this additional branch is already close to zero for $\zeta = 0.5$. Hence, there should be no intensity-contribution around $\zeta = 0.25$. Furthermore, the intensity of this additional branch is comparably high as for the original Σ_1-branch in the $La_{1.69}Sr_{0.31}NiO_4$ measurement [380]. Such a large signal would have been easily seen in this experiment - see Fig. 9.5 (a). Hence, this intensity is either so small, that it can be neglected, or it is zero. In both cases, the broadening of the energy-scans around $\zeta = 0.25$ and the anomalous dip of the corresponding phonon mode is not connected to a merging with an additional branch and can be interpreted as a coupling of the topmost Σ_1-phonon mode to the diagonal charge stripes with about equal propagation vector. On the other hand, the temperature scans indicate, that the dip in the phonon dispersion persists also above the charge ordering temperature, see Fig. 9.5 (b-f). However, there might be some dynamical stripe instability also above this temperature. Although nearly all signs point to a coupling of phonons and stripes, for a final, decisive conclusion a sam-

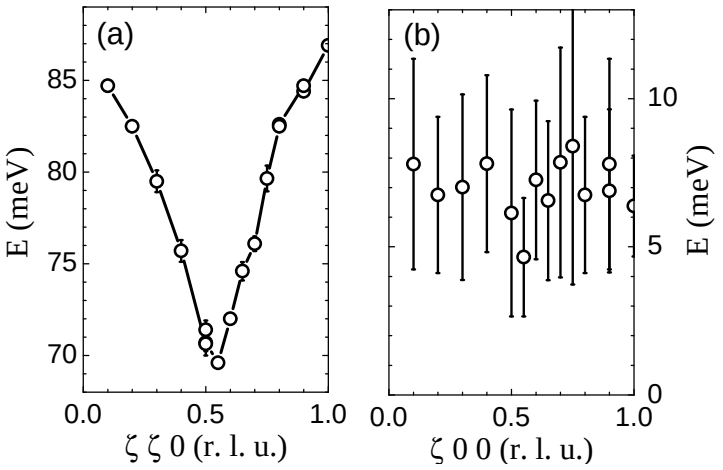

Figure 9.6: (a) Phonon dispersion of the topmost Δ_1 phonon mode and (b) peak widths (FWHM) at 2 K measured at (0 4+ζ 0) and (1 5-ζ 0) in the IN8 measurement.

ple with another hole-doping level has to be measured and compared to the results for $La_{1.8}Sr_{0.2}NiO_{4+\delta}$. Measuring time has been already granted at the 1T triple axis spectrometer at the reactor Orphée in Saclay, France. Therefore, a new $La_{2-x}Sr_xNiO_4$ single crystal with ha Sr-doping level $x = 0.12$ has been grown in this work (*ACK117*); see Chap. 5.5. For such a hole doping level of 0.12 one would expect to observe an anomaly around $\zeta = 0.12$. The $La_{2-x}Sr_xNiO_4$-sample with the lowest Sr-doping where charge ordering has been observed is a sample with $x = 0.135$ [342].

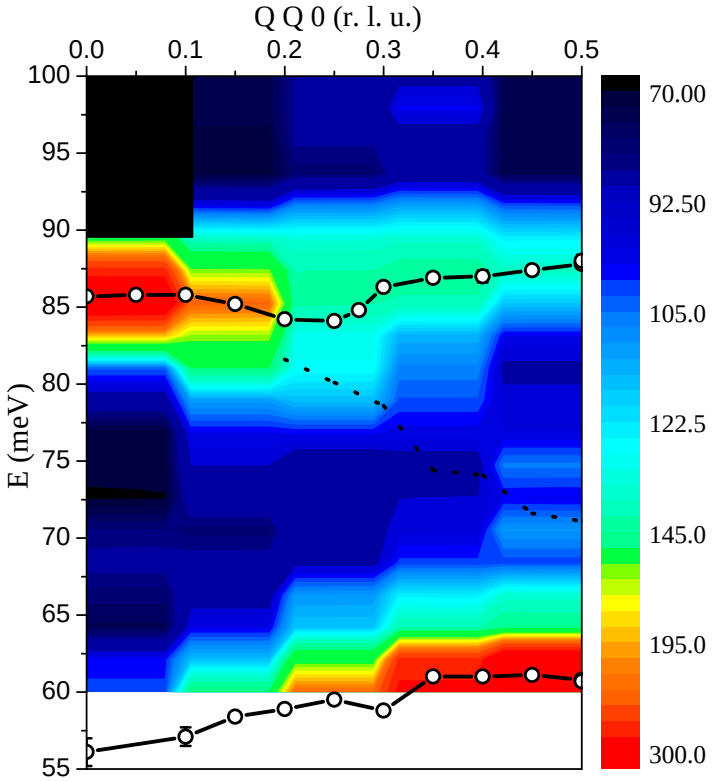

Figure 9.7: Measured neutron scattering intensity in a energy-q contour plot. The *black circles* indicate the results of gaussian fits. The black dotted line indicates an estimated dispersion of an additional (split) phonon mode according to the observations for $La_{1.69}Sr_{0.31}NiO_4$ [380] which, however, are unlike to the observations in this system.

Concluding, the inelastic neutron measurements of stripe ordered $La_{1.8}Sr_{0.2}NiO_{4+\delta}$ indicate almost no splitting of the high frequency Σ_1 phonon mode which is unlike to the observations in $La_{1.69}Sr_{0.31}NiO_4$ [380]. Instead there is clear evidence for a coupling of this topmost Σ_1-mode to the diagonal charge stripes with equal propagation vector, i. e. the dispersion $\omega(q)$ exhibits a softening at $q = \varepsilon$ and the peak width exhibits a strong broadening which might be connected to the difference for phonons propagating parallel or perpendicular to the stripes. These observations which are very different to the phonon dispersion in $La_{1.69}Sr_{0.31}NiO_4$ [380] also indicate that the dispersion in

$La_{1.69}Sr_{0.31}NiO_4$ might be dominated by commensurability effects. Furthermore, strong temperature effects are visible which appear above the stripe ordering onset temperature T_{CO}. For $q = \varepsilon$ the temperature dependency indicates an anomalous softening of $\omega(q)$ on heating above T_{CO}. Furthermore, the phonon intensity becomes very broad for $q = 1/2$ at 300 K which indicates a strong damping of this phonon mode.

magnetic excitations

Using the PUMA triple axis spectrometer the magnetic excitations of $La_{1.825}Sr_{0.175}NiO_{4+\delta}$ have been studied. Fig. 9.8 shows the incommensurability ε for charge (*black triangles*) and magnetic (*grey circles*) ordering superstructure reflections derived from elastic (H$\bar{\text{H}}$0)-scans through (0.78 2.22 0) and (1.394 -0.394 0) respectively. Additionally, in the inset of Fig. 9.8 the normalized intensity of these superstructure reflections is shown. From this intensity-temperature curve the magnetic transition temperature could be determined which is of the order of ∼100 K. As found for other LSNO-compounds, the magnetic transition temperature is well below the charge stripe ordering temperature. The incommensurability ε determined from the charge ordering superstructure reflections differs from the value determined by the analysis of the magnetic peak positions. This discrepancy remains unexplained in this work. The value of the incommensurability ε is on the one hand well below the commensurate value of 1/3 but on the other hand distinctly larger than the nominal value of 0.175 expected from the Sr-doping. Hence, this $La_{1.825}Sr_{0.175}NiO_{4+\delta}$ single crystal contains substantial interstitial excess oxygen which is of the order of $\delta \in [0.02, 0.035]$. The temperature dependency of ε exhibits the tendency to increase with rising temperature towards the commensurate value of 1/3 as was observed for other LSNO samples (see Introduction).

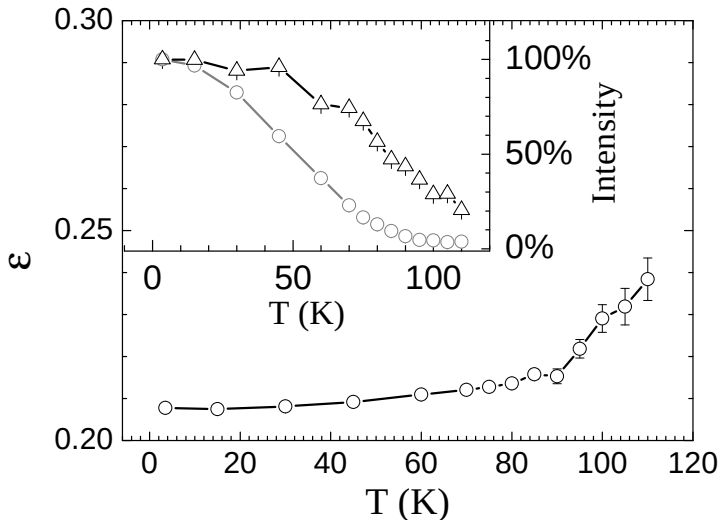

Figure 9.8: ε-temperature curve with intensity-temperature curve in the inset; *black triangles:* charge ordering superstructure reflections, *gray circles:* ε derived from the positions of the incommensurate magnetic satellites.

Recently, quasi-one-dimensional antiferromagnetic excitations have been observed in $La_{5/3}Sr_{1/3}NiO_4$ [382]. These low-energy magnetic excitations form a square-pattern in reciprocal space - see inset of Fig. 9.9 (b) - and were attributed to antiferromagnetic (AFM) spin correlations among the stripe electrons [382]. In the inset of Fig. 9.9 (b) a model of the magnetic excitations in reciprocal space is shown. The *red circles* indicate the incommensurate magnetic satellites of the $La_{1.825}Sr_{0.175}NiO_{4+\delta}$-sample and the *green*

lines indicate the diffuse magnetic scattering arising from 1D AFM correlations parallel to the stripe direction. As there are two possible stripe domains in the LSNO system (see Introduction), the solid and dashed lines indicate the magnetic scattering of these two different domains. The *blue arrow* denotes the scan direction in this inelastic neutron scattering measurement and the corresponding constant-E scans measured at 0.5 THz to 2 THz (∼2.1 meV to ∼8.3 meV) are shown in Fig. 9.9 (a). The red lines indicate fits with two gaussians [1] equidistant on both sides around the center of the diffuse magnetic scattering (crossing of the *blue arrow* with the *green dashed line*) and another independent gaussian for the contribution of the magnetic satellites (*red circles*) in order to describe the increasing intensity at the end of these scans. Spurious peaks have been neglected. In Ref. [382] also two simple gaussians have been fitted on a linear background. The intensity of this magnetic signal decreases with increasing energy and at 8.3 meV

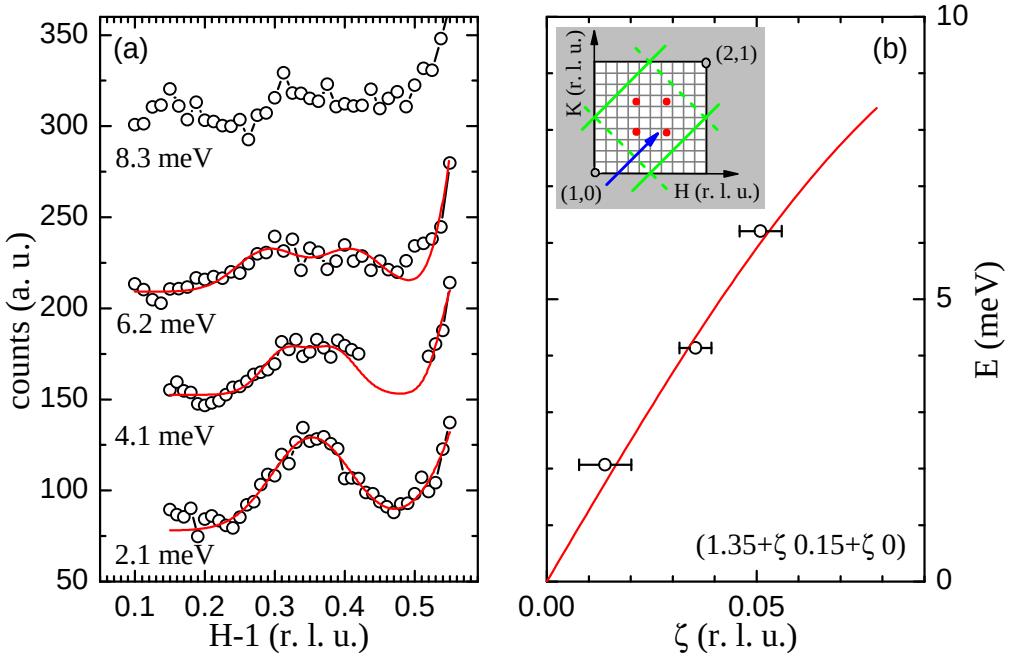

Figure 9.9: (a) Constant energy scans across the dynamic, quasi-1D antiferromagnetic correlations among the stripe electrons together with (b) the according dispersion. In the inset the scan (*blue arrow*) within the (HK0)-plane of reciprocal space is shown.

the magnetic signal is barely visible. The 8.3 meV constant-E scan has been fitted with the expected starting parameters right from the beginning but, as can be seen, the fit is not reliable (*red dotted line*). This is stressed by the large error bar of the fitted

[1] The FWHM and the intensities of both gaussian have been set equal and the peak positions have been fitted symmetrically around the center. For these fits, a self-written computer program [383] based on the Levenberg-Marquardt algorithm [384] has been used. (Similar fitting results could be obtained with Origin 7.5 [385].)

value for ζ in Fig. 9.9 (b) which is even larger than the ζ-region shown in this figure. (Probably, this data is also biased by spurious peaks etc.) These 1D AFM correlations have been measured also at various other positions in reciprocal space confirming the interpretation in terms of a quasi-one dimensional signal. Some of these scans are shown in Fig. 9.9 (a).

The dispersion obtained by these gaussian fits is shown in Fig. 9.9 (b). The *red line* indicates a fit to the measured data using the dispersion proposed in Ref. [382]:

$$E(\overrightarrow{Q}) = \pi \cdot J \cdot |sin(2\pi \cdot \overrightarrow{Q} \circ \overrightarrow{d})| \tag{9.1}$$

with J the exchange energy per spin and vector $\overrightarrow{d} = (1, 1, 0)$. For the magnetic

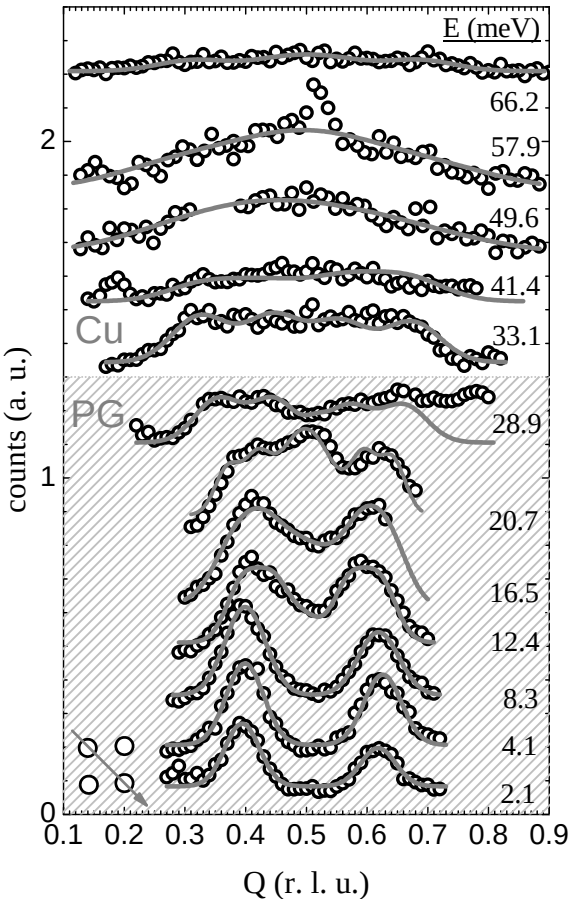

Figure 9.10: (b) Constant-E-scans in (H$\bar{\text{H}}$0)-direction measured at the PUMA spectrometer.

excitations of the other stripe domain (*solid green lines* in the inset of Fig. 9.9 (b)) this vector is $\overrightarrow{d'} = (1, -1, 0)$.

Fitting the dispersion of Eq. 9.1 to the measured data yields an exchange energy of 3.2(1) meV which is exactly the value reported for $La_{5/3}Sr_{1/3}NiO_4$ [382]. However,

the larger error bars of this dispersion indicate the accuracy of this fit and of this measurement. Compared to this, the measurement of the $La_{5/3}Sr_{1/3}NiO_4$-sample [382] exhibits stronger magnetic intensities. This may be explained by the much more stable commensurate stripe ordering of this 1/3 doped sample which may contribute to a larger signal from these 1D AFM correlations parallel to the stripes yielding a much better signal to noise ratio than in the $La_{1.825}Sr_{0.175}NiO_{4+\delta}$-sample measured in this work. However, also the measurements in this work which have been performed at various points in reciprocal space clearly confirm these 1D AFM correlations parallel to the stripes.

Also the magnetic excitation spectrum of the incommensurate magnetic order (satellites) has been studied within this PUMA measurement. For the high energy excitations a second measurement at the PUMA spectrometer has been performed using a Cu (220) monochromator. Fig. 9.10 shows large inelastic scans through $Q - \tau = (0.5\ 0.5\ 0)$ using

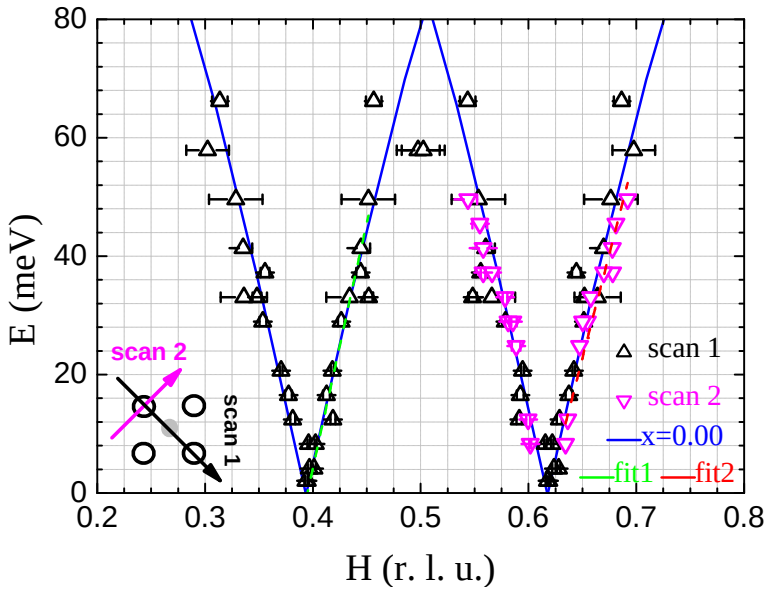

Figure 9.11: Spin-wave dispersion relation of $La_{1.825}Sr_{0.175}NiO_{4+\delta}$ determined in the PUMA measurement; the *blue line* indicates the dispersion of La_2NiO_4 from Ref. [386, 373] which is shifted to the incommensurate wave vectors of the $La_{1.825}Sr_{0.175}NiO_{4+\delta}$-sample; *magenta triangles* and *black triangles* are data points of the corresponding scans shown in the inset; this data has been measured around (1.5 -0.5 0) (*grey dot* in the inset); *green* and *red dashed lines* indicate a linear fit to data of *scan type 1* and *scan type 2*. (Note, that the magnetic peaks observed on both sides around $H = 1/2$ are not fully symetrically in the PUMA measurement.)

a PG monochromator (data on grey hatched background) and a Cu (220) monochromator for the higher energy range. The *grey lines* denote the fits to the data with gaussians of the same FWHM symmetrically placed around the incommensurable wave

vectors (H∼0.4, ∼0.6). The amplitude of the first two and of the last two gaussians was set equal in order to suppress non-physical results with the intensity deviations of the two sides describing effects due to the magnetic form factor etc. over larger regions in Q-space.

For comparison also a fit of the magnon dispersion taking the convolution of the spectrometer resolution function by the Cooper Nathans formalism and the magnetic form factor of the Ni^{2+} ion into account turned out to describe the data not so well as the data suffers from larger contributions of phonons from E = 12 meV on. Although several phonons were introduced by additional gaussians, these fits turned out to be not as good as fitting the data directly with gaussians as described above. Hence, only the gaussian fits are shown in Fig. 9.10.

The resulting spin-wave dispersions for two different kinds of scan types are plotted in Fig. 9.11 together with the dispersions of undoped La_2NiO_4 with $x = 0.00$ taken from Ref. [373, 386]. These values (*blue lines*) have been shifted to the incommensurate wave vectors of the $La_{1.825}Sr_{0.175}NiO_{4+\delta}$-sample studied in this work. A linear fit of the magnon dispersion corresponding to the *black* and *magenta data points* (belonging to *scan type 1* and *scan type 2*; see Fig. 9.11) yields very similar values for the spin wave velocity as reported in literature for undoped La_2NiO_4 [373, 386]. The spin wave velocities parallel and perpendicular to the stripes amount to $\hbar c_\perp = 357(14)$ meVÅ (*scan type 1*) and $\hbar c_\parallel = 303(10)$ meVÅ (*scan type 2*) which is close to the value of $\hbar c_0 = 340$ meVÅ for undoped La_2NiO_4 and $\hbar c_\parallel = 300(20)$ meVÅ and $\hbar c_\perp = 350(20)$ meVÅ for LSNO with $x = 0.31$ [373, 386]. Due to the lower doping the distance in-between the stripes is larger and the magnetic Bragg-peaks are closer to the antiferromagnetic zone-center. In consequence, it seems that the magnons merge at q=($\frac{1}{2}$ $\frac{1}{2}$ 0) at lower energies compared to the 31% doped sample. From the gaussian fits (see Fig. 9.10 and 9.11) this merging seems to occur around 14 THz (∼57.9 meV). If this is the case, the data at 16 Thz would be indicative for a (weak) dispersion above this merging point. But as can be seen in Fig. 9.10, phonon contaminations render the determination of the magnon-merging-point and the observation of the dispersion above rather unreliable.

However, the spin wave dispersion could be measured very well in the lower energy regime and the spin wave velocities parallel and perpendicular to the stripes are very close to the values for LSNO with $x = 0.31$ [373]. The anisotropy between the directions parallel and perpendicular to the stripes is about 15%.

In order to study the purely magnetic scattering and to get rid of the phonon contributions, an inelastic neutron scattering measurement has been performed at the IN20 spectrometer at the ILL using polarized neutrons and a Heusler monochromator and analyzer for polarization analysis. For the scans shown in Fig. 9.12 (a-b) a constant-k_f mode with $k_f = 4.099$ Å^{-1} has been chosen. The magnetic field was applied parallel to the scattering vector ($H \| Q$) and spin-flip (SF) and non-spin-flip (NSF) scattering has been detected separately. Additionally, for the 50 meV to 70 meV constant-E scans also the SF and NSF intensity for $H \perp Q$ has been detected in order to calculate the background and/or the pure magnetic scattering contribution using the following formulas for SF-scattering: $\sigma_{SF}^{H\|Q} = \sigma_{mag} + \frac{2}{3} \cdot \sigma_{nucl,incoh.} + \sigma_{backg}$ and $\sigma_{SF}^{H\perp Q} = \frac{1}{2} \cdot \sigma_{mag} + \frac{2}{3} \cdot \sigma_{nucl,incoh.} + \sigma_{backg}$. Hence, the difference intensity amounts to $\frac{1}{2} \cdot \sigma_{mag}$. With this knowledge the non-magnetic in-

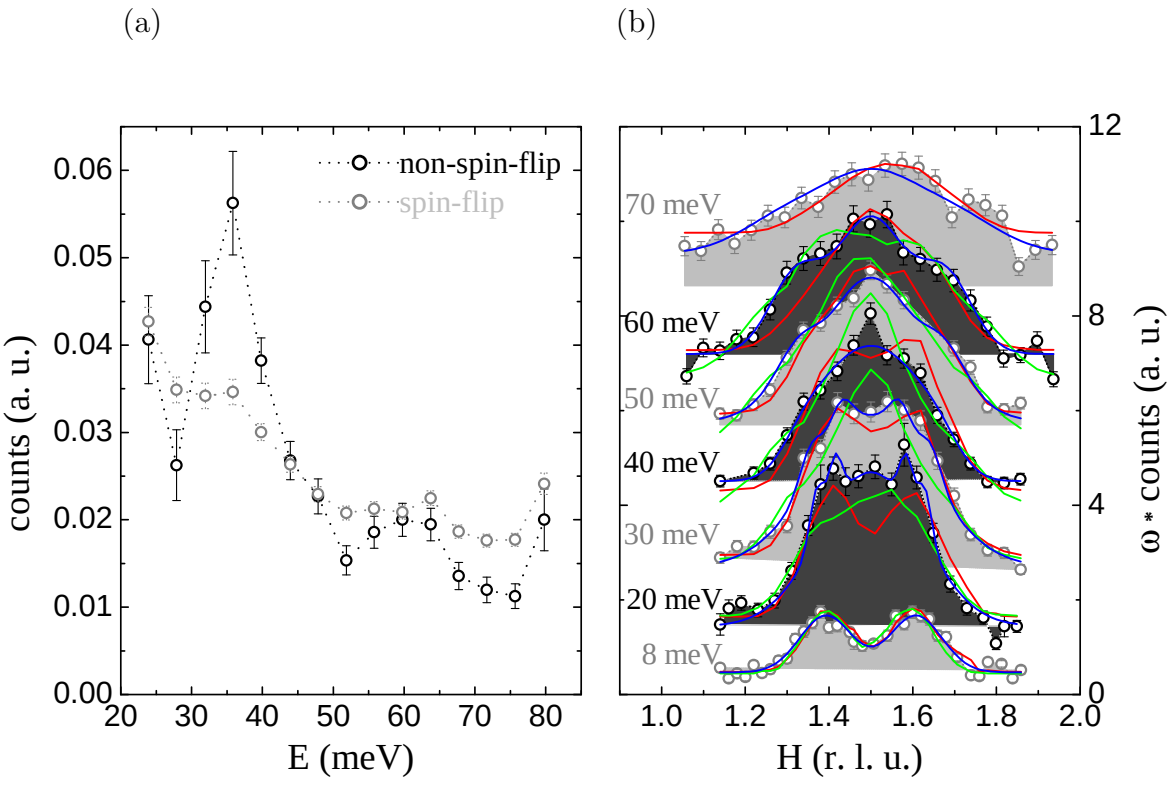

Figure 9.12: (a) Constant-Q-scans at (1.5 1.5 0). (b) Constant-E-scans in (H$\bar{\text{H}}$0)-direction; circles indicate the measured data in the spin-flip channel multiplied by the energy (ω) and shifted by a constant value. The filled areas under the data indicate the pure magnetic scattering after background subtraction. The *blue*, *green* and *red lines* denote fits of the data by pure gaussian fits (*blue*), by a conical dispersion / sine-shaped dispersion convoluted with the spectrometer resolution function (*green/red*) as described in the text.

tensity (background etc.) can be calculated and the pure magnetic intensity is indicated by the filled area under the 50 meV to 70 meV constant-E scan-curves; see Fig. 9.12 (b). For the lower energies (8 meV to 40 meV) no intensity has been measured for $H \perp Q$, but as could already be seen in the 50 meV and 60 meV data, the non-magnetic scattering (background etc.) is at about the same level as the first and last data points within these scans. Hence, the background level was estimated by connecting these data points and, thus, the estimated magnetic scattering is indicated also by a filled area under the data points; see Fig. 9.12 (b).

In Fig. 9.12 (a) a constant-Q scan is plotted as a function of energy transfer. Around 35 meV and 60 meV peaks could be observed in the NSF channel which indicate phonon contributions at these energies and explain the additional intensities (peaks) in the data of the PUMA measurement. Especially, the interpretation of a merging of the magnon branches around 60 meV which was indicated by the PUMA data is uncovered as phononic in origin by this energy scan (constant-Q scan). Hence, the PUMA data is

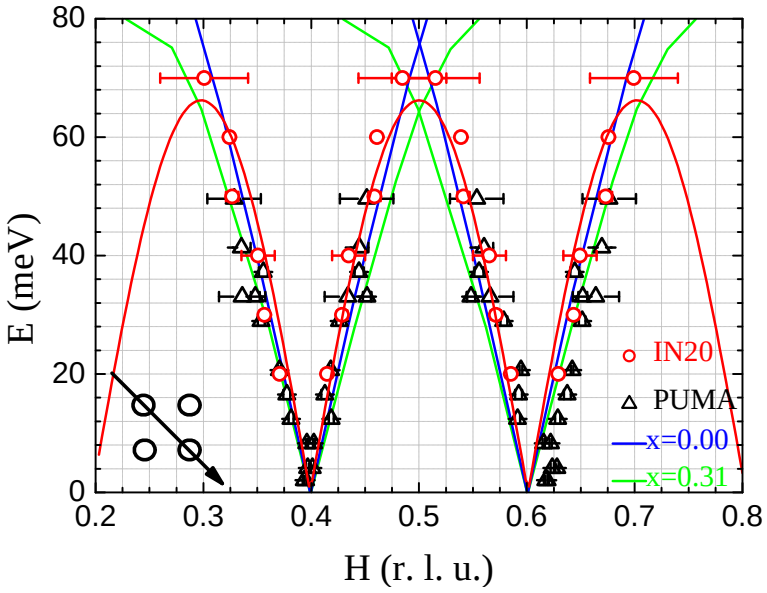

Figure 9.13: Spin-wave dispersion relation of $La_{1.825}Sr_{0.175}NiO_{4+\delta}$; *red circles:* IN20 data, *black triangles:* PUMA data; the *blue line* and the *green line* are dispersions of LSNO x =0.00 and 0.31 samples from Ref. [386] and[373] respectively which are shifted to the incommensurate wave vectors $\widetilde{q}$ of the $La_{1.825}Sr_{0.175}NiO_{4+\delta}$-sample; *red line*: $c' \cdot |\sin(\pi \cdot (0.5/\widetilde{q}_H) \cdot |H - (0.5 - \widetilde{q}_H)|)|$ (In contrast to the PUMA measurement the incommensurate magnetic peaks could be observed symmetrically around $H = 1/2$ for the IN20 measurement.)

not reliable for the 14 THz (57.9 meV) measurement. And probably also other results could have been biased by phonon contributions.

In Fig. 9.12 (b) constant-E scans are shown with a (H$\bar{\text{H}}$0) scan direction through (1.5 1.5 0). As stated above, the filled area under the curve indicates the pure magnetic scattering (above background). The *blue lines* are gaussian fits to the data.

First of all, the incommensurate magnetic peak positions have been determined by fitting the 8 meV data with two gaussian contributions $y = y_0 + I_1 * \exp(-((x-h_1)/w_1)^2) + I_1 * \exp(-((x-3+h_1)/w_1)^2)$. This proceeding can be justified as a small splitting of the magnon branches can not be resolved by the resolution within this measurement, quite similar to the PUMA measurement. Both gaussians are centered around H =1.5 and have equal values for intensity and FWHM. After a value of $h_1 = 1.393(3)$ and $h_2 = 3 - h_1$ has been determined for the incommensurate peak positions, the higher energy data has been fitted using two gaussians centered around h_1 and two other gaussians centered around h_2. The intensity and FWHM of these four gaussians has been restricted to equal values. Hence only three parameters have been refined - one positional parameter describing the absolute value of the distances to h_1 and h_2 respectively (Δh_1), one parameter for the intensity (I_1) and a third parameter for the width (w_1). One additional parameter was used for the refinement of the background level (y_0). During the refine-

ment it turned out, that there is some intensity at H =1.5 which could not be described by these four gaussians plus constant background. This additional intensity is most likely caused by resolution effects due to the admixture of intensity from the other two spin wave cones. In order to describe this effect somehow, an independent fifth gaussian which is centered at H =1.5 has been applied to the fitting procedure enhancing the number of fit parameters by two (I_5 and w_5). (Whenever possible, this fifth gaussian contribution was set to zero intensity.) Thus, the total intensity was described using Eq. 9.2.

$$y = y_0 + \sum_{\mu=0}^{1}\sum_{\nu=1}^{2}\{I_1 * \exp(-((x - h_\nu + (-1)^\mu \Delta h_1)/w_1)^2)\} + I_5 * \exp(-((x - \frac{3}{2})/w_5)^2) \quad (9.2)$$

In Tab. 9.2 the fitting parameters are listed for each constant-E scan. In Fig. 9.12 (b) the four gaussian fits (*green lines*) are shown together with the additional gaussian in the center (*blue line*).

scan	y_0	Δh_1	I_1	w_1	I_5	w_5
8 meV	0.468(35)	-	1.203(54)	0.088(4)	-	-
20 meV	1.436(97)	0.022(2)	1.070(191)	0.023(4)	3.264(159)	0.172(11)
30 meV	2.688(133)	0.036(5)	0.707(179)	0.037(11)	3.186(266)	0.198(14)
40 meV	4.510(57)	0.042(15)	1.198(180)	0.081(19)	1.524(233)	0.089(44)
50 meV	5.7	0.066(6)	0.786(331)	0.074(20)	1.956(637)	0.218(11)
60 meV	7.1975	0.068(4)	1.698(128)	0.091(7)	-	-
70 meV	9.317(320)	0.092(41)	0.762(188)	0.154(69)	-	-

Table 9.2: Fit parameters obtained by fitting Eq. 9.2 to the measured data.

The magnon dispersion derived by these fits is shown in Fig. 9.13 (*red circles*). As can be seen, the IN20 data fits quite well to the values determined in the PUMA measurement at low energy. The spin-wave dispersions of the undoped La_2NiO_4 [386] and of $La_{1.69}Sr_{0.31}NiO_4$ [373] which were shifted towards the incommensurate positions of the $La_{1.825}Sr_{0.175}NiO_{4+\delta}$-sample exhibit very similar dispersions. The spin-wave velocity derived from this dispersion amounts to 379(19) meVÅ which is close to the value of 340 meVÅ in undoped LSNO [386, 373].

In order to describe the mentioned resolution effects better, all spectra have been also modeled using the ResLib package [387], enabling a four dimensional convolution of the spectrometer resolution function with the dispersion surface. In a first model a simple conical dispersion surface with $\omega = c \cdot \Delta Q$ has been fitted to the data (*green line* in Fig. 9.12 (b)). This dispersion is not able to fit the high energy data well. Therefore, a in a second model a dispersion surface with $\omega = c \cdot \sin(\phi \cdot \Delta Q)$ has been fitted to the data (*red line* in Fig. 9.12 (b)). The spin wave dispersion derived by fits of these second model is also shown in Fig. 9.13 (*red line*). Also this model leads to some shortcoming in describing the measured data since this model can not describe the decreasing structure factor for the descending sine-branch, i. e. for H approaching 0 or 1. Such a loss of intensity for $H \rightarrow 0$, 1 has been reported in Ref. [370] where the magnon dispersion was calculated for vertical and diagonal stripes. Hence, a more sophisticated model is

needed to fit the data including also resolution effects. Also the value of the spin wave velocity obtained by these fits is somewhat enhanced: $\hbar \cdot c_\perp \approx 411$ meVÅ. The value obtained by the first methods using gaussian fits only (Eq. 9.2) yields a more reasonable value of $\hbar c_\perp = 379(19)$ meVÅ which is within the error bars in good aggreement with the results of the PUMA measurement ($\hbar c_\perp = 357(14)$ meVÅ).

However, also the LSNO single crystal with $x = 0.12$ grown in this work (*ACK117*) might be a better candidate for a measurement of the spin wave dispersion as the magnon merging point can be expected at much lower energies since the incommensurability should be about half as large as the incommensurability of the $La_{1.825}Sr_{0.175}NiO_{4+\delta}$-crystal measured in this work. Thus, the needed energy transfer can be expected to be much lower rendering the observation of the spin wave dispersion much more easy.

9.1.4 Conclusion

In conclusion, the phonon dispersion of the high frequency Σ_1 branch of $La_{1.8}Sr_{0.2}NiO_{4+\delta}$ reveals a very interesting phonon anomaly at phonon propagation vectors corresponding to the propagation vectors of the diagonal charge stripes (incommensurability ε). Hence, this is a first evidence for electron phonon coupling in a diagonal charge stripe phase and might be relevant for the study of the spin glass phase of $La_{2-x}Sr_xCuO_4$ where also a diagonal charge stripe phase was proposed.

Concluding, the inelastic neutron measurements of stripe ordered $La_{1.8}Sr_{0.2}NiO_{4+\delta}$ indicate almost no splitting of the high frequency Σ_1 phonon mode which is unlike to the observations in $La_{1.69}Sr_{0.31}NiO_4$ [380]. Instead there is clear evidence for a coupling of this topmost Σ_1-mode to the diagonal charge stripes with equal propagation vector, i. e. the dispersion $\omega(q)$ exhibits a softening at $q = \varepsilon$. Also the peak width exhibits an anomalous broadening which is in contrast to the peak widths of the Δ_1 phonon mode which can not couple to diagonal charge stripes like the Σ_1-mode. This anomalous peak broadening of the Σ_1 mode might be connected to the difference for phonons propagating parallel or perpendicular to the diagonal charge stripes. All these findings are very different to the behaviour of the corresponding Σ_1 mode in $La_{1.69}Sr_{0.31}NiO_4$ [380]. Thus, the phonon anomalies in $La_{1.69}Sr_{0.31}NiO_4$ might be dominated by commensurate effects and, hence, $La_{1.69}Sr_{0.31}NiO_4$ might not be the ideal compound to study the phonon dispersion in a diagonal charge stripe phase.

Furthermore, strong temperature effects are visible which appear above the stripe ordering temperature T_{CO}. For $q = \varepsilon$ the temperature dependency indicates an anomalous softening of $\omega(q)$ on heating above T_{CO}. And the temperature dependency of this Σ_1 phonon mode indicates a strong broadening at the zone boundary for high temperatures (300 K) which indicates a strong damping of this phonon mode.

Besides the phonon dispersion, also the magnon dispersion of $La_{1.825}Sr_{0.175}NiO_{4+\delta}$ was measured. Similar as reported for $La_{5/3}Sr_{1/3}NiO_4$-samples, the LSNO sample studied in this work exhibits also dynamic, quasi-one-dimensional antiferromagnetic correlations among the stripe electrons with an exchange energy almost identical to the value reported for $La_{5/3}Sr_{1/3}NiO_4$ [382], i. e. 3.2(1) meV. These findings support the picture of Ni^{3+}-chains in the charge stripe phase of of $La_{1.825}Sr_{0.175}NiO_{4+\delta}$.

The measurement of the magnon dispersion itself is more complicated. At low energy the picture is rather clear and the spin wave velocities parallel and perpendicular to the stripes amount to $\hbar c_\perp = 357(14)$ meVÅ and $\hbar c_\parallel = 303(10)$ meVÅ (PUMA measurement) which is close to the value of $\hbar c_0 = 340$ meVÅ for undoped La_2NiO_4 and $\hbar c_\parallel = 300(20)$ meVÅ and $\hbar c_\perp = 350(20)$ meVÅ for LSNO with $x = 0.31$ [373, 386]. Polarized neutron measurements of $La_{1.825}Sr_{0.175}NiO_{4+\delta}$ at the IN20 spectrometer indicate a slightly higher value $\hbar c_\perp = 379(19)$ meVÅ compared to the value of $\hbar c_\perp = 357(14)$ meVÅ for the PUMA measurement. However, at high energy a direct and unambiguous evidence for a merging of the magnon branches could not be found. The energies where this merging could be expected are still too high for this $La_{1.825}Sr_{0.175}NiO_{4+\delta}$-sample - 70 meV was the upper limit of the IN20 spectrometer - and the contaminations with phonons in this energy range renders the interpretation of the PUMA data (no polarization analysis) very difficult. But the growth of another LSNO crystal with $x = 0.12$ in this work might enable the observation of this magnon merging point and any possible spin wave dispersion above this merging point since the incommensurability of this crystal should be much smaller and, hence, the needed energy scale can be expected to be distinctly lower. Also for the study of the phonon dispersion this crystal is very well suited as it may extend the observations of electron phonon coupling from $La_{1.825}Sr_{0.175}NiO_{4+\delta}$ to other Sr doping concentrations [2].

[2] measuring time has already been granted at the 1T spectrometer at the reactor Orphée in Saclay, France.

[Ar] $3d^{10}$ $4s^1$
1084/2595
63.546

29 Cu
Copper

10 Cuprates

Copper is widely distributed in the earth's crust [107] and although the most important ores are oxides, sulphides and carbonates it can also be found as a free element due to it's low reactivity. Copper is together with silver the best electrical conducting metal. Besides for electronic applications it is used as an alloy in brass or bronze.

10.1 Search for charge stripes in the spin-glass phase of $La_{2-x}Sr_xCuO_4$

10.1.1 Introduction

In 1986 high-temperature superconductivity (HTSC) has been discovered in the cuprate system $La_{2-x}Ba_xCuO_4$ exhibiting a transition temperature of about 30 K [4]. This discovery has triggered enormous research activity in this field and soon other HTSC cuprates with steadily rising T_C followed among which $YBa_2Cu_3O_7$ (YBCO) with a transition temperature of 94 K which can be easily reached using liquid nitrogen has drawn a lot of attention. The cuprate with the current maximum T_C is $HgBa_2Ca_2Cu_3O_{8+y}$ with a T_C of 134 K and even 164 K under pressure [388, 389].

$La_{2-x}Sr_xCuO_4$ can be regarded as the model cuprate system as it has a very simple quasi-two-dimensional crystal structure consisting of CuO_2 layers separated by layers of $(La,Sr)_2O_2$, the so-called 214- or K_2NiF_4-structure isostructural to the nickelate system decribed in Chap. 9.1; see Fig. 9.1 (a-d). The most important modifications are listed in Tab. 9.1 and originate from the octahedral tilts among the tetragonal [110], [1-10] axes; see Chap. 9.1.

The parent compound La_2CuO_4 is an antiferromagnetic insulator with a gap of about 1.5 eV, a Néel temperature of T_N ∼325 K and very large Heisenberg exchange energies [390, 391, 31]. The Cu^{2+}-ion sitting in weakly coupled CuO_2 layers has a $3d^9$ configuration and the degeneracy of these 3d orbitals is lifted by a large crystal field splitting. Hence, the hole (S=1/2) at the Cu-site occupies the $3d_{x^2-y^2}$ orbital and the insulating properties can be understood by the Hubbard-Model.

By the successive substitution of trivalent La by divalent Sr additional holes are doped into the $La_{2-x}Sr_xCuO_4$-system and long-range antiferromagnetic (AFM) order disappears around Sr-doping levels of $x \sim 0.015$ [31]. Around $x \sim 0.055$ this system enters the superconducting regime with a maximum T_C around $x \sim 0.15$. With further

hole-doping the transition temperature decreases again, thus forming a so-called superconducting dome - see the $La_{2-x}Sr_xCuO_4$ phase diagram in Fig. 10.1. In this phase diagram also the HTT to LTO transition temperature is shown as a function of Sr doping. The electrical resistivity is very anisotropic and the in-plane resistivity ρ_{ab} which is purely metallic for $x > 0.05$ exhibits a distinct minimum for the compounds within the SG phase; see Ref. [392, 393]

The role of electron-phonon coupling in HTSC cuprates is still a matter of debate. The static stripes found in Nd codoped LSCO with $x = 0.12$ [6] indicate that electron-lattice interaction plays a role in the cuprates. However, these stripe phases exhibit only small structural distortions. In the isostructural nickelates, for example, the charge stripes are accompanied by much larger structural modulations originating from the modulation of the charges; see Chap. 9.1. The only evidence for stripe like charge (and spin) modulations with static long range order was observed by neutron, hard X-ray and resonant soft x-ray diffraction in $La_{2-x}Sr_xCuO_4$ codoped with smaller rare-earth ions and in $La_{2-x}Ba_xCuO_4$ for Sr and Ba doping levels near 1/8 [6, 365, 9, 394-401]. Here, the charge stripes are running in tetragonal [100] direction, i. e. parallel to the Cu-O bonds. Since these stripes act as a domain wall for the magnetic order yielding a phase shift, the corresponding magnetic modulations are also collinear but have a twice as large spacing, i. e. $q_{mag} = \frac{1}{2} \cdot q_{CO}$. Although no evidence for static charge stripes was found in the superconducting regime of pure $La_{2-x}Sr_xCuO_4$, the observation of collinear magnetic correlations/sattelites [402-407] indicates the existence of (dynamic) collinear charge stripes. On entering the spin-glass (SG) regime of this system ($0.02 \leq x \leq 0.05$) the magnetic satellites rotate by 45° and appear at $(\frac{1}{2} \pm \delta_m \ \frac{1}{2} \pm \delta_m \ 0)_{tet}$ pointing in a diagonal direction instead of a horizontal/vertical one [408-414]. This behaviour was also observed for similar hole doping levels in the Nd codoped $La_{2-x}Sr_xCuO_4$ system [415] and in the $La_{2-x}Ba_xCuO_4$ system [416]. Hence, a stripe phase was also proposed for the SG phase of $La_{2-x}Sr_xCuO_4$ which is right between the metallic (superconducting) and the commensurate antiferromagnetic insulating phases. As the incommensurate magnetic modulation propagates in the tetragonal [110] direction or, more accurately, in the orthorhombic [010] direction (space group *Bmab*) [413], one could also expect diagonal charge stripes similar as in the nickelate system (see Chap. 9.1). However, despite tremendous effort no concomitant structural lattice modulation and no evidence for charge ordering has been reported

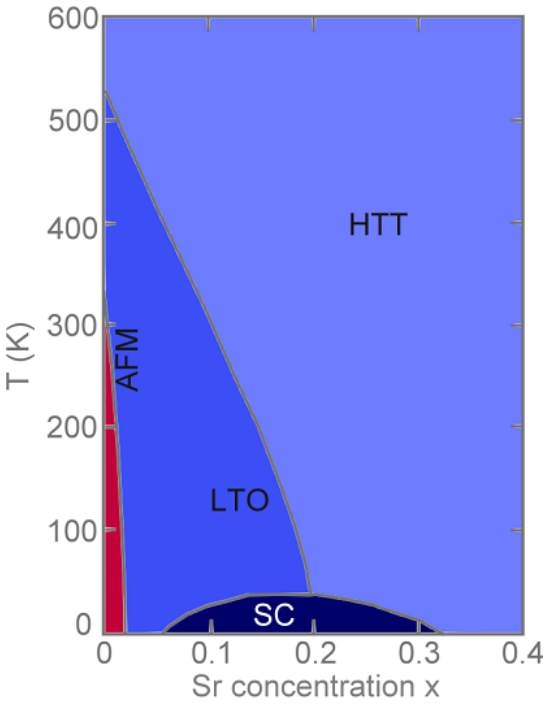

Figure 10.1: Schematic Phase diagram of $La_{2-x}Sr_xCuO_4$ (data taken from Ref. [31]).

in the SG phase of $La_{2-x}Sr_xCuO_4$ so far. Therefore, an alternative chiral explanation has been proposed for the incommensurate ordering in the SG-phase and explains the existing data as well [417-419].

Another possibility to study charge ordering phenomena than by direct observation of structural modulations etc. is the measurement of anomalies in the phonon dispersion which occur in many charge ordered perovskite transition metal oxides [420, 421]. As a charge modulation is accompanied by a modulation of the transition metal-oxygen bond distances a coupling with the longitudinal bond-stretching phonon modes may be induced, which were often called breathing modes [422]. In the HTSC cuprates the

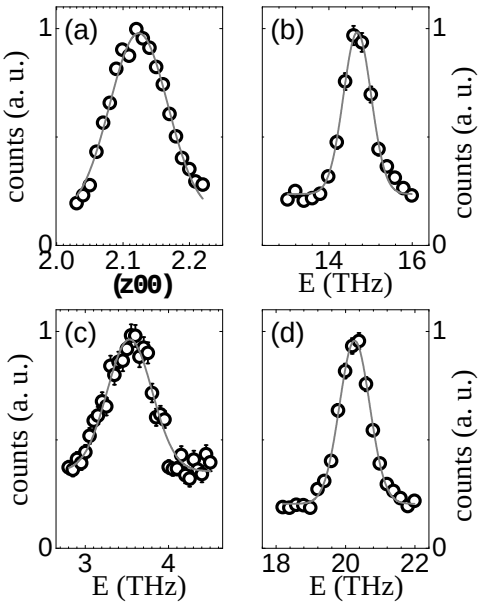

Figure 10.2: Typical constant-Q and constant-E scans.

topmost Δ_1 mode, i. e. the bond stretching phonon dispersion in tetragonal [100] direction, has a flat dispersion near the Brillouin zone centre which, then exhibits a strong anomalous decay around $q = (0.25\ 0\ 0)$ and becomes flat again afterwards for $q = (\zeta\ 0\ 0)$ with $\zeta > 0.35$. This behaviour of the compounds in the superconducting regime is in contrast to the undoped parent compound La_2CuO_4 [378] and indicates strong electron-phonon coupling. For $La_{2-x}Sr_xCuO_4$ with $x \approx 0.12$ it also correlates with the magnetic modulation [407] and coincides with the propagation vector of the static charge stripes observed in the related Nd codoped compounds [6]. Hence, in the case that there is charge ordering, a coupling of the topmost Σ_1 phonon mode to diagonal stripes could be expected for the compounds belonging to the SG phase where diagonal magnetic modulations have been observed. Such a coupling of the bond-stretching phonon mode to diagonal charge stripes has been observed for the first time in this work for the nickelate system - see Chap. 9.1. Therefore, the analysis of the corresponding phonon mode in a a sample belonging to the SG phase may give insight in the question whether diagonal charge stripe order occurs in this regime or not.

10.1.2 Experimental

Large single crystals of $La_{1.95}Sr_{0.05}CuO_4$ have been grown by K. Ikeuchi from the group of K. Yamada using the floating-zone technique. The lattice parameter of these samples have been determined by powder X-ray diffraction. The values of the room-temperature lattice parameter as well as the value of the low-temperature orthorhombic splitting determined in several neutron and hard X-ray experiments confirm the Sr concentration of $x = 0.05$ in these crystals. Also the measurement of the electrical resistivity using a four-probe setup indicates insulating properties; see Fig. 10.3 (b). Hence, the sample is definitely in the SG phase and not in the metallic (superconducting) phase which might arise from accidental oxygen doping. This is also affirmed by the measurement of the magnetical susceptibility; see Fig. 10.3 (b). Most of the literature dealing with the SG phase and the diagonal magnetic correlations is based on the study of crystals grown in the same way as the $La_{1.95}Sr_{0.05}CuO_4$ crystal in this work was grown [409, 410, 412, 411, 413, 414].

For further characterization of the sample elastic neutron scattering measurements have been performed at the triple-axis spectrometer IN8 at the ILL in Grenoble, France and at the triple-axis spectrometer PUMA at FRM-II in Garching. At the IN8 spectrometer a bent Si-monochromator has been used for these purposes and Q-scans in [1-10] direction through $[\frac{1}{2}\ \frac{1}{2}\ 0]$ have been performed at 1.8 K and at 25 K. The difference of these two scans is shown in Fig. 10.3 (a) clearly revealing the incommensurate magnetic signal at $(\frac{1}{2} \pm \delta_m\ \frac{1}{2} \mp \delta_m\ 0)$ with $\delta_m \sim 0.03$ which is in very good agreement with previous characterization of the magnetic ordering in $La_{1.95}Sr_{0.05}CuO_4$, affirming the Sr concentration $x = 0.05$ in these crystals again. (However, also some signal was found at

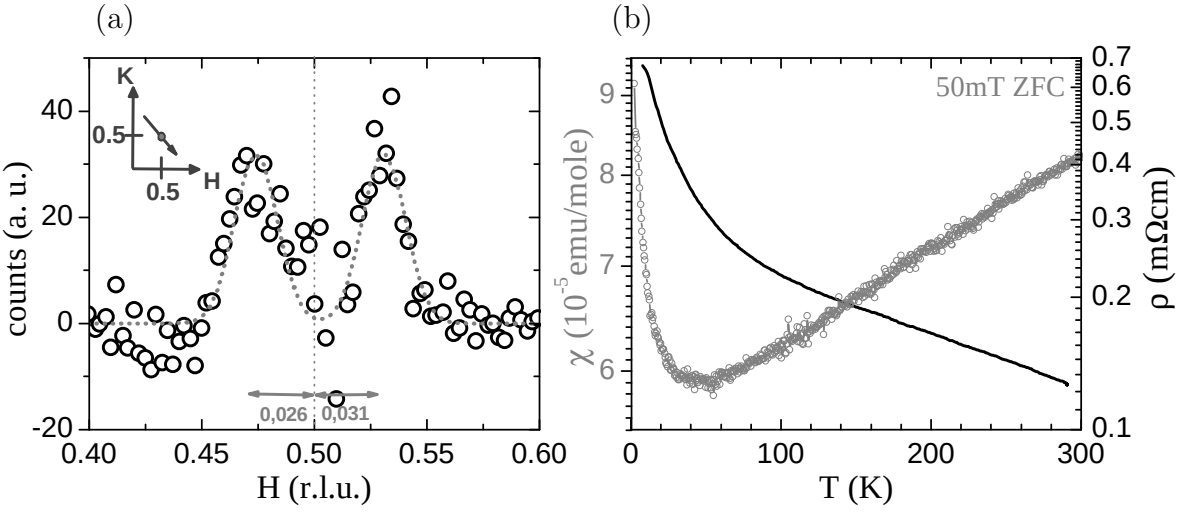

Figure 10.3: (a) The difference of the intensity of an elastic scan in [1 -1 0] direction through $(\frac{1}{2}\ \frac{1}{2}\ 0)$ at 1.8 K and 25 K. The resulting signal reveals the positions of the diagonal magnetic satellites in reciprocal space with $\delta_m \approx 0.03$. (b) Measurement of the electrical resistivity and of the magnetic susceptibility (50 mT, ZFC).

the commensurate position ($\frac{1}{2}$ $\frac{1}{2}$ 0) which is absent in the temperature difference shown in Fig. 10.3 (a) and might be due to some spurious effect like $\lambda/2$, multiple scattering etc.) Similar scans have been obtained at the PUMA spectrometer confirming the value of δ_m.

Inelastic neutron scattering measurements have been performed at the triple-axis spectrometer IN8 at the ILL in Grenoble, France. For a flux optimization a double-focusing Cu (200) monochromator and double-focusing (002) pyrolithic graphite (PG) analyzer setup has been chosen. These measurements have been performed in a constant-k_f mode with a final energy of 14.7 meV. Pyrolytic graphite filter were placed between sample/diaphragms and the analyzer in order to diminish undesirable neutrons at higher harmonic wavelengths. This filter is most efficient for the chosen final energy. For the reason of intrinsic contaminations appearing at an energy transfer of 44 meV, also a final energy of 30.5 meV with a lower resolution was chosen across this energy. Two $La_{1.95}Sr_{0.05}CuO_4$ crystals have been coaligned and mounted with the [100]/[010] axes in the scattering plane (tetragonal notation) which is optimal for the study of phonons propagating in [100] direction (Δ_1 mode) and in [110] direction (Σ_1 mode). Also, this geometry gives rise to an optimal focusing integration as the vertical divergency of the spectrometer is larger and as the phonon dispersion along c is weak. In Fig. 10.2 (a-d) typical constant-Q and constant-E scans are shown (lines are gaussian fits to the data).

For a measurement of the longitudinal acoustic branches also an inelastic neutron measurement has been performed at the cold triple axis spectrometer 4F.1 at the reactor Orphée in Saclay, France. Using cold instead of thermal neutrons a much better energy resolution could be attained. For these measurements a double PG-(002) monochromator and a PG-(002) analyzer have been used.

Additionally, a direct investigation for charge-ordering superstructure reflections in $La_{1.95}Sr_{0.05}CuO_4$ has been performed at the 4F.1 spectrometer (reactor Orphée) and at the PUMA spectrometer (FRM-II).

Furthermore, in three different measurements using ∼100 keV (*1st*: 100097 eV, *2nd*: 99999.5 eV and *3rd measurement*: 100061 eV) hard X-rays at beamline BW5 at Hasylab/DESY in Hamburg charge ordering superstructure reflections have been searched for in $La_{1.95}Sr_{0.05}CuO_4$. The results of these measurements haven been corroborated by complementary neutron measurements at the G4.3 diffractometer at the reactor Orphée in Saclay, France (λ=2.36 Å). In the first synchrotron measurement a setting with a Si analyzer crystal for maximum resolution was used. In the second synchrotron experiment a much lower resolution has been chosen with the use of a Ge-doped Si analyzer crystal in order to integrate over a larger area in Q-space and to avoid any accidental missing of very sharp reflections. In the third synchrotron measurement the same resolution setting has been applied for the comparison of the results of $La_{1.95}Sr_{0.05}CuO_4$ with a LSCO sample in the superconducting regime - $La_{1.88}Sr_{0.12}CuO_4$.

The analysis of the phonon dispersion is based on the tetragonal ($I4/mmm$) unit cell and the orthorhombic distortions will be ignored. All wavevectors Q will be given in units of reduced lattice units $2\pi/a_{tet}$. Also the results of the neutron measurements searching for superstructure reflections are also reported in tetragonal notation. However, the high resolution of the synchrotron measurements using 100 keV X-rays gives necessitates to

the exact separation of the different twin domains in the orthorhombic phase. Hence, the results of these synchrotron measurements are given in orthorhombic notation.

10.1.3 Results and Discussion

Lattice dynamics of $La_{1.95}Sr_{0.05}CuO_4$

In Fig. 10.5 constant-Q scans of the $La_{1.95}Sr_{0.05}CuO_4$ sample studied in this work are shown for the high frequency Σ_1 and Δ_1 branches. As the polarization patterns in Fig. 9.3 (a-b) indicate, these topmost Σ_1 or Δ_1 phonon modes should couple to charge stripe instabilities and, hence, this experiment mainly focuses on these phonon modes. The overall phonon dispersion obtained in all measurements is plotted in Fig. 10.4. In this figure, the Δ_1-, Δ_2-, Σ_1- and Σ_2-branches are shown where the Δ (Σ) branches denote phonon modes propagating in [100]-direction ([110]-direction) and the index 1 and 3 refer to irreducible representations containing longitudinal acoustic modes and transverse acoustic modes polarized parallel to the planes respectively [423]. Whereas the transverse modes exhibit narrow peak widths throughout the entire Brillouin zone, the longitudinal Δ_1 modes lose intensity and broaden towards the middle of the Brillouin zone which can be only partially understood with lattice dynamic model calculations and is similar in $La_{1.85}Sr_{0.15}CuO_4$ [381]. Nonetheless, the entire dispersion of the high frequency modes of $La_{1.95}Sr_{0.05}CuO_4$ in [100]- and [110]-direction is plotted in Fig. 10.6 (a-b) in detail and compared with other $La_{2-x}Sr_xCuO_4$-samples from literature with Sr doping levels $x = 0.00$, 0.07, 0.15. The corresponding peak width measured in constant-Q scans is plotted in Fig. 10.6 (c-d).

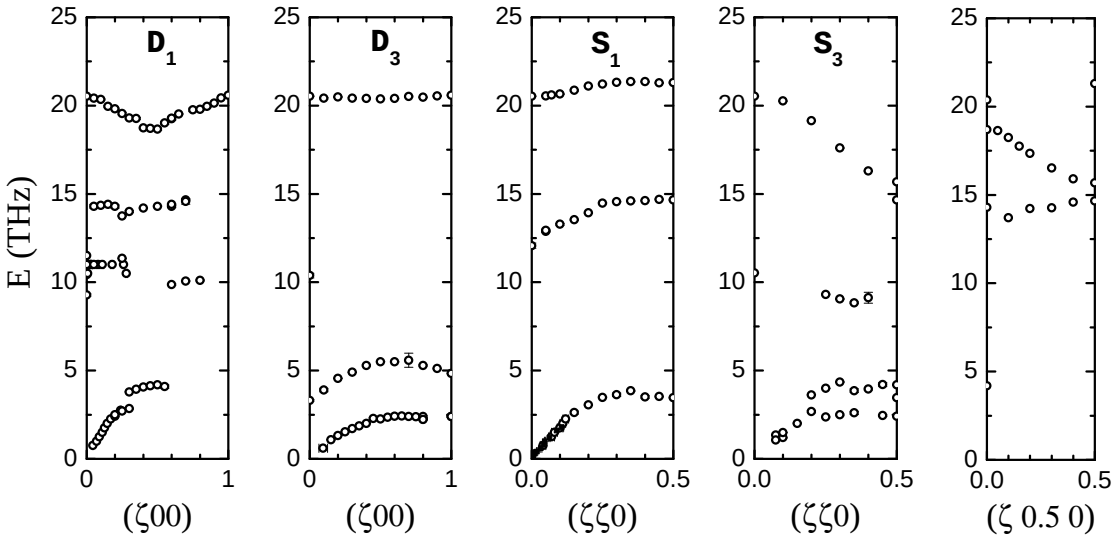

Figure 10.4: Phonon dispersion for Δ_1-, Δ_2-, Σ_1-, Σ_2- modes and a phonon dispersion in (ζ $\frac{1}{2}$ 0) direction.

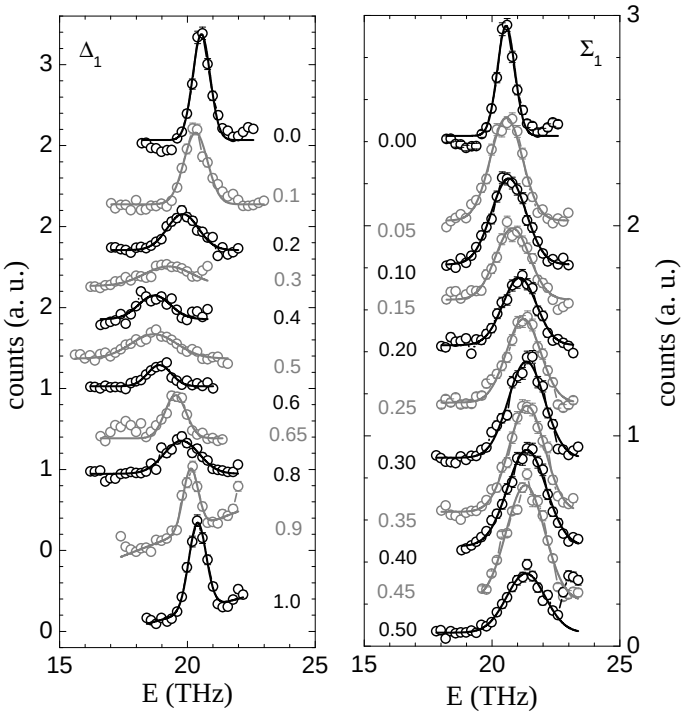

Figure 10.5: Constant-Q scans for Δ_1 and Σ_1 modes of $La_{1.95}Sr_{0.05}CuO_4$ for different values of ζ measured at 1.8 K.

The octahedral tilts in $La_{2-x}Sr_xCuO_4$ induce distortions doubling the primitive unit cell and the number of phonon branches which may be even further enhanced by twinning effects. Thus, for the phonon modes in [1 1 0]-direction a broadening can be expected. But these (small) effects are difficult to resolve in a typical neutron measurement and will be ignored in this work. Thus, the results presented in this work refer to the tetragonal notation.

The position of the magnetic satellites at $\sim(\frac{1}{2} \pm 0.03\ \frac{1}{2} \mp 0.03\ 0)$ would be indicative for diagonal charge stripes with $q_{CO} \sim (0.06\ 0.06\ 0)$. A value of $q_{CO} \sim (0.06\ 0.06\ 0)$ to $(0.07\ 0.07\ 0)$ could be also expected from the nominal Sr concentration and comparison with literature data [413]. As the bond stretching phonon modes should couple to charge stripes, one would expect phonon anomalies around $q \approx q_{CO}$ in the high frequency Σ_1 mode as has been observed for $La_{1.8}Sr_{0.2}NiO_{4+\delta}$ in this work, see Chap. 9.1. The (commensurate) stripe order in $La_{1.69}Sr_{0.31}NiO_4$ causes a clear splitting of this phonon mode; see Ref. [380]. However, the phonon dispersion of $La_{1.95}Sr_{0.05}CuO_4$ in [110]-direction exhibits no anomalies, although anomalies would have been expected in the case of diagonal stripe ordering. Also the peak widths are not indicative for any phonon anomaly in [110]-direction; see Fig. 10.6.

But surprisingly, the dispersion in [100] direction exhibits already similarities with the dispersion of metallic LSCO especially with $La_{1.93}Sr_{0.07}CuO_4$. In Fig. 10.6 (a) the

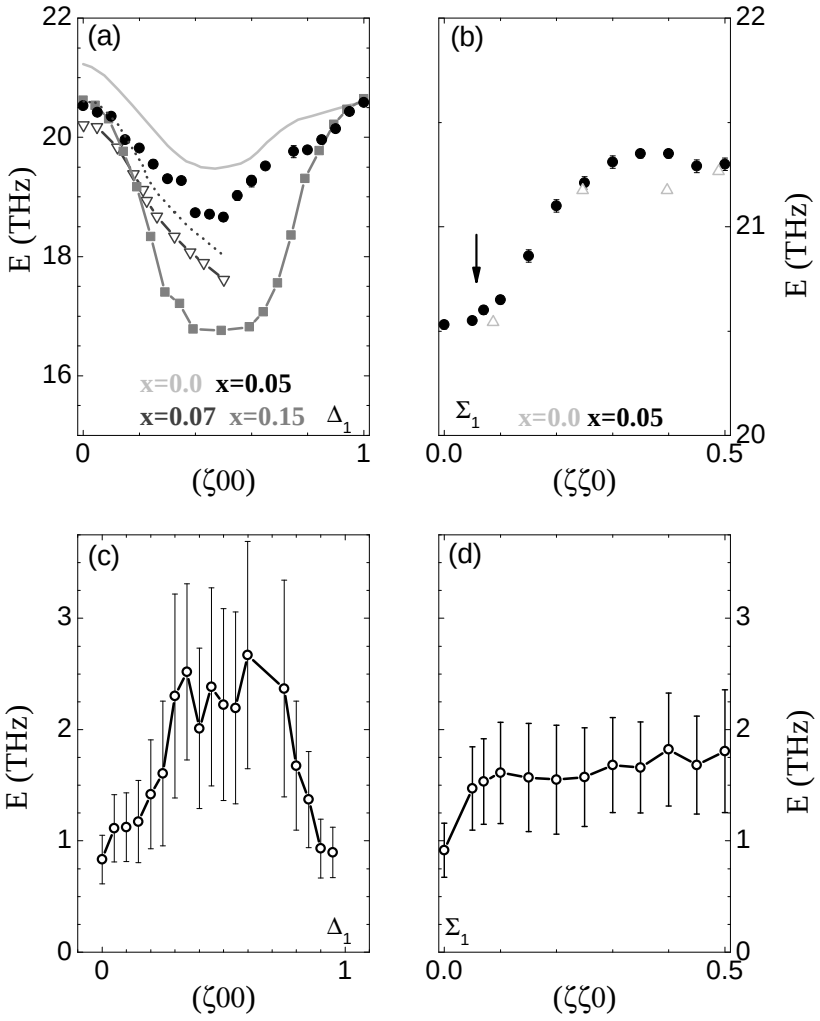

Figure 10.6: (a) Dispersion of the high-frequency Δ_1 phonon mode of $La_{1.95}Sr_{0.05}CuO_4$ (*black dots*) together with the dispersion of La_2CuO_4 (*light gray line*) [381], $La_{1.85}Sr_{0.15}CuO_4$ (*gray squares*) [381] and $La_{1.93}Sr_{0.07}CuO_4$ (*dark gray triangles* †) [13]. (b) Dispersion of the topmost Σ_1 branch of $La_{1.95}Sr_{0.05}CuO_4$ together with the dispersion of La_2CuO_4 [378]. (c-d) The width (FWHM) of the corresponding bond-stretching modes of $La_{1.95}Sr_{0.05}CuO_4$. (†: the dotted line indicates the values of $La_{1.93}Sr_{0.07}CuO_4$ shifted by 0.4 THz to higher energies/frequencies.)

dispersion of $La_{1.93}Sr_{0.07}CuO_4$ [13] shifted by 0.4 THz to higher energies is also shown (dotted line) in order to correct for a possible energy offset of the two different spectrometer IN8 and 1T: as shown in Chap. 10.2, Fig. 10.26 (c), the phonon dispersion of $La_{1.48}Nd_{0.4}Sr_{0.12}CuO_4$ measured in Ref. [13] is shifted by about $\sim$2 meV $\approx$ 0.5 THz to lower energies compared to the phonon measurement of $La_{1.88}Sr_{0.12}CuO_4$ in this work. Also the phonon dispersion of $La_{1.85}Sr_{0.15}CuO_4$ reported in Ref. [13] is almost identical

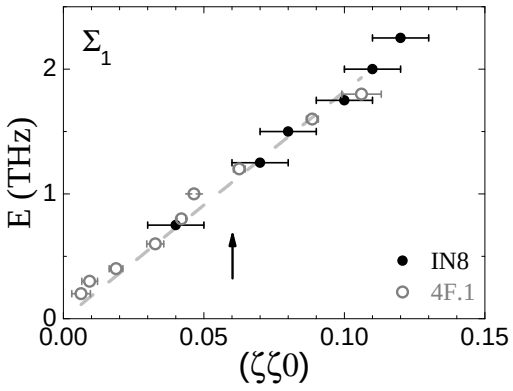

Figure 10.7: Phonon dispersion of the longitudinal acoustic Σ_1 phonon mode; *black dots*: IN8 data, *gray cricles*: 4F.1 data.

to the dispersion of $La_{1.48}Nd_{0.4}Sr_{0.12}CuO_4$ [13] indicating that this offset in energy might not be an effect of Nd co-doping. Hence, the dotted line might be a better comparison of $La_{1.93}Sr_{0.07}CuO_4$ to the 5% doped LSCO sample measured in this work.

In any case, the longitudinal bond stretching mode of $La_{1.95}Sr_{0.05}CuO_4$ exhibits a downwards dispersion which is characteristic for samples in the metallic LSCO regime. Also the full widths at half maximum show a distinct broadening which is similar as in optimum doped $La_{1.85}Sr_{0.15}CuO_4$; see Fig. 10.6 (c). And there is no evidence for a LO-TO splitting as could be expected for an insulator.

Hence, the phonon dispersion of $La_{1.95}Sr_{0.05}CuO_4$ does not exhibit any signatures supporting the picture of diagonal stripes in the SG phase of LSCO. Instead, the longitudinal bond stretching phonon dispersion exhibits a softening of the half-breathing mode which is qualitatively independent on the Sr doping level x and just the extent of this softening as well as the shape of the dispersion vary with x. The downward dispersion of the of the Δ_1 mode from the zone center $\zeta = 0$ towards $\zeta = 0.5$ (half-breathing mode) amounts to ΔE ∼1.8 THz in $La_{1.95}Sr_{0.05}CuO_4$ and ∼2.6 THz and ∼3.9 THz in $La_{1.93}Sr_{0.07}CuO_4$ and $La_{1.88}Sr_{0.12}CuO_4$ respectively; see Fig. 10.6 (a). Hence, the amplitude of the half-breathing mode softening is in very good approximation proportional to the Sr doping level x and even no effect due to the reduced metallicity of $La_{1.95}Sr_{0.05}CuO_4$ is apparent.

Thus, the dispersion of the Δ_1 mode as well as the distinct broadening of the phonon widths in the LSCO system indicates a strong electron phonon coupling for the longitudinal bond stretching mode and the softening of the half-breathing mode seems to be an intrinsic instability of the LSCO system which roughly scales with the Sr doping level x.

Additionally, the longitudinal acoustic (LA) phonons along the [110]-direction have been studied using also a cold triple-axis spectrometer (4F.1) with a better energy resolution. The results of the inelastic measurements at the thermal (IN8) and cold (4F.1) neutron sources are shown together in Fig. 10.7. Supporting the observations in the high frequency Σ_1 mode, also the LA Σ_1 phonon mode exhibits no anomalies at a prop-

agation vector which would have been expected for a diagonal charge stripe phase.

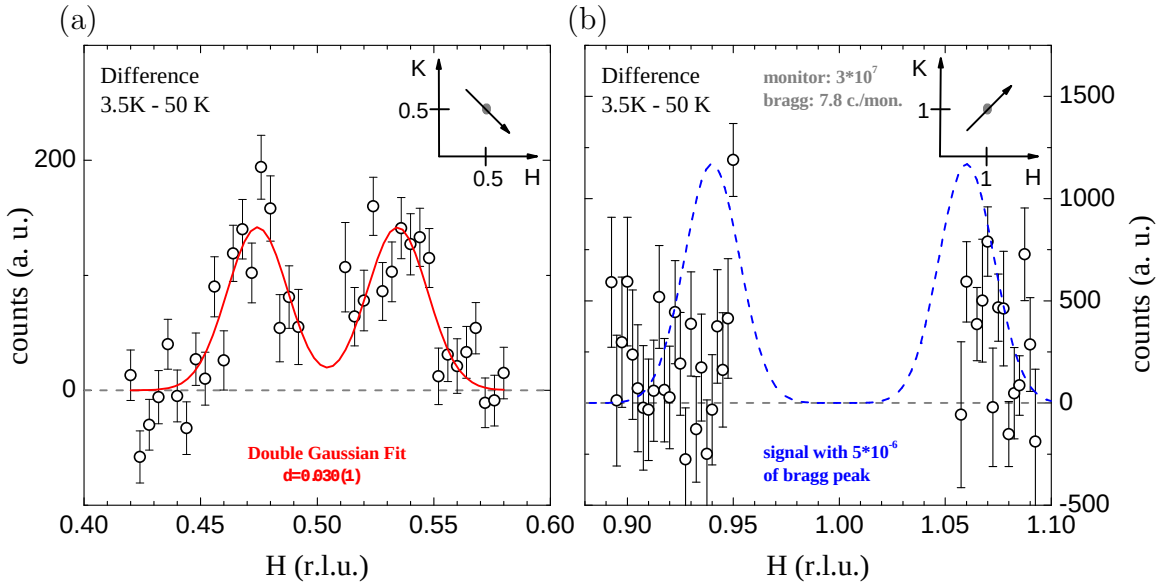

Figure 10.8: (a) The difference of the intensity of an elastic scan through $Q = (\frac{1}{2}\ \frac{1}{2}\ 0)$ at 3.5 K and 50 K (PUMA spectrometer, first measurement). The resulting signal yields $\delta_m = 0.030(1)$. (b) Difference intensity between scans measured at 3.5 K and at 50 K of a scan in [1 1 0] direction through (1 1 0). The *dashed blue line* indicates the expected intensity of a superstructure reflection with $\delta_{CO} = 2 \cdot \delta_m$, the same peak width and of the size of $5 \cdot 10^{-6}$ of a strong Bragg peak.

search for structural distortions in $La_{1.95}Sr_{0.05}CuO_4$

Besides studying the signatures of a (diagonal) stripe instability in the phonon dispersion, also several experiments have been performed in this work in order to search directly for the structural superstructure reflections of a diagonal (horizontal/vertical) charge stripe phase:

1. PUMA spectrometer (FRM-II, $\lambda = 2.35$ Å neutrons; 4 days)
2. PUMA spectrometer (FRM-II, $\lambda = 2.36$ Å neutrons; 2 days)
3. PUMA spectrometer (FRM-II, $\lambda = 2.36$ Å neutrons; 3 days)
4. 4F.1 spectrometer (reactor Orphée, $\lambda = 4.25$ Å neutrons; 7 days)
5. beamline KMC-1 (BESSY, (soft X-rays) synchrotron radiation; 2 days)
6. beamline MagS (BESSY, $\lambda \sim 1.381$ Å synchrotron radiation; 1 day)
7. beamline BW5 (Hasylab/DESY, $\lambda = 0.124$ Å synchrotron radiation; 7 days)
8. beamline BW5 (Hasylab/DESY, $\lambda = 0.124$ Å synchrotron radiation; 3 days)
9. beamline BW5 (Hasylab/DESY, $\lambda = 0.124$ Å synchrotron radiation; 2 days)
10. G4.3 diffractometer (reactor Orphée, $\lambda = 2.36$ Å neutrons; 2 days)

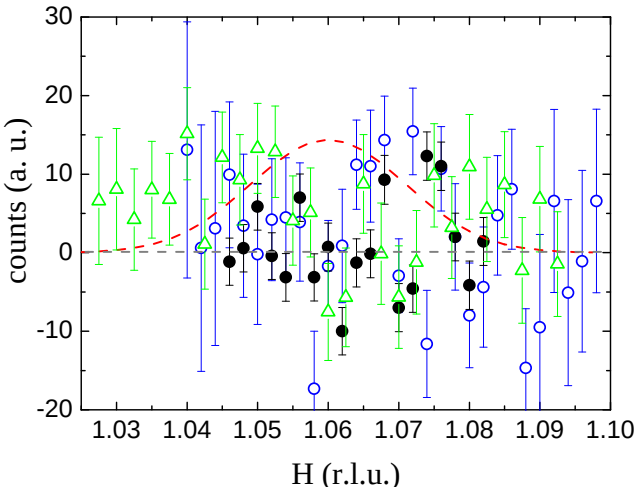

Figure 10.9: Longitudinal scans in [1 -1 0]-direction through (1 -1 L). The difference of the low-temperature data (∼2 K) minus the high-temperature data (∼50 K) is shown; *blue circles*: $L = 0$ (4F.1), *black dots*: $L = \frac{1}{2}$ (4F.1), *green triangles*: $L = 1$ (PUMA), *red dashed line*: a signal with peak width of the magnetic satellites and intensity of $1{\cdot}10^{-6}$ of the (110) Bragg peak at H = $1{+}2{\cdot}\delta_m$.

In Fig. 10.8 (a) the difference intensity of two scans through the commensurate AFM Bragg position at 3.5 K and at 50 K at the PUMA spectrometer is shown. Clearly the magnetic satellites are visible. Fitting two symmetrical gaussian with equal intensity and peak width to the data yields an incommensurability of (nearly) exactly 0.03 which is in accordance with the IN8 measurement; compare Fig. 10.3 (a). This measurement was performed in a [100]/[010] geometry with collimations of 20'-open-S-20' and flat analyzer and monochromator. In the second and third measurement at the PUMA spectrometer a 60'-24'-S-20' collimation setting was applied. The difficulty of these measurements compared to measurements of LSCO crystals with higher Sr doping where horizontal/vertical stripes appear is the vicinity of the expected diagonal charge stripe superstructure reflections to the Bragg peak. For the suppression of the Bragg tails an optimal resolution is needed. In Fig. 10.8 (b) the results of a diagonal scan (see inset) across the (110) Bragg peak is shown. The *blue dashed line* indicates a signal of the order of $5 \cdot 10^{-6}$ of a strong Bragg reflection. This signal would have been easily seen.

Further measurements across $(1\pm2\delta\ 1\pm2\delta\ L)$ with $L = 0,\ \frac{1}{2},\ 1$ and 3 have been performed at the PUMA and 4F.1 spectrometer. The measurements at the 4F.1 spectrometer benefit from the higher resolution due to the larger neutron wavelength used. The most important results are summarized in Fig. 10.9 where the difference of the low temperature data (∼2 K) and high temperature data (∼50 K or more) is shown. The *red dashed line* indicates a signal which is about $1{\cdot}10^{-6}$ of the (110) Bragg peak. As can be seen a signal of $1\text{-}2 \cdot 10^{-6}$ of a strong Bragg peak would have been detected in these experiments for $L = 0,\ \frac{1}{2}$ and 1. The intensity of the charge stripe ordering su-

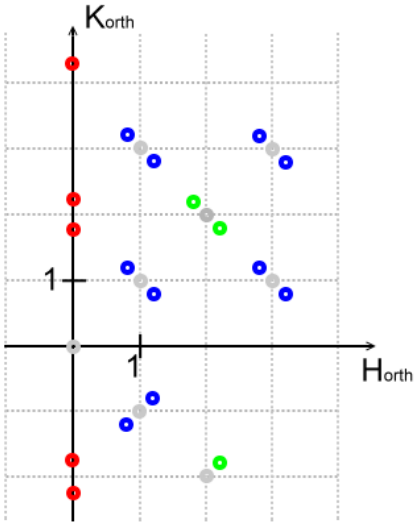

Figure 10.10: Superstructure reflections in the first two BW5 measurements.

perstructure reflection (0 2-2ε 0) observed for vertical/horizontal stripes in Ref. [6] is of the order of $\sim 10^{-6}$ times that of the strong (020) nuclear reflection. This value is about the detection limit for weak superstructure reflections in the neutron measurements of $La_{1.95}Sr_{0.05}CuO_4$ in this work. Hence, there is no support for the diagonal stripe picture

in the SG phase of LSCO from the neutron experiments performed in this work which is in accordance with the study of the phonon dispersion of this work.

There was also no sign of such diagonal stripe superstructure reflection in resonant soft X-ray diffraction measurements using synchrotron radiation at beamline KMC-1 at BESSY in Berlin which have been performed in collaboration with H. Ott and T. Burnus.

In this work, additional synchrotron radiation single crystal X-ray diffraction measurements using ∼100 keV hard X-rays have been performed at beamline BW5 at Hasylab/DESY. Due to the high resolution it was possible to orient the crystal on one orthorhombic twin domain. Hence, the results of these measurements are shown in orthorhombic notation instead of the tetragonal one.

In this experiment superstructure reflections were visible at several positions in reciprocal space: at positions in diagonal direction indicative for diagonal stripes but also in horizontal/vertical direction. In Fig. 10.10 the superstructure reflections observed in the first two BW5 measurements are summarized in the HK plane (in orthorhombic notation). The red circles denote the superstructure reflections measured at $(0\ K\ -3)_{ortho}$ which would be indicative for diagonal charge stripes with q=$(0\ 0.2\ 1)_{ortho}$. The other circles indicate superstructure reflections at vertical/horizontal q-values with $L = 2{\cdot}\mathrm{n}{+}1$ *(blue circles)* or $L{=}\ 2 \cdot n$ *(green circles)* with q=$(\pm 0.1\ \mp 0.1\ 0)_{ortho}$.

In the first high resolution BW5 measurement superstructure reflections appeared at $(0\ K\ -3)_{ortho}$. In Fig. 10.11 (a-d) several scans through these superstructure reflections are shown. These scans exhibit sharp peaks at $(0\ \pm 2 \mp 0.2\ -3)_{ortho}$with an intensity of about $\sim 8{\times}10^{-8}$ of the $(020)_{ortho}$ Bragg peak. The peak positions are qualitatively the right position for diagonal charge stripe superstructure reflections indicating a modulation in the orthorhombic b^* direction which would be in accordance with the observation in Ref. [410] that the diagonal magnetic satellites appear only in b^* direction of the LTO structure. Also the intensity could be of right order of magnitude and the

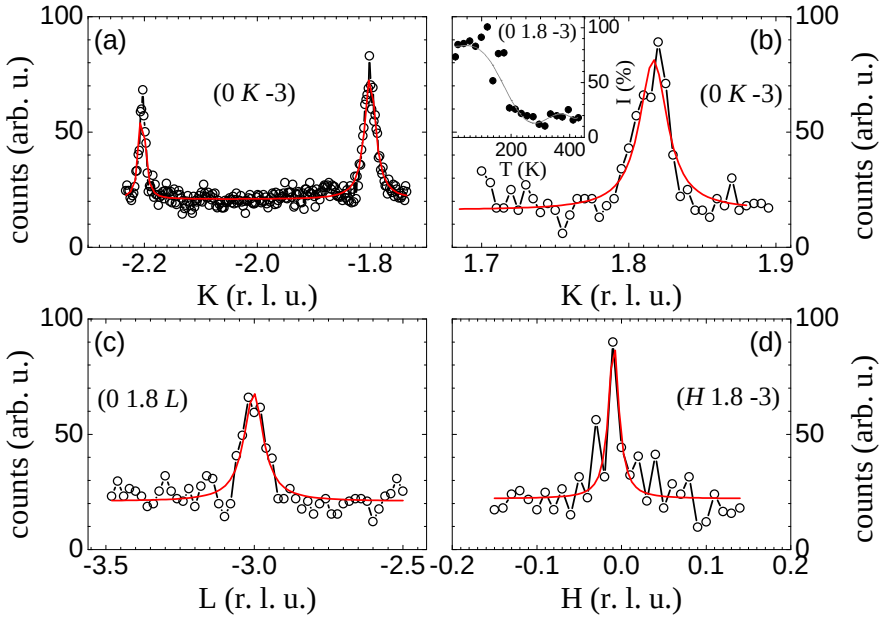

Figure 10.11: The measured superstructure reflections in the high-resolution BW5 experiment (with a q-vector pointing in b^* direction) of a diagonal charge stripe order. The *red lines* are fits with a lorentzian.

odd value of L would be indicative for a three-dimensionally ordered diagonal charge stripe phase similar as in the nickelate system (see Chap. 9.1). However, the quantitative value of q amounts to $(0\ 0.2\ 1)_{ortho}$ and, hence, diagonal magnetic satellites would have been expected at $(0\ 1\pm0.1\ 0)_{ortho}$ and $(1\ \pm0.1\ 0)_{ortho}$, or in tetragonal notation at $(\frac{1}{2}\mp0.05\ \frac{1}{2}\pm0.05\ 0)_{tet}$. But, due to the neutron measurements δ_m amounts to 0.03 which is distinctly smaller than the value of 0.05; compare Fig. 10.8 (a). Also the temperature dependency of the (0 1.8 -3) superstructure reflection which has been measured in the second BW5 measurement and which is shown in the inset of Fig. 10.11 (b) does not favour a charge-stripe order as an interpretation since the ordering temperature would be even much higher than that in $La_{5/3}Sr_{1/3}NiO_4$. Thus, these superstructure reflections probably have some other origin like Sr-ordering etc.

Hence, no superstructure reflections of a diagonal stripe phase could be detected in this first BW5 measurement with an accuracy of roughly $\sim1\times10^{-8}$ of the $(020)_{ortho}$ Bragg peak.

Besides these rather weak superstructure reflections distinctly stronger superstructure reflections appeared at positions with horizontal instead of diagonal character. The according q-values amount to $(\pm0.1\ \mp0.1\ 0)_{ortho} = (\pm0.1\ 0\ 0)_{tet}$ and most of these reflections

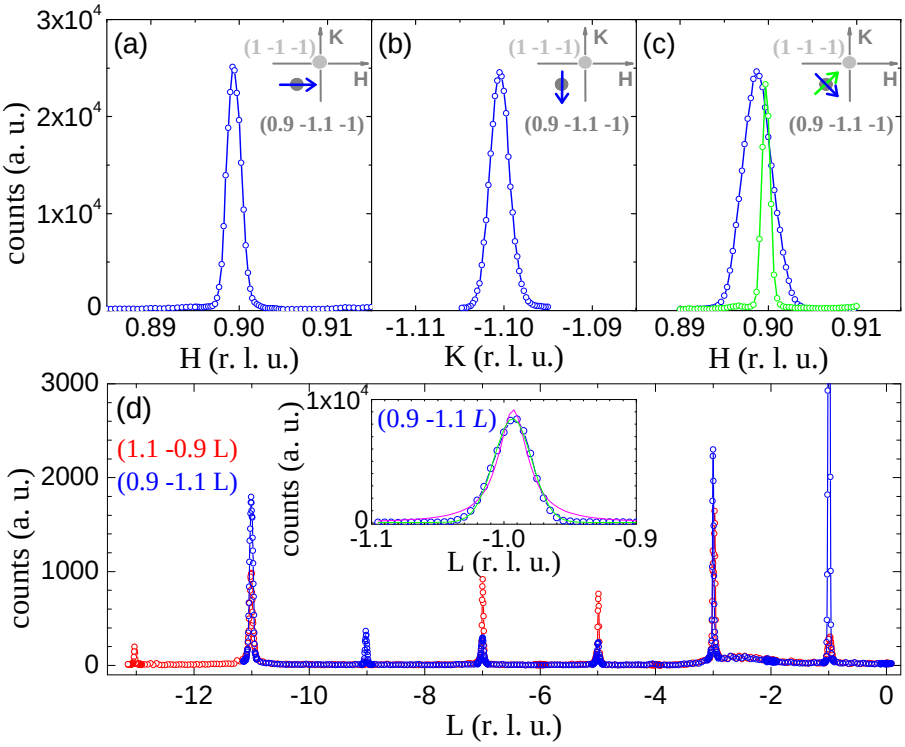

Figure 10.12: Scans in (a) [100]-, (b) [010]-, (c) [110]- and [1-10] direction through the (0.9 -1.1 -1) superstructure reflection in the (first) high-resolution BW5 experiment. In (d) L-scans at (0.9 -1.1 L) and (1.1 -0.9 -1) are shown. In the inset a more detailed L-scan through (0.9 -1.1 -1)can be seen.

have about $\sim 10^{-6}$ to $\sim$1-4$\cdot 10^{-4}$ times the intensity of the $(020)_{ortho}$ reflection. There are two superstructure reflections which are even larger: the strongest superstructure reflection found has an intensity of about 7×10^{-4} of the strong $(020)_{ortho}$ Bragg peak.

It is difficult to understand the origin of these distinctly stronger superstructure reflections since they appear at transversal positions [1] which indicates that the shifts of the modulation should be perpendicular to the propagation direction. A conventional vertical/horizontal charge stripe phase as has been found in Nd codoped LSCO [6] is not able to explain these superstructure reflections as they should appear in longitudinal scans instead of transversal ones. Also, these superstructure reflections are three orders of magnitude larger than the superstructure reflections observed for horizontal stripes in Nd codoped LSCO [6]. However, the absolute value of $q = (\pm 0.1\ 0\ 0)_{tet}$ would be in accordance with the Sr doping level of $x = 0.05$ since the superstructure reflection of the vertical stripes in Nd codoped LSCO with $x = 0.12$ was found at $q = (0\ 0.25\ 0)_{tet}$ [6].

In Fig. 10.12 (a-c) different Q-scans through such a collinear superstructure reflection are plotted. Additionally, large scans in [001]-direction reveal the L-dependency for these superstructure reflections which appear only at odd values of L in Fig. 10.12 (d). In the inset of Fig. 10.12 (d) a L-scan through (0.9 -1.1 -1) is shown. The *green/magenta lines* indicate gaussian/lorentzian fits. As can be seen, these peaks are very sharp and limited by resolution indicating very large correlation lengths.

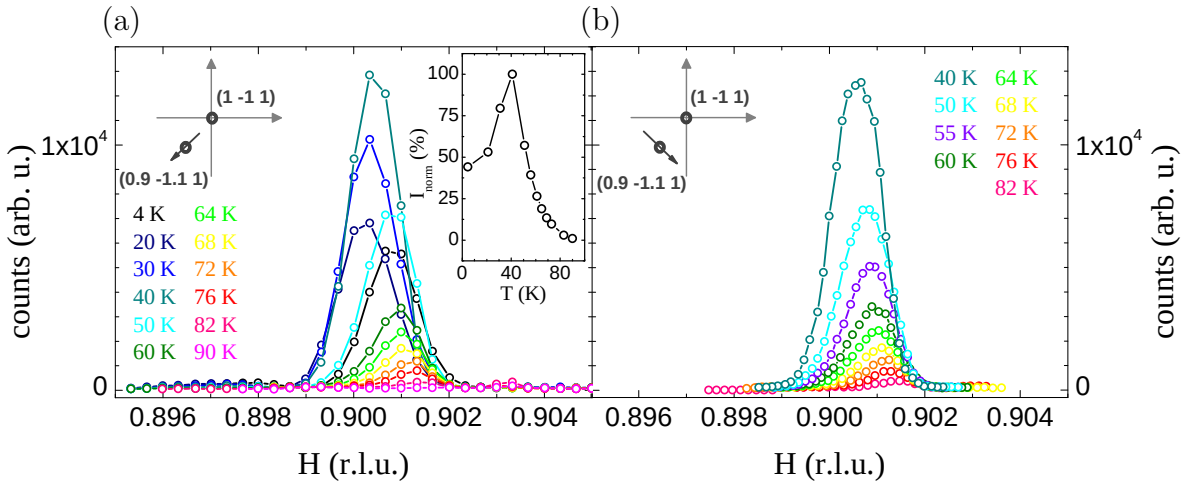

Figure 10.13: The temperature dependency of the (0.9 -1.1 1) superstructure reflection which was traced for all temperatures by (a) longitudinal and (b) transversal scans in the (first) high resolution BW5 experiment.

In Fig. 10.13 (a-b) the temperature dependency of the (0.9 -1.1 1) superstructure reflection traced by both, longitudinal and transversal scans, is shown. As can be seen from the temperature dependant scans in [110]-direction, these superstructure reflection

[1] The transversal satellites or superstructure reflections appear at $\vec{Q} = \vec{q} + \vec{\tau}$ with $\vec{q}$ being perpendicular to $\vec{\tau}$.

appear exactly at (0.9 -1.1 1) below an onset temperature of roughly 90 K. The intensity-temperature curve in the inset of Fig. 10.13 (a) exhibits a maximum at ∼40 K. Below this temperature there seems to be some kind of decrease again. From the temperature dependency of these superstructure reflections a ionic La/Sr order can be excluded, as the fully reversible rise is too sudden and rather unlikely for such kind of ordering. Any oxygen ordering can also be excluded as the sample has a Sr doping level of 5% which is close to the superconducting regime and, thus, any additional oxygen would have turned this sample superconducting which is not the case as can be seen from the electrical resistivity and magnetic susceptibility measurements; see Fig. 10.3 (b). Furthermore, the typical superstructure reflections for oxygen ordering with q-vectors having a c^* component could not be found (in a brief check) in the second low-resolution BW5 experiment.

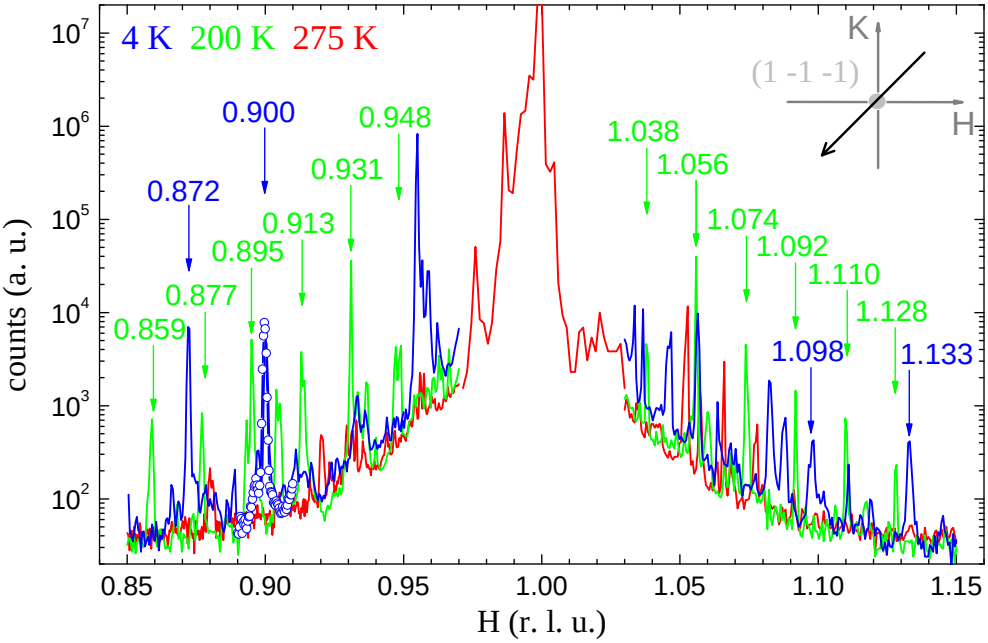

Figure 10.14: Large scans in [110]-direction through (1 -1 -1) for three different temperatures measured in the (first) high-resolution BW5 experiment.

After studying these superstructure reflections at $q = (\pm 0.1\ \mp 0.1\ 0)_{ortho}$ also the environment of these superstructure reflections in Q-space was studied in the (first) high-resolution BW5 experiment. Thus, larger transversal scans through (1 -1 -1) have been made at different temperatures. These scans are shown for three selected temperatures in Fig. 10.14. The first observation is that these superstructure reflections are not solely the only reflections that exist at lowest temperatures. Another rather strong superstructure reflection appears at positions in reciprocal space with $q \sim (\pm 0.13\ \mp 0.13\ 0)_{ortho}$. But there are also several other positions where superstructure reflections appear. These superstructure reflections vanish with increasing temperature and appear at other po-

sitions closer to the Bragg peak at higher temperatures. The superstructure reflection studied at low temperature (4 K) in great detail, see Fig. 10.12 (a-d), is indicated by the *blue open circles*.

A very interesting feature could be observed especially in the transversal scans at 200 K (*green lines*): about all superstructure reflections appear at equidistant positions as can be seen in Tab. 10.1. Note, that 0.090 is exactly 5×0.018. This astonishing result

ζ:	0.859	0.877	0.895	0.913	0.931	0.948	1.038	1.056	1.074	1.092	1.110	1.128
Δ:		0.018	0.018	0.018	0.018	0.017	0.090	0.018	0.018	0.018	0.018	0.018

Table 10.1: ζ values of the q-vectors $(\pm\zeta\ \mp\zeta\ 0)$ of the superstructure reflections measured at 200 K (see Fig. 10.14) and the difference Δ between them.

indicates that all these superstructure reflections with $q = (\pm\zeta\ \mp\zeta\ 0)_{ortho}$ are higher harmonics of a modulation with $q = (\pm 0.018\ \mp 0.018\ 0)_{ortho}$. A larger area of the HK plane around these reflections was also scanned in steps of 0.001 r. l. u. in both directions in the high-resolution BW5 experiment; see Fig. 10.15 (a). These superstructure reflections are rather sharp in longitudinal direction but smeared out in a direction transversal to $\overrightarrow{q}$. Even if this effect is mainly caused by instrumental resolution effects, some of these peaks extend over much larger regions in [1-10]-direction than others which can not be explained by resolution effects. Hence, the correlation length parallel to $\overrightarrow{q}$ is larger than the (in-plane) correlation length perpendicular to $\overrightarrow{q}$.

At low temperatures this picture is less clear. As can be seen in Fig. 10.14 also several additional peaks can be found at q-positions between expected positions for higher harmonics. But these additional reflections may be caused by an admixture of super-

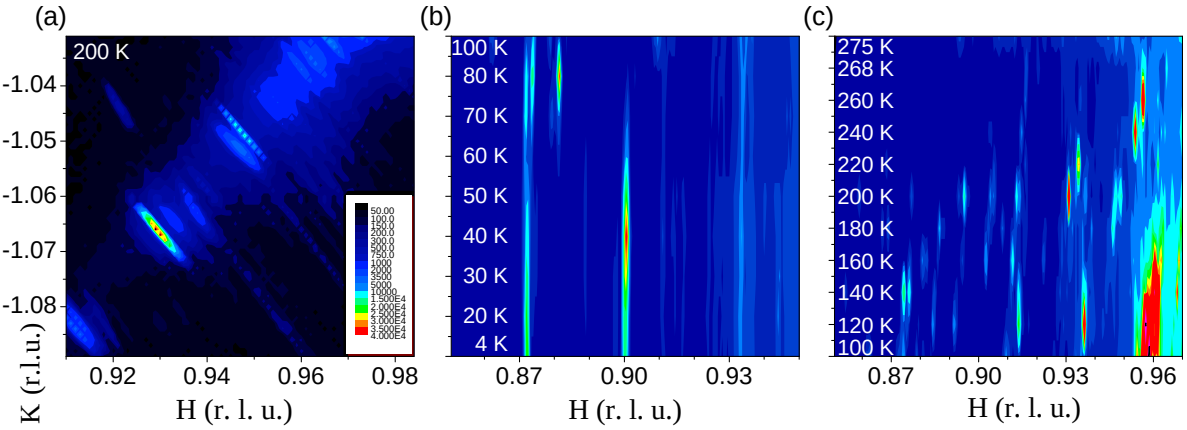

Figure 10.15: (a) Scattered intensity in the HK plane (L=-1) measured in the high resolution BW5 experiment at 200 K. The intensity was measured in steps of $\Delta H = \Delta K = 0.001$. (b-c) Intensity map of the scans in [110]-direction plotted as a function of temperature and wavevector transfer (H). The white letters denote the discrete temperature points.

structure reflections of the other twin components which induces larger effects at low temperatures since the orthorhombic splitting is distinctly larger; compare Fig. 10.16 (c-d). Also the high resolution of this first BW5 experiment may have caused a missing of some reflections. A more detailed analysis of these features was performed in the second low resolution BW5 experiment and will be discussed later.

The intensity of these superstructure reflections is similar as found for the superstructure reflections with $q = (\pm 0.1\ \mp 0.1\ 0)_{ortho}$. However, there are also some unusually strong reflections closer to the Bragg peak having an intensity of about 0.52% or 0.96% of the strong $(020)_{ortho}$ Bragg peak. If these two $\sim(0.96\ -1.04\ -1)_{ortho}$ and $\sim(2.92\ 3.08\ -11)_{ortho}$ reflections are superstructure reflections of the same type and not crystallites etc. they have an unusually large structure factor. (Also the superstructure reflection exactly at $(2.9\ 3.1\ -11)_{ortho}$ has the largest intensity compared with other superstructure

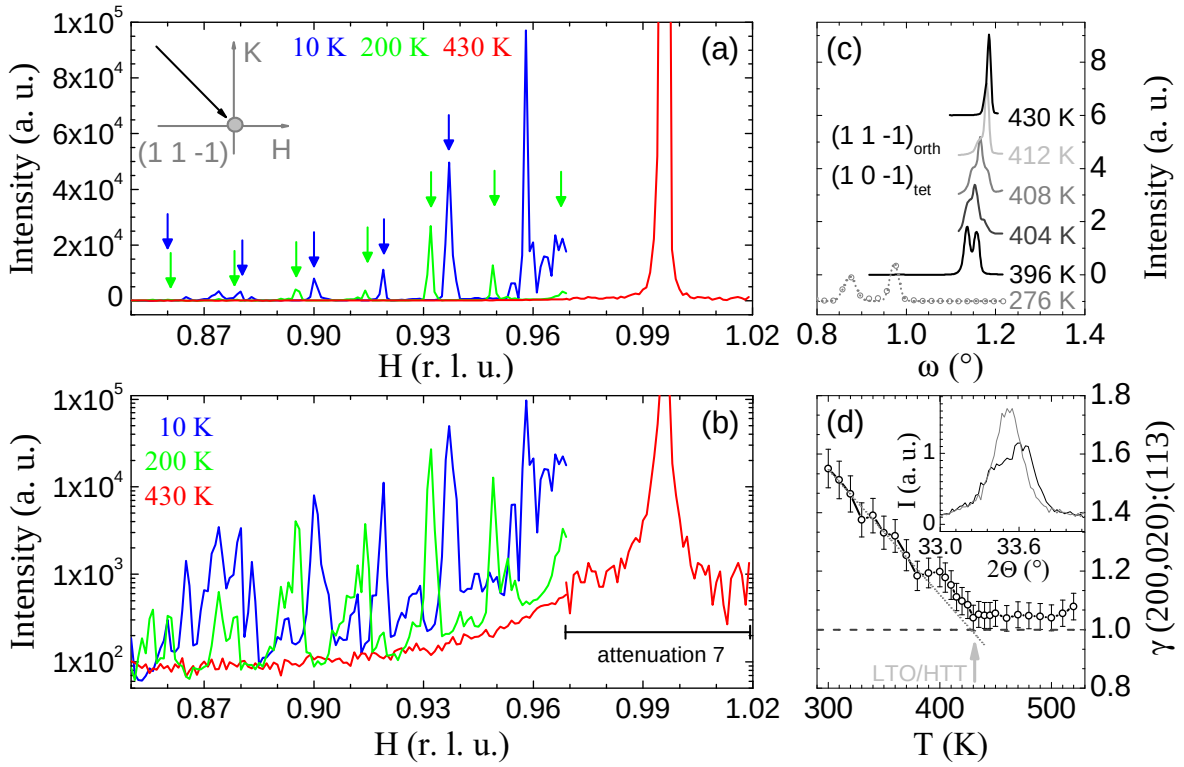

Figure 10.16: (a-b) Transversal scans through (1 1 -1) measured in the second BW5 measurement. Arrows indicate the superstructure peak positions at about equidistant positions in reciprocal space. (c) Rocking scans through the (1 1 -1) Bragg peak for different temperatures indicating the LTO → HTT phase transition (2nd BW5 experiment). (d) Ratio of the peak widths of the (2 0 0),(0 2 0) peaks and the (1 1 3) reflection measured with Cu-K_α radiation in a high temperature camera (HTK) at a conventional rotating anode powder diffractometer. The inset shows the (2 0 0),(0 2 0) peaks in the diffraction patterns measured at two different temperatures.

reflections with same q. Its intensity amounts to $4.1 \cdot 10^{-4}$ times the intensity of the strong $(020)_{ortho}$ peak.)

At higher temperatures the intensity of these superstructure reflections decreases and the positions move towards smaller values of q as can be seen in Fig. 10.14 but especially in Fig. 10.15 (b-c) where the scans in [1 1 0]-direction are plotted as a function of temperature and wavevector transfer. The superstructure reflections appear at discrete positions and vanish on heating. Instead of these other superstructure reflections appear at positions closer to the Bragg peak. In this first BW5 experiment the temperature limit was room-temperature, but in the second BW5 experiment the temperature dependency was studied in more detail and up to higher temperatures.

In the second BW5 experiment the instrumental resolution was decreased by choosing a Ge-doped analyzer crystal instead of a pure Si crystal in order to eliminate or reduce the possibility of missing the sharp superstructure reflections found in the first experiment. Also a different cryostat was used in this experiment in order to be able to heat also above room-temperature. In Fig. 10.16 (a-b) transversal scans through $(1\ 1\ \text{-}1)_{ortho}$ are shown for three different temperatures: 10 K, 200 K and 430 K. Whereas sharp superstructure peaks appear at 10 K and 200 K, no superstructure reflections are visible anymore at 430 K. The statistical spread close to the Bragg peak is caused by the large attenuation factor ($>2^7$) used to scan this region in order to protect the detector. In Fig. 10.16 (c) ω scans of the $(1\ 1\ \text{-}1)_{ortho}$ reflection are shown for different temperatures. At low temperatures, clearly a splitting is observable which decreases on heating and finally vanishes completely around 430 K. Hence, the HTT to LTO transition temperature amounts to ∼430 K. Additional powder X-ray diffraction measurements using Cu-K_α radiation (generated by a rotating anode) and a HTK heating device have been performed under application of a vacuum of roughly 10^{-4} mbar. Due to the orthorhombic splitting the (2 0 0) and (0 2 0) reflections in the LTO phase appear at slightly different values of 2Θ. In the inset of Fig. 10.16 (d) the intensity of these reflections is plotted as a function of 2Θ for two different temperatures: 300 K (*black*) and 430 K (*gray*). Obviously the resolution of this powder diffractometer is not good enough in order to separate these reflections although the used X-ray wavelength is a dozen times larger than in the BW5 synchrotron measurements. However, a small but observable peak broadening indicates the splitting of the $(2\ 0\ 0)_{ortho}$ and $(0\ 2\ 0)_{ortho}$ peaks. Unfortunately, there were no other well separated and strong peaks which could be used for a reliable determination of the LTO to HTT structural phase transition. Hence, the peak width (FWHM) of this combined $(2\ 0\ 0)_{ortho}/(0\ 2\ 0)_{ortho}$ peak has been compared to the peak width (FWHM) of a peak which is not split, the $(1\ 1\ 3)_{ortho}$ reflection. In Fig. 10.16 (d) the ratio γ of these two peak widths determined by gaussian fits is plotted as a function of temperature. From the temperature dependency of γ a transition temperature of roughly 430 K could be determined. This value is identical to the value determined in the BW5 synchrotron measurement and also fully in accordance with the phase diagram of LSCO [31] shown in Fig. 10.1.

Fig. 10.17 (a) shows a larger intensity-map of the HK plane in reciprocal space for L = -1 measured in the second BW5 experiment at 10 K. The superstructure reflections are visible and also the equidistant spacing between them is apparent. The inset shows

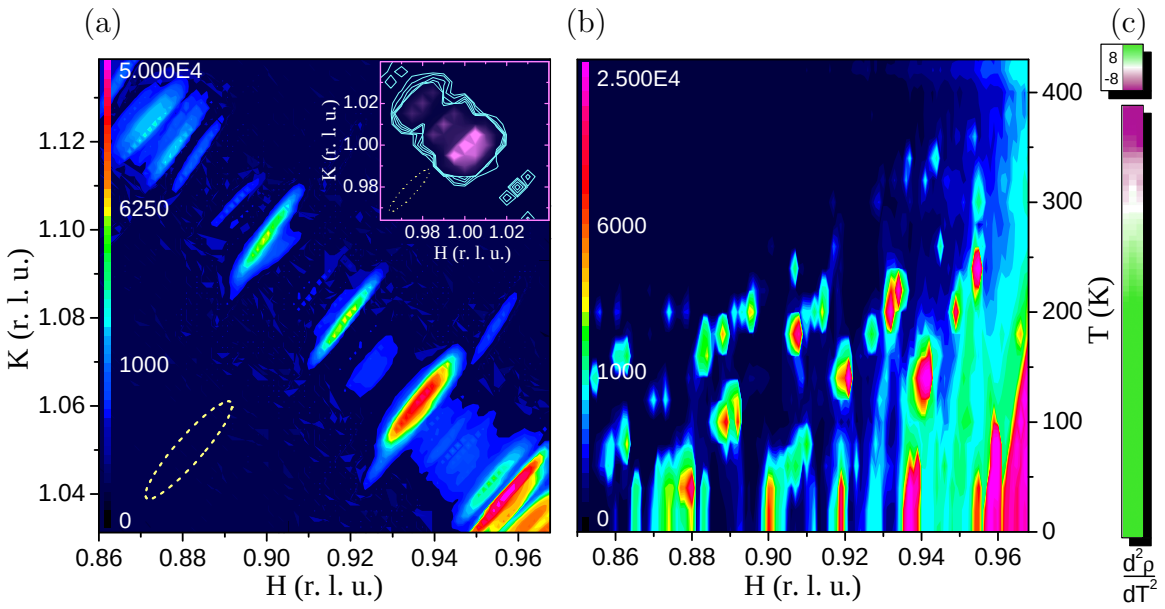

Figure 10.17: (a) HK map for L = -1 measured at 10 K in the second BW5 experiment. The data points are measured in steps of $\Delta H = \Delta K = 0.001$. The inset shows the results of similar scans which have been performed with a large attenuation in order to scan the adjacent Bragg peak. These scans have been performed rather briefly with steps of $\Delta H = \Delta K = 0.005$. The size of the elliptical dotted line in the inset corresponds to the size of the dotted ellipse in the figure. (b) Summary of scans in [1 1 0]-direction through (0.9 1.1 -1) with $\Delta H = 0.001$ measured for different temperatures in steps of 20 K. Thus, the scattered intensity is plotted as a function of temperature and wavevector transfer (H). (c) Temperature dependency of $d^2\rho_{ab}/dT^2$ depicted from Ref. [393]. The figure above indicates the range of the values from -8·10^{-6}/K^2 (*violett*) to 8·10^{-6}/K^2 (*green*).

a map of the adjacent Bragg peak measured in larger steps ($\Delta H = \Delta K = 0.005$) with an attenuation factor >2^6. The elliptically surrounded area (*light yellow*) in the inset

10 K:							
ζ:	0.958	0.937	0.919	0.900	0.880	0.860	
Δ:		0.021	0.018	0.019	0.020	0.020	
200 K:							
ζ:	0.968	0.949	0.932	0.914	0.895	0.878	0.860
Δ:		0.019	0.017	0.018	0.019	0.017	0.018

Table 10.2: ζ values of the q-vectors (-ζ ζ 0) of the superstructure reflections measured at 10 K and 200 K in the second BW5 experiment (see Fig. 10.16). Below, the difference Δ between the ζ values of the same column and the column before are listed.

corresponds to the dotted ellipse (*light yellow*) in Fig. 10.17 (a) and gives an impression of the instrumental resolution. The appearance of a three-peak structure is artificial and results from the rough-textured grid of Q points in the scans forming this map.

In Tab. 10.2 the values of q for the different superstructure reflections measured at 10 K and at 200 K are shown ($Q = (1\ 1\ \text{-}1)+q$). The value of ζ for $q = (\text{-}\zeta\ \zeta\ 0)$ is plotted in the first row and the difference of ζ for the two neighbouring reflections is listed below. Like in the first high-resolution measurement, the superstructure reflections appear at equidistant positions which resembles on the occurrence of higher harmonics. At 10 K the difference of ζ for neighbouring superstructure reflections amounts to 0.0196(5). This is indicative for higher harmonics of a modulation with $q = (\text{-}0.0196\ 0.0196\ 0)$. Indeed, also the scans shown in the inset of Fig. 10.17 (a) indicate a rather strong superstructure reflection at $q = (\text{-}0.02\ 0.02\ 0)$ which is even visible in this measurement of the Bragg peak with a high attenuation factor. On the other side of the Bragg peak there is also a superstructure reflection at at $q = (0.02\ \text{-}0.02\ 0)$ but with distinctly lower intensity (of the order of 10%). These weaker reflections have been visualized by the use of contour lines (*cyan*) for the lower intensity region. Hence, the structure factor of these superstructure reflections is not equal on both sides of the Bragg peak but the superstructure reflections from the basic modulation can be found symmetrically on both sides of the Bragg peak with $q \sim \pm(0.02\ \text{-}0.02\ 0)$. Another interesting feature is an additional peak intensity at $q \sim (\text{-}0.01\ 0.01\ 0)$. This reflection is completely absent on the other side of the Bragg peak. Most likely, this reflection originates from another twin domain (or crystallite) which can be expected at about this position. Two of the other four possible twin domains in this system could be expected exactly at (1 1 -1). The fourth twin domain should be at the other side of the Bragg peak. Obviously, this fourth twin domain is absent.

At 200 K the basic propagation vector is little smaller than at 10 K and ζ has a value of 0.0180(4). This is exactly the value determined at 200 K in the first high-resolution BW5 measurement. This value is smaller than the value at 10 K and indicates that the superstructure reflections move towards the Bragg peak on heating. In Fig. 10.17 (b) all temperature scans of the type of Fig. 10.16 (a) are summarized and plotted as a function of temperature and wavevector transfer (H). From this figure it is apparent that the superstructure reflections accelerate their movement towards the Bragg peak above 200 K and that they rapidly lose intensity and finally vanish above 350-400 K. In Fig. 10.18 (b) the incommensurability δ of the $(1\pm n\cdot\delta\ 1\mp n\cdot\delta\ \text{-}1)_{ortho}$ reflections ($n \in \aleph$) is plotted as a function of temperature. At higher temperatures the superstructure intensities strongly decrease and, thus, the determination of the peak positions becomes rather difficult. Hence, the value of the incommensurability could be determined up to 325 K only. The overall temperature dependency of δ exhibits only minor changes up to 220 K which is followed by a stronger decay at higher temperatures. At low temperature the incommensurability $\delta = 0.018$ is connected to a modulation which has a wavelength of about 55 tetragonal unit cells, i. e. a wavelength of roughly 200 Å. On heating, this value of the wavelength strongly increases accompanied by a decay of these superstructure reflection intensities at high temperatures.

Thus, in these synchrotron measurements structural superstructure reflections and

their higher harmonics could be observed which indicate an in-plane modulation with a propagation vector parallel to the Cu-O bonds. This modulation is strongly temperature dependent and exhibits a rather large modulation wavelength which even increases on heating. Most of these intensities vanish around 250 K and the remaining intensities finally vanish at the LTO → HTT phase transition.

Complementary neutron measurements have been performed at the G4.3 diffractometer using a large (twinned) single crystal of $La_{1.95}Sr_{0.05}CuO_4$. These measurements reveal a very similar picture as in the hard X-ray case. In Fig. 10.18 (a) scans in $[100]_{tet}$ di-

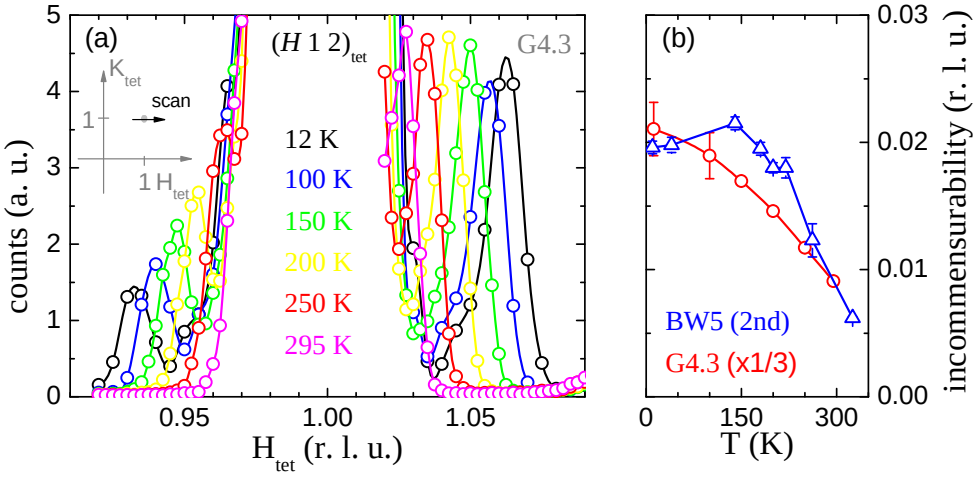

Figure 10.18: (a) Temperture dependant scans in $[100]_{tet}$-direction obtained in neutron measurements of $La_{1.95}Sr_{0.05}CuO_4$ at the G4.3 diffractometer. (b) Temperature dependence of the incommensurability δ of the superstructure reflections $(1\pm\delta\ 1\mp\delta\ -1)_{ortho}$ measured in the second BW5 measurement and $(1\pm\delta\ 1\ 2)_{tet}$ in the G4.3 measurement.

rection through $(1\ 1\ 2)_{tet}$ are shown. In orthorhombic notation this scan is equivalent to a scan in $[1\ -1\ 0]_{ortho}$-direction through the $(0\ 2\ 2)_{ortho}$ Bragg reflection. Similar as in the X-ray case, strong superstructure reflections appear at transversal positions which are indicative for some modulation parallel to the Cu-O bonds (and not diagonal). Also, these reflections shift towards the Bragg peak on heating. The incommensurability δ multiplied by the factor 1/3 (*red circles*) is plotted as a function of temperature in Fig. 10.18 (b) together with the value of δ for the basic modulation determined in the second BW5 measurement (*blue triangles*). As the resolution is much lower in the neutron case it is not possible to detect superstructure reflections close to the Bragg peak. Thus, presumably only the higher harmonics could be detected. The first reflection which can be clearly separated and fitted with two symmetrical gaussians has an incommensurability of $\delta \sim 0.06$ at 12 K. If the picture of higher harmonics is appropriate, the basic modulation would correspond to a δ value of $\sim$0.06/3. This value is very similar as the value at 10 K in the hard X-ray measurement. Also the values at

higher temperatures are in accordance with the X-ray case. However, there are some minor discrepancies around 150 K to 200 K. These might be explained by the different $La_{1.95}Sr_{0.05}CuO_4$-samples used in both measurements or by the different resolution of both measurements. The neutron measurement exhibits a much more smooth shift of the superstructure reflections towards the Bragg position whereas the synchrotron measurements indicate discrete jumps of these reflections. Possibly, the neutron measurement averages over all these effects within the large single crystal, whereas the synchrotron measurement has a much higher resolution and, thus is able to detect all tiny superstructure reflections separately.

Furthermore, the intensity of these superstructure reflections amounts to ∼1.6% of the $(1\ 1\ 2)_{tet}$ nuclear reflection and can be calculated to be approximately $4{\cdot}10^{-3}$ times the intensity of the $(0\ 2\ 0)_{ortho}$ reflection [2] in order to have a comparison with the BW5 measurement. Hence, these superstructure reflections found in the G4.3 measurement are 2-3 orders of magnitude larger than most of the superstructure reflections with a q-value of ±(0.1 -0.1 0) observed in the BW5 measurement and still one order of magnitude stronger than the strongest superstructure reflections with this q-value observed in the BW5 measurement. But these reflections found in the neutron measurement are of equal size as the unusual strong reflection observed at ∼(0.96 -1.04 -1) in the BW5 measurement which also has an intensity of $5.2{\cdot}10^{-3}$ of the $(0\ 2\ 0)_{ortho}$ peak. Thus, the neutron measurements might indicate strong modulations of the oxygen ions since neutrons are more sensitive to oxygen than X-rays. However, it is also possible that only the unusually strong superstructure reflections could be observed in the neutron measurements and that all the other 100 to 1000 times weaker reflections were not resolved in this measurement. This might explain that no higher harmonics could be observed in the neutron measurement.

Additionally, also resonant synchrotron radiation X-ray diffraction measurements have been performed at the MagS diffractometer at BESSY. A $La_{1.95}Sr_{0.05}CuO_4$ sample taken from the same crystal as in the BW5 measurement has been used for this measurement and the $(1\ 0\ 1)_{tet}$ surface has been cut and polished. In Fig. 10.19 (a) the resulting scattered intensity at 10 K in the HK-plane for $L = 1$ is shown. The major intensity is distributed along a straight line in K direction pointing towards the Bragg peak. This line is equivalent to a transversal line along $(1\text{-}\zeta\ 1{+}\zeta\ 1)_{ortho}$ in orthorhombic notation. For a comparison with the map measured in the second BW5 measurement shown in Fig. 10.17 (a), this map has to be rotated anti-clockwise by 45°. Obviously, the directions where large intensities can be found are identical. However, the MagS measurement exhibits no single superstructure reflections but a smooth intensity distribution along the positions of superstructure reflections instead. As these measurements are much more surface sensitive due to distinctly lower X-ray energies (∼8.98 keV instead of 100 keV) this might be induced by surface effects. For example the surface could be oxidized etc.

[2] For 2.36 Å neutrons and under application of a structure model for $La_{1.95}Sr_{0.05}CuO_4$ the calculated [58] structure factor of the $(0\ 2\ 2)_{ortho}$ reflection is roughly half the size of the structure factor of a $(0\ 2\ 0)_{ortho}$ reflection.

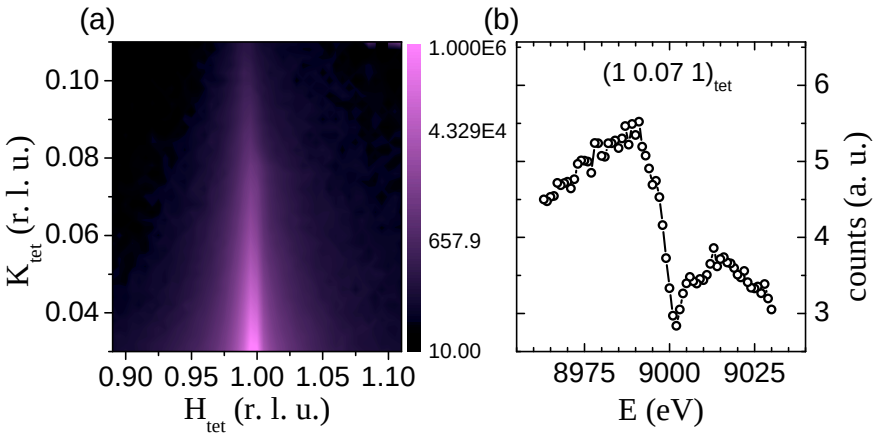

Figure 10.19: Results of resonant X-ray measurements at the Cu K edge using synchrotron radiation (beamline MagS). (a) Intensity map in the HK-plane with $L = 1$; the intensity is plotted logarithmically as indicated in the legend to the right. (b) Energy-scan at $(1\ 0.07\ 1)_{tet}$.

In Fig. 10.19 (b) an energy scan has been applied for a Q value where significant intensity was observed, i. e. at $(1\ 0.07\ 1)_{tet}$ which is right in the middle of the HK map. Obviously, there is no resonant enhancement at the absorbtion threshold. If these reflections are smeared out along the whole transversal K_{tet}-line, this observation would be in favour of o purely structural effect and, hence, support a picture like a modulation of octahedral tilting patterns etc. versus a charge stripe ordering. However, the significance of this measurement is not clear as no single superstructure reflections are visible and as the whole measurement might be biased by surface effects.

In Fig. 10.17 (c) the value of of $\mathrm{d}^2\rho_{ab}/\mathrm{dT}^2$ is shown as a function of temperature. These values have been taken from Ref. [393] where the phase diagram of LSCO was studied by resistivity curvature mapping (RCM). The temperature values at the vertical axis are the same as in Fig. 10.17 (b). Hence, both figures can be compared directly. It seems that the accelerated vanishing of superstructure reflections above ∼250 K coincides with the beginning decay of $\mathrm{d}^2\rho_{ab}/\mathrm{dT}^2$ from which the pseudogap crossover line can be determined [393]. In this temperature region there are already no superstructure reflections visible for large regions of Q-space and the incommensurability δ exhibits a strong decrease. Hence, the origin of these superstructure reflections might be connected to the electronic properties of $La_{1.95}Sr_{0.05}CuO_4$. However, so far, one may only speculate about the origin of these superstructure reflections as these superstructure reflections appear at positions neither typical for diagonal nor for vertical/horizontal charge stripes. Some theoretical possibilities one may think about are listed in the following and will be discussed only very briefly afterwards as these are just speculations.

- an unusual charge ordering
- (anti-) ferroelectric domains

- modulation of the octahedral tilt pattern (LTT)
- bipolaron stripe phase

The transversal positions of these superstructure reflections request a shift/displacement of the atoms which is transversal to the propagation direction. This is not in accordance with the general picture of a vertical/horizontal charge stripe phase where one would expect a longitudinal shift of the oxygen ions towards the charge stripes. Therefore, only a strange, unusual charge ordering might be responsible for these kind of reflections. Also the strong intensities and the temperature dependency of these superstructure reflections is unfavourable for a charge-stripe explanation. Coming to the second model, a displacement of the copper ions from the central position in the CuO_6 octahedra forming an antiferroelectric arrangement might induce such transversal superstructure reflections. Due to the large modulation wavelengths of about 200 Å this antiferroelectric pattern should have large domains of ferroelectric character with a regular arrangement of the domain walls. Also the rather high dielectric constants observed in the SG phase of LSCO would support such a picture. The third model might be the most realistic one. Here, the octahedral tilts might be modulated over the whole crystal. For example one could think of a LTT tilt pattern which appears in this modulation every $\sim$50 unit cells in a kind of LTT-stripes. These stronger oxygen displacements may explain larger superstructure reflection intensities and also the temperature dependency, as these superstructure reflections completely vanish when the octahedral tilts disappear, i. e. at the LTO $\rightarrow$ HTT transition. Finally, also a pairing of holes along charge stripes may also explain these superstructure reflections. This model starts with a conventional quarter-filled vertical stripe phase in which every second hole moves to the next neighbouring copper site parallel to the stripe in order to form hole-pairs which resemble on bipolarons. Hence, within a stripe there are two holes always separated by two normal Cu-sites. If all these hole-pairs increase their hole-hole distance for a reduction of Coulomb repulsion and rotate around their center in order to relief some stress with the neighbouring copper ions a displacement pattern results which exhibits transversal displacements with respect to the propagation direction and which can be expected to propagate through the whole crystal as also all the other neighbouring copper ions will follow this displacement pattern in order to relief some stress on their own. Therefore, larger superstructure reflection intensities could be expected for such a modulation. This model would also be rather interesting with regard to the pairing mechanism in the superconducting regime.

search for structural distortions in $La_{1.88}Sr_{0.12}CuO_4$

In order to analyze the Sr doping dependency of these superstructure reflections found in the first two BW5 measurements and to see whether these superstructure reflections vanish for LSCO samples in the superconducting regime also a third BW5 measurement using hard X-rays has been performed for a 12% Sr doped LSCO sample. Due to the use of a lower resolution by choosing a Ge-doped analyzer crystal the possibility of any accidental missing of sharp superstructure reflections has been reduced. In Fig. 10.20 (c-h) large transversal scans through six different Bragg peaks exhibiting superstructure reflections for the 5%-doped LSCO sample are shown. Here, for 12% doped LSCO, these scans do not exhibit any superstructure reflections at 8 K. For a comparison also the results of scans at 10 K (*green*) and at 430 K (*red*) of the low resolution BW5 measurements of $La_{1.95}Sr_{0.05}CuO_4$ are shown together with the measurement of $La_{1.88}Sr_{0.12}CuO_4$ at 8 K (*blue*) in Fig. 10.20 (a-b). The scan direction is plotted in the inset of Fig. 10.20 (a). Obviously no discrete superstructure reflections appear in $La_{1.88}Sr_{0.12}CuO_4$. However, there is an amount of diffuse scattering around the Bragg peak which is distinctly larger than in $La_{1.95}Sr_{0.05}CuO_4$ at 430 K. The origin of this

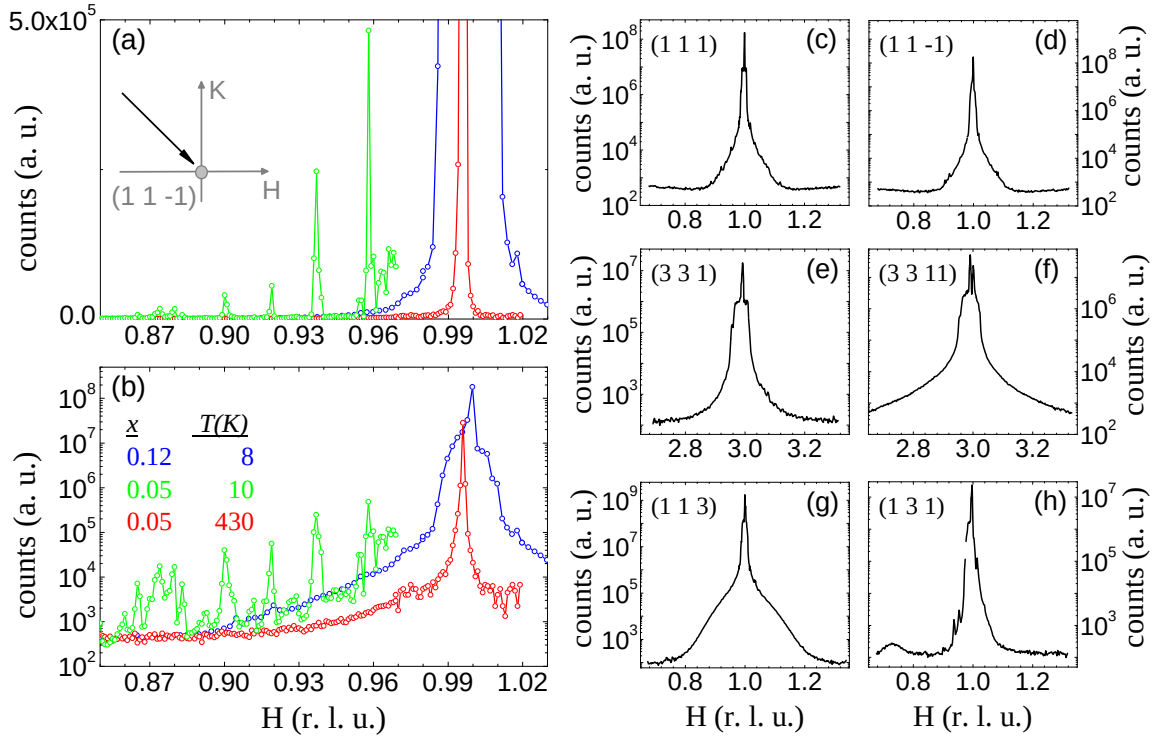

Figure 10.20: (a-b) Transversal scans through (1 1 -1); *blue*: $La_{1.88}Sr_{0.12}CuO_4$ at 8 K, *green/red*: $La_{1.95}Sr_{0.05}CuO_4$ at 10 K/430 K. (c-h) Transversal scans through different Bragg reflections for $La_{1.88}Sr_{0.12}CuO_4$ measured at ∼8 K.

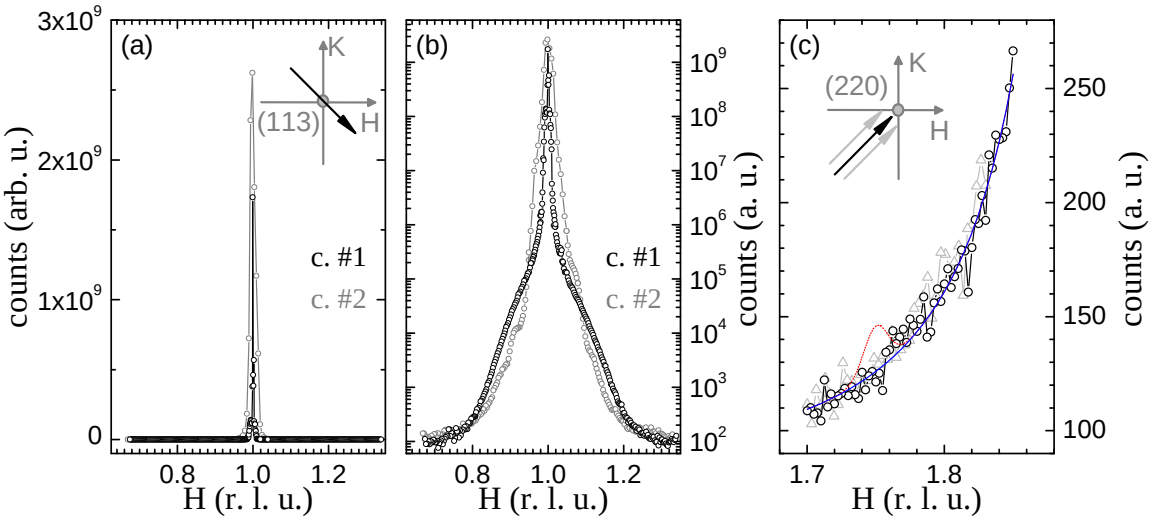

Figure 10.21: (a-b) Transversal scans through (1 1 3) for the two different $La_{1.88}Sr_{0.12}CuO_4$ *crystals #1* (*black*) and *#2* (*gray*). (c) Longitudinal scans through (1.75 1.75±p 0) with $p = 0.00$ (*black circles*) and -0.01 (*gray triangles*). (The scan with $p = +0.01$ is not shown.) The *blue line* is a lorentzian fit to the data ($p = 0.00$) and the *red line* indicates the smallest signal which would have been detected (detection limit); compare Tab. 10.3.

diffuse scattering is unclear.

For a different $La_{1.88}Sr_{0.12}CuO_4$ sample grown by F. Nakamura also the occurrence of conventional charge stripe order was studied in this third BW5 measurement. In the following, this crystal will be referred to as *crystal #2*, whereas the other $La_{1.88}Sr_{0.12}CuO_4$-crystal studied will be referred to as *crystal #1*. In order to search for conventional superstructure reflections large longitudinal scans through $Q \pm q$ have been applied with Q being a Bragg peak and $q = (0.25\ 0.25\ 0)_{ortho}$. A low resolution setting with a Ge-doped Si analyzer crystal has been chosen in order to minimize the possibility of accidentally missing a very sharp superstructure reflection due to a very high resolution. Furthermore, additional longitudinal scans parallel to the nominal scans have been performed symmetrically on both sides of the nominal scans in order to fully exclude any accidental missing of superstructure reflections. These scans run through through $Q \pm q \pm p$. In Tab. 10.3 the results of these scans are summarized. The first three lines describe the values of (Q±q) ±p which are the central points of several longitudinal scans of the type shown in Fig. 10.21 (c). In the inset of Fig. 10.21 (c) the scan direction of the central scan (*black*) and the two additional scans shifted by ±0.01 in H- or K-direction (*light gray*) are shown. The abbreviation for these three scans in Tab. 10.3 is 1.75±0.01 1.75±0.01 0. A value of $p = \pm 0.02$ indicates the maximum shifted values of p, i. e. that one additional scan is shifted by 0.01 and a further one by 0.02 in H-direction (on each side of the central scan) and not that only one scan shifted by 0.02 has been performed at each side. Finally, the value ι indicates the detection limit of

H:	2.25±0.02	1.75	1.75±0.01	2.25±0.01	1.75	2.25	2±0.03
K:	2.25±0.02	-0.25	1.75±0.01	2.25±0.01	1.75	2.25	0.25±0.03
L:	0	0	0	1/2	1	1	0
ι:	$4.8{\cdot}10^{-9}$	$1.6{\cdot}10^{-8}$	$6.5\text{-}7.6{\cdot}10^{-9}$	$8.3{\cdot}10^{-9}$	$9.6{\cdot}10^{-9}$	$9.7{\cdot}10^{-9}$	$2.4\text{-}2.5{\cdot}10^{-10}$

Table 10.3: Detection limit ι for several superstructure reflections measured in the third BW5 measurement on the second $La_{1.88}Sr_{0.12}CuO_4$-single crystal (orthorhombic notation). ι is the size of a signal relative to a strong Bragg peak which would have been detected.

this particular superstructure reflection. Its value means that ι times the intensity of a strong Bragg peak [3] would have been detected in these measurements. As can be seen in Tab. 10.3 superstructure reflections for vertical/horizontal stripes can be excluded with an accuracy of at least 10^{-8} of a strong Bragg reflection. The strength of similar superstructure reflections observed for horizontal stripes in Ref. [6] for Nd codoped LSCO samples with neutron diffraction is of the order $\sim 10^{-6}$. Such a large signal would have been easily detected in the measurements of this work.

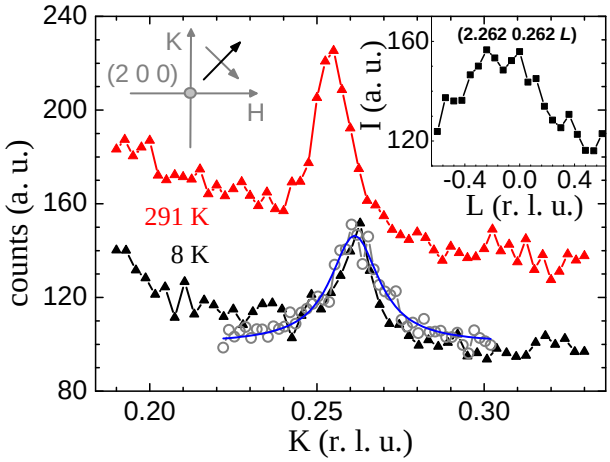

Figure 10.22: Scans in [1 ±1 0]-direction through (2.262 0.262 0) measured at ∼8 K (*black/gray*). Additionally, a scan in [1 1 0]-direction measured at 291 K (*red*) is shown (these values are shifted along the ordinate axis). The *blue line* indicates a lorentzian fit. In the inset a scan in [0 0 1]-direction is shown.

However, one superstructure reflection could be observed at $(2.262\ 0.262\ 0)_{ortho}$ which is not too far away from the expected position for vertical stripes of a 1/8 doped sample: $(2.25\ 0.25\ 0)_{ortho} = (1\ 1.25\ 0)_{tet}$ [6]. This signal has a magnitude of $1.5{\cdot}10^{-8}$ of a strong Bragg reflection. In Fig. 10.22 longitudinal (*black triangles*) and transversal scans (*gray open circles*) through this reflection measured at approximately 8 K are

[3] The reference peak is the $(1\ 1\ 3)_{ortho}$ reflection which is only slightly smaller than the $(0\ 2\ 0)_{ortho}$ reflection. Due to a calculation [58] based on a structure model, the intensity of the $(1\ 1\ 3)_{ortho}$ peak should be roughly 2/3 of the $(0\ 2\ 0)_{ortho}$ reflection.

shown. Additionally, the same longitudinal scan measured at 291 K is shown; (the values are shifted for a better comparison). In the inset of Fig. 10.22 also a scan in [0 0 1]-direction is shown. In Ref. [6] a charge stripe ordering temperature of roughly 60 K was observed for Nd codoped LSCO samples with same Sr doping level. As this signal does not vanish up to room temperature in the $La_{1.88}Sr_{0.12}CuO_4$-sample (*crystal #2*) measured in this work, this peak can not be related to vertical charge stripes since the ordering temperature would be too high (although the position in reciprocal space is very close to the expected position).

Additionally, a rather large HK map has been collected for *crystal #1* with steps of $\Delta H = \Delta K = 0.003$ and $H \in [2.16,2.31]$, $K \in [2.16,2.283]$, $L = 0$. In this large map, no superstructure reflection could be detected around (2.25 2.25 0) with a detection limit of $1.5{\cdot}10^{-8}$ of a large Bragg reflection (1 1 3).

Although nothing would indicate diagonal stripes in $La_{1.88}Sr_{0.12}CuO_4$, also a few additional scans have been performed in order to look briefly for features of such a stripe order. As expected, there are also no signs of diagonal stripes in 12 scans (0.005 steps) with a detection limit of $2.5{\cdot}10^{-10}$ of a strong Bragg reflection, compare Tab. 10.3.

10.1.4 Conclusion

In conclusion, the search of indications for a diagonal charge stripe order in a sample which is in the SG phase of LSCO, $La_{1.95}Sr_{0.05}CuO_4$, did not yield any evidence for such a stripe instability. On the one hand the phonon dispersion studied by means of inelastic neutron scattering did not reveal any signature of a diagonal stripe phase neither in the longitudinal acoustic branches nor in the bond stretching branches - there is no phonon anomaly in the high frequency Σ_1 mode (along the [1 1 0]-direction). Instead, the longitudinal bond stretching branches of insulating $La_{1.95}Sr_{0.05}CuO_4$ exhibit anomalies along the [1 0 0] direction which are very similar to that observed in the metallic/superconducting regime of LSCO: this Δ_1 branch exhibits a downwards dispersion on the half way from zone center to zone boundary. A comparison with a 7% and a 15% doped sample indicates that the softening of this so called half-breathing mode scales approximately with the Sr content x independent of metallic or insulating properties of the particular system.

Additionally, the direct search of superstructure reflections did not yield any evidence for a diagonal stripe phase. In various neutron scattering experiments such structural superstructure reflections could be excluded with an accuracy of at least $2{\cdot}10^{-6}$ of a strong nuclear reflection. Also the search of such reflections with resonant X-rays at the synchrotron did not reveal the reflections expected for diagonal stripes. Furthermore, the search of these superstructure reflections with 100 keV hard X-rays at the synchrotron yields only a few peaks, but these have propagation vectors which are not related to the propagation vectors of the magnetic satellites and the temperature dependency indicates that these superstructure reflections do not vanish up to 430 K. Hence, these reflections might reflect some other effect like Sr ordering etc. Any other diagonal charge stripe superstructure reflections can be excluded with an accuracy of about 10^{-8} of a strong Bragg peak. Thus, there is no evidence for diagonal stripes in various diffraction

measurements performed in this work.

Instead some novel superstructure reflections appear at positions rotated by 45° with respect to the positions for diagonal stripes. However, these superstructure reflections do not seem to be a signature of horizontal stripes as these reflections could be observed in transversal configuration only, i. e. the modulation vector q is perpendicular to the Bragg peak τ. Furthermore, there exists a whole series of superstructure reflections at about equidistant steps indicating that these reflections are higher harmonics of a modulation which propagates along the Cu-O bond directions with a wavelength of about 55×3.9 Å. On heating, these superstructure reflections decrease in intensity and move towards the bragg position. Many of these reflections vanish above 250 K. At the LTO to HTT phase transition, finally, all remaining reflections are gone. Hence, there might be a connection to the octahedral tilts and these superstructure reflections might indicate some modulation of these tilts. But of cause, also other interpretations are possible, as the octahedral tilts might stabilize some other kind of ordering. For example, it is well known that the octahedral tilts in the LTT phase stabilize the charge stripes in Nd codoped LSCO [6].

For a $La_{1.88}Sr_{0.12}CuO_4$-sample in the metallic/superconducting regime, these superstructure reflections vanish suggesting a close connection of these superstructure reflections to the insulating properties in $La_{1.95}Sr_{0.05}CuO_4$. Also, the second derivative of the electrical resistivity ρ_{ab} (taken from Ref. [393]) exhibits first changes when the superstructure reflections start to vanish above ∼250 K.

For another $La_{1.88}Sr_{0.12}CuO_4$-sample signatures of vertical charge stripe ordering have been searched for using 100 keV hard X-rays at the synchrotron. Superstructure reflections of these kind of stripes can be excluded with an accuracy of $\sim 10^{-8}$ of a strong nuclear reflection.

10.2 Phonon dispersion in $La_{2-x}Sr_xCu_{1-x}(Ni/Zn)_xO_4$

10.2.1 Introduction

Since the discovery of the high-temperature superconductivity (HTSC) in the cuprates [4] the pairing mechanism in still a matter of debate and the question about the role of electron-phonon coupling still a matter of controversy. First evidence for strong electron-phonon coupling in the cuprate high-temperature superconductors was found in inelastic neutron scattering (INS) experiments on $La_{2-x}Sr_xCuO_4$ (LSCO) and $YBa_2Cu_3O_7$ [424-426]. The comparison of the phonon frequencies measured on insulating and on the superconducting materials revealed a distinct shift of spectral weight [424, 427, 428]. The doping mainly induces a frequency renormalization of the modes with the highest energies which possess longitudinal bond-stretching character. The polarization patterns of the zone-boundary longitudinal modes are characterized through modulations of the bond-lengths at different Cu-sites. Therefore, they are called breathing modes and one may expect a strong coupling to charge ordering or to charge fluctuations. Polarization patterns of these longitudinal bond stretching modes (Δ_1) are shown schematically for $q = (0.25\ 0\ 0)$ and $q = (0.5\ 0\ 0)$ in Fig. 10.26 (a-b). A step-like drop in the dispersion of these high-energy modes can be observed around $q = (0.25\ 0\ 0)$ which is similar for all HTSC cuprates and even in other metallic perovskites [420]. However, the frequency renormalization seems to rise with rising T_C of these compounds. Furthermore, the value of q nicely fits to the propagation vector of the charge stripe ordering which has been observed in $La_{2-x-y}Nd_ySr_xCuO_4$ and $La_{2-x}Ba_xCuO_4$ ($x \sim 1/8$) [6, 365]. In contrast to the high-energy mode, the low and medium phonon-energy ranges exhibit less sensitivity to doping. Similar effects were also reported for the electron-doped cuprates $Nd_{1.85}Ce_{0.15}CuO_4$ (NCCO) [429, 420, 430]. Although known for a long time these phonon anomalies in the cuprates have attracted strong interest more recently, initiated through the discussion of the famous kinks in the ARPES spectra [431]. Some groups now consider electron-phonon coupling to play an important role in the cuprates [10-12]. Especially, the very recent observation of a coupling of the phonon anomaly and stripe ordering in cuprates with static charge stripe ordering [13] indicates the importance of electron phonon-coupling in the cuprates. However, the direct relevance for the pairing remains an open question.

The investigation of Zn and Ni doped cuprates may give complementary information. In $La_{2-x}Sr_xCuO_4$ the substitution of Cu with non-magnetic ions like Al, Ga and Zn as well as the substitution with magnetic ions like Fe, Co and Ni leads to a reduction of T_C as was studied in great detail for the (optimum doped) LSCO parent compound $La_{1.85}Sr_{0.15}CuO_4$ [432]. Doping with divalent Zn has the advantage that there is no additional electronic doping like in the case of Ga or Al. For a conventional superconductor, magnetic impurities have a much stronger pair-breaking ability than non-magnetic dopants. However, in LSCO 3% of doping with non-magnetic Zn leads to a suppression of superconductivity whereas 4% of doping with magnetic Ni is needed for the same effect [432, 433]. This observation would be in favour of a magnetic mechanism as the non-magnetic dopants reduce T_C about as effectively as the magnetic ones.

The Zn^{2+}-ion with a $3d^{10}$ (S=0) configuration introduces a nonmagnetic random potential in the copper-oxide planes. Doping with Zn reduces T_C even more effectively than doping with Ni and it magnifies the 1/8 anomaly [434]. Although Zn is a non-magnetic impurity it seems to induce local moments within non-superconducting islands which are separated from the superconducting regions as was interpreted by the analysis of the spin fluctuations [435]. Doping with Zn induces distinct changes on the magnetic fluctuations. In $La_{1.86}Sr_{0.14}Cu_{0.988}Zn_{0.012}O_4$ sharp coherent Bragg reflections can be observed for zero energy transfer, whereas only some weak diffuse scattering can be observed in the elastic channel of the corresponding Zn-free compound $La_{1.85}Sr_{0.15}CuO_4$ [406]. Around 2 meV energy transfer in the inelastic channel the magnetic fluctuations are very similar for these two compounds. Thus, Zn doping shifts the spectral weight of spin excitations from inelastic to (quasi-)elastic regions and finite-frequency stripe fluctuations of Zn-free compounds become observable in the elastic channel ($\omega = 0$) of the corresponding Zn doped compound. Hence, Zn is able to "pin" the stripe fluctuations [406].

On the other hand, the Ni ion enters the copper oxide planes in its three-valent magnetic state or the Ni^{2+}-ion plus a hole form a strongly bound state with Zhang-Rice character. Hence, regarding the Cu oxidation state solely, the hole-doping induced by Sr gets compensated by Ni doping. However, the average Ni/Cu oxidation state is not altered. As the Ni-ion strongly localizes the holes at the Ni-sites [436] the effective number of free, mobile holes is reduced which affects the stripe spacing and, hence, the incommensurability ε decreases with Ni doping. Thus, the incommensurability gets finally destroyed in $La_{1.95}Sr_{0.05}Cu_{1-y}Ni_yO_4$ around Ni-doping levels of $y \approx 0.03$ [436] and the compound with $y = 0.05$ exhibits only sharp magnetic Bragg peaks originating from long range antiferromagnetic order as in La_2CuO_4. The dependence of ε on the effective (free) hole concentration in Ni doped and Ni-free materials is almost equal. In Ref. [436] also a very small decrease of the incommensurability ε was observed for the Zn doped samples. But the decrease of ε is much faster on Ni doping.

10.2.2 Experimental

The Zn and Ni doped LSCO single crystals (LSCZO, LSCNO)[4] $La_{1.88}Sr_{0.12}Cu_{0.96}Ni_{0.04}O_4$, $La_{1.85}Sr_{0.15}Cu_{0.98}Ni_{0.02}O_4$ and $La_{1.88}Sr_{0.12}Cu_{0.97}Zn_{0.03}O_4$ were grown by H. Hiraka using a floating-zone image furnace. For a comparison also a Zn/Ni-free $La_{1.88}Sr_{0.12}CuO_4$ single crystal grown by M. Fujita (also from the group of K. Yamada) has been used.

Inelastic neutron scattering experiments have been performed at the IN8 triple axis spectrometer at the ILL in Grenoble, France. A Cu (200) monochromator and a pyrolytic graphite (002) analyzer was used, each of which was vertically and horizontally focused. The analyzer was used in a constant-k_f mode with a final energy of 14.7 meV. Two pyrolytic graphite filter have been placed after the sample in order to diminish higher harmonics. In summary, a double focussing $open - Cu200 - open - D - S - PG - D - PG - open$ configuration has been applied (with D: diaphragm). The sample was mounted with the tetragonal (100)/(010) axes in the scattering plane.

[4] LSCZO: $La_{2-x}Sr_xCu_{1-y}Zn_yO_4$, LSCNO: $La_{2-x}Sr_xCu_{1-y}Ni_yO_4$.

10.2.3 Results and Discussion

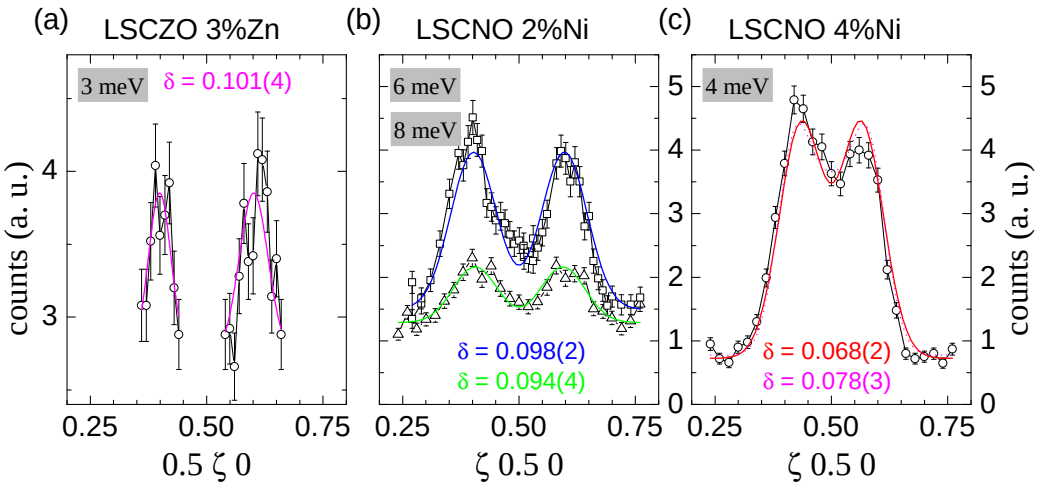

Figure 10.23: Constant-E scans over the incommensurate magnetic peaks of (a) $La_{1.88}Sr_{0.12}Cu_{0.97}Zn_{0.03}O_4$ (E = 3 meV), (b) $La_{1.85}Sr_{0.15}Cu_{0.98}Ni_{0.02}O_4$ (E = 6, 8 meV) and (c) $La_{1.88}Sr_{0.12}Cu_{0.96}Ni_{0.04}O_4$ (E = 4 meV). The intensity of the 8 meV data in figure (b) is multiplied by a factor of 1/2. In figure (c) a fit with two gaussians (*red line*) and also a fit three gaussians (*magenta dotted line*) is shown (see text).

For a characterization of the three LSCZO/LSCNO samples the positions of the magnetic satellites were determined by constant-E scans running in tetragonal $[H00]$ or $[0K0]$ direction. The resulting (magnetic) neutron scattering intensities are shown in Fig. 10.23 (a-c). Two equidistant gaussians have been fitted to these data in order to determine the incommensurability δ of the magnetic satellites. For the 3% Zn doped sample δ amounts to 0.101(4). For the 2% and 4% Ni doped samples δ amounts to 0.096(2) and 0.068(2) respectively. But also a fit with a third, additional gaussian in the center has been applied for the 4% Ni-doped sample in order to describe a possible merging of the magnetic contributions from the magnetic satellites of the other twin domains (*magenta dotted line*). The resulting incommensurability amounts to 0.078(3). These results are roughly in accordance with the nominal effective hole concentration $n = x - y$ with Sr doping level x and Ni doping level y. For example, for the 4% Ni doped sample the expected value of n amounts to $0.12 - 0.04 = 0.08$ which is in good agreement with experiment.

In order to analyze the coupling of the longitudinal bond-stretching phonon modes to the charges and the changes with Zn- and Ni-doping the topmost Δ_1 branch has been measured for $La_{1.88}Sr_{0.12}CuO_4$, $La_{1.88}Sr_{0.12}Cu_{0.97}Zn_{0.03}O_4$, $La_{1.88}Sr_{0.12}Cu_{0.96}Ni_{0.04}O_4$ and $La_{1.85}Sr_{0.15}Cu_{0.98}Ni_{0.02}O_4$. In Fig. 10.24 (a-d) constant-Q scans measured at 2 K are shown for all four samples for three selected q values between zone center and zone boundary. The full data is summarized in the intensity maps of Fig. 10.25 (a-d). The

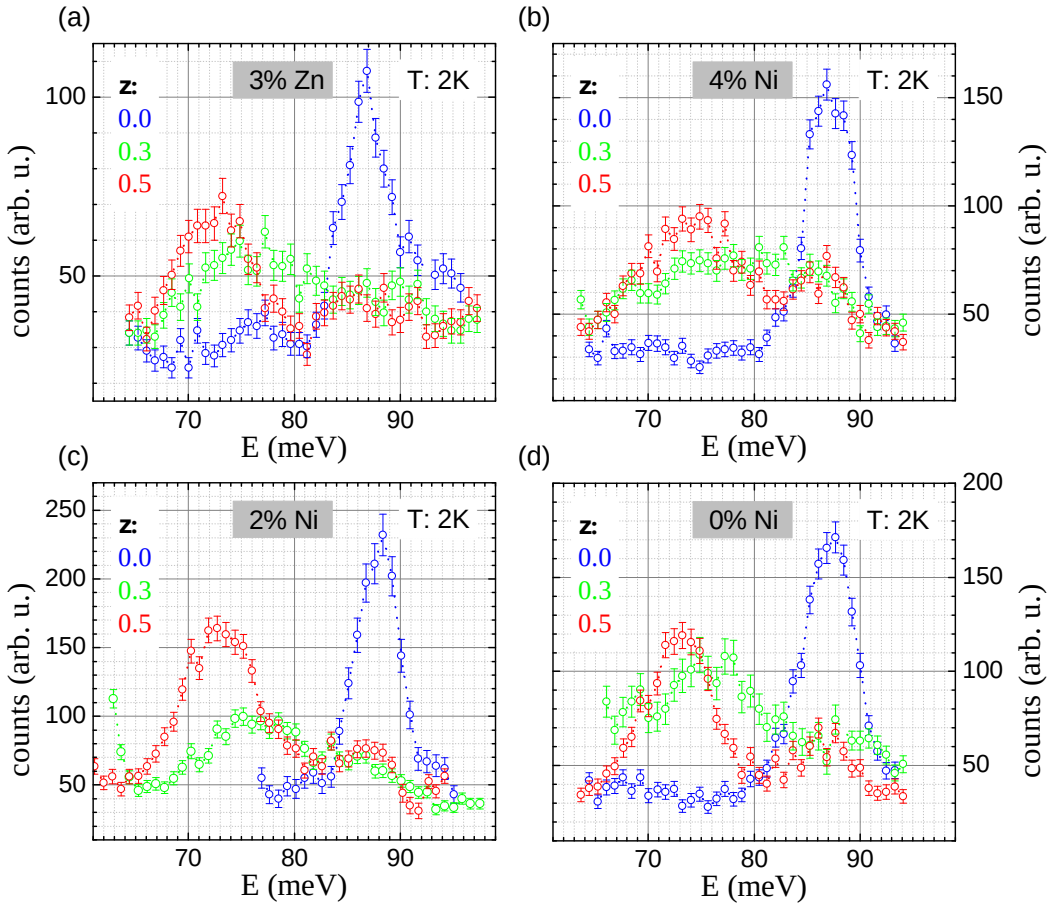

Figure 10.24: Constant-Q scans for q = 0.0, 0.3 and 0.5 of (a) $La_{1.88}Sr_{0.12}Cu_{0.97}Zn_{0.03}O_4$, (b) $La_{1.88}Sr_{0.12}Cu_{0.96}Ni_{0.04}O_4$, (c) $La_{1.85}Sr_{0.15}Cu_{0.98}Ni_{0.02}O_4$ and (d) $La_{1.88}Sr_{0.12}CuO_4$ measured at 2 K.

incommensurability ε or wavevector of the stripe order, $q_{CO} = 2 \cdot \delta$, is indicated by the vertical dashed lines (*magenta*). The total dispersion obtained by gaussian fits to the data is shown in Fig. 10.26 (c). As can be already seen in the intensity maps, Fig. 10.25 (a-d), the dispersion of the longitudinal bond-stretching branches looks quite similar in all four compounds. The dispersion shown in Fig. 10.26 (c) exhibits no major differences for all these compounds allthough the magnetic satellites appear at quite different positions, especially for the 4% Ni-doped sample. In Fig. 10.26 (a-b) the polarization patterns of the topmost Σ_1 phonon modes at q = (0.25 0 0) and (0.5 0 0) are shown. If there is any charge stripe order with a propagation vector q_{CO} = (0.25 0 0) one could assume a coupling of this phonon mode to the charges and expect some anomalies in the phonon dispersion around q_{CO}. The strong softening of this phonon dispersion around q = (0.25 0 0) which was found in (pure) 1/8 doped LBCO [13] was attributed to strong electron-phonon coupling. In this study [13] even two different

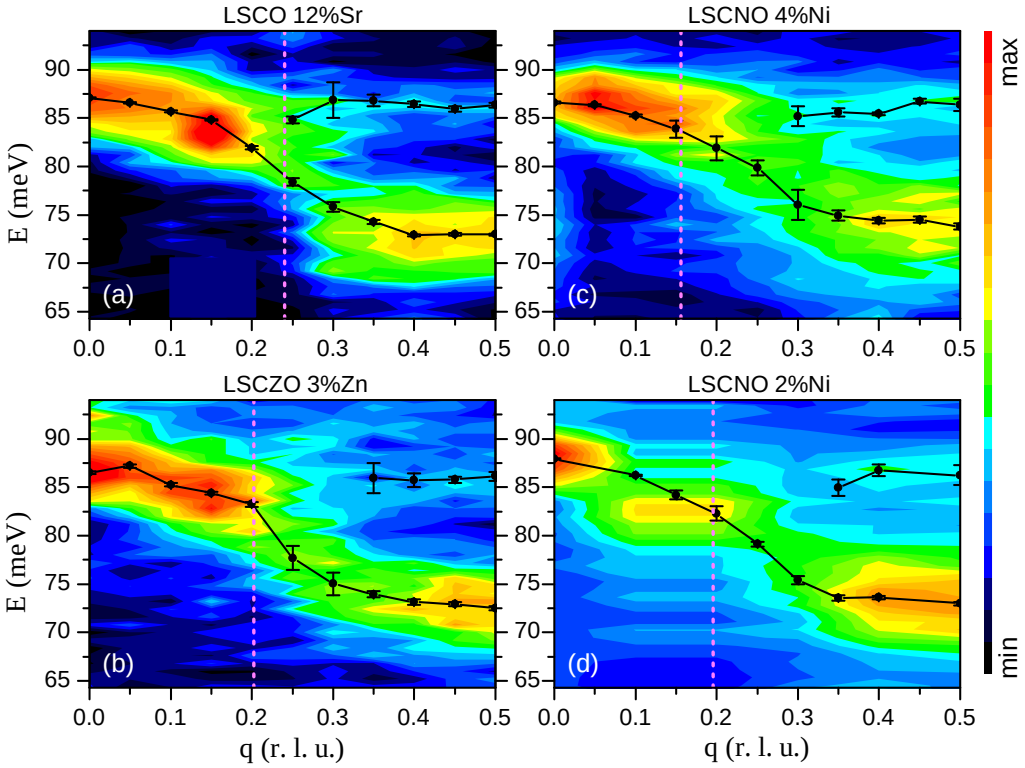

Figure 10.25: Inelastic neutron scattering intensities as a function of wavevector and energy transfer.

branches were assumed and fitted to the data - one for phonons propagating parallel and one for phonons propagating perpendicular to the stripes. However, the results of this work indicate something quite different. Although the incommensurability of the 4% Ni doped sample is fully different to the other three samples, the dispersion is about the same. Especially, the strong softening occurs still around $q = (0.25\ 0\ 0)$ and is obviously not connected to the incommensurability which is indicated by the vertical lines (magenta) in Fig. 10.25 (a-d). Hence, there is no coupling between any possible (dynamic) stripes and the renormalization of the longitudinal bond-stretching branch around $q = (0.25\ 0\ 0)$.

Furthermore, in this experiment some additional intensity could be observed in constant-Q scans above the topmost Δ_1 branch. These additional phonon branches obtained by gaussian fits are shown in Fig. 10.25 (a-d) and Fig. 10.26 (c). This effect may be either caused by some resolution effect or indicates the existence of an additional phonon branch. In the first case, the resolution ellipsoid may collect some intensities from the phonon modes connecting the Δ_1 with the Σ_3 mode. In the second case, the interpre-

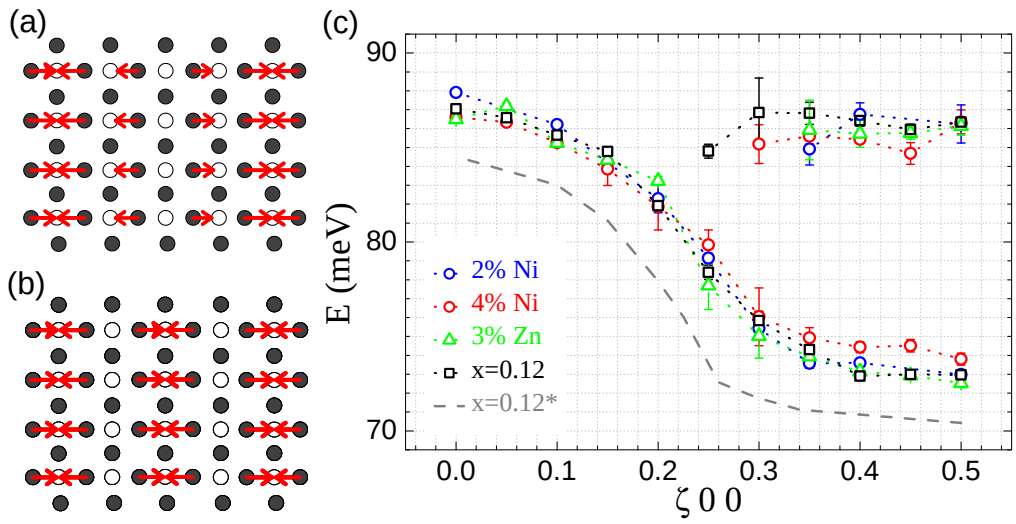

Figure 10.26: Schematic model of the polarization patterns for the topmost Δ_1-mode with propagation vector (a) $q = 0.25$ and (b) $q = 0.5$; *white/black circles*: Cu-/O-ions. (c) Dispersion for the LSCO, LSCZO and LSNO samples measured. The dashed line indicates the values observed for $La_{1.48}Nd_{0.4}Sr_{0.12}CuO_4$ in Ref. [13].

tation is not so easy, as the Ni/Zn free LSCO sample also shows some weak intensities in this region. However, in the 4% Ni doped LSCNO sample, this effect is strongest. In Ref. [437] also some additional intensities were found in the bond-stretching phonon branch of $La_{1.85}Sr_{0.15}CuO_4$ which have been attributed to a local dynamic charge ordering that is different from the charge stripes and connected to a doubling of the a-lattice parameter. As the effects are strongest for the 4% Ni doped sample studied in this work and as Ni strongly localizes charges, a dynamic local charge ordering may really have something to do with the additional phonon branch observed in this work (if it were not a resolution effect).

In Fig. 10.26 (c) also the measured dispersion for a Ni/Zn-free LSCO sample with $x = 0.12$ taken from Ref. [13] is shown. The values are systematically shifted ∼2 meV to lower energies. This difference may reflect a different energy calibration of the spectrometers used in this work (IN8) and in Ref. [13] (1T). Measurements of the phonon modes of $CuGeO_3$ which have been performed by M. Braden reveal no misadjustment of the IN8 spectrometer [438].

In Fig. 10.27 (a-h) the temperature effect on these phonon modes is shown. The additional phonon branch observed at low temperatures seems to persist up to room-temperature. At least in both Ni doped samples this effect is clearly visible. Due to this temperature-independency the explanation as a resolution effect can not be excluded.

Regarding the conventional bond-stretching phonon modes, one can observe the expected temperature effect for the phonon mode around $q = (0\ 0\ 0)$ of all four measured samples. The frequency slightly decreases on heating up to room-temperature as could be

expected from thermal expansion effects. However, no clear effect (difference in energy) is visible around $q = (0.5\ 0\ 0)$ in all four samples. Finally, also for $q \approx (0.3\ 0\ 0)$ no distinct effect is visible for the LSCNO and LSCZO samples, but there is some indication for a change in Zn/Ni-free $La_{1.88}Sr_{0.12}CuO_4$. The phonon peak for $q = (0.3\ 0\ 0)$ measured at $Q = (2.7\ 1\ 0)$ is distinctly more narrow at room-temperature (FWHM = 6.5(3.2) meV) than at 2 K (FWHM = 10.1(5.9) meV). For $q = (0.25\ 0\ 0)$ which was measured at $Q = (2.75\ 1\ 0)$ there is some contamination at higher energies in the room-temperature data set which renders a reliable determination of the peak width (FWHM) of this data set rather difficult. Nonetheless, for $Q = (2.75\ 1\ 0)$ the FWHM determined by gaussian fits amounts to 11.2(4.0) meV at 2 K and 9.5(4.1) meV at room-temperature for this data. The observation of a reduction of the peak width on heating would be in favour of the existence of (dynamic) charge stripes with a propagation vector of (0.25 0 0) in this compound with an interpretation of the peak broadening due to the difference between phonon modes propagating parallel or perpendicular to the stripes similar as in Ref. [13]. And if the charge stripes vanish with rising temperature, these phonon modes become identical and the peak becomes narrow. However, the ζ =0.25 data is somewhat contradictionary to the ζ =0.3 data and, hence, no reliable result can be drawn from this measurement. Most likely, the peak broadening at 2 K for ζ =0.3 is itself induced by some contamination (spurious peak) at lower energies. This assumption is also stressed by the finding, that phonon softening around ζ =0.25 is not coupled to the propagation vector of the stripes as discussed above. Hence, the temperature dependency of the Σ_1 phonon modes does not show any unusual effects.

10.2.4 Conclusion

In conclusion, the dispersion of the Cu-O bond stretching phonon modes probed by inelastic neutron scattering was compared for four different LSCO, LSCZO and LSCNO samples with Sr doping levels $x = 0.12$ and 0.15. The stripe spacing has been modified by the introduction of Ni. Interestingly, the dispersion of this topmost Σ_1 phonon mode exhibits about the same developing for all four samples. Especially the strong renormalization of this phonon branch is about identical for all samples although the stripe spacing is different: for the 4% Ni doped sample the incommensurability of the magnetic satellites amounts to ∼0.08 which is distinctly lower than the value for the other compounds and the expected value for the Ni-free compound which amounts to 0.12. If this phonon anomaly is related to (dynamic) charge stripes one would expect a dependency on the stripe spacing. The absence of any correlation with the propagation vector of the stripes indicates that the origin of this phonon anomaly might be different from what was thought before (see Ref. [13]) and that a coupling of the Cu-O bond stretching phonon modes to the stripes seems not to be the reason.

Furthermore, a new phonon branch was observed which was most pronounced for the Ni doped samples. It is possible that this branch reflects some coupling to local charges, which is supported by the fact that Ni strongly localizes charges. However, a simple resolution effect may also explain this observation and, hence, it can not be excluded that this additional branch is just a measurement artifact.

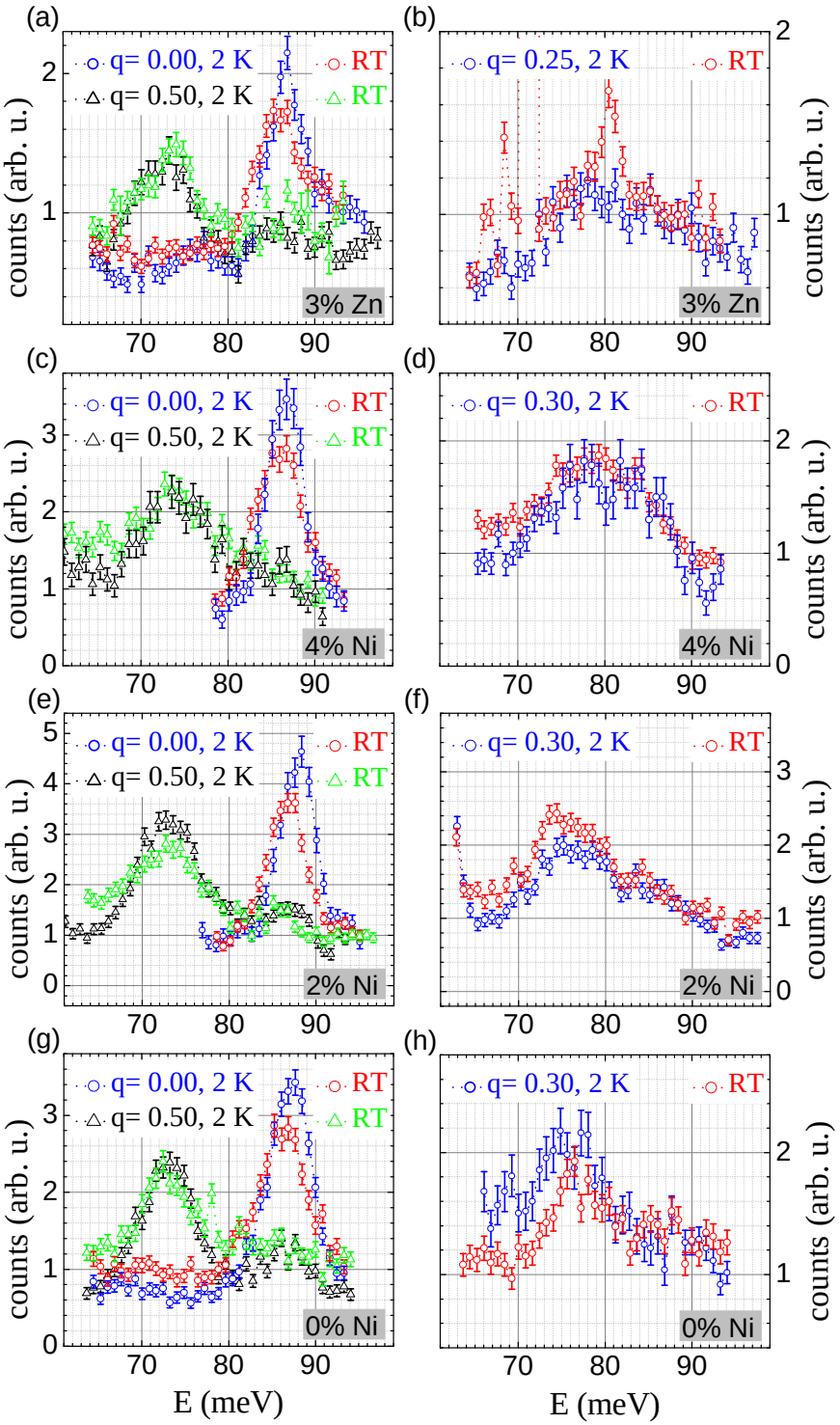

Figure 10.27: Constant-Q scans (q = 0.0, ∼0.3, 0.5) for (a-b) $La_{1.88}Sr_{0.12}Cu_{0.97}Zn_{0.03}O_4$, (c-d) $La_{1.88}Sr_{0.12}Cu_{0.96}Ni_{0.04}O_4$, (e-f) $La_{1.85}Sr_{0.15}Cu_{0.98}Ni_{0.02}O_4$ and (g-h) $La_{1.88}Sr_{0.12}CuO_4$ measured at 2 K.

11 Oxyhalides

11.1 High-pressure studies of TiOCl

11.1.1 Introduction

Low dimensional S=$\frac{1}{2}$ quantum spin systems have attracted much interest in the past years due to their challenging variety of ground states [439]. TiOCl is such a low dimensional system which exhibits interesting electronic and magnetic properties [239, 241, 242, 440]. TiOCl crystallizes in the FeOCl structure with space group $Pmmn$. As can be seen in Fig. 11.1 (a). Ti-O-bilayers are separated by Cl-ions rendering this structure quasi two-dimensional. Within these Ti-O bilayers, two different types of Ti^{3+}-chains can be observed. Whereas the chain in a-direction only allows for an interaction between the Ti^{3+} 3d-electrons via superexchange, the chain in b-direction enables direct exchange interactions. Hence, the character of the magnetic interactions is quasi one-dimensional (1D) in b-direction [439]. At high temperature, the magnetic properties can be described by a 1D spin-1/2 nearest neighbour Heisenberg model with a Bonner-Fisher type susceptibility [239]. At $T_1 = 67$ K TiOCl exhibits a transition related with a dimerization of the Ti-ions along the b-direction which has been interpreted as a spin-Peierls transition. This transition leads to a doubling of the b-lattice parameter and to a symmetry reduction to a monoclinic symmetry with space group $P2_1/m$ [439]. The second-order phase transition at $T_2 = 91$ K causes a lowering of the orthorhombic symmetry [439]. Strong orbital fluctuations [441, 442] have been proposed as an explanation. But now, an incommensurately modulated structure is well established for this intermediate phase [443, 444]. Due to the high nearest neighbour exchange coupling, TiOCl was expected to be close to a insulator-to-metal transition [239] and should be very sensitive to the application of high pressure. Recently, optical transmittance and reflectance studies in the infra-red and in the visible frequency range revealed a strong depression of the transmittance at high pressures [33] which was interpreted as an pressure-induced insulator-to-metal transition above the critical pressure $p_{c,1}$ = 12-15 GPa. This insulator-to-metal transition is accompanied by structural changes [445]. The closure of the Mott-Hubbard gap has been also observed for the related compound TiOBr [445]. This report has created a lot of controversy, lately. Whereas electrical resistivity measurements on polycrystalline samples indicate insulating properties for the whole pressure range [446] and no indications for structural changes have been found in accompanying synchrotron measurements [446], other synchrotron measurements together with *ab-initio* calculations and pressure dependent magnetic susceptibility measurements indicate a Peierls-transition above $p_{c,1}$ [447]. Furthermore, recent theoretical work using Car-Parrinello molecular dynamics

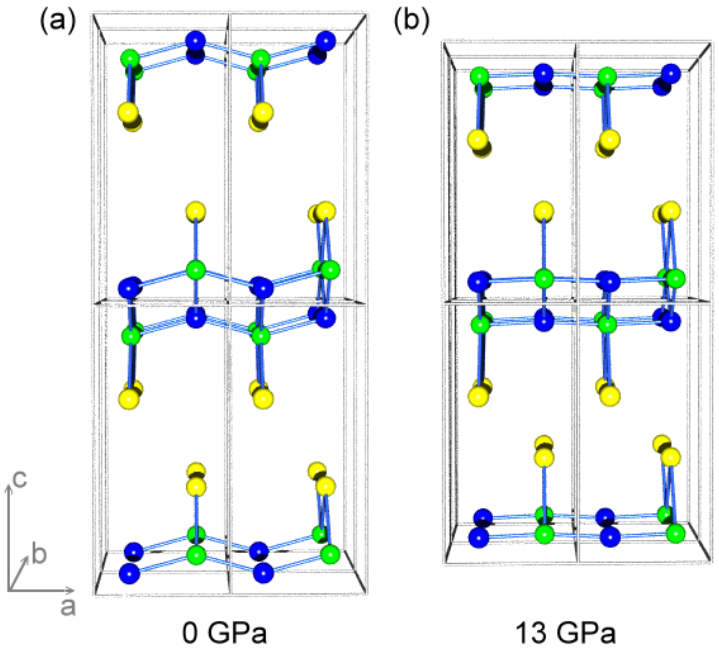

Figure 11.1: (color online) Structure of TiOCl at (a) 0 GPa and (b) 13 GPa; *green:* titanium, *blue:* oxygen, *yellow:* chlorine ions.

find an insulator-to-metal transition above $p_{c,1}$, which is driven by a widening of the bandwidth instead of a reduction of the crystal field splitting [448]. Due to these calculations, the partial density of states of the energetically lowest t_{2g} orbital which is able to overlap in b-direction still exhibits a gap, but the Fermi level crosses the partial density of states of the other two t_{2g} orbitals rendering the electronic properties of this system metallic. Furthermore, also a dimerization along b is found which explains the gap in the partial density of states of the first, energetically lowest t_{2g} orbital. These calculations are in agreement with the optical data of Ref. [33] and can also explain the superstructure reflections found in Ref. [447, 445] which are indicative for a Ti-Ti dimerization. At even higher pressures which have not been studied so far, these calculations indicate a vanishing dimerization and a purely metallic state [448].

With increasing pressure a continuous rise of the commensurate and incommensurate spin-Peierls temperatures T_1 and T_2 has been reported in Ref. [447] as indicated by pressure dependent magnetic susceptibility measurements. And the spin-Peierls transition at 67 K $= T_1(0$ GPa) is assumed to be connected to the dimerization at 300 K $= T_1(15$ GPa). However, this transition at room-temperature and very high pressures is interpreted to be a Peierls instability and *ab initio* calculations postulate an insulating state.

In this work, the pressure-induced structural changes of TiOCl were measured by neutron diffraction at the Time-Of-Flight powder neutron diffractometer PEARL at the pulsed neutron source ISIS.

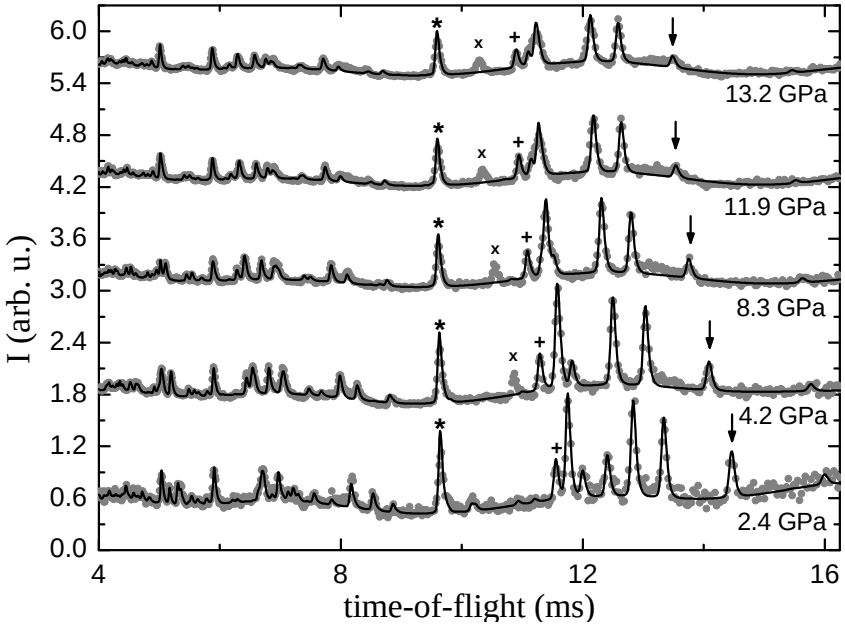

Figure 11.2: Diffraction patterns of the 3rd measurement (D_2O, D-O-CD_3, D-O-C_2D_5, Pb, double-toroidal diamond anvil cells); *gray dots*: measured data, *black line*: fit to the data, *gray star*: diamond peak, *gray x*: extra-peak, *gray +*: lead peak, *black arrow*: TiOCl (011) peak.

11.1.2 Experimental

TiOCl was prepared by the chemical vapour transport technique. The single crystals obtained were thoroughly ground, compressed under hydrostatic pressure and reground afterwards. This procedure was repeated several times in order to achieve a homogenous powder and minimize preferred orientation effects. The phase purity of the sample was checked by powder x-ray diffraction.

Three Time-of-Flight (TOF) powder neutron diffraction measurements have been performed at the PEARL diffractometer at the ISIS Facility of the Rutherford Appleton Laboratory in Didcot, United Kingdom. For the application of pressure, a Paris-Edinburgh pressure cell has been used. In the first experiment using double-toroidal diamond anvils, fluorinert has been used as a pressure medium and MgO as a pressure marker. In the second experiment using single-toroidal tungsten carbide anvils a mixture of D_2O, D-O-CD_3 and D-O-C_2D_5 with the ratio 1:16:3 has been used as the pressure medium and Pb as the pressure marker. Finally, in the third experiment using double-toroidal diamond anvils, also a mixture of methanol, ethanol and water has been used as a pressure medium and lead as pressure marker. The TOF data has been evaluated using the GSAS software.

11.1.3 Results and Discussion

In the first measurement, fluorinert was used as a pressure medium in order to minimize any reactions with the pressure medium. Unfortunately, fluorinert loses its hydrostatic properties at comparably low pressures and pressure induced peak broadening sets in above roughly 4 GPa. Also, the peaks of the pressure marker MgO merged with some TiOCl sample peaks rendering the pressure determination less accurate. Therefore in the second measurement, a mixture of methanol, ethanol and water has been tried. In this experiment the structure of TiOCl was measured at lower pressures using the tungsten carbide cells. No differences could be observed within these two experiments. Hence, there are no indications that TiOCl reacts chemically with methanol, ethanol or water - or, at least, there is no difference to fluorinert. Additional powder x-ray diffraction measurements support these observations. Thus, this mixture was also chosen as the pressure medium in the third measurement, where TiOCl has been measured at very high pressures, again. The TOF-diffraction patterns of this third measurement are shown in Fig. 11.2. As the low pressure structure of TiOCl was already measured in the second measurement, the 2.4 GPa data set was measured more rapidly with a lower statistics. An analysis of the signal in different equivalent detectors reveals that the intensities of all reflections are about equal in the different detector banks. Thus, there is no evidence for preferred orientation effects (also at high pressure) which allows a reliable structure refinement.

In this high pressure study, two main significant changes are observable. First of all, a new peak emerges above about 4 GPa as is indicated by the gray 'x' in Fig. 11.2. This new peak could not be observed in the second measurement using the tungsten carbide cell up to a pressure of 3.7(1) GPa but it is visible in this third measurement at 4.2(2) GPa and also above 3.5(2) GPa in the first measurement using fluorinert as a pressure medium. The other prominent feature in these diffractions patterns is the strong decrease of the (011) reflection with rising pressure. The (011) reflection is indicated by the black arrows in Fig. 11.2.

Recently, a pressure induced rise of the commensurate and incommensurate spin-Peierls transition temperatures T_1 (≈67 K) and T_2 (≈91 K) has been reported [447]. For the commensurate and incommensurate spin-Peierls transition temperatures the pressure dependency is $(\partial T_1/\partial P) = 2.88\times10^{-1}$ GPa^{-1} and $(\partial T_2/\partial P) = 3.64\times10^{-1}$ GPa^{-1}; see Ref. [447]. Hence, the commensurate spin-Peierls temperature T_1 is assumed to reach room-temperature at pressures $P_{c,1}$ of roughly 12-15 GPa, thus, connecting the (67 K, 0 GPa) point with the (300 K, 15 GPa) point in the (T, P)-phase diagram. If this interpretation is right, also the incommensurate spin-Peierls temperature should reach room-temperature, but at a distinctly lower pressure. Indeed, the additional peak, which has been observed in the diffraction data appears at pressures around 4 GPa which roughly fits to the pressure $P_{c,2}$ expected for $T_2(P_{c,2}) \approx 300$ K. Thus, this new peak denoted by the gray 'x' in Fig. 11.2 may be connected to the incommensurate phase. However, an unambiguous determination (indexation) of this incommensurate peak was not possible. But a (δ 2-ε 0) reflection which has also been traced with temperature in Ref. [449] describes the peak position best. The incommensurability ε was calculated

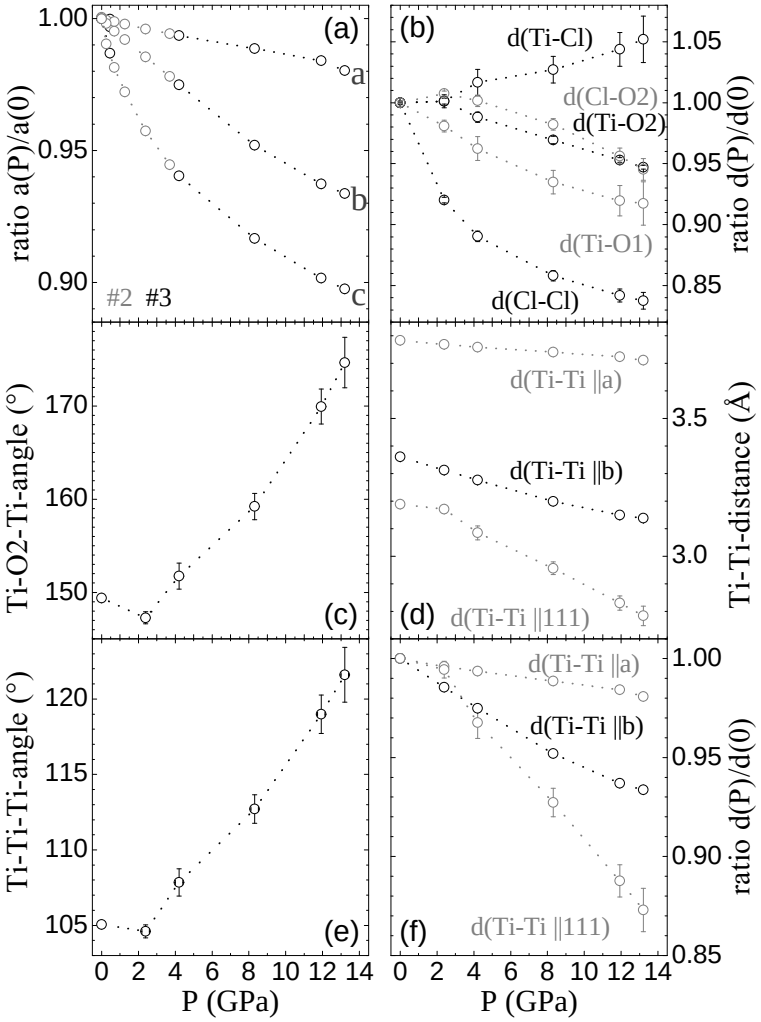

Figure 11.3: Results of the neutron diffraction measurements. (a) The relative lattice parameter as a function of pressure; (b) relative bond lengths; (c) Ti-O2-Ti bond angle indicating the flattening of the Ti-O planes; (d) Ti-Ti distances; (e) Ti-Ti-Ti angles; (f) the relative Ti-Ti distances.

from the peak position assuming that δ has a more or less constant value of 0.08 which is a quite reasonable assumption as δ seems to be the much more constant parameter compared to ε [1]; see Ref. [449]. In Fig. 11.4 the value of ε is plotted as a function of pressure. The gray data points indicate the results for the first measurement with fluorinert as a pressure medium and the black data points denote the values for the much more precise, third measurement with methanol, ethanol and water as a pressure medium. Obviously these values exhibit a significant difference. But as the TiOCl sam-

[1] Of cause, the two parameters δ and ε can not be determined independently at the same time from data which was collected as a function of only one free parameter.

ples measured in these two measurements were different, this difference might either arise from differences in the two samples or be connected to the different pressure media. In this work, the influence of this strange incommensurate superstructure reflection

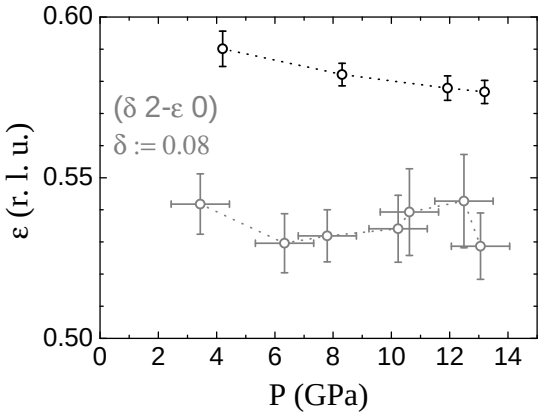

Figure 11.4: Incommensurability ε of a (δ 2-ε 0) reflection; *black:* 3rd measurement, *gray:* 1st measurement (fluorinert).

is neglected and just the fundamental structure has been fitted with an orthorhombic structure model ($Pmmn$). Although the measurements have been extended up to pressures of 13.2 GPa no commensurate superstructure reflections of the monoclinic $P2_1/m$ phase could be observed. Thus, 13.2 GPa appears to be below the value of $P_{c,1}$ for the sample measured in this work. This would be in accordance with the diffraction results of Ref. [445] where the structural phase transition is observed around 15.5 GPa. In the following, the pressure induced changes up to 13.2 GPa, i. e. close to this structural phase transition, will be discussed.

In Fig. 11.3 (a) the lattice parameters are plotted as a function of pressure. The *gray/black* data points indicate the results of the second and third measurement respectively. The pressure dependency of the lattice parameter is similar to the values reported in Ref. [446] - the a-axis is the fewest compressible axis whereas the c-axis is the most compressible one.

In Fig. 11.3 (b) the Ti-O1, Ti-O2, Ti-Cl and the Cl-Cl distances are shown. In this nomenclature the Ti-O1 bond points roughly in [011]-direction connecting an Ti ion with the oxygen ion in the neighbouring Ti-O layer and the Ti-O2 bond points in a-direction, thus, connection Ti-ions within the same Ti-O layer. As can be seen, the Ti-O1 distance exhibits a larger compressibility than the Ti-O2 distance. Thus, the neighbouring Ti-O layers within the same Ti-O bilayer get closer and the distance of these layers shrinks. Interestingly, there is one bondlength which increases with pressure - the Ti-Cl bondlength. Thus, the titanium ion which is located within a strongly distorted O_4Cl_2 octahedron moves in c-direction away from the chlorine ions towards the Ti-O layer. With increasing pressure also the chlorine ions move in c-direction towards each other and the Cl-Cl distances become much shorter. Another value which illustrates this

flattening of the Ti-O layers is the Ti-O2-Ti bond angle which connects two titanium ions within the same Ti-O layer over an oxygen ion in a direction; see Fig. 11.3 (c). This Ti-O2-Ti angle strongly increases with pressure from roughly 150° at ambient pressure to 174.7(2.7)° at 13.2 GPa. This strong effect induces an almost perfect flattening of the Ti-O bilayers as can be seen even visually in the comparison of Fig. 11.1 (a) and (b). In the diffraction patterns, this flattening of the bilayers is connected to the strong reduction of the (011) reflection which is marked by the black arrows in Fig. 11.2. The same reduction of this (011) reflection at high pressures up to 12 GPa has also been observed in the first measurement with fluorinert as the pressure medium.

Regarding the Ti-Ti distances which are plotted in Fig. 11.3 (d), the Ti-Ti distance in a direction is the fewest compressible Ti-Ti distance. The reason for this is the flattening of the Ti-O layers which induces a relative enlargement of the Ti-O distances in a direction. Hence, this flattening of the Ti-O layers is also responsible for the weak compressibility of the a lattice parameter. On the other hand, the Cl-Cl distances exhibit the strongest compressibility which is responsible for the high compressibility of the c lattice parameter. The Ti-Ti distance in b direction is more compressible, which would support a dimerization at higher pressures. However, this Ti-Ti distance is neither the shortest nor the most compressible Ti-Ti distance. The Ti-Ti distance which roughly points in [111]-direction is smaller and exhibits a distinctly larger compressibility as can be seen in Fig. 11.3 (f). This Ti-Ti distance shrinks from 3.189(4) Å at 0 GPa to 2.784(35) Å at 13.2 GPa which is smaller than the Ti-Ti distance in pure α-titanium metal at ambient pressure (2.9508 Å) [450]. High pressure studies of Ti metal observe a Ti-Ti distance of roughly 2.85 Å around 13 GPa for the α-phase and roughly 2.6 Å around 13 GPa for the shortest Ti-Ti distances in the high-pressure ω-phase of Ti metal [451]. Hence, this Ti-Ti distance in TiOCl at 13.2 GPa lies between the Ti-Ti distances of the α- and ω-phases of the pure titanium metal at similar pressures. These short Ti-Ti bonds in TiOCl form a grid of zig-zag chains running in [±110] direction. In Fig. 11.3 (e) the corresponding pressure dependent Ti-Ti-Ti angle is shown. It increases from about 105° at 0 GPa to about 121.6° at 13.2 GPa. (There are also 120° Ti-Ti-Ti bond-angles in hexagonal α- and ω-Ti.)

The chlorine ions moving away in c-directions enhance the low-dimensionality of this system. On the first view this anomalous rise of the Ti-Cl distance by 0.124(46) Å between 0 GPa and 13 GPa may seem unphysical; see Fig. 11.3 (b). But the flattening of the Ti-O bilayers induces a shift of the oxygen ions towards the chlorine ions and up to 13 GPa the Cl-O2 distance decreases by 0.184(30) Å; see Fig. 11.3 (b). Thus, the chlorine ions become repelled by the large and negative charged oxygen ions which move towards the chlorine ions as the Ti-O bilayers flatten.

The structural parameters derived in the measurement with double-toroidal diamond anvil cells and methanol, ethanol and water as a pressure medium and lead as a pressure marker (third experiment) are listed in Tab. 11.1. The '0 GPa measurement' has been made at ambient pressure using a vanadium can and the measurement at 2.4(2) GPa has been made using a tungsten carbide cell and single-toroidal diamond anvil cells (second experiment).

All these strong structural changes induced by pressure point to changes in the elec-

pressure:	SG	**a**	**b**	**c**
0 GPa	*Pmmn*	3.78395(21) Å	3.36095(17) Å	8.0496(4) Å
2.4(2) GPa	*Pmmn*	3.7688(6) Å	3.3121(5) Å	7.7062(11) Å
4.2(2) GPa	*Pmmn*	3.7594(8) Å	3.2765(6) Å	7.5698(16) Å
8.3(2) GPa	*Pmmn*	3.7410(8) Å	3.1996(6) Å	7.3789(16) Å
11.9(2) GPa	*Pmmn*	3.7244(11) Å	3.1491(8) Å	7.2566(22) Å
13.2(2) GPa	*Pmmn*	3.7114(12) Å	3.1380(9) Å	7.2231(24) Å
pressure:	*atom:*	**x**	**y**	**z**
0 GPa	Ti1	0.25	0.75	0.8795(6)
	Cl1	0.25	0.25	0.66937(24)
	O1	0.75	0.75	0.94383(33)
2.4(2) GPa	Ti1	0.25	0.75	0.8742(20)
	Cl1	0.25	0.25	0.6511(11)
	O1	0.75	0.75	0.9460(7)
4.2(2) GPa	Ti1	0.25	0.75	0.880(4)
	Cl1	0.25	0.25	0.6440(23)
	O1	0.75	0.75	0.9425(21)
8.3(2) GPa	Ti1	0.25	0.75	0.889(4)
	Cl1	0.25	0.25	0.6377(23)
	O1	0.75	0.75	0.9355(22)
11.9(2) GPa	Ti1	0.25	0.75	0.901(5)
	Cl1	0.25	0.25	0.6354(31)
	O1	0.75	0.75	0.9236(33)
13.2(2) GPa	Ti1	0.25	0.75	0.906(7)
	Cl1	0.25	0.25	0.635(4)
	O1	0.75	0.75	0.918(5)

Table 11.1: Structural parameters of TiOCl at different pressures.

tronic behaviour of TiOCl. The strong flattening of the Ti-O bilayers which, additionally, get compressed in *c*-direction supports the electron hopping and should increase the bandwidths of the t_{2g} orbitals with exception of the lowest lying t_{2g} orbital which exhibits a really small overlap in all directions. This result is fully in accordance with the calculations in Ref. [448] and, thus, supports the observation of a pressure-induced metal-to-insulator transition in Ref. [33]. However, the structural changes observed in this work are much larger than the ones calculated in Ref. [448] and may stimulate further calculations. Also the strongly reduced Ti-Ti distance in [111]-direction may be in favour of a metallic regime at high pressures. With respect to all these strong structural changes the observation of insulating electronic properties over the whole pressure regime in Ref. [446] seems questionable and may be caused by grain boundary effects within the polycrystalline samples of this presumably quasi-two-dimensional metal as it was already proposed in Ref. [448].

The dimerization at high pressures which was postulated in Ref. [447] and calculated in Ref. [448] could not be observed in the measurements of this work, as the highest pressure attained is probably too low. It is interesting to note, that the Ti-O2-Ti angle in Fig. 11.3 (c) can be extrapolated to 180° for pressures of approximately 15.9 GPa. About this pressure has been reported to be the critical pressure for the structral phase

transition of TiOCl [445]. Thus, the high-pressure phase transition in TiOCl may be connected to a complete flattening of the Ti-O bilayers. However, it appears important to note that the pressure induced structural modifications described above can go beyond the full flattening of the TiOCl layers resulting again in a corrugation but with opposed signs.

11.1.4 Conclusion

In conclusion, the high pressure structure of TiOCl has been measured with powder neutron diffraction. As there were no preferred orientation effects in these measurements, it was possible to solve the high pressure structure of TiOCl up to pressures well below the structural phase transition which has been reported to occur around 15.5 GPa in Ref. [445]. With increasing pressure, a strong flattening of the Ti-O layers and a compression of the distance of two neighbouring Ti-O layers within a bilayer occurs. This flattening of the bilayers is connected to the strong decrease of the (011) reflection in the diffraction patterns. These strong structural changes favour changes of the electronic properties of TiOCl at high pressure. An increase of the electronic bandwidth W can be expected which would support the metallic high-pressure scenario of TiOCl as was reported in Ref. [33, 448]. However, there is also the possibility for a dimerization at even higher pressures which was postulated in Ref. [447] within the scenario of a Peierls instability or calculated in Ref. [448] within a metallic scenario. Possibly, this possible dimerization is connected to a complete flattening of the Ti-O bilayers as is indicated by the extrapolation of the Ti-O2-Ti angle to 180°. Furthermore, with increasing pressure and flattening of the bilayers the chlorine ions are repelled from the Ti-O bilayers by the oxygen ions rendering this system even more low-dimensional.

11.2 Magneto-elastic coupling in VOCl

11.2.1 Introduction

The transition metal oxyhalides MOX with M = Sc, Ti, V, Cr, Fe and X = Cl, Br have re-attracted enormous interest in the past years due to the exhibition of challenging low-dimensional phenomena for one compound of this group - TiOCl [439, 239, 241, 242, 440, 444], see Chap. 11.1. The whole group of transition metal oxyhalides MOX provides a very nice system of at room-temperature crystallographically iso-structural compounds in which several electronic configurations and their interactions with the crystal lattice can be probed systematically. However, the physical properties of the MOCl compounds different from M = Ti have not been studied in great detail so far [452-456]. Like TiOCl, VOCl crystallizes in an orthorhombic structure with space group $Pmmn$, with one crystallographic V-site [457]. The V^{3+}-ions are coordinated by four oxygen atoms and two chlorine atoms forming strongly distorted VO_4Cl_2 octahedral units; see Fig. 11.6. These are linked via corners along the crystallographic b-axis and via edges along the a-axis, forming quasi two dimensional bilayers in the ab-plane. Due to the Cl-ions there is a separation of the Ti-O-bilayers which are parallel to the ab-plane, thus, turning this system low-dimensional. Due to electronic correlations all oxyhalides display rather strong electron localization, resulting in (electrically) Mott-insulating properties. In VOCl the band gap is reported to be about 1.7 eV [458]. Whereas in TiOCl direct overlap of the t_{2g}^1- ground state xy-orbitals along the crystallographic b-axis leads to one dimensional magnetic interactions [242], VOCl is believed to exhibit (quasi) two dimensional antiferromagnetic ordering below T_N (80 K) [453]. In an early powder neutron diffraction study a collinear magnetic order with the wavevector [1/2 1/2 1/2] and the magnetic moments pointing in a-direction has been reported [453]. The magnetic susceptibility was described well with a quadratic 2D-Heisenberg model. However, in this study no signs of a structural transition in VOCl have been observed down to lowest temperatures [453].

11.2.2 Experimental

The polycrystalline VOCl-samples were made by T. Taetz by the chemical transport technique; see Ref. [459]. The single crystals obtained via this route were thoroughly ground, compressed under hydrostatic pressure and reground afterwards. This procedure was repeated several times in order to achieve a homogenous powder and hence minimize preferred orientation effects. The phase purity of the sample was checked using powder X-ray diffraction.

High resolution synchrotron radiation powder X-ray diffraction measurements have been performed at beamline B2 at the synchrotron facility HASYLAB/DESY in Hamburg, Germany. Therefore, the VOCl-powder (*sample A*) was well ground and filled in glass capillaries with 0.3 mm in diameter which were sealed and mounted in Debye-Scherrer geometry in a He closed-cycle cryostat equipped with a silicon diode as temperature sensor and with a capillary spinner. A wavelength of 0.7466 Å was selected from

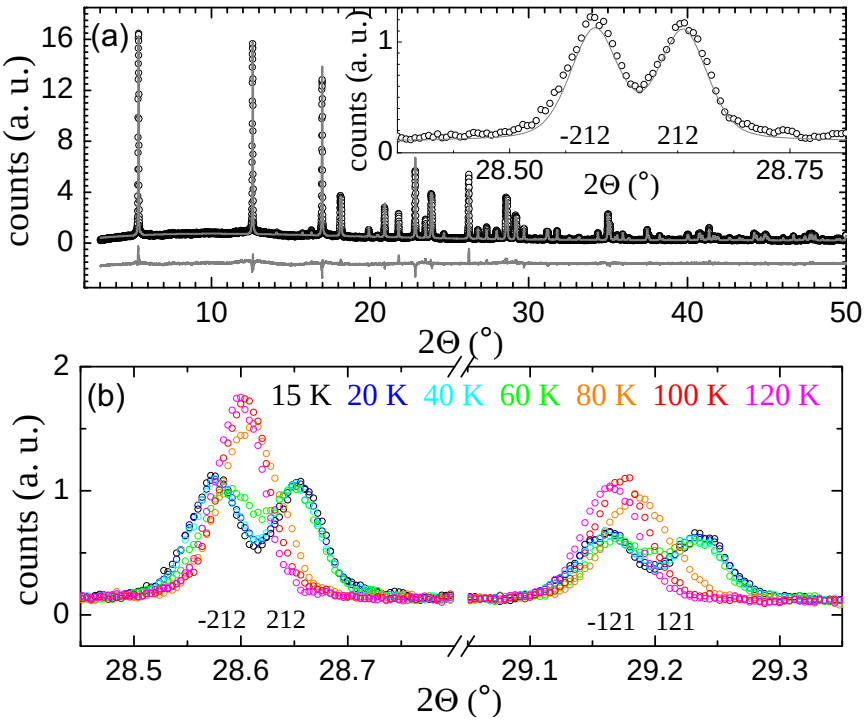

Figure 11.5: (color online) Synchrotron radiation powder X-ray diffraction patterns. (a) Rietveld fit (*gray*) to the data at 15 K (*black*) with a clip of the diffraction pattern in the inset. (b) Temperature dependency of the (±212) and (±121) reflections.

the direct white synchrotron beam using a Si (111) double flat-crystal monochromator and determined from 8 reflection positions of a LaB_6 reference sample. The diffraction patterns have been collected using an on-site readable position-sensitive image-plate detector.

Powder neutron diffraction measurements have been performed at the D20, D1A and the D2B diffractometer at the ILL in Grenoble, France (λ = 2.4233 Å, 1.91 Å and 1.594 Å respectively). The sample measured at the D20 and D2B diffractometer (*sample B*) contains some not identified impurity phases. Therefore, only the single phase sample measured at the D1A diffractometer (*sample C*) was used for a full nuclear structure refinement. Only for the magnetic structure refinement the D20 data has been used, as there was no overlapping of peaks from the impurity phases with the magnetic peaks.

11.2.3 Results and Discussion

Temperature dependent high-resolution powder X-ray diffraction measurements using synchrotron radiation with an incident wavelength of 0.7466 Å have been performed at beamline B2 at Hasylab/DESY. These measurements reveal a structural phase tran-

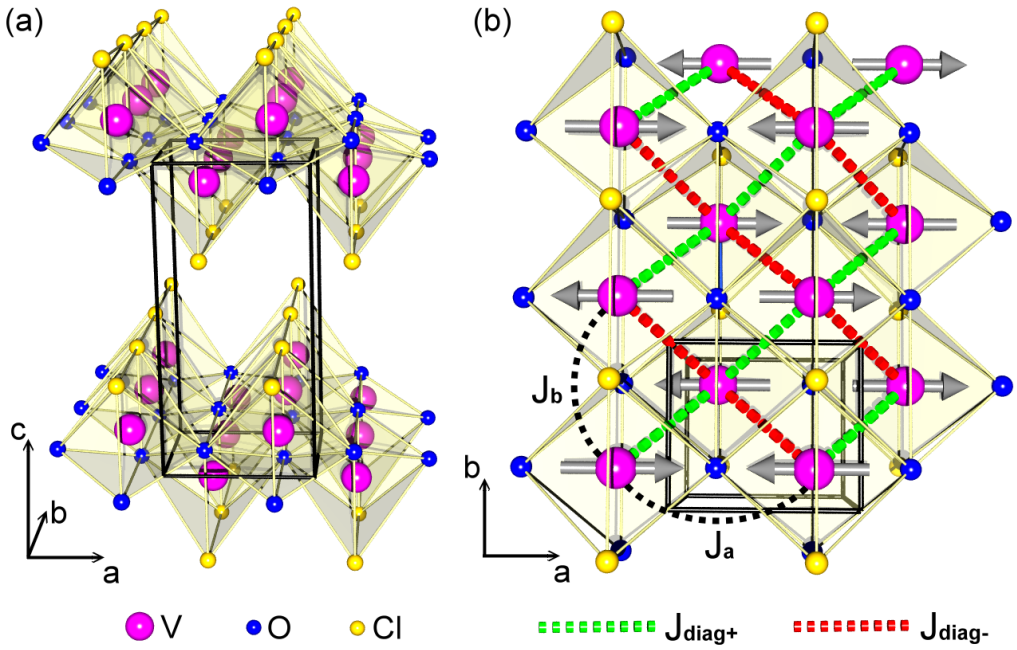

Figure 11.6: (color online) Nuclear and magnetic structure of VOCl; *yellow*: Cl-, *blue*: O-, *magenta*: V-ions; *black*: the structural unit cell. The directions of the magnetic moments at each V-site is indicated by *magenta arrows*. *Green* (*red*) *dotted lines* indicate the antiferromagnetically coupled V-V pairs in the AFM1 (AFM2) structure.

sition below 80 K. A diffraction pattern at the lowest temperature, 15 K, is shown in Fig. 11.5 (a). The open circles denote the measured data points and the line indicates the Rietveld fit of the structure model to the data using the program *FullProf/WinPLOTR* [88]. The part of the diffractogram focussing on the ($\pm$212) reflections is shown in the inset. The clearly observable splitting of the (212) reflection indicates the symmetry reduction from the orthorhombic ($Pmmn$) to a monoclinic symmetry. The data can be described with space group $P2/n$ (monoclinic setting c) and a monoclinic angle γ of 90.2°. In Fig. 11.5 (b) the ($\pm$212) and ($\pm$121) reflections are plotted for different temperatures indicating the orthorhombic to monoclinic phase transition below 80 K. The resulting lattice parameter are plotted as a function of temperature in Fig. 11.7 (a-d). A rise of the monoclinic angle γ can be observed below 80 K reaching its maximum value of about 90.2° around 40 K. These new findings are opposite to the neutron measurements reported in Ref. [453] where no phase transition has been observed at low temperatures.

Powder neutron diffraction measurements have been performed at the ILL. In Fig. 11.8 (a-c) neutron diffraction patterns of VOCl are shown. Fig. 11.8 (c) shows the splitting of the (223) reflection measured at the D2B diffractometer with an incident wavlength of 1.594 Å. This finding corroborates the results of the synchrotron measurements and verifies the occurrence of a monoclinic distortion for the sample measured at the D20

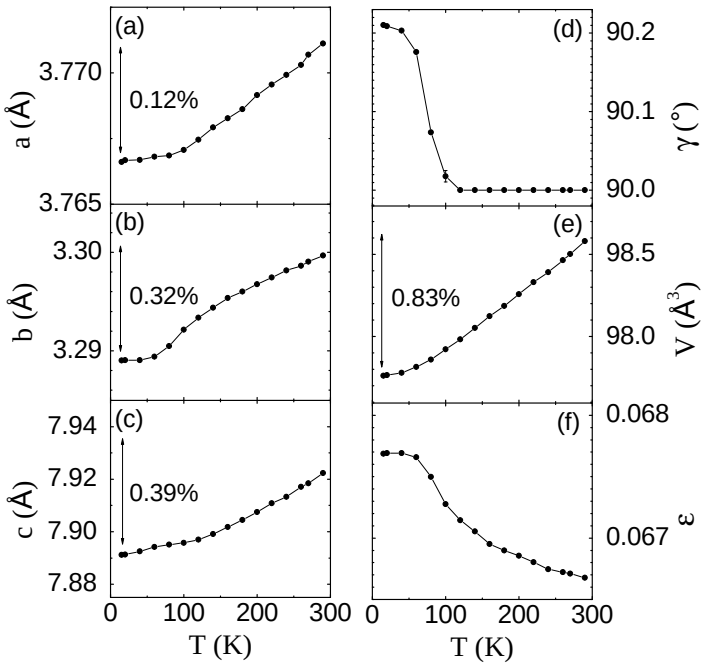

Figure 11.7: Results of synchrotron radiation powder X-ray diffraction measurements: (a-c) lattice parameter, (d) monoclinic angle, (e) unit cell volume and (f) orthorhombic splitting ε = (a-b)/(a+b). (Lines are guide to the eyes.)

diffractometer. In Fig. 11.8 (a) the strongest magnetic peaks measured at 2 K at the D20 diffractometer with an incident wavelength of 2.4233 Å are plotted. And in Fig. 11.8 (b) a diffractogram measured at 10 K at the D1A diffractometer using a neutron wavelength of 1.91 Å is shown. The structural parameters resuting from the rietveld refinement of all neutron (and synchrotron) measurements are listed in Tab. 11.2.

The structural refinement reveals increasing V-O-V bond angles in a/b-direction and a displacement of the vanadium ions away from the chlorine ions towards the oxygen ions in c-direction; see Fig. 11.10 (a-e). These displacements should increase the antiferromagnetic exchange interaction across the oxygen ions as all V-O-V bond angles increase. Indeed, a fully three-dimensional (3D) antiferromagnetic structure could be fitted to the neutron data; see Fig. 11.8 (a). The occurence of $(\frac{1}{2}\ \frac{1}{2}\ \frac{1}{2})$ and $(\frac{1}{2}\ \frac{1}{2}\ \frac{3}{2})$ reflections below T_N indicates a magnetic propagation vector $\overrightarrow{k} = (\frac{1}{2}\ \frac{1}{2}\ \frac{1}{2})$. This leads to a $2 \times 2 \times 2$ enlargement of the magnetic unit cell. A magnetic structure model with all moments between neighbouring V-ions in a-, b- and c-direction coupled antiferromagnetically and pointing in a-direction describes the data best; see Fig. 11.6. Other directions of the magnetic moment like the [110]-direction induce discrepancies in the measured intensities of the $(\pm1\pm11)$ and $(\pm1\pm13)$ reflections (in notation of the magnetic unit cell) and would not be in accordance with the magnetic susceptibility measured in Ref. [453] which indicates antiferromagnetic ordering with moments parallel to the crystallographic a-axis. The antiferromagnetic moment amounts to about 1.3 μ_B at 2 K which is in approximate

agreement with the value reported in Ref. [453] but which is a rather small value for the vanadium ion with a $3d^2$ electronic configuration. The value of the antiferromagnetic moment as a function of temperature is shown in Fig. 11.10 (h). The temperature dependency of this antiferromagnetic moment indicates a Néel-temperature of roughly 81 K. Additionally, the monoclinic angle γ is plotted below the ordered moment (*gray*). The direct coupling of γ to the antiferromagnetic moment is indicative for a magneto-elastic coupling which drives the orthorhombic to monoclinic phase transition.

According to representation theory, there are four irreducible representations for space group $P112/n$ with a magnetic ion at (-0.25 0.25 z_0) ($z_0 \approx 0.117$) and with propagation vector $\overrightarrow{k} = (\frac{1}{2}\ \frac{1}{2}\ \frac{1}{2})$. The basis vectors for these four possibilities derived from the programm *BasiRep* [88] are shown in Fig. 11.9. These four possibilities will be referred to as the antiferromagnetic structures 1 to 4 (AFM1 - AFM4). In the AFM1 structure, the magnetic moments of the V-ions within the first primitive unit cell are within the *ab*-plane and couple antiferromagnetically; see Fig. 11.9 (only the *a* direction is shown). Contrarily to this, these moments couple ferromagnetically in the AFM2 structure. As was pointed out in Ref. [453], the two magnetic structures AFM1 and AFM2 can not be distinguished with powder neutron diffraction if the crystal structure was orthorhombic ($Pmmn$) as the intensity of a powder peak is a constant and depends only on the average value of the sin^2 of the angle between magnetic moment and scattering vector. However, the structural phase transition $Pmmn \rightarrow P2/n$ observed in this work induces a (small) splitting of the ($\pm1\ \mp1\ L$) and the ($\pm1\ \pm1\ L$) reflections (L = 1, 3). The (small) splitting of these reflections allows to distinguish between the two magnetic structures. In Fig. 11.8 (a) for all magnetic models the Rietveld fits to the measured data at 2 K are shown. A rietveld fit of the AFM2 structure reveals that the calculated intensities for the first magnetic peak ($\pm1\ \pm1$ 1) are shifted to lower 2Θ values in total. Thus, the AFM2 structure fails in describing the measured data correctly. Contrarily to this, the AFM1 structure is able to describe the data well if the magnetic moments are parallel to the *a*-direction. A fit with moments in *b* direction suffers in the correct description of the intensities. Even a fit with both *a*- and *b*-components yields only within the error bars negligible values for the moment in *b*-direction: -0.14(15)μ_B. This result is in accordance with the measured magnetic susceptibility in Ref. [453] which reveals an antiferromagnetic structure with moments in *a*-direction. The AFM3 and AFM4 structures with *c*-components of the magnetic moment fail in describing the magnetic intensities; see Fig. 11.8 (a). Thus, in VOCl the AFM1 magnetic structure with moments in *a*-direction is clearly preferred against the other possible magnetic structures, especially the AFM2 structure. This result is in contrast to the results of the single crystal neutron measurements of Ref. [453] where an admixture of the AFM1 and AFM2 was found. Most likely, below T_N a twinning of both monoclinic structures occurs in the single crystal of Ref. [453] which has not been accounted for as the orthorhombic to monoclinic phase transitions has not been recognized.

The preference of the AFM1 structure can be understood with regard to the monoclinic distortions of the structure. As noted above, the magnetic moments couple antiferromagnetically along the *green* V-V bonds in Fig. 11.6 but not along the *red* ones. And

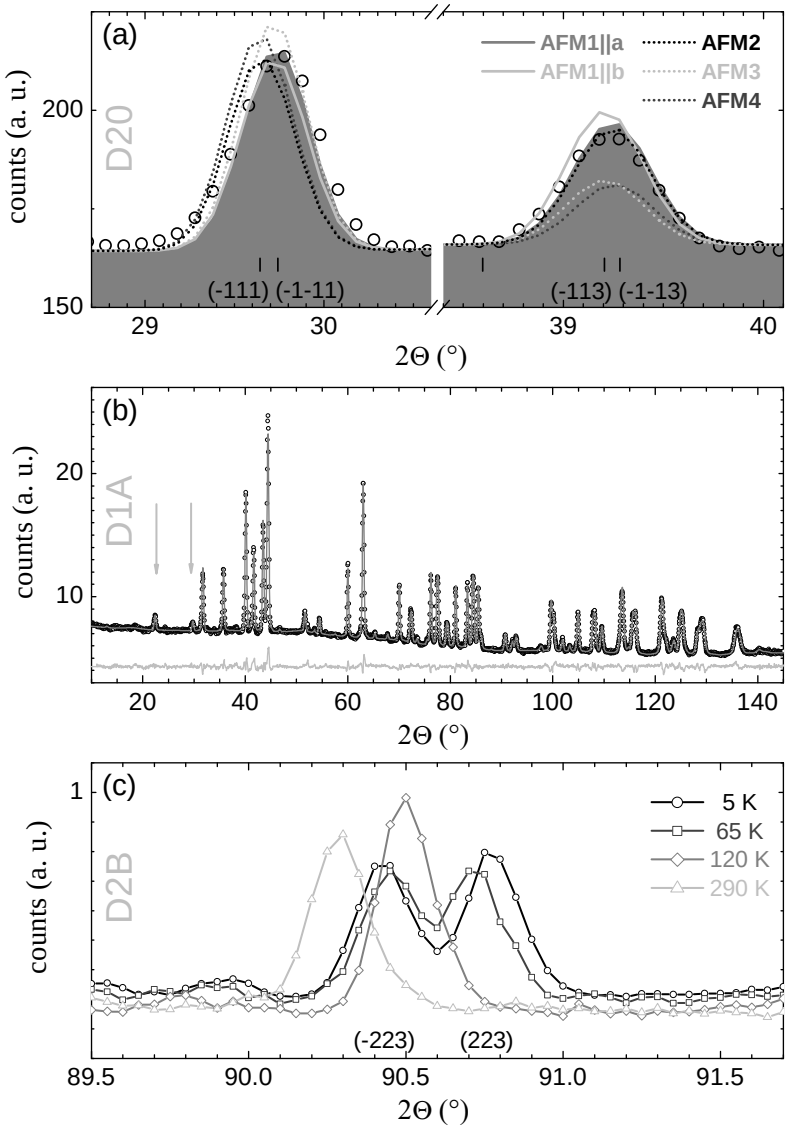

Figure 11.8: (a) Powder neutron diffraction patterns measured at 2 K (D20 diffractometer); *circles*: data points, *lines*: rietveld fits to the data with the AFM1-AFM4 structure models. The area below the AFM1-fit (moment $\|a$) is filled (*gray*). (b) Fit of the D1A measurement at 10 K; *black*: data points, *gray*: Rietveld fit to the data, *lt. gray*: difference I_{obs}-I_{calc}, arrows indicate the magnetic peaks. (c) Diffraction patterns measured at different temperatures at the D2B diffractometer.

indeed, the *red* and *green* V-V bonds in Fig. 11.6 differ by 0.0073(15) Å as can be seen in Fig. 11.10 (f). Compared to the orthorhombic structure where the *red* and *green* bonds shown in Fig. 11.6 are equivalent, these monoclinic distortions may be responsible for an

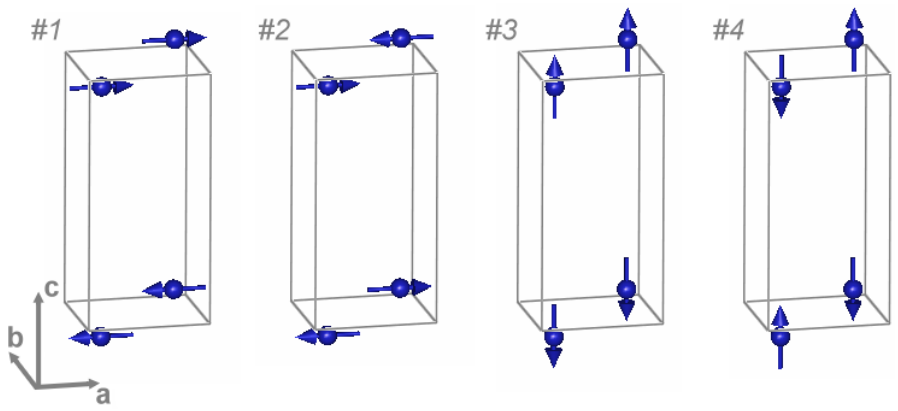

Figure 11.9: (a-d) Models of the four possible irreducible representations in space group $P112/n$ with k = ($\frac{1}{2}$ $\frac{1}{2}$ $\frac{1}{2}$) and with magnetic atoms in the primitive unit cell at (-0.25, 0.25, z_0).

enhancement of the antiferromagnetic exchange interaction across one of these bonds, i. e. the *green* V-V bonds in Fig. 11.6, as the shorter V-V distance can be expected to induce a larger orbital overlap accompanied by a stronger exchange interaction. Thus, these monoclinic distortions prefer the establishment of the AFM1 structure versus the AFM2 structure. Hence, the orthorhombic to monoclinic phase transition is connected to the magnetic phase transition and may be driven by magneto-elastic coupling of spins and lattice.

Unfortunately, these neutron measurements suffer from the small vanadium scattering length which causes enlarged error bars for all variables which are strongly dependent on one or even on two atomic V-positions. This effect is most visible in Fig. 11.10 (f). Therefore, an extremely long measurement has been performed at the D1A diffractometer in order to increase the statistics and another synchrotron radiation powder X-ray diffraction measurement at 20 K has been performed at beamline B2 at Hasylab/DESY. In this synchrotron measurement a summation of several measurements with an image plate detector with a total measuring time of more than 1 hour has been applied. As the measured sample volume is rather small in synchrotron measurements, preferred orientation effects can be expected for this quasi-2D system. Thus, also one additional parameter for a preferred orientation in *c*-diretcion has been refined which is reasonable as these crystals have a very anisotropic shape of extremely flat crystalline layers which extend in *a*-/*b*- direction. The values of this extremely accurate measurement are plotted in Fig. 11.10 (a-g). As can be seen, the error bars of these two exact measurements are much smaller and in the synchrotron case of dimensions of the symbol size only. Especially, the value of the difference in the V-V distances shown in Fig. 11.10 (e) has much smaller error bars now and corroborates the neutron results and, thus, the explanation for the preference of the AFM1 structure. The structural parameters of this synchrotron measurement and of the neutron measurements at 2 K and at 150 K are listed in Fig. 11.9 (a-g).

It is interesting to note that both diagonal V-V distances decrease on cooling which enhances the antiferromagnetic exchange interaction due to a stronger orbital overlap but that the corresponding V-O-V bond angles decrease on cooling which is less favourable for an antiferromagnetic exchange interaction; see Fig. 11.10 (c,e). This effect indicates that the diagonal V-V-distance may be directly connected with magneto-elastic coupling whereas the corresponding diagonal V-O-V bond angles play somehow a minor role than the distances. Furthermore, the (slightly) shorter diagonal V-V bonds have also about 0.3° smaller diagonal V-O-V bond angles which is less favourable for a stronger antiferromagnetic exchange interaction along the shorter diagonal V-V bonds. As stated above, in VOCl the antiferromagnetic coupling is established along the shorter diagonal V-V bonds within a V-double layer and not along the diagonal V-V bonds with larger corresponding V-O-V bond angles. This situation is contrary to the case of the spin-Peierls material $CuGeO_3$ where the dimerization is realized through modulation of the bond angles [460-463]. However, the case of VOCl may be different compared to $CuGeO_3$ as t_{2g} orbitals are involved instead of e_g orbitals.

11.2.4 Conclusion

In conclusion, synchrotron measurements as well as neutron measurements reveal a structural phase transition $Pmmn \rightarrow P2/n$ in VOCl. Orthorhombic to monoclinic phase transitions have been observed for TiOCl and TiOBr at low temperatures so far but no similar transition has been observed in the VOCl system [453]. Furthermore, the analysis of the magnetic structure within the monoclinic $2 \times 2 \times 2$ unit cell of this quasi-2D system yields a fully 3D-antiferromagnetic structure with an antiferromagnetic moment pointing in a-direction. At 2 K this moment amounts to about 1.3 μ_B which is a strongly reduced value for the $3d^2$ V-ion. The magnetic phase transition is accompanied by structural distortions inducing a splitting of two diagonal V-V bond distances which are both equivalent in the undistorted orthorhombic structure. Concomitant, a well pronounced increase of the V-O-V bond angles in a- and b-direction appears. This flattening of the VO-layers induces an enhancement of the antiferromagnetic exchange interactions in a- and b-directions whereas the shortening of one of the diagonal V-V distances within a V-bilayer implied by the monoclinic distortion induces a larger orbital overlap which increases the exchange interaction along one of the previously two equivalent exchange paths and, thus, lifts the frustration of the coupling between the two magnetic sublattices. Hence, these structural changes explain the magnetic structure which could be observed in the powder neutron diffraction measurements of this work and which could be distinguished from the other possible magnetic structures with a propagation vector of $\overrightarrow{k} = (\frac{1}{2}\ \frac{1}{2}\ \frac{1}{2})$ due to a sufficiently large monoclinic distortion with a monoclinic angle of about 90.2°.

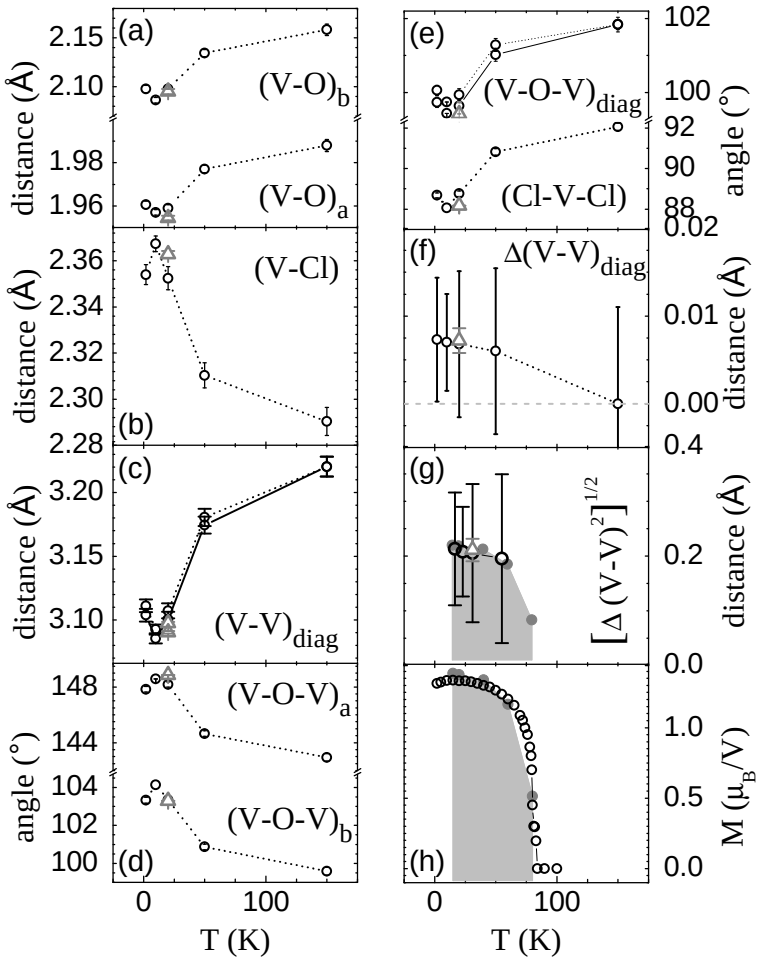

Figure 11.10: (a) V-O distances for V-O bonds in a- and b-direction. (b) V-Cl distance. (c) V-V distances for V-ions within the same V-bilayer in diagonal direction (*red* and *green* bonds in Fig. 11.6). (d) V-O-V bond angles for V-ions within the same z-plane in a-direction (V-O'-V) and in b-direction (V-O-V). (e) Cl-V-Cl angle and V-O-V angle in diagonal direction. (f) $\Delta(\text{V-V})_{diag}$: difference of the two diagonal V-V bond distances. (g) $\sqrt{(V-V)^2_{diag,1} - (V-V)^2_{diag,2}}$ plotted together with the monoclinic angle γ (*gray*). (h) The antiferromagnetic moment (*black*) together with γ (*gray*). *Black circles:* powder neutron data, *gray triangles:* synchrotron data. (Lines are guide to the eyes.)

2 K:	neutron	D1A (ILL)		
SG	**a (Å)**	**b (Å)**	**c (Å)**	γ
$P112/n$	3.76755(10)	3.29045(9)	7.89582(20)	90.21(0)
Atom	**x**	**y**	**z**	
V	-0.25	0.25	0.11678(76)	
Cl	-0.25	0.75	0.33000(4)	
O	-0.25	0.75	-0.04800(6)	

10 K:	neutron	D1A (ILL)		
SG	**a (Å)**	**b (Å)**	**c (Å)**	γ
$P112/n$	3.76776(6)	3.29076(5)	7.89611(13)	90.202(1)
Atom	**x**	**y**	**z**	
V	-0.25	0.25	0.11478(59)	
Cl	-0.25	0.75	0.33035(3)	
O	-0.25	0.75	-0.04765(3)	

150 K:	neutron	D1A (ILL)		
SG	**a (Å)**	**b (Å)**	**c (Å)**	γ
$Pmmn$	3.77001(10)	3.29656(10)	7.90713(25)	90
Atom	**x**	**y**	**z**	
V	0.25	0.25	0.12804(111)	
Cl	0.25	0.75	0.32914(5)	
O	0.25	0.75	0.95185(8)	

20 K:	synchrotron	B2 (DESY)		
SG	**a (Å)**	**b (Å)**	**c (Å)**	γ
$P112/n$	3.76670(4)	3.28912(4)	7.89098(10)	90.207(1)
Atom	**x**	**y**	**z**	
V	-0.25	0.25	0.11590(16)	
Cl	-0.25	0.75	0.33176(21)	
O	-0.25	0.75	-0.04661(57)	

Table 11.2: Results of the structural refinement of the neutron (D1A) and synchrotron (B2) measurements.

12 Summary

This work deals with the study of ordering phenomena such as charge, orbital and magnetic ordering in first row transition metal oxides (M = Ti, V, Cr, Ni, Cu) where the interplay of charge, orbital, spin and lattice degrees of freedom plays a crucial role for the variety and richness of physical properties of these systems.

On the one hand several first row transition metal oxides and oxyhalides with a $3d^1$ or $3d^2$ electronic configuration have been studied. The orbital degree of freedom plays an important role in these compounds which are also very well suited for electron density measurements since the contributions of only one or two electrons can be observed more easily. Ordering phenomena in titanates, vanadates, chromates and titanium and vanadium oxyhalides have been studied here.

On the other hand charge-stripe order in hole-doped first row $3d^8$ and $3d^9$ transition metal oxides, i. e. nickelates and cuprates with a layered perovskite structure has been studied. In contrast to the first group of systems the orbital degree of freedom is almost quenched in these systems. Whereas horizontal stripes have been observed in the cuprates [6] the nickelate system exhibits a robust diagonal charge-stripe order. In contrast to the metallic cuprates the nickelates also stay insulating up to extremely high Sr doping levels of $\sim$1 [32]. Nevertheless, this prototypical diagonal charge-stripe system is very well suited for the study of charge-stripes and phonon and magnetic excitations and, thus, for a comparison with the cuprates.

With only one electron in the 3d-shell the rare earth ***titanate*** system $RE\mathrm{TiO_3}$ is an ideal system to study the complex interplay of orbital and magnetic degrees of freedom as well as to investigate metal-insulator transitions which can be driven by hole-doping. In this work these two different aspects of the titanate system have been studied intensively. For these purposes, copious $R\mathrm{TiO_3}$ and $R_{1-x}\mathrm{Ca}_x\mathrm{TiO_3}$ (R = Gd, Tb, Dy, Y, Ho, Er, Yb, Lu) single crystals with well defined (oxygen) stoichiometry have been grown.

Regarding the first aspect, structural anomalies at the magnetic ordering temperature of $\mathbf{RTiO_3}$ have been studied by means of powder X-ray diffraction. These structural anomalies can be observed in an anomalous rise or drop of the orthorhombic a and b lattice parameters and in thermal expansion anomalies which are of opposite sign for the group of antiferromagnetic, feroorbitally ordered and the group of ferromagnetic, antiferoorbitally ordered titanates. Furthermore, within each group, the anomalies are strongest for the compounds close to the crossover between ferromagnetic and antiferromagnetic compounds, i. e. $\mathrm{SmTiO_3}$ and $\mathrm{GdTiO_3}$.

As could be verified with complementary powder neutron and single crystal X-ray diffraction measurements, the octahedral distortions which are indicative for orbital

ordering change few with decreasing temperature (290 K $\geq$ T $\geq$2 K). In contrast the structural distortions strongly change among the whole $R\mathrm{TiO_3}$-series with decreasing R-ionic radius (R = La, ..., Yb). Therefore, these compounds can be considered to be orbitally ordered already at room-temperature. This is corroborated by resonant X-ray diffraction measurements of $\mathrm{DyTiO_3}$ at the synchrotron revealing no change of the signal indicative for orbital ordering between room-temperature and 10 K. Hence, the anomalies of the lattice parameter and the thermal expansion are indicative for a magnetically driven change in the orbital arrangement which strengthens the prevalent orbital ordering already induced by the octahedral tilts and R-shifts.

With decreasing R-ionic radius from La to Yb, single crystal X-ray diffraction measurements of $R\mathrm{TiO_3}$ reveal a continuous change of octahedral tilts and rotations as well as of the two prominent distortions which are indicative for the type of orbital ordering in $R\mathrm{TiO_3}$. Hence, the R-ionic radius can be regarded as an external control parameter which continuously drives the magnetic and orbital transition from ferromagnetic and antiferroorbital ordering to antiferromagnetic and ferroorbital ordering. Thus, the transition from ferroorbitally to antiferroorbitally ordered $R\mathrm{TiO_3}$ controlled by an external ordering parameter and accompanied by a sign change of the thermal expansion with anomalies strongest at the crossover from ferroorbital to antiferroorbital ordering resembles on the observations of thermal expansion anomalies across the metamagnetic transition in $\mathrm{Ca_{2-x}Sr_xRuO_4}$ [147] or in a quantum phase transition in general [146].

Furthermore, a pressure-driven crossover of the relative a/a_0 and c/c_0 lattice parameters could be observed at lower pressures than observed for $\mathrm{YTiO_3}$ in Ref. [148]. Since $\mathrm{GdTiO_3}$ is already closer to the antiferromagnetic side of the phase diagram, the observations within this work support the model proposed in Ref. [148] where the ferromagnetic and antiferroorbitally ordered titanates are shifted by pressure into the antiferromagnetic and ferroorbitally ordered regime.

Regarding the second aspect, i. e. the metal-insulator transition in $\mathbf{R_{1-x}Ca_xTiO_3}$, this system exhibits an unusual 'inverse metal-insulator transition' with the metallic phase appearing at low temperatures. Usually, in MI-transitions the metallic phase appears at high temperatures [162, 163]. Furthermore, the doping driven MI-transition in $R_{1-x}\mathrm{Ca}_x\mathrm{TiO_3}$ appears at rather high hole doping levels x $\sim$0.39, $\sim$0.41 and $\sim$0.5 for R = Y, Er, Lu respectively. In the $\mathrm{La_{1-x}Sr_xTiO_3}$-system a hole-doping level of x $\sim$0.05 is sufficient for turning this system metallic [2, 94]. So far, this difference has been attributed to the bandwidth reduction induced by increasing tilts for decreasing R-ionic radius. But single crystal X-ray diffraction measurements in this work indicate that the octahedral tilts of these compounds strongly decrease with Ca doping. This can be explained with the larger ionic radius of the Ca^{2+} ion compared to the R^{3+}-ions and the smaller ionic radius of the Ti^{4+}-ion compared to the Ti^{3+}-ion [82]. It seems possible that additional effects - like charge ordering - enforce the insulating properties of the $R_{1-x}\mathrm{Ca}_x\mathrm{TiO_3}$-system ($R$ = Y, Er, Lu). Also in other perovskites which stay insulating up to high amounts of hole-doping sometimes charge ordering is observed [7, 160]. However, no evidence for charge ordering has been reported for a titanate system so far.

In this work, signatures of charge ordering could be observed in the crystal structure measured by means of neutron and X-ray diffraction including synchrotron experiments. In the low-temperature monoclinic phase the oxygen environment of the two distinct Ti sites is different. The nominal valency of both Ti-sites calculated by the bond-valence-sum formalism [169] indicates a difference of about 0.3 electrons for $Y_{1-x}Ca_xTiO_3$ with $x \sim 0.35$. As long as these systems remain insulating, this difference of the nominal valencies further increases with increasing hole-doping level in the $R_{1-x}Ca_xTiO_3$-system reaching a value of about 0.8 electrons for $x \sim 0.44$. This doping dependency supports the charge ordering picture since the half-doped compound should exhibit the most stable charge ordering pattern. Together with charge ordering the concomitant superstructure reflections (0 1 L) could be observed by neutron diffraction and in several resonant X-ray diffraction experiments at the synchrotron. The charge ordering temperatures T_{CO} derived from the onset temperature of these reflections rises with increasing hole-doping level towards the optimum, half-doped sample in the $R_{1-x}Ca_xTiO_3$-system which corroborates the charge ordering picture. In the resonant X-ray diffraction measurements, the charge ordering character of these superstructure reflections could be verified by energy scans and with polarization analysis. However, for all systems the metallic properties finally prevail at high doping levels since the introduction of Ca-ions strengthens the metallic properties by hole doping as well as by an increase of the electronic bandwidth W due to decreasing octahedral tilts.

Due to the large number of possible oxidation states of the vanadium ion ranging from +2 to +5 a large variety of different vanadium oxide compounds exists. In this work, three different representatives of this huge family of ***vanadates*** have been studied: $K_2V_8O_{16}$, LiV_2O_5 and ZnV_2O_4. Due to the absence of heavy ions and due to small number of d-electrons these vanadate systems appear to be well suited for electron density measurements.

The first compound, $\mathbf{K_2V_8O_{16}}$ (hollandite) is a mixed-valent vanadium oxide with an average valency of 3.75+ and a structure consisting of VO_6-double chains running in c_{tet} direction. This compound exhibits a MI-transition at about 160 K [210]. Concomitantly, the magnetic susceptibility exhibits a distinct drop by about 50% of its value above T_C [210]. This drop of χ can be either explained by antiferromagnetism or dimerization. Furthermore, in X-ray diffraction measurements superstructure reflections appear below T_C being indicative for an $\sqrt{2} \times \sqrt{2} \times 2$ enlargement of the high-temperature tetragonal ($I4/m$) unit cell [210].

Synchrotron radiation powder X-ray diffraction measurements of $K_2V_8O_{16}$ indicate a monoclinic symmetry below T_C. The analysis of single crystal X-ray diffraction measurements yields the best description with space group $I2/m$. In the low-temperature crystal structure of $K_2V_8O_{16}$ a novel dimerization of one half of all vanadium chains running in c-direction could be observed together with zig-zag-chain formation of the neighbouring vanadium chains. This resembles on the monoclinic M2-phase of VO_2 [212]. From these structural results, there is also first evidence that charge ordering occurs additionally in this system in a manner that one half of all dimerized chains contains V^{3+} ions and the

other half V^{4+} ions. The dimerization is able to explain the drop of the magnetic susceptibility below T_C and the metal-insulator transition. Furthermore, the decrease of χ by about 50% below T_C nicely fits to the dimerization of one half of all vanadium chains. The observation of dimerization of the vanadium ions in this work is corroborated by powder neutron diffraction and ESR measurements exhibiting no signs of antiferromagnetic ordering down to 2 K. Electron density measurements using a laboratory X-ray source give first evidence for an orbital occupation with large d_{xy} character. These orbitals would exhibit direct overlap in chain-direction which would be in accordance with the scenario of a Peierls instability explaining the dimerization found in this work.

In γ-$\mathbf{LiV_2O_5}$ which is iso-structural to α'-NaV_2O_5 but which has a much more corrugated crystal structure charge ordering occurs at room-temperature in a manner that magnetic V^{4+}- zig-zag chains running in b-direction are separated by non-magnetic V^{5+}-zig-zag chains.

Measurements of the electrical resistivity indicate that the charge ordering is quite robust and persists up ∼830 K. Synchrotron radiation single crystal X-ray and single crystal neutron diffraction measurements of γ-LiV_2O_5 confirm charge ordering down to ∼2 K. No further structural phase transitions could be observed in synchrotron radiation powder X-ray diffraction measurements. Neither neutron nor synchrotron measurements give any evidence for a tetramerized phase at low temperatures which was proposed by theoretical calculations [238].

Besides the search for phase transitions, an electron density measurement of this compound has been performed at 10 K at the synchrotron. A standard structure refinement and, in addition, a multipole refinement have been performed. The difference Fourier maps as well as the static multipole deformation and charge density maps indicate the occupation of a d_{xy} orbital at the V^{4+}-site in the charge ordered structure. Such a ground state could be supported by theoretical calculations based on the atomic positions derived from this synchrotron measurement [265]. Hence, this measurement can be considered to be a successful electron density measurement of a transition metal oxide.

$\mathbf{ZnV_2O_4}$ is a cubic spinel which exhibits a cubic to tetragonal phase transition at ∼50 K and which orders antiferromagnetically below ∼40 K [277]. Basically, three different theoretical orbital orbital ordering models exist for the tetragonal low-temperature phase: an 'antiferroorbital' ordering model [285], a 'ferroorbital' ordering model [286] and an 'orbital-Peierls' model [287]. Additionally a 'dimerized' model has been proposed recently [292].

For a measurement of the electron density, synchrotron radiation single crystal X-ray diffraction measurements have been performed at 70 K and at 10 K. Unfortunately, the unavoidable twinning which appears below the cubic to tetragonal phase transition prevents the measurement of the low-temperature structure of ZnV_2O_4. But the synchrotron measurement at 70 K reveals very interesting results. An excess electron density around the V-ion could be observed. This electron density extends along the three-fold roto-inversion axis in the cubic phase which might be an indication of an occupation of the trigonal a_{2g} orbital. This interesting result would give rise to completely new orbital

ordering schemes also in the low temperature tetragonal phase since a trigonal symmetry would have to be considered in a completely new orbital ordering model. But there is also another explanation for this electron density since it might be indicative for a shift of the vanadium ions along the [1 1 1]-direction and equivalent directions (former roto-inversion axes) yielding a kind of 'dimerized' phase. Indeed, the structure refinement indicates better R/R_w-values for the 'dimerized' structure model also compared to a multipole refinement of the 'undistorted' structure model. Additionally, superstructure reflections could be observed in this measurement which violate the reflection conditions for the 'undistorted' structure but which are allowed in the 'dimerized' structure.

Either the occupation of an a_{2g} orbital or the formation of V-V dimers (tetramers) in the cubic phase may stimulate new theoretical calculations for the ground state of ZnV_2O_4.

In the perovskite ***chromate*** system $\mathbf{RCrO_3}$ with divalent R-ions Ca, Sr and Pb the chromium ion has an unusual oxidation state of Cr^{4+} giving rise to interesting electronic and magnetic properties. Besides detailed structural information, for most of these compounds also no detailed knowledge about the electronic and magnetic properties exists.

The magnetic structures of all three chromate compounds have been studied by means of powder neutron diffraction and the magnetic structure of $CaCrO_3$ has been solved for the first time. The magnetic properties of $SrCrO_3$ which are reported controversially in literature [306, 307] have been reanalyzed. Finally, the magnetic structure of $PbCrO_3$ reported in literature [325] could be verified.

Below $T_N \sim 90$ K, $CaCrO_3$ exhibits a C-type antiferromagnetic order with an ordered moment of 1.09(4) μ_B pointing in the orthorhombic b-direction. For $SrCrO_3$ a C-type antiferromagnetic structure could be observed. The moment direction could be determined as the c_{tet}direction which is different from the $a_{tet}b_{tet}$-direction reported in Ref. [307]. Unlike to Ref. [307] the size of the ordered moment, ~ 0.8 μ_B, could be determined in this work. Furthermore, the magnetic properties of $SrCrO_3$ could be directly attributed to the tetragonal low temperature phase which has also been proposed in Ref. [307]. Finally, in $PbCrO_3$ a G-type antiferromagnetic structure with an ordered moment of ~ 2 μ_B could be confirmed.

Despite its semiconductive temperature dependency the electrical resistivity of $CaCrO_3$ might exhibit first indications for an itinerant character since the value of ρ for $T \rightarrow 0$ K is finite. Thus, the resistivity of polycystalline $CaCrO_3$ might be governed by grain boundary effects - a similar situation can be observed in the half metallic Cr^{4+}-compound CrO_2 [320, 321]. Also the small and nearly temperature independent magnetic susceptibility of $CaCrO_3$ [318] and the failure of Curie-Weiss fits is indicative for itinerant electron behaviour. Finally, optical reflectivity measurements of $CaCrO_3$ [322, 318] reveal its metallic character - the reflectivity extrapolates to 1 for $\omega \rightarrow 0$ [322, 318] and a moderate conductivity of several hundred to thousand $\Omega^{-1}\mathrm{cm}^{-1}$ can be observed [322, 318]. In this metallic scenario, the C-type antiferromagnetic order of $CaCrO_3$ can be explained by comparably large diagonal exchange interactions induced by a strong pd-hybridization according to band structure calculations [318]. Hence, $CaCrO_3$ is the rare case of a

metallic and antiferromagnetic transition-metal oxide with a fully three-dimensional electronic structure. The few metallic and antiferromagnetic transition metal oxides known are low dimensional with regard to their electronic structure and antiferromagnetism arises from the stacking of ferromagnetic layers [303, 304]. $SrCrO_3$ with a less distorted crystal structure and a slightly lower ordered moment should be even more metallic than $CaCrO_3$.

Since both systems are close to the crossover between itinerant and metallic properties it seems interesting to perform pressure studies [1] of the $CaCrO_3$- and $SrCrO_3$-systems. Here, synchrotron experiments have been performed in order to determine the lattice parameter as a function of pressure up to rather high pressures of ∼34 GPa. In $CaCrO_3$ these measurements indicate decreasing octahedral tilts with increasing pressure and in $SrCrO_3$ the less compressible (larger) tetragonal a_{tet}-axis ($a_{tet} > c_{tet}$) is indicative for an orbital occupation of the d_{xy} orbital which was also proposed in Ref. [307].

The ***transition metal oxyhalides*** MOX (M = Ti, V, ...) provide an interesting system of at room-temperature iso-structural compounds in which several electronic configurations and their interactions with the crystal lattice can be probed systematically. One compound of this group, TiOCl, exhibits a transition related to a dimerization of the Ti-ions at 67 K which has been interpreted as a spin Peierls transition. Thus, TiOCl might be one of the few known inorganic spin Peierls systems besides $CuGeO_3$ [439, 239].

Recently, optical transmittance and reflectance studies of **TiOCl** revealed a strong depression of the transmittance at high pressures (12-15 GPa) which was interpreted as a pressure-induced insulator-to-metal transition [33, 448]. However, there are no indications for metallic behaviour in the electrical resistivity of polycrystalline samples [446]. Furthermore, a combined study with synchrotron measurements, *ab-initio* calculations and pressure dependent magnetic susceptibility measurements indicates a Peierls-transition at high pressures [447].

In this work, pressure dependent structural studies of TiOCl have been performed by means of powder neutron diffraction up to a maximum pressure of ∼13 GPa. These measurements reveal a strong and almost full flattening of the Ti-O layers at high pressures and a concomitant compression of the distances of two neighbouring Ti-O layers within a bilayer. These strong structural changes favour changes of the electronic properties of TiOCl at high pressure and may stimulate new theoretical calculations based on these astonishing results. In general, an increase of the electronic bandwidth W can be expected which would support the metallic high-pressure scenario of TiOCl as was reported in Ref. [33, 448]. However, there is still the possibility for a dimerization at even higher pressures (than ∼13 GPa) which was postulated in Ref. [447] within the scenario of a Peierls instability or calculated in Ref. [448] within a metallic scenario.

Orthorhombic to monoclinic phase transitions have been observed for TiOCl and

[1] The pressure dependence of the unit cell volume of $CaCrO_3$ and $SrCrO_3$ up to pressures of about 8 GPa has also been reported in literature [310].

TiOBr at low temperatures but no similar transition has been observed in the isostructural **VOCl** system [453].

In this work, synchrotron measurements as well as neutron measurements reveal such a structural phase transition ($Pmmn \rightarrow P2/n$) in VOCl. The analysis of the magnetic structure with propagation vector ($\frac{1}{2}\ \frac{1}{2}\ \frac{1}{2}$) yields a fully three-dimensional antiferromagnetic structure with an antiferromagnetic moment of $\sim$1.3 μ_B pointing in a-direction. This magnetic phase transition is accompanied by structural distortions which induce an increase of the antiferromagnetic exchange interactions in general and by distortions implied by the monoclinic symmetry which lift the frustration of the previously equivalent diagonal exchange interactions by the decrease of one diagonal V-V distance versus the other and, thus, by enhancing the orbital overlap in one direction.

The discovery of charge-stripe ordering in the high-T_C superconducting cuprates [6] as well as the spin wave dispersion with a so-called 'hour-glass' shape [18-22, 367] have attracted enormous interest, recently. However, the role of this stripe instability and the spin fluctuations in the superconducting pairing mechanism is still under debate. The ***nickelate*** compounds $La_{2-x}Sr_xNiO_{4+\delta}$ are iso-structural to the cuprates with a single-layered perovskite structure. This prototypical stripe ordered system, hence, is an ideal system for a comparison with the cuprates. In the past, several compounds have been studied regarding their phonon and spin wave dispersion [380, 373]. But these studies might suffer from commensurability effects since all these compounds have hole-doping levels close to the commensurate 1/3 doped value. Here, two $La_{2-x}Sr_xNiO_{4+\delta}$ compounds with distinctly smaller hole doping levels more far away from the commensurate value and, thus, with an incommensurate stripe character have been studied: $La_{1.8}Sr_{0.2}NiO_{4+\delta}$ and $La_{1.825}Sr_{0.175}NiO_{4+\delta}$.

In contrast to the commensurate compound $La_{1.69}Sr_{0.31}NiO_4$ [380], the phonon dispersion of stripe ordered $\mathbf{La_{1.8}Sr_{0.2}NiO_{4+\delta}}$ indicates almost no splitting of the high frequency longitudinal bond-stretching Σ_1 phonon mode. But this phonon mode exhibits an extremely interesting anomaly at phonon propagation vectors corresponding to the propagation vectors of the diagonal charge-stripes ($q = \varepsilon$). The softening of this phonon mode at these propagation vectors gives evidence for electron phonon coupling in the diagonal charge-stripe phase. Concomitantly with this anomalous softening a peak broadening of the Σ_1 phonon mode could be observed which might be connected to the difference for phonons propagating parallel or perpendicular to the diagonal charge-stripes. Furthermore, strong temperature effects are visible which appear above the stripe ordering temperature T_{CO}. For $q = \varepsilon$ the temperature dependency indicates an anomalous softening of $\omega(q)$ on heating above T_{CO} and the zone boundary mode (q =1/2) becomes strongly damped at 300 K. These new findings indicating electron phonon coupling in an incommensurate diagonal charge-stripe phase might be also relevant for the study of the spin glass phase of $La_{2-x}Sr_xCuO_4$ where a diagonal charge-stripe phase was also proposed.

The measurement of the magnon dispersion in $\mathbf{La_{1.825}Sr_{0.175}NiO_{4+\delta}}$ turned out to be

more complicated. Whereas the picture is rather clear for lower energies it was difficult to measure the dispersion at higher energies. The spin wave velocities parallel and perpendicular to the stripes amount to $\hbar c_\perp = 357(14)$ meVÅ and $\hbar c_\parallel = 303(10)$ meVÅ which is close to the value of $\hbar c_0 = 340$ meVÅ for undoped La_2NiO_4 and $\hbar c_\parallel = 300(20)$ meVÅ and $\hbar c_\perp = 350(20)$ meVÅ for LSNO with $x = 0.31$ [373, 386]. At high energies it was difficult to obtain unambiguous evidence for a merging of the magnon branches since phonon contributions merged with the magnetic signal in the interesting energy regime. This could be verified with polarized neutrons. Also the observation of a magnon dispersion above this presumable merging point suffers from possible phonon contributions in the experiment without polarization analysis and could be hardly observed in the experiment with polarized neutrons since the high needed energies were at the limit of the accessible energy range.

Since the discovery of high-temperature superconductivity (HTSC) in the ***cuprates*** [4] the superconducting pairing mechanism in still a matter of debate and the question about the role of electron-phonon coupling still a matter of controversy. $La_{2-x}Sr_xCuO_4$ (LSCO) can be regarded as the model cuprate system as it has a very simple quasi-two-dimensional crystal structure consisting of CuO_2 layers separated by layers of $(La,Sr)_2O_2$. In LSCO the substitution of Cu with non-magnetic ions like Zn as well as the substitution with magnetic ions like Ni leads to a reduction of T_C [432]. For a conventional superconductor, magnetic impurities have a much stronger pair-breaking ability than non-magnetic dopants. However, this seems not to be the case for the Zn- and Ni-doped LSCO-system (LSCZO and LSCNO respectively) [432, 433] which might also be in favour of a magnetic pairing mechanism.

The search of indications for a diagonal charge-stripe order in $\mathbf{La_{1.95}Sr_{0.05}CuO_4}$, which is a compound within the spin-glass phase of LSCO, did not yield any evidence for such a stripe instability. First, the phonon dispersion studied by means of inelastic neutron scattering did not reveal any signature of a diagonal stripe phase neither in the longitudinal acoustic branches nor in the Cu-O bond-stretching branches. In contrast to that, such signatures could be observed in the diagonal charge-stripe phase of $La_{1.8}Sr_{0.2}NiO_{4+\delta}$ in this work. Instead, the longitudinal bond-stretching branches (Δ_1) of $La_{1.95}Sr_{0.05}CuO_4$ exhibit anomalies similar to the anomalies observed in the superconducting regime of LSCO. This softening of the so called half-breathing mode scales approximately with the Sr content x independent of metallic or insulating properties of the system. Second, the direct search of superstructure reflections did not yield any evidence for a diagonal stripe phase. In various neutron scattering experiments these superstructure reflections can be excluded with an accuracy of $1\text{-}2{\cdot}10^{-6}$ of a strong nuclear reflection. Resonant X-rays diffraction measurements at the synchrotron did not reveal these superstructure reflections and in synchrotron measurements using 100 keV hard X-rays such reflections could not be observed with an accuracy of about 10^{-8} of a strong Bragg peak. Instead a novel class of superstructure reflections with a large number of higher harmonics appears at positions rotated by 45° with respect to the positions for diagonal stripes. However, these superstructure reflections do not seem to reflect the typical signature of

horizontal stripes since their modulation vector q is perpendicular to the Bragg peak τ. Also the wavelength of this modulation with about 200 Å is rather large. Most of these reflections (or their higher harmonics) disappear above ∼250 K which might be connected to the electronic properties of this system since the second derivative of the electrical resistivity exhibits a strong decrease in this temperature regime [393]. Finally, after the orthorhombic to tetragonal (LTO→HTT) phase transition all superstructure reflections disappear which indicates that these superstructure reflections reflect distortions which are either directly connected to the octahedral tilts in the orthorhombic phase or which are stabilized by these octahedral tilts. Note, that the horizontal charge-stripe order in Nd codoped cuprates is stabilized by the octahedral tilts of the low-temperature tetragonal (LTT) phase [6]. These novel superstructure reflections also vanish for a $La_{1.88}Sr_{0.12}CuO_4$-sample in the metallic (superconducting) regime suggesting a close connection of these superstructure reflections to the insulating properties of $La_{1.95}Sr_{0.05}CuO_4$.

The phonon dispersion of the Cu-O bond-stretching phonon modes of three different **LSCZO** and **LSCNO** samples with Sr doping levels $x = 0.12$ and 0.15 has been studied and compared to Zn- and Ni-free $La_{1.88}Sr_{0.12}CuO_4$. The phonon dispersion of the topmost Δ_1 phonon mode exhibits strong similarities for all four samples. Especially the strong renormalization of this phonon branch is very similar for all samples. This is very astonishing since the stripe spacing is different for these samples. For example the incommensurability of the 4% Ni doped sample amounts to ∼0.08 which is distinctly lower than the value for the Ni-free compound which amounts to 0.12. If this phonon anomaly is related to (dynamic) charge-stripes one would expect a dependency on the stripe spacing, i. e. the anomaly should be observable at $q \sim 0.16$ for the 4% Ni-doped sample which is distinctly lower than the value of $q \sim \frac{1}{4}$ for the Ni-free compound. Hence, the absence of any correlation with the propagation vector of the stripes might indicate that a coupling of the Cu-O bond-stretching phonon modes to the charge-stripes is not the origin of this phonon anomaly as was thought before [13].

Concluding, this work has further contributed to uncover new properties and ordering phenomena within the wide variety of intriguing properties of transition metal oxides:

Also twenty years after the discovery of high-temperature superconductivity in the cuprates [4] it was possible to find novel ordering phenomena within the $La_{2-x}Sr_xCuO_4$-system. Furthermore, it was possible to show that the generally believed 'rule of thumb' that 3D-antiferromagnetism is observed in insulating transition metal oxide systems is not always true. Beyond, it was possible to measure the electron density of a transition metal oxide, γ-LiV_2O_5, and to observe the orbital occupation 'directly': a d_{xy} orbital. Also, it was possible to observe electron-phonon coupling in a diagonal charge stripe system, the nickelate system $La_{1.8}Sr_{0.2}NiO_4$. In addition, several other ordering phenomena have been unrevealed and studied among which charge ordering in a titanate system shall be mentioned in representation.

[Ar] $3d^6$ $4s^2$
1535/2750
55.845

26 Fe
Iron

A Appendix A: Ferrates/Ferrosilikates

Iron with a distribution of 4.7% by mass is one of the most common elements in the earth's crust [107] and also in the universe as the iron nucleus is energetically very stable. The most common ore is haematite Fe_2O_3. Iron has a very large importance for the construction of machines etc. but it is also a crucial element for life as it is the key functional element of haemoglobin.

A.1 Incommensurate magnetic order in $NaFeSi_2O_6$

A.1.1 Introduction

Materials exhibiting a sizeable magnetoelectric coupling might have a great potential for the application in new data storage devices. Hence, the study of multiferroic materials exhibiting magnetic and ferroelectric order at the same time has become a strongly studied topic in contemporary solid state physics. The observation of a large magnetoelectric interaction in $TbMnO_3$ has induced a revival in the field of multiferroics and magnetoelectrics [464]. The magnetoelectric effect which has been predicted long ago and observed first in Cr_2O_3 [465-467] describes the generation of an electric polarization P by a magnetic field or of a magnetization M by an electric field and is given in leading order by the tensor α_{ij}, which linearly couples P to an applied magnetic field H and M to an applied electric field E [1]. Since the upper limit of α_{ij} is restricted by the product of electric and magnetic susceptibilities $\chi_{ii}^{elec} \cdot \chi_{jj}^{mag}$ multiferroic materials with simultaneous ferroelectric and (anti-)ferromagnetic order can be expected to yield the strongest magnetoelectric response [465, 469]. However, a few years ago the only known multiferroic materials (like $BiFeO_3$ and some hexagonal manganites) exhibit only small macroscopic magnetoelectric effects [465, 470-473]. Only recently it has been found, that ferroelectricity can arise from some special types of magnetic ordering inducing sizeable magnetoelectric effects and the ability to switch the electric polarization by an applied magnetic field (and vice versa). In these recently studied materials magnetic frustration induces a complex magnetic structure with cycloids or spirals. Due to Dzyaloshinskii-

[1] The Landau free energy for linear magnetoelectrics contains a linear term in H and E [468]: $\phi = \phi_0 - \alpha_{ij} \cdot E_i \cdot H_j$ with the magnetoelectric susceptibility tensor α_{ij}. The electric polarization and magnetization can be derived by $P_i = -\partial\phi/\partial E_i = \alpha_{ij} \cdot H_j$ and $M_j = -\partial\phi/\partial H_j = \alpha_{ij} \cdot E_i$ respectively. (In general the free energy may contain additional higher order terms $-\frac{1}{2} \cdot \beta_{ijk} \cdot E_i \cdot H_j \cdot H_k$, $-\frac{1}{2} \cdot \gamma_{ijk} \cdot H_i \cdot E_j \cdot E_k$ resulting in a higher order magnetoelectric effect.) [468]

Moriya interaction such a spiral magnetic ordering can induce ferroelectricity and the electrical polarization is of the form

$$P = \sum_{i,j} A \cdot e_{ij} \times (S_i \times S_j) \tag{A.1}$$

where e_{ij} is the unit vector between the spins S_i and S_j [468, 474]. Hence, ferroelectricity may occur in any spiral magnet with the (magnetic) propagation vector $\overrightarrow{k}$ not perpendicular to the spin-spiral plane [468].

For example $TbMnO_3$ [2] is one of the recently discovered novel multiferroic materials where the Mn-spins order first in a longitudinal spin-density wave which in a second phase transition then transforms into a cycloid [475]. Due to the inverse Dzyaloshinski-Moriya effect [474], see Eq. A.1, the cycloid induces a polar distortion along the *c*-axis.

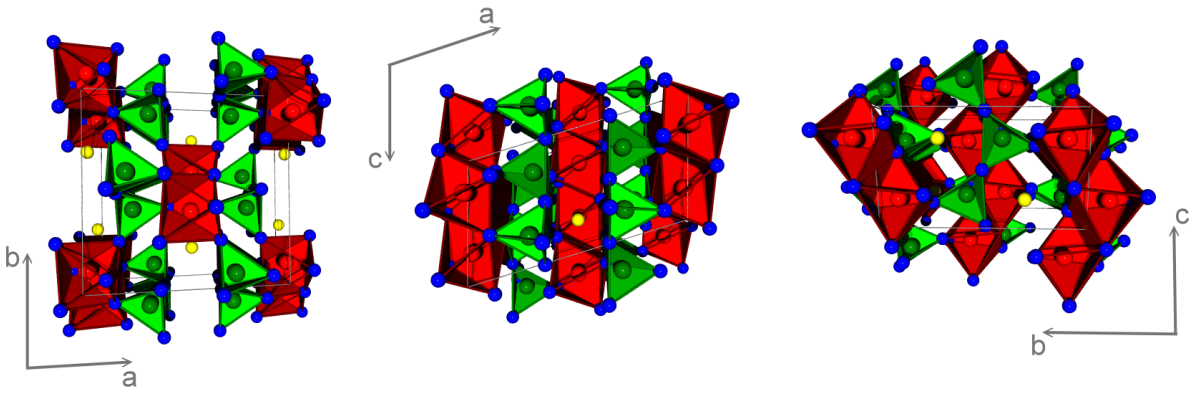

Figure A.1: Crystal structure of $NaFeSi_2O_6$; *yellow*: Na, *red*: Fe, *green*: Si, *blue*: O.

Recently, multiferroic properties have been also discovered in aegirine ($NaFeSi_2O_6$) belonging to the pyroxenes $AMSi_2O_6$ where A stands for mono- or divalent metals while M represents di- or trivalent metals [476]. Three members of this large family have been shown to be multiferroic ($NaFeSi_2O_6$) or linear magnetoelectric materials ($LiFeSi_2O_6$ and $LiCrSi_2O_6$) [476, 477].

The crystal structure of aegirine is shown in Fig. A.1 in three perspective views. In these pyroxenes zig-zag chains of edge-sharing FeO_6 octahedra running in *c*-direction are separated by tetrahedral SiO_4 chains also running in *c*-direction. As can be seen in Fig. A.1, the crystal structure is monoclinic (with space group $C2/c$, $a \sim 9.68$Å, $b \sim 8.83$Å, $c \sim 5.3$Å and $\beta \sim 107.3°$) [478]. For the compound with $A =$ Li, a further structural phase transition from $C2/c$ to $P2_1/c$ occurs at 228 K [479] and in contrast to $NaFeSi_2O_6$, $LiFeSi_2O_6$ exhibits ferroelectricity only with applied magnetic fields.

$NaFeSi_2O_6$ orders antiferromagnetically at about 8 K and exhibits additional ferroelectric ordering at about 6 K [476]. However, the yet published magnetic structure

[2] which was also grown in this work - see Chap. 5.6

can not explain the ferroelectric properties based on the inverse Dzyaloshinski-Moriya effect. In the magnetic structure reported in Ref. [478] the Fe-chains are ordered ferromagnetically (intra-chain) and neighbouring chains are coupled antiferromagnetically (inter-chain). In this model, the antiferromagnetic (AFM) inter-chain interaction is supposed to be stronger than the intra-chain interaction, thus stabilizing the ferromagnetic arrangement within the chains.

A.1.2 Experimental

The aegirine $NaFeSi_2O_6$ crystals studied in this work have been provided by the group of Prof. L. Bohatý and were cut from a high-quality natural single crystal from Mount Malosa, Malawi [476, 477]. However, the real composition of this aegirine compound has been determined to be $Na_{1.04}Fe_{0.83}Ca_{0.04}Mn_{0.02}Al_{0.01}Ti_{0.08}Si_2O_6$ [476]. Additionally, synthetic powder samples of aegirine have been grown by P. Becker-Bohatý which have been used for powder neutron diffraction measurements.

Single crystal neutron diffraction measurements of aegirine have been performed at the HEIDI diffractometer at the FRM-II in Garching ($\lambda = 0.55$ Å) and at the IN3 spectrometer at the ILL in Grenoble, France ($\lambda = 2.36$ Å). Additionally, powder neutron diffraction measurements have been performed at the G4.1 ($\lambda = 2.4226$ Å) and at the 3T.2 diffractometer ($\lambda = 1.22525$ Å) at the reactor Orphée in Saclay, France.

A.1.3 Results and Discussion

Single crystal neutron diffraction measurements have been performed at the IN3 spectrometer. These measurements reveal the appearance of incommensurate magnetic peaks below the magnetic ordering temperature. In Fig. A.2 (f) all relevant peaks found in the $HK0$-plane are shown. The *black arrows* indicate the scans which have been performed in order to study these reflections and the most important scans are labeled with letters A to E and shown in Fig. A.2 (a-f). It should be noted, that the strongest peaks in the powder diffraction patterns are absent in these single crystal measurements, i. e. the (1 0 0) and the (0 1 0) peak. Scans of type A through two incommensurate peaks are shown for different temperatures in Fig. A.2 (a-d). In Fig. A.2 (a) the intensities are plotted linearly and shifted by a constant value for each temperature. As can be seen, the first significant magnetic intensities appear below about 9 K. In Fig. A.2 (b-c) the focus is drawn on the higher temperatures where still some magnetic scattering can be observed at the incommensurate peak positions. The peak width increases for these reflections indicating short range magnetic order at higher temperatures. The intensities of these scans have been fitted with two symmetric lorentzians and the resulting peak intensity, incommensurability δ and a 'length' parameter which is indicative for the lower limit of the coherence length are plotted as a function of temperature in Fig. A.4 (a-c). Below 8 K this modulation exhibits hardly any temperature dependency. But above 8 K the incommensurability δ starts to decrease and the magnetic scattering becomes more and more diffuse. Even at 12 K two different incommensurate peaks can be distinguished. Hence, there are still magnetic correlations but with small coherence lengths

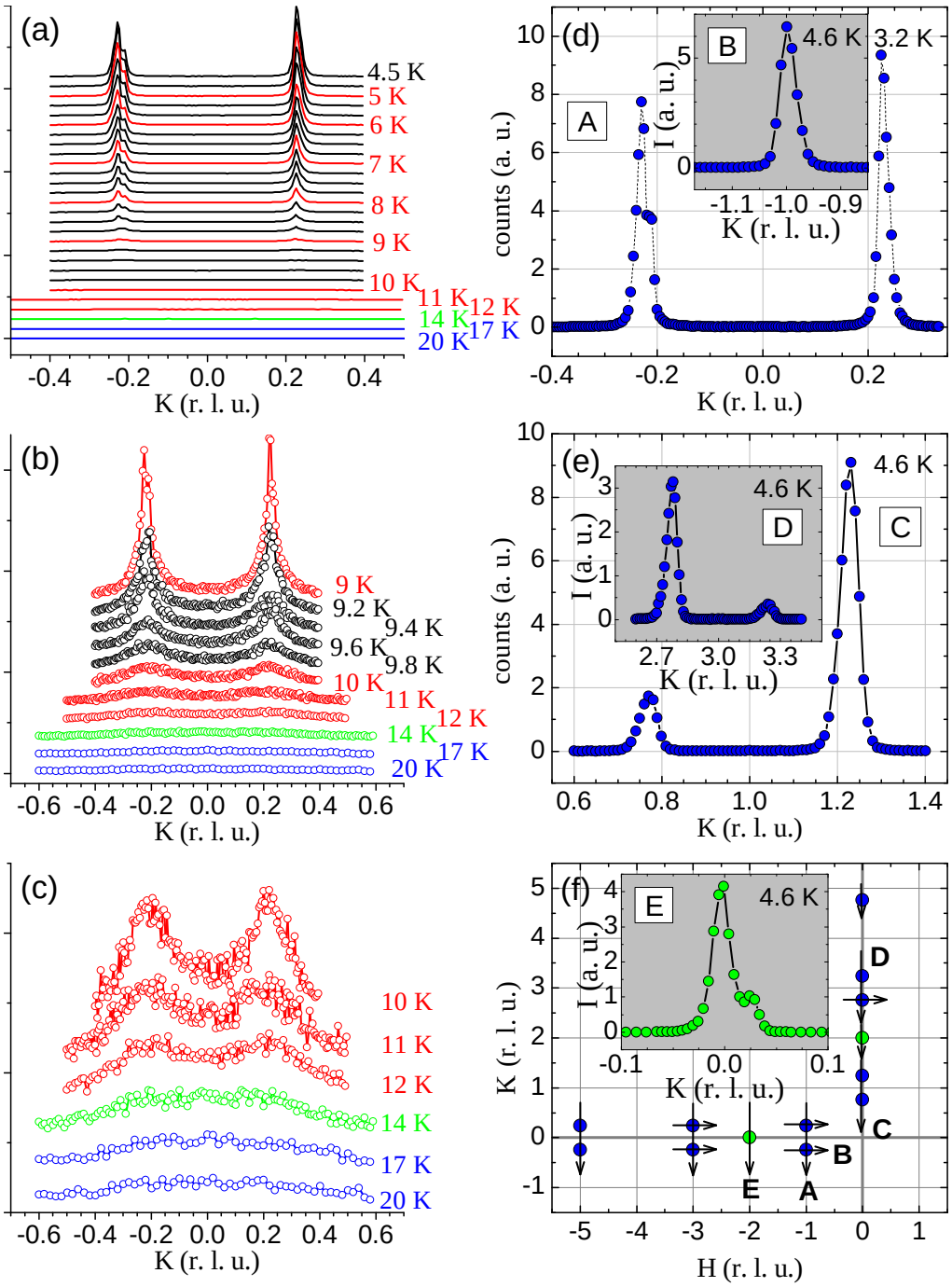

Figure A.2: Results of the IN3 experiment. The scan types A, B, C, D and E are indicated in figure (f). (a-c) Scans of type A for different temperatures. (d) Scans of type A (with type B in the inset). (e) Scans of type C (with type D in the inset). (f) HK-map indicating the incommensurate peak positions; *black arrows*: scan directions. Some important scans are labeled with letters A-E.

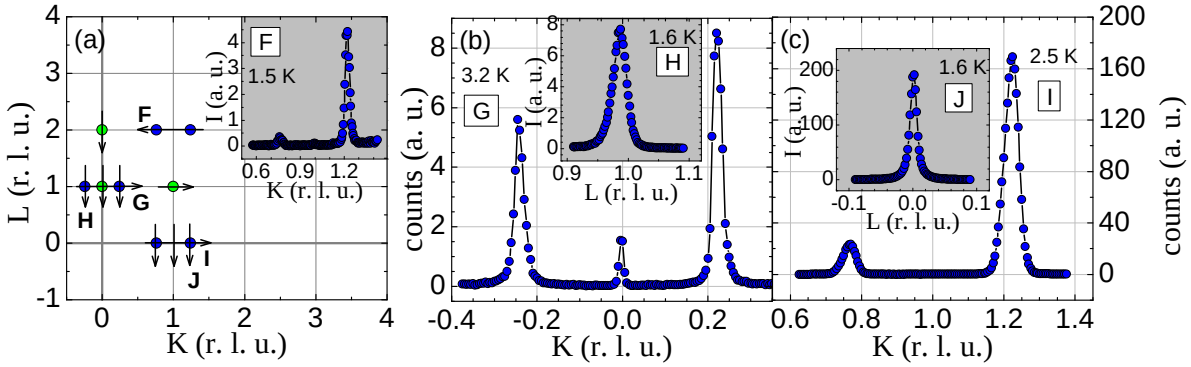

Figure A.3: Results of the IN3 measurement for the other orientation of the natural aegirine crystal. (a) HK-map showing the observed reflections. All relevant scans are indicated by *black arrows*. Some selected scans are labeled with letters F-J. The inset shows scan F. (b) Plot of scan G; the inset shows scan H. (c) Plot of scan I; the inset shows scan J.

only, i. e. short range order (correlations). The strong decrease of the coherence length around 9 K is nicely visible in Fig. A.4 (c). Some diffuse magnetic scattering can be even observed at distinctly higher temperatures of 17-20 K, see Fig. A.2 (c). In order to get an impression of the coherence lengths and intensities this diffuse scattering has also been fitted with two lorentzian fits although a significant amount of (diffuse) intensity can be observed at the commensurate peak position. The resulting values for the incommensurability might be biased by such effects as is already indicated by the larger error bars. It should be noted that the Bragg peak is asymetrically broadened (and on one side even nearly split) due to the mosaicity of this natural single crystal. A scan through the (-2 0 0) Bragg peak is shown in the inset of Fig. A.2 (f). The FWHM of this peak determined by a gaussian fit amounts to 0.028(3). Hence, the fitting parameter 'length' plotted in Fig. A.4 (c) should be regarded only as a lower limit for of the real coherence length as the *asymetric* mosaic spread was neglected in these calculations.

As the lattice is C-centered (1 0 0) and (0 1 0) are no reciprocal lattice points. Hence, magnetic satellites appear at Q-positions corresponding to an incommensurate modulation vector $q \sim$ (0 1.23 0) or (0 0.77 0) or (1 0.23 0).

Additional incommensurate reflections have been observed at various other Q-values as can be seen in Fig. A.2 (f). The most important scans (at low temperatures) are plotted in Fig. A.2 (d-e). Furthermore, similar scans have been performed in the $0KL$-plane using another orientation of the crystal. In Fig. A.3 (a) the points in reciprocal space are shown where incommensurate magnetic and commensurate nuclear reflections have been observed denoted by *blue dots* and *green dots* respectively. Similar to the other crystal orientation, *black arrows* indicate the scan directions. All these measurements [3] indicate a picture of an incommensurate magnetic ordering in aegirine

[3] One peak of unknown origin has been observed at (0 1 1). As this peak does not vanish up to 13 K it has a structural origin.

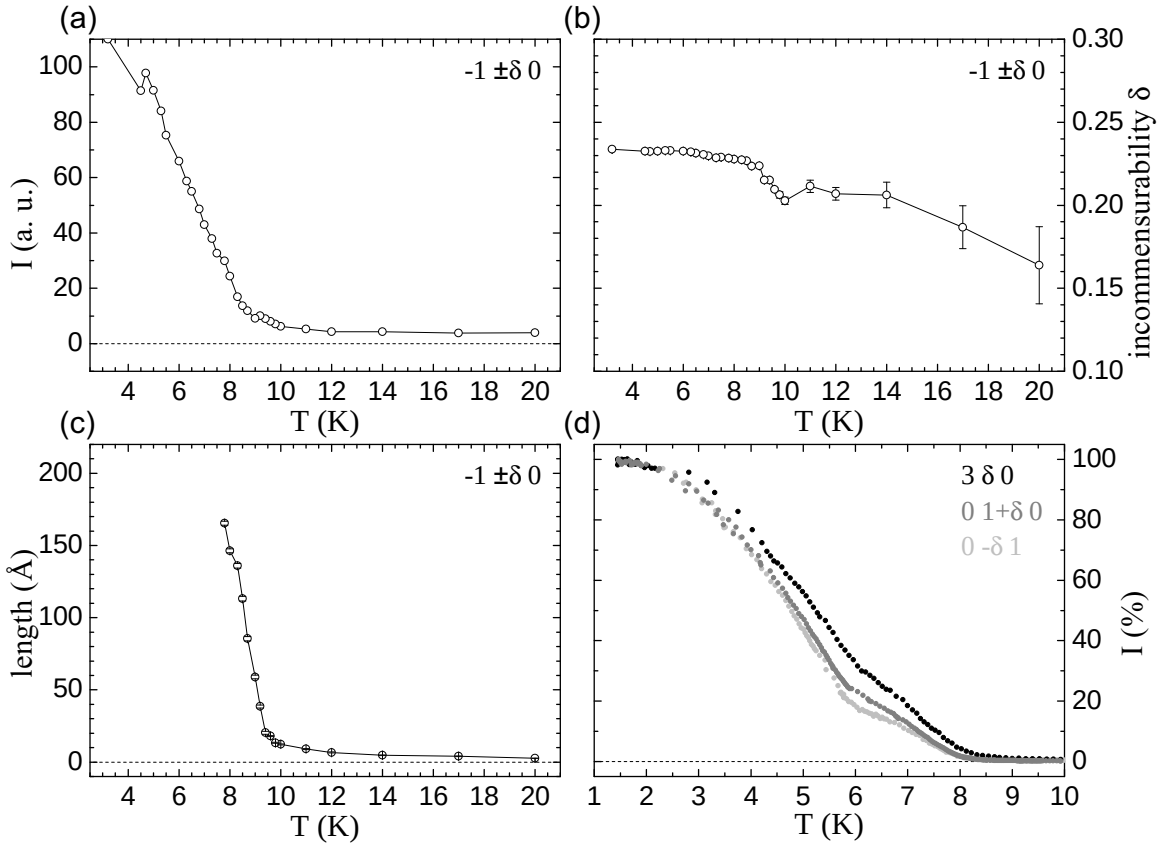

Figure A.4: Results of the IN3 measurement. (a) Temperature dependency of the intensity of the incommensurate magnetic peaks at (-1 δ 0). (b) Incommensurability δ as a function of temperature. (c) fitting parameter 'length' derived from lorentzian fits plotted versus temperature. (d) Precise temperature dependency of several incommensurate magnetic peaks. (Lines are guide to the eyes.)

($Na_{1.04}Fe_{0.83}Ca_{0.04}Mn_{0.02}Al_{0.01}Ti_{0.08}Si_2O_6$) with a propagation vector of $q \sim$ (0 1.23 0).

Complementary powder neutron diffraction measurements which have been performed at the G4.1 diffractometer have been analyzed in order to understand the origin of the incommensurate magnetic modulation. First of all, it should be mentioned that the diffractogram measured at 1.5 K is very similar to the diffractogram observed in Ref. [478]. Such a diffractogram can be seen in Fig. A.7 (a). The two most prominent magnetic peaks appear at the commensurate positions (1 0 0) and (0 1 0). Furthermore, there are several broad bumps between the commensurate peak positions which have been attributed to impurity phases in Ref. [478]. The four most apparent bumps or peaks are indicated with *blue arrows* in Fig. A.7 (a). Knowing from the IN3 experiment that an incommensurate magnetic modulation appears in this system it was possible to index these four peaks and identify them as the (0 -2 0)+q, (-1 -1 0)+q, (0 0 0)+q and

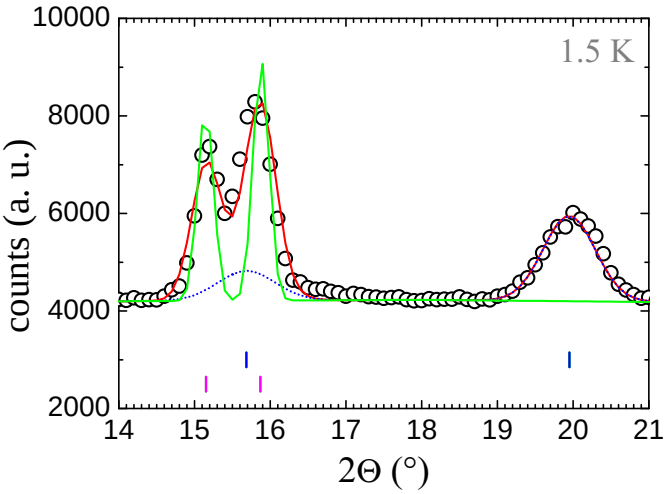

Figure A.5: Part of the diffractogram of aegirine measured at 1.5 K at the G4.1 diffractometer; *black circles*: measured data I_{obs}, *blue* and *magenta bars*: peak positions of the incommensurate magnetic and commensurate magnetic peak positions respectively; *red line*: a Rietveld fit ($I^{(1)}_{calc}$) with nuclear plus the two magnetic commensurate and incommensurate phases; *blue dotted line*: calculated contribution of the incommensurate magnetic structure (ellipt. spiral) to $I^{(1)}_{calc}$; *green line*: another Rietveld fit ($I^{(2)}_{calc}$) with a nuclear plus a single commensurate magnetic phase.

(±2 0 0)+q and (2 -2 -1)+q reflections. Hence, these magnetic peaks do not arise from an iron oxide impurity phase but are the incommensurate magnetic peaks observed in the single crystal neutron measurement on the natural crystal. Furthermore, there are some other peaks denoted by an asterisk in Fig. A.7 (a). These peaks do not vanish up to 14 K as can be seen in Fig. A.4 (e). Hence, these temperature-independent peaks which can not be indexed properly belong to an unknown impurity phase with a significant volume ratio $\gg 10\%$. These data regions were excluded from the fit in order to prevent any biasing of the results of the refinement.

The superposition of two magnetic phases has been fitted to the data in order to describe the commensurate as well as the incommensurate magnetic order. The commensurate magnetic phase is very similar to the one reported in Ref. [478] (same symmetry, moment in *ac* plane). Only the size and direction of the magnetic moments are different since the second incommensurate peak (*blue arrow* in Fig. A.7) is located between the two commensurate peak positions and overlaps with the commensurate magnetic peaks. (The other incommensurate magnetic peaks do not overlap with other commensurate peaks.) Furthermore, whereas commensurate magnetic and nuclear peaks have comparably narrow peak widths the incommensurate magnetic peaks are distinctly broader. This indicates a variation of the incommensurability δ within the powder sample and may be attributed to variations in the stoichiometry of different parts of the powder

sample which is corroborated by the fact that this sample contains a significant amount of impurity phases. (Another interpretation would be that the coherence length is rather small in this powder sample.) Thus, the peak widths of the two magnetic phases have been fitted independently.

As can be seen in Fig. A.5, the second incommensurate peak/bump which is located between the two commensurate magnetic (1 0 0) and (0 1 0) peaks is real - a Rietveld fit without an incommensurate magnetic phase (*green line*) is not able to correct for these reflections. Hence an additional incommensurate magnetic phase is needed in order to describe these peaks (*red line*). The contribution of this incommensurate magnetic phase is plotted separately in this figure (*blue dotted line*).

For the commensurate magnetic phase the magnetic structure reported in Ref. [478] has been verified. This result is not astonishing since all the incommensurate peaks do not overlap strong enough in order to biase these results. Hence, only the magnetic moments within the *ac*-plane of the commensurate magnetic structure had to be refined simultaneously with the incommensurate magnetic structure.

Various possible incommensurate magnetic structure models have been applied in order to fit the data using the program *FullProf* [88]. The symmetry analysis using the program *BasIreps* implemented in the *FullProf* suite indicates that no further symmetry elements correlate the Fe-ions sitting at the special sites $(0\ y\ \frac{1}{4})$ and $(0\ -y\ \frac{3}{4})$. (Only the C-centering remains.) The resulting vectorial Fourier components of the two irreducible representations are $(0\ u\ 0)$ and $(u\ 0\ v)$ respectively with u and v being complex numbers. The reason for the loss of symmetry elements is the incompatibility of the propagation vector q with the *c*-glide mirror plane and the inversion. (The identity and the 2-fold axis remain compatible.) But these two symmetry elements are needed in order to relate the two Fe-atoms at $(0\ y\ \frac{1}{4})$ and $(0\ -y\ \frac{3}{4})$. Hence, these two iron sites are independent, in principle. However, in this work, the moments of the two iron sites have been set equal and just the phase of the magnetic moment has been either fitted or calculated.

Thus, several magnetic structure models have been refined systematically. Most variations of helical, cycloidal or sinusoidal magnetic structures can not describe the measured data. However, a couple of possible magnetic structures were finally able to yield quite acceptable fits. These are shown in Fig. A.7 (a-e). The *green/blue/magenta bars* denote peak positions of the nuclear/incommensurate magnetic/commensurate magnetic structures. And the *red* and *blue lines* indicate the total calculated intensity and the intensity of the single incommensurate magnetic phase respectively. The corresponding incommensurate magnetic structure models of Fig. A.7 (a-e) are visualized in Fig. A.8 (a-e).

First, cycloidal magnetic structure models with magnetic moments rotating in the *br* plane with $r = (\xi\ 0\ \zeta)$ have been refined. The results for the special cycloidal magnetic structures with moments rotating in the *ab*- and *bc* plane are shown in Fig. A.7 (a-b). Obviously, these cycloidal models describe the 1st, 3rd and 4th incommensurate magnetic peaks quite well but tend to have some additional intensity at the second incommensurate peak position which overlaps with the commensurate magnetic (0 1 0) peak. Obviously, the independent refinement of the commensurate magnetic phase is not able to fully compensate these large intensities. Nevertheless, the finally obtained R-values are quite acceptable.

magnetic structure model	$\mathbf{R}_p^{(tot)}$	$\mathbf{R}_{wp}^{(tot)}$	$\mathbf{R}_{inc.}^{(mag)}$	$\mathrm{R}_{com.}^{(mag)}$	$\mathbf{R}^{(mag)}$
cycloidal with **M** in *ab*-plane	2.42%	4.53%	10.1%	11.1%	**10.6%**
cycloidal with **M** in *bc*-plane	2.53%	4.61%	15.9%	12.9%	**13.7%**
helical with **M** in *ac*-plane	2.68%	4.75%	23.3%	7.45%	**15.4%**
elliptic spiral with **M** in *ac*-plane	2.61%	4.72%	19.7%	4.21%	**12.0%**
elliptic spiral with **M** free	2.52%	4.62%	11.8%	3.06%	**7.4%**

Table A.1: Results of Rietveld refinement with Fullprof [88]. $\mathrm{R}^{(mag)}$ is the average R-value of commensurate and incommensurate magnetic structure.

In contrast to these cycloidal magnetic structures, a transverse spiral magnetic structure with the moment rotating in the *ac*-plane yields much smaller calculated intensities at this second incommensurate peak position resulting in a much better description of these peaks; see Fig. A.7 (d). However, the fourth (last) incommensurate magnetic peak marked with a *blue arrow* can not be appropriately described with this model as the calculated intensities are too low. Hence, a helical structure with the magnetic moment rotating in the *ac*-plane can be excluded. In a similar way an elliptical spiral with the moment in the *ac*-plane can not describe the data satisfactory. Hence, these two magnetic structures can be excluded although the magnetic susceptibility measurements would be indicative for a moment rotating within the *ac* plane since χ_a and χ_c exhibit a distinct drop below the magnetic ordering temperature which is in contrast to the temperature dependency of χ_b [476].

Next, other (elliptical) spiral structures with the magnetic moment rotating in a plane which is tilted out of the *ac* plane but not coplanar to the *b*-direction (like the cycloids) have been refined to the data. This tilt of the plane of the magnetic moments has also been set free in the refinement of this elliptical spiral structure. Several elliptical spirals were able to describe the data equally well. One of these fits with an elliptical spiral which is tilted by $\sim$45° out of the *ac* plane can be seen in Fig. A.7 (e). This fit yields a satisfactory description of the experimental data since the last (4th) incommensurate magnetic peak marked with a *blue arrow* has enough calculated intensity and also the second incommensurate peak overlapping with the (0 1 0) and (1 0 0) peaks is not too large yielding a quite good description of the ensemble of the (-1 -1 0)+q, (0 1 0) and (1 0 0) peaks. Also all other incommensurate magnetic peaks can be described quite well using this elliptical spiral model. For this last model the phase of the two distinct Fe-sites has been calculated from the differing y-values of the two Fe-atoms in order to describe a more simple 'coherent modulation' within the whole crystal. But in principle, this phase is not restricted by the symmetry and has been also refined for all the other models mentioned above in order to obtain the best description of the data.

As can be seen in Fig. A.8 (e) and Fig. A.6, the obtained magnetic moments are coupled antiferromagnetically within each zig-zag chain running in *c*-direction (*yellow lines*), additionally, exhibiting a sizeable canting. (Some of the magnetic moments which are not needed in the following discussion are plotted transparent in order to focus on the most important moments.) The four iron ions in the neighbouring chains (inter-chain) with same values of z are also coupled antiferromagnetically but with a distinct canting

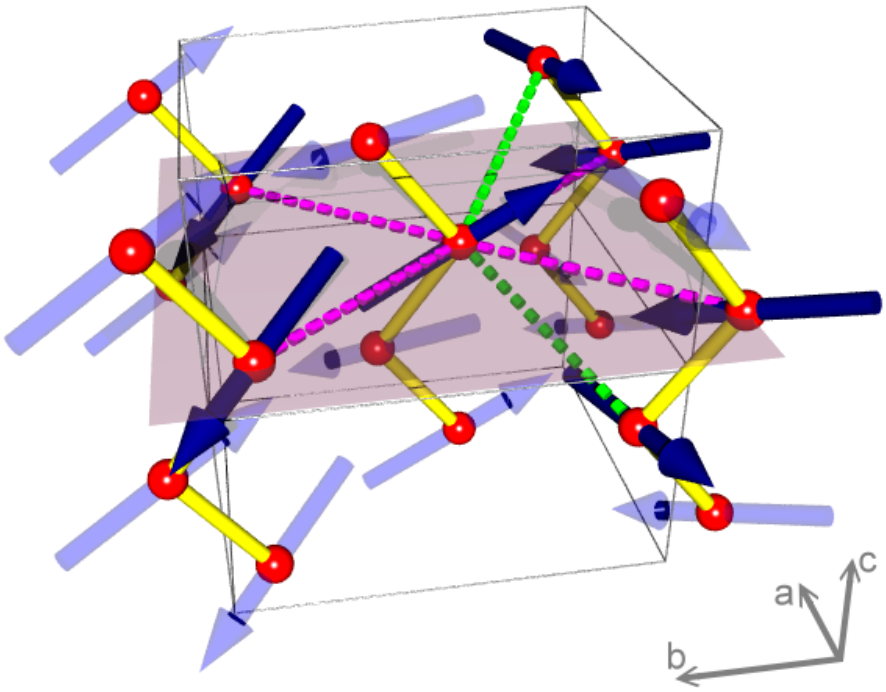

Figure A.6: Magnetic and nuclear structure for the tilted elliptical spiral model; *blue arrows:* magnetic moments, *red spheres:* Fe-ions, *yellow lines:* Fe-Fe bonds within the zig-zag chains, *green dotted lines:* the shortest inter-chain Fe-Fe distances, *magenta dotted lines:* Fe-Fe bonds within the same layer parallel to the *ab*-plane (second shortest inter-chain Fe-Fe distances).

angle (these are connected by the *magenta dotted lines* in Fig. A.6). So far, there would be no reason for frustration inducing an incommensurate magnetic structure. But, these four neighbouring Fe-ions with the same value of z are only the next-nearest inter-chain neighbours with a Fe-Fe distance of about 6.55 Å. There is one Fe-ion in the layer above and one Fe-ion in the layer below, which are closer to the central Fe-ion (*green dotted lines* in Fig. A.6). For these two Fe-ions the Fe-Fe distances amounts to 5.45 Å. All the other Fe-ions in neighbouring chains have larger Fe-Fe distances (2× ∼6.71 Å, 2× ∼7.82 Å, 2× ∼8.74 Å). Obviously these two nearest neighbouring interchain Fe-ions and the other four next nearest neighbouring inter-chain Fe-ions can not couple antiferromagnetically at the same time (unless the Fe-ions within the zig-zag chains couple ferromagnetically). Hence, there is a competition between antiferromagnetic ordering with the four Fe-ions within neighbouring chains in the same layer (parallel to the *ab* plane) and with the two nearest neighbouring Fe-ions in neighbouring chains. In this magnetic structure model, these competing exchange interactions induce frustration and, hence, the canting of the two ferromagnetically coupled moments between the nearest neighbouring inter-chain Fe-ions. Even if the elliptical spiral refined in this work might not be the perfectly accurate magnetic structure, this mechanism explains the occurrence of frustration in the aegirine system as long as one assumes, that the intra-chain coupling is antiferro-

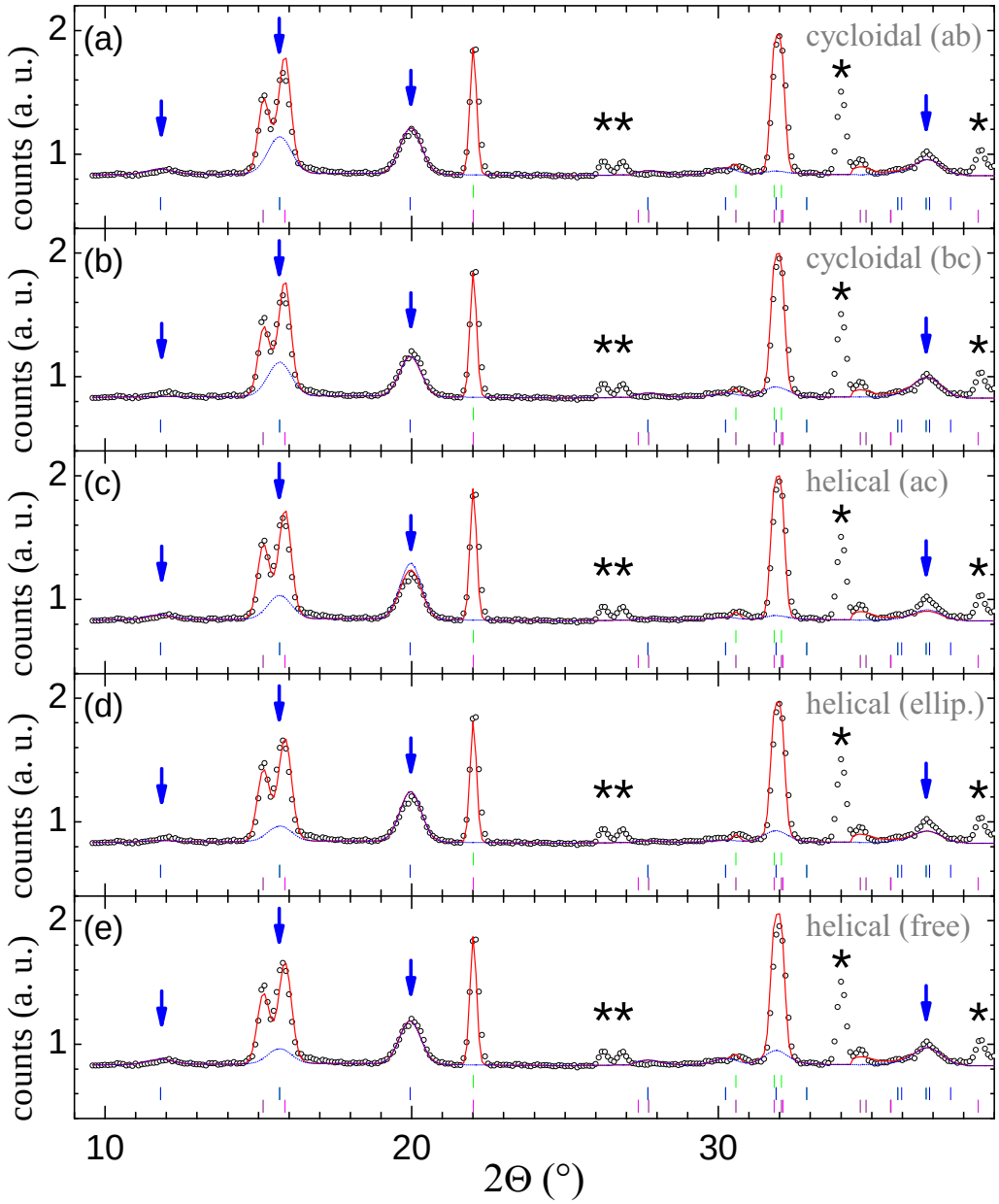

Figure A.7: Analysis of the G4.1 powder diffraction data at 1.5 K; *black circles*: measured data, (*red lines*): calculated intensities for five models: (a)/(b) a cycloidal with moments in the *ab*/*bc* plane; (c) a transverse spiral with moments in the *ac*-plane; an elliptical spiral (d) with moments in the *ac*-plane and (e) with the spiral plane tilted ∼45° out of the *ac*-plane; *blue lines*: calculated incommensurate magnetic intensities, *green/blue/magenta bars*: peak positions of the nuclear/incommensurate magnetic/commensurate magnetic phase.

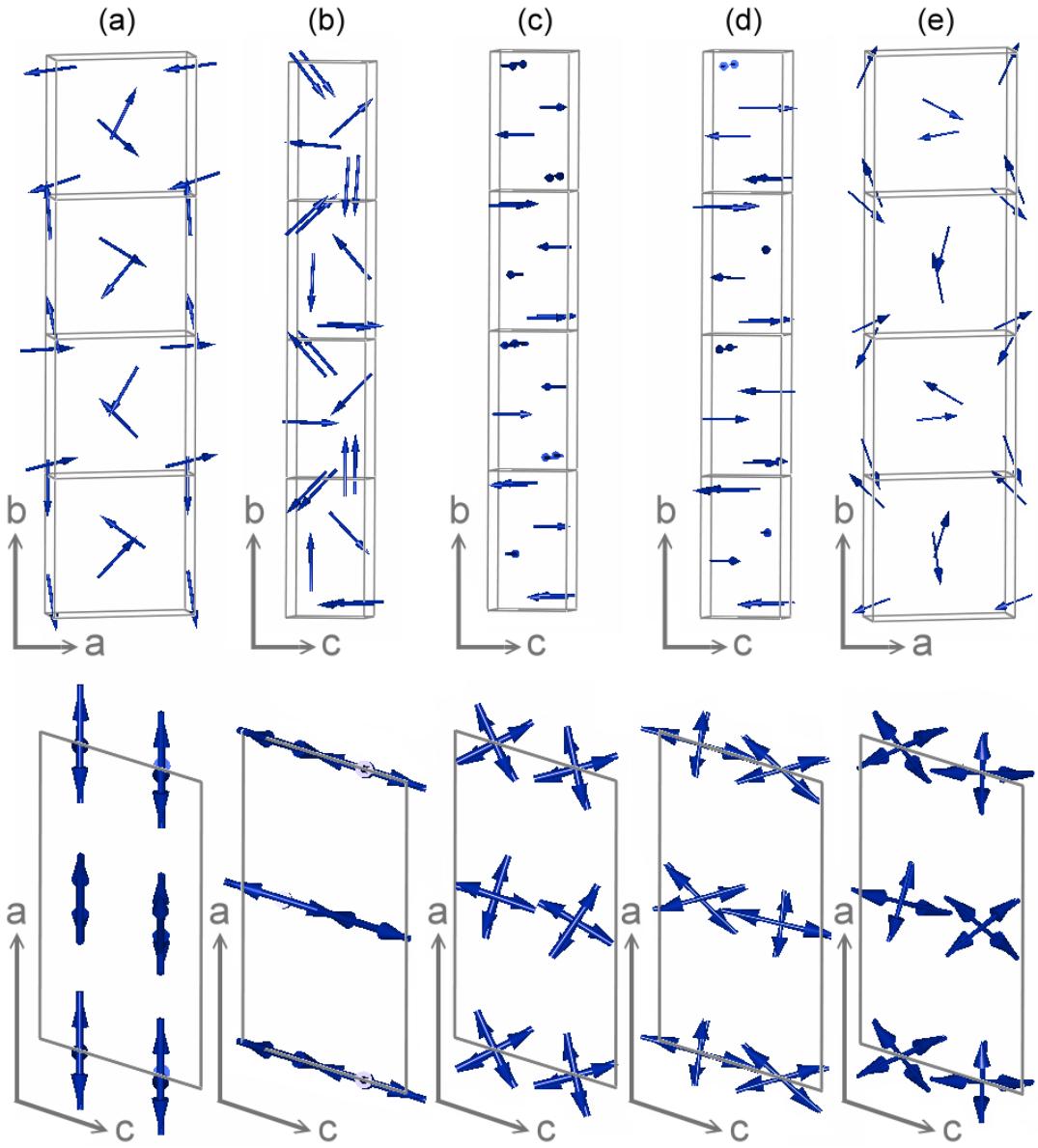

Figure A.8: (a-e) Five different models for magnetic structures in aegirine corresponding to the structure model refinement shown in Fig. A.7 (a-e). Here the projections of the magnetic moment in the *ac*-plane are shown. (a) Cycloidal with moments in the *ab*-plane, (b) cycloidal with moments in the *bc*-plane, (c) transverse spiral with moments in the *ac*-plane, (d) elliptical spiral with moments in the *ac*-plane, (e) elliptical spiral with spiral plane tilted out of the *ac*-plane.

magnetic. Of cause, this assumption is not trivial, since a ferromagnetic intra-chain coupling was proposed in Ref. [478] and only the inter-chain coupling was reported to be antiferromagnetic. However, this magnetic structure is not commensurate and, hence, also the intra-chain coupling of the commensurate magnetic phase might be either not

applicable or it might be possible, that this ferromagnetic intra-chain coupling is another possibility to release frustration in a commensurate way. Furthermore, a refinement of the same spiral magnetic structure but with ferromagnetically aligned moments within the zig-zag chains (with the same canting angle as in the AFM coupled spiral model) yields a bad description of the measured intensities.

However, there are also some uncertainties, since it was not possible to determine the exact tilting angle of the plane where the magnetic moments rotate - changes of this tilting angle yield fits with a similar good description of the data. An exact determination of this tilting angle is not within the scope of these powder neutron diffraction measurements and, hence, single crystal neutron diffraction measurements are needed for a more accurate determination of the magnetic structure. Also a sinusoidal magnetic structure with a free refinement of the magnetic moment direction is able to describe the data as well and yields almost identical results as the spiral models. However, a sinusoidal structure is not able to explain the ferroelectric order in $NaFeSi_2O_6$ [476]. But the ferroelectric ordering temperature is directly connected to the intensity of the incommensurate magnetic reflections as has been observed in the IN3 measurement: in Fig. A.4 (d) the temperature dependence of the magnetic intensities exhibits a distinct kink at the ferroelectric ordering temperature of about 6 K. It is very unlikely that this kink in the intensity of the *incommensurate* magnetic peaks is accidentally at the same temperature as the ferroelectric transition and, hence, the inverse Dzyaloshinski-Moriya effect [474] can be regarded as the mechanism inducing the ferroelectric order. But for a sinusoidal magnetic structure Eq. A.1 is always zero. Hence, a sinusoidal structure can be excluded for the 1.5 K data. It is possible that such a sinusoidal magnetic structure occurs at higher temperatures between 6 K and 8 K, but more accurate single crystal neutron data is needed in order to distinguish between the spiral and sinusoidal models.

A comparison of the magnetic R-values for all these different structure models is shown in Tab. A.1. As can be seen, the elliptical spiral magnetic structure with magnetic moments tilted out of the *ac* plane yields the smallest average magnetic R-factor of 7.4%. But also the cycloidal with the moments rotating in the *ab* plane yields a good description of the data although the average magnetic R-value is slightly larger - 10.6%. Thus, these measurements support an elliptical spiral magnetic structure with the magnetic moments rotating in a plane which is tilted distinctly out of the *ac* plane with a yet undetermined tilting angle $0° \ll \theta < 90°$. The value of θ for the spiral shown in this table amounts to $\sim 45°$, but also other values yield acceptable descriptions of the measured data. For a more accurate magnetic structure determination, single crystal neutron diffraction measurements are necessary. Especially, a cycloidal with the moments rotating in the *ab* plane seems also quite probable. However, this cycloidal is not able to explain the magnetic susceptibility measurements of the natural aegirine sample [476]: χ_a and χ_c exhibit a distinct drop for T$\rightarrow$0 K whereas no drop is observable for χ_b. Hence, a spiral model with the moments rotating in a plane slightly tilted out of the *ac* plane is also preferred by the susceptibility measurements of aegirine [476].

Thus, this spiral magnetic structure seems quite plausible - it is able to describe the measured neutron data very well, it is in accordance with the magnetic susceptibility measurements [476], it is in principle able to explain a ferroelectric polarization due to

the inverse Dzyaloshinski-Moriya effect and it also gives explanation for the frustration in this system - but it should be stressed that it is not possible to distinguish accurately between all possible incommensurate magnetic structures with this powder neutron data. As mentioned above a sinusoidal solution had to be ruled out by argumentations based on the kink in the incommensurate magnetic peak intensities of the single crystal data and not from the powder neutron data directly. Also it was not possible to determine the exact spiral plane as many different solutions were about equivalent. Hence, single crystal neutron data are needed for a more accurate magnetic structure determination and these first results of the powder diffraction data should be rather regarded as a demonstration that it is possible to describe these data with an incommensurate magnetic spiral. Also the occurrence of commensurate magnetic peaks in the powder samples remains still puzzling. Although these peaks are most likely caused by phase separation one may also think about a conical magnetic structure. But, no commensurate magnetic peaks have been observed in the single crystal neutron diffraction measurement of the natural aegirine crystals. Hence, this interpretation is rather unlikely, unless the $NaFeSi_2O_6$ powder samples are something completely different than the natural aegirine crystals ($Na_{1.04}Fe_{0.83}Ca_{0.04}Mn_{0.02}Al_{0.01}Ti_{0.08}Si_2O_6$).

Finally, the temperature dependency of the magnetic order in $NaFeSi_2O_6$ has been analyzed based on the elliptical spiral model (with tilted spiral plane) which yields a satisfactory description of the data measured at 1.5 K. In principle it can be expected that only one irreducible representation Γ_i describes the magnetic structure after the first continuous magnetic phase transition at ∼8 K, and that the data can be described with two irreducible representations $\Gamma_i \otimes \Gamma_j$ after the second magnetic phase transition at ∼6 K since the components of a second irreducible representation can be added after the second magnetic phase transition [**?**]. Therefore, in $NaFeSi_2O_6$ it may be possible that a transverse spiral with moments in the *ac* plane appears below 8 K according to the irreducible representation with vectorial Fourier components (u 0 v) and that the components of a second irreducible representation, (0 u 0), are added after the second magnetic transition at ∼6 K. With these two components the elliptical spiral which is tilted out of the *ac* plane can be described since the second component (0 u 0) is needed for a tilting of the spiral plane out of the *ac*-plane.

However, the intensities between 6 K and 8 K are much too low to distinguish between such models in this magnetic phase. Also a sinusoidal model could be applicable in this temperature regime. Hence, with this powder diffraction data only the absolute value of the magnetic moments could be refined within the elliptical spiral model with fixed moment directions etc. in order to get an imagination of the temperature dependency of the ordered moment. For an accurate determination of the intermediate magnetic phase between ∼8 K and ∼6 K it is definitely necessary to use single crystal neutron data (or to measure a sample without commensurate magnetic contributions at a high-flux powder diffractometer).

In Fig. A.9 (d-e) the powder neutron diffraction patterns measured at various temperatures above and below the phase transition are shown. In Fig. A.9 (a-c) the Rietveld fits of the elliptical spiral model (with fixed moment directions) and the commensurate magnetic structure model to this data are shown for the 1.5 K, 5.5 K and 7.0 K

measurements. As can be seen, the magnetic intensity of the incommensurate magnetic structure nearly vanishes around 7.0 K. The obtained values of the ordered magnetic moment are shown for all measured temperatures in Fig. A.4 (f). At 1.5 K the ordered moment of the commensurate magnetic structure amounts to 1.83(3) μ_B. At 1.5 K the ordered moment of the incommensurate magnetic structure amounts to 3.41(9) μ_B. The magnetic moment of this elliptical spiral rotates in a plane tilted by about 45° out of the *ac* plane between its maximal value of 4.16 μ_B in (0.125 -2.910 3.012) direction and its minimum value of 2.43 μ_B in (-2.535 -0.209 -0.857) direction, see Fig. A.8 (e) and Fig. A.6. Since the magnetic intensities are proportional to the square of the ordered moments, the 1.83(3) μ_B ordered moment in the commensurate magnetic structure indicate that a $100\times(1.83\ \mu_B)^2/(5\ \mu_B)^2$ percent volume fraction of the aegirine sample exhibits this commensurate ordering scheme (assuming that the true ordered moment of the Fe^{3+}-ion in the commensurate magnetic structure amounts to about 5 μ_B). Thus 13.4% of this aegirine powder sample exhibit a commensurate magnetic order. On the other hand, the ordered moment in the incommensurate magnetic structure has to be multiplied by a factor of about 1.075 in order to obtain the correct ordered moment of this 86.6% majority phase. After this correction, the ordered moment of the elliptical spiral amounts to 3.67 μ_B (and the maximum and minimum values amount to 4.47 μ_B and 2.72 μ_B).

A.1.4 Conclusion

Concluding, the $NaFeSi_2O_6$-system exhibits an incommensurate magnetic ordering at low temperatures. Single crystal neutron diffraction measurements reveal a distinct kink in the temperature-dependent intensity of the incommensurate magnetic reflections. This kink appears exactly at the ferroelectric ordering temperature and, thus, the inverse Dzyaloshinski-Moriya effect [474] can be regarded as the driving mechanism of the ferroelectric polarization.

Complementary powder neutron diffraction measurements at 1.5 K have been analyzed in order to determine this magnetic structure on a synthetic sample. But in contrast to the single crystal neutron data of the natural crystal also a commensurate magnetic phase could be observed in the synthetic powder. This difference to the single crystal data can not be explained so far. It might be speculated that frustration can be compensated by the incommensurate magnetic phase with antiferromagnetically coupled chains (as proposed in this work) and also by this commensurate magnetic structure with ferromagnetically coupled chains. However the absence of a commensurate magnetic phase in the natural aegirine single crystal remains unexplained. The commensurate magnetic propagation vector (0 1 0) resembles on the incommensurate antiferromagnetic propagation vector (0 0.77 0) and the magnetic symmetry reported in Ref. [478] could be confirmed and has been used for the description of this commensurate phase.

Additionally to the commensurate magnetic peaks, also incommensurate magnetic peaks could be observed in these measurements. In Ref. [478] these peaks could be also observed but have been attributed to impurity phases [478]. An incommensurate magnetic structure with character of an elliptical spiral which is tilted out of the *ac*

plane is able to describe the measured data. Also, the magnetic susceptibility data would be in accordance with such a spiral model [477]. Furthermore, the polarization in b direction [476] may arise from such a magnetic structure in principle. And finally, this model also helps to understand the frustration in this system: The coupling of the moments within the zig-zag chains (intra-chain) and the coupling between an Fe-ion and its *four* next-nearest Fe-ions in neighbouring zig-zag chains (inter-chain) have a strong antiferromagnetic character (as derived from the Rietveld refinement). However, the coupling of this Fe-ion to its *two* nearest Fe-ions in neighbouring zig-zag chains has an unfavourable ferromagnetic character. This gives rise to frustration in this system and may be responsible for the rotation of the moments away from a collinear alignment yielding the observed incommensurate structure.

Nonetheless, it should be stressed that it was not possible to unambiguously distinguish between all possible magnetic structures in these powder neutron measurements. Many possible solutions yield a very similar description of the data with very similar R-values. Especially in the elliptical spiral model it was not possible to determine the exact tilting angle of the spiral plane. Furthermore, sinusoidal magnetic structures have been excluded right from the beginning in a argumentative manner but yield also satisfactory descriptions of the measured data. Hence, these powder neutron diffraction measurements are not sufficient for an exact determination of the magnetic structure.

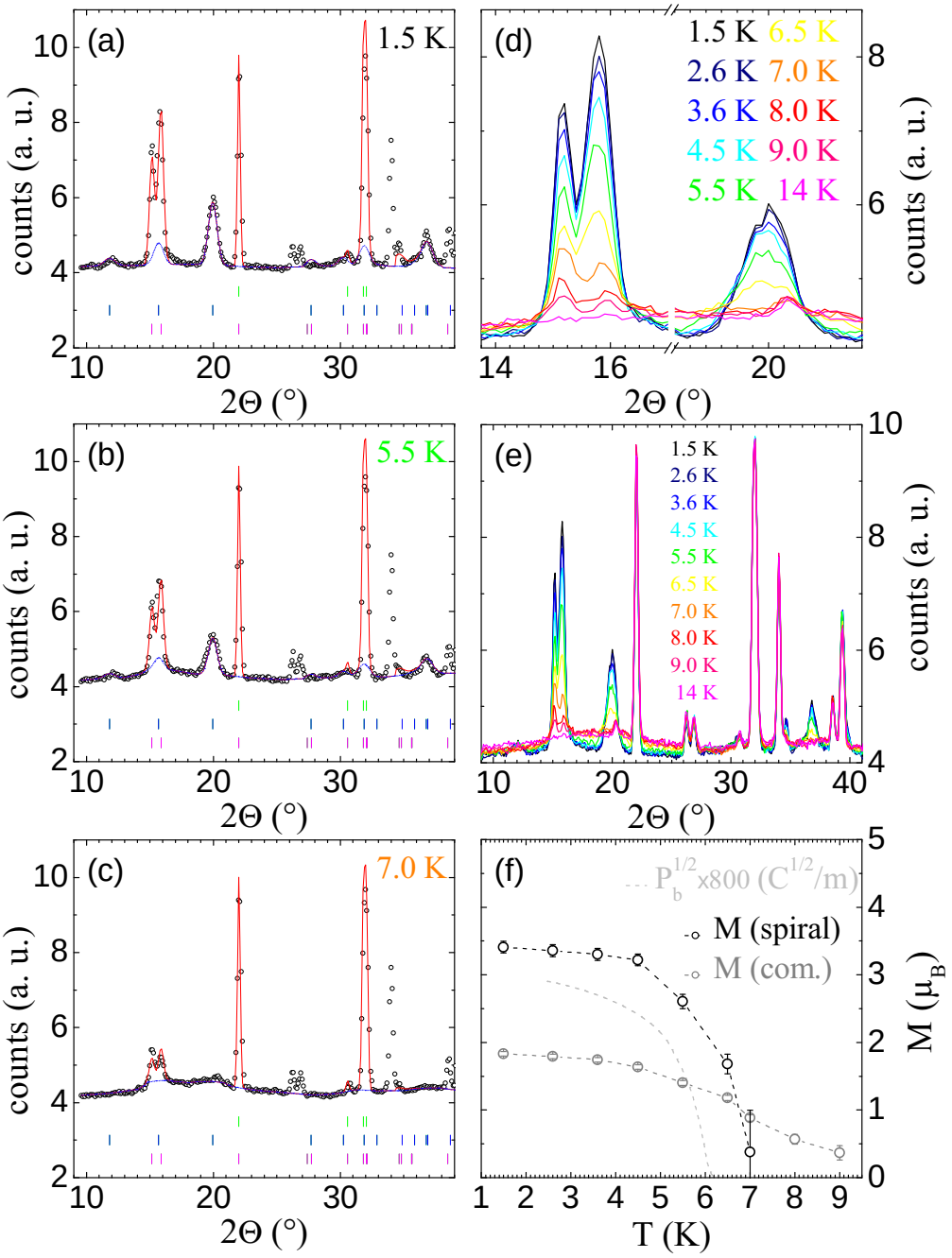

Figure A.9: (a-c) Results of Rietveld refinements with the elliptical spiral model for three different temperatures. (d-e) Powder neutron diffraction patterns collected at different temperatures. (f) Ordered antiferromagnetic moment of the elliptical spiral model (*black circles*) and of the commensurate magnetic phase (*gray circles*). Additionally, taken from Ref. [476, 477] the square root of the polarization P (multiplied by 800) is shown (in units of $\sqrt{C}/m$ instead of μ_B).

B Appendix B: 1D Titanates

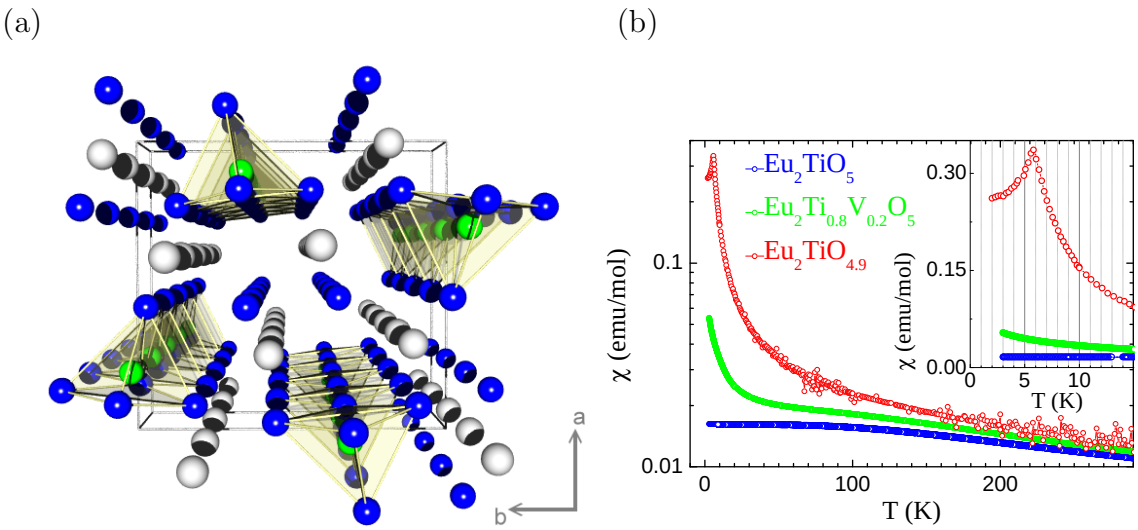

Figure B.1: (a) Structure of $Eu_2Ti_{1-x}V_xO_{5-\delta}$ (b) Magnetic susceptibility of *ACK058*, *ACK066* and *ACK124*.

Single crystals of Eu_2TiO_5 (*ACK058*), $Eu_2Ti_{0.85}V_{0.15}O_5$ (*ACK066*) and $Eu_2TiO_{4.9}$ (*ACK124*) with a quasi one-dimensional (1D) crystal structure have been grown in this work, see Fig. B.1 (a). Whereas Eu_2TiO_5 is a transparent crystal, the other two crystals are black. The structure of Eu_2TiO_5 and $Eu_2Ti_{0.85}V_{0.15}O_5$ has been measured with single crystal X-ray diffraction. The results are listed in Tab. B.1. This structure has also been confirmed for $Eu_2TiO_{4.9}$ by powder X-ray diffraction. The magnetic susceptibility measurements which have been measured by M. Reuther and S. Heiligen are shown in Fig. B.1 (b). Eu_2TiO_5 exhibits a temperature independent (Van Vleck) paramagnetic susceptibility below about 100 K presumably arising from the Eu^{3+}-ions. In contrast to 15% V-doping the susceptibility of $Eu_2TiO_{4.9}$ indicates an antiferromagnetic ordering at about 6 K. Hence, the introduction of V-ions seems to introduce localized moments only, whereas electron doping at the Ti-site seems to create some antiferromagnetic correlations either among Ti^{3+}- or between Eu^{2+}-ions.

ACK058						
refl.	107180					
2Θ$_{max}$	112.4°					
R$_{int}$	3.64%					
redun.	33.2					
R/Rw	2.65%/3.45%					
GoF	1.33					
atoms:	**occ.**	**x**	**y**	**z**	**U$_{iso}$ (Å^2)**	
Eu1	1	0.13647(3)	0.05839(3)	0.25	0.005943(19)	
Eu2	1	0.39086(3)	0.22101(3)	0.75	0.006025(19)	
Ti1	1	0.17915(4)	0.37890(3)	0.25	0.00545(5)	
O1	1	0.00672(9)	0.10388(10)	0.75	0.0299(2)	
O2	1	0.27573(10)	0.04114(9)	0.75	0.0292(2)	
O3	1	0.23294(9)	0.38170(10)	0.75	0.0302(2)	
O4	1	0.26375(9)	0.23113(8)	0.25	0.0294(2)	
O5	1	0.01491(11)	0.34203(10)	0.25	0.0350(3)	
atoms:	**U$_{11}$**	**U$_{22}$**	**U$_{33}$**	**U$_{12}$**	**U$_{13}$**	**U$_{23}$**
Eu1	0.00614(4)	0.00630(3)	0.00539(3)	-0.000525(19)	0	0
Eu2	0.00652(4)	0.00624(3)	0.00532(3)	-0.00062(2)	0	0
Ti1	0.00578(10)	0.00507(9)	0.00550(8)	-0.00029(7)	0	0
O1	0.0295(4)	0.0299(3)	0.0303(4)	-0.0010(3)	0	0
O2	0.0304(4)	0.0282(4)	0.0290(3)	0.0010(2)	0	0
O3	0.0341(4)	0.0289(4)	0.0274(3)	-0.0007(3)	0	0
O4	0.0333(4)	0.0273(4)	0.0277(3)	0.0001(3)	0	0
O5	0.0297(5)	0.0420(5)	0.0332(4)	-0.0056(3)	0	0

ACK066						
refl.	70265					
2Θ$_{max}$	113.6°					
R$_{int}$	2.65%					
redun.	22.1					
R/Rw	1.60%/1.93%					
GoF	1.34					
atoms:	**occ.**	**x**	**y**	**z**	**U$_{iso}$ (Å^2)**	
Eu1	1	0.136843(14)	0.057866(13)	0.25	0.005416(12)	
Eu2	1	0.389882(15)	0.221392(15)	0.75	0.005551(12)	
Ti1/V1	0.85/0.15	0.17830(2)	0.37898(2)	0.25	0.00255(4)	
O1	1	0.00657(10)	0.10466(10)	0.75	0.00769(17)	
O2	1	0.27514(10)	0.04067(10)	0.75	0.00712(16)	
O3	1	0.23206(11)	0.38164(9)	0.75	0.00799(18)	
O4	1	0.26388(10)	0.23119(10)	0.25	0.00733(16)	
O5	1	0.01564(11)	0.34383(13)	0.25	0.0127(2)	
atoms:	**U$_{11}$**	**U$_{22}$**	**U$_{33}$**	**U$_{12}$**	**U$_{13}$**	**U$_{23}$**
Eu1	0.00557(2)	0.00599(2)	0.004688(17)	-0.000445(14)	0	0
Eu2	0.006069(19)	0.00583(2)	0.004748(17)	-0.000676(14)	0	0
Ti1/V1	0.00253(6)	0.00231(7)	0.00283(5)	-0.00053(5)	0	0
O1	0.0070(3)	0.0076(3)	0.0085(3)	0.0009(2)	0	0
O2	0.0094(3)	0.0061(3)	0.0059(2)	0.0005(2)	0	0
O3	0.0113(3)	0.0076(3)	0.0050(2)	-0.0001(3)	0	0
O4	0.0095(3)	0.0070(3)	0.0055(2)	0.0008(3)	0	0
O5	0.0071(3)	0.0227(5)	0.0085(3)	-0.0044(3)	0	0

Table B.1: Results of single crystal X-ray diffraction measurements.

C Appendix C: $EuTiO_3$

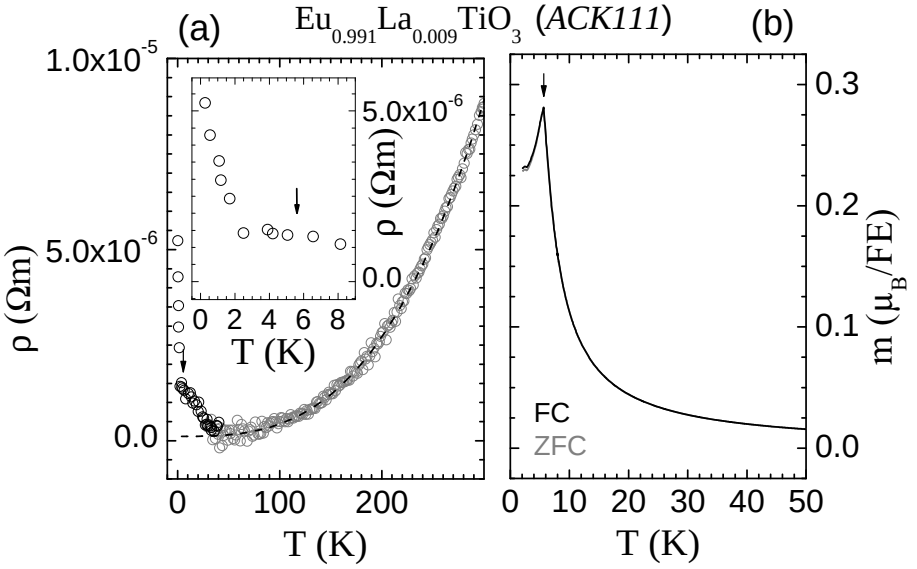

Figure C.1: (a) Electrical resistivity ρ measured with 1 mA (*gray circles*) and 50 μA in a Heliox ^{3}He evaporation insert (*black circles*). (b) Magnetic susceptibility χ of $Eu_{0.991}La_{0.009}TiO_3$.

$EuTiO_3$ has a cubic perovskite crystal structure ($Pm\bar{3}m$) with divalent Eu-ions (7 μ_B) and non-magnetic Ti^{4+}-ions and orders antiferromagnetically at 5.3 K [120]. In this work, a single crystal of $Eu_{0.991}La_{0.009}TiO_3$ (*ACK111*) has been grown which has a completely black colour. The electrical resistivity ρ and magnetic susceptibility χ measurements of this crystal *ACK111* are shown in Fig. C.1 (a-b). The measurement of ρ with a standard four-probe technique always suffered from noise at low temperatures independent of the used sample and variation of the measurement technique etc. The electrical resistivity ρ exhibits a purely metallic behaviour and can be fitted with a $\rho_0 + A \cdot T^3$ law only (*dashed black line*). The measurement of χ which has been performed by M. Reuther indicates an antiferromagnetic ordering at ~5.6 K (marked with a *black arrow*).

$EuTiO_3$ has a similar cubic crystal structure as $SrTiO_3$ and also a Ti $3d^0$ electronic configuration. $SrTiO_3$ is a band insulator with a band gap of 3.2 eV. However, the doping with a small amount of charge carriers by substitution of Ti by Nb, Sr by La or by

oxygen vacancies induces metallic properties in this system and, moreover, superconductivity with a T_C of $\sim$ 0.3 K for the optimum carrier concentration of $\sim 10^{20} cm^{-3}$ which is a rather high value of T_C for this carrier density [480, 481]. For $Sr_{0.991}La_{0.009}TiO_3$ a T_C of about 0.22 K has been reported. Although $Eu_{0.991}La_{0.009}TiO_3$ exhibits antiferromagnetic ordering and magnetism is harmful for superconductivity, the electrical resistivity of this compound has also been measured in another measurement down to very low temperatures using a Heliox ^{3}He evaporation insert. This measurement which has been performed by O. Heyer by a standard four-probe technique is denoted by the *black circles* in Fig. C.1 (a) and the inset of this figure. However, no indications for superconductivity have been found down to $\sim$0.27 K. The antiferromagnetic ordering temperature is indicated by the *black arrow*.

D Appendix D: $MnSiO_3$

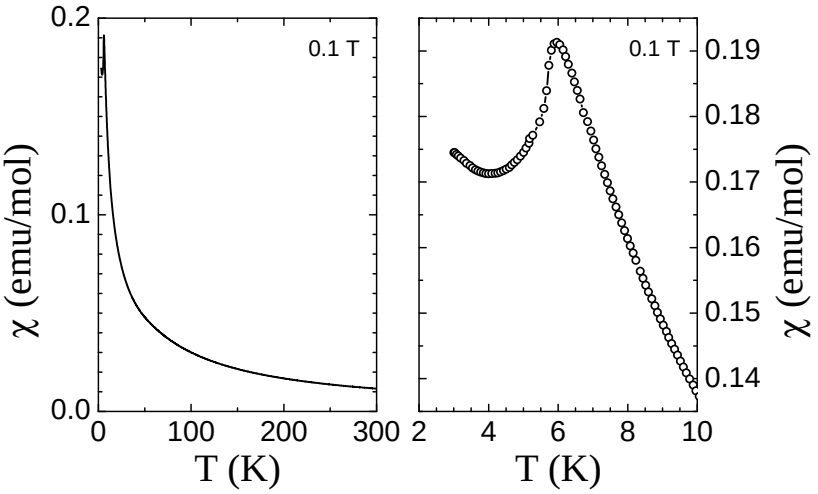

Figure D.1: Magnetic susceptibility χ of $MnSiO_3$.

$MnSiO_3$ is a silicate with rhodonite structure if synthesized at low pressures [482]. Above pressures of 30-43 kbar (depending on the temperature), this compound transforms to a high-pressure polymorph with triclinic pyroxmangite structure (a: 6.721(2) Å, b: 7.603(3) Å, c: 17.455(6) Å, α: 113°10'(6'), β 82°16'(6'), γ: 94°08'(6')) [482]. Above 70-95 kbar this compound further transforms to a compound with monoclinic pyroxene structure (clinopyroxene with SG $P2_1/c$) accompanied by a remarkable color change from light pink (pyroxmangite) to lilac (pyroxene) [482]. Finally, around 125 kbar the fourth $CaGeO_3$ garnet-like high pressure phase becomes stable [482].

Here, the magnetic susceptibility of a natural mineral of $MnSiO_3$ - pyroxmangite - with light pink color has been measured by M. Reuther using a VSM magnetometer. The susceptibility χ indicates an antiferromagnetic ordering temperature of about 6 K.

Bibliography

[1] G. Galilei, http://allezitate.com/galileo-galilei/zitate/242916 .

[2] M. Imada, A. Fujimori and Y. Tokura, Reviews of Modern Physics **70**, 1039 (1998).

[3] E. Dagotto, Science **309**, 257 (2005).

[4] J. G. Bednorz and K. A. Müller, Z. Physik B **64**, 189 (1986).

[5] R. von Helmolt, J. Wecker, B. Holzapfel, L. Schultz and K. Samwer, Phys. Rev. Lett. **71**, 2331 (1993).

[6] J. M. Tranquada, B. J. Sternlieb, J. D. Axe, Y. Nakamura and S. Uchida, Nature **375**, 561 (1995).

[7] Y. Tokura and N. Nagaosa, Science **288**, 462 (2000).

[8] G. C. Milward, M. J. Calderón and P. B. Littlewood, Nature **433**, 607 (2005).

[9] J. M. Tranquada, J. D. Axe, N. Ichikawa, A. R. Moodenbaugh, Y. Nakamura and S. Uchida, Phys. Rev. Lett. **78**, 338 (1997).

[10] T. Cuk, F. Baumberger, D. H. Lu, N. Ingle, X. J. Zhou, H. Eisaki, N. Kaneko, Z. Hussain, T. P. Devereaux, N. Nagaosa and Z.-X. Shen, Phys. Rev. Lett. **93**, 117003 (2004).

[11] T. P. Devereaux, T. Cuk, Z.-X. Shen and N. Nagaosa, Phys. Rev. Lett. **93**, 117004 (2004).

[12] X. J. Zhou, J. S. T. Yoshida, T. Cuk, W. L. Yang, V. Brouet, J. Nakamura, N. Mannella, S. Komiya, Y. Ando, F. Zhou, W. X. Ti, J. W. Xiong, Z. X. Zhao, T. Sasagawa, T. Kakeshita, H. Eisaki, S. Uchida, A. Fujimori, Z. Zhang, E. W. Plummer, R. B. Laughlin, Z. Hussain and Z.-X. Shen, Phys. Rev. Lett. **95**, 117001 (2005).

[13] D. Reznik, L. Pintschovius, M. Ito, S. Iikubo, M. Sato, H. Goka, M. Fujita, K. Yamada, G. D. Gu and J. M. Tranquada, Nature **440**, 1170 (2006).

[14] D. I. Khomskii and G. A. Sawatzky .

[15] R. P. Ozerov, V. A. Streltsov, A. N. Sobolev, B. N. Figgisc and V. L. Volkovd, Acta Cryst. Sec. B **57**, 244 (2001).

[16] Acta Cryst. A **46**, 271 (1990).

[17] E. A. Zhurovaa and V. G. Tsirelsonb, Acta Cryst. Sec. B **58**, 567 (2002).

[18] S. M. Hayden, H. A. Mook, P. Dai, T. G. Perring and Doan, Nature **429**, 531 (2004).

[19] V. Hinkov, S. Pailhès, P. Bourges, Y. Sidis, A. Ivanov, A. Kulakov, C. T. Lin, D. P. Chen, C. Bernhard and B. Keimer, Nature **430**, 650 (2004).

[20] J. M. Tranquada, H. Woo, T. G. Perring, H. Goka, G. D. Gu, G. Xu, M. Fujita and K. Yamada, Nature **429**, 534 (2004).

[21] N. B. Christensen, D. F. McMorrow, H. M. Rønnow, B. Lake, S. M. Hayden, G. Aeppli, T. G. Perring, M. Mangkorntong, M. Nohara and H. Takagi, Phys. Rev. Lett. **93**, 147002 (2004).

[22] C. Stock, W. J. L. Buyers, R. A. Cowley, P. S. Clegg, R. Coldea, C. D. Frost, R. Liang, D. Peets, D. Bonn, W. N. Hardy and R. J. Birgeneau, Phys. Rev. B **71**, 024522 (2005).

[23] H. F. Fongand, P. Bourges, Y. Sidis, L. P. Regnault, J. Bossy, A. Ivanov, D. L. Milius, I. A. Aksay and B. Keimer, Phys. Rev. B **61**, 14773 (2000).

[24] P. Dai, H. A. Mook, R. D. Hunt and F. Dogan, Phys. Rev. B **63**, 054525 (2001).

[25] C. Stock, W. J. L. Buyers, R. A. Cowley, P. S. Clegg, R. Coldea, C. D. Frost, R. Liang, D. Peets, D. Bonn, W. N. Hardy and R. J. Birgeneau, Phys. Rev. B **71**, 024522 (2005).

[26] A. Furrer, *Magnetic Neutron Scattering*, World Scientific Singapore (1995).

[27] C. Zener, Phys. Rev. **82**, 403 (1951).

[28] J. B. Goodenough, Phys. Rev. **100**, 564 (1955).

[29] J. Kanamori, J. Phys. C : Solid State Phys. **10**, 87 (1959).

[30] P. W. Anderson, Phys. Rev. **79**, 350 (1950).

[31] B. Keimer, N. Belk, R. J. Birgeneau, A. Cassanho, C. Y. Chen, M. Greven and M. A. Kastner, Phys. Rev. B **46**, 14034 (1992).

[32] R. J. Cava, B. Batlogg, T. T. Palstra, J. J. Krajewski, W. F. Peck, A. P. Ramirez and L. W. Rupp, Phys. Rev. B **43**, 1229 (1991).

[33] C. A. Kuntscher, S. Frank, A. Pashkin, M. Hoinkis, M. Klemm, M. Sing, S. Horn and R. Claessen, Phys. Rev. B **74**, 184402 (2006).

[34] A. C. Thompson, D. T. Attwood, E. M. Gullikson, M. R. Howells, J. B. Kortright, A. L. Robinson, J. H. Underwood, K.-J. Kim, J. Kirz, I. Lindau, P. Pianetta, H. Winick, G. P. Williams, J. H. Scofield and D. Vaughan, *X-Ray Data Booklet (2nd ed.)*, Lawrence Berkeley National Laboratory (2001).

[35] http://www.esrf.eu/ .

[36] G. Will, *Powder Diffraction*, Springer (2006).

[37] T. Fließbach, *Elektrodynamik*, Spektrum Akademischer Verlag Heidelberg Berlin, 3. Auflage (2000).

[38] http://hasylab.desy.de .

[39] http://www.bessy.de/ .

[40] G. Shirane, S. M. Shapiro and J. M. Tranquada, *Neutron scattering with a triple axis spectrometer*, Cambridge University Press (2002).

[41] G. L. Squires, *Introduction to the theory of thermal neutron scattering*, Dover Publications, Inc. (1978).

[42] C. Gerthsen and H. Vogel, *Physik*, Springer Verlag (1993).

[43] H. Halban and P. Preiswerk, C. R. Acad. Sci. Paris **203**, 73 (1936).

[44] D. P. Mitchell and P. N. Powers, Phys. Rev. **50**, 486 (1936).

[45] T. Chatterji, *Neutron scattering from Magnetic Materials*, Elsevier (2006).

[46] H. C. Ohanian, *Principles of Physics*, W. W. Norton and Company (1994).

[47] http://www.isis.rl.ac.uk/ .

[48] http://www.frm2.tum.de/ .

[49] http://www-llb.cea.fr/ .

[50] http://www.ill.eu/ .

[51] http://sinq.web.psi.ch/ .

[52] P. P. Ewald, *Fifty years of X-ray diffraction*, International Union of Crystallography, Utrecht, Netherlands (1962).

[53] P. Debye and P. Scherrer, Phys. Z. **17**, 277 (1916).

[54] J. D. Hanawalt, H. W. Rinn and L. K. Frevel, Ind. Eng. Chem. Anal. Ed. **10**, 457 (1938).

[55] C. G. Shull and J. S. Smart, Phys. Rev. **76**, 1256 (1949).

[56] H. M. Rietveld, J. Appl. Cryst. **2**, 65 (1969).

[57] A. C. Komarek, Diploma Thesis, University of Köln (2004).

[58] V. Petricek and M. Dusek, http://www-xray.fzu.cz/jana/jana2000 .

[59] W. Massa, *Kristallstrukturbestimmung, 3. Auflage*, B. G. Teubner (2002).

[60] A.-J. Dianoux, G. Lander, C. C. Wilson and R. S. Eccleston, *Neutron Data Booklet, second edition*, OCP Science (2003).

[61] P. Coppens, *X-ray Charge densities and Chemical Bonding*, Oxford Science Publications (1997).

[62] J. C. Hanson, L. C. Sieker and L. H. Jensen, Acta Cryst. B **29**, 797 (1973).

[63] J. de Meulenaar and H. Tompa, Acta Cryst. A **19**, 1014 (1965).

[64] R. H. Blessing, Acta Cryst. A **51**, 33 (1995).

[65] Area-Detector Absorption Correction; Siemens Industrial Automation, Inc.: Madison, WI, (1996).

[66] B. AXS, http://www.bruker-axs.de/ .

[67] M. Cwik, Dissertation (2007).

[68] M. G. Vincent and H. D. Flack, Acta Cryst. A **35**, 78 (1979).

[69] Optical floating zone system FZ - 10000 - H - VI - VP Crystal Systems Inc.

[70] W. Heywang, Z. Naturforsch. **11a**, 238 (1956).

[71] S. R. Coriell and M. Cordes, Journal of Crystal Growth **42**, 466 (1977).

[72] R. E. Green, J. Appl. Phys. **35**, 1297 (1964).

[73] A. A. Nugroho, private communication.

[74] C. H. Chun and W. Wuest, Acta Astronautica **9**, 225 (1982).

[75] *Crystal Systems Inc. model FZ-T-10000-H-VI-VP*.

[76] P. Reutler, Dissertation, RWTH Aachen (2003).

[77] U. Müller, Anorganische Strukturchemie (1996).

[78] H. Roth, Dissertation, Universität zu Köln (2008).

[79] M. Tsubota, F. Iga, K. Uchihira, T. Nakano, S. Kura, T. Takabatake, S. Kodama, H. Nakao and Y. Murakami, J. Phys. Soc. Japan **74**, 3259 (2005).

[80] V. M. Goldschmidt, Norsk. Vid. Akad., Math.-Naturvid. Kl. (1926).

[81] H. D. Zhou and J. B. Goodenough, J. Phys.: Condens. Matter **17**, 7395 (2005).

[82] R. D. Shannon, Acta Cryst. A **32**, 751 (1976).

[83] H. Roth, Diplomarbeit, Universität zu Köln (2003).

[84] A. C. Komarek, H. Roth, M. Cwik, W.-D. Stein, J. Baier, M. Kriener, F. Bourée, T. Lorenz and M. Braden, Phys Rev. B **75**, 224402 (2007).

[85] N. Hollmann, Diploma Thesis, University of Köln, (2006).

[86] T. Lorenz, private communication .

[87] J. E. Greedan, J. Less Common Metals **111**, 335 (1985).

[88] T. Roisnel and J. Rodriguez-Carvajal, WinPLOTR, FullProf (2005).

[89] E. F. Bertaut, Acta. Cryst. A **24**, 217 (1968).

[90] C. W. Turner, J. E. Greedan and M. F. Collins, J. Mag. Mag. Mat. **20**, 165 (1980).

[91] C. W. Turner, M. F. Collins and J. E. Greedan, J. Mag. Mag. Mat. **23**, 265 (1981).

[92] E. F. Bertaut and J. Maréschal, Solid State Commun. **5**, 93 (1967).

[93] C. C. Hays, J.-S. Zhou, J. T. Markert and J. B. Goodenough, Phys. Rev. B **60**, 10367 (1999).

[94] A. E. Filali, Diplomarbeit, Universität zu Köln (2004).

[95] K. Kumagai, T. Suzuki, Y. Taguchi, Y. Okada, Y. Fujishima and Y. Tokura, Phys. Rev. B **48**, 7636 (1993).

[96] Y. Taguchi, Y. Tokura, T. Arima and F. Inaba, Phys. Rev. B **48**, 511 (1992).

[97] M. Tsubota, F. Iga, T. Nakano, K. Uchihira, S. Kura, M. Takemura, Y. Bando, K. Umeo, T. Takabatake, E. Nishibori, M. Takata, M. Sakata, K. Kato and Y. Ohishi, J. Phys. Soc. Japan **72**, 3182 (2003).

[98] S. Das, A. Poddar and B. Roy, J. Alloys and Compounds **358**, 17 (2003).

[99] J. Laugier, OrientExpress 3.4 .

[100] M. Benomar, Dissertation, Universität zu Köln (2007).

[101] P. I. D. Prabhakaran and A. T. Boothroyd, J. Crystal Growth **237-23**, 815 (2002).

[102] O. Friedt, Diplomarbeit, Universität zu Köln (1998).

[103] M. Hucker, K. Chung, M. Chand, T. Vogt, J. M. Tranquada and D. J. Buttrey, Phys. Rev. B **70**, 064105 (2004).

[104] T. Finger, Dissertation, unpublished .

[105] T. Katsufuji, M. Masaki, A. Machida, M. Moritomo, K. Kato, E. Nishibori, M. Takata, M. Sakata, K. Ohoyama, K. Kitazawa and H. Takagi, Phys. Rev. B **66**, 134434 (2002).

[106] T. Kimura, G. Lawes, T. Goto, Y. Tokura and A. P. Ramirez, Phys. Rev. B **71**, 224425 (2005).

[107] S. S. Zumdahl, Chemistry, Third Edition, D. C. Heath and Company, Lexington Massachusetts Toronto (1993).

[108] http://de.wikipedia.org/wiki/Titandioxid .

[109] J. P. Goral and J. E. Greedan, J. Magn. Matter **37**, 315 (1983).

[110] G. I. Meijer, W. Henggeler, J. Brown, O.-S. Becker, J. G. Bednorz, C. Rossel and P. Wachter, Phys. Rev. B **59**, 11832 (1999).

[111] G. Amow and J. E. Greedan, Journal of Solid State Chemistry **121**, 443 (1996).

[112] G. Amow, J. E. Greedan and C. Ritter, Journal of Solid State Chemistry **141**, 262 (1996).

[113] J. D. Garrett and J. E. G. D. A. MacLean, Mater. Res. Bull. **16**, 145 (1981).

[114] M. Onoda and M. Yasumoto, J. Phys.: Condens. Matter **9**, 3861 (1997).

[115] M. Onoda and M. Yasumoto, J. Phys.: Condens. Matter **9**, 5623 (1997).

[116] C. C. Hays, J.-S. Zhou, J. T. Markert and J. B. Goodenough, Phys. Rev. B **60**, 10367 (1999).

[117] J. Akimitsu, H. Ichikawa, N. Eguchi, T. Miyano, M. Nishi and K. Kakurai, J. Phys. Soc. Japan **70**, 3475 (2001).

[118] M. Cwik, T. Lorenz, J. Baier, R. Müller, G. Andre, F. Bouree, F. Lichtenberg, A. Freimuth and E. M.-H. und M. Braden, Phys. Rev. B **68**, 060401 (2003).

[119] B. Keimer, D. Casa, A. Ivanov, J. W. Lynn, M. v. Zimmermann, J. P. Hill, D. Gibbs, Y. Taguchi and Y. Tokura, Phys. Rev. Lett. **85**, 3946 (2000).

[120] T. R. McGuire, M. W. Shafer, R. J. J. andH. A. Alperin and S. J. Pickart, J. Appl. Phys. **37**, 981 (1966).

[121] D. A. MacLean, H.-N. Ng and J. E. Greedan, J. Solid State Chem. **30**, 35 (1979).

[122] Y. Okimoto, T. Katsufuji, Y. Okada, T. Arima and Y. Tokura, Phys. Rev. B **51**, 9581 (1995).

[123] V. M. Goldschmidt, Geochemische Verteilungsgesetze der Elemente Band VII, VIII Norsk. Vid. Akad. (1927/28).

[124] E. Pavarini, S. Biermann, A. Poteryaev, A. I. Lichtenstein, A. Georges and O. Andersen, Phys. Rev. Lett. **92**, 176403 (2004).

[125] C. Ulrich, G. Khaliullin, S. Okamoto, M. Reehuis, A. Ivanov, H. He, Y. Taguchi, Y. Tokura and B. Keimer, Phys. Rev. Lett. **89**, 167202 (2002).

[126] D. I. Khomskii and G. A. Sawatzky, Solid State Commun. **102**, 87 (1997).

[127] T. Katsufuji, Y. Taguchi and Y. Tokura, Phys. Rev. B **56**, 10145 (1997).

[128] J. P. Goral and J. E. G. und D. A. MacLean, J. Solid State Chem. **43**, 244 (1982).

[129] G.Khaliullin and S. Maekawa, Phys. Rev. Lett. **85**, 3950 (2000).

[130] G. Khaliullin, Phys. Rev. B **64**, 212405 (2001).

[131] M. Moshizuki and M. Imada, J. Phys. Soc. Jpn. **70**, 2872 (2001).

[132] M. W. Haverkort, Z. Hu, A. Tanaka, G. Ghiringhelli, H. Roth, M. Cwik, T. Lorenz, C. Schüßler-Langeheine, S. V. Streltsov, A. S. Mylnikova, V. I. Anisimov, C. de Nadai, N. B. Brookes, H. H. Hsieh, H.-J. Lin, C. T. Chen, T. Mizokawa, Y. Taguchi, Y. Tokura, D. I. Khomskii and L. H. Tjeng, Phys. Rev. Lett. **94**, 056401 (2005).

[133] R. Rückamp, E. Benckiser, M. W. Haverkort, H. Roth, T. Lorenz, A. Freimuth, L. Jongen, A. Möller, G. Meyer, P. Reutler, B. Büchner, A. Revcolevschi, S.-W. Cheong, C. Sekar, G. Krabbes and M. Grüninger, New J. Phys. **7**, 144 (2005).

[134] R. Schmitz, O. Entin-Wohlman, A. Aharony, A. B. Harris and E. Müller-Hartmann, Phys. Rev. B **71**, 214438 (2005).

[135] R. Schmitz, O. Entin-Wohlman, A. Aharony, A. B. Harris and E. Müller-Hartmann, Phys. Rev. B **71**, 144412 (2005).

[136] C. W. Turner, M. F. Collins and J. E. Greedan, J. Magn. Magn. Mater. **23**, 265 (1981).

[137] M. Heinrich, H.-A. K. von Nidda, V. Fritsch and A. Loidl, Phys. Rev. B **63**, 193103 (2001).

[138] C. W. Turner and J. E. Greedan, J. Solid State Chem. **34**, 207 (1980).

[139] J. Hemberger, H.-A. K. von Nidda, V. Fritsch, J. Deisenhofer, S. Lobina, T. Rudolf, P. Lunkenheimer, F. Lichtenberg, A. Loidl, D. Bruns and B. Büchner, Phys. Rev. Lett. **91**, 066403 (2003).

[140] H. Nakao, Y. Wakabayashi, T. Kiyama, Y. Murakami, M. v. Zimmermann, J. P. Hill, D. Gibbs, S. Ishihara, Y. Taguchi and Y. Tokura, Phys. Rev. B **66**, 184419 (2002).

[141] A. Hammersley, *FIT2D*, Copyright 1987-2004 Andy Hammersley / ESRF.

[142] K. Kugel and D. Khomskii, Sov. Phys. Usp. **25**, 231 (1982).

[143] I. Solovyev, Phys. Rev. B **69**, 134403 (2004).

[144] I. Solovyev, Phys. Rev. Lett. **74**, 054412 (2006).

[145] D. Meier, N. Aliouane, D. N. Argyriou, J. A. Mydosh and T. Lorenz, New Journal of Physics **9**, 100 (2007).

[146] M. Garst and A. Rosch, Phys. Rev. B **72**, 205129 (2005).

[147] M. Kriener, P. Steffens, J. Baier, O. Schumann, T. Zabel, T. Lorenz, O. Friedt, R. Müller, A. Gukasov, P. Radaelli, P. Reutler, A. Revcolevschi, S. Nakatsuji, Y. Maeno and M. Braden, Phys. Rev. Lett. **95**, 267403 (2005).

[148] I. Loa, X. Wang, K. Syassen, H. Roth, T. Lorenz, M. Hanfland and Y.-L. Mathis, J. Phys.: Cond. Matt. **19**, 406223 (2007).

[149] N. L. Ross and R. L. Angel, Am. Mineral. **84**, 277 (1999).

[150] Neutron News **3**, 29 (1992).

[151] E. Pavarini, A. Yamasaki, J. Nuss and O. K. Andersen, New J. Phys. **7**, 188 (2005).

[152] Y. Murakami, H. Kawada, H. Kawata, M. Tanaka, T. Arima, Y. Moritomo and Y. Tokura, Phys. Rev. Lett. **80**, 1932 (1998).

[153] J.-G. Cheng, Y. Sui, J.-S. Zhou, J. B. Goodenough and W. H. Su, Phys. Rev. Lett. **101**, 087205 (2008).

[154] C. Schüßler-Langeheine, private communication .

[155] M. Braden, private communication .

[156] B. T. Thole, P. Carra, F. Sette and G. van der Laan, Phys. Rev. Lett. **68**, 1943 (1992).

[157] Z. Hu, private communication.

[158] J. G. Bednorz and K. A. Müller, Z. Physik B **64**, 189 (1986).

[159] Y. Tokura, Y. Taguchi, Y. Moritomo, K. Kumagai, T. Suzuki and Y. Iye, Phys. Rev. B **48**, 14063 (1993).

[160] J. M. Tranquada, D. J. Buttrey, V. Sachan and J. E. Lorenzo, Phys. Rev. Lett. **73**, 1003 (1994).

[161] K. Kato, E. Nishibori, M. Takata, M. Sakata, T. Nakano, K. Uchihira, M. Tsubota, F. Iga and T. Takabatake, J. Phys. Soc. Japan **71**, 2082 (2002).

[162] F. J. Morin, Phys. Rev. Lett. **3**, 34 (1959).

[163] D. Qian, L. Wray, D. Hsieh, D. Wu, J. L. Luo, N. L. Wang, A. Kuprin, A. Fedorov, R. J. Cava, L. Viciu and M. Z. Hasan, Phys. Rev. Lett. **96**, 046407 (2006).

[164] F. Iga, T. Nishiguchi and Y. Nishihara, Physica B **206,207**, 859 (1995).

[165] F. Iga, T. Naka, T. Matsumoto, N. Shirakawa, K. Murata and Y. Nishihara, Physica B **223,224**, 526 (1996).

[166] M. Tsubota, F. Iga, T. Nakano, K. Uchihira and S. Kura, J. Phys. Soc. Japan **72**, 3182 (2003).

[167] S. Arumugam, K. Mydeen, N. Manivannan, M. K. Vanji, D. Prabhakaran and A. T. Boothroyd, Phys. Rev. B **73**, 212412 (2006).

[168] W. A. Groen, F. P. F. van Berkel and D. J. W. IJdo, Acta Cryst. C **42**, 1472 (1986).

[169] I. D. Brown and D. Altermatt, Acta Cryst. B **41**, 244 (1985).

[170] M. Braden, Dissertation, Universität zu Köln (1992).

[171] V. Petricek, M. Dusek and L. Palatinus, http://www-xray.fzu.cz/jana/jana2000 (2007).

[172] R. Ali and M. Yashima, J. Solid State Chem. **178**, 2867 (2005).

[173] C. Schüßler-Langeheine, private communication .

[174] S. Grenier, J. P. Hill, D. Gibbs, K. J. Thomas, M. v. Zimmermann, C. S. Nelson, V. Kiryukhin, Y. Tokura, Y. Tomioka, D. Casa, T. Gog and C. Venkataraman, Phys. Rev. B **69**, 134419 (2004).

[175] U. Staub, G. I. Meijer, F. Fauth, R. Allenspach, J. G. Bednorz, J. Karpinski, S. M. Kazakov, L. Paolasini and F. d'Acapito, Phys. Rev. Lett. **88**, 126402 (2002).

[176] Y. Murakami, H. Kawada, H. Kawata, M. Tanaka, T. Arima, Y. Moritomo and Y. Tokura, Phys. Rev. Lett. **80**, 1932 (1998).

[177] S. Grenier, A. Toader, J. E. Lorenzo, Y. Joly, B. Grenier, S. Ravy, L. P. Regnault, H. Renevier, J. Y. Henry, J. Jegoudez and A. Revcolevschi, Phys. Rev. B **65**, 180101 (2002).

[178] K. Nakamura, T. Arima, A. Nakazawa, Y. Wakabayashi and Y. Murakami, Phys. Rev. B **60**, 2425 (1999).

[179] H. Nakao, M. Tsubota, F. Iga, K. Uchihira, T. Nakano, T. Takabatake, K. Kato and Y. Murakami, J. Phys. Soc. Japan **73**, 2620 (2004).

[180] H. Nakao, S. Kodama, K. Kiyoto, Y. Murakami, M. Tsubota, F. Iga, K. Uchihira, T. Takabatake, H. Ohsumi, M. Mizumaki and N. Ikeda, J. Phys. Soc. Japan **75**, 094706 (2006).

[181] E. Dagotto, Science **309**, 257 (2005).

[182] N. Schittner, Diplomarbeit, Universität zu Köln (2003).

[183] Y. Maeno, H. Hashimoto, K. Yoshida, S. Nishizaki, T. Fujita, J. G. Bednorz and F. Lichtenberg, Nature **372**, 532 (1994).

[184] J. F. Schooley and W. R. Hosler, Phys Rev. Lett. **12**, 474 (1964).

[185] D. G. Schlom, Y. Jia, L.-N. Zou, . Hanei, S. Briczinski, M. A. Zurbuchen, C. W. Leitz, S. Madhavan, S. WOzniak, Y. Liu, M. E. Hawley, G. W. Brown, A. Dabkowski, H. A. Dabkowska, R. Uecker and P. Reiche, SUPERCONDUCTING AND RELATED OXIDES: PHYSICS AND NANOENGINEERING III **3481**, 226 (1998).

[186] H. D. Zhou, B. S. Conner, L. Balicas and C. R. Wiebe, Phys. Rev. Lett. **99**, 136403 (2007).

[187] T. Vogt and D. J. Butterey, Phys. Rev. B **52**, R9843 (1995).

[188] J. Hemberger, P. Lunkenheimer, R. Viana, R. Böhmer and A. Loidl, Phys Rev. B **52**, 13159 (1995).

[189] W. Abriel, F. Rau and K. J. Range, Materials Research Bulletin **14**, 1463 (1979).

[190] T. Yamauchi, Y. Ueda and N. Môri, Phys. Rev. Lett. **89**, 057002 (2002).

[191] T.Yamauchi, M. Isobe and Y. Ueda, Solid State Sciences **7**, 874 (2005).

[192] Y. Ueda, M. Isobe and T. Yamauchi, J. of Phys. and Chem. of Solids **63**, 951 (2002).

[193] M. Foëx, Compt . Rend. **223**, 1126 (1946).

[194] M. Foëx, Compt . Rend. **227**, 193 (1948).

[195] R. M. Wentzcovitch, W. W. Schulz and P. B. Allen, Phys. Rev. Lett. **72**, 3389 (1994).

[196] T. M. Rice, H. Launois and J. P. Pouget, Phys. Rev. Lett. **73**, 3042 (1994).

[197] M. Marezio, D. B. McWhan, P. D. Dernier and J. P. Remeika, Phys. Rev. Lett. **28**, 1390 (1972).

[198] Y. Ueda, Y. Kitaoka, H. Yasuoka, K. Kosuge and S. Kachi, J. Phys. Soc. Jpn. **47**, 333 (1979).

[199] H. Horiuchi, M. Tokonami, N. Morimoto and K. Nagasawa, Act Cryst. B **28**, 1404 (1972).

[200] A. Byström and A. M. Byström, Acta Cryst. **3**, 146 (1950).

[201] Y. Michiue, Acta Cryst. B **63**, 577 (2007).

[202] Y. Michiue, J. Solid State Chem. **180**, 1840 (2007).

[203] M. Isobe, S. Koishi and Y. Ueda, J. Magn. and Magn. Mat. **310**, 888 (2007).

[204] H. Miura, Mineralogical Journal **13**, 119 (1986).

[205] H. U. Beyeler, Phys. Rev. Lett. **37**, 1557 (1976).

[206] A. F. Reid and A. E. Ringwood, J. Solid State Chem. **1**, 6 (1969).

[207] A. E. Ringwood, A. F. Reid and A. D. Wadsley, Acta Cryst. **23**, 1093 (1967).

[208] B. Mukherjee, Acta Cryst. **13**, 164 (1960).

[209] M. C. Cadée and G. C. Verschoor, Acta Cryst. B **34**, 3554 (1978).

[210] M. Isobe, S. Koishi, N. Kouno, J.-I. Yamaura, T. Yamauchi, H. Ueda, H. Gotou, T. Yagi and Y. Ueda, J. Phys. Soc. Japan **75**, 073801 (2006).

[211] H. T. Stokes and D. M. Hatch, *Isotropy Subgroupps of the 230 Crystallographic Space Groups*, World Scientific (1988).

[212] V. Eyert, Ann. Phys. **11**, 650 (2002).

[213] S. Minomura and H. Nagasaki, J. Phys. Soc. Japan **19**, 131 (1963).

[214] P. Y. Zavalij and M. S. Wittingham, Acta. Cryst. B **55**, 627 (1999).

[215] M. Marezio, D. B. McWhan, J. P. Remeika and P. D. Dernier, Phys. Rev. B **5**, 2541 (1971).

[216] J. P. Pouget, H. Launois, T. M. Rice, P. Dernier, A. Gossard, G. Villeneuve and P. Hagenmuller, Phys. Rev. B **10**, 1801 (1974).

[217] D. Paquet and P. Leroux-Hugon, Phys. Rev. B **22**, 5284 (1980).

[218] R. Fischer and H. Ludwiczek, Monatshefte für Chemie **106**, 223 (1975).

[219] H. M. Evjen, Phys. Rev. **39**, 675 (1932).

[220] J. M. Ziman, *Principles of the Theory of Solids*, Cambridge University Press, London, 37. Auflage (1969).

[221] S. Horiuchi, T. Shirakawa and Y. Ohta, Phys. Rev. B **77**, 155120 (2008).

[222] S. Ishiwata, J. W. G. Bos, Q. Huang and R. J. Cava, J. Phys.: Cond. Matt. **18**, 3745 (2006).

[223] R. Bachmann and H. Schulz, Acta Cryst. A **40**, 668 (1984).

[224] C. Kittel, Festkörperphysik **11** (1996).

[225] J. P. D'Haenens, D. Kaplan and P. Merenda, J. Phys. C: Solid State Phys. **8**, 2267 (1975).

[226] J. Hemberger, private communication .

[227] C. Sellier, F. Boucher and E. Janod, Solid state sciences **5**, 591 (2003).

[228] Y. Ueda and M. Isobe, J. Magn. Magn. Materials **177-181**, 741 (1998).

[229] S. Miyahara, M. Troyer, D. Johnston and K. Ueda, J. Phys. Soc. Japan **67**, 3918 (1998).

[230] B. Normand, K. Penc, M. Albrecht and F. Mila, Phys. Rev. B **56**, R5736 (1997).

[231] K. Kordonis, Dissertation, Universität zu Köln (2007).

[232] M. Hase, I. Terasaki and K. Uchinokura, Phys. Rev. Lett. **70**, 3651 (1993).

[233] Y. Ueda, Chem. Mater. **10**, 2653 (1998).

[234] M. Isobe and Y. Ueda, J. Phys. Soc. Japan **65**, 1178 (1996).

[235] M. Isobe and Y. Ueda, J. of Alloys and Compounds **262-263**, 180 (1997).

[236] J. P. Boucher and L. P. Regnault, Journal de Physique I **6**, 1939 (1996).

[237] M. C. Cross and D. S. Fisher, Phys. Rev. B **19**, 402 (1979).

[238] F. Becca, F. Mila and D. Poilblanc, Phys. Rev. Lett. **91**, 067202 (2003).

[239] A. Seidel, C. Marianetti, F. Chou, G. Ceder and P. Lee, Phys. Rev. B **67**, 020405 (2003).

[240] A. Seidel and P. Lee, Phys. Rev. B **69**, 94419 (2004).

[241] V. Kataev, J. Baier, A. Möller, L. Jongen, G. Meyer and A. Freimuth, Phys. Rev. B **68**, 140405 (2003).

[242] R. Rückamp, J. Baier, M. Kriener, M. W. Haverkort, T. Lorenz, G. S. Uhrig, L. Jongen, A. Möller, G. Meyer and M. Grüninger, Phys. Rev. Lett. **95**, 97203 (2006).

[243] A. Carpy and J. Galy, Acta. Cryst. B **31**, 1481 (1975).

[244] H. Smolinski, C. Gros, W. Weber, U. Peuchert, G. Roth, M. Weiden and C. Geibel, Phys. Rev. Lett. **80**, 5164 (1998).

[245] M. Onoda and T. Kagami, J. Phys.: Cond. Matt. **11**, 3475 (1999).

[246] P. Fertey, M. Poirier, M. Castonguay, J. Jegoudez and A. Revcolevschi, Phys. Rev. B **57**, 13698 (1998).

[247] W. Schnelle, Y. Grin and R. Kremer, Phys. Rev. B **59**, 73 (1999).

[248] S. G. Bompadre, A. F. Hebard, V. N. Kotov, D. Hall, G. Maris, J. Baas and T. T. M. Palstra, Phys. Rev. B **61**, R13321 (2000).

[249] Y. Fujii, H. Nakao, T. Yosihama, M. Nishi, K. Nakajima, K. Kakurai, M. Isobe, Y. Ueda and H. Sawa, J. Phys. Soc. Japan **66**, 326 (1997).

[250] T. Ohama, H. Yasuoka, M. Isobe and Y. Ueda, Phys. Rev. B **59**, 3299 (1999).

[251] J. Lüdecke, A. Jobst, S. v. Smaalen, E. Morré, C. Geibel and H.-G. Krane, Phys. Rev. Lett. **82**, 3633 (1999).

[252] J. L. de Boer, A. Meetsma, J. Baas and T. T. M. Palstra, Phys. Rev. Lett. **84**, 3962 (2000).

[253] H. Sawa, E. Ninomiya, T. Ohama, H. Nakao, K. Ohwada, Y. Murakam, Y. Fujii, Y. Noda, M. Isobe and Y. Ueda, J. Phys. Soc. Japan **71**, 385 (2002).

[254] H. Sawa, Y. Wakabayashi, E. Ninomiya, T. Ohama, H. Nakao, Y. Murakami, K. Ohwada, Y. Fujii, Y. Noda, M. Isobe and Y. Ueda, Physica B **329-333**, 878 (2003).

[255] N. Fujiwara, H. Yasuoka, M. Isobe and Y. Ueda, Phys. Rev. B **58**, 11134 (1998).

[256] N. Fujiwara, H. Yasuoka, M. Isobe and Y. Ueda, Phys. Rev. B **55**, R11945 (1997).

[257] M. Isobe and Y. Ueda, J. Phys. Soc. Japan **65**, 3142 (1996).

[258] J. C. Bonner and M. E. Fisher, Phys. Rev. **135**, A640 (1964).

[259] W. E. Hatfield, J. Appl. Phys. **52**, 1985 (1981).

[260] Y. Takeo, T. Yosihama, M. Nishi, K. Nakajima, K. Kakurai, M. Isobe and Y. Ueda, J. Phys. Chem. Solids **60**, 1145 (1999).

[261] Z. S. Popovic and F. R. Vukajlovic, Phys. Rev. B **59**, 5333 (1999).

[262] M. J. Konstantinovic, J. Dong, M. E. Ziaei, B. P. Clayman, J. C. Irwin, K. Yakushi, M. Isobe and Y. Ueda, Phys. Rev. B **63**, 121102 (2001).

[263] D. N. Anderson and R. D. Willett, Acta Crystallographica B **27**, 1476 (1971).

[264] P. J. Galy and A. Hardy, Acta Crystallographica B **19**, 432 (1955).

[265] H. Wu, private communication.

[266] H. . T. . Diep and H. . Giacomini, *Frustrated Spin Systems*, World Scientific Publishing Co. Pte. Ltd. Singapore (2004).

[267] A. P. Ramirez.

[268] L. Gastaldi and L. Scaramuzza, Acta Cryst. Sec. B **36**, 2751 (1980).

[269] D. Mähl, J. Pickardt and B. Reuter, Z. Anorg. Allg. Chem. **491**, 203 (1982).

[270] G. A. Samara and A. A. Giardini, Phys. Rev. **186**, 577 (1969).

[271] E. J. W. Verwey, Nature **144**, 327 (1939).

[272] L. Tang, P. Y. Zou, L. Shan, A. F. Dong, G. C. Che and H. H. Wen, Phys. Rev. B **73**, 184521 (2006).

[273] F. Fazileh, R. J. Gooding and D. C. Johnston, preprint arXiv:cond-mat/0310612v1 (2003).

[274] S. Kondo, D. C. Johnston, C. A. Swenson, F. Borsa, A. V. Mahajan, L. L. Miller, T. Gu, A. I. Goldman, M. B. Maple, D. A. Gajewski, E. J. Freeman, N. R. Dilley, R. P. Dickey, J. Merrin, K. Kojima, G. M. Luke, Y. J. Uemura, O. Chmaissem and J. D. Jorgensen, Phys. Rev. Lett. **78**, 3729 (1997).

[275] S. Kondo, D. C. Johnston and L. L. Miller, Phys. Rev. B **59**, 2609 (1999).

[276] Y. S. K. Kawakami and N. Tsuda, J. Phys. Soc. Japan **55**, 174 (1986).

[277] Y. Ueda, N. Fujiwara and H. Yasuoka, J. Phys. Soc. Jpn. **66**, 778 (1997).

[278] S.-H. Lee, D. Louca, H. Ueda, S. Park, T. J. Sato, M. Isobe, Y. Ueda, S. Rosenkranz, P. Zschack, J. I. niguez, Y. Qiu and R. Osborn, Phys. Rev. Lett. **93**(15), 156407 (2004).

[279] M. Reehuis, A. Krimmel, N. Büttgen, A. Loidl and A. Prokofiev, Eur. Phys. J. B **35**, 311 (2003).

[280] S. Niziol, Phys. Status Solidi A **18**, K11 (1973).

[281] P. G. Radaelli, New J. Phys. **7**, 53 (2005).

[282] S. D. Matteo, G. Jackeli and N. B. Perkins, Phys. Rev. B **72**, 020408 (2005).

[283] T. Maitra and R. Valenti, Physical Review Letters **99**, 126401 (2007).

[284] Y. Yamashita and K. Ueda, Phys. Rev. Lett. **85**, 4960 (2000).

[285] H. Tsunetsugu and Y. Motome, Phys. Rev. B **68**, 060405 (2003).

[286] O. Tchernyshyov, Phys. Rev. Lett. **93**, 157206 (2004).

[287] D. I. Khomskii and T. Mizokawa, Phys. Rev. Lett. **94**, 156402 (2005).

[288] T. Suzuki, M. Katsumura, K. Taniguchi, T. Arima and T. Katsufuji, Phys. Rev. Lett. **98**, 127203 (2007).

[289] T. Katsufuji, private communication.

[290] N. Nishiguchi and M. Onoda, J. Phys.: Cond. Matt. **14**, L551 (2002).

[291] D. I. Khomskii, private communication .

[292] V. Pardo, S. Blanco-Canosa, F. Rivadulla, D. I. Khomskii, D. Baldomir, H. Wu and J. Rivas, Physical Review Letters **101**, 256403 (2008).

[293] S. Ebbinghaus, J. Hanss, M. Klemm and S. Horn, J. Alloys Comp. **370**, 75 (2004).

[294] P. Pfalzer, Dissertation, Universität Augsburg (2004).

[295] T. Hahn, *TablesInternational Tables of Crystallography Vol. A*, Kluwer Academic Publishers (2002).

[296] Y. Ren, T. T. M. Palstra, D. I. Khomskii, E. Pellegrin, A. A. Nugroho, A. A. Menovsky and G. A. Sawatzky, Nature **396**, 441 (1998).

[297] C. Ulrich, G. Khaliullin, J. Sirker, M. Reehuis, M. Ohl, S. Miyasaka, Y. Tokura and B. Keimer, Phys. Rev. Lett. **91**, 257202 (2003).

[298] G. R. Blake, T. T. M. Palstra, Y. Ren, A. A. Nugroho and A. A. Menovsky, Phys. Rev. Lett. **87**, 245501 (2001).

[299] S. Ishihara, Phys. Rev. Lett. **94**, 156408 (2005).

[300] G. Khaliullin and S. Maekawa, Phys. Rev. Lett. **85**, 3950 (2000).

[301] D. I. Khomskii and T. Mizokawa, Phys. Rev. Lett. **94**, 156402 (2005).

[302] J. B. Goodenoug, Interscience publishers, New York-London (1963).

[303] Y. Yoshida, S.-I. Ikeda, H. Matsuhata and N. Shirakawa, Phys. Rev. B **72**, 054412 (2005).

[304] D. N. Argyriou, J. F. Mitchell, P. G. Radaelli, H. N. Bordallo, D. E. Cox, M. Medarde and J. D. Jorgensen, Phys Rev. B **59**, 8695 (1999).

[305] J. F. Weiher, B. L. Chamberland and J. L. Gillson, J. Solid State Chem. **3**, 529 (1971).

[306] A. J. Williams, A. Gillies, J. P. Attfield, G. Heymann, H. Huppertz, M. J. Martínez-Lope and J. A. Alonso, Phys Rev. B **73**, 104409 (2006).

[307] L. O.-S.-Martin, A. J. Williams, J. R. J. P. Attfield, G. Heymann and H. Huppertz, Phys Rev. Lett. **99**, 255701 (2007).

[308] B. L. Chamberland, Solid State Commun. **5**, 663 (1967).

[309] J. B. Goodenough, J. M. Longo and J. A. Kafalas, Mater. Res. Bull. **3**, 471 (1968).

[310] J.-S. Zhou, C.-Q. Jin, Y.-W. Long, L.-X. Yang and J. B. Goodenough, Phys. Rev. Lett. **96**, 046408 (2006).

[311] W. Baugal, W. Kunn, H. Kleischmager and F. J. Rohr, J. Power Sources **1**, 203 (1976/77).

[312] W. Feduska and A. O. Isenberg, J. Power Sources **10**, 89 (1983).

[313] W. Shafer and R. Schmidberger, High Tech Ceramics, Elsevier, Amsterdam (1987).

[314] D. B. Meadowcroft, Br. J. Appl. Phys. **2**, 1225 (1969).

[315] A. Liebsch and H. Ishida, Phys. Rev. Lett. **98**, 216403 (2007).

[316] M. Braden, G. André, S. Nakatsuji and Y. Maeno, Phys. Rev. B **58**, 847 (1998).

[317] O. Friedt, M. Braden, G. André, P. Adelmann, S. Nakatsuji and Y. Maeno, Phys. Rev. B **63**, 174432 (2001).

[318] A. C. Komarek, S. V. Streltsov, M. Isobe, T. Moller, M. Hoelzel, A. Senyshyn, D. Trots, M. T. Fernandez-Diaz, T. Hansen, H. Gotou, T. Yagi, Y. Ueda, V. I. Anisimov, M. Gruninger, D. I. Khomskii and M. Braden, Phys. Rev. Lett. **101**, 167204 (2008).

[319] N. Sakai, H. Fjellvåg and B. C. Hauback, J. Solid State Chem. **121**, 202 (1996).

[320] J. M. D. Coey and M. Venkatesan, J. Appl. Phys. **91 No. 10**, 8345 (2002).

[321] J. Dai, J. Tang, H. Xu, L. Spinu, W. Wang, K. Wang, A. Kumbhar, M. Li and U. Diebold, Appl. Phys. Lett. **77 No. 18**, 2840 (2000).

[322] T. Möller, Dissertation, Universität zu Köln, *in preparation* .

[323] G. Cao, S. McCall, M. Shepard, J. E. Crow and R. P. Guertin, Phys. Rev. B **56**, 321 (1997).

[324] B. L. Chamberland and C. W. Moeller, J. Solid State Chem. **5**, 39 (1972).

[325] W. L. Roth and R. C. DeVries, J. Appl. Physics **38**, 951 (1967).

[326] B. L. Chamberland, Solid State Commun. **5**, 663 (1967).

[327] E. Castillo-Martínez, A. Durán and M. Á. Alario-Franco, J. Solid State Chem. **181**, 895 (2008).

[328] J. P. DHaenens, D. Kaplan and P. Merenda, J. Phys. C: Solid State Phys. **8** (1975).

[329] F. D. Murnaghan, Am. J. Math. **49**, 235 (1937).

[330] F. Birch, Phys. Rev. **71**, 809 (1947).

[331] F. Birch, J. Geophys. Res. B **83**, 1257 (1978).

[332] J. Zaanen and O. Gunnarsson, Phys. Rev. B **40**, 7391 (1989).

[333] J. M. Tranquada, J. E. Lorenzo, D. J. Buttrey and V. Sachan, Phys. Rev. B **52**, 3581 (1995).

[334] S. M. Hayden, G. H. Lander, J. Zarestky, P. J. Brown, C. Stassis, P. Metcalf and J. M. Honig, Phys. Rev. Lett. **68**, 1061 (1992).

[335] C. H. Chen, S.-W. Cheong and A. S. Cooper, Phys. Rev. Lett. **71**, 2461 (1993).

[336] J. Rodriguez-Carvajal, M. T. Fernandez-Diaz and J. L. Martinez, J. Phys.: Cond. Matt. **3**, 3215 (1991).

[337] K. Ishizaka, T. Arima, Y. Murakami, R. Kajimoto, H. Yoshizawa, N. Nagaosa and Y. Tokura, Phys. Rev. Lett. **92**, 196404 (2004).

[338] R. Kajimoto, K. Ishizaka, H. Yoshizawa and Y. Tokura, Phys. Rev. B **67**, 014511 (2003).

[339] R. Kajimoto, T. Kakeshita, H. Yoshizawa, T. Tanabe, T. Katsufuji and Y. Tokura, Phys. Rev. B **64**, 144432 (2001).

[340] H. Yoshizawa, T. Kakeshita, R. Kajimoto, T. Tanabe, T. Katsufuji and Y. Tokura, Phys. Rev. B **61**, R854 (2000).

[341] T. Katsufuji, T. Tanabe, T. Ishikawa, S. Yamanouchi, Y. Tokura, T. Kakeshita, R. Kajimoto and H. Yoshizawa, Phys. Rev. B **60**, R5097 (1999).

[342] V. Sachan, D. J. Buttrey, J. M. Tranquada, J. E. Lorenzo and G. Shirane, Phys. Rev. B **51**, 12742 (1995).

[343] J. M. Tranquada, D. J. Buttrey and V. Sachan, Phys. Rev. B **54**, 12318 (1996).

[344] R. J. Birgeneau and G. Shirane, edited by D. M. Ginsberg, World Scientific, Singapore (1989).

[345] S.-W. Cheong, H. Y. Hwang, C. H. Chen, B. Batlogg, L. W. R. S. A. and Carter, Phys. Rev. B **49**, 7088 (1994).

[346] R. J. McQueeney, J. L. Sarrao and R. Osborn, Phys. Rev. B **60**, 80 (1999).

[347] T. Ido, K. Magoshi, H. Eisaki and S. Uchida, Phys. Rev. B **44**, 12094 (1991).

[348] H. Eisaki, S. Uchida, T. Mizokawa, H. Namatame, A. Fujimori, van J. Elp, P. Kuiper, G. A. S. S. Hosoya and H. Katayama-Yoshida, Phys. Rev. B **45**, 12513 (1992).

[349] S. Uchida, T. Ido, H. Takagi, T. Arima, Y. Tokura and S. Tajima, Phys. Rev. B **43**, 7942 (1991).

[350] B. Büchner, Dissertation, Universität zu Köln (1994).

[351] B. Grande, H. Müller-Buschbaum and M. Schweizer, Z. f. anorgan. u. allg. Chem. **428**, 120 (1977).

[352] J. M. Tranquada, Y. Kong, J. E. Lorenzo, D. J. Buttrey, D. E. Rice and V. Sachan, Phys. Rev. B **50**, 6340 (1994).

[353] J. M. Tranquada, D. J. Buttrey and D. E.Rice, Phys. Rev. Lett. **70**, 445 (1993).

[354] D. E. Rice and D. J. Buttrey, J. Solid State Chem. **105**, 197 (1993).

[355] J. E. Lorenzo, J. M. Tranquada, D. J.Buttrey and V. Sachan, Phys. Rev. B **51**, 3176 (1995).

[356] P. Wochner, J. M. Tranquada, D. J. Buttrey and V. Sachan, Phys. Rev. B **57**, 1066 (1998).

[357] S.-H. Lee, S.-W. Cheong, K. Yamada and C. F. Majkrzak, Phys. Rev. B **63**, 060405R (2001).

[358] S.-H. Lee and S.-W. Cheong, Phys. Rev. Lett. **79**, 2514 (1997).

[359] E. Fawcett, H. L. Alberts, V. Y. Galkin, D. R.Noakes and J. V. Yakhmi, Rev. Mod. Phys. **66**, 25 (1994).

[360] C. Schüssler-Langeheine, J. Schlappa, A. Tanaka, Z. Hu, C. F. Chang, E. Schierle, M. Benomar, H. Ott, E. Weschke, G. Kaindl, O. Friedt, G. A. Sawatzky, H.-J. Lin, C. T. Chen, M. Braden and L. H. Tjeng, Physical Review Letters **95**, 156402 (2005).

[361] J. Schlappa, Dissertation, Universität zu Köln (2006).

[362] F. C. Zhang and T. M. Rice, Phys. Rev. B **37**, 3759 (1988).

[363] K. Ishizaka, Y. Taguchi, R. Kajimoto, H. Yoshizawa and Y. Tokura, Phys. Rev. B **67**, 184418 (2003).

[364] R. Kajimoto, K. Ishizaka, H. Yoshizawa and Y. Tokura, Phys. Rev. B **67**, 014511 (2003).

[365] M. Fujita, H. Goka, K. Yamada, J. M. Tranquada and L. P. Regnault, Phys. Rev. B **70**, 104517 (2004).

[366] N. Hasselmann, A. H. C. Neto and C. M. Smith, Phys. Rev. B **69**, 014424 (2004).

[367] G. S. Uhrig, K. P. Schmidt and M. Grüninger, Phys. Rev. Lett. **93**, 267003 (2004).

[368] C. D. Batista, G. Ortiz and A. V. Balatsky, Phys. Rev. B **64**, 172508 (2001).

[369] E. W. Carlson, D. X. Yao and D. K. Campbell, Phys. Rev. B **70**, 064505 (2004).

[370] F. Krüger and S. Scheidl, Phys. Rev. B **67**, 134512 (2003).

[371] J. M. Tranquada, P. Wochner and D. J. Buttrey, Phys. Rev. Lett. **79**, 2133 (1997).

[372] A. T. Boothroyd, D. Prabhakaran, P. G. Freeman, S. J. S. Lister, M. Enderle, A. Hiess and J. Kulda, Phys. Rev. B **67**, 100407 (2003).

[373] P. Bourges, Y. Sidis, M. Braden, K. Nakajima and J. M. Tranquada, Phys. Rev. Lett. **90**, 147202 (2003).

[374] H. Woo, A. T. Boothroyd, K. Nakajima, T. G. Perring, C. D. Frost, P. G. Freeman, D. Prabhakaran, K. Yamada and J. M. Tranquada, Phys. rev. B **72**, 064437 (2005).

[375] P. G. Freeman, A. T. Boothroyd, D. Prabhakaran, C. D. Frost, M. Enderle and A. Hiess, Phys. Rev. B **71**, 174412 (2005).

[376] K. Nakajima, K. Yamada, S. Hosoya, T. Omata and Y. Endoh, J. Phys. Soc. Japan **62**, 438 (1993).

[377] L. Pintschovius, W. Reichardt, M. B. andG. Dhalenne and A. Revcolevschi, Phys. Rev. B **64**, 094510 (2001).

[378] S. L. Chaplot, W. Reichardt, L. Pintschovius and N. Pyka, Phys. Rev. B **52**, 7230 (1995).

[379] M. Braden, L. Pintschovius, T. Uefuji and K. Yamada, Phys. Rev. B **72**, 184517 (2005).

[380] J. M. Tranquada, K. Nakajima, M. Braden, L. Pintschovius and R. J. McQueeney, Phys. Rev. Lett. **88**, 075505 (2002).

[381] L. Pintschovius and M. Braden, Phys. Rev. B **60**, R15039 (1999).

[382] A. T. Boothroyd, P. G. Freeman, D. Prabhakaran, A. Hiess, M. Enderle, J. Kulda and F. Altorfer, Phys. Rev. Lett. **91**, 257201 (2003).

[383] A. C. Komarek, MultiSPEC (2005-2008).

[384] Numerical Recipes in C, Second Edition, nr.com (1992).

[385] Origin 7.5, http://www.additive-net.de/software/origin (1991-2008).

[386] K. Nakajima, K. Yamada, S. Hosoya, T. Omata and Y. Endoh, J. Phys. Soc. Japan **62**, 4438 (1993).

[387] A. Zheludev, ResLib v.2.1, Brookhaven National Laboratory (1999-2000).

[388] A. Schilling, M. Cantoni, J. D. Guo and H. R. Ott, Nature **363**, 56 (1993).

[389] L. Gao, Y. Y. Xue, F. Chen, Q. Xiong, R. L. Meng, D. Ramirez and C. W. Chu, Phys. Rev. B **50**, 4260 (1994).

[390] M. Hücker, Dissertation, Universität zu Köln (2000).

[391] M. A. Kastner, R. J. Birgeneau, G. Shirane and Y. Endoh, Rev. Mod. Phys. **70**, 897 (1998).

[392] H. Takagi, B. Batlogg, H. L. Kao, J. Kwo, R. J. Cava, J. J. Krajewski and W. F. Peck, Phys. Rev. Lett. **69**, 2975 (1992).

[393] Y. Ando, S. Komiya, K. Segawa, S. Ono and Y. Kurita, Phys. Rev. Lett. **93**, 267001 (2004).

[394] N. B. Christensen, H. M. Ronnow, J. Mesot, R. A. Ewings, N. Momono, M. Oda, M. Ido, M. Enderle, D. F. McMorrow and A. T. Boothroyd, Phys. Rev. Lett. **98**, 197003 (2007).

[395] P. Abbamonte, A. Rusydi, S. Smadici, G. D. Gu, G. A. Sawatzky and D. L. Feng, Nat. Phys. **1**, 155 (2005).

[396] N. Ichikawa, S. Uchida, J. M. Tranquada, T. Niemöller, P. M. Gehring, S.-H. Lee and J. R. Schneider, Phys. Rev. Lett. **85**, 1738 (2000).

[397] Y.-J. Kim, G. D. Gu, T. Gog and D. Casa, Phys. Rev. B **77**, 064520 (2008).

[398] M. Hücker, G. D. Gu, J. M. Tranquada, M. v. Zimmermann, H.-H. Klauss, N. J. Curro, M. Braden and B. Büchner, Physica C **460-462**, 170 (2007).

[399] S. R. Dunsiger, Y. Zhao, Z. Yamani, W. J. L. Buyers, H. A. Dabkowska and B. D. Gaulin, Phys. Rev. B **77**, 224410 (2008).

[400] J. M. Tranquada, G. D. Gu, M. Hücker, Q. Jie, H.-J. Kang, R. Klingeler, Q. Li, N. Tristan, J. S. Wen, G. Y. Xu, Z. J. Xu, J. Zhou and M. v. Zimmermann, Phys. Rev. B **78**, 174529 (2008).

[401] J. Fink, E. Schierle, E. Weschke, J. Geck, D. Hawthorn, H. Wadati, H. H. Hu, H. A. Durr, N. Wizent, B. Büchner and G. A. Sawatzky, preprint cond-mat/0805.4352 (2008).

[402] S.-W. Cheong, G. Aeppli, T. E. Mason, H. Mook, S. M. Hayden, P. C. Canfield, Z. Fisk, K. N. Clausen and J. L. Martinez, Phys. Rev. Lett. **67**, 1791 (1991).

[403] T. E. Mason, G. Aeppli, S. M. Hayden, A. P. Ramirez and H. A.Mook, Phys. Rev. Lett. **71**, 919 (1993).

[404] K. Yamada, S. Wakimoto, G. Shirane, C. H. Lee, M. A. Kastner, S. Hosoya, M. Greven, Y. Endoh and R. J. Birgeneau, Phys. Rev. Lett. **75**, 1626 (1995).

[405] M. Matsuda, K. Yamada, Y. Endoh, T. R. Thurston, G. Shirane, R. J. Birgeneau, M. A. Kastner, I. Tanaka and H. Kojima, Phys. Rev. B **49**, 6958 (1994).

[406] S. A. Kivelson, I. P. Bindloss, E. Fradkin, V. Oganesyan, J. M. Tranquada, A. Kapitulnik and C. Howald, Rev. Mod. Phys. **75**, 1201 (2003).

[407] T. Suzuki, T. Goto, K. Chiba, T. Shinoda, T. Fukase, H. Kimura, K. Yamada, M. Ohashi and Y. Yamaguchi, Phys. Rev. B **57**, R3229 (1998).

[408] K. Yamada, C. H. Lee, K. Kurahashi, J. Wada, S. Wakimoto, S. Ueki, H. Kimura, Y. Endoh, S. Hosoya, G. Shirane, R. J. Birgeneau, M. Greven, M. A. Kastner and Y. J. Kim, Phys. Rev. B **57**, 6165 (1998).

[409] S. Wakimoto, G. Shirane, Y. Endoh, K. Hirota, S. Ueki, K. Yamada, R. J. Birgeneau, M. A. Kastner, Y. S. Lee, P. M. Gehring and S. H. Lee, Phys. Rev. B **60**, R769 (1999).

[410] S. Wakimoto, R. J. Birgeneau, M. A. Kastner, Y. S. Lee, R. Erwin, P. M. Gehring, S. H. Lee, M. Fujita, K. Yamada, Y. Endoh, K. Hirota and G. Shirane, Phys. Rev. B **61**, 3699 (2000).

[411] M. Matsuda, Y. S. Lee, M. Greven, M. A. Kastner, R. J. Birgeneau, K. Yamada, Y. Endoh, P. Böni, S.-H. Lee, S. Wakimoto and G. Shirane, Phys. Rev. B **61**, 4326 (2000).

[412] S. Wakimoto, S. Ueki, Y. Endoh and K. Yamada, Phys. Rev. B **62**, 3547 (2000).

[413] M. Matsuda, M. Fujita, K. Yamada, R. J. Birgeneau, M. A. Kastner, H. Hiraka, Y. Endoh, S. Wakimoto and G. Shirane, Phys. Rev. B **62**, 9148 (2000).

[414] M. Matsuda, M. Fujita, K. Yamada, R. J. Birgeneau, Y. Endoh and G. Shirane, Phys. Rev. B **66**, 174508 (2002).

[415] S. Wakimoto, J. M. Tranquada, T. Ono, K. M. Kojima, S. Uchida, S.-H. Lee, P. M. Gehring and R. J. Birgeneau, Phys. Rev. B **64**, 174505 (2001).

[416] S. R. Dunsiger, Y. Zhao, B. D. Gaulin, Y. Qiu, P. Bourges, Y. Sidis, J. R. D. Copley, A. Kallin, E. M. Mazurek and H. A. Dabkowska, Phys. Rev. B **78**, 092507 (2008).

[417] N. Hasselmann, A. H. Castro Neto and C. Morais Smith, Phys. Rev. B **69**, 014424 (2004).

[418] O. P. Sushkov and V. N. Kotov, Phys. Rev. Lett. **94**, 097005 (2005).

[419] P.-A. Lindgard, Phys. Rev.Lett. **95**, 217001 (2005).

[420] M. Braden, L. Pintschovius, T. Uefuji and K. Yamada, Phys. Rev. B **72**, 184517 (2005).

[421] M. Braden, Y. Sidis, P. Bourges, P. Pfeuty, J. Kulda, Z. Mao and Y. Maeno, Phys. Rev. B **66**, 064522 (2002).

[422] M. Tachiki and S. Takahashi, Phys. Rev. B **39**, 293 (1989).

[423] M. Braden, W. Reichardt, Y. Sidis, Z. Mao and Y. Maeno, Phys. Rev. B **76**, 014505 (2007).

[424] B. Renker, F. Gompf, E. Gering, G. Roth, W. Reichardt, D. Ewert, H. Rietschel and H. Mutka, Z. Phys. **71**, 437 (1988).

[425] B. Renker, F. Gompf, E. Gering, N. Nücker, D. Ewert, W. Reichardt and H. Rietschel, Z. Phys. **67**, 15 (1987).

[426] B. Renker, F. Gompf, E. Gering, D. Ewert, H. Rietschel and A. Dianoux, Z. Phys. **73**, 309 (1988).

[427] L. Pintschovius and M. Braden, Phys. Rev. B **60**, R15039 (1999).

[428] W. Reichardt, J. Low Temp. Phys. **105**, 807 (1996).

[429] M. d'Astuto, P. K. Mang, P. Giura, A. Shukla, P. Ghigna, A. Mirone, M. Braden, M. Greven, M. Krisch and F. Sette, Phys. Rev. Lett. **88**, 167002 (2002).

[430] H. J. Kang, P. Dai, D. Mandrus, R. Jin, H. A. Mook, D. T. Adroja, S. M. Bennington, S.-H. Lee and J. W. Lynn, Phys. Rev. B **66**, 064506 (2002).

[431] A. Lanzara, P. V. Bogdanov, X. J. Zhou, S. A. Kellar, D. L. Feng, E. D. Lu, T. Yoshida, H. Eisaki, A. Fujimori, K. Kishio, J.-I. Shimoyama, T. Noda, S. Uchida, Z. Hussain and Z.-X. Shen, Nature **412**, 510 (2001).

[432] G. Xiao, M. Z. Cieplak, J. Q. Xiao and C. L. Chien, Phys. Rev. B **42**, 8752 (1990).

[433] H. Kimura, K. Hirota, H. Matsushita, K. Yamada, Y. Endoh, S.-H. Lee, C. F. Majkrzak, R. Erwin, G. Shirane, M. Greven, Y. S. Lee, M. A. Kastner and R. J. Birgeneau, Phys. Rev. B **59**, 6517 (1999).

[434] Y. Koike, A. Kobayashi, T. Kawaguchi, M. Kato, T. Noji, Y. Ono, T. Hikita and Y. Saito, Solid State Commun. **82**, 889 (1992).

[435] M. Kofu, H. Kimura and K. Hirota, Phys. Rev. B **72**, 064502 (2005).

[436] M. Matsuda, M. Fujita and K. Yamada, Phys. Rev. B **73**, 140503(R) (2006).

[437] R. J. McQueeney, Y. Petrov, T. Egami, M. Yethiraj, S. hirane and Y. Endoh, Phys. Rev. Lett. **82**, 628 (1999).

[438] M. Braden, private communication.

[439] M. Shaz, S. v. Smaalen, L. Palatinus, M. Hoinkis, M. Klemm, S. Horn and R. Claessen, Phys. Rev. B **71**, 100405 (2005).

[440] G. Caimi, L. Degiorgi, N. N. Kovaleva, P. Lemmens and F. C. Chou, Phys. Rev. B **69**, 125108 (2004).

[441] P. Lemmens, K. Y. Choi, G. Caimi, L. Degiorgi, N. N. Kovaleva, A. Seidel and F. C. Chou, Phys. Rev. B **70**, 134429 (2004).

[442] T. Saha-Dasgupta, R. Valentí, H. Rosner and C. Gros, Europhys. Lett. **67**, 63 (2004).

[443] S. van Smaalen, L. Palatinus and A. Schönleber, Phys. Rev. B **72**, 020105R (2005).

[444] A. Schönleber, S. v. Smaalen and L. Palatinus, Phys. Rev. B **73**, 214410 (2006).

[445] C. A. Kuntscher, A. Pashkin, H. Hoffmann, S. Frank, M. Klemm, S. Horn, A. Schönleber, S. van Smaalen, M. Hanfland, S. Glawion, M. Sing and R. Claessen, Phys. Rev. B **78**, 035106 (2008).

[446] M. K. Forthaus, T. Taetz, A. Möller and M. M. Abd-Elmeguid, Phys. Rev. B **77**, 165121 (2008).

[447] S. Blanco-Canosa, F. Rivadulla, A. Pineiro, V. Pardo, D. Baldomir, D. I. Khomskii, M. M. Abd-Elmeguid, M. A. López-Quintela and J. Rivas, preprint cond-mat/0806.0230 (2008).

[448] Y.-Z. Zhang, H. O. Jeschke and R. Valentí, Phys. Rev. Lett. **101**, 136406 (2008).

[449] A. Krimmel, J. Strempfer, B. Bohnenbuck, B. Keimer, M. Hoinkis, M. Klemm, S. Horn, A. Loidl, M. Sing, R. Claessen and M. v. Zimmermann, Phys. Rev. B **73**, 172413 (2006).

[450] R. R. Pawar and V. T. Deshpande, Acta Cryst. A **24**, 316 (1968).

[451] D. Errandonea, Y. Meng, M. Somayazulu and D. Häusermann, Physica B: Cond. Matt. **355**, 116 (2005).

[452] J. P. Vénien, P. Palvadeau, D. Schleich and J. Rouxel, Mat. Res. Bull. **14**, 891 (1979).

[453] A. Wiedenmann, J. P. Venien, P. Palvadeau and J. Rossat-Mignod, J.Phys. C.: Solid State Phys. **16**, 5339 (1983).

[454] S. M. Kauzlarich, J. L. Stanton, J. Faber and B. A. Averill, J. Am. Chem. Soc. **108**, 7946 (1986).

[455] S. R. Hwang, W.-H. Li, K. C. Lee, J. W. Lynn and C.-G. Wu, Phys. Rev. B **62**, 14157 (2000).

[456] A. N. Christensen, T. Johansson and S. Quézel, Acta Chem. Scand. A **28**, 1171 (1975).

[457] A. Haase and G. Brauer, Acta Cryst. B **31**, 2521 (1975).

[458] E. Benckiser, R. Rückamp, T. Möller, T. Taetz, A. Möller, A. A. Nugroho, T. T. M. Palstra, G. S. Uhrig and M. Grüninger, New J. Phys. **10**, 053027 (2008).

[459] H. Schäfer and F. Wartenpfuhl, J. Less. Com. Metals **3**, 29 (1961).

[460] M. Hase, I. Terasaki and K. Uchinokura, Phys. Rev. Lett. **70**, 3651 (1993).

[461] M. Braden, G. Wilkendorf, J. Lorenzana, M. Aï, G. McIntyre, M. Behruzi, G. Heger, G. Dhalenne and A. Revcolevschi, Phys. Rev. B **54**, 1105 (1996).

[462] W. Geertsma and D. Khomskii, Phys. Rev. B **54**, 3011 (1996).

[463] R. Werner, C. Gros and M. Braden, Phys. Rev. B **59**, 14356 (1999).

[464] T. Kimura, T. Goto, H. Shintani, K. Ishizaka, T. Arima and Y. Tokura, Nature **426**, 55 (2003).

[465] D. Senff, Dissertation, Universität zu Köln (2007).

[466] M. Fiebig, Journal of Physics D: Applied Physics **38**, 123 (2005).

[467] W. Eerenstein, N. D. Mathur and J. F. Scott, Nature **442**, 759 (2006).

[468] U. Adem, Dissertation, Universität Groningen (2008).

[469] J. W. F. Brown, R. M. Hornreich and S. Shtrikman, Phys. Rev. **168**, 574 (1968).

[470] F. Kubel and H. Schmid, Acta Crystallogr. B **46**, 698 (1990).

[471] M. Fiebig, T. Lottermoser, D. Frohlich, A. Goltsev and R. Pisarev, Nature **419**, 818 (2002).

[472] E. F. Bertaut and M. Mercier, Phys. Lett. **5**, 27 (1963).

[473] G. A. Smolenskii and I. E. Chupis, Sov. Phys. Usp. **25**, 475 (1983).

[474] M. Mostovoy, Phys. Rev. Lett. **96**, 067601 (2006).

[475] M. Kenzelmann, A. B. Harris, S. Jonas, C. Broholm, J. Schefer, S. B. Kim, C. L. Zhang, S.-W. Cheong, O. P. Vajk and J. W. Lynn, Phys. Rev. Lett. **95**, 087206 (2005).

[476] S. Jodlauk, P.Becker, J. A. Mydosh, D. I. Khomskii, T. Lorenz, S. V. Streltsov, D. C. Hezel and L. Bohatý, J. Phys.: Cond. Matt. **19**, 432201 (2007).

[477] S. Jodlauk, Dissertation, Universität zu Köln, *in preparation* .

[478] O. Ballet, J. M. D. Coey, G. Fillion, A. Ghose, A. Hewat and J. R. Regnard, Phys. Chem. Minerals **16**, 672 (1989).

[479] G. J. Redhammer, G. Roth, W. Paulus, G. André, W. Lottermoser, G. Amthauer, W. Treutmann and B. Koppelhuber-Bitschnau, Phys. Chem. Minerals **28**, 337 (2001).

[480] J. F. Schooley, W. R. Hosler and M. L. Cohen, Phys. Rev. Lett. **12**, 474 (1964).

[481] H. Suzuki, H. Bando, Y. Ootuka, I. H. Inoue, T. Yamamoto, K. Takahashi and Y. Nishihara, J. Phys. Soc. Japan **65**, 1529 (1996).

[482] S.-I. Akimoto and Y. Syono, Am. Mineral. **57**, 76 (1972).

Danksagung

Ein besonderer Dank gebührt an dieser Stelle meinem Doktorvater Prof. M. Braden, der mir die Möglichkeit gegeben hat an solch interessanten und aktuellen Forschungsgebieten wie z. B. den Kupraten zu arbeiten und mir gleichzeitig die Freiräume gelassen hat, um auch meine eigenen Ideen zu verfolgen. Vielen Dank auch für das entgegengebrachte Vertrauen und die wohlwollende Unterstützung bei dieser Arbeit.

Den Mitgliedern der Prüfungskommission, Prof. M. Grüninger und Prof. L. Bohatý, danke ich für ihre Bereitschaft meine Arbeit zu lesen und die Gutachten zu verfassen, sowie für ihre Zusammenarbeit auf dem Gebiet der Chromate bzw. der Ferrosilikate.

Weiterhin möchte ich Prof. D. I. Khomskii herzlich danken für die vielen sehr aufschlussreichen und interessanten Gespräche.

Desweiteren möchte ich allen Probenpräparatoren danken für die unzähligen, zumeist hervorragenden und in jedem Fall sehr spannenden Kristalle, ohne die keine Messungen möglich gewesen wären, abgesehen von den in dieser Arbeit selbst hergestellten Kristallen natürlich. In diesem Zusammenhang gilt mein besonderer Dank Prof. K. Yamada und H. Haruhiro, K. Ikeuchi und F. Fujita für die umfangreiche Kollaboration auf dem Gebiet der Kuprate und für interessante Diskussionen. Auch F. Nakamura möchte ich für einen Kuprat Kristall danken. Desweiteren möchte ich M. Benomar und A. A. Nugruho für die Nickelatkristalle sowie für die wichtigen Informationen zur Kristallzucht danken. Bei Prof. P. Becker-Bohatý möchte ich mich für die Aegirin-Kristalle bedanken. Weiterhin danke ich Prof. M. Isobe für die ganzen Hollandit Kristalle, Kalzium- und Strontium-Chromate, Zink- und Lithium-Vanadate sowie für seine überaus nette Art. M. Azuma möchte ich für das Blei-Chromat danken. Und bei T. Taetz und A. Möller möchte ich mich für das TiOCl und VOCl bedanken sowie auch für interessante Diskussionen. H. Roth danke ich für die ersten Titanatkristalle. M. Reuther möchte ich für wichtige Informationen zur Kristallzucht danken sowie für die Kooperation auf dem Gebiet der Kobaltate und nette Diskussionen und für die freundliche Durchführung so mancher Magnetisierungsmessung. Auch M. Valldor möchte ich für wichtige Informationen zur Kristallzucht sowie für nette Gespräche danken, aber auch für Zusammenarbeit bei einigen neuen Mangan- und Kobaltverbindungen.

Ein ganz besonderer Dank gilt auch C. Schüßler-Langeheine für die äußerst angenehme Zusammenarbeit auf dem Gebiet der resonanten Streuung am Synchrotron und das Korrekturlesen der entsprechenden Teile dieser Arbeit. Ich habe die gemeinsamen Aufenthalte und Messungen am BESSY sehr genossen. In diesem Zusammenhang danke ich an dieser Stelle auch recht herzlich H.-H. Wu und C. Trabant für ihre Kollaboration und Hilfsbereitschaft.

Ein großer Dank geht auch an J. Hemberger fuer die gemeinsame Zusammenarbeit bei ESR Messungen und der Suche nach interessanten Materialeigenschaften sowie steter Hilfsbereitschaft.

Weiterhin danke ich T. Lorenz und J. Rohrkamp für thermische Ausdehnungsmessungen und aufschlussreiche Gespräche.

Desweiteren danke ich Z. Hu für die Zusammenarbeit auf dem Gebiet der Titanate.

S. Jodlauk möchte ich für die langjärige Begleitung auf dem Gebiet der Physik und

für interessante Gespräche sowie auch für die gemeinsame Zusammenarbeit danken. T. Möller sei herzlich für seine Zusammenarbeit auf dem Gebiet der Chromate gedankt. M. Forthaus möchte ich recht herzlich für die Unterstützung bei der Druckmessung an Titanaten sowie für interessante Informationen zu Druckmessungen danken. M. Baum möchte ich für die Unterstützung bei der Druckmessung an Chromaten danken. O. Heyer danke ich recht herzlich für die Messung der spezifischen Wärme sowie von Messungen des elektrischen Widerstands bei ∼300 mK. S. Heiligen möchte ich für unzählige TGA Messungen sowie Magnetisierungsmessungen danken. I. Simons danke ich für EDX Messungen. H. Wu danke ich für die Rechnungen des Lithiumvanadats. N. Johansen danke ich für Hall-Effekt Messungen an Kalziumchromat. H. Kierspel und R. Dommel danke ich für die stete Versorgung mit flüssigem Helium. A. Solugubenko, M. Kriener, M. Hücker und Prof. M. Abd-Elmeguid danke ich für interessante Diskussionen. O. Schumann und neuerdings auch O. Breunig möchte ich für die Unterstützung bei Computerfragen danken.

Vor allem der gesamten Neutronengruppe aber auch den restlichen noch nicht genannten (und auch den genannten) Institutsmitgliedern danke ich recht herzlich für das gute, ruhige, angenehme Arbeitsklima.

Schlußendlich danke ich recht herzlich allen Instrumentwissenschaftlern, die mich so tatkräftig unterstützt und die Messungen am laufen gehalten haben.

Am FRM-II danke ich:
K. Hradil - vielen Dank für die wirklich große Hilfe bei den Neutronenmessungen am PUMA Spektrometer. P. Link danke ich für das große Engagement bei den Messungen am PANDA Spektrometer. M. Meven danke ich für die Unterstützung bei den Messungen am HEIDI Diffraktometer. A. Senyshyn und M. Hölzel sei für ihre Unterstützung bei Pulvermessungen am SPODI Diffraktometer gedankt. B. Pedersen danke ich für seine Hilfe bei Messungen am RESI Diffraktometer. T. Unruh möchte ich für die Hilfe bei der Messung am Time-Of-Flight Spektrometer TOFTOF danken.

Am DESY danke ich:
W. Morgenroth - Danke für die Deinen herzlichen Empfang und Deine tatkräftige Unterstützung bei den Elektronendichte- und Strukturmessungen an der beamline D3. M. v. Zimmermann - Vielen Dank für Deine Hilfe und die zusätzliche Messzeit an der beamline BW5. D. Trots - Danke für Deine Unterstützung und die erfolgreiche Zusammenarbeit an der beamline B2.

Am BESSY danke ich:
R. Feyerherm und E. Dudzik für ihre Unterstützung bei RXS Messungen an der beamline MagS

Am LLB in Saclay danke ich:
A. Cousson für seine Unterstützung bei Messungen am 5C.2 Diffraktometer sowie seine freundliche Art. F. Bourée danke ich für Messungen am 3T.1 Diffraktometer. G. André für die Unterstützung bei Messungen am G4.1 Diffraktometer. Y. Sidis danke ich für die Hilfe bei Messungen am 4F Spektrometer.

Am ILL danke ich:
M. T. Fernandez-Diaz danke ich herzlich für ihre Unterstützung bei elastischen Neutronenmessungen am D20, D2B und D1A Diffraktometer sowie darüberhinausgehender

Hilfe und freundlicher Unterstützung. A. Hiess danke ich für seine Hilfe und Zusammenarbeit bei so mancher inelastischer Messung am IN8 Spektrometer. T. Hansen danke ich für seine Unterstützung und interessante Gespräche am D20 Diffraktometer. J. R. Stewart danke ich für seine Unterstützung am Time-Of-Flight Spektrometer IN4. P. Freeman und P. Steffens sei für die Hilfe am IN20 Spektrometer gedankt. B. Ouladdiaf danke ich für die Hilfe am OrientExpress.

Am ESRF danke ich:
M. Hanfland für seine freundliche Unterstützung bei den Druckmessungen an der beamline ID09A.

An ISIS danke ich:
M. Tucker und B. Marshall für ihre Unterstützung bei diversen Messungen am PEARL Diffraktometer.

Am SINQ (PSI) danke ich:
T. Strässle für seine große Hilfsbereitschaft bei Messungen am FOCUS Flugzeitspektrometer. A. Cervellino danke ich für seine Unterstützung bei Messungen am DMC Diffraktometer.

Abstract

Ordering phenomena like charge, orbital and magnetic ordering play an important role for the understanding of the intriguing properties of transition metal oxides. In this work, the focus was on the study of such ordering phenomena in first row transition metal oxides with either one or two electrons or one or two holes in the 3d-shell, i. e. titanates, vanadates, chromates, titanium and vanadium oxychlorides on the one hand and nickelates and cuprates on the other hand. Experimentally, the pillars of this work are elastic and inelastic neutron scattering, X-ray diffraction, synchrotron measurements and crystal growth.

In the perovskite titanate system $R\mathrm{TiO_3}$ with trivalent R^{3+}-ions, anomalies in the lattice parameter and thermal expansion at the onset of magnetic ordering have been studied as a function of R-ionic radius across the boundary of ferromagnetic, antiferroorbitally ordered and antiferromagnetic, ferroorbitally ordered compounds in the phase diagram. These anomalies change sign and get strongest at the crossover of the orbital and magnetic ordering schemes which resembles on the metamagnetic transition in $\mathrm{Ca_{2-x}Sr_xRuO_4}$ or on a quantum phase transition in general. Further structural studies reveal that the distortions which are indicative for ferroorbital and antiferroorbital ordering and which distinctly change with the R-ion size and the orbital ordering schemes change much less with temperature. This also indicates that the recent scenario of an orbital liquid state in the paramagnetic phase of $R\mathrm{TiO_3}$ is questionable which could also be supported by resonant X-ray diffraction measurements of $\mathrm{DyTiO_3}$ which exhibit only few changes of orbital ordering across the magnetic transition.

In the hole-doped $R_{1-x}\mathrm{Ca}_x\mathrm{TiO_3}$-system evidence for charge ordering was found in various diffraction studies including single crystal neutron diffraction and synchrotron radiation single crystal X-ray diffraction measurements as well as in resonant X-ray diffraction measurements at the synchrotron.

In the hollandite system $\mathrm{K_2V_8O_{16}}$ a novel dimerized phase could be observed which resembles on the monoclinic M2-phase of $\mathrm{VO_2}$.

In γ-$\mathrm{LiV_2O_5}$ the electron density could be measured by means of synchrotron radiation single crystal X-ray diffraction and the occupation of a d_{xy} orbital could be observed.

In $\mathrm{ZnV_2O_4}$ an electron density measurement indicates either the occupation of a trigonal a_{2g} orbital or a 'dimerized' phase which might stimulate completely new theoretical calculations for the ground state of this compound.

Usually, in fully three-dimensional transition metal oxides antiferromagnetism can be expected to be found in insulating materials only. In $\mathrm{CaCrO_3}$, a material with an unusual Cr^{4+}-oxidation state, antiferromagnetism and metallic properties can be observed together. Also in $\mathrm{SrCrO_3}$ an antiferromagnetic structure could be affirmed. This compound should be even more metallic than $\mathrm{CaCrO_3}$.

In powder neutron diffraction measurements of TiOCl an unusual strong flattening of the TiO-planes could be observed at high pressures up to 13 GPa which should induce changes of the electronic properties of this system.

In VOCl a yet undisclosed phase transition has been observed at low temperatures which lifts the frustration across two previously equivalent diagonal magnetic exchange

'paths' (interactions) and, hence, gives rise to the exact determination of the magnetic structure.

Inelastic neutron scattering experiments on $La_{1.8}Sr_{0.2}NiO_4$ indicate electron phonon coupling in this prototypical diagonal charge-stripe system. These observations might be also relevant for the isostructural cuprate system.

For a compound in the spin-glass phase of LSCO, $La_{1.95}Sr_{0.05}CuO_4$, the phonon dispersion of the high-frequency Σ_1 and Δ_1 phonon modes has been studied. For this compound in the spin-glass phase of LSCO incommensurate magnetic peaks or satellites can be observed at diagonal positions around the the planar antiferromagnetic wave vector. Therefore, a diagonal charge stripe phase has been proposed for this compound. Here, no electron phonon coupling could be observed for the Σ_1 mode which should couple to any diagonal charge stripe ordering as was observed for the diagonal incommensurate charge stripes in $La_{1.8}Sr_{0.2}NiO_4$ in this work. Also the direct search for structural superstructure reflections which would be indicative for a diagonal charge stripe order did not reveal any evidence for such a stripe instability. Instead, synchrotron experiments with 100 keV hard X-rays and complementary neutron experiments reveal novel superstructure reflections together with a number of higher harmonic which could be observed at positions in reciprocal space which are rotated by 45° with respect to the positions where diagonal charge stripes would have been expected.

Kurzzusammenfassung

Ordnungsphänomene wie Ladungs-, orbitale und magnetische Ordnung spielen eine wichtige Rolle für das Verständnis der teils faszinierenden Eigenschaften von Übergangsmetalloxiden. Der Fokus dieser Arbeit lag auf der Untersuchung solcher Ordnungsphänomene in der ersten Reihe der Übergangsmetalloxide mit ein bis zwei Elektronen oder ein bis zwei Löchern in der 3d-Schale, daß heißt Titanaten, Vanadaten, Chromaten, Titan- und Vanadiumoxychloriden auf der einen Seite und Nickelaten und Kupraten auf der anderen Seite. Die experimentellen Methoden dieser Arbeit stützen sich im Wesentlichen auf folgende Säulen: Elastische und inelastische Neutronenstreuung, Röntgendiffraktion, Synchrotron-Experimente und Kristallzucht.

In den Titanaten $R\mathrm{TiO_3}$ mit Perowskit-Struktur und dreiwertigen R^{3+}-ionen wurden Anomalien in den Gitterkonstanten und der thermischen Ausdehnung bei der magnetischen Ordnungstemperatur in Abhängigkeit vom R-Ionenradius quer über die Grenze von ferromagnetischen, antiferroorbital geordneten und antiferromagnetischen, ferroorbital geordneten Verbindungen im Phasendiagram untersucht. Diese Anomalien werden stärker und wechseln ihr Vorzeichen an der Grenze zu dem Übergang zwischen diesen orbitalen und magnetischen Ordnungsmustern was an den metamagnetischen Übergang in $\mathrm{Ca_{2-x}Sr_xRuO_4}$ oder einen Quantenphasenübergang im allgemeinen erinnert. Weitere Strukturuntersuchungen zeigen, daß die für ferroorbitale und antiferroorbitale Ordnung typischen Verzerrungen sehr deutlich mit dem R-Ionenradius und den einhergehenden orbitalen Ordnungsmustern variieren, hingegen sehr viel weniger mit der Temperatur. Das lässt an dem kürzlich veröffentlichten Szenario einer orbitalen Flüssigkeit in der paramagnetischen Phase von $R\mathrm{TiO_3}$ zweifeln was darüberhinaus auch mittels resonanter Streuung mit Synchrotronstrahlung an $\mathrm{DyTiO_3}$ gezeigt werden konnte, welche kaum Veränderungen der orbitalen Ordnung über den magnetischen Phasenübergang hinweg zeigten.

Im lochdotierten $R_{1-x}\mathrm{Ca}_x\mathrm{TiO_3}$ System wurden mittels verschiedenster Diffraktionsexperimente, die Einkristall Neutronenstreuung sowie Röntgendiffraktion mit Synchrotronstrahlung aber auch resonante Röntgenstreuung am Synchrotron einschliessen, klare Hinweise auf Ladungsordnung gefunden.

Im Hollandit System $\mathrm{K_2V_8O_{16}}$ wurde eine neue dimerisierte Phase gefunden welche entfernt an die monokline M2-Phase in $\mathrm{VO_2}$ erinnert.

In γ-$\mathrm{LiV_2O_5}$ konnten Elektronendichtemessungen am Synchrotron durchgeführt werden welche die Besetzung eines d_{xy} Orbitals anzeigen.

Ähnliche Elektronendichtemessungen an $\mathrm{ZnV_2O_4}$ zeigen die Besetzung eines a_{2g} Orbitals oder eine 'dimerisierte' Phase an was als Grundlage für neue Berechnungen des Grundzustands dieser Verbindung dienen kann.

Üblicherweise wird in dreidimensionalen Übergangsmetalloxiden Antiferromagnetismus nur in Isolatoren erwartet. Aber in $\mathrm{CaCrO_3}$, einer Verbindung mit einer ungewöhnlichen $\mathrm{Cr^{4+}}$-Oxidationsstufe, konnte beobachtet werden, dass antiferromagnetische und metallische Eigenschaften gleichzeitig auftreten. Auch in $\mathrm{SrCrO_3}$ konnte eine antiferromagnetische Struktur bestätigt werden. Diese Verbindung sollte sogar noch deutlichere metallische Eigenschaften als $\mathrm{CaCrO_3}$ aufweisen.

In Pulverneutronenmessungen an TiOCl konnte bei hohen Drücken (bis 13 GPa) ein ungewöhnlich starkes Abflachen der Titan-Sauerstoff-Ebenen beobachtet werden, was Konsequenzen für die elektronischen Eigenschaften dieses Materials haben muß.

In VOCl wurde ein bislang nicht bekannter Phasenübergang bei tiefen Temperaturen entdeckt welcher die Frustration entlang zweier zuvor äquivalenter, diagonaler magnetischer Wechselwirkungen aufhebt und die Möglichkeit zur genauen Magnetstrukturbestimmung eröffnete.

Mittels inelastischer Neutronenstreuung an $La_{1.8}Sr_{0.2}NiO_4$ konnte Elektron-Phonon Kopplung in diesem prototypischen diagonalen Streifen-System beobachtet werden. Diese Beobachtungen dürften auch für das isostrukturelle Kuprat-System relevant sein.

Für $La_{1.95}Sr_{0.05}CuO_4$, eine Kupratverbindung in der Spinglas Phase von LSCO, wurde die Phononendispersion der ergetisch höchstliegenden Σ_1 and Δ_1 Phononenmoden untersucht. Für diese Verbindung in der Spinglas Phase von LSCO treten inkommensurable magnetische Peaks an diagonalen Positionen rings um den in der HK-Ebene liegenden kommensurablen antiferromagnetischen Wellenvektor auf. Daher wurde eine diagonale Ladungsstreifen-Phase für diese Verbindung vorgeschlagen. Hier (in dieser Arbeit) konnte keine Elektron-Phonon Kopplung der Σ_1 Phononenmode beobachtet werden, welche an diagonale Streifen ankoppeln sollte, so wie es in dieser Arbeit für die diagonalen inkommensurablen Ladungsstreifen in $La_{1.8}Sr_{0.2}NiO_4$ beobachtet wurde. Auch die direkte Suche nach Überstrukturreflexen dieser Ladungsstreifen verlief erfolglos. Stattdessen enthüllten Synchrotronexperimente mit 100 keV harter Röntgenstrahlung und komplementäre Neutronenbeugungsexperimente bislang unbekannte Überstrukturreflexe und die dazugehörigen höheren Harmonischen welche an Stellen des reziproken Raums beobachtet wurden, die um 45° gedreht sind in Bezug auf die Positionen an denen diagonale Streifen erwartet worden wären.

Offizielle Erklärung

Ich versichere, daß ich die von mir vorgelegte Dissertation selbständig angefertigt, die benutzten Quellen und Hilfsmittel vollständig angegeben und die Stellen der Arbeit - einschließlich Tabellen, Karten und Abbildungen -, die anderen Werken im Wortlautoder dem Sinn nach entnommen sind, in jedem Einzelfall als Entlehnung kenntlichgemacht habe; daß diese Dissertation noch keiner anderen Fakultät oder Universität zur Prüfung vorgelegen hat; daß sie - abgesehen von unten angegebenen Teilpublikationen -noch nicht veröffentlicht worden ist sowie, daß ich eine solche Veröffentlichung vor Abschluß des Promotionsverfahrens nicht vornehmen werde.

Die Bestimmungen dieser Promotionsordnung sind mir bekannt. Die von mir vorgelegte Dissertation ist von Prof. Dr. M. Braden betreut worden.

Köln, den

_____

(Alexander Komarek)

Liste der Teilveröffentlichungen

1. ***Strong Magneto-elastic coupling in VOCl: Neutron and synchrotron powder x-ray diffraction study***
   A. C. Komarek, T. Taetz, M. T. Fernandez-Diaz, D. M. Trots, A. Möller, M. Braden
   preprint arXiv:0902.0544v1 (2009); accepted by PRB.

2. ***CaCrO3: An Anomalous Antiferromagnetic Metallic Oxide***
   A. C. Komarek, S. V. Streltsov, M. Isobe, T. Möller, M. Hoelzel, A. Senyshyn, D. Trots, M. T. Fernández-Díaz, T. Hansen, H. Gotou, T. Yagi, Y. Ueda, V. I. Anisimov, M. Grüninger, D. I. Khomskii, and M. Braden
   Phys. Rev. Lett. **101**, 167204 (2008)

3. ***Magnetoelastic coupling in RTiO3 (R=La,Nd,Sm,Gd,Y) investigated with diffraction techniques and thermal expansion measurements***
   A. C. Komarek, H. Roth, M. Cwik, W.-D. Stein, J. Baier, M. Kriener, F. Bourée, T. Lorenz, and M. Braden
   Phys. Rev. B **75**, 224402 (2007)